LLS

DOE ER-0313 9

Fusion Reactor Materials

Semiannual Progress Report for Period Ending September 30, 1990

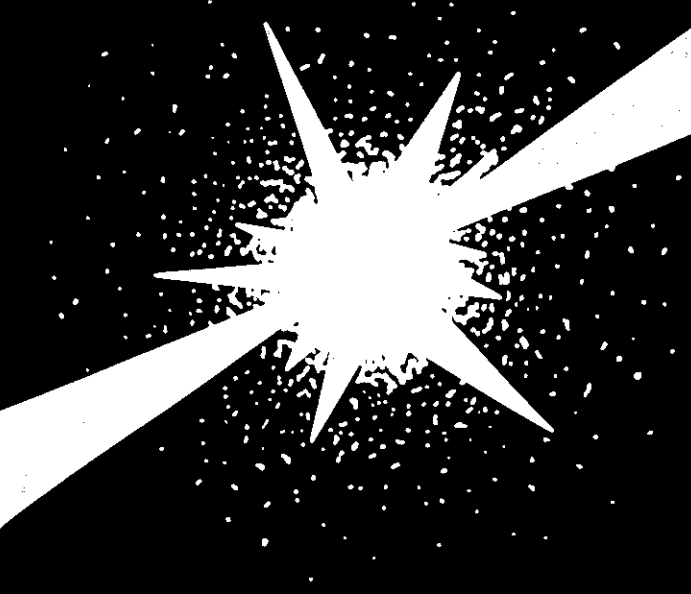

U. S. Department of Energy
Office of Fusion Energy

This report has been reproduced directly from the best available copy.

Available to DOE and DOE contractors from the Office of Scientific and Technical Information, P.O. Box 62, Oak Ridge, TN 37831; prices available from (615) 576-8401, FTS 626-8401.

Available to the public from the National Technical Information Service, U.S. Department of Commerce, 5285 Port Royal Rd., Springfield, VA 22161.

This report was prepared as an account of work sponsored by an agency of the United States Government. Neither the United States Government nor any agency thereof, nor any of their employees, makes any warranty, express or implied, or assumes any legal liability or responsibility for the accuracy, completeness, or usefulness of any information, apparatus, product, or process disclosed, or represents that its use would not infringe privately owned rights. Reference herein to any specific commercial product, process, or service by trade name, trademark, manufacturer, or otherwise, does not necessarily constitute or imply its endorsement, recommendation, or favoring by the United States Government or any agency thereof. The views and opinions of authors expressed herein do not necessarily state or reflect those of the United States Government or any agency thereof.

DOE/ER-0313/9
Distribution
Categories
UC-423, -424

FUSION REACTOR MATERIALS SEMIANNUAL PROGRESS REPORT FOR THE PERIOD ENDING SEPTEMBER 30, 1990

Date Published: April 1991

Prepared for
DOE Office of Fusion Energy
(AT 15 02 03 A)

Prepared by
OAK RIDGE NATIONAL LABORATORY
Oak Ridge, Tennessee 37831
managed by
MARTIN MARIETTA ENERGY SYSTEMS, INC.
for the
U.S. DEPARTMENT OF ENERGY
under Contract DE-AC05-840R21400

FOREWORD

This is the ninth in a series of semiannual technical progress reports on fusion reactor materials. This report combines research and development activities which were previously reported separately in the following technical progress reports:

- Alloy Development for Irradiation Performance
- Damage Analysis and Fundamental Studies
- Special Purpose Materials

These activities are concerned principally with the effects of the neutronic and chemical environment on the properties and performance of reactor materials; together they form one element of the overall materials program being conducted in support of the Magnetic Fusion Energy Program of the US. Department of Energy. The other major element of the program is concerned with the interactions between reactor materials and the plasma and is reported separately.

The Fusion Reactor Materials Program is a national effort involving several national laboratories, universities, and industries. The purpose of this series of reports is to provide a working technical record for the use of the program participants, and to provide a means of communicating the efforts of mterials scientists to the rest of the fusion community, both nationally and worldwide.

This report has been compiled and edited under the guidance of A. F. Rowcliffe and Frances Scarboro. Oak Ridge National Laboratory. Their efforts, and the efforts of the many persons who made technical contributions, are gratefully acknowledged.
F. W. Wiffen, Reactor Technologies Branch. has responsibility within DOE for the programs reported on in this document.

R. Price, Chief
Reactor Technologies Branch
Office of Fusion Energy

TABLE OF CONTENTS

FOREWORD iii

1. IRRADIATION FACILITIES, TEST MATRICES, AND EXPERIMENTAL METHODS 1

1.1 AN EVALUATION OF M E LOS ALAMOS SPALLATION RADIATION EFFECTS FACILITY (LASREF) FOR FUSION APPLICATIONS (Pacific Northwest Laboratory) 3

The appropriate role, both short-term and long-term. of the Los Alamos Spallation Radiation Effects Facility (LASREF) in the U.S. Fusion Materials Program was reviewed by a peer group in June 1990. This report presents the LASREF review committee's findings and recommendations.

1.2 OEVELOPMENT OF DISC COMPACT TENSION SPECIMENS AND TEST TECHNIQUES FOR HFIR IRRADIATIONS (University of California-SB and Oak Ridge National Laboratory) 7

Near tern irradiations or candidate alloys being planned for the High Flux Isotope Reactor (HFIR) in support of ITER and isotope tailoring experiments necessitate the use of relatlvely small fracture toughness specimens, e.g., darn to 12.5 mm in diameter. The specimens will also contain substantial amounts of helium. This work involved the application of electropotential drop techniques to determine J-resistance Curves for this purpose in HT-9 specimens with diameters of 40, 25. and 12.5 mm at temperatures ranging from 20°C to 100°C; in addition, the effects of side grooving were examined. Good agreement between J-resistance curves determined by the electropotential drop and by multiple specimen techniques was obtalned for all specimen geometries, sizes. and temperatures.

1.3 DESIGN, FABRICATION, AND OPERATION OF HFIR-MFE RB* SPECTRALLY TAILORED IRRADIATION CAPSULES (oak Ridge National Laboratory and Midwest Technical. Inc.) 13

Design and fabrication of four HFIR-MFE RB* capsules (60, 200, 330, and 400°C) to accommodate specimens previously irradiated in spectrally tailored experiments in the ORR are proceeding satisfactorily. These capsula designs incorporate provisions for removal, examination. and re-encapsulation of specimens at an intermediate exposure level of 16 displacments per atom (dpa) en route to a target exposure level of 24 dpa. With the exception of the 60°C capsule, where the test spedmens are in direct contact with the reactor cooling Water. the specimen temperatures (monitored by 21 thermocouples) are controlled by varying the thermal Conductance or a small gap region between the specimen holder and the containment tube.

1.4 APPLICATION OF BALL PUNCH TESTS TO EVALUATING FRACTURE MODE TRANSITION IN FERRITIC STEELS (University of California-SB) 15

An investigation was mad8 or the applicability of a ball punch test to evaluating the fracture mode transition in ferritic steel specimens equivalent to transmission electron microscopy (TEM) discs. Both static and dynamic test conditions were Mamined in specimens with and without several intentional defects. High displacement rates (>4 mm/s) resulted in adiabatic heating of the specimen during testing. Smooth specimens were found to provide more reproducible and useful data than specimens containing holes and grooves. A good correlation was found between the absorbed energy beyond maximum load and fracture mode transition, with the latter characterized by either fracture appearance or Charpy impact energy.

1.5 DEVELOPMENT OF PRESSURIZED TUBE SPECIMEN FOR CREEP TESTING OF BERYLLIUM (Lawrence Livermore National Laboratory, Westinghouse Savannah River Company. and Pacific Northwest Laboratory) 20

The ability to fabricate a pressurized tube specimen from beryllium was successfully demonstrated. The specimen failed at a midwall hoop stress of about 32 ksi in a burst test at 500°C.

2. DOSIMETRY, DAMAGE PARAMETERS, AND ACTIVATION CALCULATIONS 29

2.1 NEUTRON DOSIMETRY FOR THE MOTA-IF EXPERIMENT IN FFTF (Pacific Northwest Laboratory) 31

Neutron fluence and spectral measurements are reported for the MOTA-1F experiment in the Fast Flux Test Facility (FFTF). The irradiation was conducted from November 18, 1987, to January 8, 1989, far a total exposure of 335.4 EFPD. The maximum fluence was 12.7 × 10^{22} nlcm', 9.56 × 10^{22} above 0.1 MeV producing 39.1 dpa in iron. Neutron energy spectra were adjusted at three positions and gradients were measured at nine other locations.

3. MATERIALS ENGINEERING AND DESIGN REQUIREMENTS 37

No contributions.

4. FUNOAMENTAL MECHANICAL BEHAVIOR 39

No contributions.

5. RADIATION EFFECTS: MECHANISTIC STUDIES, THEORY, AND MODELING 41

5.1 MOLECULAR DYNAMICS OF COLLISION CASCADES WITH COMPOSITE PAIR/MANY-BODY POTENTIALS (University of California. Los Angeles) 43

An empirical, composite interatomic potential is developed to describe interaction of energetic particles by pair potentials at high energies and many-body potentials at low energies. Molecular-dynamics studies of low-energy collision cascades are performed. The displacement threshold surface in copper is investigated and compared to experimental data. Our computer simulations show good agreement with the experimental results of King and Benedek at 10 K.

5.2 INFLUENCE OF COLD WORK AND PHOSPHORUS CONTENT ON NEUTRON-INDUCED SMELLING OF Fs-Cr-Ni ALLOYS (Pacific Northwest Laboratory) 50

Phosphorus additions can either Increase or decrease void swelling of Fe-Cr-Ni alloys, depending on irradiation temperature, phosphorus level and cold work level. The role of cold work is not always to suppress swelling in Fe-Cr-Ni-P alloys. however, particularly at relatively higher irradiation temperatures, where cold working often increases swelling substantially.

5.3 HELIUM MEASUREMENTS FOR THE MFE-4 SPECTRAL TAILORING EXPERIMENT (Pacific Northwest Laboratory and Rockwell International) 58

Measurements of helium concentration have been made on Fe-15.1Cr-34.5Ni specimens irradiated at 330. 400, 500, and 600°C after irradiation in ORR to displacement levels ranging from 12.6 to 13.8 dpa. The measurements compare well to Previously calculated Values. being 4 to 8% lower. Minor differences in helium content were also observed between specimens from capsules that were assumed to have possessed identical spectral environments.

5.4 THE INFLUENCE OF HELIUM ON MECHANICAL PROPERTIES OF MODEL AUSTENITIC ALLOYS, DETERMINED USING ^{59}Ni ISOTOPIC TAILORING AND FAST REACTOR IRRADIATION (Pacific Northwest Laboratory and Rockwell International) 61

Tensile testing and microscopy Continue on specimens removed from the first. second, and third discharges of the ^{59}Ni isotopic doping experiment. The results to date indlcate that helium/dpa ratios typical of fusion reactors (4 to 19 appm/dpa) do not lead to significant changes in the yield strength of model Fe-Cr-Ni alloys. Measurements of helium generated in undoped specimens from the second and third discharges show that the helium/dpa ratio increaser during irradiation in FFTF due to the production of ^{59}Ni. In specimens doped with ^{59}Ni prior to irradiation, the helium/dpa ratio can increase, decrease or remain the same during the second irradiation interval. This behavior occurs because the Cross sections for the production and burnout of ^{59}Ni are very sensitive to core location and the nature of neighboring conponents.

5.5 CORRELATION OF MECHANICAL PROPERTY CHANGES IN NEUTRON IRRADIATED PRESSURE VESSEL STEELS ON THE BASIS OF SPECTRAL EFFECTS (Pacific Northwest Laboratory) 69

Comparisons are made of tensile data on specimens of A212B and A302B pressure vessel steels irradiated at low temperatures (40-90°C) and to low doses (<0.1 dpa) with 14 MeV D-T fusion neutrons in the Rotating Target Neutron source (RTNS-II), with fission reactor neutrons in the mega West Reactor (OWR) and the Oak Ridge Research Reactor (ORR), and with the highly thermal spectrum at the pressure vessel surveillance positions of the High Flux Isotope Reactor (HFIR). For each neutron spectrum, damage cross sections are determined for several defect production functions derived from atomistic computer simulations of collision cascades. Displacements per atom (dpa) and the numbers of freely migrating defects are tested as damage correlation parameters for the tensile data. The data from RTNS-II, OWR and ORR correlate fairly well when compared on the basis of dpa, but the data from HFIR show that only about one-sixth as many dpa are needed to produce the same radiation-induced yield stress changes as in the other neutron spectra. In the HFIR surveillance position a Significant fraction of the displacments is produced by recoils resulting from thermal neutron Captures. Having energies of about 400 eV, these recoils are much more efficient per unit energy at producing freely migrating defects than the high energy recoils responsible for most of the displacements in the other neutron spectra considered, A significantly better correlation of data from HFIR with those from the other spectra is achieved when the property changes are compared on the basis of the production of freely migrating self-interstitial defects. This parameter may better represent the defects participating in the radiation strengthening process in this temperature and fluence regime.

5.6 LOW EXPOSURE SPECTRAL EFFECTS EXPERIMENT: IRRADIATIONS AT 473 K IN OMEGA WEST REACTOR (Pacific Northwest Laboratory) 17

Tensile tests have been performed on specimens from the last ret of mega West Reactor (OWR) irradiations performed as part of the Low Exposure Spectral Effects Experiment (LESEX). Tensile data are reported.

5.7 NEW INSIGHTS ON THE MEWNISMS CONTROLLING THE NICKEL DEPENDENCE OF SWELLING IN IRRADIATED Fe-Cr-Ni ALLOYS (Washington State University and Pacific Northwest Laboratory) 81

In a previous report the interstitial and vacancy biases for an edge dislocation in a binary alloy were examined, assuming the existence of an equilibrium Cottrell atmosphere around the line defect. The Larche and Cahn treatment of stress relaxation due to a solute atmosphere was employed with the Wolfer and Ashkin formulation for the bias of an edge dislocation to compute the bias as a function of nickel concentration in the Fe-Ni system. Using the minimum critical void radius Concept, the concentration-dependent bias was shown to offer a plausible explanation for the minimum in welling observed at intermediate nickel levels and the gradual increase in swelling at higher nickel levels. In this report, a more realistic description of the conposition dependence of vacancy diffusion has also been included, an addition Which improves the model substantially.

5.8 THE INFLUENCE OF NICKEL CONTENT ON MICROSTRUCTURES OF Fe-Cr-Ni AUSTENITIC ALLOYS IRRMIATED WITH NICKEL IONS (Kyushu University and Pacific Northwest Laboratory) 87

Ion-irradiated Fe-15Cr-XNi (X = 20, 35, 45. 60, 75) ternary alloys and a 15Cr-85Ni binary alloy were examined after bombardment at 675°C and compared to earlier observations made on these same alloys after irradiation in EBR-II at 510 or 538°C. The response of the ion-irradiated *microstructures* to nickel content appears to be very consistent with that of neutron irradiation even though there are four orders of magnitude difference in displacement rate and over 200°C difference in temperature. It appears that the transition to higher rates of swelling during both types of irradiation is related to the operation of some mechanism that is *not* directly associated With void nucleation.

6. DEVELOPMENT OF STRUCTURAL ALLOYS 95

6.1 Ferritic Stainless Steels 95

6.1.1 IMPACT BEHAVIOR OF 9Cr-1MoVNb AND 12Cr-1MoVW STEELS IRRADIATED IN HFIR (Oak Ridge National Laboratory) 97

Charpy impact specimens of 9Cr-1MoVNb and 12Cr-1MoVW steels and these steels with 2% Ni (9Cr-1MoVNb-2Ni and 12Cr-1MoVW-2Ni) were irradiated in the High Flux Isotope Reactor (HFIR) at 300°C up to 34 dpa and at 400°C to 42 dpa. Nickel was added to the standard conposition to study the effect of transmutation helium formed by reaction of ^{58}Ni with thermal neutrons in the mixed-spectrum of HFIR. Helium levels approaching 400 appm were achieved in the steels containing 2% Ni. Irradiation caused large increases in the DBTT of a11 four steels. A saturation in the shift in DBTT with increasing fluence that was observed in fast reactor irradiations does not apply to specimens irradiated in HFIR. Shifts in DBTT of over 300°C were observed at 400°C for 9Cr-1MoVNb-2Ni and 12Cr-1MoVW-2Ni; shifts of over 200°C were observed for the standard steels. For all steels, the increase was greater at 400°C than at 300°C. The shifts are the largest ever recorded for this type of steel and are attributed to the higher helium concentrations.

6.1.2 THE DEVELOPMENT OF FERRITIC STEELS FOR FAST INDUCED-RADIOACTIVITY DECAY (Oak Ridge National Laboratory) 106

Irradiation of ferritic steels with neutrons at temperatures up to ~450°C causes a loss of toughness. This can be measured in a Charpy impact test. where an increase in the ductile-brittle transition temperature (DBTT) and a decrease in the upper-shelf energy is observed after irradiation. Reduced-activation Cr-W steels with chromium concentrations varying from 2.25 to 12% were irradiated at 365°C to ~7 dpa in the Fast Flux Test Facility. Steels With 2.25% Cr and 9 combination of 2% W and 0.25% V were less severely affected by irradiation than steels with vanadium and no tungsten. tungsten and no vanadium, or with 1% W and 0.25% V. Two steels with 9% Cr showed the most resistance to a loss of toughness. A 9% Cr steel with 2% W and 0.25% V showed an increase in DBTT of 68°C. This same composition with an addition of 0.07% Ta developed an increase in DBTT of only 4°C. These values compare to increaser of over 100°C for the rest of the Steels.

6.1.3 COMPARISON OF THE EFFECTS OF LONG-TERM THERMAL AGING AND HFIR IRRADIATION ON THE MICROSTRUCTURAL EVOLUTION OF 9Cr-1MoVNb STEEL (Oak Ridge National Laboratory) 113

Both thermal aging at 482-704°C for uP to 25.000 h and HFIR irradiation at 300-600°C for up to 39 dpa produce substantial changes in the as-tempered microstructure of 9Cr-1MoVNb martensiticiferritic steel. However, the changes in the dislocation/subgrain boundary and the precipitate Structures caused by thermal aging or neutron irradiation are quite different in nature. During thermal aging, the as-tempered lathlsubgrain boundary and carbide precipitate structures remain stable below 650°C, but coarsen and recover somewhat at 650-704°C. The formation of abundant intergranular Laves phase, intra-lath dislocation networks, and fine dispersions of VC needles are thermal aging effects that are superimposed upon the as-tempered microstructure at 482-593°C. HFIR irradiation produces dense dispersions of very small "black-dot" dislocation loops at 300°C and produces helium bubbles and voids at 400°C. At 300-500°C, there is considerable recovery of the as-tempered lath/subgrain boundary structure and the microstructural/microcompositional instability of the as-tempered carbide precipitates during irradiation. By contrast, the as-tempered microstructure remains essentially unchanged during irradiation at 600°C. Comparison of thermally aged with irradiated material suggests that the instabilities of the as-tempered lathisubgrain boundary and precipitate structures at lower irradiation temperatures are radiation-induced effects, whereas the absence of both Laves phase and fine VC needles during irradiation is a radiation-retarded thermal effect.

6.1.4 MICROSTRUCTURE AND PROPERTIES OF WELDED W, V, AND Ta MODIFIED FERRITIC STEELS WITH FAST INDUCED-RADIOACTIVITY DECAY (Auburn University) 133

Sheet specimens of W, V. Ta modified low activation ferritic steels were welded using the gas tungsten arc welding (GTAW) process. Autogenous bead-on-plate welds were produced on samples of 2¼CrV, 2¼Cr-1WV, 2¼Cr-2W, 2¼Cr-2WV, 5Cr-2WV, 9Cr-2WV, 9Cr-2WVTa, and 12Cr-2WV. Sound autogenous welds were obtained in all low activation 2¼% Cr bainitic steels and the 5% Cr martensitic steel. Bend tests of the welds yielded insufficient toughness at the fusion zone in the low activation 9 and 12% Cr martensitic steels. A port-weld heat treatment is recommended for the 9 and 12% Cr low activation steels to restore toughness.

6.2 Austenitic Stainless Steels 143

6.2.1 IRRADIATION EFFECTS OF GRAIN BOUNDARY CHEMISTRY OF MANGANESE STABILIZED MARTENSITIC STEELS (Muroran Institute of Technology and Pacific Northwest Laboratory) 145

The effect of neutron irradiation (10 dpa at 638 K, FFTF/MOTA) on solute Segregation to the grain boundaries in reduced-activation 9Cr-1W-2Mn and 12Cr-1W-6Mn martensitic steels was investigated using Auger electron spectroscopy (AES). The AES spectrum obtained from the grain boundaries in both martensitic steels was influenced by neutron irradiation. Neutron irradiation caused marked increases in the amount of intergranular segregation of Si in 9Cr and Mn in 12Cr steel, respectively. while no significant increase in S and/or P Segregations were found in either steel. Large shifts in DBTT to high tenperatwe caused by neutron irradlation observed in these two martensitic steels are interpreted in terms of site canpetition between C and Si resulting from irradiation-inducedlenhanced Segregation of Si in 9Cr steel and weakening of grain boundary strength by irradiation-inducedlenhanced segregation of Mn in 12Cr steels, respectively.

6.2.2 SWELLING BEHAVIOR OF AUSTENITIC STAINLESS STEELS IRRADIATED AT 400°C IN ORR MFE-7J CAPSULE BY SPECTRALLY TAILORED NEUTRONS (Japan Atomic Energy Research Establishment and Oak Ridge National Laboratory) 152

Several Japanese austenitic stainless steels. including specimens taken from the electron beam (EB) welds. have been irradiated in the Oak Ridge Research Reactor (ORR) in Special spectrally tailored experiments. The first batch of specimens have been retrieved at the damage level of 7.4 dpa and helium level or 102 appm in a type 316 stainless steel, and 130 appm He in JPCA with 16 wt % Ni. This irradiation produced significant alloy-to-alloy differences in Swelling at 400°C. One low-carbon steel and an experimental ternary alloy have shown higher values of swelling. Irradiation in HFIR of the sane set of alloys caused very high levels of void swelling only at 500°C and above. Metallurgical efforts to suppress such swelling (1.e., cold working and/or increased carbon level) were effective at this tenperature range. The present results suggest that appropriate care also needs to be taken for the fusion application of this kind of alloy at lower temperatures like 400°C. Welds in this experiment Showed no measurable degradation in swelling resistance compared to their base metals.

6.2.3 DETERMINATION OF CREEP-SWELLING COUPLING COEFFICIENTS FOR IRRADIATED STAINLESS STEELS (University of California-Berkeley, Pacific Northwest Laboratory, and Westinghouse Hanford Conpany) 160

Irradiation creep data at ~400°C Were analyzed for two 20% Cold-worked titanium-modified type 316 stainless steels. One of these Steels was the fusion Prime candidate alloy designated PCA. The analysis was based an the assumption that the B_0 + DS creep model applies to these steels at this tenperature. This assumption was found to be valid. A creep-Swelling coupling coefficient of D = 0.6 × 10-' MPa^{-1} was found for both steels, Which is in excellent agreement with the results of earlier studies conducted using annealed AISI 304L and also 10% and 20% cold-worked AISI 316 stainless steels. There appears to be some enhancement of swelling by stress. leading to an apparent but misleading nonlinearity of creep with respect to stress. The dependence of the creep-swelling coupling coefficient an irradiation tenperatwe for temperatures greater than 400°C has not yet been established.

6.3 Refractory Metal Alloys 167

6.3.1 FFTF/MOTA IRRADIATION OF REFRACTORY ALLOYS UNDER CONSIDERATION AS PLASMA FACING COMPONENTS (Pacific Northwest Laboratory) 169

A refractory alloy irradiation series involving four discharges of the Materials open Test Assembly (MOTA-1B through MOTA-1E) has been canpleted. This experiment contains pure Mo, Mo-41Re, TZM, arid Nb-1Zr. Irradiation temperatures in this experiment ranged from 404 to 730°C with neutron exposures yielding 8.7 to 110.8 dpa. Measurement of density changes and disk bend testing are planned to begin shortly.

6.3.2 SWELLING DEPENDENCE OF NEUTRON-IRRADIATED VANADIW ALLOYS ON TEMPERATURE. NEUTRON FLUENCE. AND THERMOMECHANICAL TREATMENT (Argonne Natlonal Laboratory and Tohoku University) 172

Swelling of vanadium alloys was determined after Irradlation at 420 and 600°C to neutron fluences ranging from 0.3 x 10^{27} neutrons/m^2 (17 @a) to 1.9 x 10^{27} neutrons/m^2 (114 dpa). Binary and ternary vanadium alloys With Cr. Ti, Mo, W, Ni, Fe, Zr, and Si additions were irradlated in either the fully annealed, partially annealed. or 10% cold-worked condition. Upon irradiation at 600°C, the swelling of vanadium to which Cr had been added was greatly exacerbated. Whereas the swelling of vanadlum to which Ti. Mo, W and NI (3-20%) had been added was rot signlficantly affected. Swelling of V-Cr alloys upon Irradiatlon at 600°C was substantially reduced (<0.1% per dpa) by the addition of Ti (1-15%). Upon Irradiation at 420°C, the swelling of the vanadium alloys was <0.2% per dpa. Partial annealing or 10% cold-working had no significant effect on swelling of the alloys.

6.4 Copper Alloys 177

6.4.1 MECHANICAL PROPERTY CHANGES AND MICROSTRUCTURES OF DISPERSION-STRENGTHENED COPPER ALLOYS AFTER NEUTRON IRRADIATION AT 411, 414, AND 529°C (University of Illinois and Pacific Northwest Laboratory) 179

Dispersion strengthened copper alloys have shown promise for certain hlgh heat flux applications in both near term and long term fusion devices. Thls study examines mechanical properties changes and microstructural evolution in several oxide dispersion strengthened alloys whlch were subjected to high levels of irradiation-induced displacement damage. Irradiations were carried out in FFTF to 34 and 50 dpa at 411-414°C and 32 dpa at 529°C. The alloys Include several oxide dispersion-strengthened alloys based on the Cu-Al system, as well as ones based on the Cu-Cr and Cu-Hf systems. Of this group, certain of the Cu-Al alloys. those produced by an Internal oxidation technique to contain alumina weight fractions of 0.15 to 0.25% outperformed the other alloys in all respects. These alloys, designated CuAl15, CuAl20, and CuAl25, were found to be resistant to void swelling up to 50 dpa at 414°C, and to retaln their superior mechanical and physical properties after extended irradiation. The major factor which controls the stability during irradiation was found to be the dispersoid volume fractlon and distribution. The other alloys examined were less resistant to radiation-induced properties changes for a variety of reasons. Some of these Include dispersoid redistribution by ballistic resolution. effects of retained dissolved oxygen. and nonuniformity of dispersion distribution. The effect of laser welding was also examined. Thls joining technique was found to be unacceptable since it destroys the dispersoid distribution and thereby the resistance of the alloys to radiation-induced damage.

6.4.2 BRAZING OF COPPER-ALWINA ALLOYS (Auburn University) 196

An induction braze has been developed to join copper-alumlna alloys. Thls brazing technique is proposed to replace current furnace brazlng methods that have yielded poor results because of silver ingression along the flne graln boundaries of the copper-alumlna alloys. The induction braze (because of the short braze time) severely restricts silver ingression along the grain boundarles of the alloy. Tensile tests of induction brazed lap joints fail in the base material rather than the braze Indicating good braze properties.

6.4.3 A BRIEF REVIEW OF CAVITY SWELLING AND HARDENING IN IRRADIATED COPPER AND COPPER ALLOYS (Oak Ridge National Laboratory) . 201

The literature on radiation-induced swelling and hardenlng in copper and its alloys is reviewed. Vold formation does rot occur during irradiation of copper unless suitable impurity atoms such as oxygen or helium are present. Void formation occurs for neutron Irradiatlon temperatures of 180 to 550°C, with peak swelling occurring at ~320°C for irradiation at a damage rate of 2 x lo-' dpa/s. The port-translent swelling rate has been measured to be ~0.5%/dpa at temperatures near 400°C. Dispersion-strengthened copper has been round to be very resistant to vold swelling due to the high sink denslty associated with the dispersion-stabilized dislocation Structure. Irradiation of copper at temperatures below 400°C generally causes an increase in strength due to the formation of defect clusters which inhibit dislocation motion. The radiation hardenlng can be adequately described by Seeger's dispersed barrier model, with a barrier strength for small defect clusters of $a \approx 0.2$. The radiatlon hardenlng apparently saturates for fluences greater than ~10^{24} n/m^2 (~0.1 dpa) during Irradiatlon at room tmperature due to a saturation of the defect cluster density. Grain boundarles can modify the hardenlng behavlor by blocking the transmission of dislocation slip bands. leading to a radiatlon-modified Hall-Petch relation between yield Strength and grain size. Radiation-enhanced recrystallization can lead to softening of cold-worked copper alloys at temperatures above 300°C.

6.5 Environmental Effects on Structural Alloys 217

6.5.1 ELECTROCHEMICAL AND MICROSTRUCTURAL CHARACTERIZATION OF AN AUSTENITIC STAINLESS STEEL IRRADIATED BY HEAVY IONS AT 515°C (Oak Ridge National Laboratory and Japan Atomic Energy Research Institute) 219

The electrochemical and microstructural behavior of a solution-annealed, heavy-ion-irradiated. austenitic stainless steel, designated LS1A, have been investigated at 515°C after doses of 1, 10, and 30 displacements per atom (dpa). Changes in electrochemical properties due to radiation induced segregation in thin radiation-affected layers of the material were detected by the electrochemical potentiokinetic reactivation (EPR) technique using transmission electron microscopy (TEM) disk specimens. At all doses, the Flade potential and reactivation charge were greater than those measured for thermally aged control specimens. Flade potentials increased with increasing dpa while the reactivation charge did not increase beyond 10 dpa. Grain face etching, similar to that found on EPR-tested neutron-irradiated austenitic stainless steels, was observed on all specimens after testing. Grain boundaries were etched after doses of 10 and 30 dpa. The extent of grain face etching increased with increasing dose. Duplicate heavy-ion-irradiated specimens were also examined by high resolution analytical electron microscopy (AEM). The 1-dpa specimen showed only a high density of small faulted dislocations (~10 nm), and no grain boundary precipitation was observed nor was any grain boundary segregation detected. AEM confirmed chromium depletion at grain boundaries as measured by EPR for the 10- and 30-dpa specimens. Depletion widths of approximately 10 nm and grain boundary chromium compositions of less than 10% by weight were found. Molybdenum was also depleted near the boundary, whereas nickel, silicon, and iron were enriched for the 10- and 30-dpa irradiations. Precipitation of G and eta phases and larger dislocation loops (~60 nm) were observed in the 10- and 30-dpa specimens.

6.5.2 ENVIRONMENTAL EFFECTS ON AQUEOUS STRESS CORROSION OF CANDIDATE AUSTENITIC STEELS FOR ITER STRUCTURAL APPLICATIONS (Argonne National Laboratory) 228

Susceptibility of Types 316 NG, 316, and 304 stainless steel to SCC was investigated at several temperatures between 50 and 150°C in slow-strain-rate-tests (SSRTs) in oxygenated water that simulates important parameters anticipated in first-wall/blanket systems. The water chemistry was based on a computer code that yielded the nominal concentrations of molecular radiolytic species produced in an aqueous environment under conditions likely to be found in the ITER. To be conservative, however, the SSRTs were performed in a less benign, more oxidizing reference environment. Predominantly ductile fracture was observed in crevice specimens of Type 316 stainless steel (SS) strained to failure in a reference ITER water chemistry. The failure behavior of Type 304 SS crevice specimens heat-treated to yield sensitization values of 2, 3, or 20 C/cm^2 by electrochemical potentiokinetic reactivation (EPR) demonstrated that degree of sensitization had a dramatic effect on intergranular SCC (IGSCC) susceptibility. Type 304 SS specimens sensitized to the highest value exhibited shorter failure times, lower maximum stresses, and lower reduction in area values than did less-sensitized Type 304 SS or Type 316 NG SS specimens. Scanning electron microscopy showed minimal evidence of SCC in the Type 316 NG and solution-annealed Type 316 SS but clear evidence of IGSCC in moderately sensitized (EPR ≈ 20 C/cm^2) Type 304 SS specimens in these environments. Ranking for resistance to SCC in simulated ITER Water by electron microscopy and SSRT parameters (e.g., total elongation, ultimate strength, and reduction in area) is: 304 SS (EPR ≈ 20 < 2 C/cm^2) < 316 NG SS.

6.5.3 SEGREGATION IN THERMALLY AGED TYPE 304L ALLOYS FOR THE ICG-IASCC ROUND ROBIN (Oak Ridge National Laboratory) 236

Grain boundary segregation in thermally aged type 304 stainless steels has been investigated by X-ray microanalysis. In one commercial alloy sensitized at low temperature, narrow (<10 nm) zones depleted of chromium, silicon, and molybdenum have been observed along with enrichment of phosphorus and nickel. For high purity alloys doped with either sulfur or phosphorus, no significant segregation of either impurity was detected. In a second commercial alloy Which exhibited no grain boundary precipitation, segregation of phosphorus, chromium, and molybdenum to boundaries was observed along with a corresponding depletion of iron. The occurrence of phosphorus segregation in the two commercial alloys and absence in the high-purity, phosphorus-doped alloys seems to indicate some synergism of phosphorus Segregation with either chromium or carbon segregation or with the precipitation of $M_{23}C_6$ at the grain boundaries.

6.5.4 MEASUREMENT OF RADIATION-INDUCED SEGREGATION IN NEUTRON-IRRADIATED AUSTENITIC STAINLESS STEELS (Oak Ridge National Laboratory and Japan Atomic Energy Research Institute) 239

X-ray microanalysis of RIS to grain boundaries and large dislocation loops in neutron-irradiated USPCA has indicated enrichment of silicon and nickel and depletion of chromium and iron. However, there are numerous artifacts which can lead to erroneous results and must be recognized and avoided. Some of these effects include surface films, preferential etching, overlapping RIS profiles from different defects, as well as the more obvious hole count and induced radioactivity of neutron-irradiated material. For irradiated EP838, silicon, nickel, and iron are enriched at boundaries, whereas manganese replaces chromium as the strongly depleted element. Preliminary measurements of RIS profiles at grain boundaries by parallel electron energy loss spectroscopy (PEELS) are discussed. The relative advantages and disadvantages of EDS and PEELS for such measurements are considered.

6.5.5 RADIATION-INDUCED GRAIN BOUNDARY SEGREGATION AND SENSITIZATION OF A NNTRON-IRRADIATED AUSTENITIC STAINLESS STEEL (Oak Ridge National Laboratory and Japan Atomic Energy Research Institute) 244

Analytical electron microscopy and electrochemical potentiokinetic reactivation (EPR) testing were applied to the radiation-induced segregation (RIS) and sensitization of a titanium-modified austenitic stainless steel irradiated to 9 dpa at 420°C in the Materials open Test Assembly (MOTA) of the Fast Flux Test Facility (FFTF). The EPR testing of both solution annealed (SA) and 25% cold-worked (CW) materials indicated a significant Increase in the reactivation charge (P_a). Both optical and scanning electron microscopy of the specimen surface after EPR testing indicated preferential attack at grain boundaries, indicative of sensitization. In addition. localized attack of the matrix was observed. Though precipitates were occasionally present on grain boundaries. they were not chromium-rich $M_{23}C_6$, but nickel- and silicon-enriched G phase. Faulted loops, fine Y' precipitates, and isolated cavities were observed in the matrix. X-ray microanalysis indicated significant RIS at high-angle boundaries in both materials. Depletion of chromium to apparent levels of 10 at. % was observed in the irradiated SA material. The boundaries were enriched in nickel, silicon. and titanium (up to 28, 6, and 1 at. %, respectively) and depleted of iron and molybdenum (as low as 54 and 0.7 at. %, respectively). The width of the Segregation zone was very narrow (<6 nm). Similar grain boundary RIS was observed in the Cold-worked material. There was also evidence for boundary migration in the cold-worked material (boundary facetting and asymmetric conposition profiles). Voids and faulted dislocation loops in the SA material also exhibited similar RIS.

6.5.6 DEVELOPMENT OF CERAWIC COATINGS FOR LIQUID METAL BLANKET APPLICATIONS (National Chung Hsing University and Argonne National Laboratory) 252

Based on a preliminary survey of more than 15 oxides and nitrides, four materials (CaO, MgO, Y_2O_3, and BN) were identified as candidates for insulator coating development. Additionally, Cr_2O_3, V_XO, and $(V,Ti)_XN$ were included for study because of their Chemical stability in liquid lithium and their potential as corrosion inhibitors. These ceramic compounds were fabricated by a variety of techniques and exposed to flowing lithium at 400°C to assess chemical compatibility. Preparation technologies included hot-press-sintering of MgO, CaO, and Y_2O_3; diffusion coating of Cr_2O_3; oxidation of vanadium; and reactive sputtering of BN. Among the three hot-pressed-sintered materials. only Y_2O_3 displayed acceptable corrosion resistance when exposed to high purity lithium. A ferritic substrate alloy (HT-9. coated with a l-pa-thick BN layer) was immersed in flowing lithium at 400°C for 1 h, after which its physical stability and chemical conpatibility were determined to be unacceptable. Chromized V-20Ti and oxidized V-20Ti immersed in flowing lithium at 410°C for 100 h showed greater potential for further development than did the BN insulator coating. Preliminary work has begun in the development of in-situ-formed insulator coatings. The first step has been to examine the characteristics of $(V,Ti)_XN$ reaction prohrct layers formed after exposure of V-Ti specimens to flowing lithium. Work is also in progress to test a self-regenerating $CaO{\cdot}V_2O_5$-type insulator coating on a vanadium substrate.

7. SOLID BREEDING MATERIALS 261

7.1 LITHIUM MASS TRANSPORT IN CERAWIC BREEDER MATERIALS (Argonne National Laboratory) 263

The transport of lithium by vaporization of LiOH(g) from lithium ceramics, particularly $Li_2O(s)$, poses a constraint on tha maximum operating temperature of the blanket. Experimental measurements have shown that, depending on temperature, moisture pressure, and proximity of structural steels. the lithium transport process is complex. For conditions wherein the $Li_2O(s)$ is "free standing," the lithium vaporization is controlled by the Li_2O/H_2O system thermodynamics that are already well established. Simply stated lithium transport as LiOH(g), increases with increasing temperature and higher partial pressures of moisture. In the proximity of stainless steel. there is an added Chemical potential driving force due to formation of Li_2CrO_2, $LiFeO_2$ and $LiNiO_2$. The transport of LiOH(g) to the stainless steel is driven by the concentration gradient of LiOH(g) from that at the $Li_2O(s)$ surface and that at the steel surface. This gas-solid reaction may become important for blanket designs where the structural steel is very close to the $Li_2O(s)$ ceramic.

7.2 DESORPTION CHARACTERISTICS OF THE $LiAlO_2$-$H_2O(g)$ SYSTEM (Argonne national Laboratory) 268

The energetics and kinetics of the evolution of $H_2O(g)$ and $H_2(g)$ from $LiAlO_2$ are being studied by the temperature programed desorption technique. The concentrations of H_2, H_2O, N_2, and O_2 in a helium stream during a tqerature ramp are measured simultaneously With a mass spectrometer. The amount of H_2 adsorptionldesorption is small compared to the amount of H_2O adsorptionldesorption. After prolonged treatment with helium containing 990 ppm H_2 at 400°C, H_2O evolution into the He-H_2 stream was observed during 473 to 1023 K (200 to 750°C) ramps at rates of 2 or 5.6 K/min. The different peak shapes reflecting this process were deconvoluted to show that they are composites of only 2 or 3 reproducible processes. The activation energies and pre-exponential terms were evaluated. The different behavior originates in the differences among different surface sites for adsorption. The interpretation of higher temperature peaks [above 873 K (650°C)] must still consider the possibility of contributions from interactions with the steel walls.

7.3 TRITIUM RELEASE FROM LITHIUM CERAMICS (Argonne National Laboratory, CEA/CEN, ENEAICRE, and Karlsruhe) 274

Recent in-pile tritium extraction experiments from lithium ceramics have investigated the effects of tmperature. material microstructure, purge gas composition, and tritium generation rate on the kinetics of tritium release. The relationship between the tritium release characteristics and sample microstructure indicates desorption is the dominant mechanism controlling tritium release for the conditions Investigated. Literature results indicate that this desorption Step may be second Order and the activation energy of desorption nay vary signlficantly with surface coverage. The changes in inventory with variations in the key parameters mentioned above were investigated to determine the applicability of these reports to in-pile tritium release. The results suggest tritium release is first order, and that the desorption activation energy is dependent on the surface coverage.

7.4 IN-SITU TRITIUM RECOVERY FROM Li_2O IRRADIATED IN FAST NEUTRON FLUX - BEATRIX-II INITIAL RESULTS (Japan Atomic Energy Research Institute, Pacific Northwest Laboratory, and Chalk River Laboratories) 279

The BEATRIX-II experiment in FFTF is an in-situ tritium recovery experiment to evaluate the tritium release characteristics of Li_2O and its stability under fast neutron irradiation to extended burnups. This experiment includes two specimens: a thin annular ring specimen capable of temperature transients and a larger temperature gradient specimen. During the first 85 days of the operating cycle of the reactor, the tritium recovery rate of a temperature transient capsule was examined as a function of temperature, gas flow rate, gas composition and burnup. Temperature changes in the range from 500 to 650°C resulted in decreasing tritium inventory with increasing temperature. Lower gas flow rates resulted in slightly lower tritium release rates while gas composition changes affected the tritium release rate significantly, more than either flow rate or temperature changes. Three different sweep gases were used: He-0.1% H_2, He-0.01% H_2, and pure He. Decreasing the aumunt of hydrogen in the sweep gas decreased the steady-state release rate by as much as a factor of two.

8. CERAMICS 289

8.1 IEA WORKSHOP ON IN-SITU MEASUREMENT OF ELECTRICAL PROPERTIES OF IRRADIATED CERAMICS (LOS Alamos National Laboratory) 291

This International Energy Agency workshop was held in Los Alamos, NM June 27-29, 1990. In attendance were 14 participants representing fusion ceramics programs in Spain, the U.K., Japan and the U.S. The workshop was divided into four Sessions: Background, Current In-Situ Work. Plans and Goals for Future work, and Recommenations. Informal discussion sessions on various subjects were also included in tho workshop. Studies of in-situ electrical properties have accelerated since the last gathering of this group, with recent findings demonstrating that dielectric breakmwn as well as enhanced conductivity can be induced by concurrent irradiation. Eased on present knowledge, recommendations were made to designers of NET and ITER on materials selection and anticipated Performance, as well as on design-related considerations.

8.2 IN-SITU MEASUREMENT OF RADIATION INDUCED CONDUCTIVITY IN CERAMICS (Los Alamos National Laboratory) 295

This report describes our experimental plan and schedule for measuring the radiation induced Conductivity (RIC) in ceramics while being irradiated with 3 MeV protons. In the initial experiments, dielectric constant and loss will be measured in pure and in Ti-doped sapphire. The measurements will be made at room temperature, at frequencies between 100 Hz and 10 MHz, with and without an applied DC bias, and as a function of radiation flux and fluence. The Ion Beam Materials Laboratory (IBML) ion source at Los Alamos will be used with beam currents up to 1 micro-ampere. Ye expect initial results to be available for the next semi-annual Progress Report.

8.3 MILLIMETER-WAVE TESTING OF ISOTOPICALLY ENRICHED ALUMINA (Los Alamos National Laboratory and Oak Ridge National Laboratory) 297

In a Special fusion-neutron Irradiation simulation experiment, ^{17}O has been substituted for ^{16}O in 99.5% alumina to be neutron-irradiated in the High Flux Isotope Reactor (HFIR) at Oak Ridge for raising the potentially deleterious helium gas yield to levels closer to those expected from the neutrons of deuterium-tritium (D-T) fusion reactions. Earlier. we reported values of complex dielectric constant k* measured at Los Alamos at millimeter-wave (MMW) frequencies for conventional (unenriched) 99.5% alumina test specimens, There specimens were made under the same conditions applying to the present report of k* measured for ^{17}O-enriched specimens based on the same alumina system. The present alumina has lower dielectric losses than that reported in the earlier work. Furtherumre. we corroborate the earlier finding that k* is a sensitive nondestructive measure of the quality of alumina being considered for rf-window use -- and the overall quality of high-purity ceramics in general.

8.4. WORKSHOP ON CERAMIC MATRIX COMPOSITE MATERIALS FOR STRWTURAL APPLICATIONS IN FUSION REACTORS (Pacific Northwest Laboratory and university of California-SB) 302

The workshop to assess the potential application of ceramic matrix composites (CMCs) for structural applications in fusion reactors was held on May 21-22, 1990, at University of California, Santa Barbara. Participants included individuals familiar with materials and design requirements in fusion reactors, ceramic composite processing and properties and radiation effects.

Clear advantages for the use of CMCs (i.e., SiC/SiC) are high-temperature operation. which would allow a high-efficiency Rankine cycle, and low activation. Limitations to their use are material Costs. fabrication complexity and costs, lack of familiarity with these materials in design. and the lack of data on radiation stability at relevant temperatures and fluences. Fusion-relevant feasibillty issues were identified.

8.5 DEVELOPMENT OF THIN-SECTION PUSH-OUT TECHNIQUE FOR USE ■ MEASURING RADIATION-INDUCED MODIFICATION OF CMPOSITE INTERFACES (Rensrelaer Polytechnic Institute and Oak Ridge National Laboratory) 306

A technique for measuring the interfacial properties for extremely thin composite sections is presented. The data shown is for a single composite section of 22 μm thickness. By employing a Nanoindenter microhardness tester. composite fibers were individually loaded and the debond and frictional Sliding Strength measured. It is shown that such a technique can discriminate between the debond and frictional components of the interfacial band. The technique presented is a substantial improvement over previous techniques in both thickness of composite section. fiber loading accuracy, and percentage of fiber failures. Though the data presented is only for a single section. the results are typical of other sections tested. A statistical analysis of the data suggests that a Weibull treatment is more appropriate to interfacial data than the commonly used normal distribution.

8.6 MEASUREMENT OF DIELECTRIC PROPERTIES IN ALUMINA UNDER IONIZING AND DISPLACIVE IRRADIATION CONDITIONS (Oak Ridge National Laboratory) 317

Several experiments have been completed in Which the dielectric properties of alumina have been measured in the presence of ionizing and displacive irradiation. Spent fuel elements from the High Flux Isotope Reactor (HFIR) at the Oak Ridge National Laboratory were Used to provide an intense source of ionizing irradiatlon for some of the measurements. The TRIGA reactor at the University of Illinois was used to provide an irradiation field that produced both ionization and atomic displacements. The results of these in situ measurements indicate that the dielectric properties of alumina are more severely degraded by displacive irradiation than was indicated by earlier. post-irradiation measurements.

8.7 DISLOCATION LOOP FORMATION IN ION-IRRADIATED POLYCRYSTALLINE SPINEL AND ALMINA (Oak Ridge National Laboratory) 323

The microstructure of magnesium aluminate spinel ($MgAl_2O_4$) and alumina (Al_2O_3) has been examined with transmission electron microscopy following ion irradiation to damage levels of 0.1 to 5 keV/atom (1 to 50 dpa) at room temperature and 650°C. The ion irradiatlon produced interstitial dislocation loops of types a/4<110>{110} and a/4<110>{111} in spinel along with a very low density of a/6<111>{111} loops. Dislocation loops of types a/3[0001](0001) and a/3<1100>{1100} were tentatively identified in alumina. The loop size increased and the density decreased gradually with increasing fluence in spinel irradiated at 650°C, with the net result that the concentration of interstitials contained in the loops remained nearly Constant at ~0.1 at. %. Defect-free regions were observed adjacent to grain boundaries and the irradiated surface in spinel irradiated at 650°C. The denuded zone width was very small for spinel Irradiated at 25°C and Al_2O_3 irradiated at 650°C. For a given irradiation tenperature, tho loops in spinel were larger and of much lower density than the loops in Al_2O_3.

8.8 TECHNIQUE FOR PREPARING CROSS-SECTION TRANSMISSION ELECTRON MICROSCOPE SPECIMENS FRCU ION-IRRADIATED CERAMICS (Oak Ridge National Laboratory) 334

The general techniques necessary to produce [illegible] ceramic specimen for transmission electron microscope observation are outlined. A particularly inportant point is that the width of the glued region between faces of the ceramic specimen must be <0.2 μm to prevent loss of the near-surface region during ion milling. A recently developed vise for gluing ceramic Cross-section specimens is described, and some examples of the effect of glue thickness on specimen quality are shown.

1. IRRADIATION FACILITIES, TEST MATRICES, AND EXPERIMENTAL METHODS

AN EVALUATION OF THE LOS ALAMOS SPALLATION RADIATION EFFECTS FACILITY (LASREF) FOR FUSION APPLICATIONS - D. G. Doran (Pacific Northwest Laboratory)[a]

OBJECTIVE

To evaluate the appropriate role, both short-term and long-term, of the Los Alamos Spallation Radiation Effects Facility (LASREF) in the U.S. Fusion Materials Program.

PROGRESS AND STATUS

Evaluation Committee

The makeup of the evaluation committee was as follows:

Members

D. G. Doran, PNL, chairman

F. A. Garner, PNL, radiation effects in metals and alloys, and chair of the Program Advisory Comnittee for Materials Science at LAMPF

L. R. Greenwood, PNL, neutron environment characterization

M. W. Guinan, LLNL, cryogenic radiation experimentation

G. E. Lucas, UCSB, radiation effects on mechanical properties and specimen miniaturization

A. F. Rowcliffe, ORNL, radiation effects in alloy development

Advisors

F. W. Clinard, LANL, radiation effects in ceramics and diagnostics

R. Prael, LANL, high energy transport codes, viz. LAHET

W. F. Sommer, LANL, LASREF description and operation

F. W. Wiffen, DOE/OFE, fusion materials programs oversight

Facility Overview

The Los Alamos Meson Physics Facility (LAMPF) is an 800-MeV, nominally 1-mA (usually 0.6 to 0.8 mA), linear proton accelerator with many experimental stations appended to it. When the residual proton beam is finally dissipated in the beam stop, neutrons are produced by spallation, fission, and evaporation. LASREF was designed to permit materials to be neutron-irradiated in the near vicinity of the beam stop, subject, of course, to the operation of LAMPF. A unique feature of the facility is the large irradiation volume, accessible via vertical "inserts" that can be tailored for specific experiments, including instrumentation if desired. The minimum irradiation temperature, without refrigeration, is about 40°C. Ancillary capabilities include remote handling equipment and hot cells.

Findings (abbreviated from full report)

1. The operation of LAMPF was budget limited to 2500 hours in FY90 and current projections suggest it may be limited to only 1900 hours in FY91. However, the U.S. Department of Energy (DOE) anticipates perhaps 3000 hours in FY92, according to J. N. Bradbury, the acting leader of the MP Division. This is still short of Bradbury's "reasonable goal" of 4000 hours (last achieved in FY84).

2. The proton beam is pulsed with both coarse and fine structure. Each 0.5 to 0.8-msec pulse recurring at 120 Hz (8.3-msec period) contains 0.3-nsec pulses at about 200 MHz (5-nsec period).

(a) Pacific Northwest Laboratory operated for U.S. Department of Energy by Battelle Memorial Institute under Contract DE-AC06-76RLO 1830.

The fine structure is of no concern for materials irradiations. The coarse structure off-time of 8 msec, however, may be of the same order as the vacancy lifetime at high temperatures in some materials with high sink densities, and is orders of magnitude larger than interstitial lifetimes. The inability to achieve equilibrium defect concentrations may affect the microstructural evolution, which in turn may affect dimensional stability, mechanical properties, and the establishment of the gradients that drive grain boundary segregation. Consideration of possible effects of pulsing should precede any LASREF irradiation.

The pulsed nature of the beam could possibly be used to advantage in ceramic insulators by providing some information on charge carrier lifetimes.

In addition to the intrinsic pulsing, the beam experiences random interruptions at the following typical rates: 30 "fast protects" (i.e., with automatic restart) of several seconds duration and 1 to 3 interrupts of perhaps 20 minutes each per 24 hours.

3. A characteristic of the neutron energy spectra produced by a spallation neutron source is a "high-energy tail" extending, with rapidly decreasing intensity, to hundreds of MeV. The precise shape of the spectrum depends on the location along the beam direction (the highest energy neutrons are produced in the forward direction), on the material of the beam stop (raising the atomic number increases the yield while softening the spectra), and the material surrounding the beam stop. Measurements near the position of maximum flux have shown that, with the current copper target, about 5% of the neutrons are above 20 MeV. This percentage can be decreased by several means, but these neutrons, which account for perhaps 15% of the displacements, produce most of the helium so are necessary if fusion-relevant helium/dpa ratios are to be obtained.

The high-energy tail will produce displacement cascades and transmutation reactions that are not characteristic of a fusion reactor. Both modeling and experiment suggest that observable effects of displacement phenomena in metals and alloys are unlikely, although this remains to be demonstrated conclusively. Atypical transmutation reactions, and factors of two uncertainties in their calculated rates, are not believed to be an important concern because attainable fluences are so low.

A third effect of a high-energy tail is to increase the proportion of ionizing events, which could be a consideration in interpreting radiation-induced conductivity measurements in LASREF.

The full report contains an appendix which discusses the characterization of the LASREF neutron environment.

4. The maximum displacement damage rate attainable in the current configuration is about 0.3 dpa (iron) per year if operated at 4000 hours per year. This rate drops radially approximately as $1/r^2$ and much less rapidly along the beam direction.

5. LASREF is unique in providing a large experimental volume that can be exploited for in situ measurements, in having the potential for cryogenic irradiations, and in having a high ratio of neutrons to gammas (total heating is less than 1 W/g in iron). This large volume--12 vertical inserts, each having a volume of 12 X 25 X 50 cm^3--is accessible only when LAMPF is down, although a small diameter (about 11 mm) rabbit tube has been used for brief irradiations during accelerator operation (a furnace has been designed to fit this tube). A larger "rabbit," about 7 X 10 x 10 cm^3, has been designed for a proposed experiment.

6. An experiment at LASREF that requires a new insert and furnace is estimated to cost about $100K on a full cost recovery basis. The neutrons are free at the present time, and installation of an experiment should cause no interference with accelerator operation.

7. Potential upgrades of LASREF have been scoped but not developed in detail. Calculations indicate that the peak flux could be increased a factor of five to about 1.5 dpa (iron)/yr at 4000 hours per year by reducing the beam stop diameter and replacing the copper stop with a tungsten alloy. The estimated cost of such an upgrade, lasting 1½ to 2 years, is about $600K. An additional estimated expense of $150K to modify the isotope production stringers at LAMPF might raise the damage rate another factor of two.

The operating cost of LASREF for a sustained program of irradiations is estimated to be about $800K per year for staff and $80K per year for hardware, assuming four inserts are used per year.

The flux (in the MeV range and below) could also be increased through use of a neutron multiplier and/or neutron reflector. This option has not been scoped, but the damage rate might be raised by another factor of two or three.

8. There is no sustained mission for LASREF in the metals and alloys segment of the fusion materials program; the damage rates are too low even with a significant upgrade, and there is a question of pulse effects at elevated irradiation temperatures. If damage rates were raised to 3 to 5 dpa/yr, useful mechanical property data might be obtained in the 40 to 300°C temperature range; however, a research program to evaluate effects of the high-energy tail would have to precede heavy program use.

9. There is a potential mission for LASREF in meeting the critical need of the CIT and ITER projects for testing magnet materials and ceramic insulators, and for more general studies of special purpose materials.

The large irradiation volume makes possible instrumented in situ measurements on materials and, most importantly, on components and subassemblies. Electronic noise at LASREF is high but should be controllable.

For CIT, studies of the shear strength of organic insulators are needed to a dose of 1000 MGy over the temperature range of 77 K to 300 K. Since there is experimental evidence that neutrons are more damaging than gammas per unit energy deposition, neutron exposures of 300 to 1000 MGy, which should easily be reached at LASREF, are required. The high neutron/gamma ratio at LASREF is important for assessing neutron versus gamma damage. The establishment of a liquid nitrogen capability at LASREF looks relatively straightforward. This would permit testing of RF windows at ITER-relevant temperatures as well as magnet materials.

For ITER, doses of only 30 MGy are required for organic insulators, but shear testing under a compressive load is needed at 4 K. In addition, studies of composite superconductors (i.e., superconductor, matrix, and stabilizer) are needed to firmly establish exposure limits of candidate commercial materials. This work is probably feasible at LASREF.

Any upgrade in flux would expand the types of materials that could be tested and would permit in situ tests at more realistic fluxes.

(The full report contains further discussion of in situ testing and details on CIT/ITER needs for irradiation testing of magnet materials.)

10. There has been some use of LASREF by foreign laboratories. Interest in future experiments has been expressed from a laboratory in the Peoples Republic of China (in situ mechanical testing), Tohoku University (in situ creep) and KfA Jülich (JET/NET). The Japanese (Monbusho) program might indeed find LASREF irradiations an appropriate bridge between their earlier RTNS-II irradiation program and the current FFTF program.

11. The potential for having an FMIT-like, accelerator-based neutron source in the U.S. in 1995-6 should not influence any actions regarding LASREF.

Recomnendations to OFE

1. Formulate a decision quickly regarding significant use of LASREF or the opportunity to take advantage of the rather extensive capabilities developed there may be lost.

2. Do not establish a sustained program for alloy development for fusion applications at LASREF at this time. The current damage rates are too low and pulse effects may introduce uncertainties at elevated irradiation temperatures. To take advantage of a significant upgrade would require not only funding of the upgrade and the LANL staff to support it, but also of a research program to evaluate spectral and pulsing effects. While the large irradiation volume and near-room temperature capability are attractive, they do not justify a diversion of funds from current reactor irradiation programs.

3. Define, in conjunction with LASREF personnel, a potential LASREF irradiation program designed to meet CIT/ITER needs for in situ testing of insulators, magnet components, and diagnostics (see Appendices 4 and 5 of full report). Funding should come from these projects.

- 3.1 Determine feasibility of developing a 77 K capability and estimate cost (rough estimate by Los Alamos is $100K) and schedule.
- 3.2 Determine feasibility of developing a 4 K capability and estimate cost and schedule, unless the Office of Basic Energy Sciences (OBES) plans to operate the cryogenic facility in the Bulk Shielding Reactor (BSR) at Oak Ridge. In the latter case, assurance of sufficient irradiation time for fusion experiments is needed.
- 3.3 Determine cost effectiveness of proposed LASREF upgrades in light of CIT/ITER needs.
- 3.4 Estimate operating costs for various scenarios.

4. Evaluate analytically the potential for increasing the peak flux through the use of a neutron multiplier and/or reflector. The cost should be low if the large amount of Cray time required is made available at the National Energy Research Supercomputer Center (NERSC) at Livermore. (Significant flux upgrades, with the exception of decreasing the diameter of the beam stop, will soften the spectra; helium/dpa ratios lower than fusion reactor first wall values are likely, though not so low as encountered in fission reactors.)

A decision on whether to proceed with a preliminary design and cost estimate for implementing this approach would be dependent on its calculated benefits and the need as perceived in Recommendation 3.

5. Examine the potential for international participation--Monbusho, NET/ITER team laboratories--in LASREF facility development and utilization.

6. Modify and further test the LAHET (high-energy transport) code if significant use of LASREF is contemplated. (A suggested approach is given in Appendix 3 of the full report. Some measurements will be made shortly of helium concentrations in LASREF-irradiated specimens; these will provide a preliminary check of calculated transmutation rates.) In addition, expanded calculations will be needed of the spatial dependence of damage rates.

FUTURE WORK

The work of the committee has been completed and its report ("Report of the LASREF Evaluation Comnittee", PNL-SA-18584, July 1990) given wide distribution. Further copies are available from the chairman.

DEVELOPMENT OF DISC COMPACT TENSION SPECIMENS AND TEST TECHNIQUES FOR HFIR IRRADIATIONS.

C. Elliott, M. Enmark, G. E. Lucas, G. R. Odette (University of California, Santa Barbara) and A. Rowcliffe (Oak Ridge National Laboratory)

OBJECTIVE

The objective of this work is to develop techniques for evaluating fracture toughness from specimens compatible with the HFIR irradiation environment.

SUMMARY

Near term irradiations of candidate alloys being planned for the High Flux Isotope Reactor (HFIR) in support of ITER and isotope tailoring experiments necessitate the use of relatively small fracture toughness specimens, eg. down to 12.5 mm in diameter. The specimens will also contain substantial amounts of helium. This work involved the application of electropotential drop techniques to determine J-resistance curves for this purpose in HT-9 specimens with diameters of 40, 25 and 12.5 mm at temperatures ranging from 20 °C to -100 °C; in addition, the effects of si& grooving were examined Good agreement between J-resistance curves determined by the electropotential drop and by multiple specimen techniques were obtained for all specimen geometries, sizes, and temperatures.

PROGRESS AND STATUS

Introduction

Irradiations in the High Flux Isotope. Reactor (HFIR) are being planned for several purposes. One is to develop data pertinent to anticipated operating conditions for the International Experimental Tokamak Reactor (ITER), where irradiation temperatures in the range 60-350°C are needed.[1] The other is to systematically determine the effects of He/dpa ratio on the microstructural evolution and mechanical properties of ferritic and austenitic steels using isotope tailoring.[2] In both cases it is desirable to obtain fracture toughness data on irradiated material. However, because of irradiation volume and/or material constraints, it is anticipated that fracture toughness data will have to be obtained from J-resistance (J-R) curves developed from single specimens having diameters as small as 12.5 mm. Huang and co-workers [3-5] have developed elecmpotential drop techniques for obtaining fracture toughness from small specimens. Our effort was undertaken to evaluate some subsequent improvements to the electropotential drop technique for specimen geometries of interest to HFIR irradiations, and to examine possible ways of lead attachment to specimens anticipated to contain significant amounts of helium.

Experiments

Tests m date have been performed on specimens taken from the ESR heat of HT-9. Compact tension (CT) specimens with the geometry shown in Figure 1 were fabricated from 16 mm thick plate in the stress relieved condition, for which microstructures have previously been examined [6,7]. As tabulated, three. sizes were machined, having thicknesses of 12.8 mm, 8 mm and 4 mm. In addition, two initial notch depths were fabricated, with crack length to specimen width ratios (a/w) nominally 0.3 and 0.5. For the a/w = 0.5

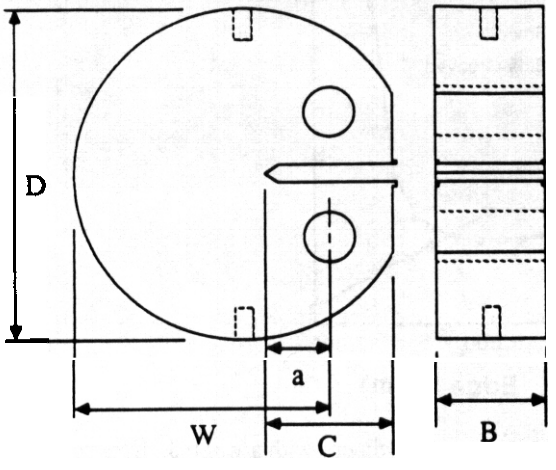

Dimensions (in mm)

D	a	W	a/W	B	C
40.0	13.6	30.0	0.45	12.8	21.0
40.0	7.5	30.0	0.25	12.8	15.0
25.0	7.9	18.8	0.42	8.0	12.5
25.0	4.7	18.8	0.25	8.0	9.4
12.5	3.0	9.4	0.32	4.0	5.5
12.5	2.3	9.4	0.25	4.0	4.8

Figure 1. Disc compact specimen geometry, and tabulated specimen dimensions.

specimens, several specimens were side grooved 20% (= B-B_o/B) with a 45° notch and a root radius of 0.25 mm. Small nubs were machined onto the faces of each disc compact tension specimen for the purpose of attaching the voltage measurement leads accurately and, hence, measuring potentials reproducibly. [8] Finally, for purposes of comparison, 12 mm thick square compact tension specimens with the geometry given in ASTM Standard E399 were fabricated with an a/w of 0.5. Direct current leads were attached to the top and bottom of each specimen by screws. Voltage leads made of 0.25 mm diameter 410 steel wire were spot welded to the nubs on the specimen faces. The selection of lead wire was chosen to approximate the composition of HT-9 and hence reduce thermoelectric emf contributions to the voltage signal.[9] The highest sensitivity to crack length changes, and lowest sensitivity to lead location and crack shape was found for leads attached to opposite sides of the specimen across the crack plane; this is in agreement with previously reported results.[9] As discussed below, separate reference potential drop measurement leads were found to be unnecessary. Previous experience with austenitic stainless steels suggests that difficulties may be encountered in welding leads to steels containing a few appm helium; consequently, various welding techniques are currently being investigated using steels doped with helium via the tritium trick.

AU specimens were pre-cracked and tested on a closed-loop, servohydraulic load frame. The specimens were attached to the load frame by pin and clevis grips; and the load train was electrically insulated from the machine by ceramic washers. DC currents of 10.5 and 3 A were applied from a stable current source to the 12.8 mm, 8 mm and 4 mm thick specimens, respectively. Each specimen was fatigue pre-cracked at ambient temperature at a AK of approximately 24 MPa√m to the desired initial crack length (either a/w ~0.3 or 0.5). Following pre-cracking specimens were tested at ambient temperature by monotonic loading under displacement-control conditions at a displacement rate of 5 μm/s to a final desired crack length, and specimens were tested at low temperatures by submersion in an alcohol bath during similar monotonic loading at a rate of 2.5 μm/s. Crack lengths were monitored both by optical measurements of surface cracks at ambient temperature and by potential drop measurements at all temperatures, each requiring calibration to provide absolute measures of crack extension as discussed below. Load-ram displacement and potential-ram displacement data were recorded on a computerized data acquisition system. Because the voltage leads hindered attachment of a clip gage, ram displacement was converted to specimen load-line displacement through a calibration of system compliance. Following testing, unbroken specimens were heat tinted in air, fatigued and then fractured at liquid nitrogen temperatures. The initial notch length (ai), fatigue-precrack(a_o) and final crack length (a_f) were measured from the fracture surface. Nine point averages of crack length were obtained for the smooth specimens, and 18 point averages for the side-grooved specimens because of the larger variation of crack length with position as discussed below.

Multiple specimen J-Aa curves were obtained, when possible, from fractographically measured values of average crack length change Δa, and J_{IC} was determined using the procedures outlined in ASTM Standard E813. In addition, a variety of potential drop-crack length calibrations were considered and evaluated as described below. Once calibrated, the potential drop data were used along with the load-displacement data to evaluate J-Aa curves, and hence J_{IC}, from single specimens by methods recommended by Hacken et al.[10] In both cases, the tearing modulus T was determined from $T = dJ/da\ (E/\sigma_o^2)$, where E is the elastic modulus and σ_o the yield strength, and dJ/da the slope of the J-Δa curve used to determine J_{IC}.

Results

The crack shapes evolved in very different ways in the smooth and side-grooved specimens. As illustrated in Figure 2, the cracks in the smooth specimens showed some tunneling. Tunneling was more pronounced under monotonic loading than fatigue, and slightly greater in the largest specimens. However. in the side-grooved specimens, the tunneling profile was inverted, with the crack growing much more rapidly at the surface of the side-groove than in the interior.

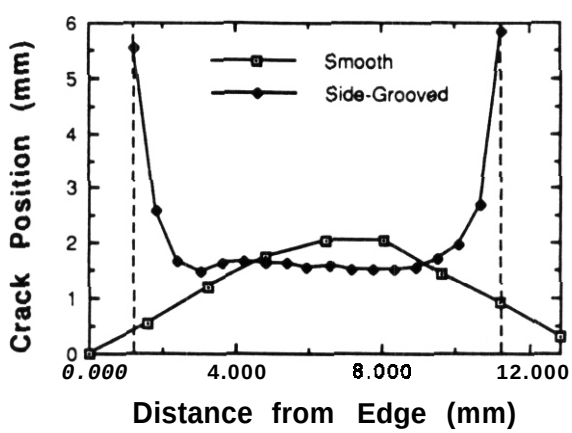

Figure 2. Comparison of crack shape geometries for smooth and side-grooved specimens with a/w = 0.5. Data shown here are for 12.8 mm thick specimens.

The a/w = 0.3 specimens showed anomalously high J_{IC} and tearing modulus data, indicative of arm bending.[11] Consequently, these specimens were only used to extend the calibration curve between crack lengths and potential drops over a wider range of initial crack lengths. We examined several different approaches to calibrating potential drop measurements with crack length. Early workers developed calibrations between potentials normalized by a reference potential (U_o) and crack lengths normalized by either initial crack lengths or specimen dimensions. For example, Ritchie [8] and others [12] have used the product of the specimen width and voltage gradient in an uncracked region of the specimen for U_o; whereas Huang [3-5] and others [12,13] have used the initial value of potential drop for U_o. However, the former method requires an additional set of leads and measurements, while the latter can lead to calibration curves that are sensitive to crack and specimen geometry. Indeed, we found that normalization against initial values of potential and crack length gave calibration curves which were very sensitive to specimen geometry (especially smooth versus side-grooved specimens), and slightly sensitive to crack geometry (especially fatigue pre-cracked versus blunted). More recently it has been suggested that using a potential drop at a fixed value of crack length to width ratio (a/w) for U_o results in a calibration curve that is less sensitive to material and geometry.[9,10] Accordingly, we found that the potential data were collapsed when the crack length was normalized by specimen width and the potential drop data were normalized against the potential drop at an a/w = 0.5 for a particular specimen geometry (ie, size and either grooved or ungrooved). This is shown in figure 3. This calibration was used to evaluate single specimen J-Δa curves.

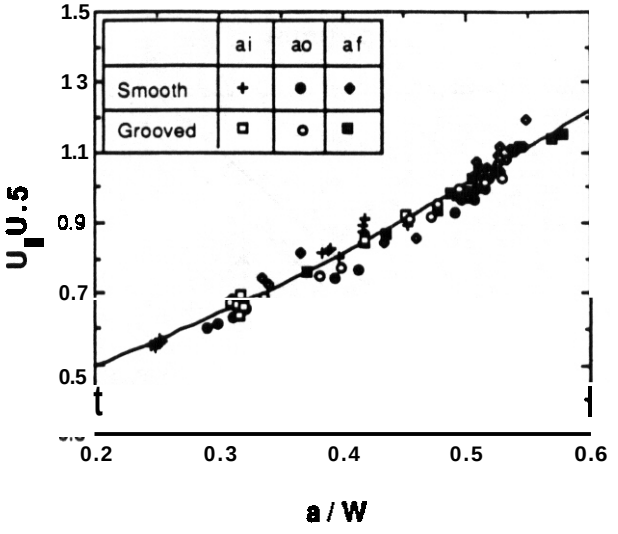

Figure 3. Potential drop normalized by values at a/w=.5 versus crack length to specimen width ratio. The fit to the data is shown as the solid line.

Representative single specimen J-Δa curves are shown for several specimen geometries in Figure 4. The end point data in Fig. 4 were obtained from fractographic measurements of Δa. The procedure outlined by Hacken et. al. [10] fixes the end points (a_o and a_f) to the directly measured values, and hence the values of Δa determined from potential drop measurements agree exactly here. This procedure also calculates J incrementally from load-displacement data and values of a between a_o and a_f calculated from potential drop, and hence the end point values of J differ slightly in some cases. The largest source of uncertainty in the procedure is in establishing the point of crack initiation. However, where comparisons could be made, fractographic indications of initiation were in agreement with predictions based on potential drop measurements. Although to date there are insufficient data to compare single specimen J-Δa curves to multiple specimen curves for all the specimen geometries we investigated, where comparisons could be made there was reasonably good agreement. This is shown in Table 1.

The dependence of J_{IC} and T on specimen size and side grooving is also shown in Table 1. The values of J_{IC} for the 12 mm thick specimens were in reasonable agreement With the values obtained fmm multiple specimen tests on the square CT specimen (220 kJ/m^2). This is larger than the value of J_{IC} = 95 kJ/m^2 for m-9 reported by Huang and Wire [3], hut the particular heat treatment investigated here results in a somewhat lower yield strength and higher ductility, so that a higher J_{IC} is not unexpected. There appears to be a systematic decrease in J_{IC} With specimen size in the smooth specimens and it is somewhat aggravated in the side-grwved specimens. Because of the relatively large toughness and low flow smss σ_f of the material examined, the minimum thickness required to meet the ASTM validity criteria for J_{IC} (ie, B > 25 J_{IC}/σ_f) is approximately 9 mm, which is larger than the two smallest specimen sizes, smooth and side-grooved. Although there have been arguments to suggest that J_{IC} should increase with decreasing size below the minimum thickness, the opposite has been observed in a number of instances, particularly when the test material has high toughness relative to strength. [15,16] On the other hand, side grooving decreases the tearing modulus, but there appears to be less of a systematic dependence of T on specimen size.

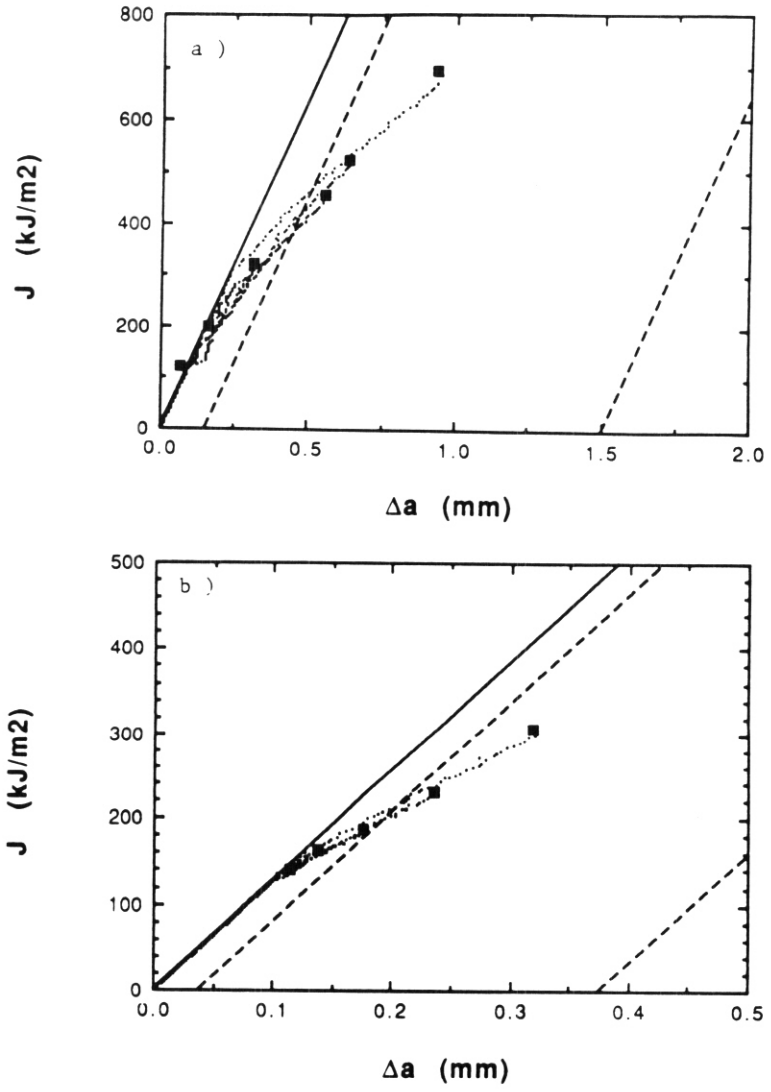

Figure 4. Representative J-Δa curves obtained from potential drop data for the a) 12.8 mm and b) 4 mm thick specimens.

Table 1
Comparison of Potential Drop and Multi-Specimen Data

B	SG?	J_{IC} (kJ/m^2)		T	
		PD[1]	MS[2]	PD[1]	MS[2]
12mm	No	262	239	376	406
	Yes	249	277	225	221
8mm	No	180	165	377	397
	Yes	113	---	326	---
4mm	No	158	113[3]	439	555
	Yes	77	---	299	---

[1]Potential Drop Test
[2]Multi-Specimen Test
[3]Based on Limited Data

In any event, the relatively good agreement between potential drop and multispecimen data and the insensitivity of the calibration curve to specimen and crack geometry suggest these techniques will be applicable to irradiated specimens. This is supported by results from low temperature testing which are shown in figure 5. Here, J_{IC} values obtained from the three specimen sizes are plotted as a function of test temperature along with data obtained from large specimens. These large specimen data were converted from valid K (ASTM E399) data by $J_{IC} = K_I^2/E(1-\nu^2)$. The validity lines for 4 mm, 8 mm, and 12 mm thick specimens are also superimposed. (Data below these lines meet the ASTM size criteria.). As can be seen at the lower temperatures where J_{IC} is reduced and σ_o increased relative to the values of the material at ambient temperature, the J_{IC} data matches well with values determined using ASTM *standard* E399 and specimens meet E813 size requirements for all specimen sizes.

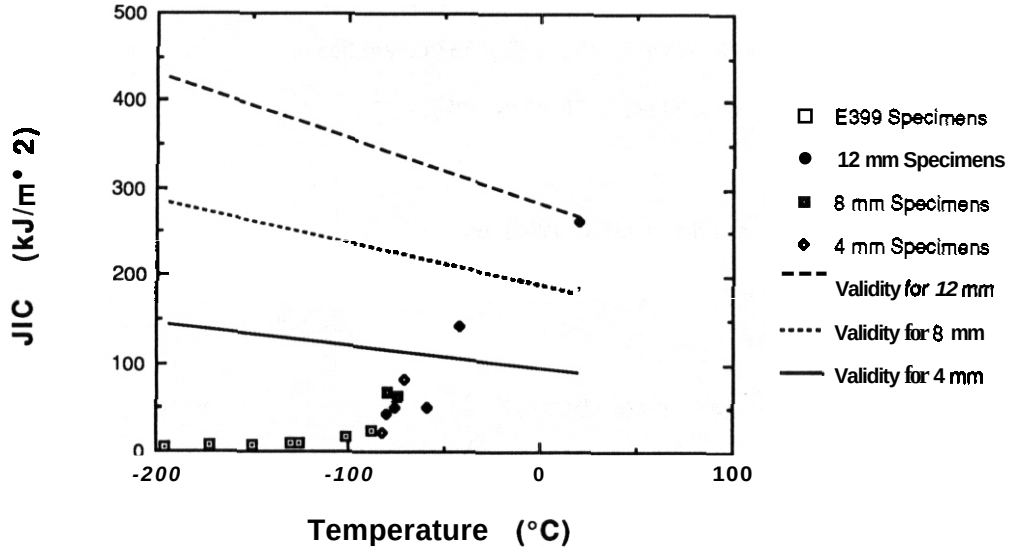

Figure 5. Low temperature test results for all specimen sizes.

SUMMARY AND CONCLUSIONS

We have investigated the applicability of electropotential drop techniques in obtaining J-Δa curves from single specimens compatible in volume and geometry with HFIR irradiation volumes. Both smooth and side-grooved specimens were examined. When the crack length was normalized against specimen width and the potential was normalized against a reference potential obtained at a crack to width ratio of a/w = 0.5 for a given specimen geometry, the data were collapsed for the range of specimen geometries investigated. J-Δa curves obtained from potential drop data were in good agreement with multispecimen data. A systematic decrease in J_{IC} with specimen thickness was observed for both side-grooved and smooth specimens. The tearing modulus was reduced by side grooving but was less dependent on specimen size. Smaller values of J_{IC} and larger values of flow stress obtained at lower test temperatures resulted in satisfaction of the ASTM size criteria for obtaining fracture toughness information for even the smallest specimens. Similar material property changes anticipated in irradiated materials should permit the use of smaller specimens in *HFIR* irradiations.

FUTURE WORK

Work will continue on both ferritic and austenitic steels, with an emphasis on identifying viable techniques for lead attachment in specimens containing helium.

REFERENCES

1. D. L. Smith, MRS Bulletin, V XIV, 7 (1989) 48.

2. G. R. Odette, J. Nucl. Mater., 141-143 (1986) 1011.

3. F. Huang and G. L. Wire, J. Eng. Mat. Tech., 101 (1979) 403.

4. F. Huang and G. L. Wire, J. Nucl. Mater., 104 (1981) 1511.

5. F. Huang, ASTM-STP-888 (1986) 290.

6. G. R. Odette, et al, J. Nucl. Mater., 122/123 (1984) 442.

7. C. Elliott, et al, J. Nucl. Mater., 141-143 (1986) 794.

8. G. H. Aronson and R. O. Ritchie, J. Test and Eval., 7, 4 (1978) 208.

9. G. M. Wilkowski, J. O. Wambaugh, K. Prabhat, ASTM-STP-833 (1984) 553.

10. W. M. Hackett, M. T. Kirk, R. A. Hays, NUREG/CR-4540 (1986).

11. J. Landes, Met Trans (in press).

12. C-Y Li and R. P. Wei, Mater. Res. and Standards, 6 (1966) 392.

13. H. H. Johnson, Mater. Res. and Standards, 5, 9 (1965) 442.

14. G. E. Lucas, et al ASTM-STP-888 (1986) 305.

15. W. R. Andrews and C. F. Shih, ASTM-STP-668 (1979) 421.

DESIGN, FABRICATION, AND OPERATION OF HFIR-MFE RB* SPECTRALLY TAILORED IRRADIATION CAPSULES • A. W. Longest, D. W. Heatherly, E. D. Clemmer (Oak Ridge National Laboratory), and J. E. Corum (Midwest Technical, Inc.).

OBJECTIVE

The objective of this work is to design, fabricate, and operate irradiation capsules for irradiating magnetic fusion energy (MFE) first-wall materials in the High Flux Isotope Reactor (HFIR) removable beryllium (RB') positions. Japanese and U.S. MFE specimens are being transferred to RB* positions following irradiation to 7.5 dpa at temperatures of 60, 200, 330, and 400°C in Oak Ridge Research Reactor (ORR) experiments ORR-MFE-6J and -7J.

SUMMARY

Design and fabrication of four HFIR-MFE RB* capsules (60,200,330, and 400°C) to accommodate specimens previously irradiated in spectrally tailored experiments in the ORR are proceeding satisfactorily. These capsule designs incorporate provisions for removal, examination, and re-encapsulation of specimens at an intermediate exposure level of 16 displacements per atom (dpa) en route to a target exposure level of 24 dpa. With the exception of the 60°C capsule, where the test specimens are in direct contact with the reactor cooling water, the specimen temperatures (monitored by 21 thermocouples) are controlled by varying the thermal conductance of a small gap region between the specimen holder and the containment tube.

Irradiation of the 60 and 330°C capsules was successfully started upon return of the HFIR to full power operation on July 17, 1990. As of September 30, 1990, these two capsules had completed 1 1/2 cycles of their planned 14-cycle irradiation to a damage level of 16 dpa. Fabrication of parts for the other two (200 and 400°C capsules) is nearing completion. Assembly of the 200 and 400°C capsules is scheduled for completion by the end of FY 1991; operation of these two capsules will follow the first two (60 and 330°C).

Capsule design and preparation of fabrication drawings for re-encapsulation of the MFE specimens after 16 dpa into two dual-temperature capsules (60/200 and 330/400°C) are scheduled to be completed in FY 1991.

PROGRESS AND STATUS

Introduction

A series of spectrally tailored irradiation capsules are being designed, fabricated, and operated as part of the U.S./Japan collaborative program for testing MFE first-wall materials in mixed-spectrum fission reactors. The test specimens are being irradiated in the new RB* facility' of the HFIR.

The first four HFIR-MFE RB* capsules were designed to accommodate Japanese and U.S. specimens previously irradiated to 7.5 dpa at temperatures of 60, 200, 330, and 400°C in the ORR in spectrally tailored experiments ORR-MFE-6J and -7J. Details of these ORR experiments, including descriptions of the test matrix, mechanical property specimens, and techniques of spectral tailoring, have been reported elsewhere.[2,3]

The first four HFIR-MFE RB* capsules will be irradiated in pairs (first the 60 and 330°C capsules, then the 200 and 400°C capsules) to a damage level of 16 dpa. After these four irradiations, the test specimens will be removed, examined, and approximately one-half of them re-encapsulated into two dual-temperature capsules (60/200 and 330/400°C) for irradiation to 24 dpa. Hafnium liners are being used to tailor the neutron spectrum to closely match the helium production-to-atom displacement ratio (14 appm/dpa) expected in a fusion reactor first wall.

60°C Capsule

The 60°C capsule, designated HFIR-MFE-60J-1, is an uninstrumented capsule with the test specimens in contact with the reactor cooling water. Capsule design, assembly, and details of the specimen loading were described previously.'

Irradiation of this capsule began July 17, 1990, at the start of HFIR cycle 289. As of September 30, 1990, 1 1/2 cycles of its planned 14-cycle irradiation to a damage level of 16 dpa had been completed. Specimen operating temperatures in this capsule are predicted to be within 10°C of 60°C.

330°C Cansule

The 330°C capsule, designated HFIR-MFE-330J-1, is an instrumented and singly contained capsule where the specimen temperatures are monitored by 21 thermocouples and controlled by adjusting the thermal conductance of a small gas gap region between the specimen holder outer sleeve and the containment tube. This capsule is cooled with 49°C reactor cooling water flowing downward over the containment tube surface. Capsule design, assembly, and details of the specimen loading were described previously.[5,6]

Irradiation of this capsule began on July 17, 1990, at the start of HFIR cycle 289. As of September 30, 1990, 1 1/2 cycles of its planned 14-cycle irradiation to a damage level of 16 dpa had been completed. Measured temperatures from the 21 thermocouples in the aluminum alloy specimen holder indicate that specimen operating temperatures are within 25°C of 330°C, which satisfies the temperature criterion for these experiments.

200 and 400°C Capsules

The 200 and 400°C capsule designs were described previously' and are basically the same as that of the 330°C capsule. The main differences in the three capsule designs are associated with (1) the number and spacing of the specimen holder slots and holes to accommodate the different specimen loadings, (2) the width of the temperature control gas gap region between the specimen holder outer sleeve and containment tube to obtain the desired specimen temperatures, and (3) the test piece included in the aluminum plug and holder above the test specimen holder to obtain extra information.

Fabrication of parts for both capsules is nearing completion. Assembly of the capsules is scheduled for completion by the end of FY 1991. Operation of these two capsules will follow the first two (a0 and 330°C).

HFIR-MFE RB* Facilities

Facility preparations required for operation of the HFIR-MFE RB* capsules were completed during the report period. Preparations completed included final checkout of Materials Irradiation Facility No.3 (MIFJ), which is being used for the HFIR-MFE-330J-1 capsule; connection of the instrumented 330°C capsule to the MIF-3 facility; and installation of a storage rack for HFIR RB* capsules at the west end of the HFIR pool.

FUTURE WORK

Assembly of the 200 and 400°C capsules is scheduled to be completed in FY 1991.

Capsule design and preparation of fabrication drawings for re-encapsulation of specimens after 16 dpa into two dual-temperature capsules (60/200 and 330/400°C) are scheduled to be completed in FY 1991.

REFERENCES

1. K. R. Thoms et al., "HFIR Irradiation Facilities Improvements - Completion of the HIFI Project," J. Nucl. Mater., 155-157 (1988) 1340-45.

2. J. L. Scott et al., pp. 12-20 in *ADIP* Semiann. Prog. Rep., March 31, 1985, DOE/ER-0045/14, U.S. DOE, Office of Fusion Energy.

3. J. L Scott et al., *Second* Annual Prog. Rep. *on* United *States-Japan* Collaborative resting in the High Flux Isotope Reactor and the Oak Ridge Research Reactor, Sept. 30, 1985, ORNL/TM-10102.

4. A. W. Longest et al., "Design and Fabrication of HFIR-MFE RB* Spectrally Tailored Irradiation Capsules," in Fusion Reactor Materials Semiann. Prog. Rep., March 31, 1988, DOE/ER-0313/4, U.S. DOE, Office of Fusion Energy.

5. A. W. Longest et al., "Design and Fabrication of HFIR-MFE RB* Spectrally Tailored Irradiation Capsules," in Fusion Reactor Materials Semiann. Prog. Rep., Sept. 30, 1987, DOE/ER-0313/3, U.S. DOE, Office of Fusion Energy.

6. A. W. Longest et al., "Design and Fabrication of HFIR-MFE RB* Spectrally Tailored Irradiation Capsules," in Fusion Reactor Materials Semiann. Prog. Rep., Sept. 30, 1988, DOE/ER-0313/5, U.S. DOE, Office of Fusion Energy.

7. A. W. Longest et al., "Design and Fabrication of HFIR-MFE RB* Spectrally Tailored Irradiation Capsules," in Fusion Reactor Materials Semiann. Prog. Rep., March 31, 1989, DOE/ER-0313/6, U.S. DOE, Office of Fusion Energy.

APPLICATION OF BALL PUNCH TESTS TO EVALUATING FRACTURE MODE TRANSITION IN FERRITIC STEELS,
J. McNaney, G. E. Lucas, G. R. Odette (University of California. Santa Barbara)

OBJECTIVE

The purpose of this study was to examine ball punch test techniques for determining fracture d e transition behavior in ferritic steel specimens as small as TEM discs.

SUMMARY

An investigation was made of the applicability of a ball punch test to evaluating the fracture mode transition in ferritic steel specimens equivalent to transmission electron microscopy (TEM) discs Both static and dynamic test conditions were examined in specimens with and without several intentional defects. High displacement rates (> 4 mm/s) resulted in adiabatic heating of the specimen during testing. Smooth specimens were found to provide more reproducible and useful data than specimens containing holes and grooves. A good correlation was found between the absorbed energy beyond maximum load and fracture mode transition, with the latter characterized by either fracture appearance or Charpy impact energy.

PROGRESS AND STATUS

Introduction

A variety of techniques have been examined for extracting mechanical properties from specimens with relatively small volumes for the purpose of optimizing irradiation volumes available to fusion reactor materials development efforts.[1] For this purpose. several studies have examined ball punch tests applied to transmission electron microscopy (TEM) disc geometries to evaluate strength and ductility parameters, and in some instances fracture mode transition.[2-7] In this study, we were particularly interested in using the ball punch test to characterize fracture mode transition in ferritic steels. Fracture mode transition is a phenomena that may be potentially limiting to ferritic steels in fusion reactor environments,[8] and we have a number of inadiation experiments either planned or completed which include TEM-disc-type specimens of ferritic steels. However, most of the ball punch tests reported in the literature to date have been conducted under slow strain rate conditions on s m t h specimens. We wanted to investigate the applicability of the technique under both static and dynamic conditions on specimens containing a number of different intentional defects, and to identify the most important test parameters for characterizing fracture d e transition.

Experiment

Tests were performed on specimens taken from five ferritic steels. two of which were in two different metallurgical Conditions. The steels and their nominal compositions are listed in Table 1. The A302B plate, A508 forging, and Linde 80 weld were low alloy, pressure vessel steels with a tempered bainite microstructure.[9] The A508 material was in the as-forged condition as well as re-austenitized at 1038°C for 1 h.[10] In addition, the Linde 80 weld was available in both unirradiated and irradiated conditions. The irradiated material had been exposed to a neutron flux of 3.6 x 10^{12} n/cm^2-s to a fluence of 2.6 x 10^{19} n/cm^2 at a temperature of 305 °C.[9] The HT-9 was taken from the stress-relieved condition of the ESR heat, and had a tempered martensitic structure.[11] The HSLA steel was an ASTM A710 class of steel with a polygonal ferrite structure.[12] These steels were selected to provide a range of mechanical properties and microstructures. In addition, mechanical property and fracture mode transition data were available for these steels from previous studies.[9,10,12,18]

Table 1

MAJOR CONSTITUENTS OF ALLOYS
(weight %)

Alloy	C	Cu	Ni	Mn	Si	Cr	Mo	V	Nb
A302B	0.23	0.20	0.17	1.47	0.26	0.05	0.52	--	--
WELD	0.12	0.40	0.60	1.36	0.51	0.04	0.44	--	--
A508	0.22	0.02	0.63	0.64	0.28	0.34	0.58	0.02	--
HSLA	0.04	1.18	0.97	0.60	0.28	0.73	0.18	--	0.04
HT-9	0.20	0.07	0.51	0.51	0.17	12.1	1.04	0.28	--

Specimens were fabricated from each material by sectioning coupons from available material, lapping the coupons to the desired thickness and punching 3 mm diameter disc specimens from the lapped coupons. The coupons were lapped to thicknesses between 0.25 to 0.28 mm, except the Linde 80 weld, which was already available as lapped coupons 0.45-0.53 mm thick. In punching the discs, the coupons were clamped between the punch and follower rod with a force of 150 N. The resulting specimens were flat with a thickness variation less than 1% across the disc.

The effects of two intentional defects were examined in some detail. Concentric through holes were machined into specimens with a 0.2 mm diameter carbide drill. In addition, annular troughs were machined into specimen surfaces with a hardened steel trepanning tool. The resulting concentric troughs were 1 mm in diameter, with a trapezoidal cross section 0.13 mm in nominal width at the base, 0.2 mm at the top and 0.1 mm deep. It was anticipated that such defects would concentrate elastic stresses by as much as a factor of 2.[13]

Specimens were tested on both a screw-driven instrumented load frame (for static and intermediaterate tests) and on a drop tower (for dynamic tests). In each case, the specimens were deformed within a punch fixture placed within a temperature bath. The punch fixture is shown in Figure 1. It consisted of an upper and lower die which clamped the specimen in a recess in the lower die. The specimen temperature was monitored by a thermocouple placed within 1 mm of the specimen circumference. A hardened steel punch tipped with a 1 mm diameter ball was used to deform the specimen into a shouldered recess 2 mm in diameter. For temperatures of 75 K and 298 K down to 140 K, a liquid nitrogen-organic solvent bath was used to immerse the entire punch fixture. For temperatures between 75 K and 140 K, a concentric dual bath was used. The outer bath was filled with liquid nitrogen. The inner bath was maintained dry (to avoid icing of the fixture) with forced, pre-cooled nitrogen gas. This cooled the specimen down to about 75 K. The desired specimen temperature was achieved by adjusting current through heating tape imbedded in the specimen fixture. Specimen temperatures were maintained to within +1 °C during the course of a test in either environment. Load on the specimen was monitored as a function of punch displacement throughout each test. Following testing, selected specimens were examined by scanning electron microscopy.

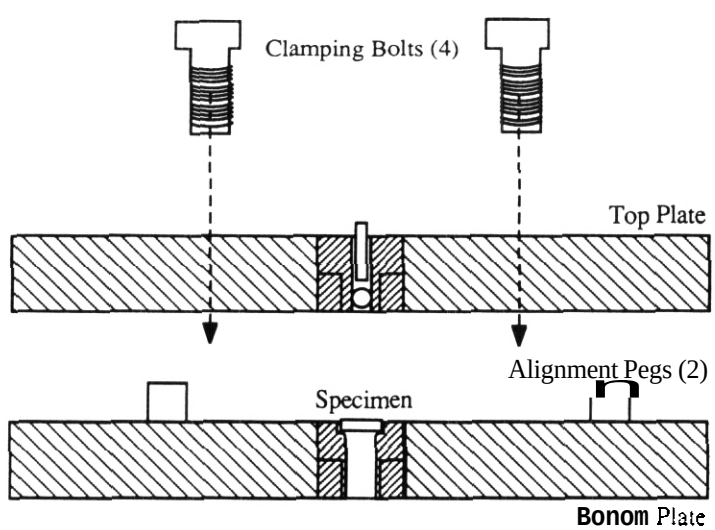

Figure 1. Schematic illustration of the ball punch fixture

Results

Materials varied in their reproducibility in load-displacement behavior, with HT-9 and the HSLA steel showing the best and A302B the worst. A typical set of load-displacement curves as a function of test temperature are shown for the HSLA steel in Figure 2. At ambient temperature, the load-displacement curve is characteristic of a ductile metal, showing a) an initially linear-elastic regime followed by b) a deviation from linearity, c) an inflection in the rising load-displacement curve, d) a maximum and e) a sudden drop in load. These have been interpreted as a) an initially elastic response, b) the formation and spread of yield zones to form a plastic hinge at the specimen center, c) work hardening and the transition from bending to membrane stretching, d) localized necking and e) fracture, respectively.[3,17] At ambient temperature it is clear that failure occurs by ductile fracture at the circumference of the contact area were plastic strains are maximum.[14,15] As the test temperature decreases, the effective flow stress of the material, and hence the load for a given punch displacement, increases; however, the punch displacement at maximum load and at failure decreases. At the lowest temperatures, the specimen fractures at the maximum load largely by cleavage. However, it is imponant to note that even at these low temperatures both the load-displacement curves and the SEM micrographs showed evidence of yielding and substantial plastic deformation prior to fracture. The increase and decrease in maximum load with decreasing temperature is analogous to the behavior of maximum load in instrumented Charpy testing of ferritic steels.[19]

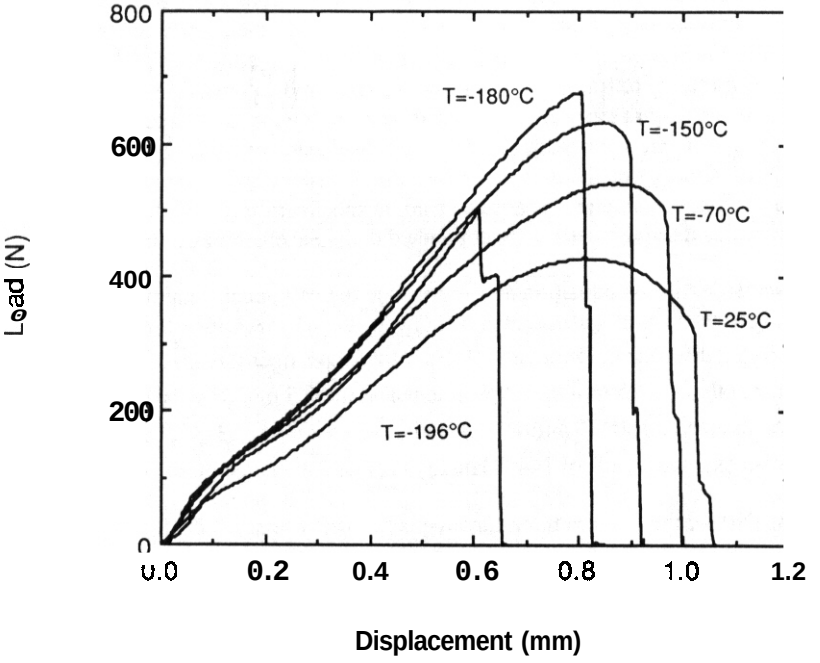

Figure 2. Load-displacement curves as a function of test temperature for the HSLA steel.

We analyzed the data several ways for each material m correlate changes in the fracture mode with changes in the load-displacement curve. This included examining total displacement to failure, displacement to maximum load, and plastic energy absorbed in deforming the specimen up to the maximum load and beyond the maximum load. Each of these shows a transition from relatively low values at low temperatures to higher values at temperatures approaching ambient. The most dramatic "transition," however, was evidenced by the energy absorbed beyond maximum load (ΔE). An example is given in Figure 3 for the A508 steel. With decreasing test temperature, a very steep transition to $\Delta E = 0$ occurs when cleavage fracture becomes predominant.

Increasing deformation rate and intentional defects were found to degrade the utility of the ball punch data for monitoring fracture d e transition. Tests performed under dynamic conditions (ie, displacement rates of a b u t 4 · 200 mm/s) were found to change the fracture d e at 75 K from cleavage to ductile fracture in the steels examined. Simple calculations indicated that heating from plastic deformation

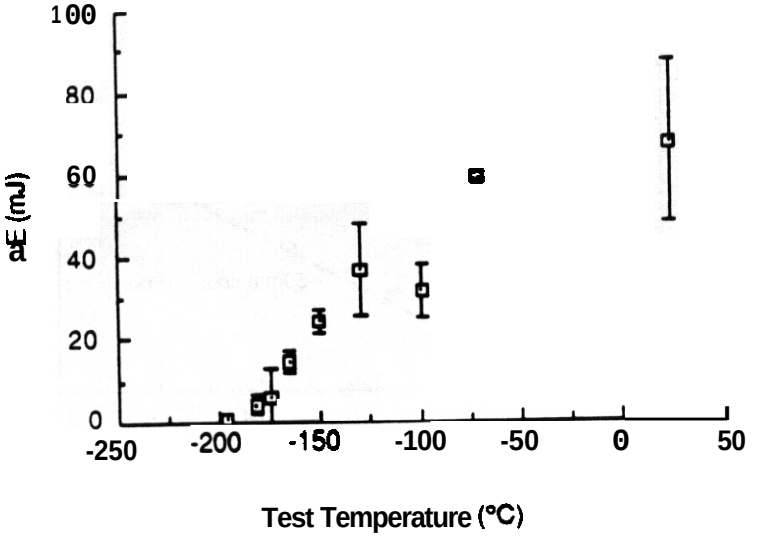

Figure 3 Absorbed energy beyond maximum load as a function of test temperature for the A508 steel.

was sufficiently adiabatic under dynamic conditions to elevate the specimen temperature above the transition. The effect of a concentric hole was to indeed promote fracture, presumably by stress intensification; however, once initiated, cracks grew radially. At low temperatures, the stress field falls off in the radial direction,[14] and hence the cracks grew stably. This produced loaddisplacement curves with no obvious features corresponding to fracture, even when the fracture mode was cleavage. Finally, the presence of an annular trough also promoted fracture and lead to rapid crack propagation around the trough circumference, thus producing a marked drop in the load-displacement curve. However, differences between loaddisplacement curves obtained at high and low test temperatures were less pronounced in specimens containing troughs than those without. Consequently, the optimum test conditions for monitoring fracture mode transition in these small disc specimens appear to be smooth specimens tested under static conditions. To ensure optimum data resolution and temperature control, subsequent tests were conducted at displacement rates of 0.04 mm/s.

Several approaches were taken toward identifying transition temperatures in the ball punch data that were correlatable to Charpy V-notch (CVN) data The correlation leading to the best fit was found to be between the 41 J transition temperature (T_{41}) in a CVN test and temperatures (TSP) at AE = 4.5 and 9 mJ for the 0.25 mm and 0.5 mm thick specimens, respectively. This correlation is shown in Figure 4. The slope of the curve for both the 0.25 mm thick specimens and the 0.5 nun thick specimens is 0.189 °C/°C. Accordingly, for the A508 steel re-austenitization induced a 150 "C shift in T_{41}, and a corresponding 33 °C change in TSP was observed; and in the Linde 80 weld, irradiation induced an estimated shift of 144°C in T_{41} [18], and a change of 29 °C in TSP was measured.

As can be seen in Figure 4, TSP for the 0.5 mm thick specimens lies below that for the 0.25 mm thick specimens. A possible reason for this is as follows. It has been argued that the applied tensile stress should exceed some critical value σ_f^* for cleavage initiation in smooth and blunt notch specimens.[8] Values of σ_f^* have been previously measured for the steels investigated here and range from 1800 MPa to 2400 MPa.[10] A number of analytical and numerical calculations of the stress and strain dismbution in a sheet specimen undergoing hemispherical punching indicate the maximum stresses achieved during punching are of the order 0.7κ, where κ is defined in the constitutive relation $\sigma = \kappa\varepsilon^n$.[14-16] From previous analyses of tensile and instrumented Charpy data on these steels,[9-12] upper estimates of values of κ at temperatures corresponding to AE = 0 are of the order 2000 MPa, and hence, maximum calculated stresses at cleavage fracture would be in the range of 1400 MPa to 1600 MPa. This suggests that some stress intensification occurs, probably due to local necking, with stress intensification factors of the order 1.2 - 1.4. Indeed, this is consistent with the significant plastic deformation and surface roughening observed to occur prior to cleavage fracture in our tests. Moreover, it is expected that for a given amount of local necking, the stress intensification would be smaller in the thicker specimens, thus requiring a lower test temperature to achieve conditions for cleavage fracture. Moreover, this small degree of stress intensification relative to stress intensification factors of about 2.2 in Charpy testing[19] is consistent with the smallerchanges in transition temperature (by about 5 times) exhibited in the disc specimen test compared to CVN tests. That is, increasing stress intensification (M) should increase the slope of the temperature dependent yield stress (σ_y) relation at the point where Mo, $= \sigma_f^*$, and hence, increase the change in the temperature at which this equality is satisfied for the changes in either σ_y or σ_f^*

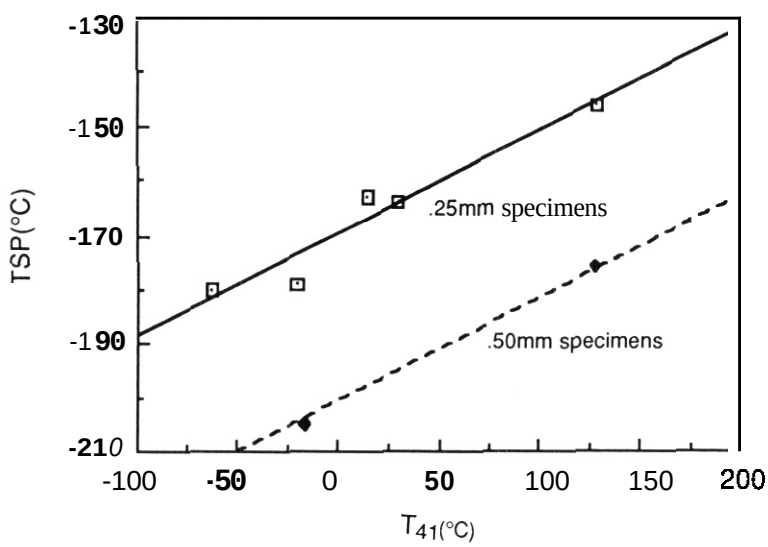

Figure 4. Correlation between the 41 J transition temperature in CVN specimens and the temperature at 4.5 mJ and 9 mJ of absorbed energy beyond maximum load in the ball punch tests on 0.25 mm and 0.5 mm thick specimens, respectively.

CONCLUSIONS

We have investigated several test parameters pertinent to obtaining fracture mode transition information on ferritic steel disc specimens from a ball punch test. It was found that dynamic testing of such small specimens leads to adiabatic heating, and hence testing was limited to static rates. While small concentric holes indeed promote crack initiation, the cracks grow stably into a falling radial stress field, and fracture mode uansition is not obvious from load displacement data. Annular troughs also promote fracture, but the differences in *load-displacement behavior* between ductile fracture and cleavage fracture regimes are reduced. Hence, the bulk of the testing was performed on smooth specimens. It was found that test temperatures at values of absorbed energy AE = 4.5 mJ for 0.25 mm thick specimens and 9 mJ for 0.5 mm specimens correlate well with the 41 J transition temperature in CVN tests, and hence changes in transition temperature induced by either thermal conditioning or irradiation could be monitored by ball punch techniques. However, the ball punch test is less sensitive to changes in transition temperature than the conventional CVN test,

FUTURE WORK

The test is being considered for several irradiation experiments.

REFERENCES

1. G. E. Lucas, Met. Trans. (in press)
2. F. H. Huang, et al, Nucl. Tech.. 57 (1982) 234.
3. M. P. Manahan. et. al, ASTM-STP-888 (1986) 17.
4. A. Okada, et. al, Trans JIM, 29.2 (1988) 99
5. G. Khose, et al. J. Nucl. Matl., 141/143 (1986) 513.
6. T. Misawa, et. al., J. Nucl. Mater., 150 (1987) 194.
7. J. M. Baik, et. al., ASTM-STP-888 (1986) 110.
8. G. R. Odette, G. E. Lucas, J. Nucl. Mater., 117 (1983) 264.
9. G. R. Odette and G. E. Lucas, EPRI NP-6114 (1989).
10. G. E. Lucas, et al, Fus. Tech.. 10, 3, parts 2A&2B (1986) 728.
11. G. R. Odette, et al, J. Nucl. Mater., 122/123 (1984) 442.
12. G. E. Lucas. et al, Mic. Sci., 13 (1986) 55.
13. S. Timoshenko, Strength of Materials, II, Van Nostrand, NY (1941) 156.
14. N. M. Wang, J. Appl. Mech.. (1970) 431.
15. J. R. Knibloe, R. H. Wagoner, Met. Trans., 20A (1989) 1509.
16. S. Levy, et al, ASTM-STP-647 (1978) 238.
17. G. E. Lucas. A. Okada, M. Kiritani, J. Nucl. Mater., 141-143 (1986) 532.
18. R. Lott, et. al, ASTM-STP-909 (1986) 242.
19. R. A. Wullaert, et al, ASTM-STP-484 (1970) 20.

DEVELOPMENT OF PRESSURIZED TUBE SPECIMEN FOR CREEP TESTING OF BERYLLIUM - W. S. Neef, R. W. Moir (Lawrence Livermore National Laboratory), E. K. Opperman (Westinghouse Savannah River Company), and M. L. Hamilton (Pacific Northwest Laboratory)

PURPOSE

The purpose of this work was to demonstrate that creep tests could be performed on beryllium in the same pressurized tube geometry as is commonly used in the FFTF/MOTA.

SUMMARY

The ability to fabricate a pressurized tube specimen from beryllium was successfully demonstrated. The specimen failed at a midwall hoop stress of about 32 ksi in a burst test at 500°C.

PROGRESS AND STATUS

Introduction

Most of the proposed ITER blanket designs call for the use of bervllium as a neutron multiolier to increase the tritium breeding ability of the blanket. In addition to its excellent neutron multiplication characteristics, it is also a low activation material with high thermal conductivity. The main issues related to the use of beryllium focus on thermal and tritium transport, mechanical performance, and compatibility.[1] As a nonstructural material that will probably rely on stainless steel for its support, the most important performance questions concern deformation, stress on structural components and thermally induced cracking. Due to the previous use of beryllium in both the fission reactor and aerospace programs, a significant data base exists for the thermal, mechanical, physical and irradiation behavior of beryllium, primarily in the form of relatively dense material containing 1 to 2 weight percent BeO. Lower density forms of beryllium are proposed, however, for ITER blanket designs.

The baseline physical properties of beryllium are fairly well understood.[1] Mechanical properties, however, are rather sensitive to microstructural variations as well as impurities, both of which are dependent on fabrication techniques. While beryllium will not be a structural component in the blanket, it is nonetheless important to identify conditions of differential thermal expansion, swelling and creep where the material will crack. Only minimal data are available on the effects of radiation on the properties of beryllium in the temperature range of interest. In particular, irradiation creep needs to be determined to predict the stress relief arising from stresses generated by differential swelling and by contact between beryllium and steel.

Creep data on beryllium are virtually non-existent, particularly under neutron irradiation. One of the most successful means of generating irradiation creep data has been through the use of pressurized tubes in the FFTF/MOTA. The current effort was designed to demonstrate not only that such specimens could be successfully fabricated from beryllium but also that burst tests on such specimens would provide valid data, i.e., that failures would occur in the main body of the tube rather than in association with the end hardware attachments.

Experimental Procedure

Pressurized tube specimens comprise a tube and two end caps, one of which has a small machined hole which is closed with a laser weld after specimen pressurization. The end caps are typically made of the same material as the tube and are welded to the tube by an electron beam process. Welding in this case was viewed as undesirable due to the likelihood of enhanced susceptibility to radiation damage in the recrystallized zone occurring in the weld joint. Brazing was considered unacceptable because no suitable braze material is compatible with the sodium coolant in FFTF. A diffusion bonding technique was therefore developed to enable the end caps to be attached to the beryllium tube.[2] The bonds were leak checked to verify the integrity of the bonding technique and a pressure test was performed to demonstrate the strength of the bonds. While a number of the specimens were actually fabricated, ultimately only one leak-tight specimen was obtained.

Results and Discussion

Brush Wellman provided the beryllium used for specimen fabrication. It was made to Lawrence Livermore National Laboratory specification MEL 1319, which is similar to Brush Wellman specification S-65. It contains ~1% BeO and has an average grain size (i.e., was fabricated from an average powder size) of ~12 μm. Nominal room temperature values of yield strength and fracture toughness are 35 ksi (minimum) and 10 ksi(in)$^{1/2}$, respectively (241 MPa and 11 MPa(m)$^{1/2}$).

Drawings of the specimen components are shown in Figure 1a. The beryllium tube and end caps were machined from solid rod stock to very tight tolerances to ensure a successful diffusion bond. The thermal expansion characteristics employed are given in Figure 2. The tube specimen was nominally 0.1800 ± 0.0005 inches (4.572 ± 0.0127 mm) in diameter with a wall thickness of 0.0145 inches (0.3683 mm). The wall thickness was reduced slightly (0.0005 inches, or 0.0127 mm) at the ends to create a ledge on which the end caps rested. The end caps were straightforward plugs, i.e., similar to the standard end cap but without grooves for radiography, etc. The components were diffusion bonded at 1100°C for one hour in a vacuum chamber that measured 10^{-6} to 10^{-7} torr at room temperature.

The first bonding attempt employed a molybdenum fixture split at its center plane and bolted together. The thin film of release agent between the two halves of the fixture led to a slight loss of axial symnetry within the fixture and resulted in small leaks in the finished specimen at positions located 90° from the split line of the fixture.

The second attempt successfully employed both beryllium rings and molybdenum backup rings, as shown in Figure 1b. The beryllium rings were placed on the outside of the specimen to facilitate the bonding process, as shown in Figure 1b, while the molybdenum backup rings were used to hold the assembly together. No attempt was made to prevent the beryllium ring from bonding to the outside of the beryllium tube; while the ring was left in place for the current demonstration, it was to be machined away for any creep tests placed in the FFTF/MOTA. The molybdenum rings were allowed to fall off the assembly as it cooled from the diffusion bonding temperature.

The molybdenum rings were 0.25 inch (6.35 mm) thick and measured 1.0 inch in outer diameter by 0.50 inch inner diameter (25.4 x 12.7 mm). The beryllium rings were 0.25 inch thick, 0.50 inch in outer diameter, and 0.18 inch inside diameter (6.35 X 12.7 x 4.57 mm). No drawings exist for these components; rather, the rings were machined to fit the tube so the nominal diametral clearance was 0.001 inch (0.025 mm) at both the 0.18 and 0.50 inch (4.57 and 12.7 mm) diameters.

A Cu-Ni tube was brazed with Q-SIL (28% copper, balance silver) to the fill plug to pressurize the specimen for this demonstration as shown in Figure 1b. Titanium hydride powder was mixed in a 30:1 ratio with a lacquer-based carrier and painted on the surfaces to be brazed to enhance the wetting of the beryllium by the braze. Brazing a fill tube was chosen in this case instead of using the standard laser-welded fill hole to facilitate leak testing of the assembly with helium prior to the burst test. The specimen was soaked at 760°C for five minutes prior to brazing, which was performed at temperatures that ranged from 780 to 810°C in a vacuum chamber that measured 10^{-6} to 3 x 10^{-7} torr at room temperature. If the wetting agent had not been used, much higher temperatures would have been required. The specimen was allowed to cool overnight after brazing the pressurization tube into place. Several views of the finished assembly are shown in Figure 3.

The burst test was performed at 500°C in air after stabilizing at the test temperature for about four hours. The pressurizing medium was helium. The pressure was increased two times per minute, as shown in Figure 4, at an average rate of about 0.775 ksi/minute (5.3 MPa/minute) until failure occurred at an internal pressure of 6.52 ksi (45 MPa), corresponding to a midwall stress of about 32 ksi (220 MPa).[2] The tube ruptured with ~3% ductility.

The ruptured tube is pictured in Figure 5. The burst was a small rupture in the middle of the tube, shown at higher magnification under a scanning electron microscope in Figure 6. Figure 7 shows a view inside the crack at the location indicated by the arrow in Figure 6. An optical metallograph is shown in Figure 8 of the diffusion bonds between the tube and both the end plug and ring, taken at the end of the tube.

Figure 8 demonstrates that the bond between the tube and the end cap was quite good, with no visible gaps in the metallographic section. A large amount of porosity is evident on the surface of the tube in Figure 6. The same porosity is visible in Figure 8, where it is clear that the pores on the outer walls of the tube have opened up significantly, presumably during the burst test. The fracture surface shown in Figure 7 appears to show a reasonable amount of localized deformation, most likely a result of shearing individual grains until the pores link up.

CONCLUSIONS

Pressurized tubes can be fabricated from beryllium with beryllium end plugs. Failure in a pressure ramp test at 500°C occurred at a stress of 32 ksi (220 MPa).

FUTURE WORK

Specimen fabrication should be further refined to provide pressurized tubes without beryllium rings on the ends. The parameters for welding of the laser fill hole should be developed.

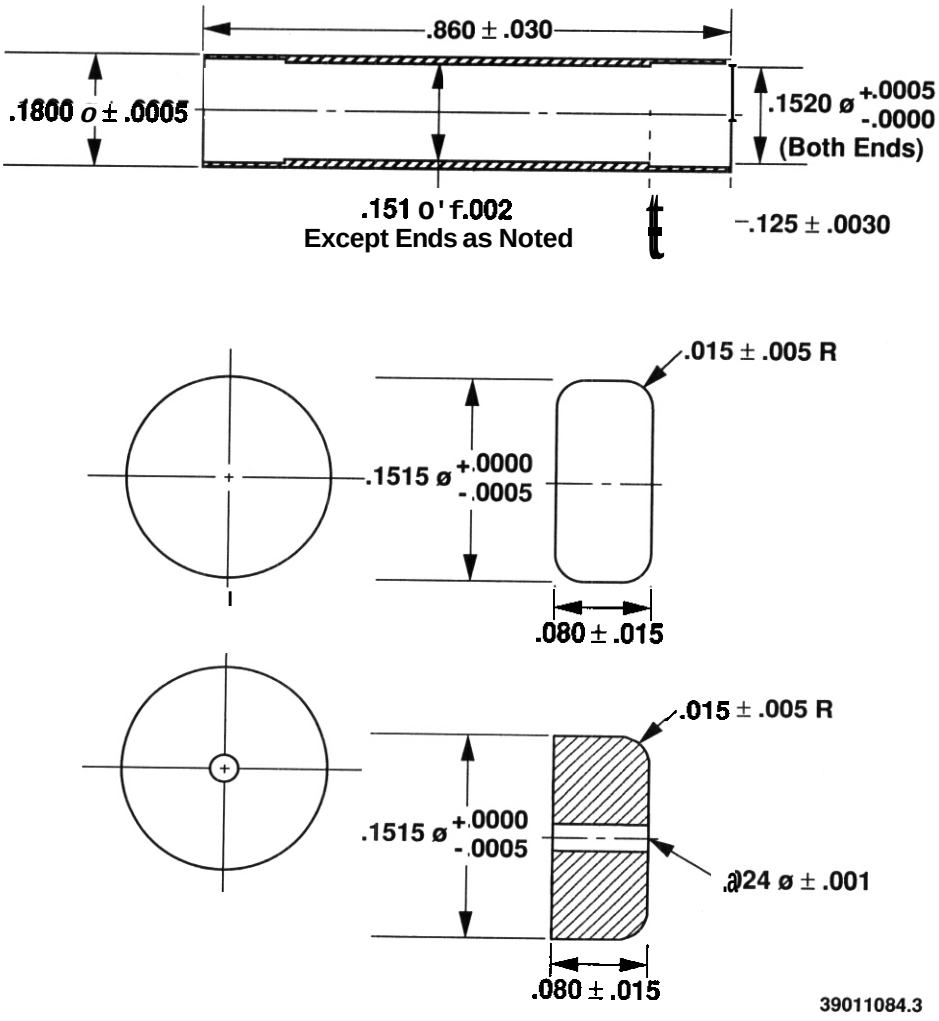

Figure la. Components of beryllium pressurized tube specimen: beryllium tube, bottom plug and top fill plug. Dimensions given in inches.

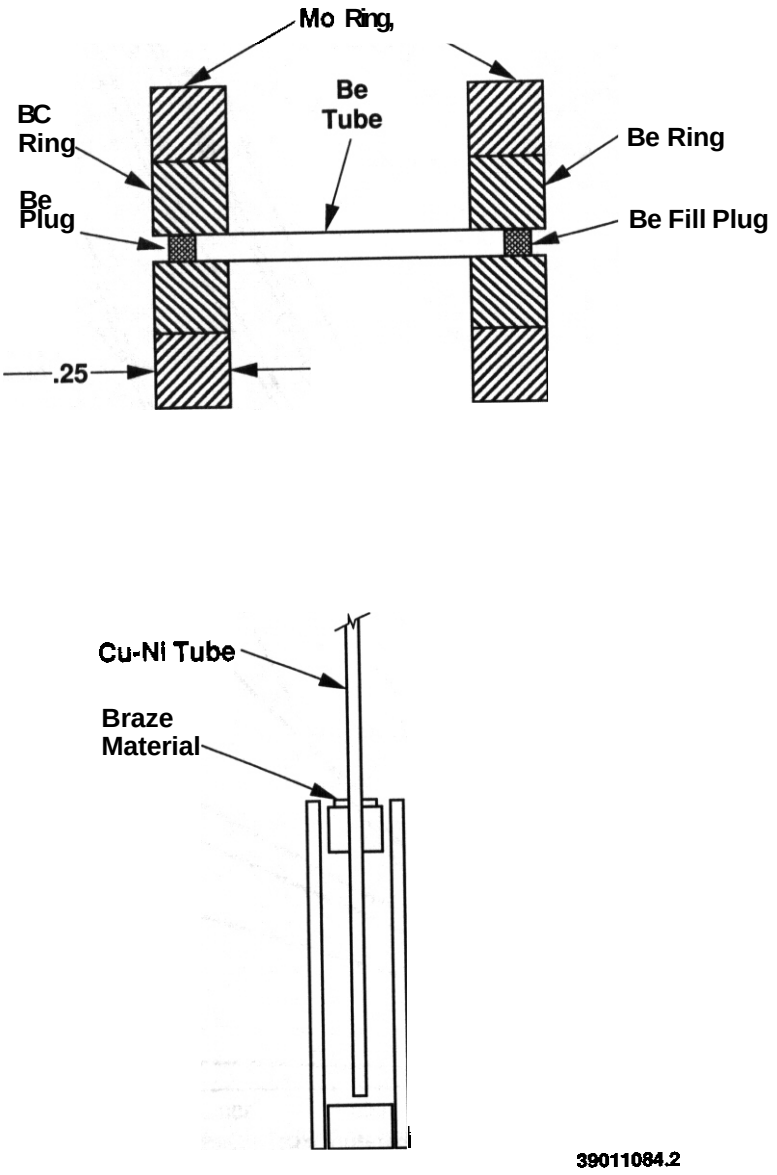

Figure lb. Pressurized tube assembly with beryllium rings and molybdenum backup rings. Dimensions given in inches.

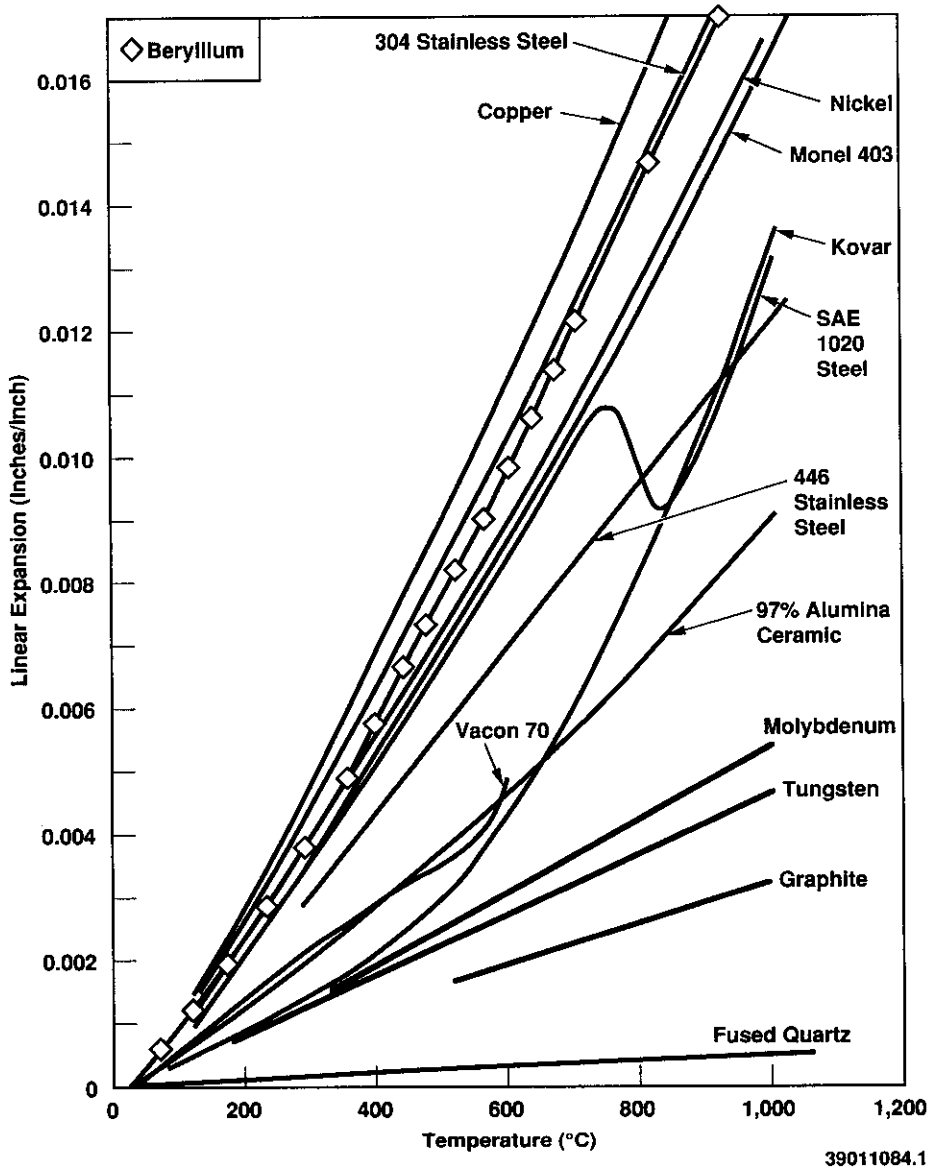

Figure 2. Thermal expansion characteristics of beryllium compared to other materials.

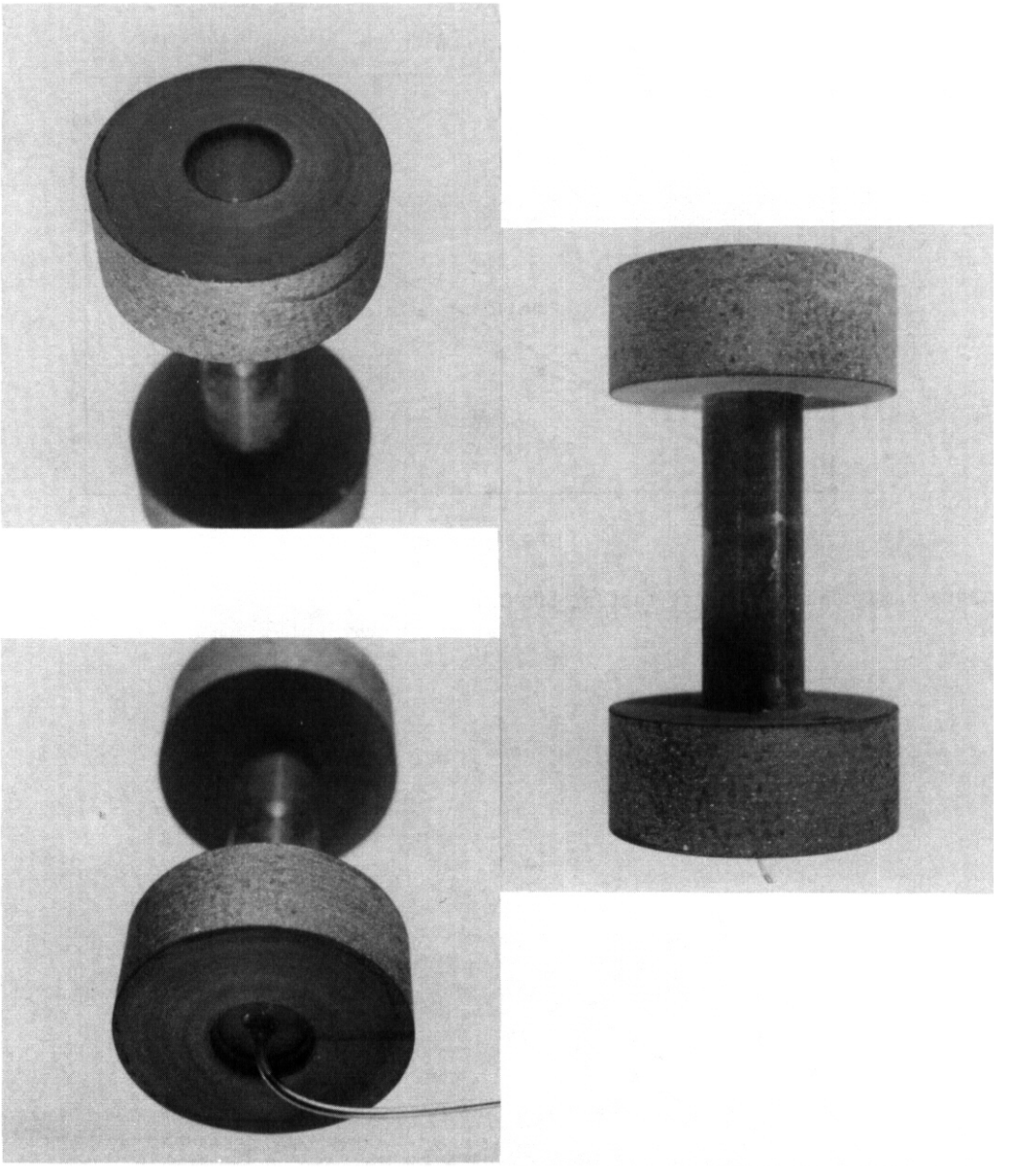

Figure 3. Pressurized tube of beryllium after removal of molybdenum backup rings, showing beryllium rings attached to ends of specimen.

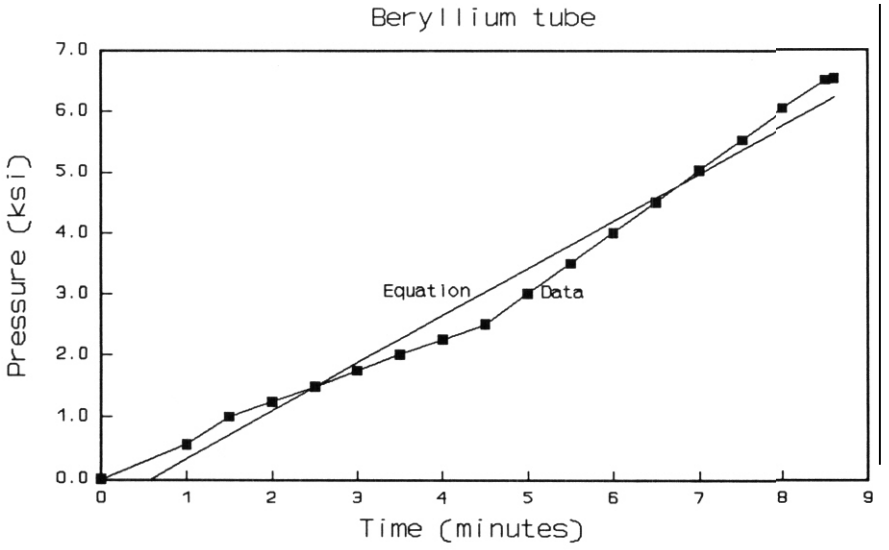

Figure 4. Pressure ramps data for burst test at 500°C.

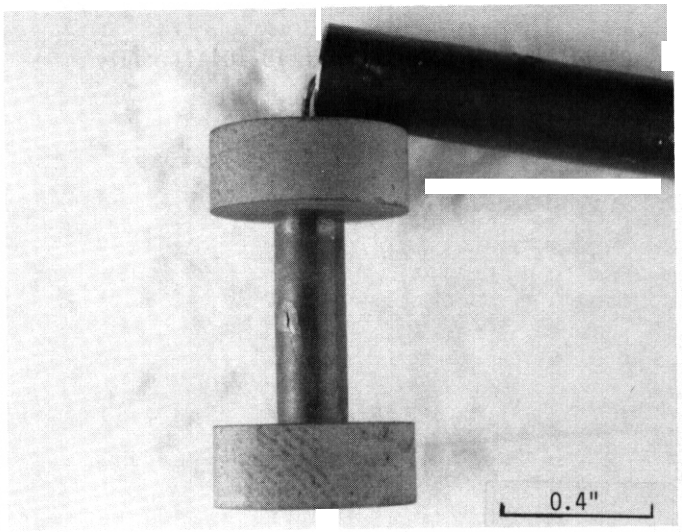

Figure 5. Rupture tested specimen of beryllium showing failure location

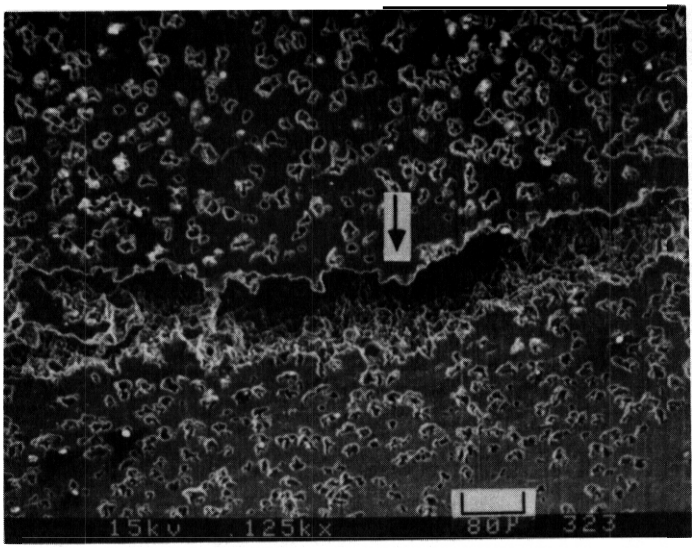

Figure 6. Scanning electron micrograph of crack in beryllium burst test tube.

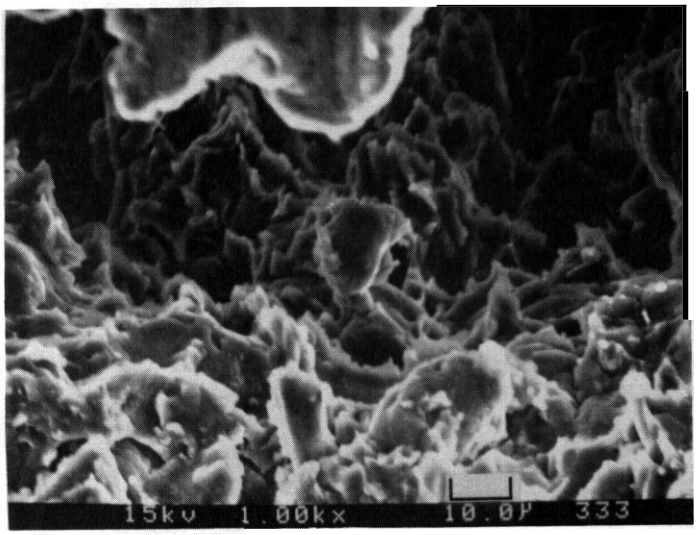

Figure 7. Scanning electron mictograph of inside of crack at location shown by arrow in previous figure.

Figure 8. Optical metallograph showing porosity, bond between beryllium ring and berryllium tube (left arrow), and bond between beryllium tube and beryllium end cap (right arrow).

REFERENCES

1. ITER Materials Data Base Report, to be published.

2. W. S. Neef, Beryllium Pressure Vessels for Creep Tests in Magnetic Fusion Energy, UCRL-ID-104441, July 20, 1990.

2. DOSIMETRY, DAMAGE PARAMETERS, AND ACTIVATION CALCULATIONS

NEUTRON DOSIMETRY FOR THE MOTA-IF EXPERIMENT IN FFTF - L. R. Greenwood and L. S. Kellogg, Pacific Northwest Laboratory[a]

OBJECTIVE

To provide dosimetry and damage analysis for fusion materials irradiation experiments.

SUMMARY

Neutron fluence and spectral measurements are reported for the MOTA-IF experiment in the Fast Flux Test Facility (FFTF). The irradiation was conducted from November 18, 1987, to January 8, 1989, for a total exposure of 335.4 EFPD. The maximum fluence was 12.7 x 10^{22} n/cm^2, 9.56 x 10^{22} above 0.1 MeV producing 39.1 dpa in iron. Neutron energy spectra were adjusted at three positions and gradients were measured at nine other locations.

PROGRESS AND STATUS

Twelve dosimetry capsules were positioned at different axial locations in the MOTA-IF assembly. Each stainless steel capsule measured about 2.1 cm long by 0.48 cm o.d. and contained dosimetry wires for either spectral or gradient measurements. The three spectral capsules contained Fe, Ti, Ni, Cu, 0.1% Co-A1 alloy, 0.13% Sc in MgO, 0.825% ^{235}U in V, 0.936% ^{239}Pu in MgO, and ^{237}Np oxide monitors; the gradient capsules contained Fe and 0.1% Co-A1 alloy wires. The Co, Sc, U, Pu, and Np materials were separately encapsulated in V.

Following irradiation, each dosimetry capsule was opened in a hot cell and each individual monitor was identified and mounted for gamma analysis. The measured activities were then converted to saturated activities by correcting for the sample weight, atomic weight, isotopic abundance, gamma absorption, reactor power history, and fission yield, as needed. Neutron self-shielding effects were not significant since the Co, Sc, U, and Pu were dilute alloys and the FFTF neutron spectrum has few neutrons at lower neutron energies.

Neutron burnup effects were found to be quite significant for the fission monitors and a small correction was necessary for the ^{59}Co(n,g) reaction. In the case of ^{59}Co, this correction can be applied using an iterative procedure since the reaction itself is the sole source of the burnup. Hence, the burnup must be at least as great as predicted by the measured value, namely exp(-st), where s is the reaction rate and t the total exposure time. Having corrected the reaction rate, the procedure can thus be repeated until it converges. This iterative approach works quite well except for very lengthy exposures where we go beyond the equilibrium activity. The procedure also includes the burnup of the product isotope (e.g., ^{60}Co). If we can determine the approximate ratio of the burnup reaction rate of the product isotope to that of the target isotope, then we can simply maintain this ratio during the iterative procedure. This approach is generally sufficient since the net corrections are not so sensitive to the reaction rates for the product isotope. In the case of the ^{59}Co(n,g) reaction, the maximum burnup effect was 2.8%.

Neutron burnup effects were found to be much larger and more difficult for the fission reactions. In all three cases, the fission reaction is not the sole source of the burnup since the (n,gamma) cross section must also be included. Unfortunately, we have no measure of the (n,gamma) reaction rate. However, we can readily calculate the rates using calculated neutron spectra. At each spectral location, neutron spectra were provided by R. Simons (Westinghouse Hanford) based on the cycle 9A irradiation.' These spectra were used with the STAY'SL computer code' to determine reaction rates for both the fission and gamma reaction. Since the absolute measured fission rates were not known, we assumed that the ratios of gamma to fission were the same as the calculations and determined the total burnup cross sections from the measured fission rates. Corrections were done separately for each fission product in order to account for the separate decay and burnup rates for each product isotope. The results were then averaged to obtain a first order correction to the burnup effects. An iterative procedure was used to determine a second order correction, which was found to be sufficient. The burnup corrections were thus determined to be between 10 and 25%. It should be noted that although metal fuel was used in the IF irradiation, the 9A calculations were based on the previous oxide fuel loadings. The effects of these changes are unknown.

In the case of ^{237}Np, there is also concern that we can breed ^{238}Pu, which will then also contribute to the fission yields. Using the calculated reaction rates derived from the calculated neutron spectra, we estimate that this effect may be as large as 4%. However, if the ^{238}Pu fission yields are similar to those from

---

(a) Pacific Northwest Laboratory is operated for the U.S. Department of Energy by Battelle Memorial Institute under Contract DE-AC06-76RLO 1830.

^{237}Np, then there may be only a small difference in the true fission rates for ^{237}Np. It is also possible that (gamma,n) effects are present; however, past experiments have shown that this effect is not significant at in-core positions.

The corrected reaction rates are listed in Tables 1 and 2. The values have an estimated absolute uncertainty of about 5%. although there is an additional uncertainty of about 5% for the fission reactions due to problems in determining the burnup rates. These rates appear to be in reasonable agreement with previous measurements[3,4] except for the fission reactions. Neither of the previous experiments made any attempt to determine neutron burnup corrections for the fission reactions. Hence, our values are about 20-30% higher than previous measurements, allowing for differences in reactor power and core changes. As noted previously, the present results are for metal fuel, whereas both previous experiments were for oxide fuels.

The measured activities were used as input to the STAY'SL computer code to adjust the neutron spectra calculated for cycle 9A. STAY'SL performs a generalized least-squares adjustment of all measured and calculated values including the measured activities, calculated spectra, and neutron cross sections. Neutron cross sections and their uncertainties were generally taken from ENDF/B-V, although new data were available from ENDF/B-VI for the $^{46}Ti(n,p)$ and $^{63}Cu(n,a)$ reactions. The adjusted neutron fluence values are listed in Table 3. The neutron spectral adjustments for the three positions are shown in Figures 1-3 where the solid line is the calculated spectrum and the dotted line the adjusted spectrum. In all three cases, there were significant spectral adjustments. In general, the adjusted spectra reduce the flux at lower neutron energies but increase the flux from about 0.1 up to several MeV. The fast neutron flux is thus higher than previously reported, mainly due to the burnup effects for the fission detectors.

Damage calculations were also performed for the three spectral positions using the SPECTER computer code.[5] Opa and helium rates for Fe are shown in Table 3. Damage parameters for other elements or compounds are also available.

Table 1
Activity Measurements at Spectral Positions (values in atom/atom-s at 291 MW)

Material Reaction	M66 -59.4 cm	M67 -2.6 cm	M68 t66.3 cm
$^{54}Fe(n,p)^{54}Mn$	3.21E-12	2.72E-11	1.06E-12
$^{58}Fe(n,g)^{59}Fe$	3.17E-11	3.50E-11	1.72E-11
$^{46}Ti(n,p)^{46}Sc$	3.55E-13	2.92E-12	1.14E-13
$^{45}Sc(n,g)^{46}Sc$	9.05E-11	1.15E-10	4.61E-11
$^{58}Ni(n,p)^{58}Co$	4.34E-12	4.05E-11	1.48E-12
$^{59}Co(n,g)^{60}Co$	1.41E-09	2.15E-10	8.13E-10
$^{63}Cu(n,a)^{60}Co$	1.76E-14	1.75E-13	5.54E-15
$^{58}Ni(n,x)^{57}Co$	8.89E-15	8.17E-14	3.13E-15
$^{60}Ni(n,p)^{60}Co$	7.81E-14	6.96E-13	2.67E-14
$^{235}U(n,f)$	7.58E-09	8.18E-09	3.19E-09
$^{239}Pu(n,f)$	5.99E-09	8.16E-09	3.32E-09
$^{237}Np(n,f)$	5.65E-10	2.02E-09	1.75E-10

Table 2
Activity Gradients for FFTF MOTA-IF (values in atom/atom-s at 291 MW)

Capsule	Ht., cm	$^{54}Fe(n,p)^{54}Mn$	$^{58}Fe(n,g)^{59}Fe$	$^{59}Co(n,g)^{60}Co$
69	-67.6	1.317E-12	3.264E-11	1.785E-09
66	-59.4	3.213E-12	3.168E-11	1.442E-09
70	-47.1	1.068E-11	3.295E-11	9.688E-10
71	-39.0	1.854E-11	2.758E-11	4.196E-10
72	-23.2	2.783E-11	3.172E-11	2.452E-10
67	-2.7	2.719E-11	3.497E-11	2.153E-10
73	15.7	2.205E-11	3.147E-11	2.201E-10
74	24.1	1.850E-11	2.833E-11	1.877E-10
68	66.3	1.062E-12	1.719E-11	8.237E-10
75	74.8	5.103E-13	1.314E-11	6.624E-10
76	108.0	4.015E-14	5.000E-12	2.751E-10
77	122.3	1.626E-14	3.607E-12	1.927E-10

Table 3
Neutron Fluences and Damage Parameters (MOTA-IF, 335.4 EFPD, 291 MW)
(Uncertainties in %included in parentheses)

Position	Ht., cm	Neutron Fluence x10^{22} n/cm^2 Total	>0.1 MeV	>1 MeV	Damage in Fe dpa	He, appm
66	-59.4	5.62 (29)	3.24 (34)	0.295 (22)	11.3	0.32
67	-2.6	12.7 (13)	9.56 (18)	1.74 (17)	39.1	3.07
68	+66.3	2.16 (28)	1.27 (35)	0.096 (21)	4.22	0.102

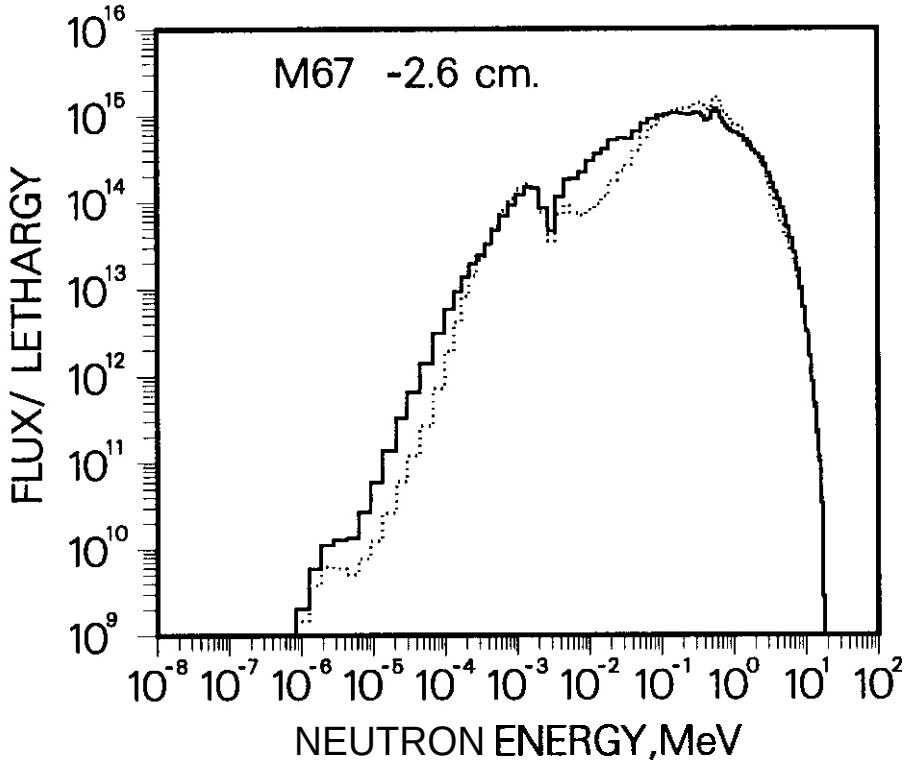

Figure 1. Calculated (solid line) and STAY'SL-adjusted (dotted line) neutron energy spectrum for capsule 67 at -2.6 cm in the FFTF MOTA-1F assembly.

The flux and damage gradients at other positions can be found from the activity gradient data in Table 2, which is shown in Figure 4. Note that the ^{58}Fe and ^{59}Co(n,g) reactions peak outside of the core since they are sensitive to the lower energy neutrons. The unusual behavior of the Co reaction is due to resonance effects.

The fluence above 0.1 MeV was determined from the activity for the ^{54}Fe(n,p) reaction. The spectral-averaged cross section was determined at each of the three spectral positions. Since the spectral changes are quite large, we assumed a linear dependence of the spectral-averaged cross section on the height. The fluence above 0.1 MeV was then determined by dividing the ^{54}Fe(n,p) activity by the calculated spectral-averaged cross sections. The resultant fast fluences are shown in Figure 5. Similarly, the ^{58}Fe(n,g) and ^{59}Co(n,g) reactions were used to determine the fluence below 0.1 MeV and the total fluence gradients are also shown in Figure 5. Dpa in Fe was then determined assuming a fixed ratio of dpa to fluence above 0.1 MeV; the dpa gradients are also shown in Figure 5. These procedures are only approximate since we only had three spectral measurements. Additional spectral monitors have been included with future runs in cycles 11 and 12 so that we can determine the fluence and damage gradients more precisely.

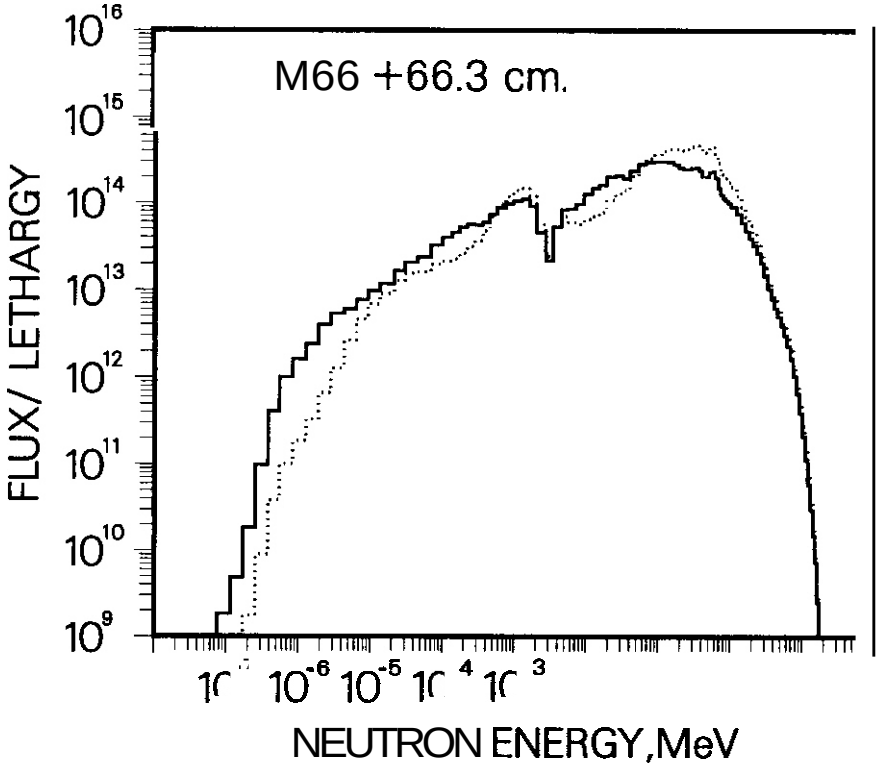

Figure 2. Calculated (solid line) and STAY'SL-adjusted (dotted line) neutron energy spectrum for capsule 66 at -59.4 cm in the FFTF MOTA-IF assembly.

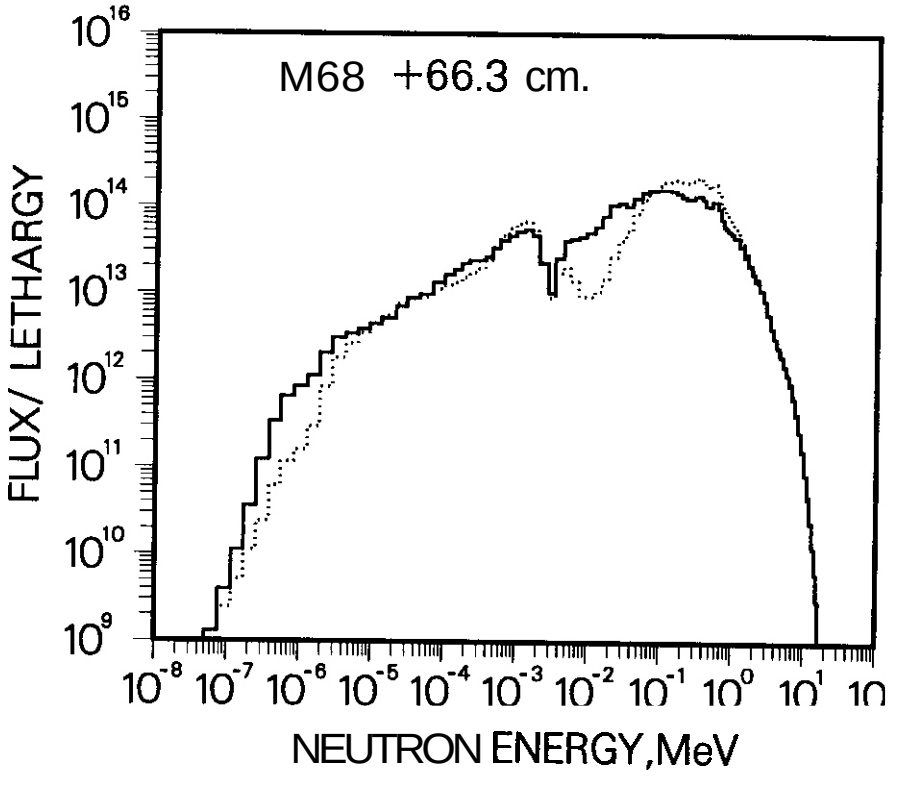

Figure 3. Calculated (solid line) and STAY'SL-adjusted (dotted line) neutron energy spectrum for capsule 68 at +66.3 cm in the FFTF MOTA-IF assembly.

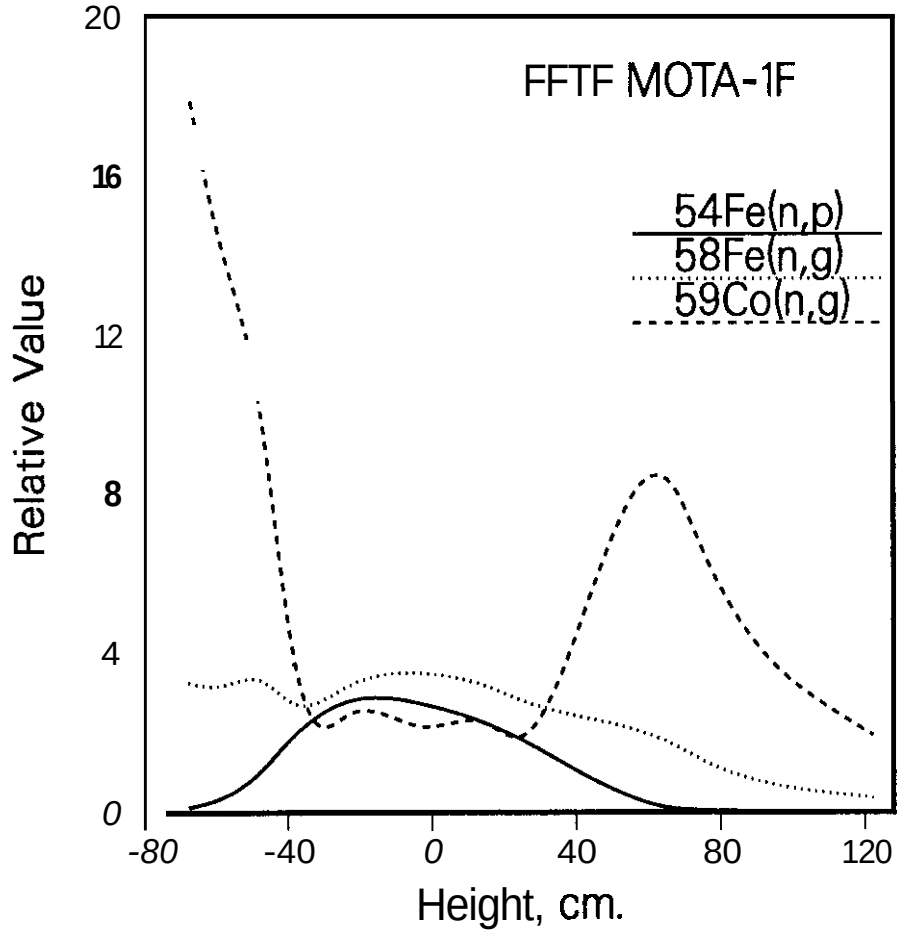

Figure 4. Activity gradients are shown as a function of height for the $^{54}Fe(n,p)$, $^{58}Fe(n,g)$, and $^{59}Co(n,g)$ reactions.

FUTURE WORK

Dosimetry is now being fabricated for the MOTA-28 in FFTF for irradiation with cycle 12 starting in about May 1991. More comprehensive dosimetry will be available from cycle 11, which contains 12 spectral and 21 flux gradient sets. These samples should be received in about June 1991. We are also providing dosimetry for the MFE-RB-200J1, -400J1, and JP-17, 18, and 19 experiments in the High Flux Isotopes Reactor at Oak Ridge National Laboratory.

REFERENCES

1. Private communication, R. Simons, Westinghouse Hanford Company, May 1990.

2. F. G. Perey, Least Squares Dosimetry Unfolding: The Program STAY'SL, ORNL/TM-6062 (1977).

3. R. L. Simons, Damage Analysis and Fundamental Studies Quarterly Progress Report, DOE/ER-0046/21, pp. 10-14, May 1985.

4. L. S. Kellogg, W. M. Mc Elroy, and W. Y. Matsumoto, FERRET-SAND II Physics-Dosimetry Analysis for the FTR MOTA-1E Experiments, PNL-NOC Report, December 1989.

5. L. R. Greenwood and R. K. Smither, SPECTER: Neutron Damage Calculations for Materials Irradiations, ANL/FPP-TM-197, January 1985.

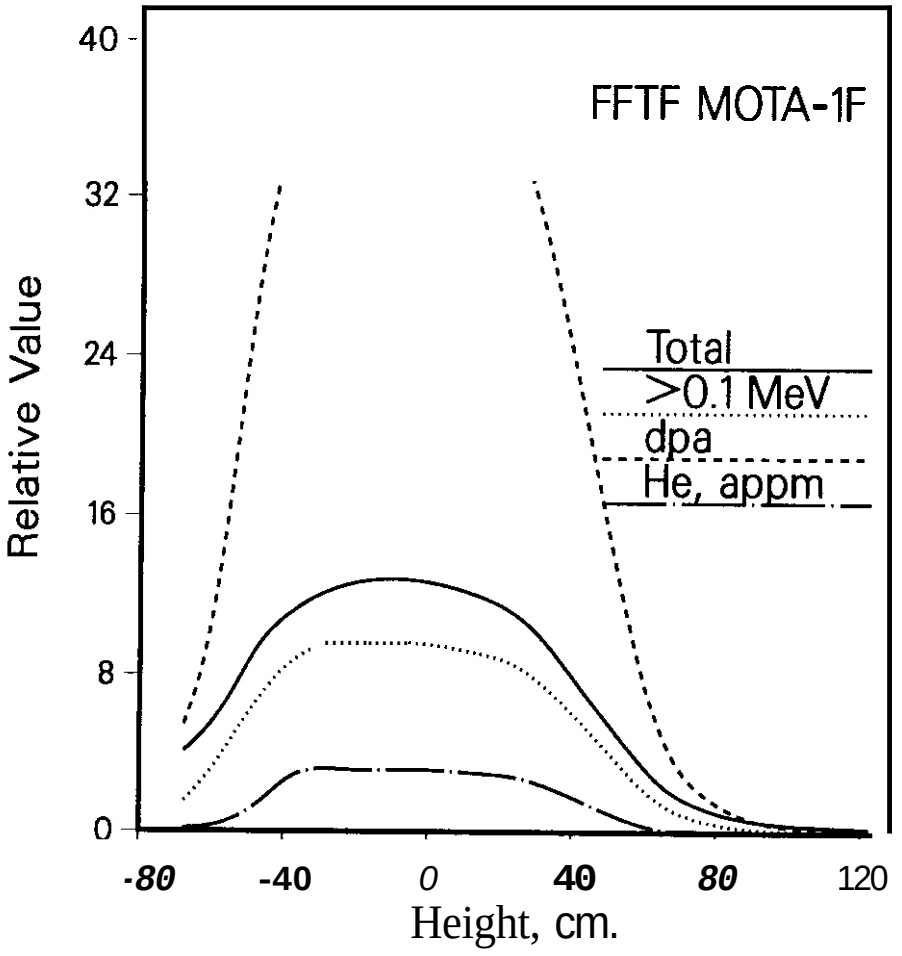

Figure 5. Fast (> 0.1 MeV) and total neutron fluences and Fe (dpa) and He (appm) gradients are shown as a function of height in the MOTA-IF assembly.

PUBLICATIONS

The following papers were presented at the Seventh ASTM-EURATOM Symposium on Reactor Dosimetry in Strasbourg, France, August 27-31, 1990, and will be published in the proceedings.

L. R. Greenwood and D. L. Bowers, Measurements of Activation Cross Sections for Fusion Reactor Applications.

D. L. Smith, J. W. Meadows, and L. R. Greenwood, Microscopic Integral Cross Section Measurements in the Be(d,n) Neutron Spectrum for Applications in Neutron Dosimetry, Radiation Damage, and the Production of Long-Lived Radionuclides.

E. M. Zsolnay, H. J. Nolthenius, L. R. Greenwood, and E. J. Szondi, Reference Data File for Neutron Spectrum Adjustment and Related Radiation Damage Calculations.

3. MATERIALS ENGINEERING AND DESIGN REQUIREMENTS

No contributions.

4. FUNDAMENTAL MECHANICAL BEHAVIOR

No contributions.

5. RADIATION EFFECTS: MECHANISTIC STUDIES, THEORY, AND MODELING

MOLECULAR DYNAMICS OF COLLISION CASCADES WITH COMPOSITE PAIR/MANY-BODY POTENTIALS - S. P. Chou and N. M. Ghoniem (University of California, Los Angeles)

OBJECTIVE

The displacement damage threshold and the size of void-defect recombination volume are two important parameters for a fundamental understanding of radiation effects. This work is aimed at a new molecular-dynamics code, CASC-MD, for low-energy ion collisions in solids. A composite pair/many-body potential is developed and used for simulations of low-energy collision cascades in copper. Good agreement is obtained with experimental data at 10 K.

SUMMARY

An empirical, composite interatomic potential is developed to describe interaction of energetic particles by pair potentials at high energies and many-body potentials at low energies. Molecular-dynamics studies of low-energy collision cascades are performed. The displacement threshold surface in copper is investigated and compared to experimental data. Our computer simulations show good agreement with the experimental results of King and Benedek at 10 K.

PROGRESS AND STATUS

1. Introduction

Pair-interaction potentials for the description of collision-cascade dynamics have been widely used to investigate the transport of ions in solids and the generation of atomic displacements. Satisfactory results have been achieved by using numerical simulation techniques such as the Monte Carlo and molecular dynamics (MD) methods [1-14]. Displacement threshold energies, however, are generally in the range of few times the lattice binding energy. Therefore, many-body effects are expected to be important in the sub- to tens-of-eV range where pair potentials do not provide an accurate description of atomic interactions. Furthermore, the many-body interaction of atoms at low energy can affect the morphology of the collision cascade because its range of influence is greater than that of pure pair potentials. Therefore, in order to accurately treat cascade dynamics, it is necessary to develop a more realistic treatment of atomic interactions at low energies. A simple many-body potential based on the embedded atom method (EAM) is used in this work.

At high incident-ion energies, the interaction between the incident ion and a stationary one is primarily that of a pair-interaction type. As the kinetic energy decreases, the effects of the surrounding lattice become more significant and the interaction must contain many-body (local) contributions.

The EAM approach has been successfully applied to a variety of problems where the solid is very near its equilibrium configuration. However, the method is not ab *initio*, but rather can be viewed as a phenomenological approach that is based on density functional theory. The Hohenberg-Kohn theorem [19] states that the total energy $E[\rho(r)]$ is a functional of the electron density $\rho(r)$. The exact form of the functional dependence is not unique, and empirical approaches must be followed to determine constants associated with the assumed form. Although simpler approaches to the determination of the embedding functional and associated constants have recently been reported in the literature [20,21], we will use the EAM approach as originally developed by Daw and Baskes [15,16] and the approximations of Foiles [17]. It is recognized that the many-body contributions to the potential are reasonably well represented by the EAM. However, the atomic displacement process requires further knowledge of the potential at atomic separation distances that are shorter than the range of EAM applicability. In Section 2, we describe an empirical method to determine a suitable composite potential for copper that covers all ranges of interatomic distances. The computational method is then described in Section 3. Results of cascade simulation in copper are given in Section 4, and conclusions follow in Section 5.

2. Composite Potential

In order to treat the atomic interaction in a continuous manner, a potential that preserves the nature of established interatomic potentials at the two energy extremes must be used. In our approach, Ziegler's pair potential [22] is selected to describe the atomic interactions at the high-energy end and an approximation to the EAM many-body potential at the low-energy end. For the transition region, a cubic-spline potential is used which allows continuity of this composite potential throughout the entire energy range. The high-energy pair potential is represented by Ziegler *et al.* [22] in the form

$$\phi_Z(R_{ij}) = \frac{Z_i Z_j e^2}{r} \sum_{k=1}^{4} c_k e^{-b_k R_{ij}/a_0} \quad , \tag{1}$$

where Z_i and Z_j are the atomic numbers of the interacting particles i and j, respectively, and R_{ij} is the separation distance between them; e is the electron charge; c_k and b_k are constants; and a_0 is the screening length [22].

The approximate many-body EAM potential is derived by Foiles [17], based on the EAM framework originally developed by Daw et al. [15,16], and it has the form

$$\phi_{EAM}(R_{ij}) = \phi_{ij}(R_{ij}) + 2\frac{\partial F_i(\bar{\rho}^a)}{\partial \rho}\rho^a_{ij}(R_{ij}) + \frac{\partial^2 F_i(\bar{\rho}^a)}{\partial \rho^2}[\rho^a_{ij}(R_{ij})]^2 \quad , \tag{2}$$

where F_i is the embedding function for atom i, $\rho^a_{ij}(R_{ij})$ is the average local electron-density contribution from atom j on atom i at a separation distance of R_{ij}, ϕ_{ij} is the core-core pair repulsive potential between interacting atoms i and j, and $\bar{\rho}^a$ is the total average local background electron density from all of the neighboring atoms on atom i.

A transitional cubic-spline potential which bridges the Ziegler and EAM potentials is assumed as

$$\phi_S(R_{ij}) = \sum_{k=0}^{3} d_k R_{ij}^k \quad , \tag{3}$$

where d_k are splining constants. This assumed spline potential satisfies the following constraints:

$$\phi_Z(R_{ij})|_{R_{ij}=r_1} = \phi_S(R_{ij})|_{R_{ij}=r_1} \quad ,$$

$$\phi_{EAM}(R_{ij})|_{R_{ij}=r_2} = \phi_S(R_{ij})|_{R_{ij}=r_2} \quad ,$$

$$\frac{\partial \phi_Z(R_{ij})}{\partial R_{ij}}|_{R_{ij}=r_1} = \frac{\partial \phi_S(R_{ij})}{\partial R_{ij}}|_{R_{ij}=r_1} \quad ,$$

$$\frac{\partial \phi_{EAM}(R_{ij})}{\partial R_{ij}}|_{R_{ij}=r_2} = \frac{\partial \phi_S(R_{ij})}{\partial R_{ij}}|_{R_{ij}=r_2} \quad .$$

The interatomic potential and force are thus continuous functions of the interatomic separation distance. The values of r_1 and r_2 are chosen so as to reduce drastic force variations when a particle moves from one potential regime to another. This is very critical because the force for the cubic-spline potential is only piece-wise continuous. A proper selection of r_1 and r_2 can reduce the degree of discontinuity in force derivatives at these parametric distances. The interaction of two lattice atoms at a separation r is completely described by the composite potential of the form:

$$\phi(R_{ij}) = \phi_Z(R_{ij}) \quad , \quad 0 < R_{ij} \le r_1 \quad ,$$

$$= \phi_S(R_{ij}) \quad , \quad r_1 \le R_{ij} \le r_2 \quad ,$$

$$= \phi_{EAM}(R_{ij}) \quad , \quad r_2 \le R_{ij} \le r_c \quad ,$$

where r_c is the cutoff distance - 5.0 Å) for the low-energy many-body potential. It is worth mentioning that this spline potential is flexible enough for extensions to other combinations of high-energy pair potentials and of low-energy many-body potentials. Possible candidates for high-energy pair interactions are the Moliere and Kr-C potentials [22]. The distances r_1 and r_2 are chosen to be 1.5 Å and 2.0 Å, respectively. The spline potential is not only a function of the interatomic separation, but is also a function of the total average local electron density. For instance, in sputtering simulations, near-surface atoms sit in different total average local electron densities than atoms in the bulk because of their neighboring atom configurations.

Table 1 gives a typical set of fitting-parameters, d_k, for equilibrium lattice atoms in bulk copper. The total average local electron density, $\bar{\rho}^a$, is 0.0276 $Å^{-3}$. The local electron density for copper with an FCC structure is based on the quantum mechanical wave functions of Clementi and Roetti [23], and the embedding function for copper is derived from the work of Foiles et al. [18].

figure 1 shows plots of the composite potential as a function of the interatomic separation, and at total average local electron densities of 0.02, 0.0276, and 0.03 $Å^{-3}$.

Table 1. Spline-Potential Parameters for Equilibrium Local Electron Density

Index, k	d_k
0	60.559
1	119.58
2	-162.68
3	61.414

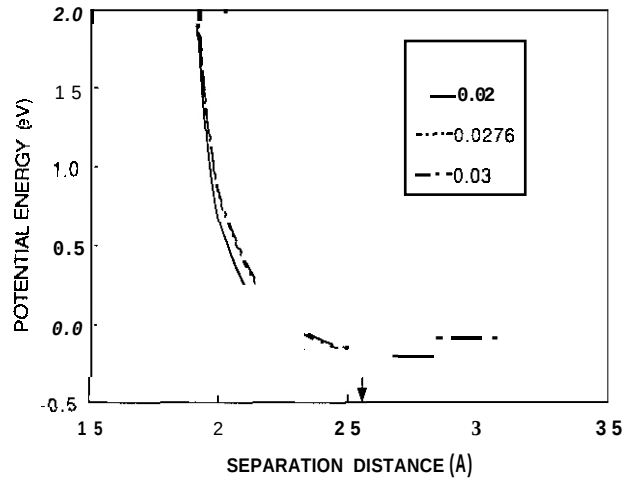

Fig. 1. Composite pair/many-body potential for copper as a function of the interatomic separation. The potential is shown for total average local electron density, $\bar{\rho}$, of 0.02, 0.0276, 0.03 Å-3.

3. Computational Method

Because of computational constraints (e.g., the computer memory size and its speed, computing cost, and the desired turnaround time), the MD technique can only simulate a small ensemble of atoms. It is important, therefore, to develop appropriate boundary conditions so that simulation results are nearly size-independent. The energy introduced by the primary knock-on atom (PKA) must be accurately dissipated in the form of atomic displacements and at the computational cell boundaries. If rigid boundaries are used, reflective energy exchange with the rigid boundaries is likely to influence subsequent dynamics.

A new MD computer code, CASC-MD, has been developed to study low-energy collision cascades. With this code, appropriate energy dissipation to below ~ 1 eV is ensured in the following ways:

1. The computational cell size is varied to show that the collisional phase of the cascade dynamics is accurately represented.
2. Two extra atomic planes are added to the computational box in the form of special viscoelastic "boundary" atoms; thus atoms up to third nearest neighbors are included. Atoms on the third extra plane are beyond the cutoff range of the EAM potential and therefore are not necessary.

The boundary atoms experience an incomplete configuration of neighboring atoms. To avoid the relaxation of boundary atoms from their equilibrium positions, a balancing external force must be introduced. A spring constant is also introduced which allows boundary atoms to oscillate around their equilibrium positions. This spring constant k (a detailed derivation is given in the appendix) is given by

$$k = \frac{EM_0}{N_c} \quad , \tag{4}$$

where E is the modulus of elasticity (Young's modulus), M_0 is the lattice constant, and N_c is the number of atoms in a unit cell. The equations of motion (EOMs) for boundary atoms are given by:

$$\frac{\partial \vec{X}_i}{\partial t} = \vec{V}_i \quad , \tag{5}$$

$$\sum \vec{\nabla}\phi_{ij} - \mu\vec{V}_i - k(\vec{X}_i - \vec{X}_{ie}) + \vec{F}_b \quad , \tag{6}$$

where $\vec{X}_i$ and $\vec{V}_i$ are the current position and velocity of particle i, ϕ_{ij} is the potential for particle j on i, $\vec{X}_{ie}$ is the equilibrium position, and $\vec{F}_b$ is the net balancing force. A damping constant, μ, is selected so that the damping time constant is greater than the cascade propagation time across the computational box. The main function of this fictitious force is to reduce the cascade energy reflection from cell boundaries.

The EOMs are integrated using Euler and leapfrog methods [24,25]. The time step is chosen to be small enough so that within each integration step, interatomic forces and potentials are near constant for all particles in the system. This allows atoms in the Ziegler potential regime to move a small fraction of the screening length for each time step. The time step is therefore dynamically computed throughout the whole cascade simulation. A consequence of the use of dynamic time steps is that both the Euler and leapfrog methods are accurate only to first order.

4. Results

Figure 2 shows atomic trajectories at different times after the initiation of a 60-eV Cu PKA in copper along the [110] direction in a (001) plane at 300 K. The initial and ending positions of lattice atoms are marked by open circles. Their trajectories in between are connected using line segments. In this figure we do not show boundary atoms for clarity of demonstration. The figure shows that the length of the linear replacement collision sequence (RCS) reaches its final value after ~ 0.15 ps. A linear replacement chain of 10.5 displaced atoms, the equivalent of a net displacement of about 25 Å along the [110] direction, is produced. The initial speed of the PKA is 135 Å/ps. The average kinetic energy available for the RCS is about half of the initial PKA energy. The average speed is about 95 Å/ps. If the subsequent slowing down of the RCS is considered, it is clear that the propagation speed of the RCS is faster than can be explained by the speed derived from the kinetic energy alone.

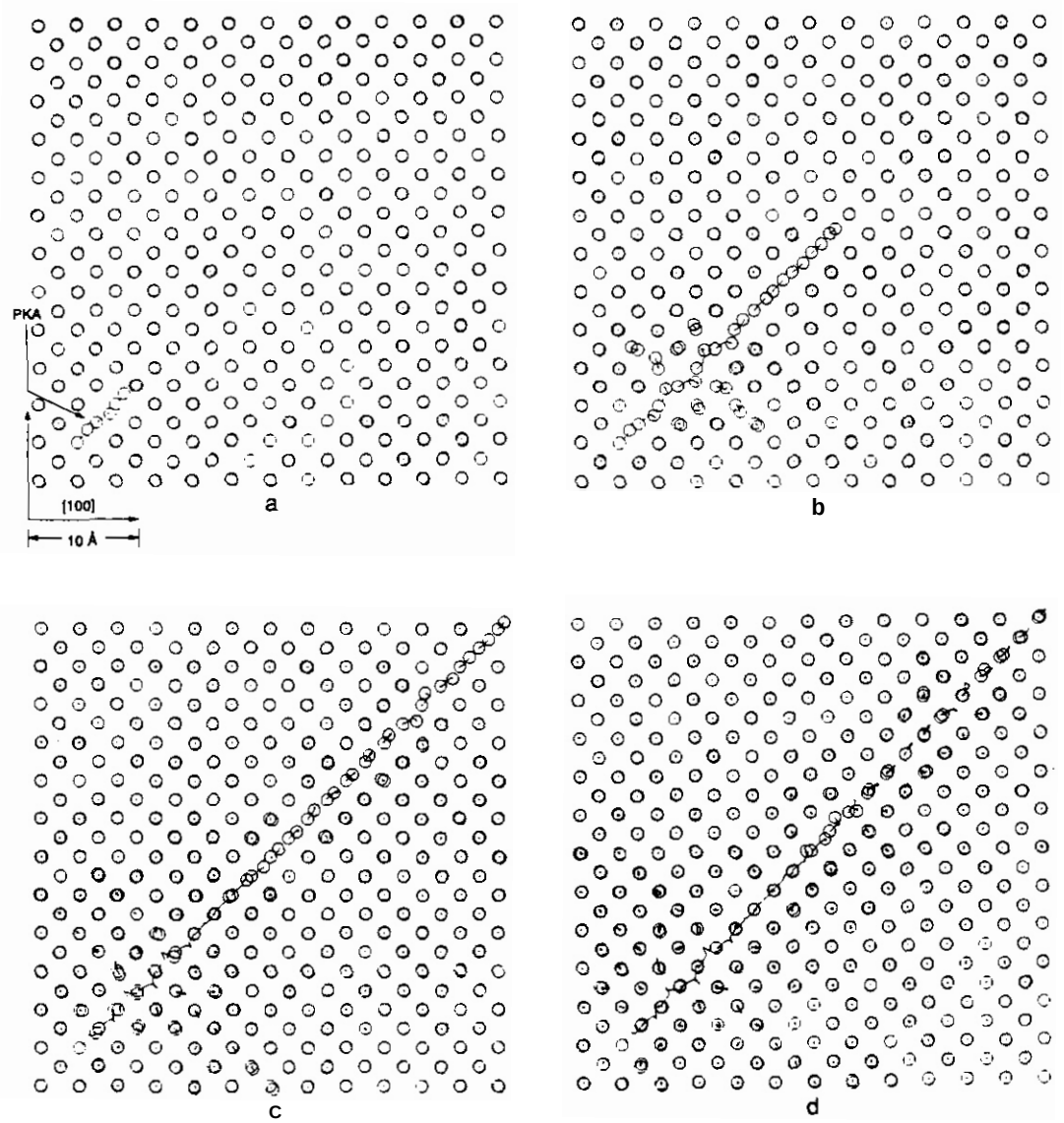

Fig. 2. Cascade trajectories at various times after the initiation of a 60-eV Cu PKA in copper at 300 K (t = 0.03, 0.14, 0.29, 0.50 ps for, respectively, a, b, c, d).

Figure 3 shows the total energy for the same 60-eV cascade as a function of time. The total energy of the system starts at about 160 eV, which includes 60 eV of PKA energy; the balance represents the thermal energy content of the system of particles. The energies displayed in Fig. 3 are divided into kinetic and potential components to show the exchange of these components as the cascade slows down. The total system energy remains constant until boundary effects become significant at about 0.3 ps. Beyond that time, a fraction of the cascade energy is dissipated in boundary regions. It is also shown that the exchange of potential and kinetic energies occurs on a time scale of about 0.05 ps.

Figure 4 shows the RCS and the elastic (sound) wave as functions of time. Also included is the expected position of the PKA, if we assume that its energy is not dissipated in the cascade and that it is free streaming at the initial speed. The propagation of the RCS clearly indicates that in near-displacement-threshold interactions, focused collision sequences subside very fast (on a time scale of about 0.1 ps). The speed of cascade-energy propagation is much faster than the average thermal phonon (sound) speed. The elastic wave speed, v_s, is calculated for isotropic copper using the relationship [26],

$$v_s = (E/\rho)^{1/2} \quad , \tag{7}$$

where E is the modulus of elasticity and ρ is the specific density for copper. The speed of cascade-energy propagation is also faster than the speed of higher order knock-on atoms. The collective motion of participating atoms in a linear RCS through the simultaneous potential field is responsible for this propagation speed. The many-body interaction helps in this collective motion because of its long-range nature.

Figure 5 shows the total cascade kinetic energies for all of the atoms in the simulation system (including boundary atoms) and for the atoms in the computational cell only (excluding boundary atoms) for the same 60-eV cascade. It can be seen that boundary atoms are not influenced by the existence of a collision cascade until the end of the collisional phase. Therefore, the total system energy remains unchanged until the cascade energy reaches the boundary. The total system energy for the computational cell decreases because a fraction of the energy is channeled into the boundary atoms. This behavior also ensures that there is no energy reflection to interfere with the cascade dynamics and indicates that the selected size of the computational cell is adequate.

Figure 6 shows the maximum kinetic energy associated with any of the recoils in two computational cell sizes (545 and 1301 atoms) for the same 60-eV collision cascade. Both simulations show that the duration of the collisional phase is approximately 0.15 ps. The kinetic energy of any of the atoms, at the end of this collisional phase, is well below the energy necessary to cause an atomic displacement. Figure 7 shows the cascade kinetic energy for two computational cell sizes. The cascade kinetic energy for the larger computational cell is summed over atoms which correspond to those in the smaller computational cell. At 300 K, the initial thermal energy content in the small computational cell is about 20 eV. Near thermalization is achieved at the end of the kinetic phase.

In Fig. 8, we compare the results of our calculations to the experimental measurements of King and Benedek [12] on copper at 10 K. Our simulations indicate that while the displacement threshold energy is around 20 eV for copper, substantially larger energy is needed to displace copper atoms along the [111] and between the [110] and [100] directions. Our calculations are quite consistent with the experiments of King and Benedek [12], who used a defect resistivity value of $\sim 2.8 \times 10^{-4}$ ohm-cm to obtain the displacement threshold surface.

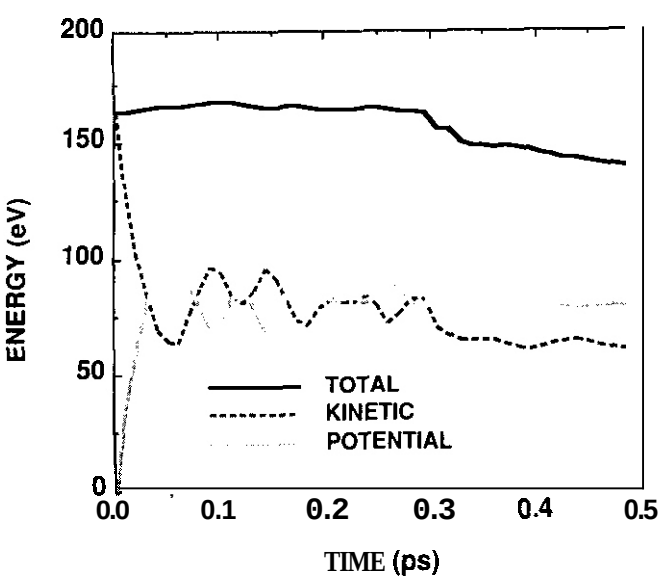

Fig. 3. Total, kinetic, and potential energies as functions of time for a collision cascade induced by a 60-eV Cu PKA in copper.

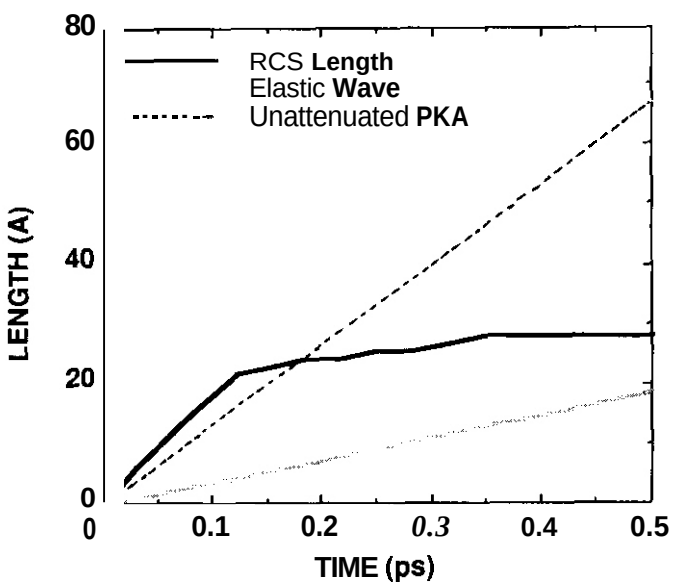

Fig. 4. Comparison of RCS propagation with those of an elastic (sound) wave and the initial PKA.

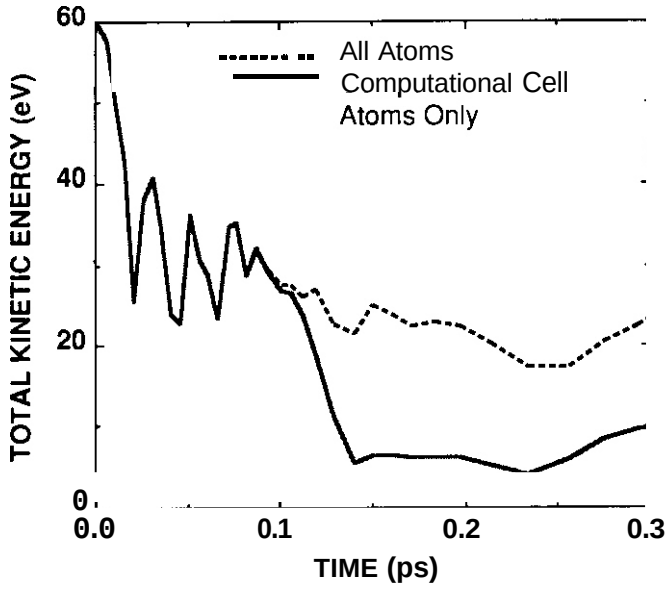

Fig. 5. Kinetic energy partitioning as a function of time for the collision cascade.

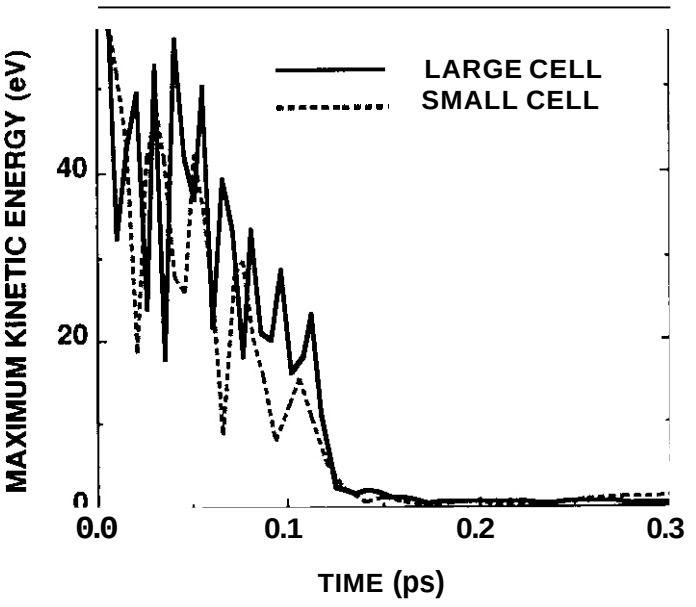

Fig. 6. The maximum kinetic energy associated with any of the atoms during the collisional phase of cascade evolution initiated by a 60-eV Cu PKA in copper.

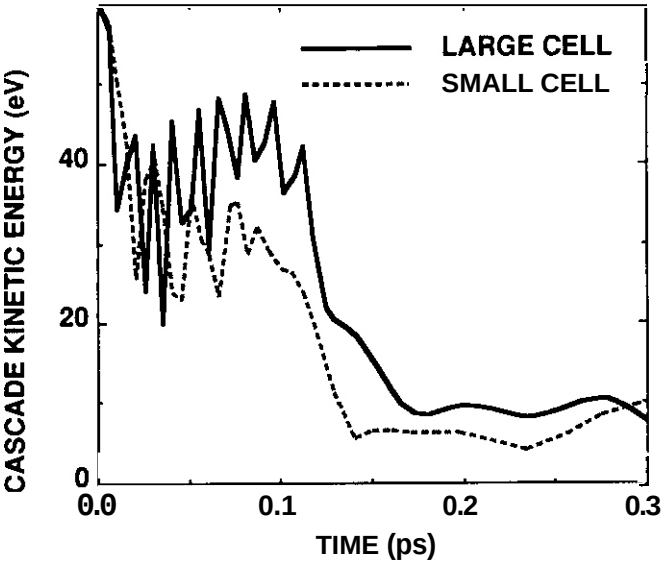

Fig. 7. Cascade kinetic energies as functions of time for two computational cell sizes.

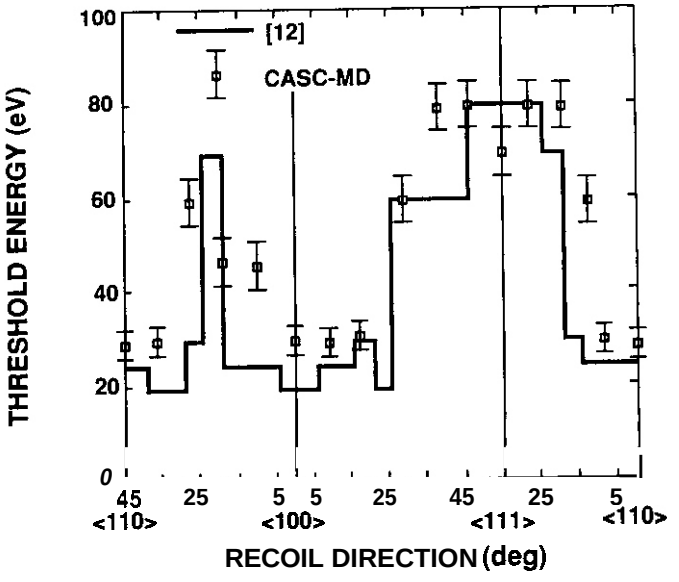

Fig. 8. Comparison between calculated displacement threshold energies along different directions at 10 K, and experimental data of King and Benedek [12]. A defect resistivity value $\sim 2.8 \times 10^{-4}$ Ω cm is used in obtaining the experimental data.

5. Conclusions

This study of the collisional phase of low-energy cascade evolution shows the following: (1) The development of a replacement collision sequence (RCS), which leads to a stable Frenkel pair, is completed in about 0.1 ps. (2) The initial propagation of an RCS is much faster than the elastic (sound) wave in copper and is even faster than the initial PKA speed, showing that cascades propagate through collective atomic motions. (3) The close agreement of our MD results with the experimental data on the displacement threshold surface indicates the usefulness of this composite potential for the simulation of low-energy ion-solid interactions.

Appendix

The spring constant k is derived as follows. The uniaxial stress-strain relation is given by:

$$\sigma = E\epsilon \quad ,$$

where σ is the stress, E is the modulus of elasticity, and ϵ is the strain, given by $\sigma = F/A$ and $\epsilon = \delta M/M$, where F is the force, A is the area where the force is exerted, M is the length, and δM is the elongation. Considering a slab of unit area, and a length of a lattice constant M_0, we can rewrite the first equation as

$$F = E(\delta M/M_0) \quad .$$

The total number N_a of atoms contained in this slab is:

$$N_a = \frac{V}{M_0^3} N_c = \frac{1 \times M_0}{M_0^3} N_c = \frac{N_c}{M_0^2} \quad ,$$

where N_c is the number of atoms in a unit cell. The last two equations yield the force per atom f as

$$f = \frac{F}{N_a} = \frac{EM_0\delta M}{N_c} = k\delta M$$

The "equivalent" spring constant is then given by

$$k = \frac{EM_0}{N_c} \quad .$$

Acknowledgment

This work was supported by the U.S. Department of Energy, Office of Fusion Energy, Grant No. DE-FG03-84ER52110, with the University of California, Los Angeles.

References

[1] M. Yoshida, J. Phys. Soc. Jpn. 16 (1961) 44.
[2] O. Oen and M. T. Robinson, J. Appl. Phys. 34 (1964) 2515.
[3] T. Ishitani, R. Shimuzu, and K. Murata, Jpn. J. Appl. Phys. 11 (1972) 125.
[4] H. L. Heinisch. J. Nucl. Mater. 103/104 (1981) 1325; also J. Nucl. Mater. 117 (1983) 46.
[5] S. P. Chou and N. M. Ghoniem, J. Nucl. Mater. 117 (1983) 55.
[6] J. B. Gibson, A. N. Goland, M. Milgram, and G. H. Vineyard, Phys. Rev. 120 (1960) 1229.
[7] J. R. Beeler, Jr., Phys. Rev. 150 (1966) 470.
[8] R. N. Stuart, N. W. Guinan, and B. J. Borg, Radiat. Eff. 30 (1976) 129.
[9] J. D. Schiffgen and R. D. Bourquin, J. Nucl. Mater. 69/70 (1978) 790.
[10] A. Tenenbaum and N. V. Doan, J. Nucl. Mater. 69/70 (1978) 775.
[11] T. Diaz de la Rubia, R. S. Averbeck, and H. Hsieh, J. Mater. Res. 4 (1989) 579.
[12] W. E. King and R. Benedek, Phys. Rev. B23 (1981) 6335.
[13] W. E. King and R. Benedek, in: Point Defects and Defect Interactions in Metals, Eds. J. Takamura, M. Doyama, and M. Kiritini (University of Tokyo Press, Tokyo, 1982) p. 807.
[14] W. E. King and R. Benedek, J. Nucl. Mater. 117 (1983) 26.
[15] M. S. Daw and M. 1. Baskes, Phys. Rev. Lett. 50 (1983) 1285.
[16] M. S. Daw and M. I. Baskes, Phys. Rev. B29 (1984) 6443.
[17] S. M. Foiles, Phys. Rev. B32 (1985) 7685.
[18] S. M. Foiles, M. I. Baskes, and M. S. Daw, Phys. Rev. 833 (1986) 7983.
[19] P. Hohenberg and K. Kohn, Phys. Rev. 136 (1964) B864.
[20] R. A. Johnson, Phys. Rev. B37 (1988) 3924.
[21] D. J. Oh and R. A. Johnson, J. Mater. Res. 3 (1988) 471.
[22] J. F. Ziegler, J. P. Biersack, and U. Littmark, The Stopping and Range of Ions in Solids (Pergamon Press, New Vork, 1985) p. 48.
[23] E. Clementi and C. Roetti, Atomic and Nuclear Data Table 14 (1974) 177.
[24] D. E. Potter, Computational Physics (John Wiley, London, 1973) p. 37.
[25] H. L. Berk and K. V. Roberts, "The Water-Bag Model," in: Methods in Computational Physics, Vol. 9, Eds. B. Alder, S. Fernbach, and M. Rotenberg (Academic Press, New Vork, 1970) p. 111.
[26] M. Alonso and E.J. Finn, Physics (Addison-Wesley, Reading, MA, 1970) p. 534.

FUTURE WORK

The methodology used in this work will be extended to the study of collision cascade interaction in ceramic composite materials such as SiC.

INFLUENCE OF COLD WORK AND PHOSPHORUS CONTENT ON NEUTRON-INDUCED SWELLING OF Fe-Cr-Ni ALLOYS - F. A. Garner (Pacific Northwest Laboratory)(")

OBJECTIVE

The overall objective of this effort was to determine the origin of the sensitivity of void swelling and microstructural evolution in irradiated metals to environmental and material variables. A more specific objective was to assist in the interpretation of the results of the ^{59}Ni doping experiment designed to study the separate and synergistic effects of helium and other variables. Two of these variables are cold working and phosphorus content.

SUMMARY

Phosphorus additions can either increase or decrease void swelling of Fe-Cr-Ni alloys, depending on irradiation temperature, phosphorus level and cold work level. The role of cold work is not always to suppress swelling in Fe-Cr-Ni-P alloys, however, particularly at relatively higher irradiation temperatures, where cold working often increases swelling substantially.

INTRODUCTION

Frequently one can generalize the action of a particular variable on a given physical process in terms of its most often observed behavior, which would indicate a single major role for that variable. For example, it is well established that the addition of either phosphorus or silicon generally suppresses the onset of void swelling in austenitic alloys. Recently, however, it has been shown that under some conditions the addition of relatively low levels of either solute can substantially increase swelling in simple Fe-Cr-Ni alloys,[1,2] as shown in Figures 1 and 2. This complex behavior is thought to indicate that two or more competing mechanisms involving these elements are operating to control swelling and that in some cases the competition is dominated by a secondary or tertiary mechanism.

As reviewed in reference 1, phosphorus forms precipitates at relatively high temperatures and concentration levels and strongly interacts with both vacancies and interstitials at all temperatures. Phosphorus also acts to maintain dislocations induced by cold working, although this latter possibility has not been explored previously in simple austenitic alloys. A search was therefore initiated for previously irradiated specimens that would allow study of the interactive effects of phosphorus and cold work.

The most extensive set of such specimens was found in the ^{59}Ni-doping helium effects experiments conducted in FFTF on Fe-15Cr-25Ni and Fe-15Cr-25Ni-0.04P (wt%).[3-5] Unfortunately, the major influence of phosphorus in increasing swelling lies in the range below 0.04% and at temperatures below ~500°C. In this temperature range of the ^{59}Ni experiment, density data have been measured only for the first discharge at 5.2 dpa, which is below the threshold of significant swelling. Higher exposure data are now being accumulated.

In another experiment, however, four nominally identical Fe-15Cr-25Ni alloys, varying primarily in phosphorus content, were irradiated as TEM disks in the FFTF fast reactor to doses in excess of 30 dpa at 420, 520 and 600°C (±5°C) in both the annealed and 30% cold worked conditions. The compositions of these alloys in Table 1, are identical to those that were irradiated in EBR-II and shown in Figure 1. Immersion density measurements were performed on two identical specimens at each condition.

One of the alloys in this experiment, E104 (Fe-15Cr-25Ni-0.055P), was also irradiated as TEM disks in EBR-II in the AA-XIV experiment to 14 dpa at 425, 500 and 600°C. In this experiment the alloys were irradiated in each of the annealed (975°C/10m/WQ), 30% cold worked, and the cold worked and aged (650°C/10m/WQ) conditions. Immersion density measurements were performed on one specimen each of every combination of starting condition and irradiation temperature.

RESULTS

Swelling values for the FFTF irradiation were calculated from density change data and are shown in Figure 3. Each data point, with one exception, represents the average of two separate but identical disks, whose densities agree within the ±0.16% established as the convergence criterion for this measurement technique. The exception was the cold worked alloy E33 (lowest phosphorus level) at 420°C, where some variability was observed.

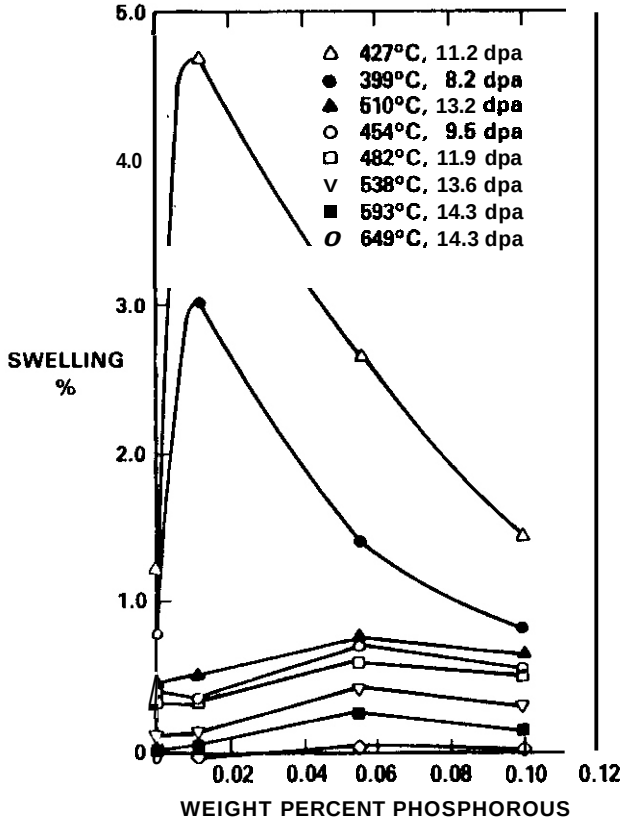

FIGURE 1. Influence of Phosphorus on Neutron-Induced Swelling in EBR-II (AA-IX experiment) of Fe-25Ni-15Cr at Various Combinations of Temperature and Fluence[1]

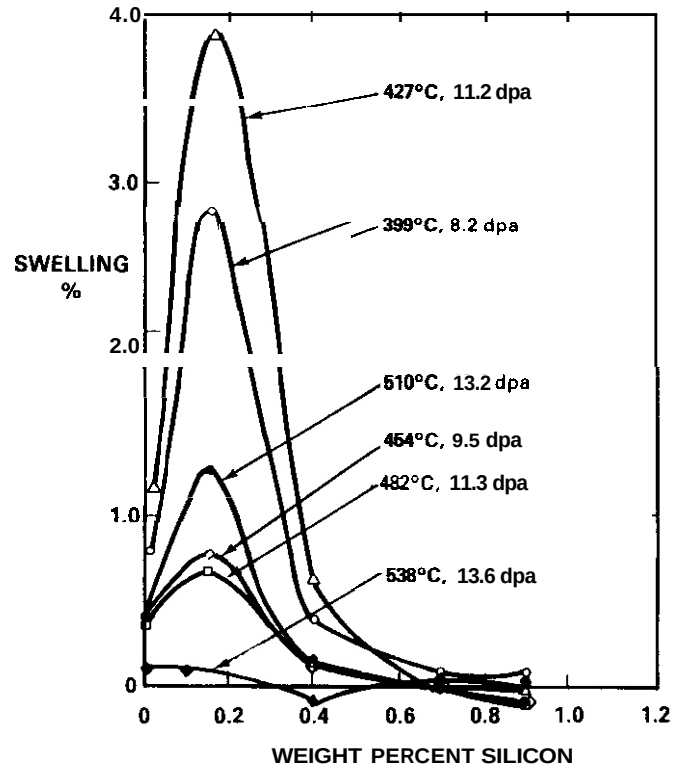

FIGURE 2. Influence of Silicon on Neutron-Induced Swelling in EBR-II (AA-IX experiment) of Fe-25Ni-15Cr at Various Combinations of Temperature and Fluence[1]

TABLE 1. Phosphorus-Modified Alloys Irradiated in FFTF-MOTA to >30 dpa

E33	Fe-25.8Ni-14.8Cr (≤ 0.005P)
E103	Fe-24.1Ni-14.7Cr-0.013P
E104	Fe-25.0Ni-15.2Cr-0.055P
E105	Fe-24.7Ni-15.3Cr-0.10P

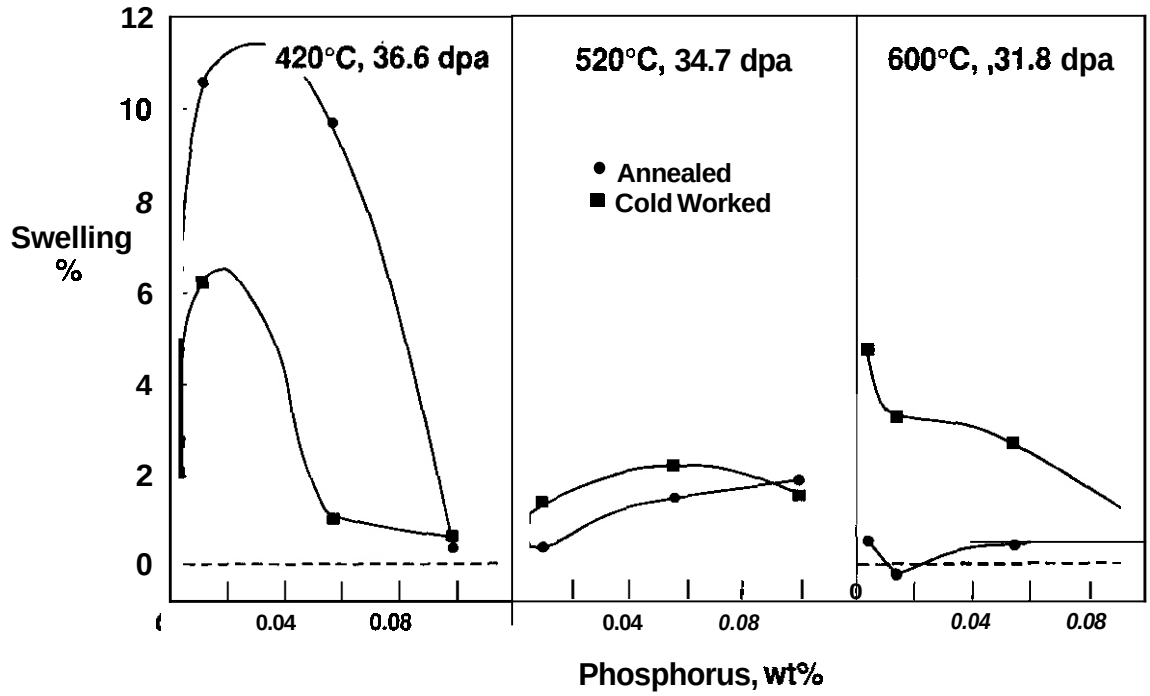

FIGURE 3. Swelling of Phosphorus-Modified Fe-15Cr-25Ni Alloys Observed in FFTF

At 420°C and 36.6 dpa the swelling behavior observed in FFTF in both the annealed and cold worked specimens mirrors that seen in the same alloys when irradiated in the annealed condition in EBR-II at 399 and 427°C, illustrating once again the various outcomes of the competition of those mechanisms associated with phosphorus. Cold working reduces swelling at 420°C, in agreement with the general observation of cold work's influence. The swelling falls quickly at higher temperatures in the annealed low phosphorus alloy, as was also observed in EBR-II. The curves for annealed materials at 520 and 600°C also exhibit the same dependence on phosphorus content as those observed in EBR-II.

There were several unusual features observed in these data, however. First, the cold worked condition swelled more than the annealed condition at 520 and 600°C. Second, and possibly even more important, the reversal in swelling behavior with cold work was observed even in the lowest phosphorus alloy E33. Third, in the cold worked condition alloy E33 swelled more at 600% and 31.8 dpa than at 520°C and 34.7 dpa, as illustrated in Figure 4. This behavior with temperature was unexpected and indicates that the interactions of cold work with both phosphorus and temperature are more complex than previously envisioned.

The density change data of alloy E104 from the EBR-II AA-XIV experiment are shown in Table 2. The decrease of swelling with cold work at 420°C is consistent with the behavior observed in FFTF. The influence of increasing temperature at this low dose level does not yield the increase in swelling observed in FFTF, however.

DISCUSSION

The effects of cold working on complex alloys have been studied in many investigations, but only a few studies have explored the effects of cold working on single Fe-Cr-Ni ternary alloys. In one recent study conducted at very high helium/dpa ratios in ORR, Fe-25Ni-15Cr suffered a reduction in swelling from 1.04 to 0.29% upon 30% cold working and irradiation at 500°C to 13.6 dpa.[6] Swelling at other irradiation temperatures in this experiment was too low to observe the influence of cold work. Similar behavior was observed in Fe-35Ni-15Cr at 500°C, falling from 0.55 to -0.11% with cold work.

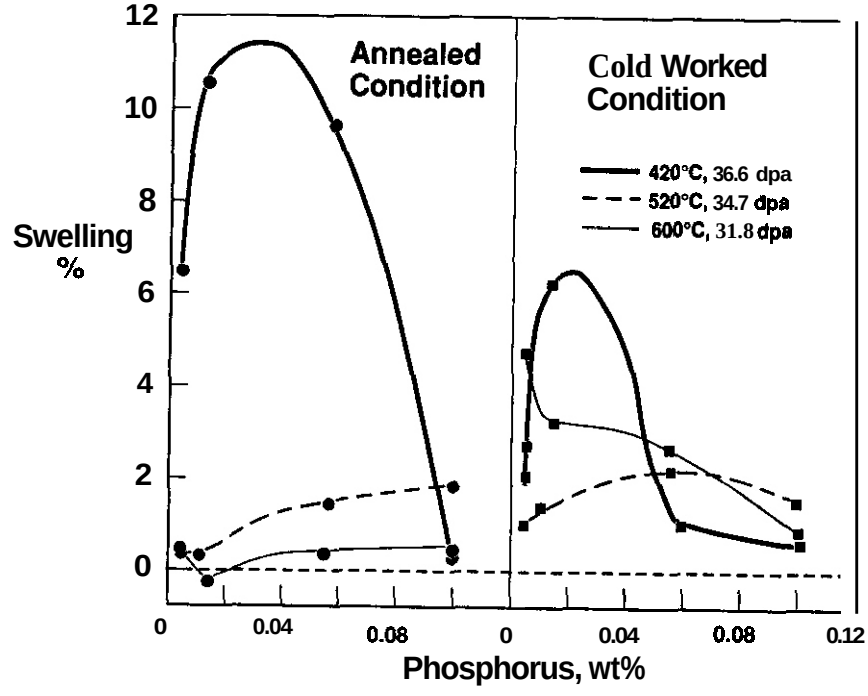

FIGURE 4. Data from Figure 3 Replotted to Emphasize the Effect of Temperature on Swelling

TABLE 2. Swelling (in %) of Alloy E104 (Fe-15Cr-25Ni-0.055P) in the MXIV Experiment Irradiated in EBR-II to 14 dpa

TemDerature. °C	Annealed	Cold Worked	Cold Worked and Aaed
420	1.79	0.28	-0.36
500	-0.21	-0.28	NA[a]
600	-0.03	NA[a]	NA[a]

(a) NA = not available.

The ^{59}Ni-doping experiment at 495°C and 14 dpa showed a reduction in swelling with cold work in Fe-15Cr-25Ni in the undoped condition and essentially no difference in the doped condition, which experienced a higher helium/dpa ratio.[5] At 600°C and 8.8 dpa this experiment did not produce sufficient swelling in Fe-15Cr-25Ni to assess the impact of cold work.[4] However, there did appear to be a slight enhancement of swelling in both the cold worked and annealed undoped conditions with phosphorus addition at 600°C, in agreement with the present study.

The previously published EBR-II studies from the AA-VII experiment[1,7] all involved the irradiation of ternary Fe-Cr-Ni alloys in the annealed condition. In one experiment designated AA-XII, however, both the annealed and 30% cold worked conditions of alloy E20 (Fe-24.4Ni-14.9Cr with ≤0.005 P) were irradiated side-by-side in EBR-II at 425 and 540°C to 18.5 and 24.5 dpa, respectively.") The E20 alloy and the E33 alloy of the current study are quite similar alloys prepared by the same vendor at the same time.

Note in Table 3 that the E20 alloy in EBR-II behaved the same as the E33 alloy in FFTF, showing a reduction in swelling with cold work at 425°C and an increase in swelling at 540°C. Figure 5 compares the behavior of E20 in this and the earlier experiment. Note also that there is some variability in the response of the cold worked alloy. Such variability is frequently observed in cold worked alloys.

Table 3 also shows some previously unpublished results of another irradiation of the E20 alloy in the MXIV experiment. At 14 dpa cold working decreases swelling at 425 and 500°C but increases it at 600°C, once again demonstrating the reversal in the influence of cold work at higher temperatures.

TABLE 3. Swelling Observed in Alloy E20 (Fe-24.4Ni-14.9Cr) in the AA-XI and AA-XIV Experiments in EBR-II

Temperature, °C, and Experiment	Displacement Level, dpa	Alloy Condition	Swelling, %
425 AA-XI	18.5	annealed	12.8[a]
425 AA-XI	18.5	30% CW	3.8[a]
540 AA-XI	24.5	annealed	1.14[a]
540 AA-XI	24.5	30% CW	4.81[b]
			3.61[b]
425 AA-XIV	14.0	annealed	9.69[c]
425 AA-XIV	14.0	30% CW	2.85[c]
500 AA-XIV	14.0	annealed	1.80[c]
500 AA-XIV	14.0	30% CW	-0.01[c]
600 AA-XIV	14.0	annealed	0.35[c]
600 AA-XIV	14.0	30% CW	2.56[c]

(a) Average swelling of four identical specimens exhibiting very small differences in density.
(b) Separate measurements on two nominally identical specimens.
(c) Measurement on one specimen only.

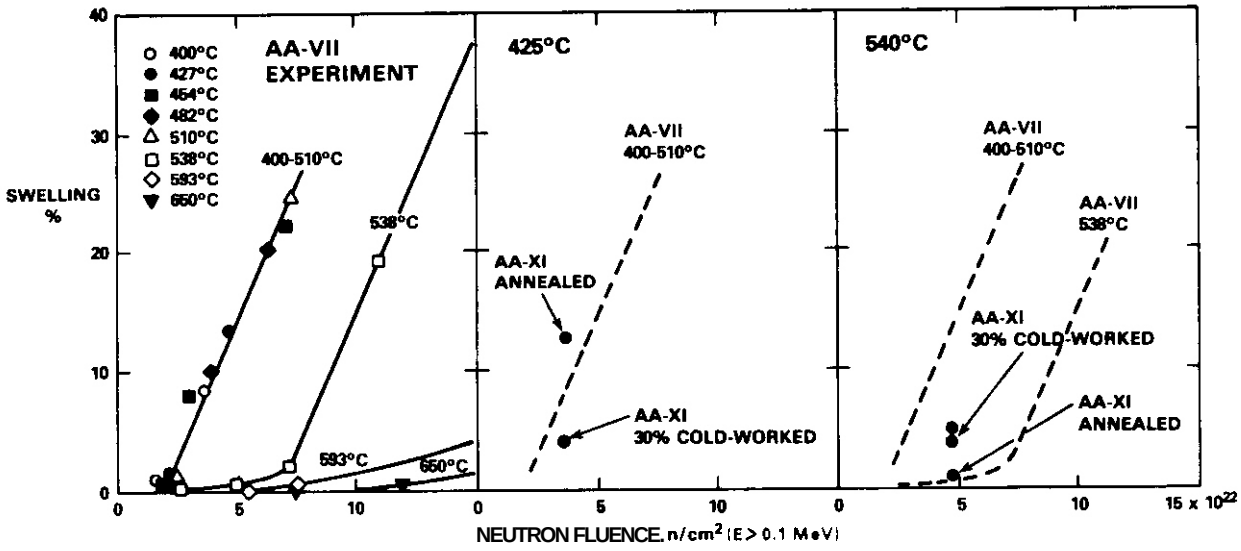

FIGURE 5. Swelling of Alloy E20 (Fe-24.4Ni-14.9Cr) in Two Separate EBR-II Experiments. Note in the two right hand figures that the influence of cold work reverses between 425 and 540% in the AA-XI experiment. (8)

The action of cold work in enhancing swelling at higher temperatures may be similar to that observed recently in pure nickel,[9] as shown in Figure 6. Microscopy studies now in progress show that the effect of cold work on the swelling of nickel at 500 and 600°C is to make it easier to establish (and maintain at higher temperatures) a saturation density of dislocations early in the irradiation, a condition which promotes early void nucleation. Swelling tends to saturate in pure nickel later in the irradiation because the dislocation density drops sharply once void swelling begins. Swelling of cold worked materials at high exposure therefore exhibits very little dependence on temperature.

Another comparison of the influence of cold work is shown in Table 4, which indicates that in FFTF Fe-7.5Cr-35Ni exhibited the expected behavior at 420 and 520°C but that large increases in swelling were observed at 600°C. The variability of swelling when enhanced by cold work is again highlighted by the fact

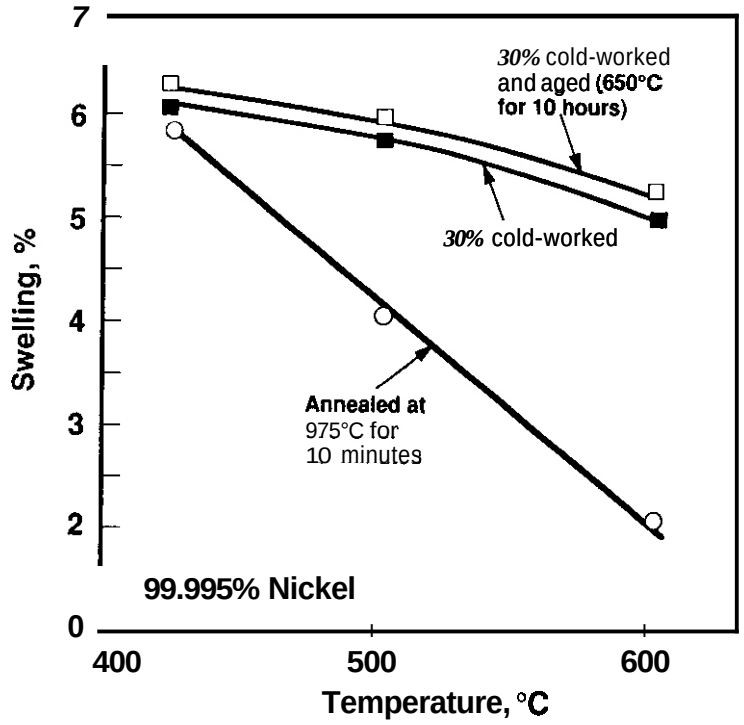

FIGURE 6. Swelling of 99.99% Nickel Irradiated to 14 dpa in the EBR-II AA-XIV Experiment.[9] The cold worked and cold worked and aged conditions do not exhibit the strong temperature dependence seen in the annealed steel.

TABLE 4. Swelling Observed in Alloy E37 (Fe-7.5Cr-35Ni) in FFTF[a]

Temperature, °C	Displacement Level, dpa	Alloy Condition	Swelling, %
420	9	annealed	-0.16
420	9	30% CW	-0.26
420	46.5	annealed	0.09
420	46.5	30% CW	-0.09
420	70	annealed	0.09
420	70	30% CW	0.09
520	14	annealed	0.16
520	14	30% CW	0.00
520	49.6	annealed	0.30
520	49.6	30% CW	-0.36
520	75	annealed	0.02
520	75	30% CW	-0.14
600	14	annealed	-0.01
600	14	30% CW	NM[b]
600	35	annealed	0.20
600	35	30% CW	2.50
600	60	annealed	0.12
600	60	30% CW	1.78

(a) Measurements on one specimen each.
(b) NM = not measured.

that swelling was increased relative to that of the annealed condition at 600°C at both 35 and 60 dpa, but was less at 60 dpa. It is not felt that swelling actually decreased on the average between 35 and 60 dpa; rather, it is believed that the enhancement process is very sensitive to uncontrolled variables in the experiment, often varying between nominally identical specimens irradiated in the same specimen packet.

The Fe-15Cr-25Ni alloy has been used as a standard material in a variety of irradiation studies conducted in the U.S. fusion and breeder reactor programs. One study not mentioned previously involved the use of this alloy in a correlation experiment between charged particle and neutron irradiations.[10,11] In that study the softness of this material was highlighted, indicating the ease with which dislocations were introduced during specimen preparation and also the difficulty of maintaining them near specimen surfaces. Therefore, there may be some merit to the comparison between the behavior of nickel and Fe-15Cr-25Ni with respect to the influence of cold work at higher irradiation temperatures. Since phosphorus has been shown in type 316 stainless steel to assist in maintaining during irradiation the dislocation densities induced by cold work,[9] this may account for the strong increase in swelling at relatively high phosphorus levels observed in Figures 3 and 4, especially at higher temperatures where dislocations are more mobile.

Another series of ion irradiation studies by Lee and Mansur also highlighted the action of phosphorus to maintain dislocation densities.[13,14] In their first study it was shown that two alloys (Fe-13.7Cr-15Ni both with and without 0.05 wt% phosphorus) both swelled at comparable levels when irradiated in the annealed condition to ~90 dpa at 675% with nickel ions.[13] This is in agreement with the neutron studies, since the phosphorus-related peak in swelling was found to exist between these two phosphorus levels. Three other phosphorus-modified alloys with silicon, titanium and carbon additions were each found to exhibit less swelling in the annealed condition when subjected to a variety of irradiation sequences, some of which involved helium coinjection. The compositions of these alloys are listed in Table 5.

In the second of these studies,[14] the latter three alloys were irradiated at 675% in the cold worked condition, but with higher levels of helium coinjection. Figure 7 compares the swelling of these alloys in the annealed and cold worked conditions, each data set taken from separate publications.[13,14] Although it is not possible to make a comparison involving only a single variable due to the variations in helium injection

TABLE 5. Ion-Irradiated Alloys Studied by Lee and Mansur[13,14]

Alloy	Comoosition
B10	Fe-13.64Cr-15.15Ni-0.050P
B11	Fe-13.63C4-15.20Ni-0.049P-0.18Ti-0.041C
B12	Fe-13.58Cr-15.15Ni-0.049P-0.17Ti-0.044C-0.83Si

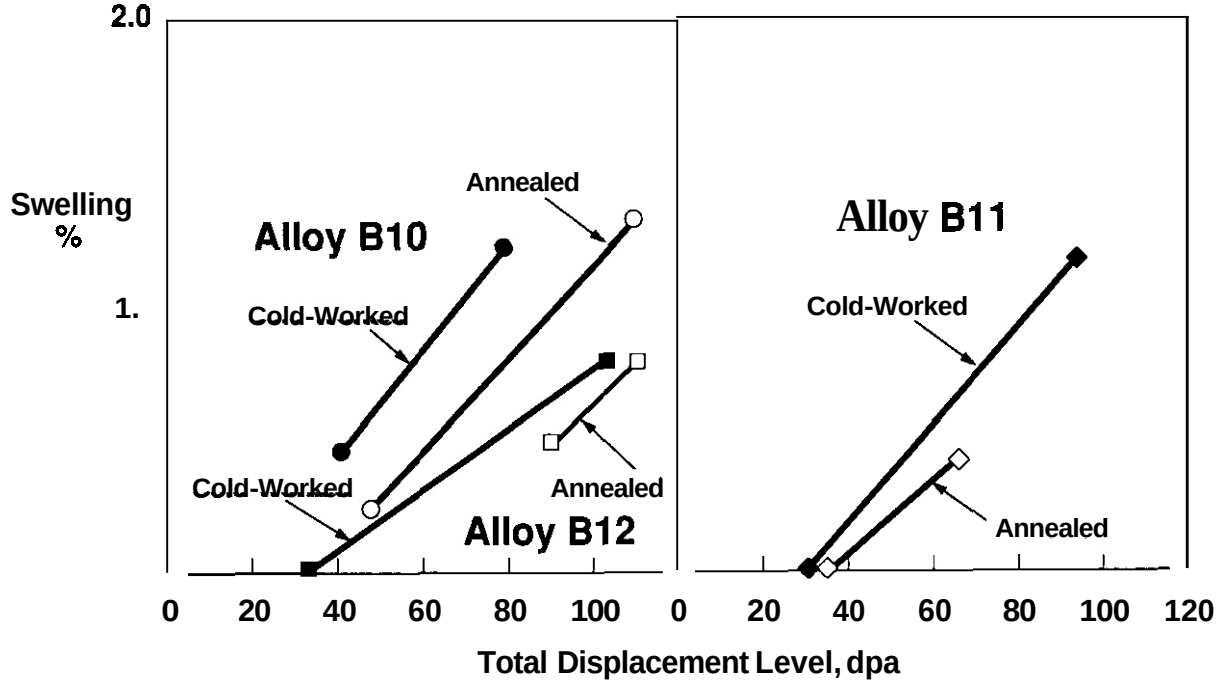

FIGURE 7. Comparison of Ion-Induced Swelling of Various Phosphorus-Modified Alloys Irradiated at 675°C, Showing That Cold Working Generally Increases Swelling[13,14]

schedules, Lee and Mansur noted their expectation that both cold working and higher cavity densities induced by helium injection should depress swelling. Note in Figure 7 that if the differences in helium are ignored the opposite result is obtained; the cold worked condition of each alloy swells more than the annealed condition. This appears to confirm the conclusion of the current study concerning the interactive roles of cold work and phosphorus on void swelling.

CONCLUSIONS

Phosphorus additions can either increase or decrease void swelling of Fe-Cr-Ni alloys, depending on irradiation temperature, phosphorus level and the cold work level of the alloy. The role of cold work is not always to suppress swelling, however, particularly at relatively higher irradiation temperatures where swelling actually increases upon cold working. The dividing point where cold working reverses its role on swelling appears to lie between 520 and 540°C for displacement rates typical of fast reactor irradiation.

FUTURE WORK

This effort will continue, focusing on microscopy examination on specimens irradiated in either FFTF or EBR-II.

REFERENCES

1. F. A. Garner and A. S. Kumar, ASTM-STP 995 (1987) 289.
2. T. Muroga, F. A. Garner and J. M. McCarthy, J. Nucl. Mater., 168 (1989) 109.
3. F. A. Garner, M. L. Hamilton, R. L. Simons and M. K. Maxon, J. Nucl. Mater. 176 (1990) in press, also DOE/ER-0313/8 (1990) 108.
4. H. Kawanishi, F. A. Garner and J. F. Stubbins, J. Nucl. Mater., 176 (1990) in press.
5. J. F. Stubbins, J. F. Nevling, F. A. Garner and R. L. Simons, ASTM-STP 1046 (1989) 147.
6. M. L. Hamilton, A. Okada and F. A. Garner, J. Nucl. Mater., 176 (1990) in press
7. F. A. Garner and H. R. Brager, ASTM STP 870 (1985) 187.
8. F. A. Garner and H. R. Brager, DOE/ER-0046/19 (1984) 62.
9. F. A. Garner, DOE/ER-0313/8 (1990) 125.
10. F. A. Garner, J. Nucl. Mater., 117 (1983) 177
11. F. A. Garner and seventeen coauthors, in Proceedings of a Workshop on Correlation of Neutron and Charged Particle Damage, CONF-760673, Oak Ridge, TN, June 1976, 177.
12. M. Itoh, S. Onose and S. Yuhara, ASTM STP 955 (1987) 114.
13. E. H. Lee and L. K. Mansur, J. Nucl. Mater., 141-143 (1986) 695.
14. E. H. Lee and L. K. Mansur, Phil. Mag. A, 61 (1990) 733.

HELIUM MEASUREMENTS FOR THE MFE-4 SPECTRAL TAILORING EXPERIMENT - F. A. Garner (Pacific Northwest Laboratory)[a] and B. M. Oliver (Rockwell International)

OBJECTIVE

The objective of this effort is to determine the role of helium on microstructural development and changes in mechanical properties of model Fe-Cr-Ni alloys.

SUMMARY

Measurements of helium concentration have been made on Fe-15.1Cr-34.5Ni specimens irradiated at 330, 400, 500 and 600°C after irradiation in ORR to displacement levels ranging from 12.6 to 13.8 dpa. The measurements compare well to previously calculated values, being 4 to 8% lower. Minor differences in helium content were also observed between specimens from capsules that were assumed to have possessed identical spectral environments.

PROGRESS AND STATUS

Introduction

In a companion report on ^{59}Ni isotopic doping, it is shown that three simple Fe-Cr-Ni alloys irradiated in FFTF do not exhibit a significant difference in mechanical properties when exposed to both breeder-relevant and fusion-relevant helium/dpa ratios[1]. In another experiment conducted in ORR at much larger helium generation rates, however, a significant increase in yield strength was observed (see Figure 1) relative to that of a similar experiment in EBR-II.[2,3] In ORR these and several other Fe-Cr-Ni alloys were exposed tb environments whose calculated He/dpa ratios ranged from 21 to 58 appm/dpa. This range reflects not only the neutron spectra but also the variation in nickel content (20 to 45 wt%). These values were calculated using dosimetry calculations and measurements provided in reference 4 for individual elements.

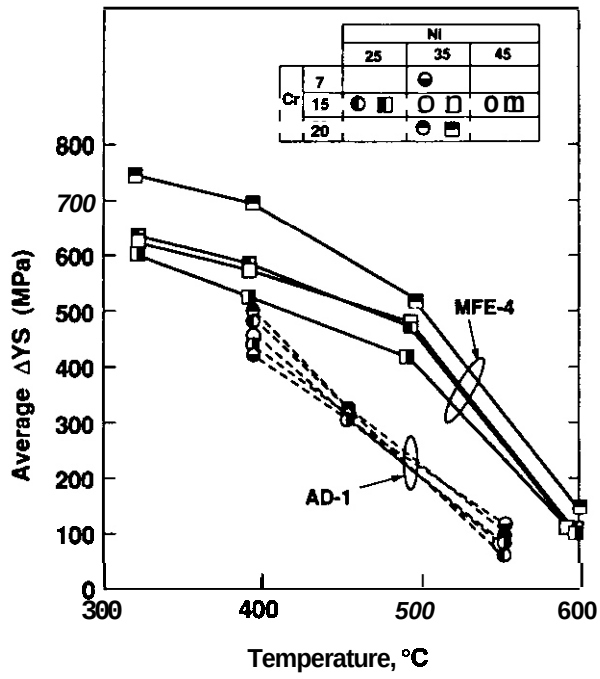

FIGURE 1. Comparison of Radiation-Induced Changes in Yield Strengths of Fe-15Cr-XNi and Fe-YCr-35Ni Alloys Irradiated in the AD-1 Experiment in EBR-II and the MFE-4 Experiment in ORR[2].

(a) Pacific Northwest Laboratory is operated for the U.S. Department of Energy by Battelle Memorial Institue under Contract DE-AC06-76RLO 1830.

Table 1 lists the displacement and helium levels reported earlier for the ORR portion of this experiment. Note that it was assumed that the 330 and 400°C irradiation sequences proceeded in the same spectral environment and also that the 500 and 600°C sequences were irradiated together. Detailed microstructural analyses of the ORR and EBR-II specimens are now in progress; the early results indicate that the larger than fusion-relevant levels of helium in the ORR experiment caused an extensive refinement of the microstructure, leading to suppression of swelling at the two lower irradiation temperatures and significant increases in hardening at all four irradiation temperatures.

Table 1

Calculated Displacement and Helium Levels[a] for the MFE-4 Experiment in ORR[2,3]

	330 and 400°C		500 and 600°C	
Composition. wt%	dpa	He. appm	dpa	He, appm
Fe-19.7Ni-14.7Cr	13.4	371	12.2	332
Fe-24.4Ni-14.9Cr	13.6	463	12.4	414
Fe-30.1Ni-15.1Cr	13.8	555	12.6	495
Fe-34.5Ni-15.1Cr	14.0	647	12.7	573
Fe-45.3Ni-15.0Cr	14.3	832	13.1	740

(a) These values were calculated for the maximum flux position using dosimetry calculations and measurements provided in reference 4 for individual elements. Note that the dpa levels increase with nickel content, reflecting the contributions of the ^{56}Fe recoil atom during helium production.

Further analysis requires confirmation of the calculated helium levels. Using standardized procedures at Rockwell International,[5,6] measurements were made on Fe-34.5Ni-15.1Cr specimens from each of the four irradiation temperatures. The specimens for analysis were cut from the gauge section of previously tested and broken tensile specimens.

Results

Table 2 lists the measured values of helium concentration for Fe-34.5Ni-15.1Cr at each irradiation temperature. When compared to the previously calculated values for the maximum flux position it is obvious that some small differences in neutron spectra and flux exist between the specimen locations in the 330 and 400°C capsules and also between the specimen locations in the 500 and 600°C capsules as well. The measured values are uniformly lower (4-8%) than the calculated values for all four of the irradiation capsules. These relatively small differences in concentration reflect the impact of small differences in position between the maximum flux position and that of the gauge sections of the tensile specimens.

CONCLUSIONS

Slight differences in helium generation rate occurred in the various canisters used in the MFE-4 spectral tailoring experiment. The helium concentrations measured for Fe-34.5Ni-15.1Cr are lower but within 4 to 8% of the previously reported values calculated from dosimetry results. These differences arose from slight differences in position between the specimens and the maximum flux position.

FUTURE WORK

This effort will continue, focusing on completion of the microscopy effort and on prediction of strength increases from measured microstructural densities.

THE INFLUENCE OF HELIUM ON MECHANICAL PROPERTIES OF MODEL AUSTENITIC ALLOYS, DETERMINED USING ^{59}Ni ISOTOPIC TAILORING AND FAST REACTOR IRRADIATION - M. L. Hamilton and F. A. Garner, Pacific Northwest Laboratory;[a] B. M. Oliver, Rockwell International.

OBJECTIVE

The objective of this effort is to study the separate and synergistic effects of helium and other important variables on the evolution of microstructure and macroscopic properties during irradiation of structural metals.

SUMMARY

Tensile testing and microscopy continue on specimens removed from the first, second and third discharges of the ^{59}Ni isotopic doping experiment. The results to date indicate that helium/dpa ratios typical of fusion reactors (4 to 19 appm/dpa) do not lead to significant changes in the yield strength of model Fe-Cr-Ni alloys. Measurements of helium generated in undoped specimens from the second and third discharges show that the helium/dpa ratio increases during irradiation in FFTF due to the production of ^{59}Ni. In specimens doped with ^{59}Ni prior to irradiation, the helium/dpa ratio can increase, decrease or remain the same during the second irradiation interval. This behavior occurs because the cross sections for the production and burnout of ^{59}Ni are very sensitive to core location and the nature of neighboring components.

PROGRESS AND STATUS

Introduction

Until recently it has been impossible to conduct experiments in which spectrum-related parameters such as helium/dpa ratio were varied without also accepting variations in other important parameters such as displacement rate and temperature history. A technique currently being used, however, allows the study of the influence of helium alone on density change, microstructural evolution and mechanical properties. This technique utilizes isotopic tailoring to vary the helium production rate without introducing changes in neutron spectrum or displacement rate.[1,2] By producing alloys whose only difference is the presence or absence of ^{59}Ni, an isotope that does not occur naturally, and irradiating doped and undoped specimens side by side in the appropriate reactor spectra, it is possible to generate substantial variations in He/dpa ratio without varying any other important parameter.

A particular advantage of isotopic doping experiments is that one need not be concerned with the details of temperature history, which is now known to heavily influence the outcome of some fission-fusion correlation experiments.[3] Since both doped and undoped specimens are irradiated side by side, the primary variable is only the helium/dpa ratio. The production rate of helium in doped specimens is also nearly constant throughout the experiment, providing that no changes occur in the neutron environment.

This report addresses the tensile data obtained from a subset of the specimens irradiated in a larger experiment currently being conducted in the Fast Flux Test Facility (FFTF) utilizing the Materials Open Test Assembly (MOTA). A previous report addressed the results of the first discharge of this experiment from FFTF; this report includes the first results of the second and third discharges.[4] The results of helium measurements from the second and third discharges are also presented in this report.

ExDerimental Detai1s

The alloys employed in this study were nominally Fe-15Cr-25Ni, Fe-15Cr-25Ni-0.04P and Fe-15Cr-45Ni (wt%) in both the cold worked and annealed conditions. These alloys were chosen to complement those in several earlier studies, one in the Experimental Breeder Reactor-I1 (EBR-II), designated the AD-1 experiment,[5,6] and another conducted in the Oak Ridge Research (ORR) Reactor, designated MFE-4.[6] The acquisition of the ^{59}Ni, the production of the ^{59}Ni-doped tensile specimens and their irradiation conditions are described in Reference 1. Microscopy disks were also prepared and irradiated; the results of examination of the first discharge of these specimens are described in detail in References 7 and 8. The miniature tensile specimens measured 5.1, 1.0 mm and 0.25 mm in gauge length, width and thickness, respectively. They were tested at room temperature at a strain rate of 4.7×10^{-4} sec^{-1} in a horizontal test frame described in Reference 9. Yield strengths were determined at 0.2% offset. In some cases more than one tensile specimen was tested, but the majority of tests to date have involved only a single test specimen.

(a) Pacific Northwest Laboratory is operated for the U.S. Department of Energy by Battelle Memorial Institute under Contract DE-AC06-76RLO.

Table 2

Helium Concentration in the Gauge Section of Fe-34.5Ni-15.1Cr Tensile Specimens

Soecimen	Temperature °C	Specimen Mass[a] (mg)	^{4}He Measured (10^{15} atoms)	Helium Concentration (appm)[b] Measured	Average[c]	Calculated[d]
JNOO-A	330	1.230	7.913	600.1	597	647
-B		2.089	13.30	593.9	±4	
JN09-A	400	1.736	11.47	616.3	611	647
-B		2.610	16.95	605.8	±7	
JN13-A	500	1.548	8.818	531.4	533	573
-B		2.157	12.38	535.4	±3	
JN19-A	600	1.461	8.722	556.9	552	573
-B		1.196	7.011	546.8	27	

(a) Mass uncertainty is ±0.001 mg.
(b) Measured helium concentration in atomic parts per million (10^{-6} atom fraction) with respect to the calculated number of atoms in the specimen.
(c) Mean and 1σ standard deviation of duplicate analyses.
(d) From Table 1.

REFERENCES

1. M. L. Hamilton, F. A. Garner and B. M. Oliver, "The Influence of Helium on Mechanical Properties of Model Austenitic Alloys, Determined Using ^{59}Ni Isotopic Tailoring and Fast Reactor Irradiation," this report.

2. M. L. Hamilton, A. Okada and F. A. Garner, "Tensile Behavior and Swelling of Ternary Austenitic Alloys Irradiated in Different Neutron Spectra, J. Nucl. Mater. 176 (1990), in press.

3. N. Sekimura, F. A. Garner and R. D. Griffin, "The Effect of Helium on Microstructural Evolution in Austenitic Stainless Steels as Determined by Spectral Tailoring Experiments," DOE/ER-0313/8 (1990) pp. 114-119.

4. L. R. Greenwood, "Dosimetry and Damage Calculations for the ORR-MFE 4A/4B Spectral Tailoring Experiments," DOE/ER-0313/6 (1989) pp. 29-35.

5. Harry Farrar IV and B. M. Oliver, "A Mass Spectrometer System to Determine Very Low Levels of Helium in Small Solid and Liquid Samples," J. Vac. Sci. Technol. A4 (1986) 1740.

6. B. M. Oliver, J. G. Bradley and Harry Farrar IV, "Helium Concentration in the Earth's Lower Atmosphere," Geochim. Cosmochim. Acta 48 (1984) 1759.

Results of Tensile Tests

Figure 1 presents a schematic representation of the various irradiation sequences of the ^{59}Ni experiment, each defined by their irradiation temperature and their location in FFTF-MOTA. Tensile tests have been completed on unirradiated specimens of all three alloys in both the annealed and 20% cold worked conditions.

Three tensile tests on unirradiated specimens were conducted for each undoped alloy in both the cold worked and the annealed conditions. Since the availability of doped specimens was rather limited, only one was tested for each combination of doped alloy and thermomechanical starting condition. Figure 2 shows that the range of yield strengths in the undoped specimens is not large and that the single doped specimen in each condition did not exhibit any significant difference in behavior. Also shown in Figure 2 are the yield strengths exhibited by the larger specimens of the unirradiated annealed alloys irradiated in the AD-1 and MFE-4 experiment,[6] demonstrating excellent agreement among the three experiments.

Tests on several subsets of irradiated specimens have also been completed. These subsets are the first two discharges at both 365 and 495°C (i.e., after MOTA-ID and MOTA-1E) and a single discharge at 600°C (after MOTA-ID). The 600°C sequence was not continued to higher radiation exposure due to a large overtemperature event in MOTA-10, reaching 806°C for fifty minutes. The 495% sequence also suffered an overtemperature, reaching 629°C for fifty minutes, but was continued in the irradiation sequence along with a replacement sequence at 495°C to explore the impact of the temperature excursion on the experiment. The sequence at 365°C did not experience a temperature excursion.

Figures 3-5 show the yield strengths measured at room temperature of specimens irradiated at nominal temperatures of 365, 495 and 600°C. The width of the error bars at zero dpa corresponds to the variation seen in Figure 2 and provides a basis for determining whether variations observed between doped and undoped specimens are significant compared to the scatter associated with the measurement technique.

The most significant features of the data shown in Figures 3-5 are, first, the relative unimportance of isotopic doping at all three temperatures in determining the yield strength, and second, the convergence at

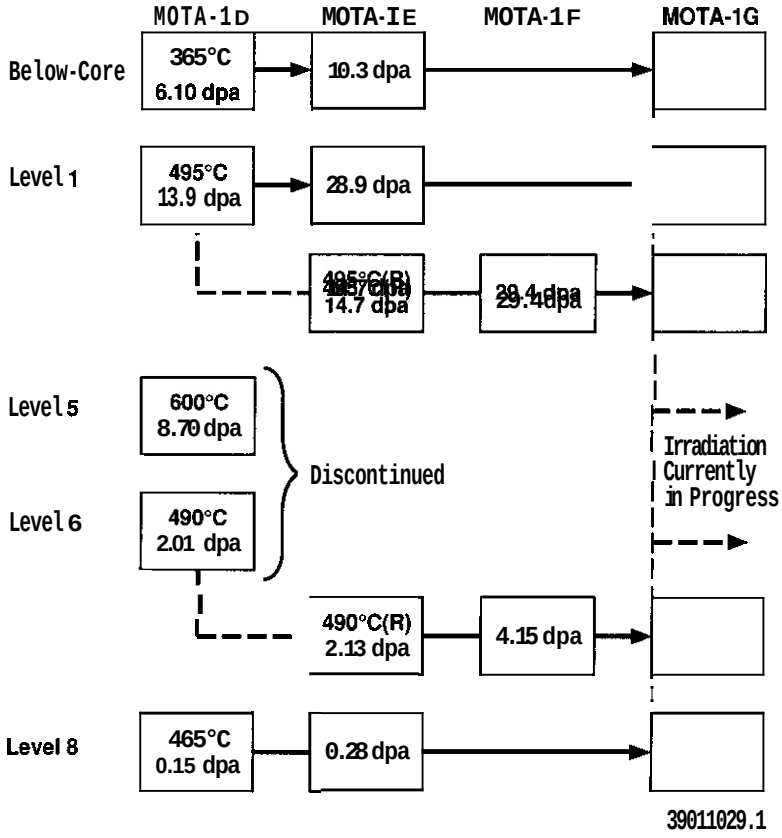

Figure 1. Schematic representation of irradiation sequences for the ^{59}Ni isotopic tailoring experiment. "495°C(R)" and "490°C(R)" refer to the replacement sequences inserted for the original sequences at 495 and 490%

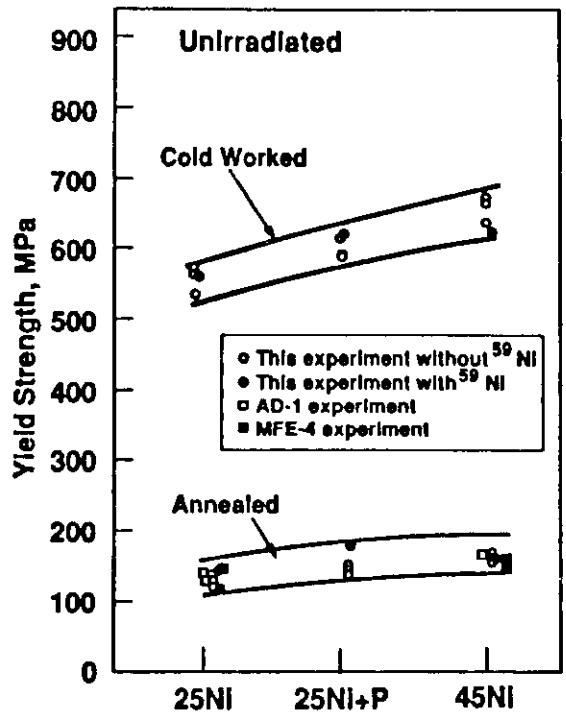

Figure 2. Yield strength data on unirradiated specimens from the FFTF/MOTA ^{59}Ni experiment and two related experiments conducted in other reactors

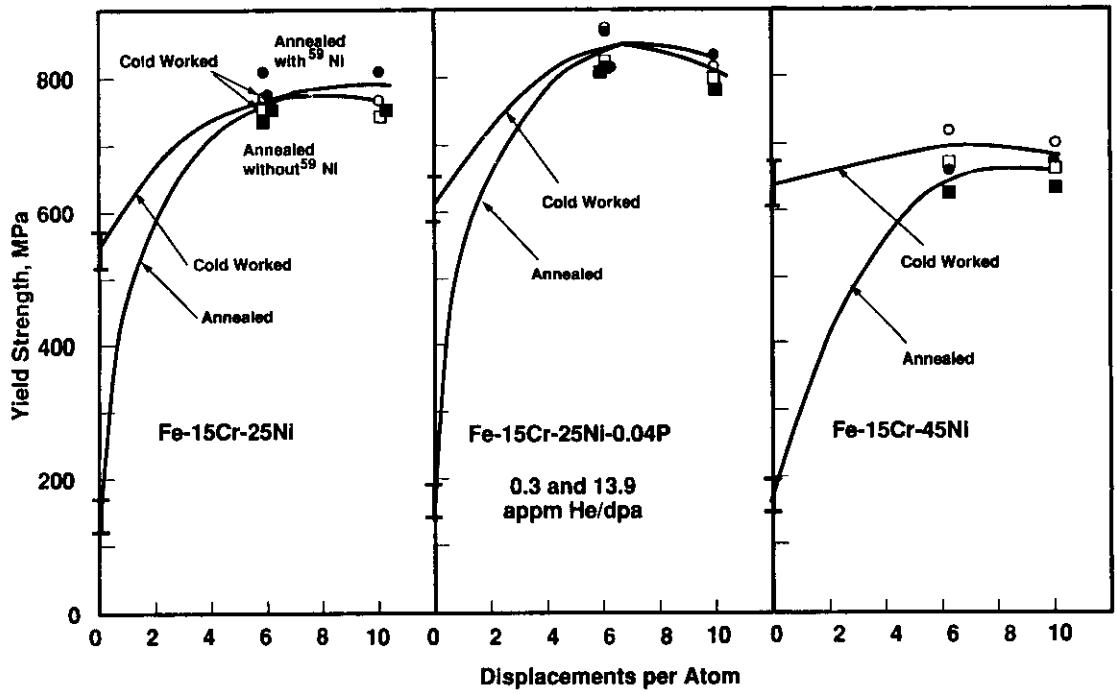

Figure 3. Influence of thermomechanical starting state and isotopic doping on yield strength of three alloys irradiated at 365°C. Open and closed symbols denote cold worked and annealed alloys, respectively; circles denote ^{59}Ni-doped specimens; squares denote undoped alloys

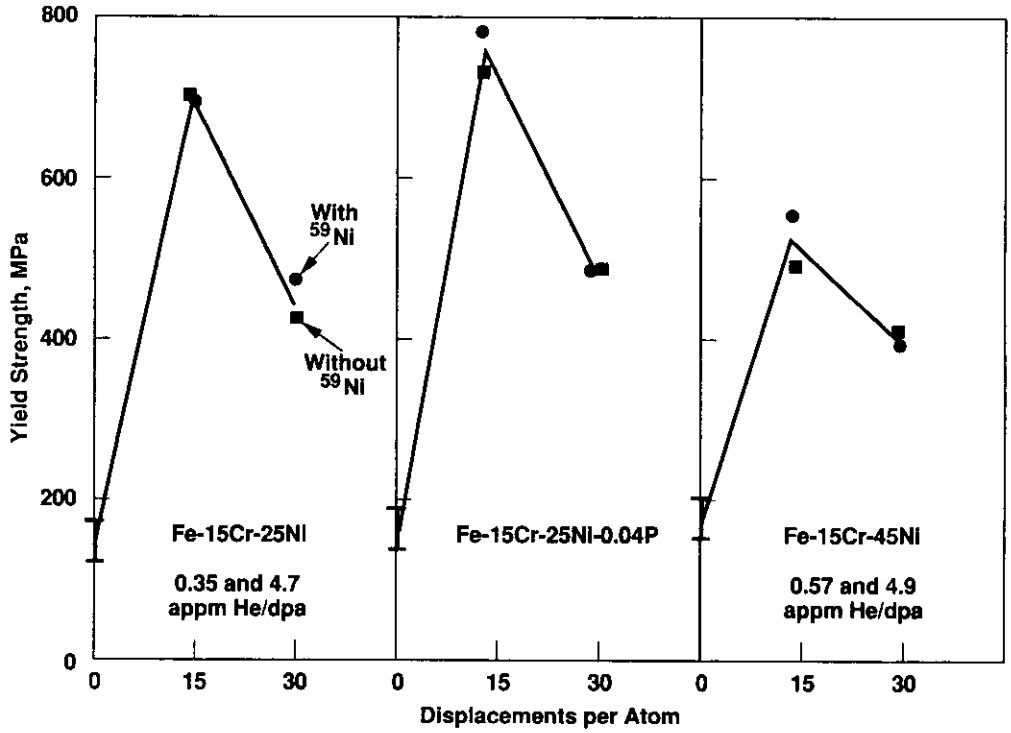

Figure 4. Influence of isotopic doping on yield strength of three annealed model alloys irradiated at 495°C

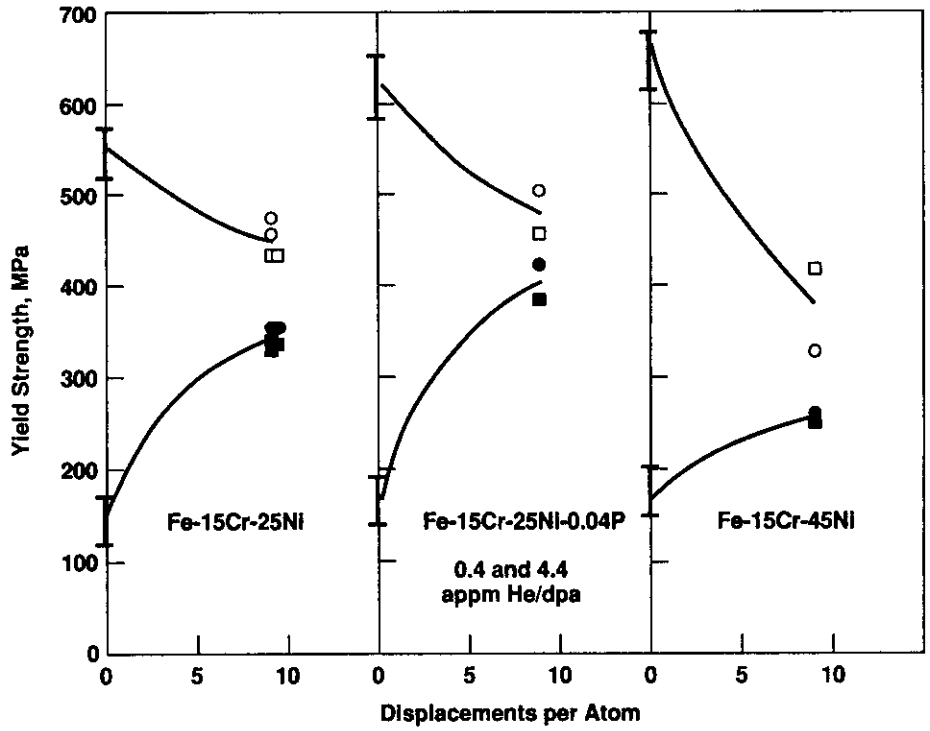

Figure 5. Influence of thermomechanical starting state and isotopic doping on yield strength of three alloys irradiated at 600°C. Open and closed symbols denote cold worked and annealed alloys, respectively; circles denote ^{59}Ni-doped specimens; squares denote undoped alloys.

365 and 600°C of both annealed and cold worked specimens to strength levels that depend only on irradiation temperature. A similar convergence has been observed previously in 316 stainless steel over a wide range of irradiation temperatures, with convergence levels sensitive to both temperature and displacement rate.[10]

At 495°C only annealed tensile specimens were irradiated and therefore it is not possible to determine whether convergence occurs at this temperature. TEM disks were irradiated at 495°C in both the annealed and cold worked conditions, however, and convergent microstructures appear to have developed.[7,8] There is one unusual feature at 495°C that was not observed previously in 316 stainless steel, however, in that the yield strength first increased and then later decreased somewhat, implying that the saturation level was initially overshot and the strength later relaxed toward the saturation level. Such behavior might arise from early nucleation of a high density of Frank loops, which later unfault to form a somewhat lower density of network dislocations. It might also result from void number densities that are initially rather high but later reduced by coalescence. An example of the latter possibility has been observed previously in Fe-15Cr-20Ni during ion-irradiation.[11] The relative independence of the tensile behavior of annealed specimens on helium content tends not to support softening behavior dominated by void coalescence, however. On the other hand, microstructural data compiled from microscopy observations of specimens from the first discharge show that the line length of loops at 495°C in both the cold worked and annealed specimens is comparable to the line length of network distributions.' This suggests that further unfaulting of loops might lead to the possibility of softening. Microscopy is now in progress on the second discharge and should confirm whether the preceding speculations are correct.

Results of Helium Measurements

Helium levels were measured, using standard techniques,[12,13] at Rockwell International on cold worked Fe-15Cr-25Ni specimens from all irradiation temperatures in the second and third discharges (ie., after MOTA-1E and -1F, respectively) and on cold worked Fe-15Cr-45Ni specimens at 365 and 490°C in the second discharge. Helium production was not measured in the latter alloy for the first discharge (MOTA 10); instead, helium levels for Fe-15Cr-45Ni in the first discharge were calculated from composition ratios and measurements made on Fe-15Cr-25Ni.

Tables 1-3 present the helium concentrations obtained on two samples cut from each specimen from the second two discharges of the ^{59}Ni doping experiments. Note that the measurements made on specimens removed from three of the second discharge groups (at 365, 495 and 465°C) and both of the third discharge groups [495°C(R) and 490°C(R)] represent the average helium levels for irradiation during two MOTA irradiation cycles (1D and 1E or 1E and 1F). Since the first and second sets of specimens discharged at each temperature were originally irradiated side by side it is possible to calculate the average helium formation rate that occurred in the second MOTA irradiation cycle only. These values are shown in parentheses in Table 2.

As shown in Table 2, the helium generation rates in both undoped and doped Fe-15Cr-25Ni specimens at 365°C (below the core) increased substantially in MOTA-1E compared to the rates observed in MOTA-ID. No change in position occurred between the two irradiation cycles, although some changes were made in the surrounding components. The average helium generation rates observed in Fe-15Cr-25Ni and Fe-15Cr-45Ni after the second discharge at 365°C exhibited the expected dependence on nickel content, (1.24 and 16.5 appm/dpa predicted vs. 1.20 and 16.7 measured for Fe-15Cr-45Ni) which tends to confirm the validity of helium/dpa ratios calculated previously for Fe-15Cr-45Ni in the first discharge. As we shall see later, however, this conclusion applies fully only to situations where the 25Ni and 45Ni specimens remain closely side by side throughout the full irradiation sequence.

In the original 495°C irradiation sequence in level 1, smaller but significant increases in helium generation rates were observed in both undoped and doped specimens relative to the increases observed at 365% below core. These specimens were moved from the 1D4 position in MOTA-10 to the 1A4 position in MOTA-1E with no significant consequence on the helium production rate of the undoped specimens.

The replacement irradiation sequence at 495°C started in position 1A4 in MOTA-1E, along with the second irradiation cycle of the original 495°C series, and continued in position 1C3 in MOTA-IF. In the undoped replacement specimen, cumulative helium/dpa ratios of 0.44 and 0.57 appm/dpa were reached in the first and second segments. These are higher than the 0.35 (position 1D4) and 0.41 values (positions 104 and then 1A4) reached in the original series. This implies that in level 1 some spectral variation occurred between 104 of MOTA-ID and 1C3 of MOTA-IF. When the 495°C replacement series was moved to position 1C3 in MOTA-IF for its second irradiation cycle, however, this caused a substantial decrease in the helium production rate for the doped specimens. This probably reflects changes in the spectrum due to neighboring experiments. The production rate for the undoped specimens increased, however, reflecting the continued build-up of ^{59}Ni, a process that would continue in all reactor positions.

In the 490°C replacement sequence, the helium production rate rose between MOTA 1E and MOTA 1F for both the undoped and doped specimens. No change in position occurred during this irradiation sequence. Both the original and replacement sequences proceeded in position 6E2, which is an above-core position possessing a large axial gradient in neutron flux and apparently significant changes in the details of the spectrum that affect the burnout and production of ^{59}Ni.

Table 1
Helium Concentration in Cold Worked TEM Disks from Isotopic Tailoring Experiment

Temperature (°C)	Nickel (wt%)	Doped With ^{59}Ni	dpa	Specimen Mass[a] (mg)	^{4}He Measured (10^{14} atoms)	Helium Concentration (appm)[b] Measured	Average[c]
365	25	No	10.3	1.937 2.966	1.493 2.263	7.157 7.084	7.12 t0.05
365	25	Yes	10.3	2.744 3.186	48.86 56.34	165.3 164.2	165 ±1
365	45	No	10.3	2.562 3.024	3.375 4.015	12.35 12.44	12.4 ±0.1
365	45	Yes	10.3	1.996 3.339	36.48 61.24	171.3 171.9	172 ±1
495	25	No	28.9	1.733 3.410	2.546 5.016	13.64 13.66	13.7 t0.1
495	25	Yes	28.9	2.482 3.316	36.22 48.46	135.5 135.7	136 ±1
495(R)[d]	25	No	14.7	2.644 3.374	1.834 2.385	6.441 6.563	6.50 ±0.09
495(R)	25	Yes	14.7	3.174 3.554	23.82 26.28	69.68 68.66	69.2 ±0.7
495(R)	25	No	29.4	2.087 2.360	3.797 4.247	16.89 16.71	16.8 ±0.1
495(R)	25	Yes	29.4	2.826 2.983	36.49 38.66	119.9 120.3	120 ±1
490(R)	25	No	2.13	2.881 4.212	0.1383 0.1974	0.4457 0.4352	0.440 ±0.007
490(R)	25	Yes	2.13	2.861 3.643	6.691 8.386	21.71 21.37	21.5 t0.2
490(R)	45	No	2.13	2.709 3.241	0.1865 0.2197	0.6452 0.6353	0.640 t0.007
490(R)	45	Yes	2.13	2.785 3.555	7.296 8.959	24.55 23.62	24.1 i.0.7
490(R)	25	No	4.15	2.348 3.797	0.3590 0.5808	1.420 1.420	1.42 ±0.00
490(R)	25	Yes	4.15	2.735 3.177	16.87 19.28	57.27 56.35	56.8 ±0.7
465	25	No	0.28	2.825 3.129	0.02223 0.02438	0.07306 0.07235	0.0727 ±0.0005
465	25	Yes	0.28	2.780 2.746	5.201 5.134	17.37 17.36	17.4 ±0.1

(a) Mass uncertainty is ±0.001 mg. Two samples were cut from each original TEM specimen.
(b) Measured helium concentration in atomic parts per million (10^{-6} atom fraction) with respect to the calculated number of atoms in the specimen.
(c) Mean and 1σ standard deviation of duplicate analyses.
(d) R denotes replacement series.

Table 2
Helium Generation Rates Determined in Fe-15Cr-25Ni

Temperature (°C)	Helium Generation Rate (appm/dpa) MOTA-1D Undoped	MOTA-1D Doped	MOTA-1E Undoped	MOTA-1E Doped	MOTA-1F Undoped	MOTA-1F Doped
365	0.30	13.9	0.69[a] (1.26)[b]	16.0[a] (19.1)	no discharge	
495	0.35	4.69	0.47[a] (0.59)	4.71[a] (4.73)	no discharge	
495(R)[c]	not irradiated		0.44	4.71	0.57[a] (0.70)	4.08[a] (3.45)
600	0.40	4.4	not irradiated		not irradiated	
490	0.28	19.8	not irradiated		not irradiated	
490(R)[c]	not irradiated		0.21	10.1	0.34[a] (0.46)	13.7[a] (17.2)
465	0.14	54.3	0.26[a] (0.40)	62.1[a] (71.1)	no discharge	

(a) He/dpa level given is average for two cycle irradiation sequence.
(b) Helium/dpa levels in parentheses represent average values calculated for second MOTA cycle only.
(c) R denotes replacement series.

Table 3
Cumulative Helium Generation Rates Determined in Fe-15Cr-45Ni After Discharge from MOTA-1E

Temperature	appm/dpa Undoped	appm/dpa Doped	Neutron damage (dpa) MOTA-1D	Neutron damage (dpa) MOTA-1E	Neutron damage (dpa) Total
365	1.20	16.7	6.1	4.2	10.3
490R	0.30	11.3	0.01	2.13	2.13

Several consequences of changes in the neutron environment can be seen in the two irradiation sequences at 490°C. First, the helium/dpa ratios for both specimen types in the replacement sequence are somewhat lower than that of the original sequence, probably reflecting differences in the loading of nearby components during the operation of MOTA-1D and MOTA-1E. Second, based on the measured MOTA-1E production rates in undoped Fe-15Cr-25Ni, we would expect the production rate in undoped Fe-15Cr-45Ni to be 0.38 appm/dpa, whereas only 0.30 appm/dpa was measured. The difference between helium levels in the 25Ni and 45Ni doped specimens is also somewhat larger than expected. These observations imply that the 45Ni specimens, which were in a separate packet from the 25Ni specimens, experienced a slightly different spectral environment, even though they were in the same basket. This in turn suggests that radial gradients in spectral parameters must also exist and that the specimens may not have been closely side by side.

The 465% low fluence sequence was conducted in above core position 8F1 in both MOTA-1D and MOTA-1E. In this case the production rates of both the doped and undoped specimens increased. Note that the production rates in the doped specimens are quite large, 54 and 71 appm/dpa in Fe-15Cr-25Ni in MOTA-1D and MOTA-1E, respectively.

Review of the data in Tables 1 and 2 leads to the following overall conclusions: 1) helium production in undoped specimens containing only natural nickel is greatest for irradiation within the core; 2) significant increases in helium production rate occur with increasing exposure in undoped specimens regardless of location with respect to the core. The percentage increases are greatest for irradiations outside the core. 3) helium production rates in specimens doped with ^{59}Ni dopant prior to irradiation tend to increase also, but are much more sensitive to changes in neutron spectrum arising from changes in position or changes in

neighboring components. In some cases the helium production rate can actually decrease even though undoped specimens in the same reactor position experience increases in helium production. This difference is due to the fact that ^{59}Ni production varies roughly as the second power of the dpa level, while the burn-out of ^{59}Ni is roughly linear with dpa.[14] Both reactions are separately but strongly sensitive to fine details of the neutron spectra.

Status of Other Types of Examination

Electron microscopy has been performed by Prof. J. F. Stubbins (NORCUS assignee at PNL from the University of Illinois) on all twelve specimen conditions of the second discharge at 365°C. Data analysis is now in progress. Density change measurements are in progress on TEM specimens from MOTA-1E at 365°C. 495°C (original) and 495°C (replacement) and the second discharge of the 495°C (replacement) from MOTA-1F.

REFERENCES

1. R. L. Simons, H. R. Brager and W. Y. Matsumoto, J. Nucl. Mater. 141-143 (1986) 1057-1060.

2. G. R. Odette, J. Nucl. Mater. 141-143 (1986) 1011-1017.

3. M. Kiritani, J. Nucl. Mater. 160 (1988) 135-141.

4. F. A. Garner, M. L. Hamilton, R. L. Simons and M. K. Maxon, "Isotopic Tailoring with ^{59}Ni to Study the Influence of Helium/dpa Ratio on Tensile Property Changes," DOE/ER-0313/8, pp. 108-113.

5. H. R. Brager, F. A. Garner and M. L. Hamilton, J. Nucl. Mater. 133 & 134 (1985) 594-598.

6. M. L. Hamilton, A. Okada and F. A. Garner, "Tensile Behavior and Swelling of Ternary Austenitic Allays Irradiated in Different Neutron Spectra." Proceedings 4th International Conference on Fusion Reactor Materials, Kyoto, Japan, Dec. 3-8, 1989, J. Nucl. Mater. (in press).

7. J. F. Stubbins and F. A. Garner, "The Relative Influence of Helium/dpa Ratio and Other Variables on Neutron-Induced Swelling at Fe-Ni-Cr Alloys at 495°C and 14 dpa." Proceedings 4th International Conference on Fusion Reactor Materials, Kyoto, Japan, Dec. 3-8, 1989, J. Nucl. Mater. (in press).

8. H. Kawanishi, F. A. Garner and R. L. Simons, "Synergistic Effects of Helium and Other Variables on Microstructure Change in Neutron-Irradiated Fe-Ni-Cr Alloys Doped with Nickel-59." Proceedings 4th International Conference on Fusion Reactor Materials, Kyoto, Japan, Dec. 3-8, 1989, J. Nucl. Mater. (in press).

9. N. F. Panayotou, S. D. Atkin, R. J. Puigh and B. A. Chin, The Use of Small-scale Specimens for Testing Irradiated Material, ASTM STP 888, W. R. Corwin and G. E. Lucas, Eds., American Society for Testing and Materials, Philadelphia, 1986, pp. 201-219.

10. F. A. Garner, M. L. Hamilton, N. F. Panayotou and G. D. Johnson, J. Nucl. Mater. 103 & 104 (1981) 803-808.

11. F. A. Garner, H. R. Brager, M. L. Hamilton, R. A. Dodd and D. L. Porter, Radiation Effects 101 (1986) 37-53.

12. H. Farrar IV and B. M. Oliver, "A Mass Spectrometer System to Determine Very Low Levels of Helium in Small Solid and Liquid Samples," J. Vac. Sci. Technol. A4, (1986), 1740.

13. B. M. Oliver, J. G. Bradley, and H. Farrar IV, "Helium Concentration in the Earth's Lower Atmosphere," Geochim. Cosmochim. Acta 48, (1984), 1759.

14. L. R. Greenwood, J. Nucl. Mater. 115 (1983) 137.

FUTURE WORK

This effort will continue, concentrating on microscopy and additional tensile testing.

ACKNOWLEDGEMENTS

This work was supported by the U.S. Department of Energy under Contract DE-AC06-76RLO 1830.

CORRELATION OF MECHANICAL PROPERTY CHANGES IN NEUTRON IRRADIATED PRESSURE VESSEL STEELS ON THE BASIS OF SPECTRAL EFFECTS - H. L. Heinisch (Pacific Northwest Laboratory)[a]

PURPOSE

To investigate the effects of the neutron spectrum on mechanical property changes in metals.

SUMMARY

Comparisons are made of tensile data on specimens of A212B and A302B pressure vessel steels irradiated at low temperatures (40-90°C) and to low doses (< 0.1 dpa) with 14 MeV D-T fusion neutrons in the Rotating Target Neutron Source (RTNS-II), with fission reactor neutrons in the Omega West Reactor (OWR) and the Oak Ridge Research Reactor (ORR), and with the highly thermal spectrum at the pressure vessel surveillance positions of the High Flux Isotope Reactor (HFIR). For each neutron spectrum, damage cross sections are determined for several defect production functions derived from atomistic computer simulations of collision cascades. Displacements per atom (dpa) and the numbers of freely migrating defects are tested as damage correlation parameters for the tensile data. The data from RTNS-II, OWR and ORR correlate fairly well when compared on the basis of dpa, but the data from HFIR show that only about one sixth as many dpa are needed to produce the same radiation-induced yield stress changes as in the other neutron spectra. In the HFIR surveillance position a significant fraction of the displacements is produced by recoils resulting from thermal neutron captures. Having energies of about 400 eV, these recoils are much more efficient per unit energy at producing freely migrating defects than the high energy recoils responsible for most of the displacements in the other neutron spectra considered. A significantly better correlation of data from HFIR with those from the other spectra is achieved when the property changes are compared on the basis of the production of freely migrating self-interstitial defects. This parameter may better represent the defects participating in the radiation strengthening process in this temperature and fluence regime.

PROGRESS AND STATUS

Introduction

A critical issue in the development and testing of nuclear materials is the prediction of the radiation-induced changes in properties of a material under one set of irradiation conditions from information obtained under a different set of irradiation conditions. A good example of the importance of this is the recent discovery' that pressure vessel steel in surveillance positions of the High Flux Isotope Reactor (HFIR), irradiated in a very soft spectrum at very low flux, has embrittled much faster than predicted from design data obtained at higher fluxes with harder spectra. This has raised concerns[2] that light water reactor vessel supports may be subject to a similar underestimate of their embrittlement. The HFIR embrittlement data were compared to the materials test data on the basis of displacements per atom (dpa), a damage parameter that is widely used and has been found to account for differences in neutron spectra extremely well in most cases.

A common reasonable assumption when data cannot be correlated on the basis of dpa (assuming material variables and temperatures are constant) has been that differences in the magnitude of the neutron flux, which virtually always accompany spectral differences, are responsible. In this paper, however, spectral effects beyond dpa will be considered. HFIR surveillance data will be compared with test data from other spectra using damage parameters based on the production of freely migrating point defects.

Radiation effects data correlation and extrapolation are also important issues in the development of materials for fusion reactors. So far, direct comparisons of fission and fusion neutron damage have been possible only at extremely low doses (< 0.1 dpa) relative to expected service conditions. In recent direct comparisons,' irradiations of metals and alloys were performed with 14-MeV D-T neutrons at the Rotating Target Neutron Source (RTNS-II) and with pool type reactor neutrons at the Omega West Reactor (OWR). A302B pressure vessel steel was included among the alloys in that experiment. A212B, the HFIR pressure vessel steel, was also included in OWR irradiations, and its irradiation hardening was compared with that of A302B.[4]

A320B and A212B have very similar compositions, especially with respect to the elements suspected of affecting embrittlement. The compositional differences are discussed in Ref. 4, where it is shown that A212B and A302B steels displayed the same fluence dependence of irradiation hardening when irradiated in OWR. At fluences low enough that impurity type and concentration are not affected by transmutations, it is reasonable to assume that A212B will harden the same as A302B in any neutron spectrum. By making this assumption in the present study, the data base for low-dose radiation-induced yield stress changes of A302B and A212B is effectively broadened to include four very different neutron spectra (see Table 1).

(a) Pacific Northwest Laboratory is operated for the U.S. Department of Energy by Battelle Memorial Institute under Contract DE-AC06-76RLO 1830.

Table 1

Characteristics of Neutron Spectra

	HFIR[a]	ORR[b]	OWR[c]	RTNS-II[d]
Total Flux (n/cm²/s)	1.2×10^{10}	2.2×10^{14}	1.9×10^{14}	1.0×10^{12}
Thermal Flux Fraction (E < 0.414 eV)	0.96	0.72	0.42	0.0
Flux Fraction (E > 0.1 MeV)	0.022	0.11	0.32	1.0
Flux Fraction (E > 1.0 MeV)	0.015	0.055	0.17	1.0
Damage Rate in Iron (dpa/s)	3.9×10^{-13}	1.8×10^{-8}	5.7×10^{-8}	3×10^{-9} to 3×10^{-11}

(a) Surveillance position, key 7, location 7, at pressure vessel.
(b) Location P8, outside core.
(c) In core.
(d) Peak flux; fluxes in RTNS-II vary with distance from the source.

In this report the radiation-induced changes in yield stress occurring in all four neutron spectra will be compared on the basis of several damage parameters, including defect production functions derived from atomistic modeling results. In making these comparisons it is assumed that any differences in behavior due to the differences in irradiation temperatures (90°C and 50°C) are small.

The Neutron Spectra

Data discussed here are for materials irradiated in RTNS-II, OWR, the surveillance positions in HFIR, and in an out-of-core position in the Oak Ridge Research Reactor (ORR). Characteristics of the four neutron spectra used in the computations are listed in Table 1. The variation in neutron spectra is quite extreme: the HFIR pressure vessel surveillance flux is dominated by thermal neutrons, while the RTNS-II flux consists entirely of 14 MeV neutrons.

The damage rates in dpa/s in iron vary over 5 orders of magnitude. In RTNS-II the magnitude of the neutron flux decreases with distance from the source, so doses varying by about a factor of 100 were achieved by placing specimens at increasing distances from the source during the same run. Damage rates in RTNS-II varied from 3×10^{-11} to 3×10^{-9} dpa/s, placing the damage rates in RTNS-II between those of HFIR and the other reactors. In an earlier comparison of the tensile data from these irradiations,' it was found that there was no apparent effect of damage rate for the OWR, ORR and RTNS-II irradiated material. Thus, if the "accelerated embrittlement" of the HFIR surveillance material is due to a rate effect, then this effect is important only at extremely low fluxes.

Damaae Correlation Parameters

Perhaps the earliest attempts to account for the effects of the spectrum of neutron energies were to compare property changes on the basis of the measured fast neutron fluence (commonly E > 1 MeV or E > 0.1 MeV). This damage parameter, still in wide use, requires only limited knowledge of the neutron spectrum and relies on the fact that, generally, most of the defects are produced by the higher energy neutrons. Of course, comparisons on the basis of fast neutrons are strictly valid only if the high energy portions of the spectra involved have the same shape.

In specific cases a significant fraction of the defects can be produced by other than the higher energy neutrons. For example, thermal neutron capture by an iron atom results in a recoil atom of about 400 eV, which produces displacement damage in iron or steels. Thus, in a highly thermal neutron spectrum, the fast neutron fluence gives a poor representation of the displacement damage in iron.

Dpa was developed as a spectrum-sensitive exposure index and has been used as a highly successful correlation parameter. Dpa is superior to fast neutron fluence because it takes into account the spectral shape and includes some measure of the response of the material. Dpa is calculated measure of the average number of times an atom of the material can be displaced during an irradiation, and it takes into account the fraction of recoil energy lost to inelastic processes that cannot produce displacement damage. To obtain dpa values, the displacement cross section must be known for the given neutron spectrum and material.[5] Calculation of the dpa cross section for a given material requires a neutron spectrum, a set of neutron

reaction cross sections, a model of the kinematics of the reactions that produce primary atomic recoils, a model for the dissipation of the primary recoil energy as electronic excitation and damage energy, and a model for the conversion of damage energy into dpa. Displacement per atom cross sections for iron are routinely reported with dosimetry information, and they can be calculated for most elements in the specified neutron spectrum using a computer code such as SPECTER.[6]

Dpa is a calculated measure of the potential to create point defects. It is not generally equal to, nor necessarily even proportional to, the number of residual point defects. The actual number of radiation-induced point defects present in a material at any time depends on the number of defects initially produced by each recoil atom and on defect interactions that occur after the displacement events (which depend on the spatial distribution of defects, crystal structure, material composition, time, temperature, and the material's radiation and deformation history).

The fraction of initially displaced atoms that become residual defects varies with primary recoil energy because the nature of collision cascades is energy dependent. Within a collision cascade created by a high energy recoil, a significant fraction of the hundreds of initially produced point defect pairs recombines as the locally high energy density in the cascade region dissipates in about 10^{-11} s (cascade quenching). At this point the measured number of residual defect pairs (at low temperatures where defects are immobile) resulting from a cascade is about 30-40% of the number of calculated dpa for the cascade.[7,8] Most of the residual defects form into clusters (the stability of which depends on the crystal temperature). During continued local annealing for a short time within the cascade region, additional clustering and recombination takes place, while a small fraction of the residual defects escapes the cascade region, becoming freely migrating defects.[9]

This picture of defect production in collision cascades has evolved over the past 25 years, aided especially by atomic-level computer simulations. Early derivations of damage functions that reflect the numbers of residual defects observed in computer simulations were performed by Doran et al.,[10,11,12] who developed damage functions for residual defects/dpa and freely migrating vacancies/dpa for iron. Heinisch, et al.[3,9] performed significantly improved simulations for copper and produced the functions for freely migrating defects used in the present paper.[13]

Above a threshold recoil energy (about 50 keV in iron) cascades tend to form multiple, separated damage regions or subcascades.[14] As a result, the fractions of initially produced defects that recombine or become freely migrating defects are constant with energy above the threshold recoil energy for subcascade formation. At the other end of the energy scale, low energy recoils create only a few defect pairs. The energy density in these cascades is not high enough to drive significant correlated recombination or clustering, so during short-term annealing nearly all the point defects produced become freely migrating defects. Thus, the efficiency of production of freely migrating defects relative to calculated dpa values is a function of recoil, energy, becoming constant at higher energies.

Figure 1 shows the production of freely migrating defects and displacements as a function of recoil energy in copper. The curves for freely migrating interstitials and vacancies are the functions determined from atomistic computer simulations of displacement cascades,[13] and they are given in terms of the expression for

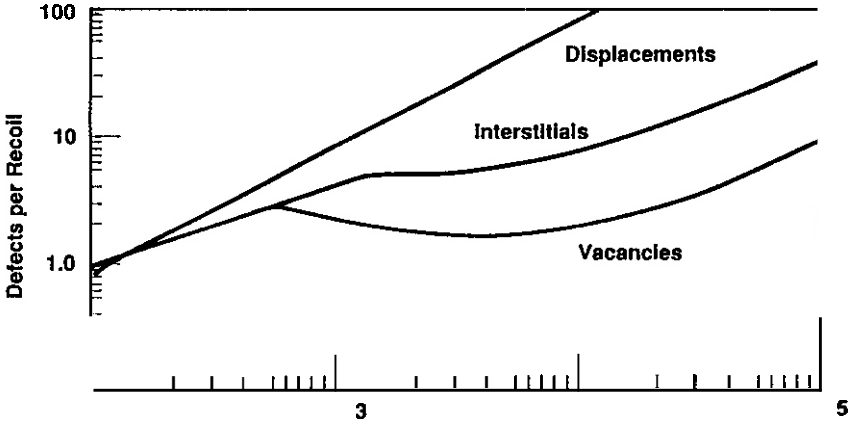

FIGURE 1. The numbers of calculated disolacements. freely miaratina vacancies and freely miaratina self-interstitials per recoil as a function of recoil energy. The free defect values are calculated with functions from atomistic computer modeling, Ref. 6.

total residual defects extracted by Simons' from resistivity measurements. It was determined in the modeling that short-term annealing in the cascade region at room temperature reduces the number of residual point defects by 22% at all energies. The displacement curve is calculated using the familiar NRT expression.[15]

Opa can be an effective damage correlation parameter only if the mechanism responsible for the property change of interest is proportional to dpa. This proportionality is influenced by the temperature and by the rate of damage production as well as by the neutron energy spectrum. Since environments with different neutron spectra usually have different damage rates, spectral and rate effects are very difficult to isolate from each other. The failure of mechanical property change data to correlate on the basis of fast fluence or dpa has often been attributed to rate effects. For example, the initial comparison' of HFIR pressure vessel surveillance Charpy data with reference data at higher damage rates was made on the basis of fast neutron fluence. The "accelerated embrittlement" of the HFIR pressure vessel steel was attributed to unspecified rate effects. Comparison of the HFIR data with recent low fluence tests by Nanstad et al.[16] in ORR showed the same accelerated embrittlement in both tensile and Charpy tests when compared on the basis of fast fluence (and dpa obtained from the fast fluence). They concluded that the results could be explained by either rate effects or spectral effects, but not unambiguously, since the effects are concurrent and inseparable in this case.

Failure of these data to correlate on the basis of dpa should not be surprising. At low doses property changes are likely to be sensitive to the total number of residual point defects, the numbers of freely migrating defects, or the numbers of defect clusters contained in collapsed displacement cascades. All of these quantities vary with the recoil energy and are proportional to dpa only at high recoil energies.

Computations

In the absence of comparable information for iron, the damage correlation functions for copper reported in Reference 13 were used, with modifications, for the pressure vessel steels. The magnitudes of surviving defect fractions are expected to be somewhat different for iron and copper since the point defect distributions initially produced by collision cascades in iron are somewhat more diffuse than those in copper.[14] In iron a smaller fraction of defect pairs recombines as the cascade region cools. To account for this, parameter values in the expression for total residual defects were modified according to Simons' prescription' to reflect more appropriate values for iron. The recoil-energy-dependent damage functions that describe the partitioning of the residual defects. Parameters for these functions were taken to be the same for iron as for copper. Thus, at high energies, residual defects are 40% of the calculated dpa, freely migrating interstitials are 5.6% and freely migrating vacancies are 1.4%.

The functions of copper in Reference 13 were based on short-term annealing of individual cascades through Stage III recovery (approximately room temperature, where vacancies and divacancies are mobile. In iron (and pressure vessel steels) vacancies are not mobile at the irradiation temperatures considered here, so the freely migrating vacancies should really be considered as 'potentially freely migrating vacancies."

Greenwood's SPECTER computer code[6] was used to generate the primary recoil spectra for iron into which the damage correlation functions were folded. For most cases for which the code was developed, thermal neutrons have been thought to have little effect. Thus, in calculating some quantities, including the recoil spectra, the code omits the contributions due to thermal neutron captures. They can easily be added manually, at least to the level of precision necessary for the present investigation. The neutron spectra for ORR and HFIR had 56 energy groups, with a single energy group below 0.414 eV. Calculations utilizing the recoil spectra are estimated to lead to variations on the order of 20-30% in calculating the defect production cross sections. The extreme cases of neutron spectra here are so different that such differences are negligible for our purposes.

Results

Irradiation temperatures for HFIR and ORR were 49% and 43°C respectively, while the RTNS-II and OWR irradiations were at 90°C. All the tensile tests were done at room temperature on flat miniature tensile specimens. The specimens used at ORNL for HFIR and ORR were somewhat larger than those for the RTNS-II and OWR tests done at PNL. The ORNL specimens with a gauge width of 1.5 mm and thickness of 0.75 mm have a cross sectional area about four times larger than the PNL specimens at 1.02 mm gauge width and 0.25 mm thickness. While the specimen size, fabrication techniques and testing procedures may affect the measured values of the yield stress in the two situations, the measured changes in yield stress due to irradiation hardening have been found to be the same for both types of specimens.[4]

Defect production cross sections were calculated for dpa, residual defects per atom at 4K (rdpa), freely migrating interstitials per atom (fmipa) and freely migrating vacancies per atom (fmvpa). The calculated values are in Table 2.

Table 2

Spectral Averaged Defect Production Cross Sections for Iron

Neutron Spectrum	Cross Sections, b dpa	rdpa	fmipa	fmvpa
RTNS-II	2900	1200	170	42
OWR	250	110	19	8
ORR	77	36	11	7
HFIR	30	17	a	7

In Figure 2 the radiation-induced yield stress changes at room temperature in A3026 and A2126 pressure vessel steels are plotted as a function of fast neutron fluence (E > 1 MeV) in the various irradiation environments. Each point is the result of an individual test. The hand-drawn curve is simply to aid visual organization. It is reproduced in the same position relative to the OWR data in Figures 2-4.

While the general trend of radiation hardening is observed in the data for all spectra in Figure 2, the data are not well-correlated. In particular, in HFIR the fast fluence necessary to produce a yield stress change of 50 MPa is less by about an order of magnitude than that in the other spectra, reflecting the "accelerated embrittlement" in the HFIR surveillance tests.'

In Figure 3 the data are replotted as a function of calculated dpa. For all but HFIR, the data grouping is much tighter, being within a factor of 2 in dpa.

Figure 4 shows the yield stress data replotted as a function of fmipa using the calculated defect production function shown in Figure 1. On the basis of fmipa the HFIR data are correlated to within a factor of two of the OWR, ORR and RTNS-II data. Relative to the comparison in Figure 3, the HFlR data have been shifted toward the RTNS-II data by a factor of 4.5.

Plots for rdpa and fmvpa are not shown. Using rdpa, the HFIR data shift toward RTNS-II by a factor of 1.4, only a slight difference from dpa. Using fmvpa, the HFIR data shift by a factor of 16, resulting in an over-correction, i.e., implying there is less hardening in HFIR than in other spectra.

Discussion

Of the damage functions examined in this paper, fmipa produces the best correlation of the yield stress changes of HFIR pressure vessel steel with those in different neutron spectra (Figure 4). Since the Charpy test data and tensile test data exhibit a similar dependence on fluence,' the same correlation will occur for embrittlement when fmipa is used as a damage parameter.

The dramatic improvement toward correlation of the HFIR data when fmipa is used as a damage parameter is a result of the 96% thermal neutron spectrum at the HFIR surveillance positions, combined with the increased efficiency of freely migrating defects per dpa at low energies. Thermal neutron captures in iron produce recoils with an average energy of 395 eV, enough to make about 4 displacements per recoil. Of the displaced atoms, an average of 2.4 displaced atoms per recoil become freely migrating interstitials (according to the model shown in Figure 1). In contrast, the average recoil from 14 MeV neutrons, about 200 keV, produces on average about 1100 displacements but only 63 freely migrating interstitials. Even fewer vacancies potentially escape the cascades, but they are not expected to be sufficiently mobile below 100°C to be considered as freely migrating defects.

The hardening centers responsible for the increases in yield stress and embrittlement of A2128 irradiated in HFIR and ORR are too small to be imaged by transmission electron microscopy.' A survey of post-irradiation annealing studies on A2128[1] showed recovery beginning about 300°C. Thus, at irradiation temperatures below 100°C small clusters are expected to be relatively stable.

Hardening centers can consist of defect clusters formed both immediately within cascades and by diffusion of the freely migrating defects. The freely migrating defects can recombine, go to existing sinks, form clusters or form complexes with interstitial impurities. Assuming that vacancy migration is negligible, interstitial-impurity complexes may be the most effective hardening centers. This is consistent with the much improved correlation of the HFIR tensile data on the basis of freely migrating interstitials.

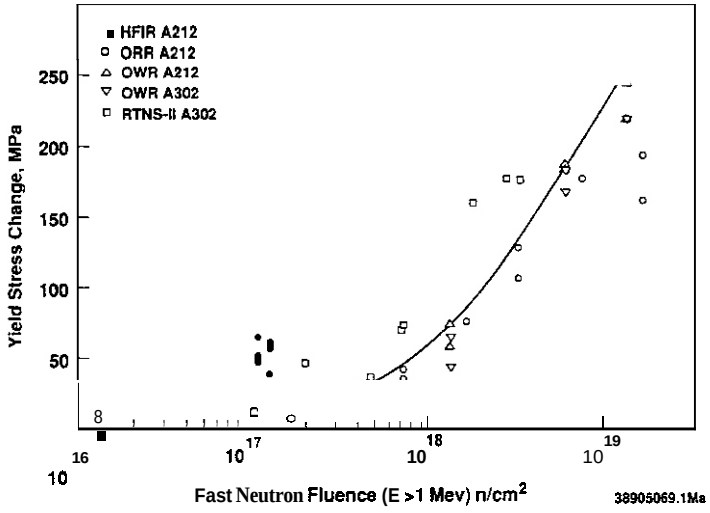

Figure 2. Change in 0.2% offset yield stress of A302B and A212B pressure vessel steels as a function of fast neutron fluence (E > 1 MeV). The hand-drawn curve is simply to aid visual organization. It is reproduced in the same position relative to the OWR data in Figures 2-4.

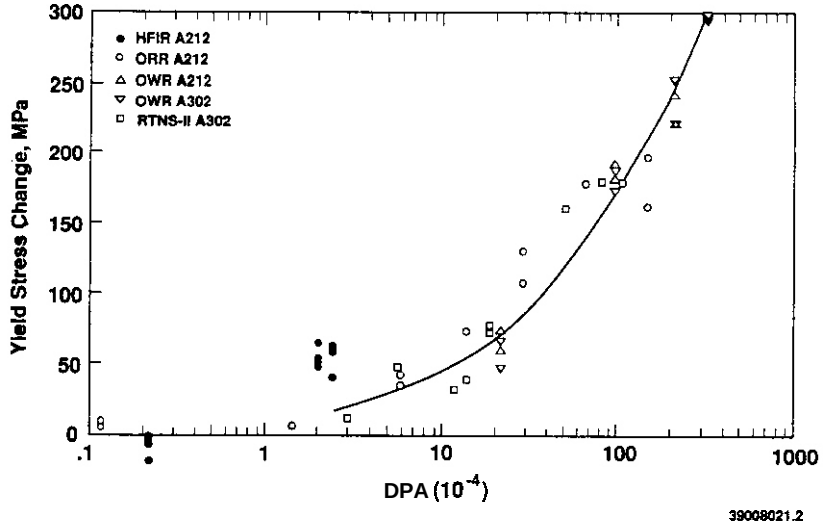

Figure 3. Change in 0.2% offset yield stress of A302B and A212B pressure vessel steels as a function of dpa.

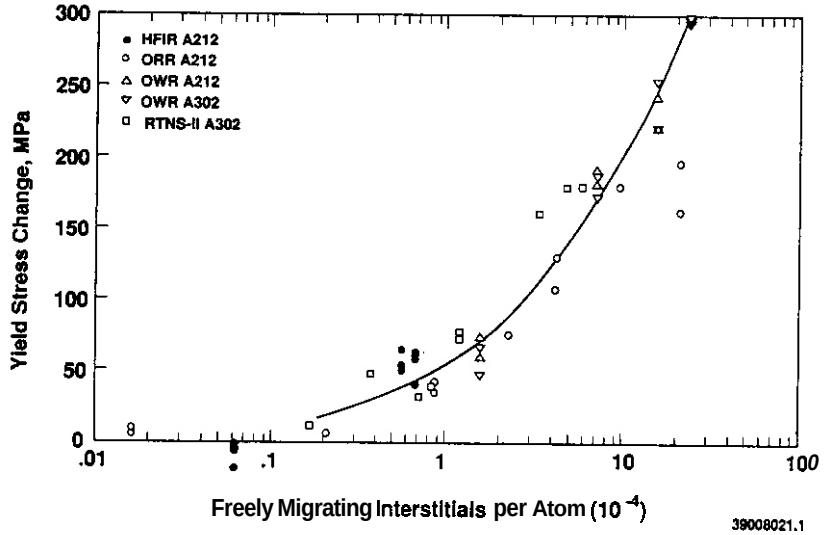

Figure 4. Change in 0.2% offset yield stress of A302B and A212B pressure vessel steels as a function of freely migrating interstitials per atom (fmipa).

The RTNS-II and OWR data correlate well on the basis of dpa (Figure 2), but less well on the basis of fmipa (Figure 3). In these much harder spectra the defect clusters fnrmed directly within cascades probably provide a greater contribution to the yield stress changes at low temperatures and doses than the small number of freely migrating defects. Thus, it may be inappropriate to compare radiation hardening data from all four spectra on the same basis, since the contributions of various hardening mechanisms are probably different. Perhaps a better damage correlation parameter for comparing the data from all four spectra would be an appropriately weighted combination of freely migrating interstitials and clusters produced directly in cascades.

A marked improvement in correlation of the HFIR and ORR embrittlement data was also achieved by Mansur and Farrell,[11] who compared the data empirically as a function of thermal neutron fluence. That correlation was achieved because in these spectra most of the freely migrating defects are produced by the low energy recoils from thermal neutron captures.

Inferences of freely migrating defect fractions from experimental measurements may be very useful for developing damage correlation functions. Wiedersich[18] has devised a simple empirical function to describe the energy dependence of concentrations of freely migrating defects extracted from solute segregation experiments. Cascades were produced by ion bombardment at much higher temperatures than the neutron irradiations dealt with here. Wiedersich's function and the function used here have the same general characteristics: a large fraction of the residual defects from low energy recoils are freely migrating, but a very small fraction of defects from high energy cascades are freely migrating. The primary difference between the empirical and the modeling-derived functions is in the value of the fraction at high energies. Computer simulations[9] gave limiting values for the fractions of freely migrating defects for individual, isolated cascades in Cu. About 3% (relative to calculated dpa) of the interstitials always escaped the cascades regardless of the parameter settings for clustering and recombination. Interpretations of the solute segregation experiments[19] imply that less than 1% of interstitials are freely migrating. Continued investigation is needed to develop this approach for damage correlation, but the concept of diminished free defect production at high energies is definitely well-established.

A single, easily calculated spectral correlation parameter, applicable in all neutron spectra, seems unlikely. Dpa works well if the spectra are not radically different. If secondary aspects of defect production in cascades, such as fmipa, are to be used as damage parameters, then their relationships to the mechanisms of mechanical property changes under various irradiation conditions must be appreciated. At the very least, researchers and test engineers should be aware that dpa is not always an appropriate damage correlation parameter for spectral effects.

ACKNOWLEDGMENTS

The author is most grateful to L. R. Greenwood for guidance in using the SPECTER code and for providing the OWR and RTNS-II neutron spectra, to R. L. Childs for the ORR and HFIR neutron spectra, to K. Farrell for providing valuable assistance, and to D. G. Doran for helpful comments on the manuscript. This work was supported by the U.S. Department of Energy under Contract DE-AC-76RLO 1830.

REFERENCES

1. "Evaluation of HFIR Pressure-Vessel Integrity Considering Radiation Embrittlement," R. D. Cheverton, J. G. Merkle and R. K. Nanstad, eds., ORNL/TM-10444 (1987).

2. R. D. Cheverton, F. B. Kam, R. K. Nanstad and G. C. Robinson, Nucl. Eng. Des. 117, 349 (1989).

3. H. L. Heinisch, J. Nucl. Mater. 155-157, 121 (1988).

4. M. L. Hamilton and H. L. Heinisch, Proceedings of the 14th ASTM International Symposium on Radiation Effects in Metals, Andover, MA, June 27-29, 1988, ASTM-STP-1046, 45 (1990).

5. D. G. Doran and N. J. Graves, "Displacement Cross-Sections and PKA Spectra: Tables and Applications," HEDL-TME 76-70 (1976).

6. L. R. Greenwood and R. K. Smither, "SPECTER: Neutron Damage Calculations for Materials Irradiation," ANL/FPP/TM-197 (1985).

7. R. L. Simons, J. Nucl. Mater. 141-143, 665 (1986).

8. J. H. Kinney, M. W. Guinan and Z. A. Munir, J. Nucl. Mater. 122-123, 1028 (1984).

9. H. L. Heinisch, J. Nucl. Mater. 117, 46 (1983).

10. D. G. Doran, Trans, ANS 15, 241 (1972).

11. D. G. Doran, Nucl. Ens. Desisn 33, 55 (1975).

12. D. G. Doran, R. L. Simons and W. N. McElroy, ASTM STP-570, 290 (1976).

13. H. L. Heinisch and F. M. Mann, J. Nucl. Mater. 122-123, 1023 (1984).

14. H. L. Heinisch and B. N. Singh, in proc. Fourth International Conference on Fusion Reactor Materials, Kyoto, Japan, December 4-8, 1989.

15. M. J. Norgett, M. T. Robinson and I. M. Torrens, Nucl. Eng. Design 33, 50 (1975).

16. R. K. Nanstad, K. Farrell, D. N. Braski and W. R. Corwin, J. Nucl. Mater. 158, 1 (1988).

17. L. K. Mansur and K. Farrell, J. Nucl. Mater. 170, 236 (1990).

18. H. Wiedersich, in proc. Fourth International Conference on Fusion Reactor Materials, Kyoto, Japan, December 4-8, 1989.

19. L. E. Rehn, P. R. Okamoto and R. S. Averback, Phvs. Rev. B 30, 3073 (1984).

PUBLICATIONS

This paper has been accepted for publication in The Journal of Nuclear Materials

LOW EXPOSURE SPECTRAL EFFECTS EXPERIMENT: IRRADIATIONS AT 473 K IN OMEGA WEST REACTOR - H. L. Heinisch and M. L. Hamilton (Pacific Northwest Laboratory)[a]

PURPOSE

The purpose of this work is to determine the effect of the neutron spectrum on radiation induced changes in mechanical properties of metals.

SUMMARY

Tensile tests have been performed on specimens from the last set of Omega West Reactor (OWR) irradiations performed as part of the Low Exposure Spectral Effects Experiment (LESEX). Tensile data are reported.

PROGRESS AND STATUS

Introduction

The LESEX experiment was designed to allow direct comparisons of the damage caused by both fission and fusion neutrons on the tensile properties and microstructures of metals and alloys.'.' During the lifetime of the Rotating Target Neutron Source (RTNS-II), miniature tensile specimens and TEM disks of pure copper, 316 stainless steel, A302B pressure vessel steel and various copper alloys were irradiated with 14 MeV d-t fusion neutrons to doses ranging from 0.0003 to 0.04 dpa at temperatures of 25, 90, 150, 200, 290, and 450°C. Companion irradiations with fission reactor neutrons to comparable doses in these materials were performed at OWR at temperatures of 90, 200 and 290°C.

Tensile tests and microscopy were performed previously on specimens irradiated in both environments at 90 and 290°C.' The final OWR irradiations were performed at 200°C to three fluence levels. Mechanical difficulties with the OWR irradiation vehicle, including the burn-out of the electrical resistance heating coils, precluded its use for further irradiations, and it was decommissioned.

Exuerimental Procedures and Results

Tensile tests were recently performed at room temperature on the specimens irradiated at 200°C in OWR using the same procedures as in the previous tests.[1] The results are given in Table 1.

As is shown in the table, the thickness measurements on each batch of specimens were generally quite consistent, varying by less than 0.025 mm from specimen to specimen. The exceptions to this are the A302B specimens, which were punched from slices of bar that varied in thickness much more than the rolled sheet typically used for punched specimens. In addition, the two Cu5Ni specimens irradiated in capsule 014 (PX68 and PX71) appeared to be slightly thinner than those irradiated in capsules 012 and 013. No explanation is readily available for this observation.

A number of specimens exhibited a relatively sharp 'yield point' relative to the remainder of the tests, where 'yield point' is used here to refer to a fairly sharp turn-over in the load-displacement trace at the end of the initial elastic loading, followed by a brief plateau at approximately constant load before the more typical increase in load observed with increasing strain. All of the SA316 specimens irradiated in both OWR and RTNS-II have exhibited this phenomenon, the effect becoming stronger with increasing dose. The duration of the plateau in terms of strain ranged from roughly 0.2 to 1%. The SA316 specimens irradiated in 014 actually exhibited a small (-3.5 MPa) yield drop rather than just a plateau. Other SA316 specimens in this experiment have exhibited yield drops as well, especially at the higher doses and higher irradiation temperatures. The Cu5Ni specimens irradiated in 013 and 014, i.e., to the two higher dose levels, also exhibited yield points. The fact that the Cu5Ni specimens exhibited the yield point plateau at only the higher dose levels, coupled with the transition in the SA316 from a plateau to a drop in load, suggests that the phenomenon is real, that it is a result of microstructural changes induced by neutron radiation, and that it is probably similar in nature to the yield drops traditionally produced by the pinning of dislocations by interstitial atmospheres.

Discussion

Figure 1 shows a comparison of the yield strength data from RTNS-II and OWR for solution annealed 316 stainless steel as a function of displacements per atom (dpa). Individual data points are shown only for the current tests. Trend lines are shown for 200% along with those for 90°C and 290°C for comparison. At

---

(a) Pacific Northwest Laboratory is operated for the U.S. Department of Energy by Battelle Memorial Institute under Contract DE-AC06-76RLO 1830.

Table 1.
Room Temperature Tensile Data on Specimens Irradiated in OWR at 200°C

Alloy	Specimen ID	Capsule ID	Fluence (10^{18} n/cm^2)	Thickness (mm)	YS (MPa)	UTS (MPa)	UE (%)	TE (%)
cu	--	--	0.0		4824	205211		
	c59	012	8.5	0.257	126	204	18.8	23.2
	C60	012	8.5	0.244	134	223	23.3	27.1
	C64	013	37.8	0.234	185	244	16.2	21.3
	C65	013	37.8	0.241	170	225	16.2	20.0
	C70	014	82.8	0.236	197	236	13.4	17.1
	c73	014	82.8	0.236	193	238	10.9	14.0
SA316	--	--	0.0	--	220211	574±20		
	A58	012	8.5	0.295	303	616	46.7	54.5
	A59	012	8.5	0.274	319	629	**54.6**	62.4
	A63	013	37.8	0.277	398	687	42.9	53.6
	A64	013	37.8	0.297	336	625	39.5	NA
	A68	014	82.8	0.297	446	681	36.1	42.6
	A69	014	82.8	0.302	449	696	39.6	50.5
A3028	--	--	0.0	--	49524	645±10		
	E63	012	8.5	0.274	557	645	3.8	7.6
	P64	012	8.5	0.244	512	571	4.6	6.5
	E68	013	37.8	0.373	650	705	2.5	4.1
	P65	013	37.8	0.338	652	729	4.0	7.0
	P55	014	82.8	0.241	732	756	0.5	0.9
A2128	--	--	0.0	--	428210	565±6		
	H19	012	8.5	0.277	455	519	3.3	4.7
	H20	012	8.5	0.277	**350**	417	3.0	4.5
	H31	014	82.8	0.244	471	525	3.5	4.7
	H32	014	82.8	0.274	409	435	1.9	3.0
Cu5Al	--	--	0.0	--	50±6	219±15		
	sx49	012	8.5	0.249	103	229	25.7	30.8
	SX50	012	8.5	0.244	110	244	31.6	33.3
	SX56	013	37.8	0.239	124	244	26.5	31.7
	SX61	013	37.8	0.236	137	**246**	22.4	26.1
	SX68	014	82.8	0.226	125	214	13.7	16.5
	SX71	014	82.8	0.213	137	239	14.1	16.5
Cu5Mn	--	--	0.0	--	6622	23528		
	CX62	012	8.5	0.241	133	270	22.9	25.6
	CX64	012	8.5	0.236	131	269	20.9	23.8
	CX68	013	37.8	0.231	146	273	20.1	22.5
	CX69	013	37.8	0.236	145	283	22.5	25.9
	cx73	014	82.8	0.246	140	270	22.6	24.6
	cx74	014	82.8	0.241	139	268	20.7	23.9
Cu5Ni	--	--	0.0	--	50±4	219±2		
	PX55	012	8.5	0.246	134	231	22.2	27.8
	PX56	012	8.5	0.234	108	237	22.5	25.7
	PX62	013	37.8	0.241	173	245	20.4	26.4
	PX66	013	37.8	0.241	191	251	18.0	24.6
	PX68	014	82.8	0.201	225	278	15.0	18.1
	PX71	014	82.8	0.198	203	240	13.1	16.8
CuAl25	--	--	0.0	--	417±16	456±16		
	JX21	012	8.5	0.274	545	571	0.6	4.4
	JX22	012	8.5	0.254	509	575	0.7	3.3
	JX29	013	37.8	0.257	543	566	0.6	3.6
	JX38	013	37.8	0.259	531	547	0.6	2.7
	JX63	014	82.8	0.259	540	***566***	0.6	2.5
	JX70	014	82.8	0.257	541	547	0.6	2.6

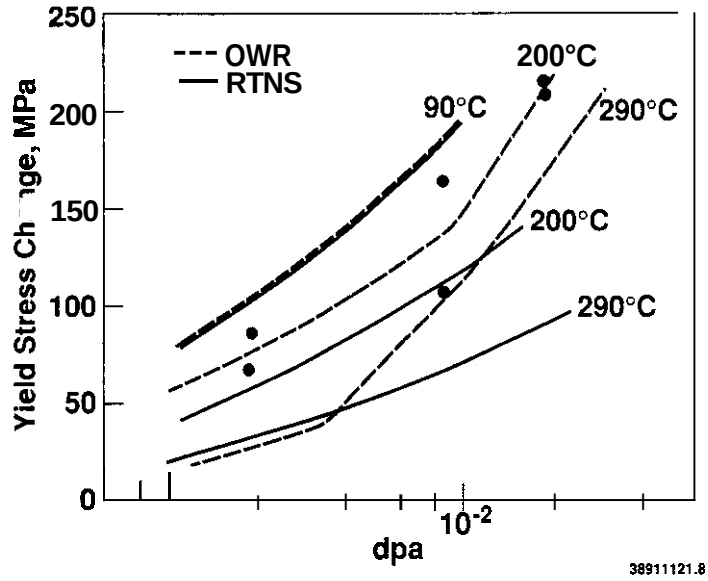

Figure 1. The changes in 0.2% offset yield stress of solution annealed 316 stainless steel irradiated at 90, 200 and 290°C in RTNS-II and OWR as a function of dpa. Individual data points are shown for only the 200°C irradiation in OWR.

90°C the yield strength change data from RTNS-II and OWR correlate well on the basis of dpa, while at 290 and 200°C irradiation in OWR produces more hardening per dpa than in RTNS-II. The trend line for 200°C in OWR is placed midway between the two data points at each exposure. Considering the scatter in the data, the difference in hardening in OWR and RTNS-II below 10^{-2} dpa implied by the trend lines may not be real. When the microstructures of specimens from RTNS-II and OWR at 90 and 290°C were examined by TEM,[3] it was determined that the very small clusters of point defects that were observed could account for the radiation induced hardening, independent of irradiation temperature. It was suggested that these clusters nucleated in OWR at temperatures below the target irradiation temperature during the daily ascent to power. This effect would be expected to be small at 90°C, and indeed, no difference in the OWR and RTNS-II data was observed. The temperature history effect, however, may well be responsible for the differences at 200°C. Such a mechanism is consistent with the observed variation in the threshold for the divergence in hardening, i.e., ~10^{-2} dpa at 200°C and ~4 x 10^{-3} dpa at 290°C. Examination of the microstructures of the SA316 TEM specimens irradiated at 200°C will provide additional information for understanding this behavior.

Detailed analysis of the yield stress data on copper, the copper alloys and the pressure vessel steels is in progress. Some preliminary information on trends in the data are reported below.

At 200°C the yield stress changes of A3028 pressure vessel steel irradiated in RTNS-II and OWR correlate well when compared on the basis of dpa. This was also observed at 90°C and 290°C.[1] The yield stresses for A212 pressure vessel steel are anomalously low. At 90°C A302 and A212 were found to behave the same.[4] An assortment of difficulties were encountered during the testing of the A212 specimens irradiated at 200°C. Fortunately, several more irradiated specimens are available for testing.

Yield stress changes of pure copper irradiated in RTNS-II and OWR at 200°C do not correlate on the basis of dpa. A factor of 10 less dose in dpa is needed in OWR to produce the same yield stress change as in RTNS-II. This is quite different from the factor of 2 more dpa needed to produce the same effect at 90°C.[1] At 290°C the data from the two spectra were found to correlate with dpa.' These results may be a further indication of temperature history effects in the OWR irradiations.

The binary copper alloys in OWR show a variety of temperature sensitivities. Cu5Mn shows essentially no difference in yield stress with increasing dose at 200°C, while Cu5Al shows a slight increase with dose. At 90°C these alloys display yield stress changes similar to that of pure copper. Cu5Ni displayed about the same changes in yield stress at 200°C as at 90°C, indicating very little temperature dependence in this fluence and temperature range.

CONCLUSIONS

The yield stress data for the 200°C OWR irradiations of the Low Exposure Spectral Effects Experiment show very interesting differences from what would be expected based on projections from the earlier data at 90°C and 290°C. At least some of the apparent inconsistencies might be related to temperature history effects we

suspect were occurring during the daily ascent to power of the OUR. Since the various materials have responded in different ways to the temperature history, at least on the basis of tensile property changes, the data may be quite useful in sorting out the operation of specific mechanisms involved in the effects. Characterization of the microstructures using TEH will provide additional information to consider in the analysis.

FUTURE WORK

Microstructural analyses and further tensile data analyses will be done on the materials irradiated at 200-c.

REFERENCES

1. H. L. Heinisch, S. D. Atkin and C. Martinez, J. Nucl. Mater. 141-143 (1986) 807.

2. H. L. Heinisch, J. Nucl. Mater. 155-157 (1988) 121.

3. N. Yoshida, H. L. Heinisch, T. Muroga, K. Araki and M. Kiritani, DOE/ER-0313/8 and in J. Nucl. Mater., in press.

4. M. L. Hamilton and H. L. Heinisch, ASTM-STP 1046, Vol II (1990) 45.

NEW INSIGHTS ON THE MECHANISMS CONTROLLING THE NICKEL DEPENDENCE OF SWELLING IN IRRADIATED Fe-Cr-Ni ALLOYS

J. J. Hoyt, Washington State University and F. A. Garner, Pacific Northwest Laboratory[a]

OBJECTIVE

The object of this effort is to determine the origins of radiation-induced changes in structural materials.

SUMMARY

In a previous report[1] the interstitial and vacancy biases for an edge dislocation in a binary alloy were examined, assuming the existence of an equilibrium Cottrell atmosphere around the line defect. The Larche' and Cahn treatment of stress relaxation due to a solute atmosphere was employed with the Wolfer and Ashkin formulation for the bias of an edge dislocation to compute the bias as a function of nickel concentration in the Fe-Ni system. Using the minimum critical void radius concept, the concentration-dependent bias was shown to offer a plausible explanation for the minimum in swelling observed at intermediate nickel levels and the gradual increase in swelling at higher nickel levels. In this report, a more realistic description of the composition dependence of vacancy diffusion has also been included, an addition which improves the model substantially.

PROGRESS AND STATUS

Introduction

The swelling behavior of irradiated metals is strongly dependent on composition. For example, in Fe-Cr-Ni alloys the swelling at relatively high temperatures decreases strongly with nickel until some intermediate level of 40-60% nickel is reached.[2] Thereafter, increases in nickel result in a more gradual increase in swelling. The strong decreases observed in swelling of austenitic alloys can be partially explained by the effect of various solute additions (Ni, Si, P) on vacancy diffusivity.[3-7] However, at present, no mechanism has been advanced for the slow upturn at higher nickel levels.

Although many studies have investigated the concentration dependence of various material parameters, few have considered the effect of compositional variations on microstructural bias factors. The interaction of a point defect, interstitial or vacancy, with the stress field of a given defect sink determines the bias toward one point defect over the other. Since the stress field is altered in the presence of a solute species, one would intuitively expect the bias to be dependent on its concentration.

Consider a binary alloy in which the solute atoms are oversized; i.e., the lattice parameter of the solute in the pure state is larger than that of the host species in its pure state. To reduce the total strain energy of a dislocation, the solute will tend to segregate on the tensile side and be repelled from the compressive side. In equilibrium a Cottrell atmosphere is established. Although this effect has long been known, it was only recently shown that the change in the stress field around a dislocation could be computed for concentrated solutions. We examine here the effect this change *in* stress field has on bias factors for edge dislocations in Fe-Ni alloys.

Marwick[8] computed the bias for a free surface due to solute redistribution by numerically solving the diffusion equations for solute, vacancy and interstitial species. The Marwick scheme is the preferred method of computing bias factors, but for a general distribution of defect sinks with non-homogeneous stress fields, the numerical solutions to the diffusion equations become quite intractable. We shall take a simpler approach and compute an **initial** bias by estimating the change in the stress field around an edge dislocation due to a Cottrell atmosphere. The emphasis on the word **initial** arises from the knowledge that sinks often become further enriched in various solutes via radiation-induced segregation.

Theoretical Background

Larche' and Cahn[9] have developed a general theory for the thermochemical equilibrium of solids under nonhydrostatic stress. A Cottrell atmosphere is one application of the theory and it was shown that the

---

[a] Pacific Northwest Laboratory is operated For the U.S. Department of Energy by Battelle Memorial Institute under Contract DE-AC06-76RLO 1830.

stress field with the solute atmosphere present is given by the stress field for a pure material but with the various elastic constants replaced by the open-field elastic constants. These constants, denoted by *, are given by

$$E^* = E/(1 + \chi\eta^2 E) \quad (1a)$$

$$\nu^* = (\nu - \chi\eta^2 E)/(1 + \chi\eta^2 E) \quad (1b)$$

$$(\kappa^{-1})^* = 3(1 - 2\nu^*)/E^* \quad (1c)$$

where linear elasticity has been assumed. The parameters E, κ and ν are, respectively, the elastic and bulk moduli and Poisson's ratio. The quantity η is the fractional change in the lattice parameter (a) with composition (c); i.e.,

$$\eta = \frac{1}{a}\left(\frac{da}{dc}\right) \quad (2)$$

Finally, χ is given as $(f'')^{-1}$, where f'' is the second derivative of the free energy with composition. All parameters are evaluated at the average concentration.

To model in an approximate way the Fe-Ni system, the various material parameters need to be evaluated. In general, E, κ and ν are dependent on the average concentration, but for simplicity we assume they are constant. The values employed for the subsequent computations are the same as employed in an earlier study and represent conditions typical of fast reactor irradiation.[12] The fractional change in lattice parameter is found by assuming a linear dependence vs. the concentration of Ni; i.e., Vegard's law. Lattice parameters of pure Ni and pure Fe are readily obtained.

To estimate χ, a model for the free energy of mixing in Fe-Ni must be assumed. (Since we are ultimately concerned with the second derivative, the free energy and free energy of mixing can be used interchangeably.) The simplest nontrivial free energy model is the regular solution approximation with a free energy of mixing of the form

$$f = \omega c(1 - c) + RT(c \ln c + (1 - c)\ln(1 - c)) \quad (3)$$

where c is the Ni concentration, R is the gas constant and ω is an interaction parameter. The first term on the right of Equation 3 is the temperature-independent enthalpy of mixing, ΔH. By adjusting ω to fit the experimentally measured ΔH, a better approximation to ΔH is established.

Figure 1 shows the enthalpy of mixing data for Fe-Ni measured by Kubaschewski et al.[11] and the assumed model used in the calculations (ω = 8510 J/mol). The assumed ΔH vs. c model is a reasonable approximation up to the Invar concentration but is rather poor at higher Ni levels. Nevertheless, for the first evaluation we expect the results to be qualitatively correct.

Using a perturbation technique for non-linear diffusion equations, Wolfer and Ashkin[13] derived the bias of an edge dislocation. In the absence of applied stress the bias is

$$Z_{i,v} = 1 + \left(\frac{Bo_{i,v}}{kt}\right)^2 / [16a^2 \ln(\frac{R}{a})] \quad (4)$$

where R and a are outer and inner cutoff radii respectively, measured in units of the Burgers vector and k is the Boltzmann's constant. The subscript i or v refers to interstitial or vacancy. The quantity $Bo_{i,v}$ is given by

$$Bo_{i,v} = v_{i,v} K (1 - 2\nu)/2\pi(1 - \nu) \quad (5)$$

where $v_{i,v}$ is the difference between the defect volume and atomic volume.

Equation 5 was derived assuming a stress field around a dislocation in an compositionally homogeneous alloy. We now examine the change in Z when the stress field relaxation is due to a solute atmosphere. Thus, Equations 1-3 are employed in conjunction with Equations 4 and 5 to arrive at the initial bias as a function of average Ni concentration.

Figure 2 shows the ratio of Z_i over Z_v vs. concentration of Ni (C_{Ni}) at various temperatures. The curves are symmetric about C_{Ni} = 0.5, a direct consequence of employing the regular solution approximation. The magnitude of the change in Z_i/Z_v is only a few percent, but this small change can have a large effect on the swelling behavior.[13-14] Note that the change of Z_i/Z_v is more pronounced at lower temperatures. Recall, however, that the bias is only one factor which controls void nucleation and growth.

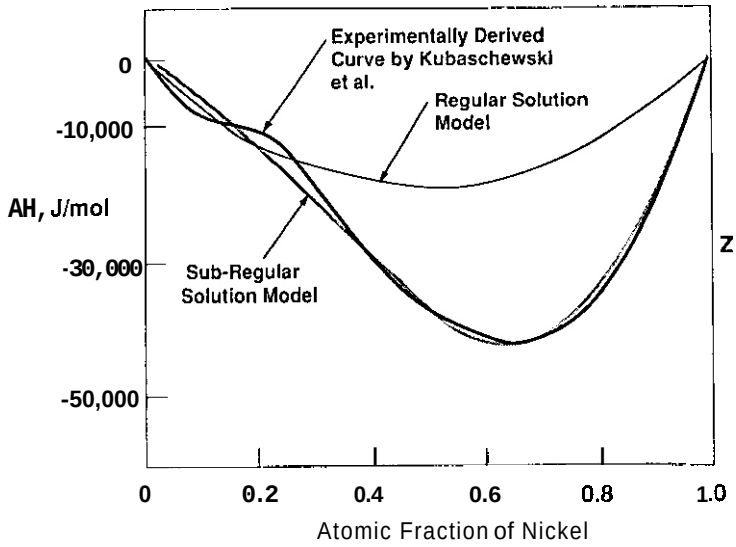

FIGURE 1. Mixing Enthalpies of Solid Fe-Ni Alloys, as Published by Kubaschewski and Coworkers[11] and the Regular and Sub-Regular Models Assumed in This Study for Illustration Purooses.

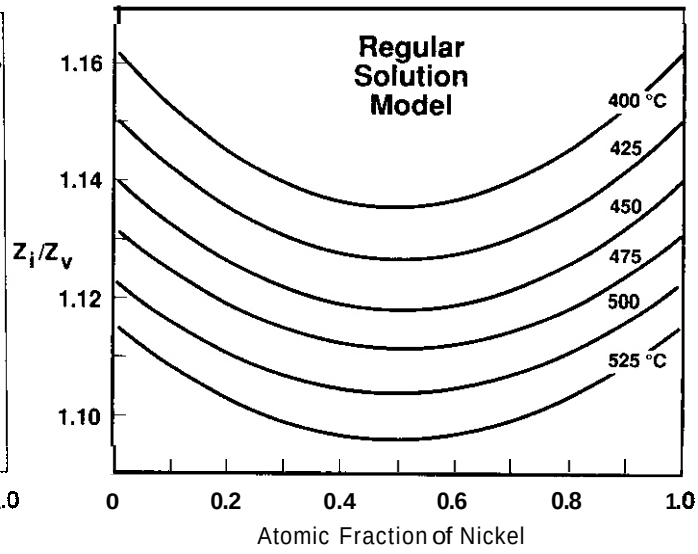

FIGURE 2. Calculated Ratio of Z_i/Z_v vs. Nickel Concentration for Various Irradiation Temperatures.

The interactive effect of a concentration-dependent bias factor and other relevant parameters on swelling behavior can be examined using the concept of a minimum critical radius, R_{mc}. For a void to grow it must nucleate as a vacancy cluster and reach a critical size. Below this critical size, a cavity will spontaneously decrease in size unless stabilized by gas atoms.

The bubble to void conversion idea was first discussed by Sears[13], and later developed by Odette and Stoller[14] and Coghlan and Mansur.[10] It was also employed by Coghlan and Garner[10] to examine the effect of Ni concentration on R_{mc} in simple austenitic alloys. The latter study focused on the effect of compositional changes in vacancy diffusivity on the minimum critical radius. The equations involved in the computation of R_{mc} are lengthy and the reader is referred to reference 13 for details. The various material and kinetic parameters needed are identical to those of reference 10. In the following it is assumed that the system bias is equal to the bias of an edge dislocation; i.e., that the ratio of void bias for an interstitial to that of a vacancy is unity. This may not be completely accurate but it is a common assumption and simplifies the calculation.

Figure 3 shows the critical radius of Fe-Ni alloys vs. C at 475°C. Again due to the symmetric form chosen for the free energy, a peak is observed at C_{Ni} = 0.5 with an approximately 10% increase in R_{mc} over that of the pure metals. Figure 3 suggests that the swelling behavior of Fe-Ni would also be symmetric. However, this conclusion neglects changes in vacancy diffusivity, the importance of which has been stressed in earlier papers.[2-7] In particular, it was shown that changes in the pre-exponential factor D_v^o with Ni content are very important. As shown in Figure 4 D_o is a moderately strong function of nickel content in Fe-Ni alloys, peaking at intermediate nickel levels.

Esmailzadeh and Kumar[5] define the effective vacancy diffusion coefficient as

$$D^{eff} = D_{Fe,v} C_{Fe} + D_{Ni,v} C_{Ni} \quad (6)$$

where C is the concentration and $D_{Fe,v}$ is the tracer diffusion coefficient normalized by the equilibrium concentration of vacancies; i.e., $C_v^{eq} = \exp(-\Delta H_f/kT)$.

Thus,

$$D_v^{eff} = [D_o^*(Fe)\, C_{Fe} + D_o^*(Ni)\, C_{Ni}] \exp(-\Delta H_m/kT) \quad (7)$$

where the term in brackets is D_v^o.

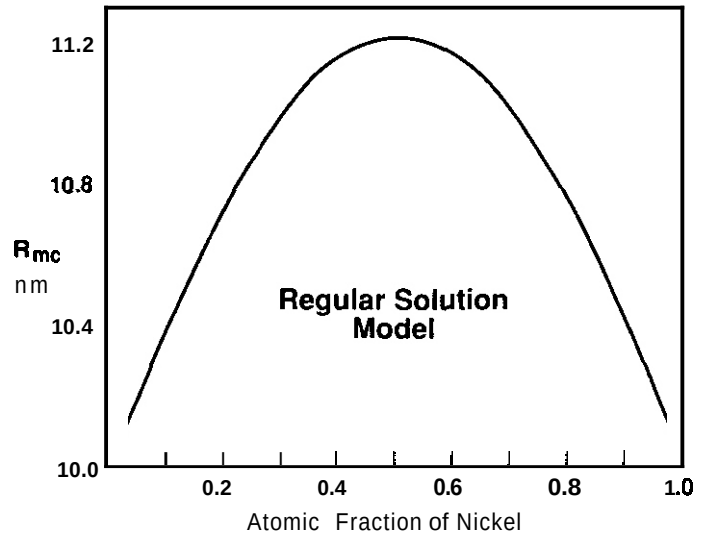

FIGURE 3. Calculated Values of Minimum Critical Radius of FeNi Alloys at 475°C, Assuming the Regular Solution Model.

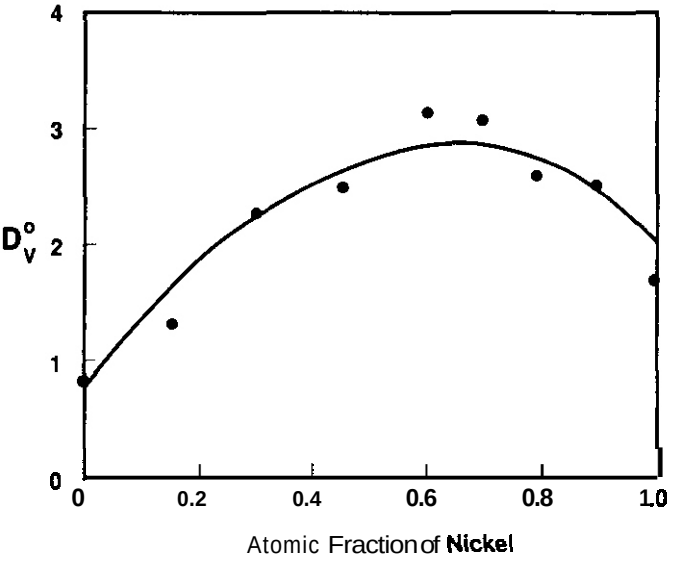

FIGURE 4. Dependence of D_v^o in Fe-Ni Alloys, on Nickel Content, Derived from D_v^* Values of Ruzikova', Million and Kucera.[16]

The quantities D_a^* for Fe and Ni in Fe-Ni binaries are given by Ruzikova', Million and Kucera[16] and were used to calculate D^o in Figure 4. The parabolic fit also shown in 4 was used with the sub-regular solution model for the enthalpy of mixing to calculate the bias factors for an edge dislocation (Figure 5) and the resulting minimum critical radius (Figures 6 and 7). In the sub-reaular model the interaction oarameter ω is assumed to be concentration dependent. In Figure 1 a sub-regula; model fit was obtained by assuming that ω varied linearly with nickel concentrations.

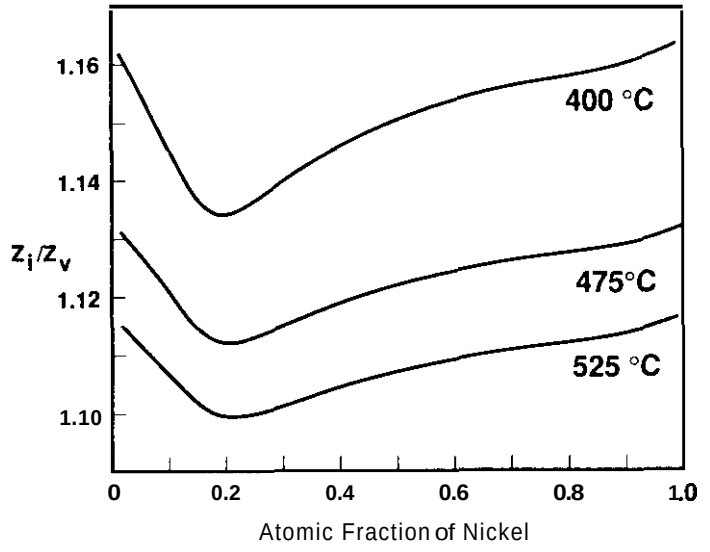

FIGURE 5. Calculated Values of Z_i/Z_v vs Nickel Concentration for Various Irradiation Temperatures, Using the Sub-Regular Solution for Mixing Enthalpy.

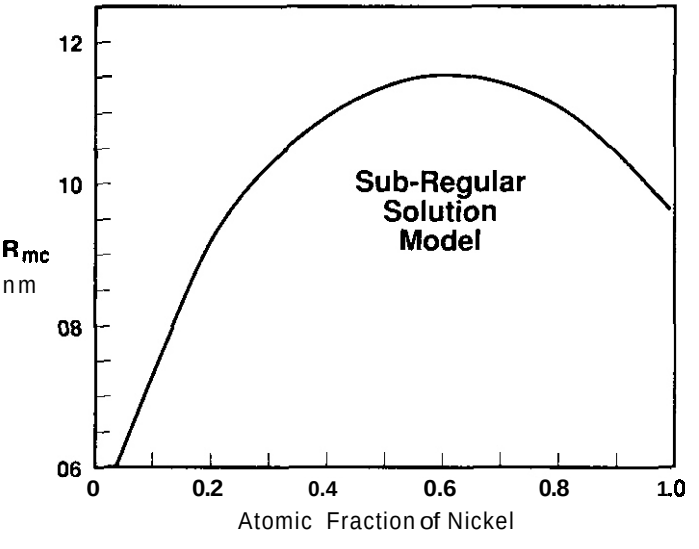

FIGURE 6. Calculated Values of Minimum Critical Radius of FeNi Alloys at 475%.

The change in R_{mc} with nickel content is also a function of temperature and increases strongly at higher temperatures. Note that the asymetric maxima in Figures 6 and 7 offer a plausible explanation for the observed gradual upturn in swelling at high Ni levels. A similar conclusion cannot be drawn by considering solely the impact of changes in D_v^o.

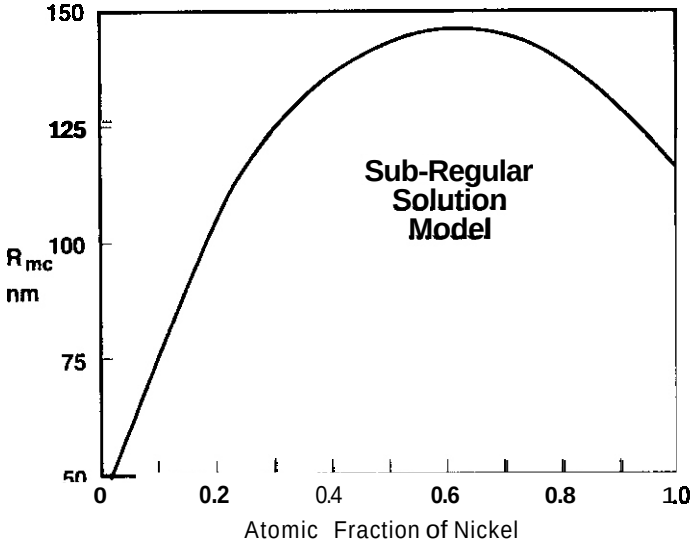

FIGURE 7. Calculated Values of Minimum Critical Radius of FeNi Alloys at 525°C. Note Large Increase of Radius Relative to That at 475°C.

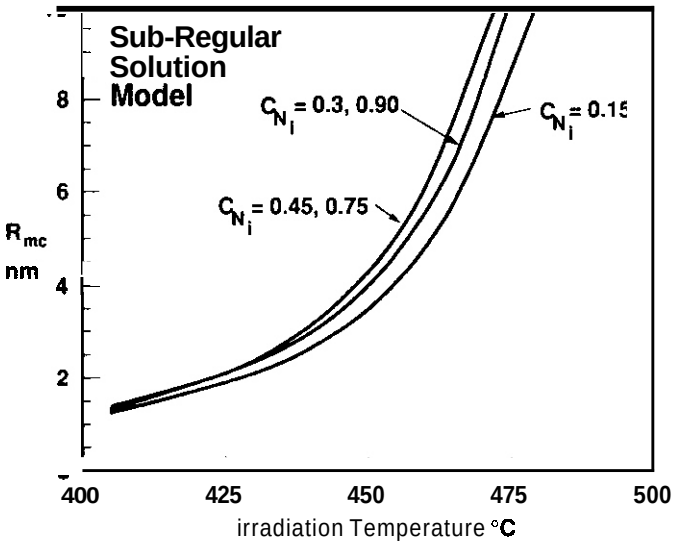

FIGURE 8. Minimum Critical Radius as a Function of Irradiation Temperature and Composition, Calculated Using Composition-Dependent Values of D_v^o and ω.

Figure 8 shows a plot of R_{mc} vs. temperature for various nickel levels. These curves show that very sensitive to nickel or temperature at relatively low temperatures, but is a steep function% & ture at higher temperatures while being moderately sensitive to nickel, all in agreement with experimental observat ions[5].

Discussion

It must be stressed that the composition-dependent bias presented in this work refers to an initial bias. The Larche' and Cahn formalism for the solute atmosphere around an edge dislocation refers to a system in thermal equilibrium. During irradiation, a material cannot be considered in equilibrium, and dynamic factors such as the inverse Kirkendall effect or solute drag become important. In the Fe-Ni-Cr system, nickel always segregates at microstructural sinks. It would be unjustified to extend the above ideas to the steady-state swelling behavior at late times without incorporating the time dependence of C_{Ni} at the sinks. Wolfer and coworkers have shown that segregation of nickel at sinks changes their bias.[17,18]

CONCLUSIONS

Changes with composition of the pre-exponential coefficient for vacancy diffusion have previously been invoked to explain the rapid decrease in swelling with Ni additions in irradiated steels. However, this factor alone cannot explain the gradual increase in swelling with Ni content for $C_{Ni} \geq 0.5$. It has been shown that the combined effect of a concentration-dependent bias factor and changes in D_v^o offers one possible explanation for the swelling behavior in Fe-Ni. The change in bias was assumed to arise from the existence of a Cottrell atmosphere of nickel atoms around the dislocations.

FUTURE WORK

This effort will continue, exploring the interaction between the Cottrell atmosphere effect and other composition-dependent operating mechanisms.

ACKNOWLEDGMENTS

J. J. Hoyt thanks the Northwest College and University Association for Science for financial support under U.S. Department of Energy Contract DE-AM-06-76-RL02225. F. A. Garner's participation was sponsored by the U.S. Department of Energy under Contract DE-AC06-76RLO 1830.

REFERENCES

1. J. J. Hoyt and F. A. Garner, Fusion Reactor Materials Semiannual Progress Report DOE/ER-0313/8, 1990, pp. 120-124.

2. F. A. Garner and A. S. Kumar, ASTM STP 955 (1987) 289.

3. F. A. Garner and W. G. Wolfer, J. Nucl. Mater. 102 (1981) 143.

4. F. A. Garner and W. G. Wolfer, J. Nucl. Mater. 122 & 123 (1984) 201.

5. B. Esmailzadeh and A. Kumar, ASTM STP 870, (1985). 468.

6. B. Esmailzadeh, A, Kumar and F. A. Garner, J. Nucl. Mater. 133 & 134 (1985) 590

7. F. A. Garner and H. R. Brager, J. Nucl. Mater. 133 & 134 (1985) 511.

8. A. D. Marwick, J. Nucl. Mater. 135 (1985) 68.

9. F. C. Larche' and J. W. Cahn, Acta Metall. 21 (1973) 1051; 26 (1978) 53; 30 (1982) 1835; 33 (1985) 331.

10. W. A. Coghlan and F. A. Garner, in Reference 5, 289.

11. O. Kubaschewski, K. H. Geiger and K. Hack, Z. Metallk. 68 (1977) 337.

12. W. G. Wolfer and M. Ashkin, J. Appl. Phvs. 47 (1976) 791.

13. V. F. Sears, J. Nucl. Mater. 39 (1971) 18-26.

14. G. R. Odette et al., J. Nucl. Mater. 85 & 86 (1979) 533-545, also 103 & 104 (1981) 1361-1366 and 122 & 123 (1984) 514-519.

15. W. A. Coghlan and L. K. Mansur, J. Nucl. Mater. 122 & 123 (1984) 495.

16. J. Ruzikova', B. Million and J. Kucera, Met. Mater. 19, (1981) 3.

17. A. Si-Ahmed and W. G. Wolfer, ASTM STP 782 (1982) 1008.

18. W. G. Wolfer, F. A. Garner and L. E. Thomas in Reference 15, 1023-1041.

THE INFLUENCE OF NICKEL CONTENT ON MICROSTRUCTURES OF Fe-Cr-Ni AUSTENITIC ALLOYS IRRADIATED WITH NICKEL IONS

- T. Muroga and N. Yoshida, Kyushu University, F. A. Garner, Pacific Northwest Laboratory[a]

OBJECTIVE

The objective of this effort is to identify the mechanisms involved in the radiation-induced evolution of microstructure in materials intended for fusion applications. The results of this study are useful in interpreting the results of several other ongoing experiments involving either spectral or isotopic tailoring to study the effects of helium on microstructural evolution.

SUMMARY

Ion-irradiated Fe-15Cr-XNi (X = 20, 35, 45, 60, 75) ternary alloys and a 15Cr-85Ni binary alloy were examined after bombardment at 675% and compared to earlier observations made on these same alloys after irradiation in EBR-II at 510 or 538°C. The response of the ion-irradiated microstructures to nickel content appears to be very consistent with that of neutron irradiation even though there are four orders of magnitude difference in displacement rate and over 200°C difference in temperature. It appears that the transition to higher rates of swelling during both types of irradiation is related to the operation of some mechanism that is not directly associated with void nucleation.

PROGRESS AND STATUS

Introduction

In an earlier report, the microstructures were examined for a series of Fe-15Cr-XNi (X = 15, 19, 21, 30, 35, 45, 75) ternary alloys and a 15Cr-85Ni binary alloy after irradiation in the EBR-II reactor at 510 and 538°C.[1] At 510°C it was obvious that void nucleation was complete prior to the onset of steady-state swelling at all nickel levels, implying that some process other than void nucleation determines when the relatively rapid void growth associated with steady-state swelling occurs. At both 510 and 538°C a protracted loop dominance at intermediate nickel levels was observed in the dislocation microstructure along with a relatively low void density, suggesting a reduced bias toward preferential interstitial absorption as a possible mechanism to produce lower swelling in this nickel range. The void densities also closely mirrored the total swelling behavior as a function of nickel content. Figures 1-4 show the relationships observed between loop and void densities, swelling, dislocation density and matrix nickel content.

It was decided to test the generality of such observations over a broad range of irradiation conditions. The first results of some other neutron irradiation studies are presented elsewhere.[2] A more rigorous test of the generality of these microstructural relationships was provided by microscopy observations of a series of specimens which were ion bombarded at much higher displacement rates, then thinned and observed by Johnston, Rosolowski, Turkalo and Lauritzen.[3] These specimens were found to be in excellent condition more than 15 years after their original examination.

ExDerimental Details

The materials examined in this study were Fe-15Cr-XNi (X = 20, 35, 45, 60, 75) ternary alloys and a 15Cr-85Ni binary alloy. These alloys were prepared separately by Johnston and coworkers and thus are nominally but not fully identical *to* those used in the neutron studies. The irradiations were performed with either 4 or 5 MeV Ni^+ ions at 675°C reaching 30 to 190 dpa at a displacement rate of about $2x10^{-2}$ dpa/s. Prior to irradiation, 20 appm of helium had been preinjected to depths where the microscopy was to be performed. The regions of the specimen examined by TEM were 700 to 850 nm from the ion-incident surface of the specimen. Due to depth-dependent changes in displacement rate characteristic of heavy ion bombardment, variations in depth of the foil from the incident surface resulted in variations in total dose. The alloys and irradiation conditions examined are listed in Table 1. The microstructure and microchemistry of these specimens were examined with a JEM-2000FX TEM equipped with an EDS system.

RESULTS AND DISCUSSION

Since ion milling was performed by Johnston and coworkers at the final stage of specimen preparation, high densities of small dots were observed in all specimens. Stereoscopic observations were carried out to distinguish between heavy ion-induced microstructure inside the specimen and near-surface defect clusters induced by ion milling. Micrographs of the damage structures will be presented in another report.[5]

(a) Pacific Northwest Laboratory is operated for the U.S. Department of Energy by Battelle Memorial Institute under Contract DE-AC06-76RLO 1830.

Table 1

Alloys (Fe-15Cr-XNi or 15Cr-85Ni) and Heavy Ion Irradiation Conditions. The irradiation temperature is 675°C.

Ni level (wt%)	20	35	35	35	45	45	45	60	75	85
Ni^+ ion energy (MeV)	5	4	4	5	4	5	4	5	5	5
Dose	30	30	53	110	58	120	190	111	116	115

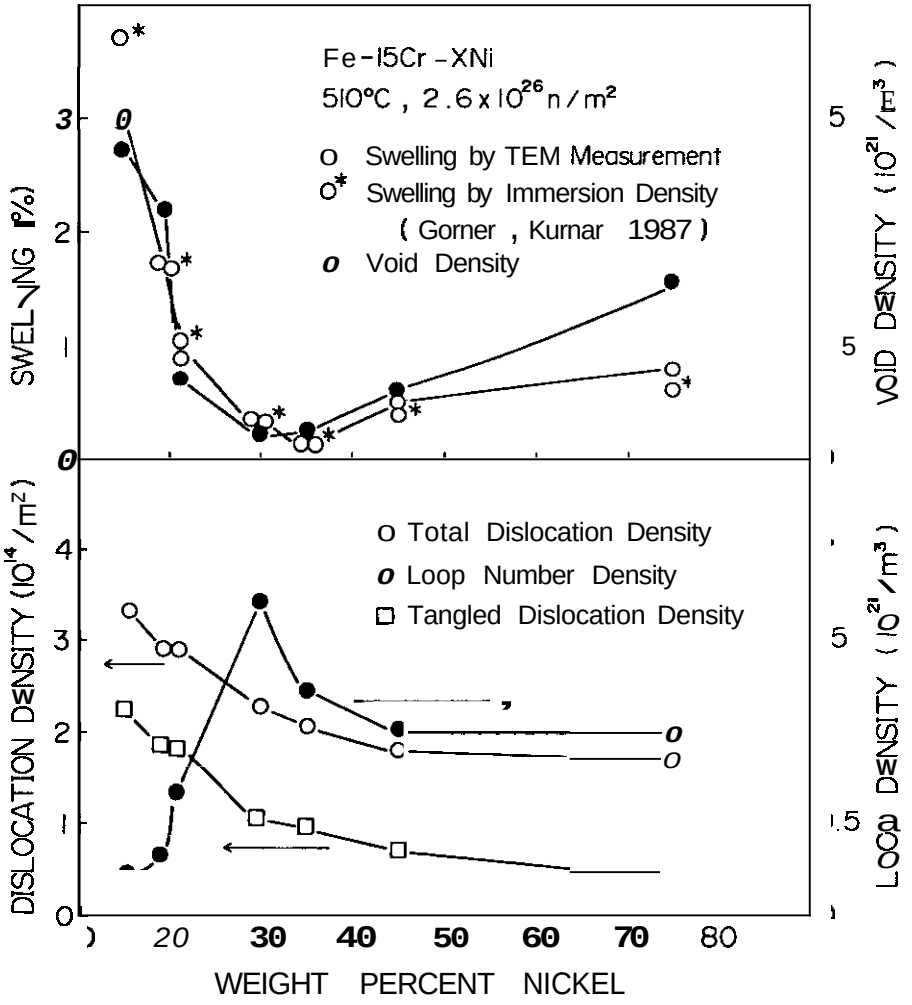

Figure 1. Dependence of microstructural parameters on nickel content at 510°C and 2.6 x 10^{26} n/m² (E > 0.1 MeV).[1]

Figure 5 shows the measured microstructural parameters as a function of nickel content. Although only lower dose microstructures were available for 20Ni and 35Ni alloys, the results concerning the nickel dependence are qualitatively similar to those shown in Figures 1 and 2 except that both void density and swelling for the 85Ni binary alloy are higher than those of the 75Ni ternary alloy. Garner[6] has shown that irradiation of 85Ni-15Cr with either ions or neutrons yields different results, depending on whether the irradiation is performed above or below 550°C, the order-disorder transition temperature for this alloy. Thus one would expect some difference in behavior for neutron irradiations conducted at 510°C or 538°C and ion irradiations conducted at 675%.

Figure 6 shows the dose dependence of both swelling and void density for the 35 and 45Ni ternary alloys. The swelling under the accelerated irradiation conditions of ion bombardment at higher temperature indeed

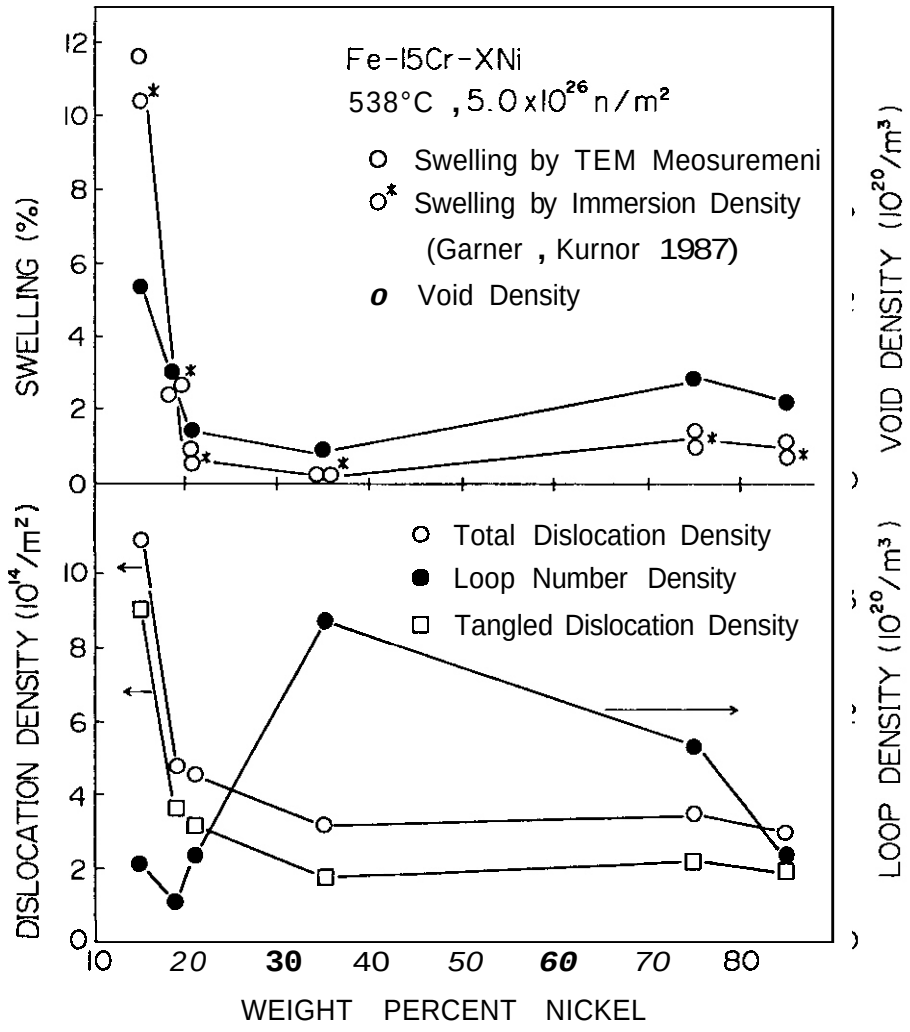

Figure 2. Dependence of microstructural parameters on nickel content at 538°C and 2.6 X 10^{26} n/m² (E > 0.1 MeV).[1] Swelling data obtained by immersion density by Garner and Kumar[4] are also shown.

appears to obey the kinetics of transient and post-transient rapid increase observed in neutron irradiation at lower displacement rate and temperature. Figure 6 also shows that the change in void density is small during the transition between these two regimes, similar to the behavior of the neutron-irradiated specimens shown in Figure 3.

Profiles of nickel concentration across voids of about 100 nm in diameter are presented in Figure 7 for a variety of nickel levels. The enrichment of nickel at voids is most prominent for lower nickel alloys. Figure 8 shows, for the 45Ni ternary alloy, the dose dependence of swelling as well as the dose dependence of nickel concentration at void surfaces and in the matrix. The nickel deoletion in the matrix coincides with the onset of rapid swelling, once again consistent with the behavior of the neutron irradiated 30Ni ternary alloy shown in Figure 4.

CONCLUSION

The nickel-dependent microstructural response of Fe-Cr-Ni alloys irradiated under very different conditions appears to be quite consistent. It appears that void densities tend to saturate at nickel dependent levels rather early in the irradiation. The transition to higher rates of swelling seems to require the later operation of some other mechanism not directly associated with void nucleation.

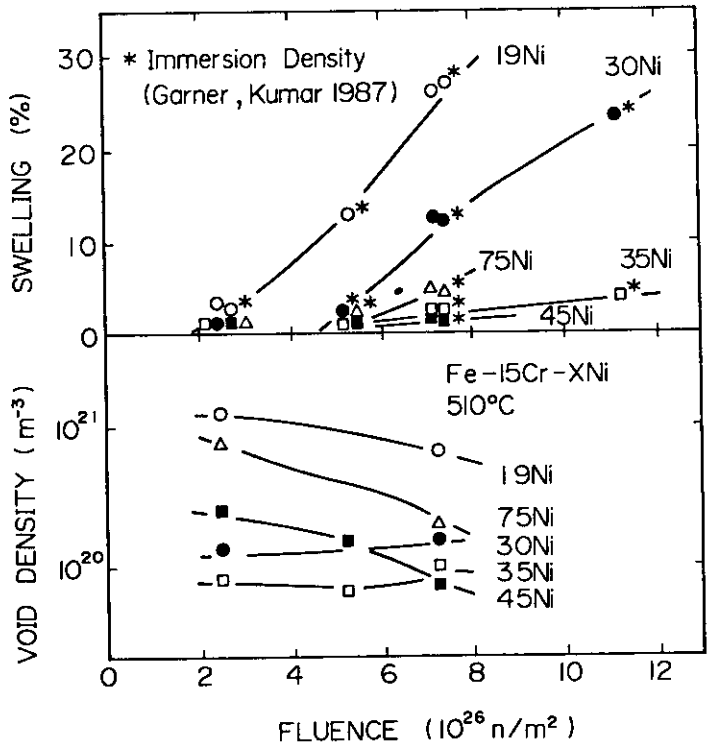

Figure 3. Fluence dependence of swelling and void density at 510°C.[1] Swelling data obtained by immersion density by Garner and Kumar[4] are also shown.

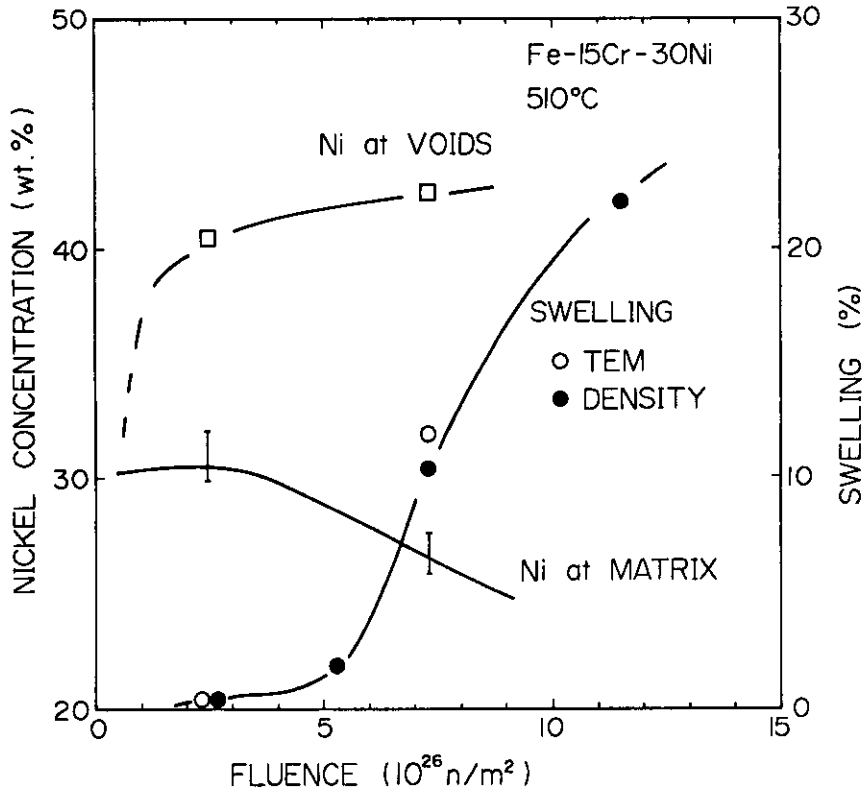

Figure 4. The fluence dependence of swelling and nickel concentration at void surfaces and in the matrix of Fe-15Cr-30Ni irradiated at 510°C[1]

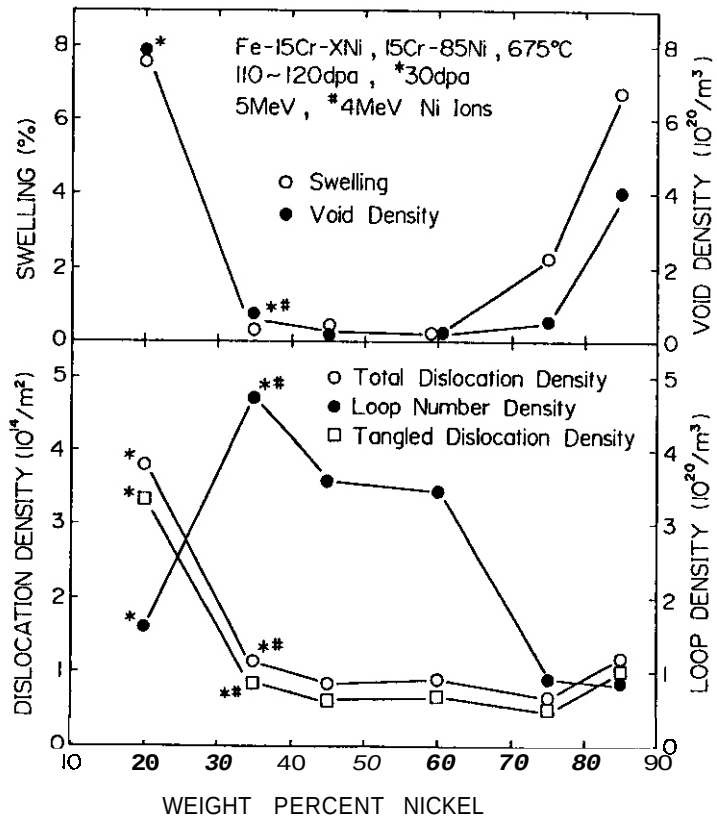

Figure 5. Dependence of microstructural parameters on nickel content at 675% and either 30 or 111-120 dpa after irradiation with either 5 or 4 MeV Ni ions.

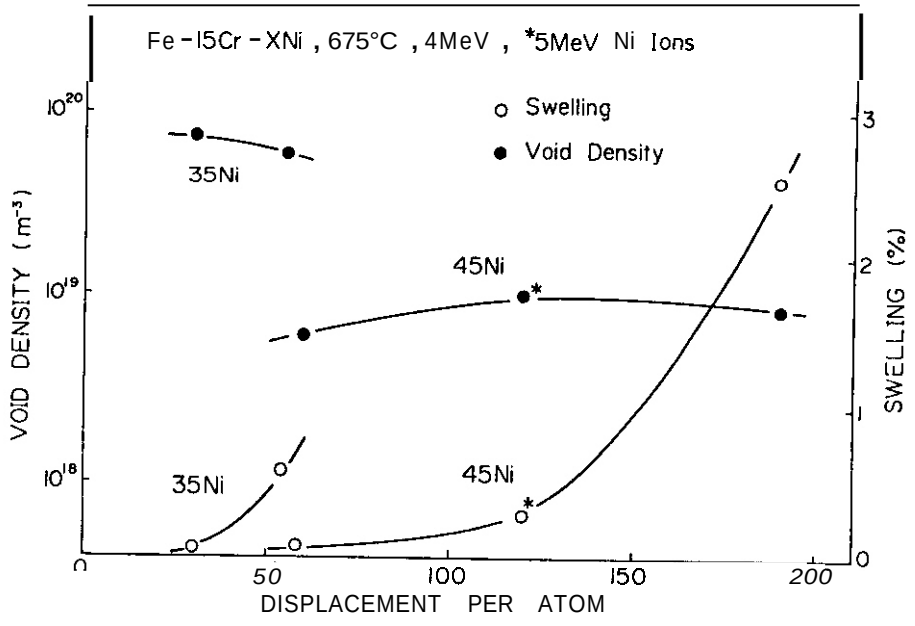

Figure 6. Dose dependence of swelling and void density in Fe-15Cr-XNi alloys irradiated with either 4 or 5 MeV Ni ions at 675°C

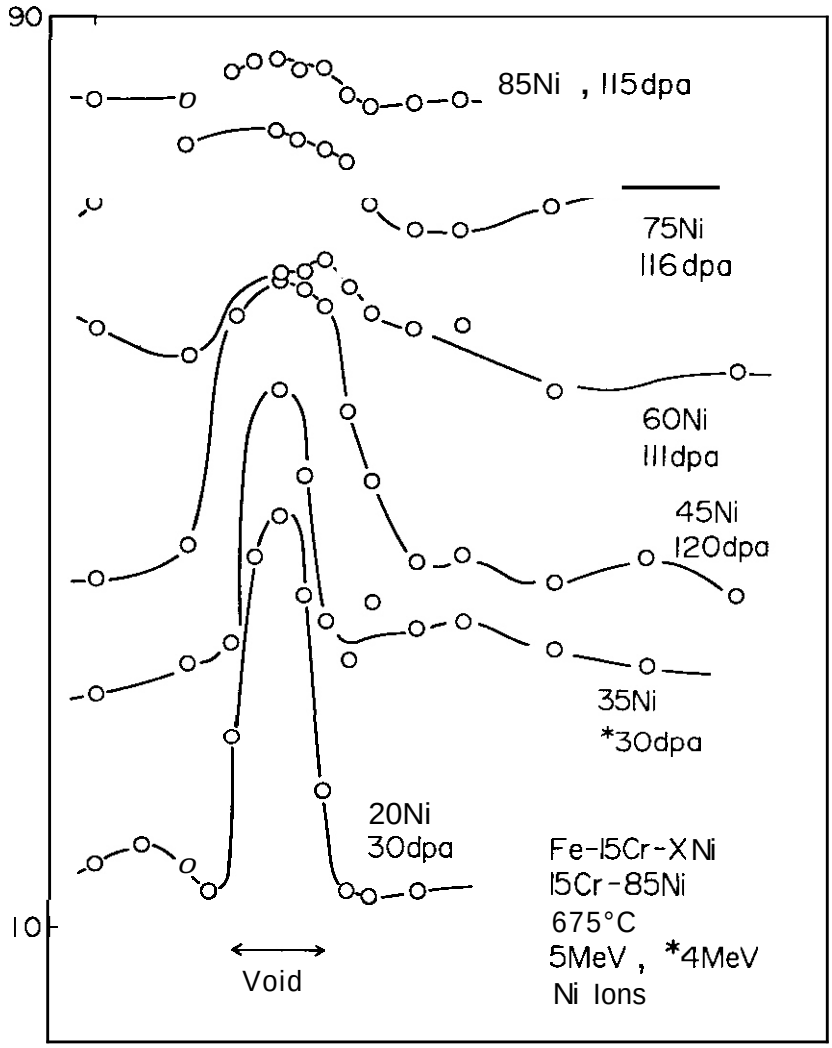

FUTURE WORK

These results will be combined with the early neutron results and some theoretical analysis. These will then be published in the proceedings of the 15th ASTM Symposium on Effects of Radiation on Materials.'')

ACKNOWLEDGMENTS

This work was supported in part by the Japan-USA Fusion Cooperation in "Fundamental Studies of Irradiation Effects in Fusion Materials Utilizing Fission Reactors" sponsored by Monbusho, the Japanese Ministry of Education, Science and Culture. The work was also supported by the U.S. Department of Energy under Contract DE-AC06-76RLO 1830.

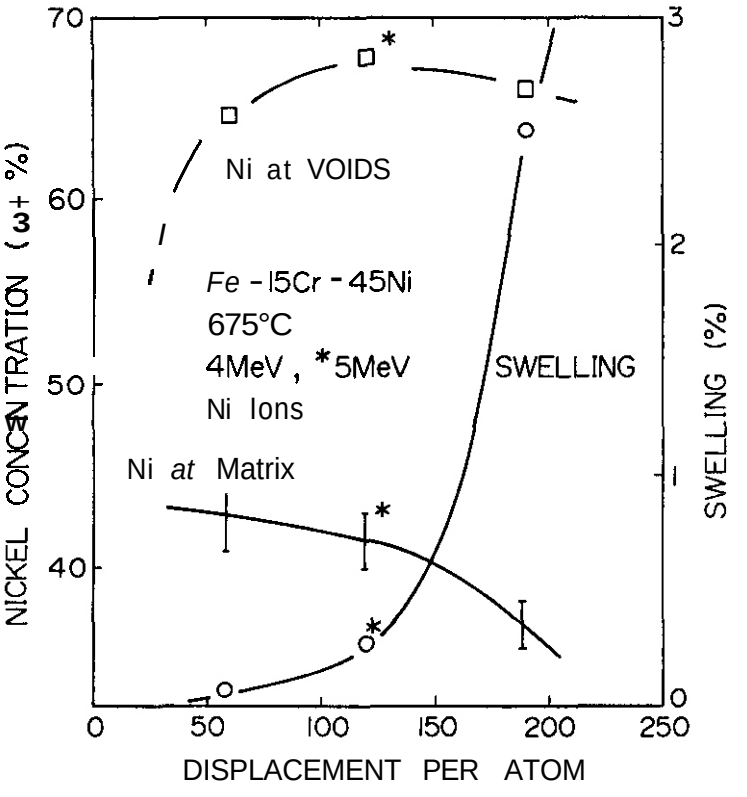

Figure 8. The dose dependence of swelling and nickel concentration at void surfaces and in the matrix of Fe-15Cr-45Ni irradiated with 4 or 5 MeV Ni ions at 510°C

REFERENCES

1. T. Muroga, F. A. Garner and S. Ohnuki, "Microstructural Investigation of Swelling Dependence on Nickel Content in Fast Neutron Irradiated Fe-Cr-Ni Austenitic Ternaries," DOE/ER-0313/7 (1989), pp. 95-101; also J. Nucl. Mater. 176 (1990) in press.

2. N. Sekimura, F. A. Garner and R. D. Griffin, "The Effect of Helium on Microstructural Evolution in Austenitic Steels as Determined by Spectral Tailoring Experiments," DOE/ER-0313/8 (1990) pp. 114-119.

3. W. G. Johnston, J. H. Rosolowski, A. M. Tarkalo and T. Lauritzen, J. Nucl. Mater. 54 (1974) pp. 22-40.

4. F. A. Garner and A. S. Kumar "The Influence of Both Major and Minor Element Composition on Void Swelling in Austenitic Steels," Effects of Radiation on Materials: 13th International Symposium, ASTM STP 955, F. A. Garner, N. H. Packan and A. S. Kumar, Eds., American Society for Testing and Materials, Philadelphia, PA, 1985, pp. 289-314.

5. T. Muroga, F. A. Garner, J. M. McCarthy and N. Yoshida, "The Influence of Nickel Content on Microstructures of Fe-Cr-Ni Austenitic Ternaries Irradiated with Fast Neutrons or Heavy Ions," Proceedings of 15th ASTM Symposium on Effects of Radiation on Materials, June 17-23, 1990, Nashville, TN, in press.

6. F. A. Garner, "The Possible influence of Order-Disorder Transformations on the Swelling of 85Ni-15Cr Nichrome Alloy, J. Nucl. Mater. 148 (1987) pp. 288-293.

6. DEVELDPMENT OF STRUCTURAL ALLOYS

6.1 Ferritic Stainless Steels

IMPACT BEHAVIOR OF 9Cr-1MoVNb AND 12Cr-1MoVW STEELS IRRADIATED IN HFIR -- R. L. Klueh and O. J. Alexander (Oak Ridge National Laboratory)

OBJECTIVE

The goal is the evaluation of the impact behavior of irradiated ferritic steels and to relate the changes to irradiation damage and transmutation helium.

SUMMARY

Charpy impact specimens of 9Cr-1MoVNb and 12Cr-1MoVW steels and these steels with 2% Ni (9Cr-1MoVNb-2Ni and 12Cr-1MoVW-2Ni) were irradiated in the High Flux Isotope Reactor (HFIR) at 300°C up to 34 dpa and at 400°C to 42 dpa. Nickel was added to the standard composition to study the effect of transmutation helium formed by reaction of ^{58}Ni with thermal neutrons in the mixed-spectrum of HFIR. Helium levels approaching 400 appm were achieved in the steels containing 2% Ni. Irradiation caused large increases in the OBTT of all four steels. A saturation in the shift in DBTT with increasing fluence that was observed in fast reactor irradiations does not apply to specimens irradiated in HFIR. Shifts in DBTT of over 300°C were observed at 400°C for 9Cr-1MoVNb-2Ni and 12Cr-1MoVW-2Ni; shifts of over 200°C were observed for the standard steels. For all steels, the increase was greater at 400°C than at 300°C. The shifts are the largest ever recorded for this type of steel and are attributed to the higher helium concentrations.

PROGRESS AND STATUS

Introduction

Because ferritic/martensitic steels are relatively immune to void swelling, they are being considered as possible structural materials for the first wall and blanket structure of future fusion reactors. A major concern involves the effect of irradiation on impact properties. Irradiation can cause a large increase in the ductile-brittle transition temperature (OBTT) and a decrease in the upper-shelf energy (USE). Even if the DBTT is below room temperature before irradiation, it can be well above room temperature after irradiation.[1-7]

A steel in a fusion reactor first wall will experience displacement damage from the high-energy neutrons from the fusion reaction. In addition, large amounts of transmutation helium will form in the material. To study the effect of simultaneously produced displacement damage and transmutation helium. nickel has been added to 9Cr-1MoVNb and 12Cr-1MoVW steels.[8] When these nickel-doped steels are irradiated in a mixed-spectrum reactor such as HFIR, displacement damage is produced by the fast neutrons in the spectrum, and helium is produced by a two-step transmutation reaction of ^{58}Ni with the thermal neutrons in the spectrum. For a ferritic steel containing 2% Ni, the He/dpa ratio produced during irradiation in HFIR is similar to that produced in a tokamak reactor. This technique has been used to examine the effect of helium on tensile properties of specimens irradiated at 50, 300, 400, and 500°C,[8,9] and on the impact properties of Charpy specimens irradiated at 50°C.[6]

Previously, we presented data for the standard 9Cr-1MoVNb and 12Cr-1MoVW steels irradiated at 300 and 400°C in HFIR up to 42 dpa (ref. 7). The shifts in OBTT observed after irradiation at 400°C were the largest ever observed for these steels. In this report, impact properties for nickel-doped 9Cr-1MoVNb and 12Cr-1MoVW steels irradiated in HFIR at 300 and 400°C will be presented, and the results will be compared with results from the irradiations of the undoped steels.[7]

Experimental Procedure

Specimens were obtained from 25-kg electroslag-remelted (ESR) heats of standard 9Cr-1MoVNb (heat XA 3590) and standard 12Cr-1MoVW (heat XAA 3587) compositions that were prepared by Combustion Engineering, Inc., Chattanooga, Tennessee. Similar compositions with 2% Ni added were also prepared by ESR; these heats have been designated 9Cr-1MoVNb-2Ni (heat XA 3591) and 12Cr-1MoVW-2Ni (heat XAA 3589). Chemical compositions are given in Table 1.

Table 1. Composition of 9Cr-1MoVNb and 12Cr-1MoVW Steel

Element	Concentration,[a] wt %			
	9Cr-1MoVNb		12Cr-1MoVW	
	0% Ni[b] (XAA 3590)	2% Ni (XAA 3591)	0% Ni[b] (XA 3587)	2% Ni (XA 3589)
C	0.09	0.064	0.21	0.20
Mn	0.36	0.36	0.50	0.49
P	0.008	0.008	0.011	0.011
S	0.004	0.004	0.004	0.004
Si	0.08	0.08	0.18	0.14
Ni	0.11	2.17	0.43	2.27
Cr	8.62	8.57	11.99	11.71
Mo	0.98	0.98	0.93	1.02
V	0.209	0.222	0.27	0.31
Nb	0.063	0.066	0.018	0.015
Ti	0.002	*0.002*	0.003	0.003
co	0.013	0.015	0.017	0.021
cu	0.03	0.04	0.05	0.05
Al	0.013	0.015	0.030	0.028
8	<0.001	<0.001	<0.001	<0.001
W	0.01	0.01	0.54	0.54
As	<0.001	<0.001	<0.001	<0.002
Sn	0.003	0.003	0.002	*0.002*
Zr	<0.001	<0.001	<0.001	<0.001
N	0.050	0.053	0.020	0.017
0	0.007	0.006	0.005	0.007

[a] Balance iron.
[b] Standard steel with no nickel added.

Charpy impact specimens were obtained from hot-rolled plate in the normalized-and-tempered condition. The normalizing treatment for the 9Cr steels was 0.5 h at 1040°C and for the 12Cr steels 0.5 h at 1050°C, after which they were air cooled. The 9Cr-1MoVNb steel was tempered 1 h at 760°C; the 12Cr-1MoVW steel was tempered 2.5 h at 780°C. The 9Cr-1MoVNb-2Ni and 12Cr-1MoVW-2Ni steels were tempered 5 h at 700°C Tempered martensite microstructures were obtained by such heat treatments. Details on heat treatment and microstructure have been published.[4,8]

Miniature Charpy V-notch specimens were machined from the heat-treated plate in the longitudinal (LT) orientation. The subsize specimens were essentially one-half the standard size; they measured 5 by 5 by 25.4 mm and contained a 0.76-mn-deep 30" V-notch with a 0.05- to -0.08-mn-root radius. Such miniature specimens show a transition from ductile to brittle fracture similar to that found in full-sized Charpy specimens, although over a different temperature range.[10,11]

Two capsules, each containing 16 specimens of the nickel-doped and undoped 9Cr-1MoVNb and 12Cr-1MoVW steel specimens, were irradiated in HFIR at the nominal irradiation temperatures of 300 and 400°C. One capsule contained the 9Cr-1MoVNb series, and the other contained the 12Cr-1MoVW series. For irradiation, specimens were enclosed in stainless steel holders, and the holders were placed inside aluminum sleeves. To achieve the desired temperature, the outer diameters of the steel specimen holders were adjusted to compensate for the variation in nuclear heating rate along the length of the capsule. Nuclear heating of the specimens and stainless steel holders provides enough heat to raise the sample temperatures to the desired values. A thermal gradient exists from the interior to exterior surface of the specimens, but this has been calculated to be less than 45°C. Three flux monitors were loaded into each capsule, and these were analyzed to determine the fluences achieved.

The capsules were irradiated in HFIR peripheral target positions for 20 cycles to a maximum total fluence of *20.2* $\times 10^{26}$ n/m^2 and a maximum fast fluence of 5.6 $\times 10^{26}$ n/m^2 (E > 0.11 MeV). At the capsule midplane, a displacement-damage level of approximately 42 dpa was obtained. However, the fluence decreases with distance from the midplane, and the displacement-damage levels at the ends of the capsules were approximately *20* dpa. Displacement-damage levels for specimens between the midplane and the ends varied between these limits. Similarly, helium levels also varied, depending on the position of the specimens in the capsule and the amount of nickel present in the alloys. Up to ~390 appm He was present in the steels with *2%* Ni.

Tests were carried out in a pendulum-type impact machine specially modified to accommodate subsize specimens.[9] To obtain the DBTT and upper-shelf energy (USE), impact energy-temperature curves were generated by fitting the data with a hyperbolic tangent function.

Because of space limitations in the irradiation capsules, a limited number of irradiated specimens were available (five each for the 9Cr-1MoVNb and 12Cr-1MoVW steels, but only three specimens each for these steels to which *2%* Ni had been added). The major objective of these studies was the determination of the shift in DBTT. Consequently, the USE often had to be estimated. The DBTT was calculated for the energy corresponding to one half of the USE and at fixed energy levels of 5.5 and 9.2 J (analogous to the 41 and 68 J often used for full-size Charpy specimens).[11]

Results

Charpy impact results for the specimens irradiated in HFIR are given in Table 2. Also given are the displacement-damage levels and helium concentrations for each set of specimens. Because the new results on the nickel-doped steels are to be compared with the results for the standard steels irradiated in the same capsules but previously published,' the results for the standard steels are also given in the table. As seen, the specimens irradiated at 400°C had damage levels of 38 to 42 dpa, while those irradiated at

Table 2. Impact Properties of Cr-Mo Steels Irradiated in HFIR

Conditions			Transition Temperature (°C)			ΔDBTT[a] (°C)	USE (J)
Temperature (°C)	Displacement (dpa)	He (appm)	1/2 USE	5.5J	9.2J		
12Cr-1MoVW (Heat XAA 3587)							
Control	0	0	-18	-58	-35		26
300	20-34	51-90	87	86	87	105	15
400	38-42	99-111	224	226	--	242	8
12Cr-1MoVW-2Ni (Heat XAA 3589)							
Control	0	0	-32	-57	-25		17
300	20-31	184-284	130	132	153	162	10
400	38-42	353-391	296	323	--	328	6[b]
9Cr-1MoVNb (Heat XA 3590)							
Control	0	0	-29	-49	-37	25	
300	20-34	16-27	138	136	138	167	20
400	37-42	30-34	175	174	182	204	12
9Cr-1MoVNb-2Ni (Heat XA 3591)							
Control	0	0	-77	-115	-90	24	
300	20-31	184-284	141	149	--	218	8
400	38-42	353-391	271	--	--	348	4[b]

[a]Calculated from 1/2 USE OBTT.
[b]Estimated because of the small number of specimens

300°C were only 20 to 34 dpa. Helium concentrations varied considerably, depending on the amount of nickel in the steel and the fluence. Because the standard 9Cr-1MoVNb steel contained only about 0.1% Ni compared to the 0.5% in the standard 12Cr-1MoVW (Table 1), the 9Cr-1MoVNb contained less helium than the 12Cr-1MoVW after a similar irradiation.

Figures 1 through 4 show the Charpy curves for each steel before and after irradiation; AOBTT values determined using the DBTT determined as one-half USE are shown in Table 2. Increases in DBTT of over 100°C occurred at 300°C and over 200°C at 400°C for all four steels. The largest change for each steel occurred after irradiation at 400°C, and a larger change occurred for the nickel-doped steels (the ones with the higher helium levels) than the undoped steels.

From Figs. 2 and 4, the difficulty is evident in estimating a USE from only three test specimens for 9Cr-1MoVNb-2Ni and 12Cr-1MoVW-2Ni steels, especially at 400°C. It is also difficult to estimate the DBTT at 400°C. Errors in the estimate in DBTT at 400°C would appear to be such as to lead to a lower value than might result were more specimens available. Nevertheless, the curves were fitted by the hyperbolic tangent function and were used to estimate a DBTT, which is given in Table 2.

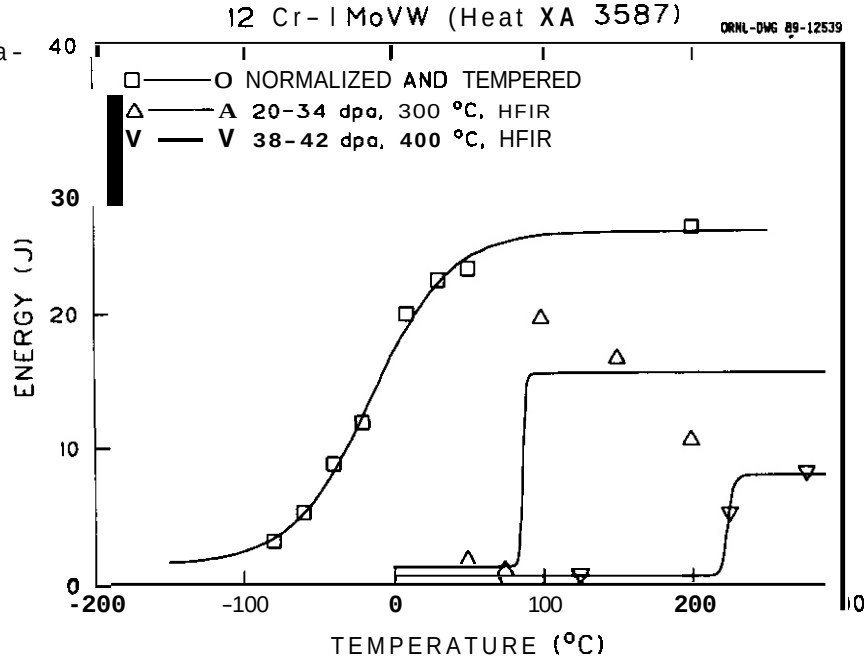

Fig. 1. Charpy impact properties of 12Cr-1MoVW steel in the unirradiated condition and after irradiation to 20-34 dpa (51-90 appm He) at 300°C and to 38-42 dpa (99-111 appm He) at 400°C in HFIR.

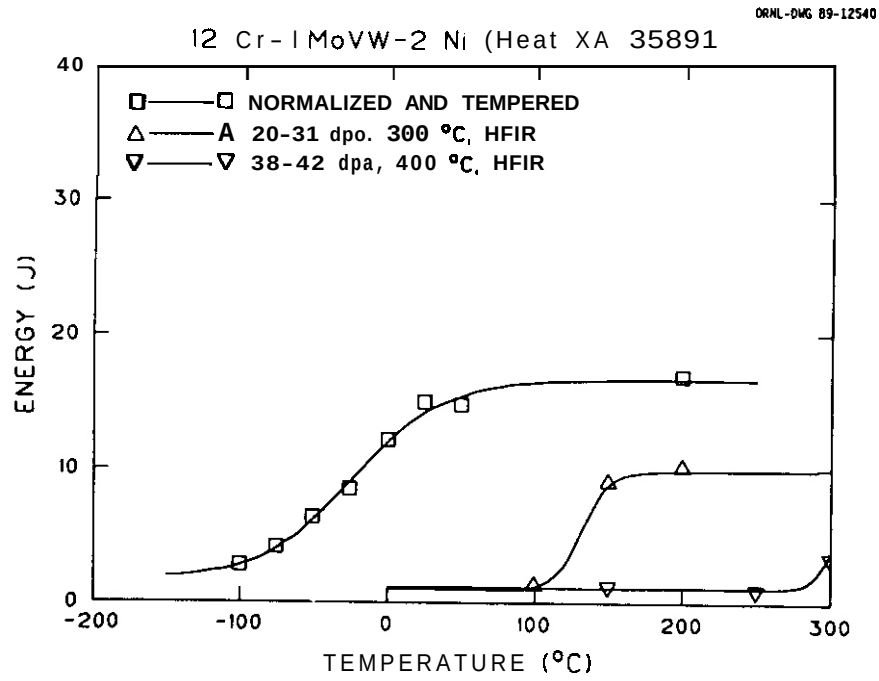

Fig. 2. Charpy impact properties of 12Cr-1MoVW-2Ni steel in the unirradiated condition and after irradiation to 20-31 dpa (184-284 appm He) at 300°C and to 38-42 dpa (353-391 appm He) at 400°C in HFIR.

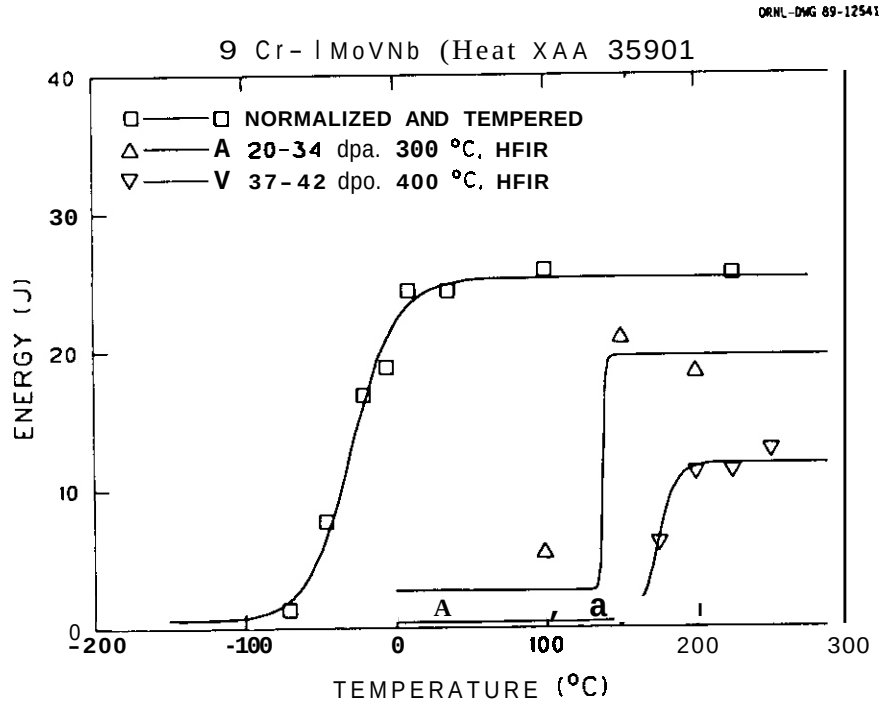

Fig. 3. Charpy impact properties of 9Cr-1MoVNb steel in the unirradiated condition and after irradiation to 20-34 dpa (16-27 appm He) at 300°C and to 37-42 dpa (30-34 appm He) at 400°C in HFIR.

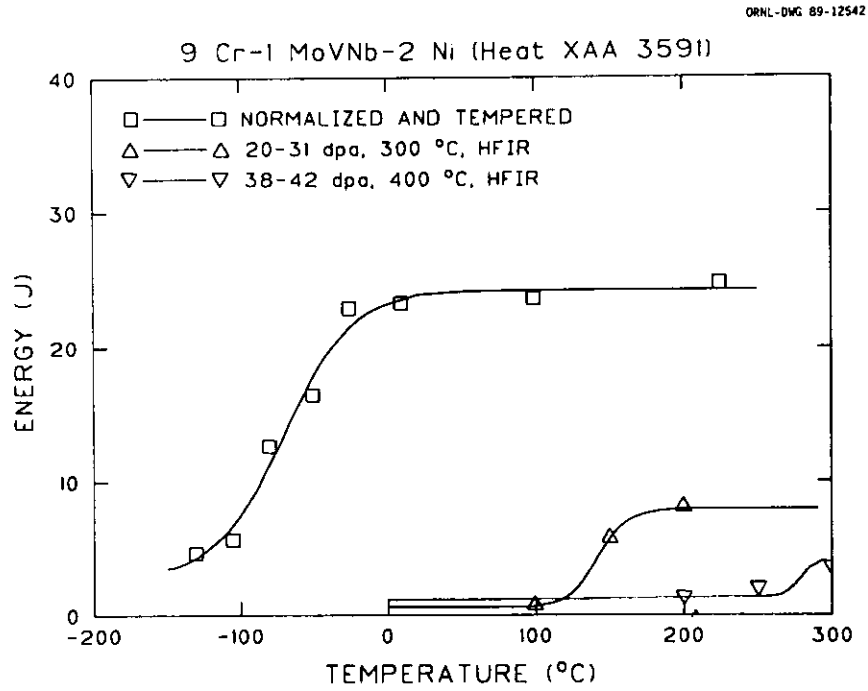

Fig. 4. Charpy impact properties of 9Cr-1MoVNb-2Ni steel in the unirradiated condition and after irradiation to 20-31 dpa (184-284 appm He) at 300°C and to 38-42 dpa (353-391 appm He) at 400°C in HFIR.

Discussion

The objective in irradiating the nickel-doped and undoped 9Cr-MoVNb and 12Cr-MoVW steels in HFIR was the determination of the effect of helium on properties. Transmutation helium is generated by an (n,α) reaction between ^{58}Ni and thermal neutrons in the HFIR spectrum. From previous work on the nickel-doped steels, it was tentatively concluded that helium may intensify the effect of irradiation on the shift in DBTT when irradiated at 50°C.[6] That experiment, like the present one, suffered from the limited number of specimens that were irradiated. A similar conclusion that helium affected the results was reached when the standard steels were irradiated in HFIR[4,7] and compared with results obtained after irradiation in fast reactors.[5]

For any test condition, Table 2 shows that the nickel-doped steels always had a larger ΔDBTT than the standard steel. A possible conclusion from this observation is that helium caused the difference. Because of the limited amount of data, such a conclusion can only be considered tentative; nevertheless, it is worthwhile to examine the results in light of all data that bear on such a conclusion.

The most important question concerning the irradiation of the nickel-doped and undoped steels is: What is the effect of helium and what is the effect of nickel? Previous work addressed this question by examining the unirradiated microstructures and the microstructures after irradiation to ~39 dpa in HFIR, where substantial helium formed, and to ~47 dpa in FFTF, where little helium formed.[12] That study showed no major differences in the evolution of the microstructures in the different reactors, with the exception of the formation of voids and bubbles in the HFIR-irradiated steels. The formation of these cavities was attributed to helium.

Differences in thermal aging behavior of the steels with and without nickel additions caused by elevated-temperature exposure during irradiation are not expected to significantly affect the DBTT. Aging for up to 2500 h at 400°C had no effect on the impact properties of any of the steels.[4,5] Also, normalized-and-tempered 9Cr-1MoVNb and 12Cr-1MoVW-2Ni steel specimens from the heats used in the present experiment were aged for 13,000 h at 300 and 400°C with only a relatively minor effect on the DBTT and USE (Fig. 5).

Charpy impact specimens of these same heats of 12Cr-1MoVW and 12Cr-1MoVW-2Ni steels were previously irradiated at 390°C to 12 dpa in EBR-II, where < 3 appm He was generated.[5] Shifts in DBTT of 122 and 90°C were observed for the 12Cr-1MoVW and 12Cr-1MoVW-2Ni, respectively. The similarity of the shift in DBTT in 12Cr-1MoVW and 12Cr-1MoVW-2Ni when irradiated in EBR-II was interpreted to mean that nickel did not significantly affect the properties and therefore should not affect them when irradiated in HFIR.[5] However, when the ΔDBTTs determined after irradiation at 390°C in EBR-II are compared with those observed after irradiation at 400°C in HFIR, it is obvious the ΔDBTT for both steels irradiated in HFIR is considerably greater (242°C for 12Cr-1MoVW and 348°C for 12Cr-1MoVW-2Ni). Either the higher fluence or the higher helium concentration produced in the HFIR experiment caused the larger ΔDBTT.

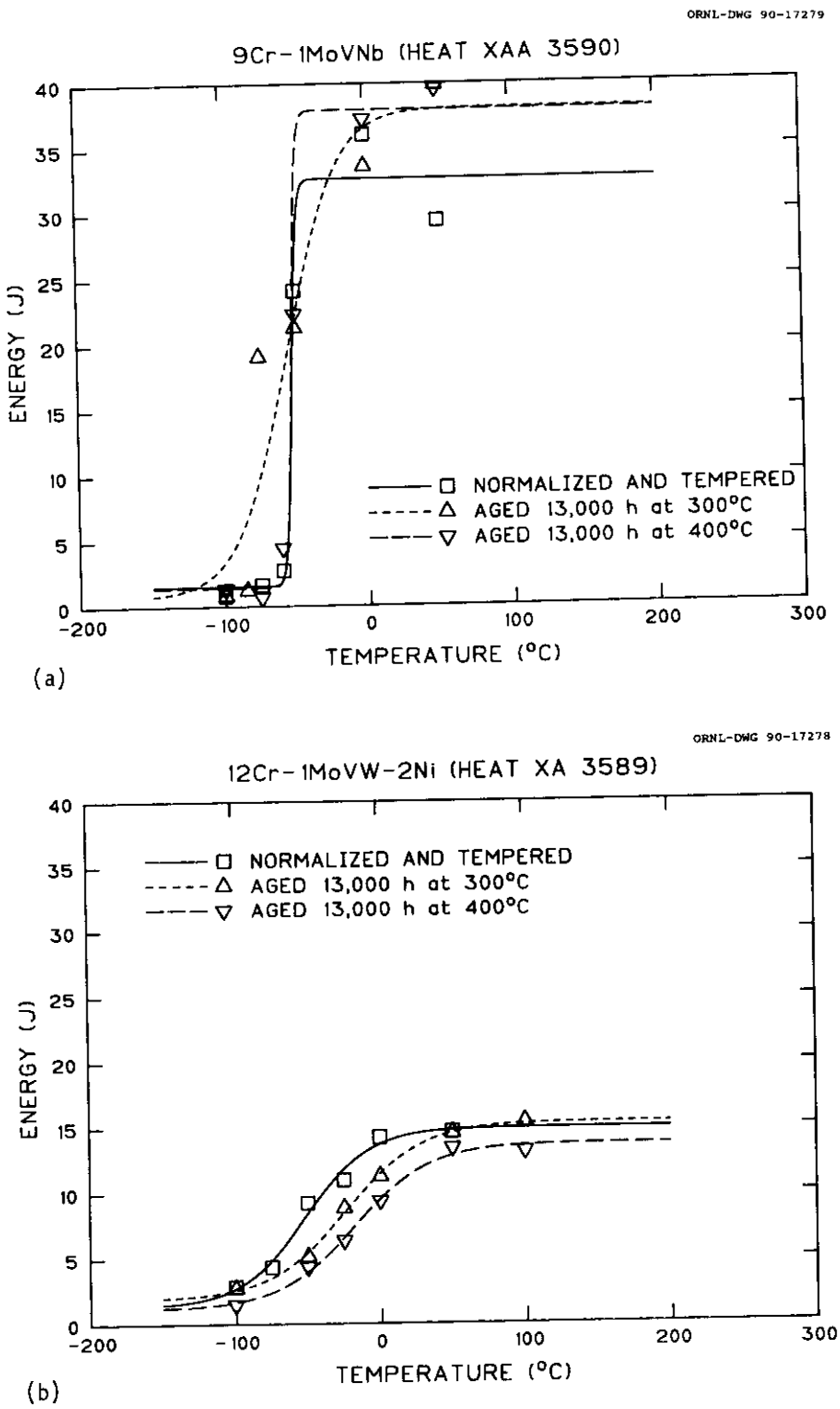

Fig. 5. Charpy impact properties for (a) 9Cr-1MoVNb and (b) 12Cr-1MoVW-2Ni steels in the normalized-and-tempered condition and after aging for 13,000 h at 300 and 400°C.

Nickel was shown by Odette and Lucas[13] to have an embrittling effect (measured as an increase in the OBTT) on pressure vessel steels irradiated in light-water reactors to fluences of ~1-3 × 10^{22} n/m^2 (note the fluence is more than three orders of magnitude less than the fluences used in the present experiment). These authors concluded that nickel acts synergistically with copper for high copper contents, but acts independently at low contents (<0.1% Cu). Although the exact mechanism for embrittlement is unknown, it is believed to be caused by "irradiation-induced fine-scale microstructural features."[13] For copper-bearing steel, 1 nm copper-rich precipitates (containing nickel when nickel is present in the steel) were established by small-angle neutron scattering. Low-copper steels also contain irradiation-induced defects, although their precise character is as yet undetermined.[13]

Such embrittlement caused by nickel is not believed to cause the effects observed in the present experiment. First, if nickel caused the effect, similar effects would be expected for irradiations in EBR-II (fast reactor) and HFIR (mixed-spectrum reactor) when irradiated to similar fast fluences. Second, the effect in the pressure-vessel steels occurs with the formation of defects so small they cannot be observed by TEM, but only by small-angle scattering." When the steels used in the present experiments are irradiated at 400°C in both fast reactors and mixed-spectrum reactors, dislocation loops are generated and precipitate reactions occur.[12,14] However, the only significant difference in microstructure ever detected when microstructures were compared for steels irradiated in a fast reactor and a mixed-spectrum reactor is that the cavity concentration is greater in steels irradiated in the mixed-spectrum reactor, an observation that has been attributed to helium.[12]

The possibility of a transmutation reaction in HFIR, other than the (n,α) reaction with ^{58}Ni to form helium, was considered. Two reactions that occur in HFIR but not in the fast reactors are (n,γ) reactions with ^{50}Cr to produce ^{51}V and ^{55}Mn to form ^{56}Fe. There is also an (n,p) reaction with ^{54}Fe to form ^{54}Mn. However, the results of any such reactions on properties should be the same for steels with and without nickel additions, because with the exception of the nickel, compositions are identical in the undoped and doped steels.

The nickel-doped steels were also used to study the effect of helium on tensile behavior, and it was concluded that helium affected the strength after irradiation in HFIR at 50 (ref. 15) and 400°C (refs. 9,16) These conclusions followed from comparing the effect of irradiation on the steels with different nickel content, although the conclusion on the 400°C tests was reached by also comparing the results from irradiation in HFIR at 400°C (ref. 9) to specimens irradiated in EBR-II at 390°C (ref. 16), where essentially no helium was produced. It should be pointed out, however, that the effect on tensile properties attributed to helium did not appear to be as large as the effect on the impact behavior observed in the present investigation.

Results from the present studies on the 9Cr-1MoVNb and 12Cr-1MoVW steels irradiated at 400°C are significantly different from those obtained by Hu and Gelles[2] on different heats of these steels irradiated at 390°C in EBR-II (the EBR-11-irradiated steels contained little helium). After 9Cr-1MoVNb steel was irradiated to 13 and 26 dpa, Hu and Gelles found a AOBTT of *52* and 54°C, respectively. The change observed for 9Cr-1MoVNb after ~40 dpa in the present experiment was 204°C. Likewise, for the 12Cr-1MoVW steel, Hu and Gelles[2] found ΔDBTTs of 124 and 144°C after 13 and 26 dpa, respectively, compared with 242°C found in the present study.

These EBR-II data indicate that a saturation in ADBTT occurred by 13 dpa for 9Cr-1MoVNb and 12Cr-1MoVW steels.[2] Likewise, recent results for 12Cr-1MoVW irradiated in FFTF at 365°C indicated a saturation in ADBTT occurred in 10 dpa (ref. 17). That saturation does not apply for the steels irradiated in HFIR. This comparison between HFIR and EBR-II irradiations also suggests that fluence or helium concentration are responsible for the differences in the shift in OBTT.

With respect to a saturation in ADBTT in HFIR, irradiations to higher dpa levels are required to determine if saturation occurs. Irradiation of another heat of 12Cr-1MoVW steel in HFIR to 4-9 dpa and *25* appm helium' resulted in a ADBTT of 195°C at 400°C. indicating that some increase occurred at the higher dpa and helium concentration used in the present experiment.

According to results in Tabie *2* for the HFIR irradiations, the ADBTT was always larger after irradiation at 400°C than at 300°C. This was true for both the 9Cr-1MoVNb and 12Cr-1MoVW steels, with and without the nickel additions. However, the irradiation fluences for the specimens irradiated at 300°C were less than those irradiated at 400°C (an average displacement damage of about *25* dpa occurred at 300°C compared to 40 dpa at 400°C). Linear extrapolation of the ADBTT data at 300°C to the higher fluence indicates that the shift would still be considerably less at 300°C than 400°C for the 12Cr-1MoVW and 12Cr-1MoVW-2Ni. The shift for the 9Cr-1MoVNb-2Ni is calculated to be similar at the two temperatures, and it would be slightly greater at 300°C for the 9Cr-1MoVNb.

Previous results led to the conclusion that the ADBTT for 12Cr-1MoVW steel went through a maximum with irradiation temperature around 400°C (refs. 4,6). Such a conclusion was based on a combination of data obtained from EBR-II and HFIR.[4,6] Because of differences in the behavior of steels in the two reactors, the use of the two types of data to reach such a conclusion is questionable. Based on HFIR data only, a maximum may occur for 12Cr-1MoVW at 400°C. That tentative conclusion is based on the extrapolation of the

300 and 400°C data of Table 2 discussed above and data at 4-9 dpa that indicated that the shift at 400°C exceeded that at 300°C and the shift at 300°C exceeded that at 50°C (refs. 4,6). More data from HFIR are required to verify this observation and to determine if a similar maximum occurs in the 9Cr-1MoVNb steel. Indications from the present experiment indicate the possibility of a broad peak around 300 to 400°C for 9Cr-1MoVNb.

One explanation for a maximum is that it is caused by the irradiation-induced dislocation and precipitation structure that results when the steel is irradiated near 400°C (refs. 12.14). This structure could have a maximum effect near 400°C, because at lower temperatures precipitate formation is inhibited by unfavorable kinetics and at higher temperatures softening occurs because of precipitate coarsening. This implies that the helium effect on ADBTT is superimposed on the effect due to the precipitate and dislocation structure.

The microstructures of the steels with and without the nickel additions irradiated in HFIR to 37-39 dpa at 300, 400, 500, and 600°C have been examined.[12] Irradiation of the 9Cr and 12Cr steels at 300 to 500°C produced a dense dislocation structure, which achieved its maximum density at 400°C. The largest amount of precipitate was observed at 400°C. There was a difference in the 9Cr and 12Cr steels in that subgrain coarsening occurred in the 9Cr-1MoVNb and 9Cr-1MoVNb-2Ni steels irradiated at 300 to 500°C. This coarsening was accompanied by the dissolution of some of the finer MC precipitates. Subgrain coarsening and dissolution was not observed for the 12Cr-1MoVW and 12Cr-1MoVW-2Ni steels at 300 and 400°C. Such microstructural changes would be expected to exacerbate the loss of toughness, and that change along with the effect of helium superimposed on these changes could cause the observed maximum. In the microstructural studies for the specimens irradiated to 37-39 dpa at 300 to 600°C. a maximum in void swelling was observed at 400°C (ref. 12) Swelling was found to be enhanced by the presence of helium.[12]

If helium is the cause of the large ADBTT for the steel irradiated in HFIR, the relative effect on the ΔDBTTs for the standard 9Cr-1MoVNb and 12Cr-1MoVW steels at first appears incongruous. Although the 9Cr-1MoVNb steel contained considerably less helium (16-27 appm) than the 12Cr-1MoVW (51-90 appm), the ADBTT of the 9Cr-1MoVNb after irradiation at 300°C exceeded that for the 12Cr-1MoVW. The AOBTT for the 12Cr-1MoVW exceeded that for 9Cr-1MoVNb after irradiation at 400°C, but the difference (38°C) was quite small, considering that the 12Cr-1MoVW contained about three times as much helium after irradiation at this temperature.

These observations on the possible relative effect of helium in 9Cr-1MoVNb and 12Cr-1MoVW steels with and without nickel added are in agreement with the swelling observations for these steels. After irradiation to 37-39 dpa in HFIR to form ~32 appm He in 9Cr-1MoVNb and 87 appm He in 12Cr-1MoVW, swelling was noticeably greater in 9Cr-1MoVNb than 12Cr-1MoVW (0.19% vs. 0.07%).[12,18] Helium was concluded to enhance swelling in both steels. An explanation for both the enhanced swelling and shift in DBTT for the 9Cr steels may again be the difference in microstructures formed in the two steels during irradiation. Subgrain coarsening would be expected to raise the DBTT. Such coarsening, which involves the movement of dislocations, might also result in the agglomeration of helium, which could then enhance swelling. Subgrain coarsening may be connected to the precipitate dissolution observed in the 9Cr steels;[19] perhaps it does not occur as readily in the 12Cr steels, because they have a higher carbon concentration.

Mechanisms by which helium affects strength, and thus toughness, have been speculated upon.[9] When helium is in an interstitial position, it can readily diffuse through an alloy.[20] However, the interstitial helium can become immobilized when trapped by a vacancy into a substitutional position. At temperatures <100°C, detrapping can occur either directly or by irradiation (by a neutron collision or by the knock-on process).[21] At somewhat higher temperatures, detrapping can involve replacement b a self interstitial. Helium-vacancy clusters can form when the helium and vacancies are mobile."" There are also indications that helium refines the scale of loop nucleation and prolongs loop stability to high fluences. [22]

It is expected that helium in interstitial positions could cause an increase in strength, as could the refinement of the scale of loop nucleation. If the helium effect is primarily associated with the loop structure and the promotion of a higher loop saturation concentration, then a strength saturation should occur at higher displacement-damage levels. The effect of interstitial helium would perhaps continue with increasing fluence and be more persistent, although saturation should again occur. Helium-vacancy clusters will form as the helium concentration builds up. At some point, no new clusters will form, and the newly generated helium will be incorporated in existing clusters and cause them to grow.

Finally, an inconsistency is observed when the data for 12Cr-1MoVW steel specimens irradiated at 300°C in HFIR to 4-9 dpa (ref. 4) are compared to those irradiated to 20-34 dpa. Although different heats of steel were involved, the ADBTT for the steel irradiated to the lower dpa had the highest DBTT. Although we cannot rule out the possibility that the ADBTT goes through a maximum with fluence at 300°C, this is not expected. Data for the 300°C tests for both of these heats of steel displayed considerable scatter in the upper shelf area. Perhaps this scatter coupled with the limited number of specimens available made an accurate determination of the DBTT impossible. The 400°C data appear to be consistent.

CONCLUSIONS

Charpy impact studies were conducted on specimens of 9Cr-1MoVNb, 9Cr-1MoVNb-2Ni, 12Cr-1MoVW, and 12Cr-1MoVW-2Ni steels irradiated at 300 and 400°C in HFIR to displacement-damage levels of up to 42 dpa. Because of the nickel present in the steels, irradiation in HFIR produced up to 390 appm He. The ADBTT values of 204 and 242°C observed for 9Cr-1MoVNb and 12Cr-1MoVW steels, respectively, after irradiation at 400°C in HFIR were the largest values ever observed for these steels. They were considerably larger than any shift observed after irradiation in a fast reactor, where a saturation value of ADBTT ~54°C was observed for 9Cr-1MoVNb and ~144°C for 12Cr-1MoVW after ~13 dpa. It was concluded that this difference for irradiation in the two reactors was either due to the larger displacement-damage level reached in the HFIR experiment, or else it was due to the large amount of helium generated in these specimens. The latter conclusion is preferred based on the observations. Irradiation in HFIR to a still-larger displacement-damage level is required to determine if a saturation of ADBTT occurs under radiation conditions in this reactor.

Regardless of whether the effect of helium is accepted, the shift in DBTT after irradiation at 400°C of 204 and 242°C for the 9Cr-1MoVNb and 12Cr-1MoVW steels, respectively, are the largest shifts ever observed for these steels. If the ADBTT of the steels with *2%* Ni are representative of these steels irradiated to He/dpa ratios typical of those expected in a fusion reactor, then a ADBTT approaching 350°C is much larger than any increase ever expected for these steels. Therefore, before these steels are considered for use as a first-wall material, this possibility of helium affecting toughness must be more fully investigated and understood.

REFERENCES

1. F. A. Smidt, Jr., J. R. Hawthorne, and V. Provenzano, in: Effects of Radiation on Materials, STP 725, Eds. D. Kramer, H. R. Brager, and J. S. Perrin (American Society for Testing and Materials, Philadelphia, 1981) p. 269.
2. W. L. Hu and D. S. Gelles, in: Influence of Radiation on Material Properties: 13th International Symposium (Part II), ASTM STP 956, F. A. Garner, C. H. Henager, Jr., and N. Igata, Eds. (American Society for Testing Materials, Philadelphia, 1987) p. 83.
3. D. S. Gelles, J. Nucl. Mater. 149 (1987) 192.
4. J. M. Vitek, W. R. Corwin, R. L. Klueh, and J. R. Hawthorne, J. Nucl. Mater. 141-143 (1986) 948.
5. W. R. Corwin, J. M. Vitek, and R. L. Klueh, J. Nucl. Mater. 149 (1987) 312.
6. R. L. Klueh, J. M. Vitek, W. R. Corwin, and D. J. Alexander, J. Nucl. Mater. 155-157 (1988) 973.
7. R. L. Klueh and D. J. Alexander, J. Nucl. Mater. to be published.
8. R. L. Klueh, J. M. Vitek, and M. L. Grossbeck, in: Effects of Irradiation on Materials: Eleventh Conference. ASTM STP 782. H. R. Brager and J. S. Perrin. Eds. (American Societv for Testing Materials, Philadelphia, 1982) p. 648.
9. R. L. Klueh and J. M. Vitek, J. Nucl. Mater. 150 (1987) 272.
10. W. R. Corwin, R. L. Klueh, and J. M. Vitek, J. Nucl. Mater. 122 & 123 (1984) 343.
11. W. R. Corwin and A. M. Hougland, in: The Use of Small-Scale Specimens for Testing Irradiated Material, ASTM STP 888, W. R. Corwin and G. E. Lucas, Eds., (American Society for Testing and Materials, Philadelphia, 1986) p. 325.
12. P. J. Maziasz, R. L. Klueh, and J. M. Vitek, J. Nucl. Mater. 141-143 (1986) 929.
13. G. R. Odette and G. E. Lucas, Effects of Irradiation on Materials: Fourteenth International Symposium (Volume II) ASTM STP 1046, N. H. Packan, R. E. Stoller, and A. S. Kumar, Eds. (American Society for Testing Materials, Philadelphia, 1990) p. 323.
14. D. S. Gelles and L. K. Thomas, in: Ferritic Alloys for use in Nuclear Energy Technologies, J. W. Davis and D. J. Michel, Eds. (Metallurgical Society of AIME, Warrendale, PA, 1984) P. 559.
15. R. L. Klueh and J. M. Vitek, J. Nucl. Mater. 161 (1989) 13.
16. R. L. Klueh and J. M. Vitek, J. Nucl. Mater. 141-143 (1986) 960.
17. R. L. Klueh and D. J. Alexander, Effects of Radiation on Materials: Fifteenth Conference (American Society for Testing Materials, Philadelphia), to be published.
18. J. M. Vitek and R. L. Klueh, J. Nucl. Mater. 122 & 123 (1984) 254.
19. P. J. Maziasz and R. L. Klueh, Effects of Radiation on Materials: Fifteenth Conference (American Society for Testing Materials, Philadelphia), to be published.
20. L. K. Mansur, E. A. Lee, P. J. Maziasz, and A. F. Rowcliffe, J. Nucl. Mater. 141-143 (1986) 633.
21. N. M. Ghoneim, S. Sharafat, and L. K. Mansur, Point Defects and Defect Interactions in Metals, J. Takamura, M. Doyama, and M. Kiritani, Eds. (University of Tokyo Press, Tokyo. 1982) p. 865.
22. P. J. Maziasz, Effects of Helium Content on Microstructural Development in Type 316 Stainless Steel Under Neutron Irradiation, Oak Ridge National Laboratory, ORNL-6121 (1985).

THE DEVELOPMENT OF FERRITIC STEELS FOR FAST INDUCED-RADIOACTIVITY DECAY -- R. L. Klueh and D. J. Alexander (Oak Ridge National Laboratory)

OBJECTIVE

Induced radioactivity in the first-wall and blanket-structure materials of a fusion reactor will make these components highly radioactive after their service lifetime, leading to difficult radioactive waste-management problems. One way to minimize the disposal problem is to use structural materials in which radioactive isotopes induced by irradiation decay quickly to levels that allow simplified disposal techniques. We are assessing the feasibility of developing such ferritic steels.

SUMMARY

Irradiation of ferritic steels with neutrons at temperatures up to ~450°C causes a loss of toughness. This can be measured in a Charpy impact test, where an increase in the ductile-brittle transition temperature (DBTT) and a decrease in the upper-shelf energy is observed after irradiation. Reduced-activation Cr-W steels with chromium concentrations varying from 2.25 to 12% were irradiated at 365°C to ~7 dpa in the Fast Flux Test Facility. Steels with 2.25% Cr and a combination of 2% W and 0.25% V were less severely affected by irradiation than steels with vanadium and no tungsten, tungsten and no vanadium, or with 1% W and 0.25% V. Two steels with 9% Cr showed the most resistance to a loss of toughness. A 9% Cr steel with 2% W and 0.25% V showed an increase in DBTT of 68°C. This same composition with an addition of 0.07% Ta developed an increase in DBTT of only 4°C. These values compare to increases of over 100°C for the rest of the steels.

PROGRESS AND STATUS

Introduction

A program is in progress to develop reduced-activation or fast induced radioactivity decay (FIRD) ferritic steels that can be more readily disposed of or recycled than conventional alloys.[1] Such alloys cannot use molybdenum and niobium, which are present in the compositions of the conventional Cr-Mo steels presently of interest for fusion reactor applications (2¼Cr-1Mo, 9Cr-1MoVNb, and 12Cr-1MoVW). Compositions for proposed experimental steels were based on variations of the compositions of the Cr-Mo steels, with tungsten proposed as a replacement for molybdenum, and vanadium, titanium, and tantalum as replacements for niobium. Various experimental alloys were preopsed as a way of determining the effect of different alloying elements on properties; these compositions are given in Table 1, along with the designation for each alloy.

Table 1. Proposed nominal compositions for fast induced-radioactivity decay steel development program

Alloy	Nominal Chemical Composition,[a] (wt %)				
	Cr	W	V	Ta	C
2.25CrV	2.25		0.25		0.1
2.25Cr-1WV	2.25	1	0.25		0.1
2.25Cr-2W	2.25	2			0.1
2.25Cr-2WV	2.25	2	0.25		0.1
5Cr-2WV	5	2	0.25		0.1
9Cr-2WV	9	2	0.25		0.1
9Cr-2WVTa	9	2	0.25	0.12	0.1
12Cr-2WV	12	2	0.25		0.1

[a]Balance iron.

A range of chromium compositions from ~2.25 to 12% (all compositions are in weight percent) was proposed.' As a maximum level for tungsten, an atom-for-atom replacement of molybdenum by tungsten was chosen; this required 2 wt % W, since the atomic weight of tungsten is approximately twice that of molybdenum. A 0.25% V content was used to obtain a favorable vanadium/carbon ratio for carbide formation: a significantly higher vanadium concentration above that necessary to tie up the carbon would make it difficult to dissolve the vanadium during the normalization treatment, thus decreasing the hardenability. Experimental alloys with 0, 1, and 2% W were proposed to determine the effect of tungsten, and an alloy with tungsten and no vanadium and one with vanadium and no tungsten were suggested to determine the effect of these elements on properties.' Tantalum was added to a 9Cr-2WV steel to get a steel analogous to the 9Cr-1MoVNb steel. A carbon level of 0.1-0.15% was proposed for all steels to help ensure weldability. Of the Cr-Mo steels presently in the fusion-reactor materials program, only the 12Cr-1MoVW steel has more carbon. That steel contains 0.2%C, which along with 0.5% Ni is used to eliminate delta-ferrite in this high-chromium alloy.

We previously reported on the microstructure,[2] tempering and tensile behavior,[3] and Charpy impact behavior[4] of these experimental Cr-W* steels in the unirradiated condition. We also reported on the effect

*As a generic designation, the new class of steels will be referred to as Cr-W steels. (The only exception is the 2¼CrV steel, which contains no tungsten.) This follows the procedure used for the Cr-Mo steels, after which these steels are patterned, even though both types of steel may contain other alloying elements.

of irradiation at 365°C in the Fast Flux Test Facility (FFTF) on the hardening behavior of the steels as measured in tensile tests.[5] In this report, the effect of irradiation at 365°C in FFTF on impact behavior is presented. For fusion-reactor applications, impact behavior is extremely important, because neutron irradiation causes an increase in the ductile-brittle transition temperature (DBTT) and a decrease in upper-shelf energy (USE) of ferritic steels. Developing steels that show only small changes in these parameters is of utmost importance if ferritic steels are to be useful as structural materials for fusion reactors.

Experimental Procedure

Eight heats of steel similar to those given in Table 1 were prepared by Combustion Engineering, Inc., Chattanooga, Tennessee. Melt compositions are given in Table 2. These are the same steels used in the previous studies.[2-5] In addition to the nominal compositions of Cr, V, W, C, and Ta desired, the concentrations of other elements such as Mn, P, Si, etc., were adjusted to levels typical of commercial practice.

Table 2. Composition of fast induced-radioactivity decay ferritic steels

Element	Chemical Composition,[a] wt %							
	2.25Cr-0.25V (heat 3785)	2.25Cr-1W-0.25V (heat 3786)	2.25Cr-2W (heat 3787)	2.25Cr-2W-0.25V (heat 3788)	5Cr-2W-0.25V (heat 3789)	9Cr-2W-0.25V (heat 3790)	9Cr-2W-0.25VTa (heat 3791)	12Cr-2W-0.25V (heat 3792)
C	0.11	0.10	0.11	0.11	0.13	0.12	0.10	0.10
Mn	0.40	0.34	0.39	0.42	0.47	0.51	0.43	0.46
P	0.015	0.015	0.016	0.016	0.015	0.014	0.015	0.014
S	0.006	0.006	*0.005*	0.006	0.005	0.005	*0.005*	*0.005*
Si	0.17	0.13	0.15	0.20	0.25	0.25	0.23	0.24
Ni	0.01	0.01	<0.01	<0.01				
Cr	2.36	2.30	2.48	2.42	5.00	8.73	8.72	11.49
Mo	0.01	<0.01	<0.01					
V	0.25	*0.25*	0.009	0.24	0.25	0.24	0.23	0.23
Nb	<0.01	<0.01	<0.01					
Ta	<0.01	<0.01	<0.01				0.075	
Ti	<0.01	<0.01	<0.01					
co	*0.005*	0.006	0.008					
cu	0.02	*0.025*	0.03					
Al	*0.02*	*0.02*	*0.02*	0.021	0.03	0.03	0.03	0.028
B	<0.001	<0.001	0.001					
W		0.93	1.99	1.98	2.07	2.09	2.09	2.12

[a]Balance iron.

All heats were air melted and then electroslag remelted (ESR) to obtain about 18 kg of usable material. The ESR ingot was hot rolled to 15.9-mm-thick plate that was heat treated and used for making the impact specimens.

A normalizing and tempering heat treatment was used. The 2.25Cr-2W steel was normalized by annealing 1 h at 900°C and air cooling. The other seven heats were annealed 1 h at 1050°C and air cooled; the higher temperature was used for these steels to assure than any vanadium carbide present was dissolved during the austenitization. The 2¼CrV, 2¼Cr-1WV, and 2¼Cr-2W were tempered 1 h at 700°C, and the other five heats were tempered 1 h at 750°C.

Irradiation of the six Charpy specimens from each heat was in the FFTF in the below-core specimen canister of the Materials Open Test Assembly (MOTA). This is a sodium "weeper" that operates at ~365°C, which is slightly above the coolant ambient temperature. Because specimens were at slightly different positions in the canister, not all specimens received the same fluence. All of the 2¼Cr steels were irradiated to about 1.98 × 10^{26} n/m^2, ~7.3 dpa. The 5Cr-2WV and 9Cr-2WV steels were irradiated to about 2.05 × 10^{26} n/m^2, ~7.6 dpa, and the 9Cr-2WVTa and 12Cr-2WV steels were irradiated to about 1.82 × 10^{26} n/m^2, ~6.7 dpa. Less than 1 appm He was formed during irradiation.

Subsize Charpy specimens were irradiated and tested. These were essentially one-third the standard size and measured 3.3 mm by 3.3 mm by 25.4 mm and contained a 0.51-mm-deep 30° V-notch with a 0.05- to 0.08-mm-root radius. All specimens were taken from the normalized-and-tempered 15.9-mm-thick plate along the rolling direction with the notch running transverse to the rolling direction (L-T orientation). Surface material was machined equally from both sides of the plate to allow for two rows of specimens to be machined from the center of the plate.

Details on the test procedure for the subsize Charpy specimens have been published.[6] Each individual Charpy data set was fitted to a hyperbolic tangent function for obtaining the transition temperature and upper-shelf energy.

Results

Results from the Charpy impact tests on the irradiated and control specimens are given in Table 3. This table gives the USE and the DBTT for each of the eight steels in the unirradiated condition and after irradiation at 365°C; the shift in DBTT (ADBTT) is also given. The DBTT was determined at an energy that is half the difference between the upper- and lower-shelf energies. Because the lower-shelf energy is only a few tenths of a joule, the value determined by this method is essentially the same as that determined at half the upper shelf energy, a value which is often used.

Table 3. Impact properties of Cr-W steels irradiated in FFTF at 365°C

Alloy Designation	Specimen Condition[a]	DBTT[b] (°C)	ADBTT (°C)	Upper-Shelf Energy (J)
2.25CrV	N&T	14		10
	I	250	236	4.2
2.25Cr-1WV	N&T	-28		11.8
	I	192	220	5.6
2.25Cr-2W	N&T	-19		9.2
	I	140	159	4.6
2.25Cr-2WV	N&T	4		9.1
	I	111	115	5.2
5Cr-2WV	N&T	-70		9.2
	I	33	103	6.5
9Cr-2WV	N&T	-60		8.4
	I	8	68	6.4
9Cr-2WVTa	N&T	-88		11.2
	I	-84	4	8.6
12Cr-2WV	N&T	-18		8.3
	I	156	174	5.9

Figure 1 shows the Charpy curves for the 2¼Cr steels. All four of these steels show a large increase in DBTT and large decrease in USE. The shift appears to be affected by the composition. Although there was a difference between the DBTT after irradiation for the 2¼CrV steel, the one without tungsten [Fig. 1(a)], and the 2¼Cr-1WV steel, which only contained 1%W [Fig. 1(b)], there was little difference in the ADBTT for these two steels. Irradiation had a similar effect on the reduction of USE for these two steels. The steel without vanadium, the 2¼Cr-2W, showed a significantly smaller shift in DBTT [Fig. 1(c)] than the other two steels. Finally, the 2¼Cr-2WV steel, which contained a combination of 2% W and 0.25% V, showed the least shift [Fig. 1(d)] of the 2¼Cr steels.

In Fig. 2, the Charpy curves for the high-chromium steels are shown. These steels also show a variation in ADBTT, with the 12Cr-2WV steel [Fig. 2(d)] showing the largest shift, followed by the 5Cr-2WV steel [Fig. 2(a)]. The 9Cr-2WV steel [Fig. 2(b)] shows a still smaller shift. Finally, irradiation of the 9Cr-2WVTa steel resulted in a ADBTT of only 4°C [Fig. 2(c)], even though the only difference between the 9Cr-2WVTa and the 9Cr-2WV steel is that the former contains 0.07% Ta.

Discussion

Optical microstructures of these eight steels when normalized-and-tempered as 15.9-mm-thick plate were previously discussed.[2] The microstructure of the 2¼CrV contained 30 to 35% tempered bainite, with the remainder being polygonal or proeutectoid ferrite. The 2¼Cr-1WV steel contained ~55% tempered bainite and 45% polygonal ferrite. Less ferrite was observed in the 2¼Cr-2W and 2¼Cr-2WV steels: the 2¼Cr-2W steel was essentially 100% bainite and the 2¼Cr-2WV steel contained 15-20% polygonal ferrite.[2] The 5Cr-2WV, 9Cr-2WV, and 9Cr-2WVTa steels were 100% tempered martensite.[2] However, the 12Cr-2WV steel contained approximately 25% delta-ferrite, with the balance being martensite. The only major difference observed in the martensite of these latter four steels by optical microscopy was that the 9Cr-2WVTa had a much finer prior austenite grain size than the other three steels.[2]

Since the shift in DBTT is expected to be related to the hardening caused by radiation, it is of interest to consider the effect of irradiation on the tensile behavior. Specimens of the steels were tensile tested after irradiation to ~7 dpa (ref. 5). (Note that in this case the steels were heat treated in the tensile specimen geometry, and because of the thinner sections, all the 2¼Cr steels were 100% bainite.) All steels hardened during irradiation. Observations on the Cr-W steels indicated that steels containing 2¼% Cr and a combination of vanadium and tungsten hardened less than those to which only vanadium or tungsten were added. For the steels containing 2.25, 5, 9, and 12% Cr and the combination of 2% W and 0.25% V, the steel with 12% Cr hardened the most, while the other three steels hardened significantly less. These three steels showed similar amounts of hardening. The 9Cr-2WVTa steel hardened the least of all of the reduced-activation steels. The results on the Cr-W steels were compared to the 9Cr-1MoVNb and 12Cr-1MoVW steels, which were similarly irradiated. It was found that analogous steels hardened similar amounts: the 9Cr-2WVTa and 9Cr-1MoVNb steels showed similar amounts of hardening, as did the 12Cr-2WV and the 12Cr-1MoVW steels.[5]

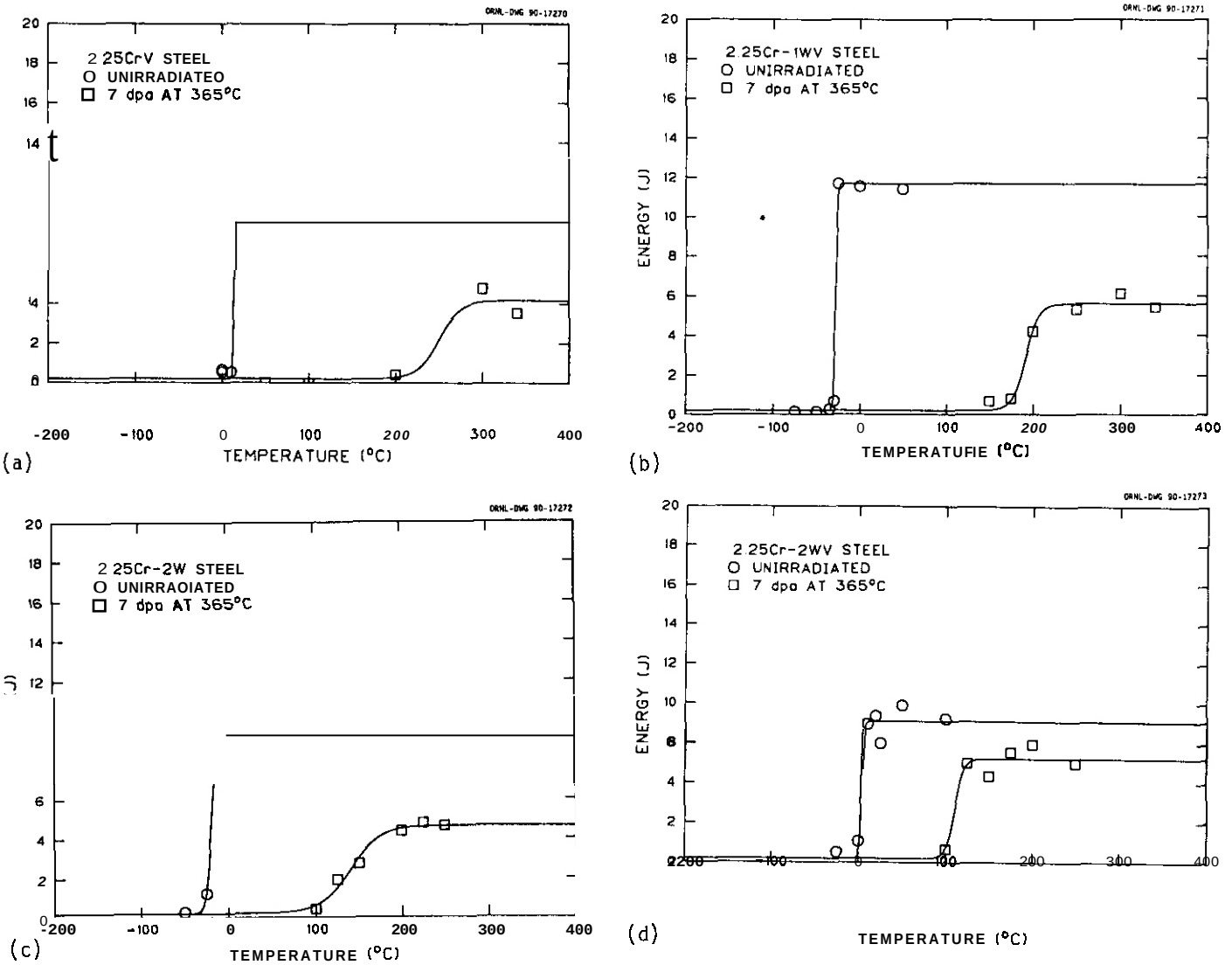

Fig. 1. Charpy impact curves of the normalized-and-tempered steel and for the steel after it was irradiated to ~7 dpa at 365°C for (a) 2¼CrV, (b) 2¼Cr-1WV, (c) 2¼Cr-2W, and (d) 2¼Cr-2WV steels.

From the observations on the Charpy tests on the 2¼Cr steels. there would also appear to be an effect of composition on the shift in DBTT. That is, it appears that the combination of tungsten and vanadium has a larger effect than vanadium alone, and 2% W has a larger effect than 1%W in combination with 0.25% V. Finally, a combination of 2% W and 0.25% V appears to have an advantage over a steel with only tungsten or with a comhination of only 1%W and vanadium.

Although these conclusions follow from the results in Table 3, their validity is unclear. because of the difference in the microstructures of the different 2¼Cr steels. The steels contain different amounts of polygonal ferrite, and we previously showed that the amount of ferrite in a mostly bainitic microstructure can adversely affect the toughness in the unirradiated condition: as the amount of polygonal ferrite decreases, the DBTT decreases and the USE increases.' Not only is the amount of polygonal ferrite a factor, but it has also been shown that the type of bainite formed can affect toughness. 7

Another complication in the comparison of the 2¼Cr steels is that the 2¼Cr-2WV steel was tempered at 750°C, compared to 700°C for the other 2¼Cr steels. Nevertheless, the comparison of these steels with 2¼Cr-2WV has validity. because even after this higher tempering temperature, the strength of the 2¼Cr-2WV is either slightly greater or equivalent to the strengths of the three steels tempered at 700°C (ref. 3). Furthermore, if the other three 2¼Cr steels were tempered at 750°C, the strengths developed would be too low for these steels to be of interest for fusion applications.

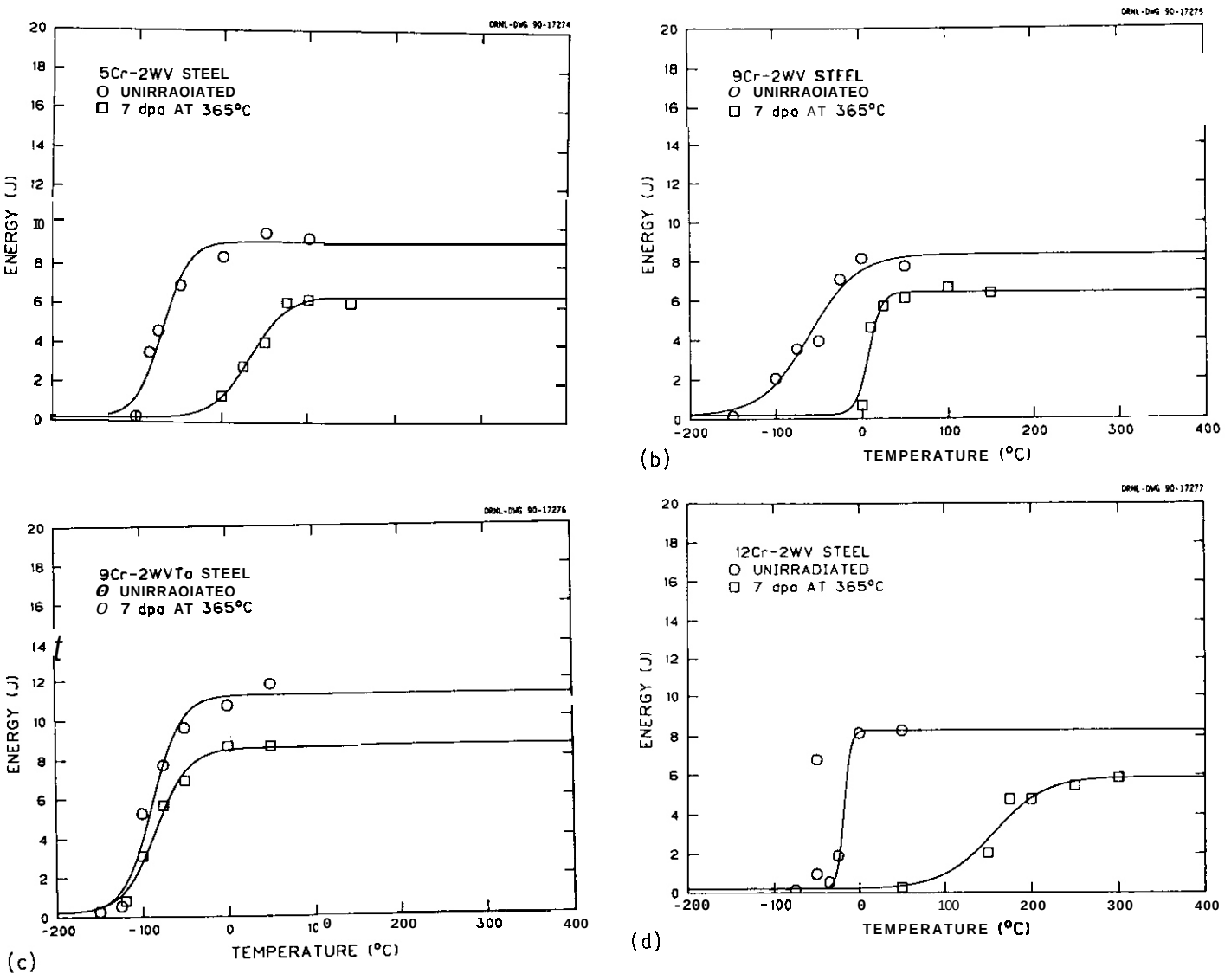

Fig. 2. Charpy impact curves of the normalized-and-tempered steel and for the steel after it was irradiated to ~7 dpa at 365°C for (a) 5Cr-2WV, (b) 9Cr-2WV, (c) 9Cr-2WVTa, and (d) 12Cr-2WV steels.

Consider now the four high-chromium steels and the 2¼Cr-2WV steel. These steels were all normalized and tempered similarly, and the 2¼Cr-2WV steel is the strongest of the eight steels -- slightly stronger than 9Cr-2WVTa (ref. 3). For the four steels that contained only tungsten and vanadium, the 12Cr-2WV steel shored the largest ADBTT. This is in qualitative agreement with the observations on the hardening due to irradiation.[5] The 2¼Cr-2WV and 5Cr-2WV steels showed similar shifts in OBTT, but the shift for the 9Cr-2WV steel was significantly less. Finally, although the ΔDBTT of the 9Cr-2WV steel was relatively small. the addition of the small amount of tantalum had a marked effect in reducing the AOBTT. This observation that the toughness of the 9Cr-2WVTa is least affected by irradiation also agrees with the observation on the effect of irradiation on tensile properties, where this steel showed the least amount of hardening when irradiated.[5]

The reason for the apparent effect of tantalum is unclear. Optical microscopy indicated that the Prior austenite grain size of the 9Cr-2WVTa was less than that of the 9Cr-2WV steel.[2] This smaller grain size could be caused by undissolved TaC restricting the grain growth of the austenite during normalization. Because of the variable nature of the microstructures, it was difficult to quantify large difference in the lath structure of the martensite of the two steels using transmission electron microscopy (TEM): qualitatively, the average lath size of the 9Cr-2WVTa steel appears to be significantly less than that of the 9Cr-2WV. Precipitates in both steels were a combination of $M_{23}C_6$ and MC, and slightly more precipitate formed in the 9Cr-2WV steel.' The MC in the 9Cr-2WV was vanadium-rich while the MC in the 9Cr-2WVTa was a combination of vanadium-rich and tantalum-rich particles.' In the unirradiated condition, the 9Cr-2WVTa steel had a slightly higher strength[3] and slightly lower DBTT (Table 3) (ref. 4). which could possibly be attributed to the smaller prior austenite grain size and/or the smaller lath size.

Prior austenite grain size and lath size offer an explanation for the reduced effect of irradiation on hardening in the 9Cr-2WVTa steel. Such boundaries act as sinks for defects (vacancies and interstitials) generated by irradiation. These defects cause the hardening, which, in turn, cause the shift in DBTT. A decrease in the lath size and prior austenite grain size results in a larger amount of boundary area available to act as a defect sink, thus reducing the defect concentration in the lattice. Fewer defects result in less hardening and a smaller ADBTT. The observation of such a small increase in DBTT for the 9Cr-2WVTa steel indicates that it may be possible to develop steels that resist a loss of toughness when irradiated -- at least for irradiation in a fast reactor.

In a previous experiment, third-size specimens of 12Cr-1MoVW and 2¼Cr-1Mo steels were also irradiated at 365°C. Increases in DBTT of 151 and 173°C were observed for 12Cr-1MoVW and 2¼Cr-1Mo, respectively,[8] much larger than the shift for 9Cr-2WVTa. Previous work has shown that the AOBTT for half-size Charpy specimens of 9Cr-1MoVNb steel irradiated in EBR-II to 13 dpa at 390°C was less than that for 12Cr-1MoVW steel.' A ADBTT of 52°C was observed for 9Cr-1MoVNb, compared with 124°C for 12Cr-1MoVW steel. Irradiation to 26 dpa showed little further increase in DBTT, which indicated that a saturation had occurred by 13 dpa. Assuming saturation is being approached for the 9Cr-2WVTa (specimens are presently being irradiated to determine saturation), this makes the slight change observed at 365°C for this steel especially significant, since ADBTT increases with decreasing irradiation temperature when irradiated in a fast reactor such as EBR-II[9] and FFTF.[8]

Cannon et. al[10] and Gelles" reported on Charpy impact tests of Six reduced activation steels irradiated in FFTF to 10 dpa at 365°C. These steels had the following nominal compositions: 2Cr-1.5V-0.1C, 7.5Cr-2W0.15C, 9Cr-1V-0.1C, 9Cr-1W-0.1C, 12Cr-6Mn-1V-0.1C, and 12Cr-6Mn-1W-0.1C. Although there are significant differences between these steels and those of the present investigation, there were some similarities. The 7.5Cr-2W and 9Cr-1W steels showed the least change in properties upon irradiation with shifts in DETT of 24 and 32°C, respectively. The 9Cr-1V steel developed a ADBTT of 62°C, while the 2Cr and 12Cr steels had ADBTT values in excess of 200°C.

When the observations from the previous experiments[10,11] are combined with those of the present investigation, it appears that a chromium concentration of around 7-9% is favorable to minimize ADBTT. Results from the present investigation indicate that tantalum affects that behavior, whereas the results of Cannon et. al[10] indicate that tungsten in the absence of vanadium is important, while high vanadium concentration in the absence of tungsten has a detrimental effect on 9% Cr steels. Note that these latter steels in the work of Cannon et. al are significantly different from those of the present experiment due to the much higher vanadium concentration used. Such a large vanadium concentration would make it extremely difficult to dissolve all the vanadium carbide when these steels are heat treated. This could affect the size of carbides present in the steel and subsequently affect the toughness.

The results of the present and past investigations should not be used to rule out the possibility of using a low-chromium steel for fusion applications, especially since the 2¼Cr-2WV steel was the strongest of the eight heats in Table 1 (ref. 1). This is especially true if tantalum could not be used in FIRD steels. Tantalum is allowed under the Nuclear Regulatory Commission regulation 10CFR61, for which FIRD alloying elements have been determined. However, tantalum develops radioactive isotopes that have an extremely high activity immediately after irradiation, and it may be eliminated for safety reasons. Without tantalum, the 9Cr steels are substantially weaker than 2¼Cr-2WV steel.[2]

It has been shown that the DBTT and USE of 2¼Cr-2WV steel before irradiation can be substantially improved when it is heat treated to obtain an all bainitic microstructure.[5] Such a heat treatment lowered the DETT to ~52°C from 4°C and increased the USE to 11 J from 9 J (ref. 5). As shown for 2¼Cr-1Mo steel,' it is possible to achieve good unirradiated and irradiated toughness on a low-chromium steel. Before irradiation, 2¼Cr-1Mo steel had a DETT of -107°C. After irradiation, the DBTT was still lower than that for 12Cr-1MoVW steel specimens irradiated similarly in FFTF, even though the latter steel had a lower ADBTT. Furthermore, after irradiation the USE of the 2¼Cr-1Mo steel remained higher than that for 12Cr-1MoVW steel before irradiation.[8] Thus, it appears that if a steel can be developed with a sufficiently low DBTT and high USE before irradiation, the saturation value of ADBTT may not be too high after irradiation for the steel to be of use. Just as tantalum appears to have a significant effect on producing radiation resistance for a 9Cr steel, it may be possible to use composition variation to achieve greater radiation resistance in a low chromium steel.

Finally, there is still a question of how large the saturation ADBTT might be in a fusion reactor -- as opposed to a fast reactor of the type used in the present studies. In a fusion reactor, large amounts of transmutation helium will form in conjunction with displacement damage. Experiments to simulate the effect of the simultaneous formation of displacement damage and helium have been attempted. This was done by irradiating 9Cr-1MoVNb and 12Cr-1MoVW steels with and without nickel additions in the High Flux Isotope Reactor (HFIR). Thermal neutrons from the mixed spectrum of HFIR form helium in a two-step reaction with ^{58}Ni, while the fast neutrons in the spectrum form displacement damage (displacement damage without significant amounts of helium is formed in a fast reactor such as FFTF or ERR-11). Such studies have indicated that helium affects toughness.[10] For the 9Cr-1MoVNb steel, irradiation to 13 and 26 dpa (<5 appm He) at 390°C in ERR-I1 resulted in shifts in DBTT of 52 and 54°C (ref. 9). However, irradiation to 40 dpa at 400°C in HFIR, where 35 appm He was generated, resulted in a ADBTT of 204°C (ref. 12). Thus, the saturation in ADBTT observed for the fast reactor irradiation does not apply. A similar effect was

observed for 12Cr-1MoVW steel after irradiation to 13 and 26 dpa, where a saturation value of 144°C was observed in EBR-II at 390°C (ref. 9), but a value 242°C was observed after irradiating in HFIR at 400°C to 40 dpa and 110 appm He (ref. 12). At present, the difference in behavior in the two reactors has been attributed to the helium.[12] A similar helium effect would then be expected to occur in a fusion reactor. There is no reason to believe the FIRD alloys should be different from the conventional ferritic steels.

SUMMARY AND CONCLUSION

Miniature Charpy specimens from eight reduced-activation Cr-W ferritic steels were irradiated to ~7 dpa in FFTF at 365°C. Alloys containing 2% W and 0.25% V with chromium levels of 2.25, 5, 9, and 12% (designated 2¼Cr-2WV, 5Cr-2WV, 9Cr-2WV, and 12Cr-2WV) were irradiated. A 9Cr-2WV steel with 0.07% Ta (9Cr-2WVTa) and 2¼Cr steels with 0.25% V and 0 and 1% W (2¼CrV, and 2¼Cr-1WV) and with 2% W and no vanadium (2¼Cr-2W) were also irradiated. Irradiation resulted in an increase in the DBTT and a decrease in USE. From observations on the 2¼CrV, 2¼Cr-1WV, 2¼Cr2W, and 2¼Cr-2WV, it was concluded that vanadium may exacerbate the shift in the absence of 2% W. These conclusions were complicated by differences in the overall microstructure (amount of bainite and polygonal ferrite) of the steels and differences in tempering conditions. Since toughness of the low-chromium steels can be affected by the amounts of bainite and polygonal ferrite in the microstructure, it may be possible to promote improved irradiation resistance if the microstructures of the steels are entirely bainite. For the high-chromium steels, the 12Cr-2WV steel showed the largest change in properties, followed by the 5Cr-2WV steel. The 9Cr steels showed the least change, with the 9Cr-2WVTa showing only a 4°C increase in DBTT, indicating that tantalum had a favorable effect on the properties. The results are encouraging in that they indicate that the effect of irradiation on toughness can be favorably affected by changing the composition.

REFERENCES

1. R. L. Klueh and E. E. Rloom, Alloy Development for Fast Induced Radioactivity Decay for Fusion Reactor Applications, Oak Ridge National Laboratory, ORNL/TM-8894, (March 1984).
2. R. L. Klueh and P. J. Maziasz, Met. Trans. 20A (1989) 373.
3. R. L. Klueh, Met. Trans. 20A (1989) 463.
4. R. L. Klueh and W. R. Corwin, J. Materials Eng. 11 (1989) 169.
5. R. L. Klueh, J. Nucl. Mater. to be published.
6. W. R. Corwin and A. M. Hougland, in: The Use of Small Scale Specimens for Testing Irradiated Material, ASTM STP 888, Eds. W. R. Corwin and G. E. Lucas (American Society for Testing and Materials, Philadelphia, 1986), p. 325.
7. R. L. Klueh and D. J. Alexander, J. Nucl. Mater. to be published.
8. R. L. Klueh and O. J. Alexander, in: Proceedings of the 15th Symposium on Effects of Radiation on Materials (American Society for Testing and Materials, Philadelphia, 1991), to be published.
9. W. L. Hu and O. S. Gelles, in: Influence of Radiation on Material Properties: 13th International Symposium (Part II), ASTM STP 956, Eds. F. A. Garner, C. H. Henager, Jr., and N. Igata (American Society for Testing Materials, Philadelphia, 1987), p. 83.
10. N. S. Cannon, W. L. Hu, and D. S. Gelles, Fusion Reactor Materials Semiannual Progress Report, March 31, 1987, DOE/ER-0045/16, U. S. Department of Energy, Washington, O. C., p. 119.
11. D. S. Gelles, in: Reduced Activation Materials for Fusion Reactors, Eds. R. L. Klueh, D. S. Gelles, M. Okada, and N. H. Packan (American Society for Testing and Materials, Philadelphia, 1990) p. 113.
12. R. L. Klueh and O. J. Alexander, J. Nucl. Mater. to be published.

COMPARISON OF THE EFFECTS OF LONG-TERM THERMAL AGING AND HFIR IRRADIATION ON THE MICROSTRUCTURAL EVOLUTION OF 9Cr-1MoVNb STEEL -- P.J. Maziasz and R.L. Klueh (Oak Ridge National Laboratory)

OBJECTIVE

The purpose of this work is comparison of reactor-irradiated and long-term thermally aged specimens of 9Cr-1MoVNb steel to distinguish displacement damage effects from those due to elevated-temperature exposure alone.

SUMMARY

Both thermal aging at 482-704°C for up to 25.000 h and HFIR irradiation at 300-600°C for up to 39 dpa produce substantial changes in the as-tempered microstructure of 9Cr-1MoVNb martensitic/ferritic steel. However, the changes in the dislocation/subgrain boundary and the precipitate structures caused by thermal aging or neutron irradiation are quite different in nature. During thermal aging, the as-tempered lath/subgrain boundary and carbide precipitate structures remain stable below 650°C, but coarsen and recover somewhat at 650-704°C. The formation of abundant intergranular Laves phase, intra-lath dislocation networks. and fine dispersions of VC needles are thermal aging effects that are superimposed upon the as-tempered microstructure at 482-593°C. HFIR irradiation produces dense dispersions of very small "black-dot" dislocations loops at 300°C and produces helium bubbles and voids at 400°C. At 300-500°C. there is considerable recovery of the as-tempered lath/subgrain boundary structure and microstructural/microcompositional instability *of* the as-tempered carbide precipitates during irradiation. By contrast. the as-tempered microstructure remains essentially unchanged during irradiation at 600°C. Comparison of thermally aged with irradiated material suggests that the instabilities of the as-tempered lath/subgrain boundary and precipitate structures at lower irradiation temperatures are radiation-induced effects, whereas the absence of both Laves phase and fine VC needles during irradiation is a radiation-retarded thermal effect.

PROGRESS AND STATUS

Introduction

Since the early 1970s. there has been increased worldwide interest in the use of 9-12 Cr martensitic/ferritic steel as alternatives to austenitic stainless steels for elevated temperature applications up to about 600°C in both nuclear and fossil energy systems.[1,2] The 9Cr-1MoVNb steel was developed jointly by the Oak Ridge National Laboratory (Oak Ridge, TN) and Combustion Engineering (Chattanooga, TN) in response to the mandate in 1974 by the U.S. Liquid Metal Fast Breeder Reactor (LMFBR) Materials Program for a better steam generator material.[1,5,6]. Also designated T-91, this steel *offers* better tensile and creep strength at 600°C relative to standard 9Cr-1Mo (F9) or other modified 9Cr steels (i.e., 9Cr-2MoVNb or EM-12) with better impact properties at lower temperatures.[3] Because the martensitic/ferritic class of steels also demonstrate outstanding resistance to radiation-induced void swelling,[7-11] these steels have also been considered for in-core LMFBR applications. Void swelling resistance plus good thermal conductivity and low thermal expansion have made 9Cr-1MoVNb an attractive candidate first-wall material for Magnetic Fusion Reactor (MFR) applications as well.[11-12]

Many of the mechanical properties limitations that occur during long-term thermal aging or neutron irradiation of 9Cr martensitic/ferritic steels can be related to changes in the as-tempered microstructure caused by such exposure. Long-term aging of 9Cr-1Mo steel produces embrittlement by increasing the ductile-to-brittle transition temperature (DBTT), which can be related to Laves phase precipitation along grain boundaries.[13-15] Radiation-induced increases *of* DBTT in 9-12Cr steels appear caused by matrix hardening related to a variety of fine, radiation-produced microstructural defects.[16-20]

The purpose of this paper is to characterize the microstructural evolution of 9Cr-1MoVNb steel after irradiation in HFIR at 300-600°C to 37-39 dpa (about 10,000 h) and after long-term thermal aging at 482-704°C for 10,000 and 25,000 h. Particular emphasis is given to characterization of the precipitate component of the microstructure using analytical electron microscopy (AEM). The comparison of the long-term aging data with reactor-irradiation data allows radiation-induced microstructural changes to be separated from those that are radiation-enhanced, -modified or -retarded thermal effects. Correct phenomenological assessment combined with microstructure-properties correlations in future work can provide insight to guide further optimization of 9Cr-1MoVNb steels for either nuclear or non-nuclear applications.

EXPERIMENTAL

The compositions *of* two heats (30176 and 30394) of 9Cr-1MoVNb steel produced by Carpenter Technology (CarTech) and one heat (XA 3590) produced by Combustion Engineering (CE, Chattanooga, TN), which were investigated

in this work, are given in Table 1. The major difference is that heats 30176 and XA 3590 both contain less Si than heat 30394, but all fall within the T-91 specification.' All of the steels were finished in a normalized (0.5 h at 1040°C. He quenched to room temperature) and tempered (1 h at 760°C) condition. Tensile, creep and Charpy-impact specimens were fabricated from plate-stock of heats 30176 and 30394 and aged stress-free at 482, 538. 593, 650 and 706°C for 10,000 and 25,000 h. Material of heat XA 3590 was first processed into 0.25-mm-thick sheet stock from which standard 3-mm-diam transmission electron microscopy (TEM) disks were punched. These disks were then also normalized and tempered prior to irradiation in the HFIR-CTR-30 experiment. Disks were irradiated at temperatures of 300, 400, 500 and 600°C to fluences of fast and thermal neutrons that produced 36.5 to 38.5 dpa and 30-32 at. ppm He in about 10,000 h.

TEM disks were punched from slices cut from thermally aged tensile (shoulder) or Charpy-impact specimens. Precipitates were electrolytically extracted onto carbon films from the TEM disks prior to electropolishing, and suspended on either copper, beryllium or carbon-coated nylon grids for analysis using x-ray energy dispersive spectroscopy (XEDS). The remainder of the slice was used for bulk electrolytic extraction of precipitates to quantitatively measure the weight fraction of residue. Only extraction replica and thin-foil specimens could be made from the highly radioactive HFIR-irradiated TEM disks.

Table 1. Compositions of Comnercial Heats of 9Cr-1MoVNb

	Heat Designation		
	30176	30394	XA 3590[b]
	Alloy Composition[a] wt %		
Cr	8.6	8.6	8.6
Mo	0.9	1.0	1.0
V	0.21	0.20	0.21
Nb	0.072	0.073	0.063
Mn	0.37	0.46	0.36
Ni	0.09	0.09	0.1
Si	0.11	0.4	0.08
C	0.081	0.084	0.09
cu	0.04	0.04	
W	<0.01	0.05	0.01
P	0.01	0.01	
N	0.0055	0.053	0.05

[a]Balance iron. [b]0.002 Ti.

Thin-foil specimens were examined using a JEM 100C TEM equipped with an AMG objective lens pole piece to minimize ferromagnetic displacements and stigmatism of the electron beam. Phase identification and quantitative microcompositional analysis of both individual particles and large areas with thousands of particles (broad-beam analysis) on the replica specimens were performed using a Philips EM400T/FEG (100 kV, field-emission gun, with < 10 nm probe size) AEM with an EDAX 9100 analysis unit and a JEM 2000FX (200 kV, LaB_6 gun) AEM with a TN-5500 Series II analysis unit. Only the normalized composition of metallic elements heavier than Al were analyzed using XEDS. More details concerning analysis techniques can be found elsewhere.[21-24]

RESULTS

As-Tempered Microstructure of 9Cr-1MoVNb

The as-tempered microstructure of both heats of 9Cr-1MoVNb martensitic/ferritic steel consisted of small intragranular lath-shaped ferrite subgrains within larger grains from prior austenite (Fig. 1a). Tempering produced about 1.4-1.8 wt.% precipitation[25] (Table 2), distributed as mainly coarse $M_{23}C_6$ and some finer MC particles along grain and lath/subgrain boundaries (Fig. 1b). XEDS analysis of individual precipitate particles extracted onto carbon replica films showed Cr-rich $M_{23}C_6$ and V- and Nb-rich MC phases (Fig. 1b). Quantitative broad beam XEDS analysis indicated that 85-90 vol.% of the extracted precipitates were $M_{23}C_6$ and 10-15% were MC, with most of the MC particles being VC. The as-tempered lath/subgrains contained dislocation networks, with densities that varied from $1\text{-}7 \times 10^{13}$ m^{-2} in larger subgrains to less in smaller ones. The lath/subgrain boundaries were also planar honeycomb arrays of dislocations with a much higher density.

Microstructural Evolution of 9Cr-1MoVNb Durins Thermal Asing

Microstructural changes were observed in the 9Cr-1MoVNb steel at ail aging temperatures in the range of 482-704°C after 25,000 h. The data can easily be separated into two temperature regimes of quite different aging effects. At the lower temperatures of 482-593°C, there was little change in the as-tempered lath/boundary and carbide precipitate structures, while at 650 and 704°C, there was detectable recovery and coarsening of the lathlsubgrain boundary structure, and coarsening of the as-tempered carbide precipitates. A considerable amount of new precipitation and an increase in the concentration of dislocation networks were observed within subgrains in the lower temperature regime, while no new precipitate phases were observed at 650 and 704°C in the lower Si heat of steel (Table 2).

Dislocation density within many subgrains increased during aging at 538°C for 25,000 h relative to the as-tempered material (Fig. 2a and 2b). By contrast, aging for 25,000 h at 650°C produced almost no change in microstructure relative to as-tempered material (Fig. 2c). Aging for 25,000 h at 704°C caused recovery and coarsening of the as-tempered lath subgrain structure into larger, equiaxed subgrains (cf. Figs. 1a and 3). Quantitative data on the weight percent of extracted

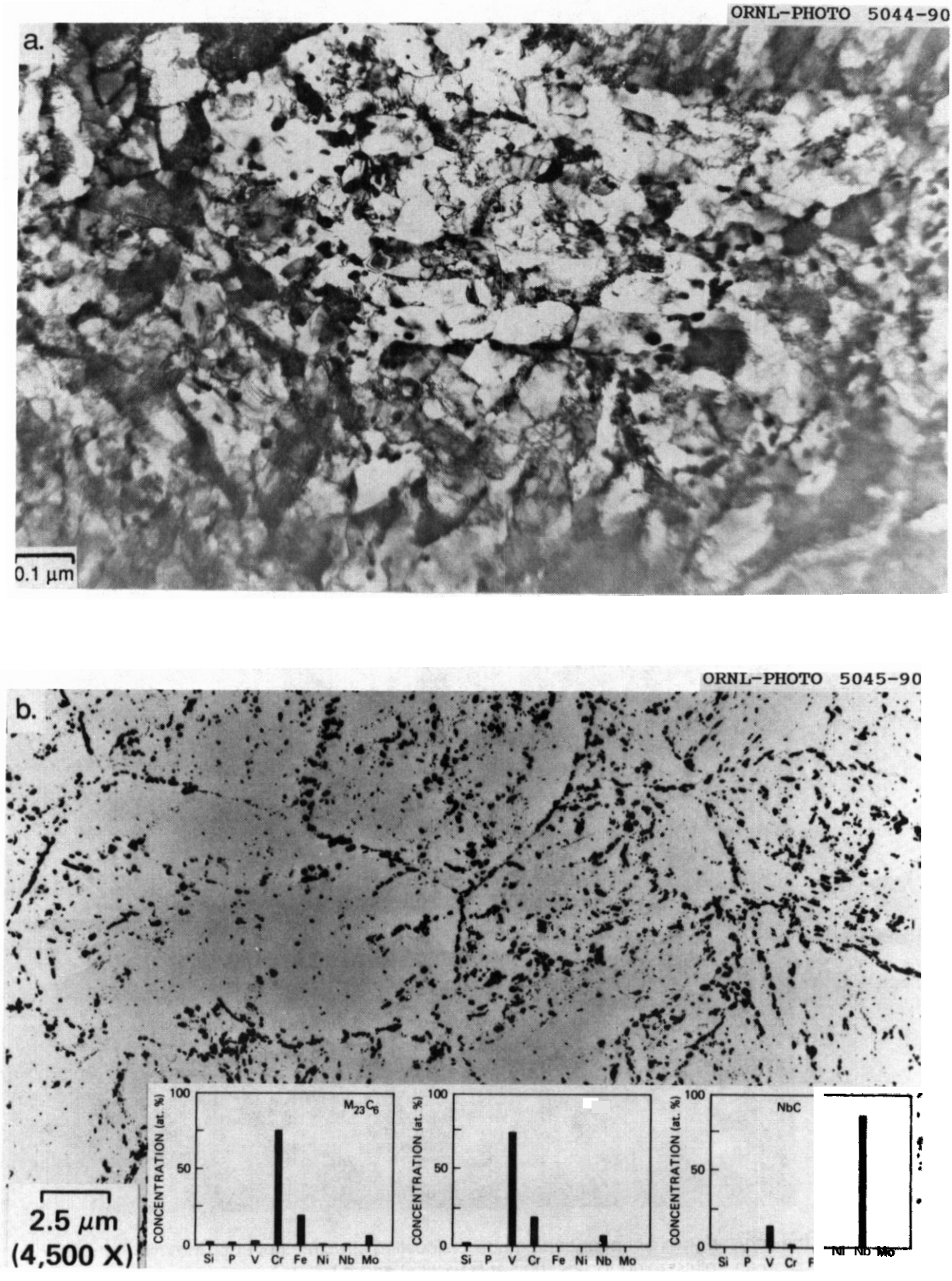

Fig. 1. The microstructure produced in 9Cr-1MoVNb steel (heat 30176) after tempering for 1h at 760°C. a.) TEM of a thin-foil specimen. and b.) TEM of precipitates extracted onto a carbon replica film (with histograms of phase compositions from quantitative XEDS analysis),

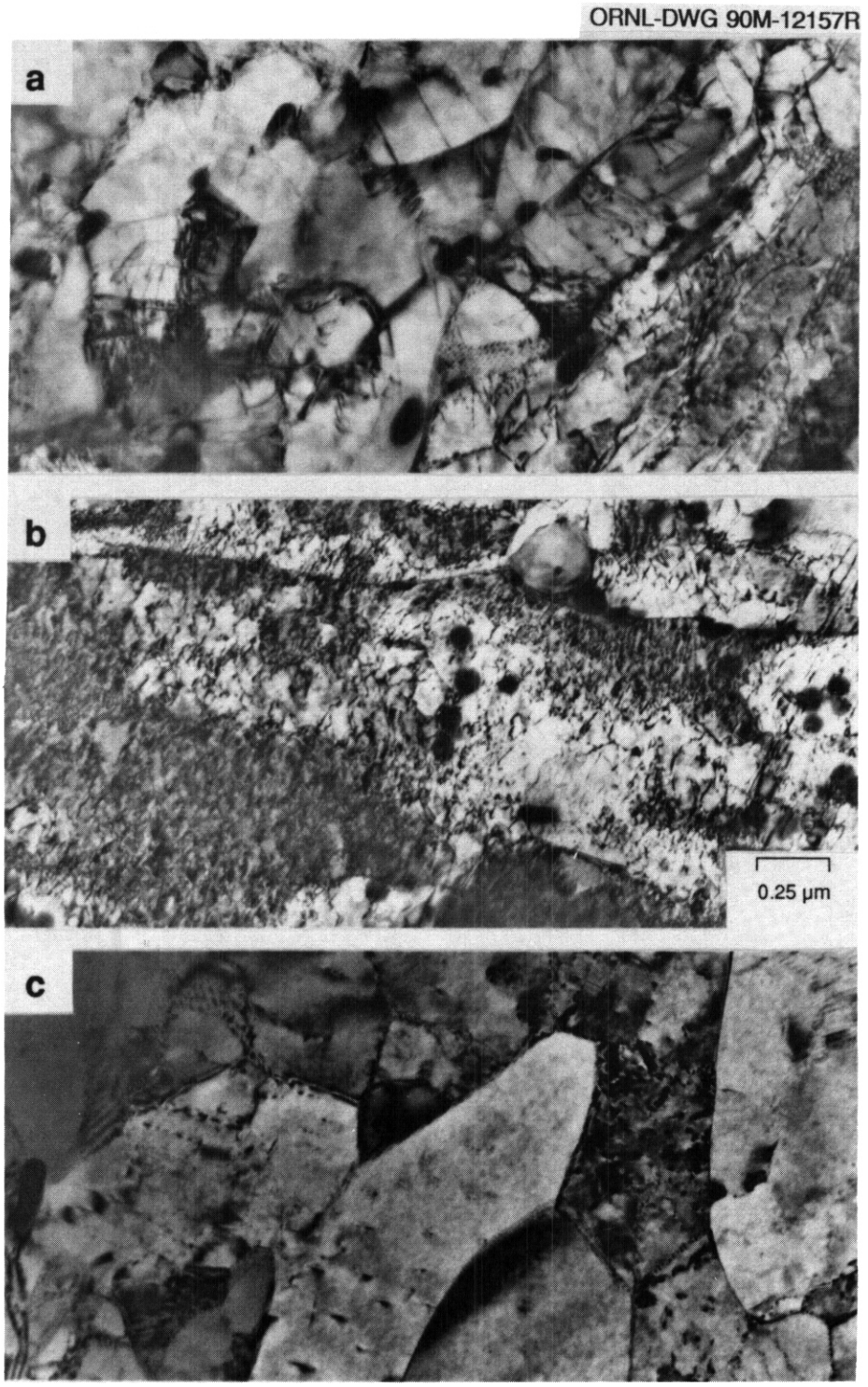

Fig. 2. TEM of the lath/subgrain boundary and matrix dislocation structures of 9Cr-1MoVNb (heat 30176) steel in a.) the as-tempered condition and after aging for 25,000h at b.) 538°C and c.) 650°C.

Table 2. Precipitation Data on Thermally Aged 9Cr-1MoVNb Specimens

Specimen Designation	Aging Conditions: Temperature (°C)	Aging Conditions: Time (h)	Bulk Precipitate Extraction (wt %)	Phases Observed on Extraction Replicas via XEDS[a]
		Heat 30176 (0.1 wt % Si)		
T-20	As-tempered	(1 h @ 760°C)	1.713	$M_{23}C_6$ + VC + NbC
24047	482	25,000	2.087	$M_{23}C_6$ + Laves + VC + NbC + $Cr_2(X)$?
T-214	538	10.000	2.027	$M_{23}C_6$ + Laves + VC
T-344	538	25,000	2.358	$M_{23}C_6$ + Laves + VC + some fine Fe-Cr phase
T-362	593	25.000	2.247	$M_{23}C_6$ + Laves + VC + NbC
T-246	650	10,000	1.748	$M_{23}C_6$ + VC + NbC
T-378	650	25,000	1.810	$M_{23}C_6$ + VC + NbC
T-394	704	25.000	1.786	$M_{23}C_6$ + VC + NbC
		Heat 30394 (0.4 wt % Si)		
T-19	As-tempered	(1 h @ 760°C)	1.833	$M_{23}C_6$ + VC + NbC
23985	482	25.000	3.137	$M_{23}C_6$ + Laves + VC + NbC
T-19	As-tempered	(1 h @ 760°C)	1.833	$M_{23}C_6$ + VC + NbC
23985	482	25,000	3.137	$M_{23}C_6$ + Laves + VC + NbC
T-616	538	25.000	3.183	$M_{23}C_6$ + Laves + VC + NbC + some fine Fe-Cr phase
1-313	650	10,000	1.802	$M_{23}C_6$ + VC + Nbc
T-584	650	25,000	2.729	$M_{23}C_6$ + Laves + VC + NbC

[a]Phase identifled by characteristic spectra from individual particle analysis: relative phase fraction determined from broad-beam XEDS of many particles. Order represents decreasing phase fractlon.

Fig. 3. TEM of the lath/subgrain structure of 9Cr-1MoVNb (heat 30176) steel after aging for 25,000h at 704°C.

precipitation from Table 2 are plotted in Fig. 4a. The amount of precipitation showed a significant increase at the lower aging temperatures.

Both thin-foil TEM and quantitative AEM analysis on extraction replicas revealed abundant Laves phase formation (Fe_2Mo type) during aging. Quantitative data from XEDS broad-beam and individual particle analyses on extraction replicas are given in Tables 3 and 4, respectively. Laves phase is highly enriched in molybdenum, and contains much more molybdenum than the carbide phases. Therefore, Laves phase is best detected by monitoring the molybdenum content of the broad-beam XEDS spectra. Correlation of broad-beam molybdenum content (so plotted as a function of aging temperature in Fig. 4b) with the weight fraction of precipitate demonstrates that the increase in precipitation during aging was due mainly to the formation of Laves phase.

Below 600°C, significantly more Laves phase was found in the heat of 9Cr-1MoVNb with more silicon (heat 30394) than in the lower silicon heat (heat 30176) (Fig. 4a). The Laves phase composition did not show significant temperature dependence in either heat of steel. However, the Laves phase composition is lower in molybdenum and higher in silicon in the high silicon heat of steel (Table 4). No Laves phase was observed in the lower silicon heat of steel at 650°C after 25,000 h. By contrast, while no Laves phase was observed in the higher silicon steel after 10,000 h at 650°C, a large amount of Laves precipitated after 25,000 h.

Laves phase was microstructurally distributed as thin films along grain and subgrain boundaries at 482 and 538°C (Figs. 5 and 6). Laves phase formed as coarser particles at 593 and/or 650°C. In the higher silicon heat of steel, Laves phase often formed as massive, globular particles that engulfed coarse boundary carbide particles at 482 and 538°C (Fig. 6b), and as boundary films.

Fine VC needles were also produced by aging at 482-593°C for 25,000 h in both heats of steel, but not at 650°C and above. Fine needles were also detected in the low-silicon heat of steel after 10,000 h at 538°C. The fine VC precipitates were distributed uniformly within larger lath/subgrains, but were heterogeneously distributed on a coarser scale because groups or packets of cells would have them while others would not. They were detectable only with higher-magnification TEM, both in thin-foil and on extraction replica specimens, as shown in Fig. 7, because they made virtually no contribution to the weight fraction of extracted precipitate or the XEDS broad-beam spectra. Compositionally, they were very similar to the larger VC precipitates, although often they had slightly more chromium and less vanadium (Table 5).

The major changes produced by aging at 650°C and above were structure recovery and precipitate coarsening, particularly at 704°C after 25,000 h (Fig. 3). Although the total weight fraction of precipitate remains about equal to that

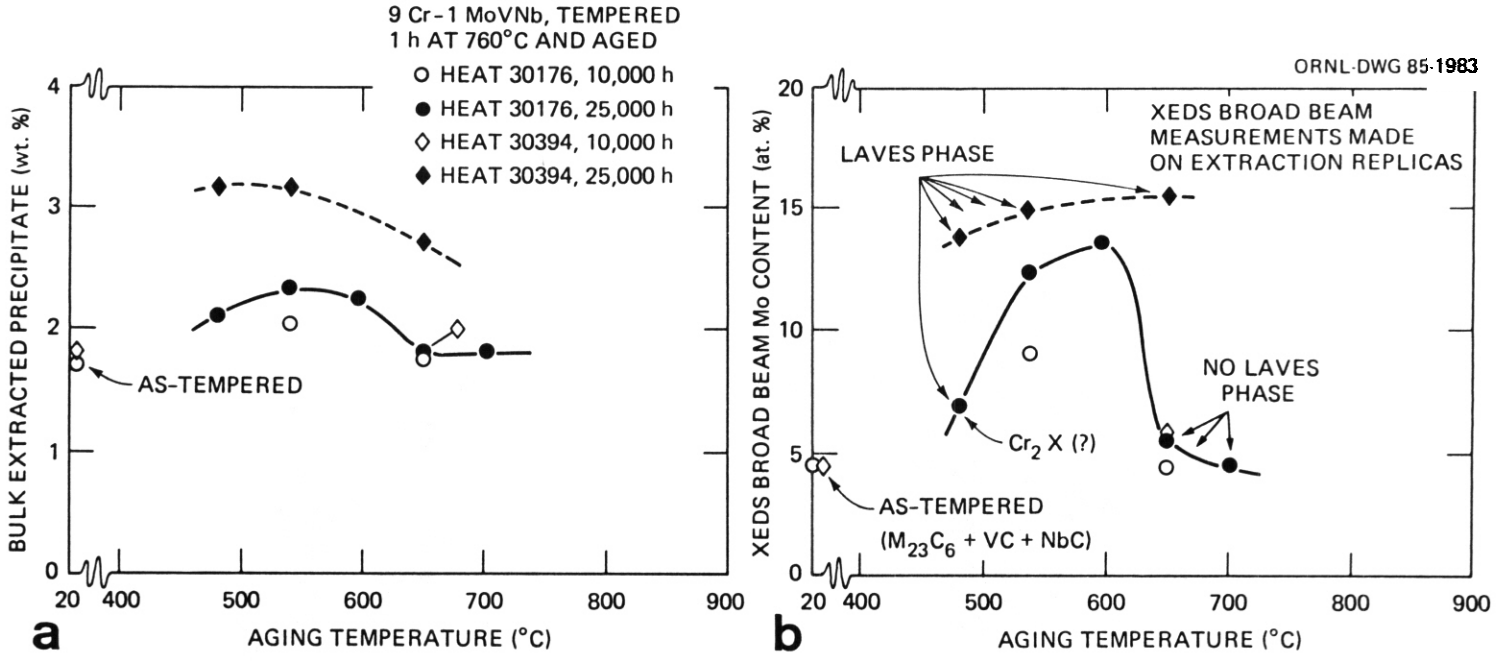

Fig. 4. Plots of a.) weight fraction (wt.%) of precipitate extracted from bulk specimens and b.) the molybdenum concentration from quantitative broad-beam XEDS analysis of precipitates on extraction replicas, both from specimens of the two heats of 9Cr-1MoVNb steel after various aging treatments.

Table 3. Broad-Beam Compositional Averaging via XEOS of Precipitates Extracted onto Replicas from Aged 9Cr-1MoVNb Steel

Aging Conditions			Alloy Composition,[a] at. %									
Temperature (°C)	Tine (h)	Phases	Si	P	Ti	V	Cr	Mn	Fe	Ni	Nb	Mo
			Heat 30176									
As-tempered		$M_{23}C_6$ + VC + NbC	4.0	0.5	0.1	**8.3**	54.5	0.2	25	**0.2**	3.0	4.5[2][b]
482	25,000	$M_{23}C_6$ + Laves + VC + Nbc + $Cr_2(X)$?	**0.5**	0.9	0.1	8.2	54.2	0.1	24.8	0.1	4.1	7.0[2]
538	10.000	$M_{23}C_6$ + Laves + VC	2.7	**2.3**	0.1	7.0	48.0	1.5	27.4	0.4	1.8	9.0[2]
538	25,000	$M_{23}C_6$ + Laves + VC + fine Fe-Cr phase	2.4	1.3	0.1	6.6	45.6	0.6	29.3	0.1	1.8	12.3[2]
593	25,000	$M_{23}C_6$ + Laves + VC + NbC	**3.7**	2.1	0.1	**5.5**	44.7	**0.5**	27.5	0.1	2.1	13.7[2]
650	10,000	$M_{23}C_6$ + VC + NbC	4.5	1.4	0.2	6.6	63.2	1.2	17.0	0.3	**2.3**	4.4[2]
650	**25,000**	$M_{23}C_6$ + VC + NbC	4.3	0.7	0.1	8.8	61.5	0.4	16.1	0.2	2.9	5.3[2]
704	25,000	$M_{23}C_6$ + VC + NbC	1.5		0.1	**11.0**	**59.2**	1.4	16.2	0.6	5.6	4.4[3]
			Heat 30394									
As-tempered		$M_{23}C_6$ + VC + NbC	2.8	1.3		7.5	**56.4**	**1.3**	24.5	0.1	**1.3**	4.5[2][b]
482	25.000	$M_{23}C_6$ + Laves + VC + NbC	**3.8**	**1.2**	0.1	9.4	39.6	**0.6**	27.4	0.2	3.9	13.8[2]
538	25,000	$M_{23}C_6$ + Laver + VC + NbC + some fins Fe-Cr	5.6	2.0	0.1	4.9	39.5	0.8	**30.8**		1.3	15.0[2]
650	10,000	$M_{23}C_6$ + VC + NbC	1.3	1.6	0.2	8.5	59.7	1.3	17.9	0.4	**3.8**	5.4[2]
650	25,000	$M_{23}C_6$ + Laves + VC + NbC	5.5	1.6	0.1	4.7	41.6	0.6	28.9	0.1	1.3	15.7[2]

[a] Normalized, averaged composition for elements heavier than aluminum.
[b] The number of spectra obtained from different areas of the replica for the average broad-beam composition.

Table 4. XEOS Composition of the Laves Phase Extracted on Replicas from Aged 9Cr-1MoVNb Steel

Aging Conditions		comments'	Composition[b] (at. %)									
Temperature (°C)	Time (h)		Si	P	Ti	V	Cr	Mn	Fe	Ni	Nb	Mo
			Heat 30176									
482	**25,000**	Large[2]	2.4	4.6	0.1	0.1	17.8	1.0	39.0	0.3	0.2	34.5
538	10,000	Large[3]	7.6	5.2	0.1	0.4	**12.8**	1.4	43.4	0.4	0.3	28.3
538	**25,000**	Large[3]	7.1	2.8	0.2	**0.6**	**13.2**	**0.9**	**43.0**	**0.2**	***0.3***	31.8
593	25.000	Large[2]	8.2	3.4	**0.2**	0.1	9.6	0.6	45.1	0.2	0.3	**32.3**
			Heat 30394									
538	25,000	Large[3]	13.4	3.6		2.2	13.5	**0.8**	**38.3**	**0.1**	0.5	27.0
650	25.000	Large[4]	11.5	3.2	0.1	0.3	12.8	0.6	42.6	0.7	0.7	28.1

[a] Large Particles are usually greater than 200 nm in size (numbers in brackets indicate the number of individual particle spectra analyzed).

[b] Normalized, averaged conposition for elements heavier than aluminum.

produced during tempering, both TEM and AEM analysis of extraction replicas indicated coarsening of the carbide precipitates, particularly the MC particles.' Broad-beam analysis at 704°C indicates an increase in the relative volume fraction of MC to $M_{23}C_6$ phases compared to the as-tempered material (more V and Nb. Table 3). While neither carbide phase showed any significant compositional change when they were stable at lower aging temperatures, both showed detectable compositional changes when they become unstable at 650-704°C. The $M_{23}C_6$ phase (average as-tempered composition -- 62% Cr-29%Fe-5.5%Mo-1% V, with detectable Si, Nb and Mn as well) contained slightly more chromium and less iron at 650 and 704°C. The VC particles become richer in niobium at the expense of chromium and vanadium at 704°C relative to the as-tempered condition (Table 5), and the fraction of mixed V- and Nb-rich MC particles also appeared to increase.

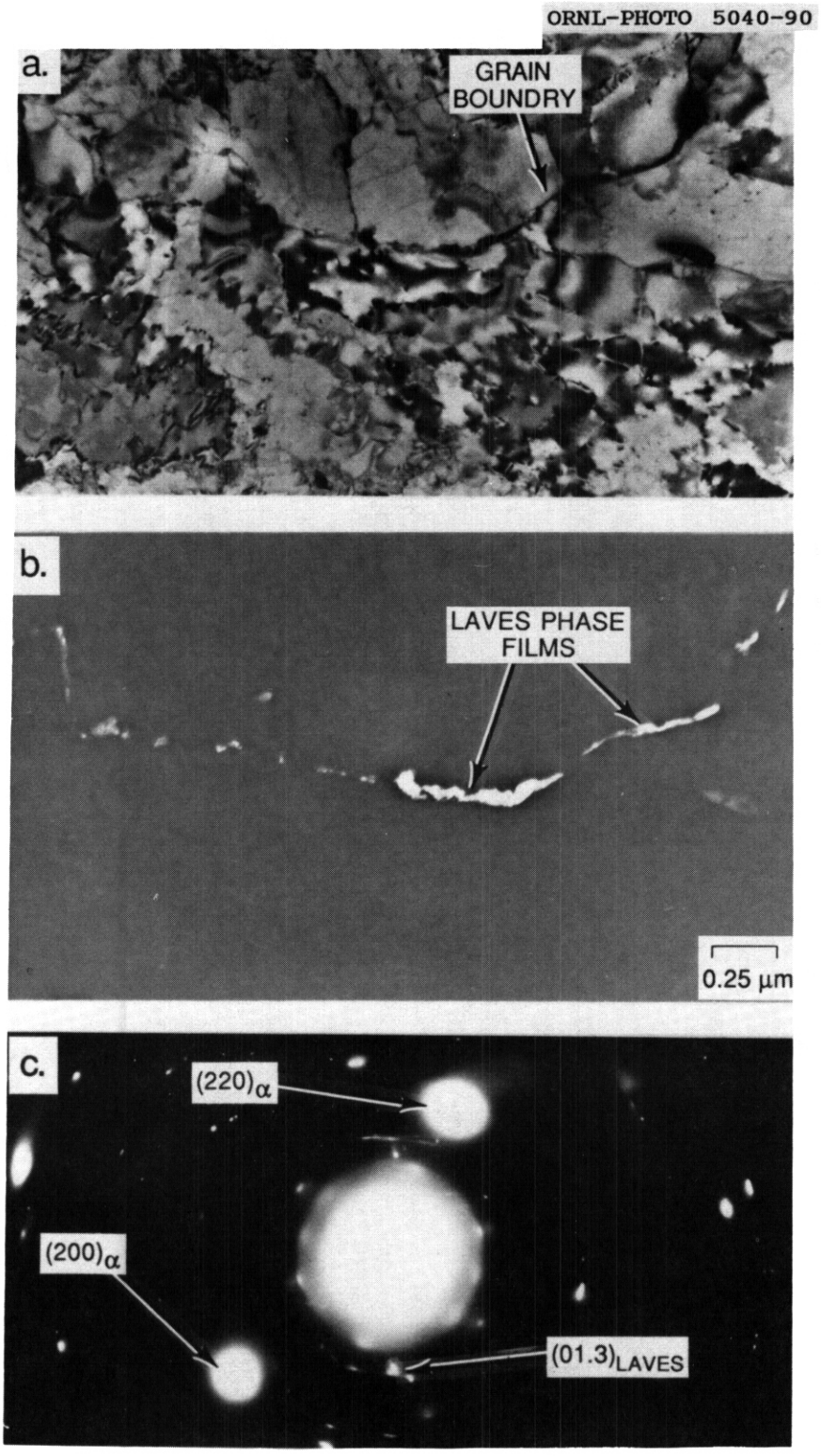

Fig. 5. Precipitation of Laves phase as films along grain boundaries in 9Cr-1MoVNb (heat 30394) steel aged for 25,000h at 538°C, as shown with TEM in a.) bright-field, b.) precipitate dark-field and c.) selected area diffraction (SAD) modes.

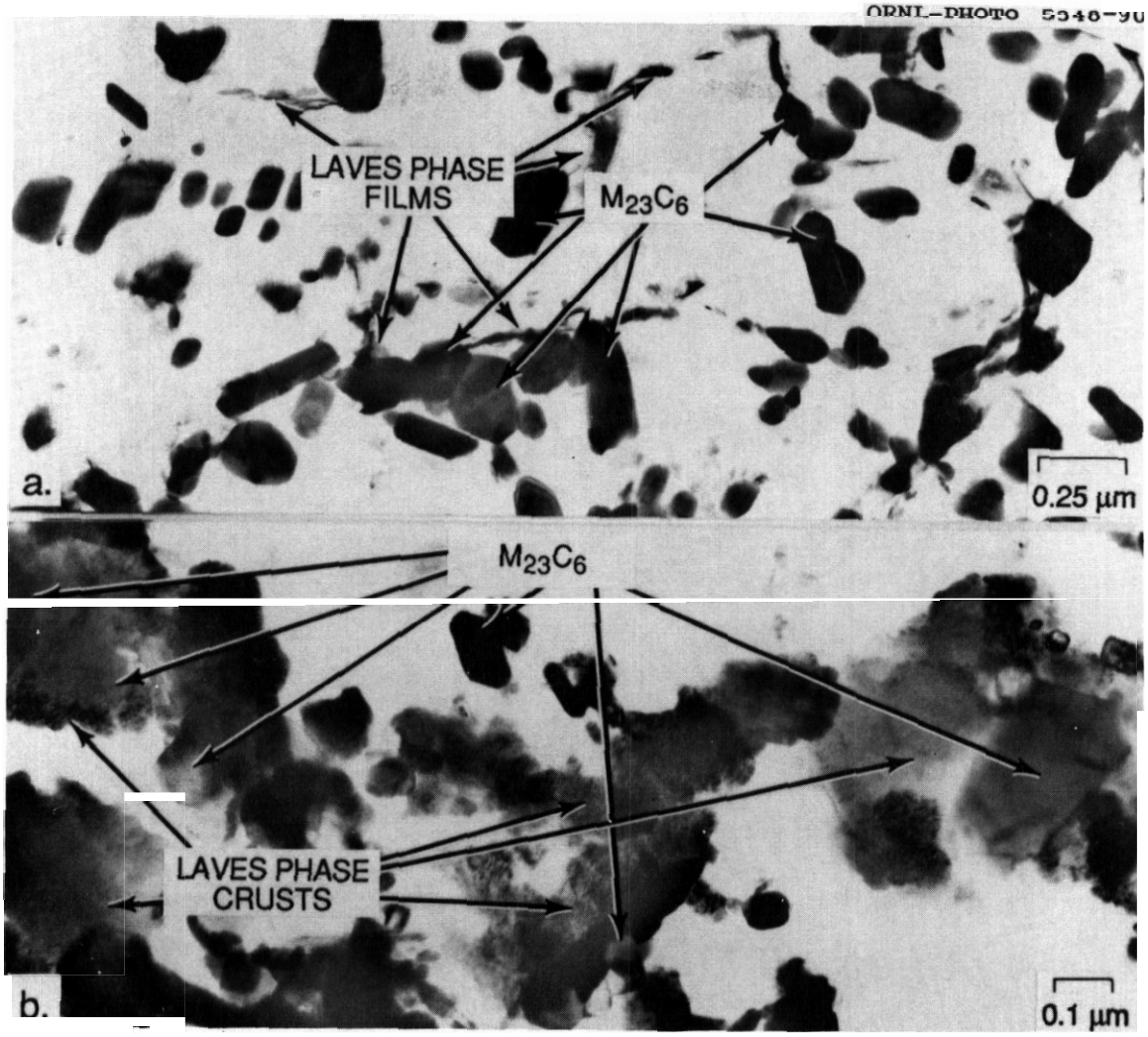

Fig. 6. Comparison of differences in the amount and distribution of Laves phase in different heats of 9Cr-1MoVNb steel during aging at 538°C for 25,000h. a.) heat 30176 (0.1 wt.% Si) and b.) heat 30394 (0.4 wt.% Si). Both specimens are extraction replicas.

Microstructural Evolution of 9Cr-1MoVNb During HFIR Irradiation

Microstructural changes due to irradiation of the low-silicon heat of 9Cr-1MoVNb in HFIR to 37-39 dpa (about 10,000 h) were observed primarily at 300-500°C; irradiation at 600°C produced almost no change relative to the as-tempered microstructure. Radiation-induced dislocation loop and void formation were confined to very narrow ranges of temperature. Tiny "black-dot" dislocation loop damage was observed only at 300°C (Fig. 8), while helium bubbles and voids were only observed to form at 400°C (Fig. 9). By contrast, changes in matrix dislocation concentration, lath/subgrain boundary structure, and carbide distribution and composition occurred as continuous functions of irradiation temperature from 300 to 500°C.

The matrix dislocation density of the 9Cr-1MoVNb steel irradiated in HFIR followed a normal temperature dependence, with the highest dislocation concentration (a mixture of loops plus network) at 300°C (Fig. 8d), less at 400 and 500°C (network only) (Figs. 9a and 10), and the lowest concentration at 600°C (Fig. 11). Quantitative measurements of dislocation concentration showed the network after irradiation at 400°C falling consistently to the higher side of the wide range observed in as-tempered material (6×10^{13} and $<1\text{-}7 \times 10^{13}$ m^{-3}, respectively).[11] The concentration of dislocation networks after HFIR irradiation at 500 and 600°C was very similar to that found in the as-tempered condition.

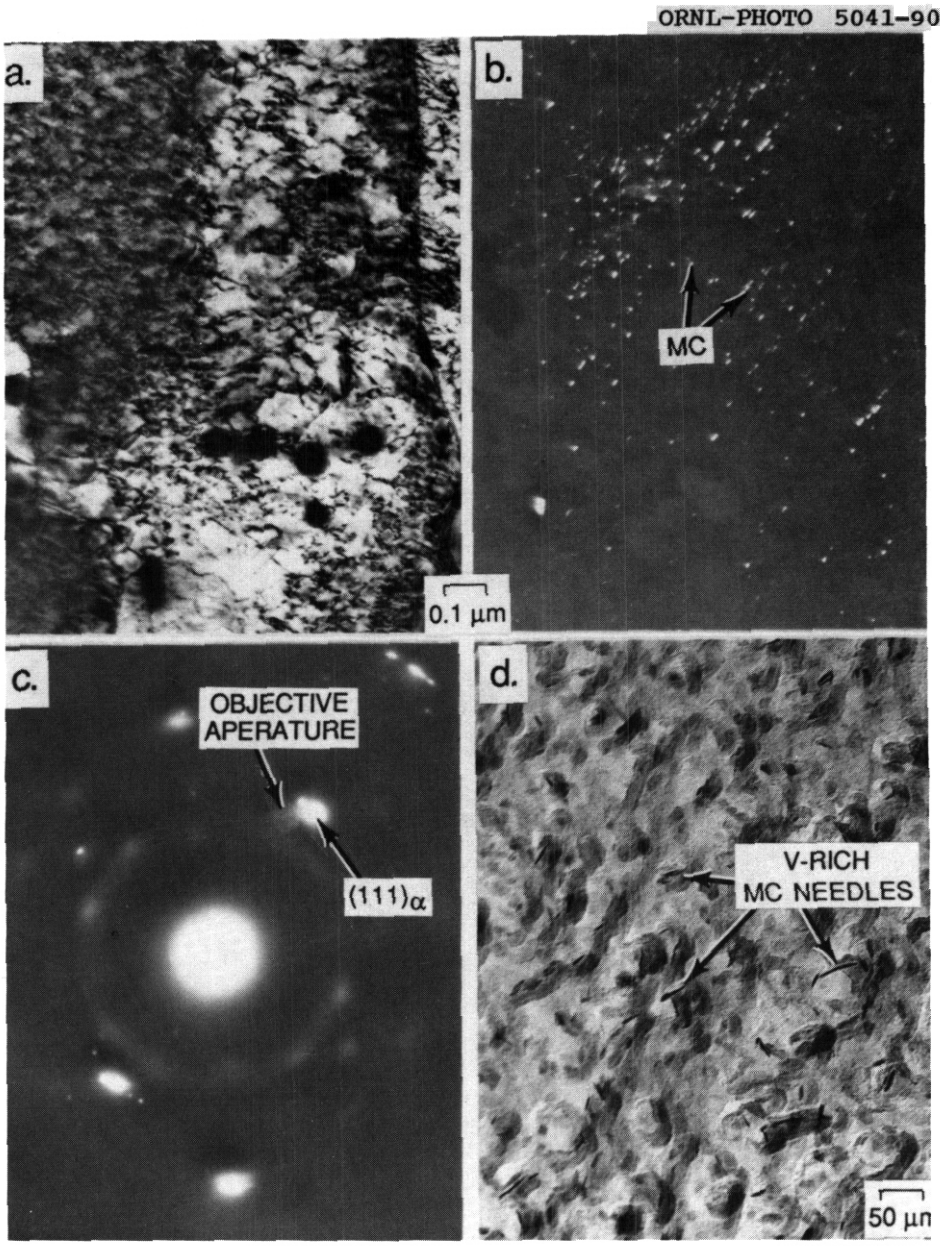

Fig. 7. Fine MC precipitation formed during aging of 9Cr-1MoVNb steel at 538°C for 25,000h. a.) bright-field. b.) precipitate dark-field and c.) SAD TEM analysis from a thin-foil specimen of heat 30176 and d.) TEM of an extraction replica specimen of heat 30394.

While the radiation-produced dislocation density followed a normal temperature dependence, recovery and coarsening of the as-tempered lath/subgrain boundary structure was observed to follow an inverse temperature dependence during HFIR irradiation at 300-500°C. Recovery of the cellular subgrain structure was greatest at 300°C (Fig. E) and least at 500°C, and at 600°C there was no discernible difference between HFIR-irradiated and as-tempered material (Figs. 8b and 11). Evidence for recovery of the subgrain structure is best seen from comparison of lower and higher magnification TEM of an as-tempered specimen with one irradiated in HFIR at 300°C in Fig. 8. At higher magnification. the small cell boundaries. which often consist of dense honeycomb networks, were a dominant microstructural feature in as-tempered material, but were almost completely absent after HFIR irradiation at 300°C (cf. Fig. Eb and Ed). Many large regions of matrix were also free of subgrain structure after irradiation at 400°C (Fig. 9a).[24] Alter irradiation at 500°C most of the initial subgrain boundary Structure remained (Fig. 10), but subgrain size was slightly coarser than found in either as-tempered material or material irradiated at 600°C. One subtle hint that irradiation at 500°C had altered the structure is the fact that many carbide precipitate particles were not associated with boundaries, as was the case in as-tempered material. At lower magnification, it can be seen that coarser packet boundaries established during tempering and prior austenite grain boundaries (both usually heavily decorated with carbide precipitates) were still visible after irradiation at 300°C (Fig. 8a and 8c).

Table 5. XEDS Composition of MC Individual Particles Extracted on Replicas from Aged 9Cr-1MoVNb Steel

Aging Conditions		Phases and Comments[a]	Composition[b] (at. %)									
Temperature (°C)	Time (h)		Si	P	Ti	V	Cr	Mn	Fe	Ni	Nb	Ho
			Heat 30176									
As-tempered		Small VC [5]	1.4	0.1	0.1	74.0	16.9		0.5		6.3	0.6
		Larger NbC[1]				12.2	2.2		0.4		84.7	0.5
		Small NbC[2]				15.3	3.3		0.5		80.2	0.6
482	25,000	g.b.[c] VC [3]	0.5	0.8	0.1	65.8	19.3		3.6		7.1	2.7
		Larger matrix VC[1]	1.2	0.6		68.2	16.1		4.6	0.1	8.7	0.7
		Very fine VC [3]	5.4	1.5	0.2	59.0	23.6		2.8	0.1	3.9	3.5
		Larger matrix NbC[1]		5.9		16.4	3.4	0.1	0.6	0.1	72.5	0.8
		Larger matrix MC[1]		3.0	0.3	51.6	12.8		1.1	0.1	26.9	4.2
538	10.000	Small VC[5]	0.5	0.5	0.2	68.0	20.8		2.3	4.8	3.7	3.6
538	25.000	Larger VC[4]		0.6	0.1	60.4	22.4		3.1	0.1	4.3	1.0
		Very fine VC[1]	8.1	0.2		52.5	23.1		9.3	0.1	2.7	4.0
593	25.000	Larger VC[2]	3.3	0.8	0.2	72.0	12.5	0.1	0.7		9.8	0.6
		Small VC[1]	3.6	1.0	0.2	73.8	14.1	0.1	0.5	0.1	5.8	0.8
		Larger NbC[1]	1.8	1.5	0.3	14.8	3.0	0.2	0.6	0.1	77.6	0.3
650	10,000	Small VC [3]	2.5	0.8		75.8	14.6		0.3		5.1	0.8
650	25.000	Larger VC[5]	1.3	1.1	0.1	67.2	16.2		1.3		12.1	0.7
		Small VC[9]	2.8	0.0	0.1	75.1	13.5		0.6		6.6	0.6
		Small NbC[2]		6.5	0.1	14.0	2.7		0.4		76.6	0.7
704	25,000	Larger VC [2]	1.1		0.7	66.4	6.6		0.7	0.5	23.6	0.2
		Small VC[4]	0.5		0.7	70.7	12.1		0.9	0.6	14.0	0.6
		Larger MC[3]	1.7		0.5	48.5	5.5		0.5	0.7	42.3	0.3
		small MC[3]	1.8		0.4	49.2	5.2		0.5	0.6	41.0	0.6
		Larger NbC[1]	3.6		0.4	8.1	1.7		0.6	0.9	84.0	0.4
			Heat 30394									
As-tempered		Small VC[1]	1.2	2.1	0.0	75.3	14.2		0.1		5.6	0.7
		Small NbC[1]	6.4	2.0		15.2	3.0		0.5		71.6	1.1
538	25,000	Small VC[6]		1.0		77.6	15.3				5.5	0.3
650	10,000	Larger VC[2]	1.4	2.8	0.1	71.2	0.9		0.4		14.4	0.9
		Small VC[2]	3.1	3.4	0.1	64.2	10.0		0.7	0.1	16.5	1.9
650	25,000	Small VC[5]	3.2	1.0	0.1	70.3	15.0	0.1	0.9		7.5	0.9

[a]Larger particles are greater than ~50 to 60 nm in size, small particles are less than ~30 to 40 nm in size, and very fine particles are usually rods, ~5-nm-thick, 40- to 100-nm-long (numbers in brackets indicate the number of individual particle spectra analyzed).

[b]Normalized, averaged composition for elements heavier than aluminum. [c]g.b. = grain boundary.

ORNL-DWG 90M-12158R

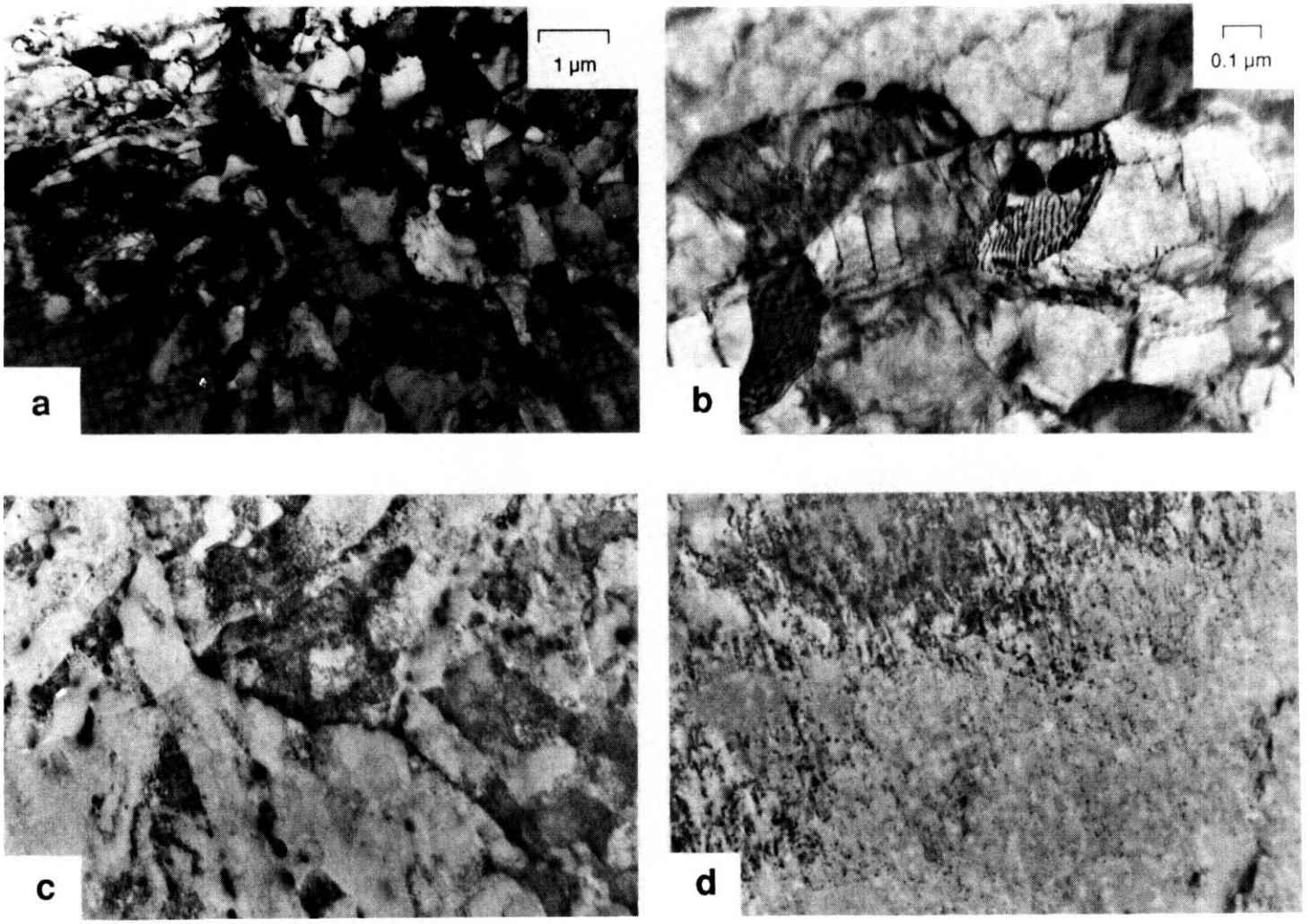

Fig. 8. TEM of the lath/subgrain boundary and matrix dislocation structures of 9Cr-1MoVNb (heat XA 3590) steel a.) and b.) as-tempered, and c.) and d.) after HFIR irradiation at 300°C to about 37 dpa, at both lower (a,c) and higher (b,d) magnifications.

HFIR irradiation produced no new precipitate phases in the 9Cr-1MoVNb steel (Table 6). There were, however, changes in the as-tempered carbide structure that were parallel to the recovery and coarsening of the lath/subgrain boundary structure, particularly in terms of temperature dependence. Microstructurally, there appeared to be dissolution of many of the smaller $M_{23}C_6$ particles during irradiation at 300 and 400°C (Figs. 8d and 9a), which were associated with the lath/subgrain boundary structure in the as-tempered condition. Most of the coarser $M_{23}C_6$ particles decorating packet boundaries or prior austenite grain boundaries appeared unaffected by the irradiation, even at 300°C (Fig. 8c). Partial dissolution of $M_{23}C_6$ carbides exhibited the same inverse temperature dependence during irradiation as found for recovery and coarsening of the lath/subgrain boundary structure. Dissolution of small $M_{23}C_6$ particles was most noticeable at 300 and 400°C, but did not appear to be occurring at 500 and 600°C. Despite these changes in precipitate microstructure, XEDS studies of extraction replicas indicated no change of the $M_{23}C_6$ phase composition during irradiation over the temperature range of 300-600°C.

While the fine MC component of the precipitate structure was too difficult to observe consistently by TEM of the complex microstructure of the irradiated thin-foil specimens, significant microstructural and microcompositional changes caused by irradiation were observed by AEM analysis of these particles on extraction replica specimens. Previously, quantitative data showed that MC particle sizes ranged from 17 to 60 nm in the as-tempered material, with more particles at the smaller end of the size range.[24] By comparison, the MC particle sizes ranged from 30 to 120 nm after HFIR irradiation at 400°C, with more particles at the larger side of the size range. The MC coarsening also had an inverse temperature dependence, because maximum effects of irradiation were observed at 300 and 400°C, while there was no detectable effect of irradiation at 600°C.

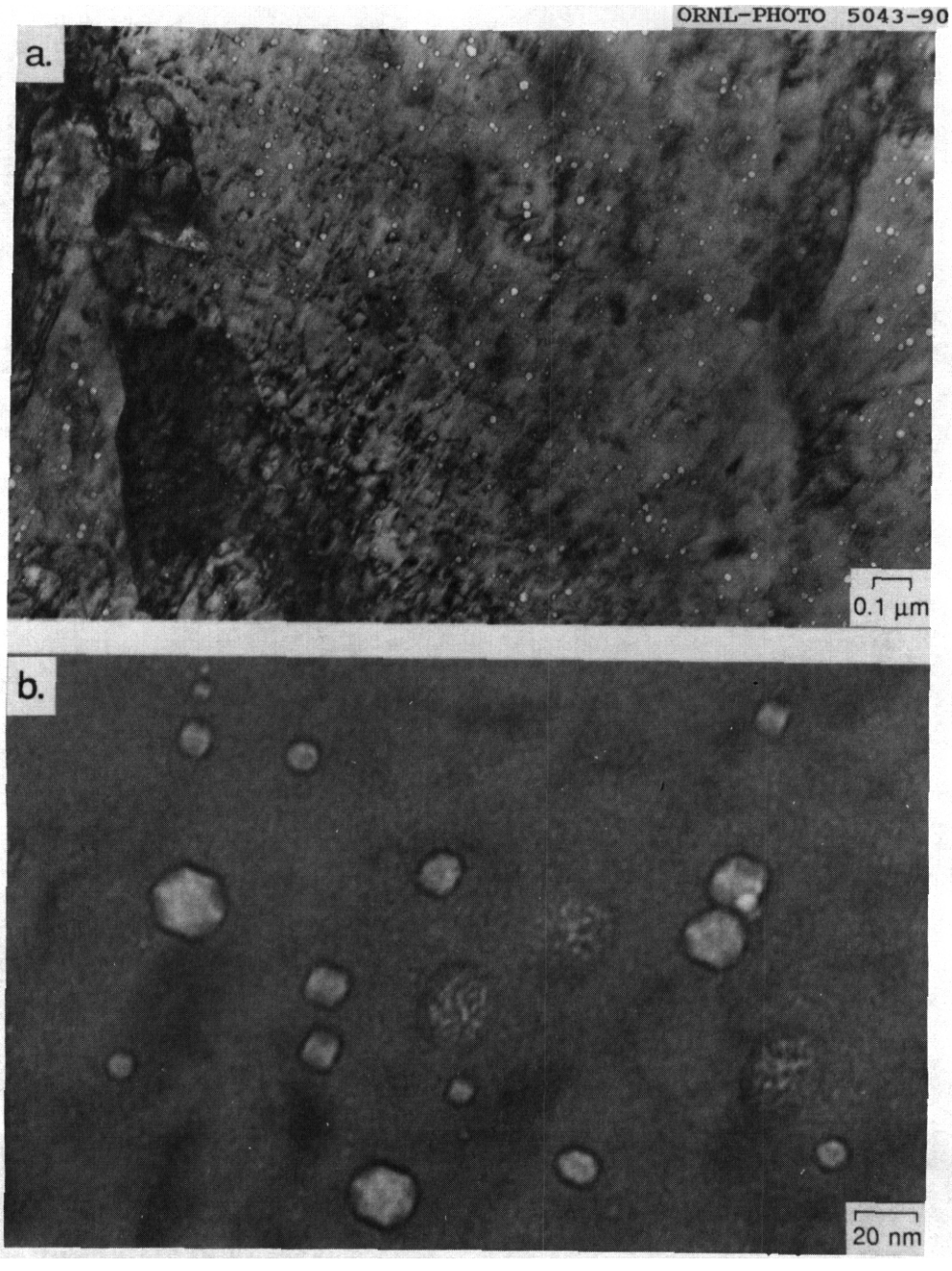

Fig. 9. TEM of larger voids and finer helium bubbles formed in 9Cr-1MoVNb (heat XA 3590) steel after HFIR irradiation at 400°C to about 37 dpa, at lower (a) and higher (b) magnifications.

Irradiation dramatically changed the V and Cr concentrations of the MC phase particles in the 9Cr-1MoVNb steel, and this effect also had a strong, inverse temperature dependence. The pronounced increase in Cr at the expense of V that occurs in MC particles during HFIR irradiation at 400°C is shown clearly in Fig. 12. Irradiation appears to strongly affect only the V and Cr concentrations. This effect of irradiation on MC composition is similar for both V-rich or mixed V- and Nb-rich particles (Fig. 12). Both Table 7 and Fig. 13 show that the effect of irradiation on Cr and V content of MC particles was very stong at 300-500°C, but then becomes weaker at 600°C. The radiation-induced Cr-enrichment was maximum at 400°C and more temperature sensitive than V-depletion. which was greatest at 400-500°C. Clearly the MC composition during irradiation at 600°C moved much closer to the MC composition observed during thermal aging, although an effect of irradiation was still noticeable.

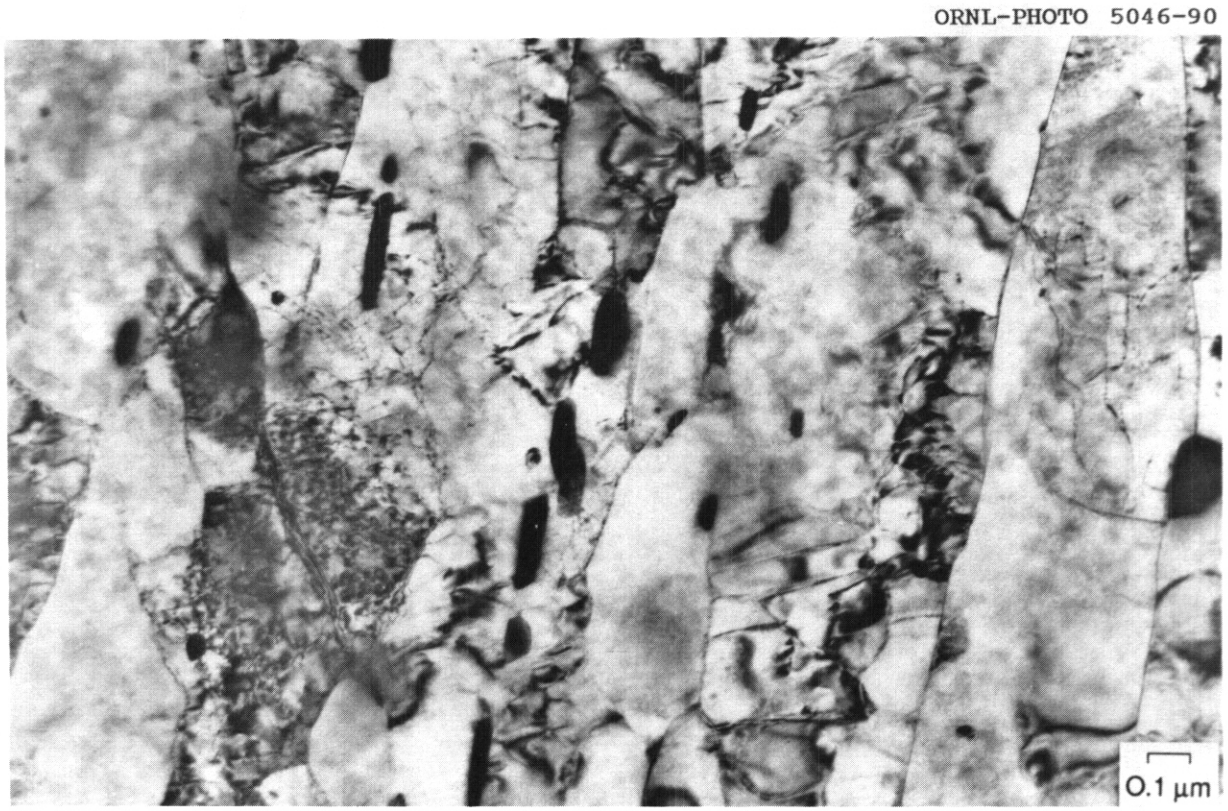

Fig. 10. TEM the lath/subgrain boundary, dislocation and precipitate structures of 9Cr-1MoVNb (heat XA 3590) steel after HFIR irradiation at 500°C to about 39 dpa.

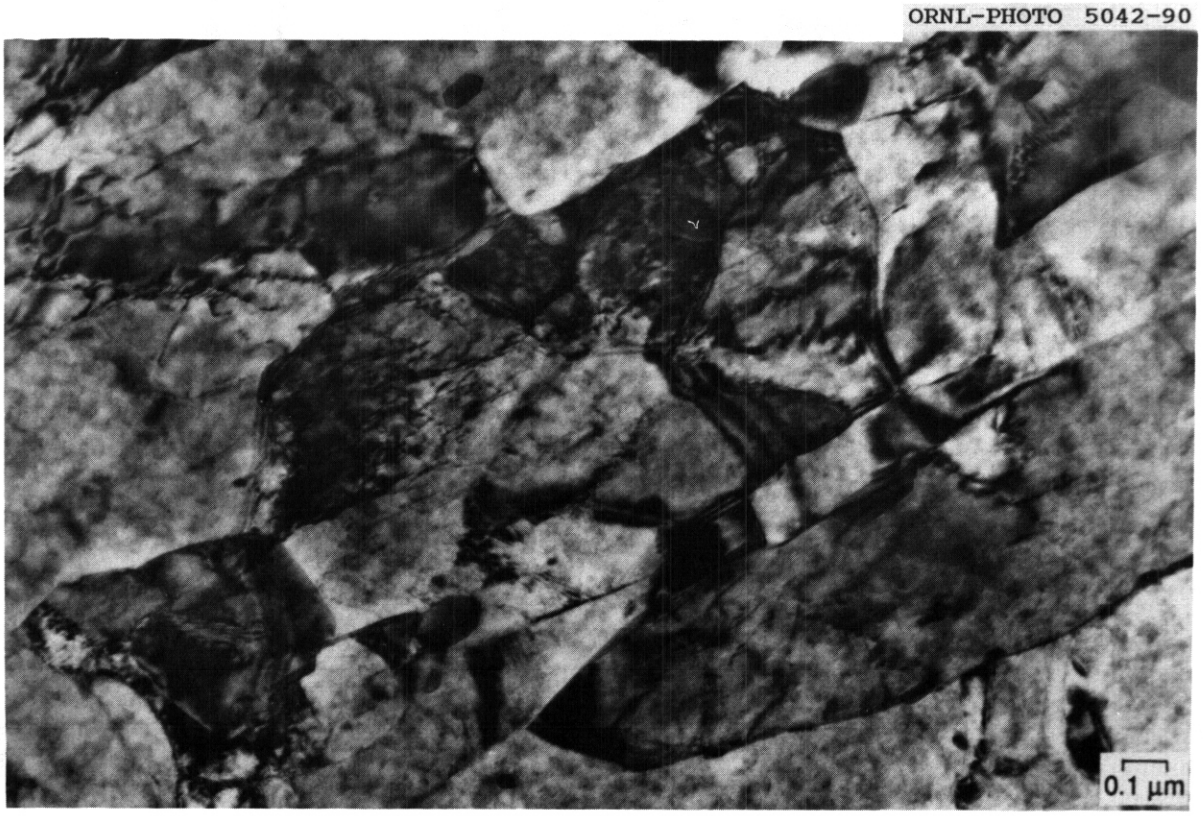

Fig. 11. TEM the lath/subgrain boundary, dislocation and precipitate structures of 9Cr-1MoVNb (heat XA 3590) steel after HFIR irradiation at 600°C to about 39 dpa.

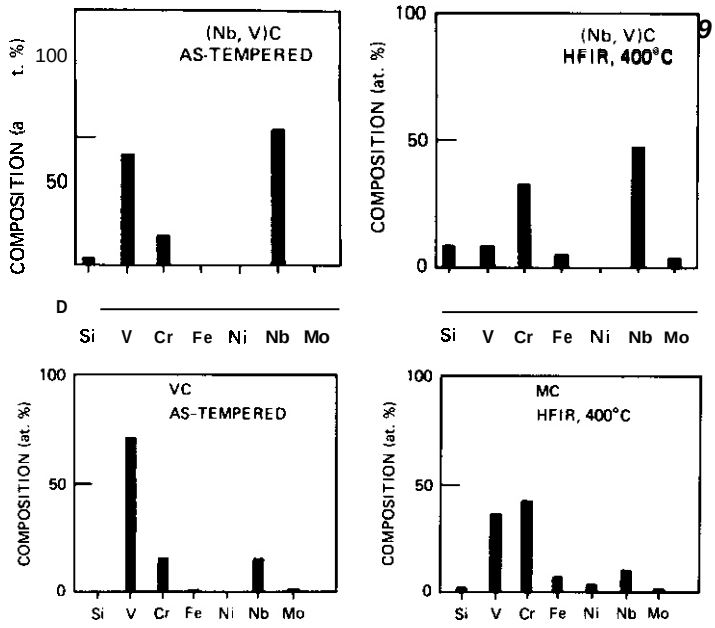

Fig. 12. Histograms of MC phase composition from quantitative XEDS analysis of precipitate particles on extraction replicas from 9Cr-1MoVNb (heat XA 3590) steel in the as-tempered condition and after HFIR irradiation at 400°C to about 37 dpa.

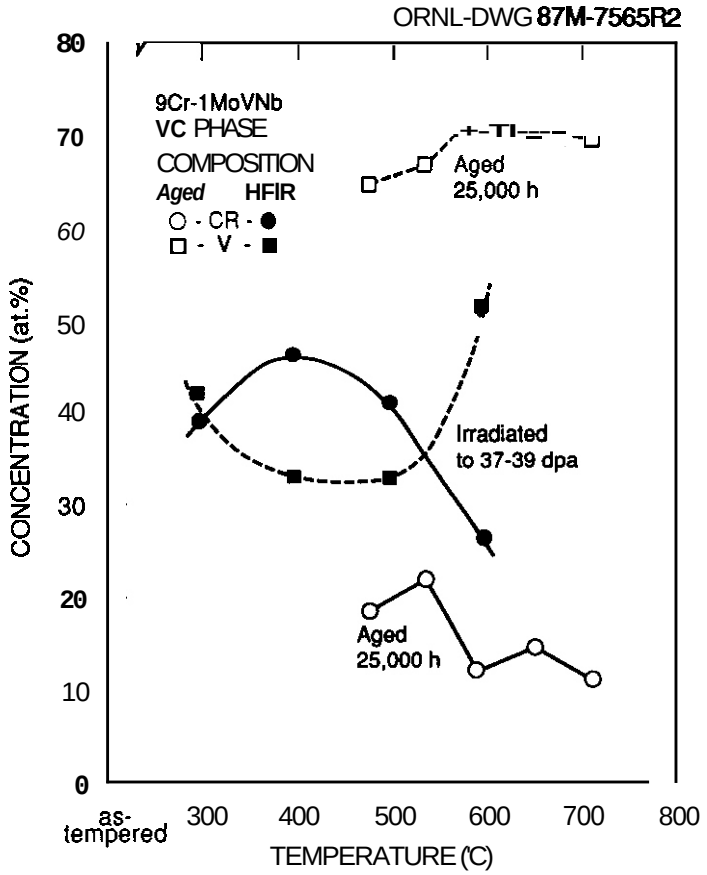

Fig. 13. A plot of the average chromium and vanadium concentrations of MC particles as functions of exposure temperature, obtained from quantitative XEDS analysis of extraction replicas made from 9Cr-1MoVNb (heat XA 3590) steel specimens which had been thermally aged or irradiated in HFIR.

The XEDS broad beam compositions of extracted precipitates showed little difference after irradiation, except for irradiation at 300°C (Table *6)*. Given the MC phase composition produced during irradiation, analysis of the broad-beam data for relative phase fractions suggested a slight increase in the amount of MC relative to $M_{23}C_6$ at 300°C (17 and 83%, respectively). The amounts of MC relative to $M_{23}C_6$ in specimens irradiated at 400-600°C were similar to that found in the as-tempered steel (10-12 and 88-90%, respectively). Bulk extraction measurements could not be performed on radioactive material, so quantitative changes in the total amount of precipitation could not be observed.

DISCUSSION

The data on 9Cr-1MoVNb steel indicate that the microstructural and microcompositional changes produced by HFIR irradiation and by thermal aging are quite different. However, it should also be obvious that the mechanisms driving such changes are also different in each exposure environment. The microstructural differences between thermally aged and HFIR irradiated 9Cr-1MoVNb steel can be summarized as follows: a.) the as-tempered subgrain boundary and precipitate structures are stable during aging at 600°C and below, but unstable during HFIR irradiation at 300-500°C; b.) Laves phase forms abundantly during aging below 600°C. but not at all during HFIR irradiation; c.) additional fine VC needles form during aging at 593°C and below, but not during HFIR irradiation; d.) the MC phase undergoes radical compositional changes during irradiation at 300-500°C that are not observed

Table 6. Broad-Beam Compositional Averaging via XEOS of Precipitates Extracted onto Replicas from HFIR-Irradiated 9Cr-1MoVNb Steel

Aging Conditions		Phases	Composition[a] (at. %)								
Temperature (°C)	Dose (dpa)		Si	Ti	V	Cr	Mn	Fe	Ni	Nb	Mo
As-tempered		$M_{23}C_6$ + MC[2][b]	0.9	0.4	9.7	53.3	0.1	26.5	0.4	3.4	4.8
300	36.5	$M_{23}C_6$ + MC[3]	**2.0**	0.1	10.5	53.8	**0.6**	25.6	0.1	2.6	**3.6**
400	**36.5**	$M_{23}C_6$ + MC[5]	1.9	0.06	5.7	61.7	**0.7**	**23.2**	0.5	*2.6*	**3.6**
500	38.5	$M_{23}C_6$ + MC[2]	2.8	**0.3**	5.8	58.6	0.1	22.1	**2.0**	**3.2**	4.6
600	38.5	$M_{23}C_6$ + MC[3]	**1.4**	**0.3**	**6.9**	60.7	3.9	22.6	0.1	**1.1**	3.1

[a]Normalized, averaged composition for elements heavier than aluminum.

[b]The number of separate Spectra obtained from different areas of the replica for the average broad-beam composition. [c]None detected.

Table 7. *XEDS Composition of Individual MC Particles Extracted onto Replicas from HFIR-Irradiated 9Cr-1MoVNb Steel*

Aging Conditions		Comments[a]	Composition[a] (at. %)							
Temperature (°C)	Dose (dpa)		Si	TI	V	Cr	Fe	Ni	Nb	Mo
As-Tempered		Small[b] VC[6][c]	1.6	**0.6**	64.0	16.6	1.6	nd[d]	**1.3**	5.2
		Small NbC[2]	**2.3**	2.3	**33.5**	***9.2***	1.1	0.1	50.5	1.3
300	**36.5**	Small VC[4]	1.5	0.4	**42.3**	36.8	8.9	0.08	8.0	1.0
		Small NbC[3]	2.2	*0.2*	11.4	17.2	10.0	0.3	53.9	3.1
400	36.5	Small VC[9]	3.2	0.5	35.0	46.5	5.5	0.4	7.4	1.4
		Small NbC[2]	0.4	1.2	8.8	34.2	4.5	0.8	46.1	3.5
500	38.5	Small VC[9]	2.5	0.1	33.9	41.9	10.0	1.0	7.5	1.5
		Small NbC[2]	**2.6**	**1.1**	9.8	27.5	7.4	0.8	46.3	3.1
600	38.5	Small MC[8]	2.1	0.4	53.6	27.9	1.0	nd[c]	7.3	1.4

[a]Normalized, averaged composition for elements heavier than aluminum.

[b]Particles are less than 50 to 60 nm in diameter

[c]The number of separate spectra obtained from different particles for the average phase composition.

[d]None detected

during aging at any temperature; e.) more dislocations are produced within the lath/subgrains during long-term thermal aging at 483-593°C than are produced during HFIR irradiation at 400-600°C. The radiation-induced loops at 300°C and cavities at 400°C are, of course, also important differences between aged and neutron-irradiated material. However, these microstructural features are the expected by-products of interstitial point-defects or helium atoms (from transmutation reactions) produced by neutron irradiation, and will not be discussed further here. Helium effects on bubble and void formation in 9 and 12 Cr steels irradiated in HFIR and FFTF have been extensively discussed elsewhere.[**]

The instability of the as-tempered carbide precipitate and subgrain boundary structures and the compositional changes of the MC phase during HFIR irradiation at 300-500°C appear to be coupled microstructural phenomena. The inverse temperature dependence suggests that these are radiation-induced effects rather than radiation-enhanced thermal effects, Both the as-tempered MC particle distribution and subgrain boundary structure coarsen during long-term aging, but only at the highest temperatures. Both the degree of coarsening during lower-temperature irradiation and the associated dissolution of $M_{23}C_6$ particles and compositional changes of MC phase during coarsening (more Cr instead of less) also consistently point to phenomena that are radiation-induced and essentially non-thermal in nature. Moreover, there is a consistent correlation between changes of precipitate and subgrain boundary structures during aging and during irradiation. This would imply that the precipitates pin the boundaries so that subgrain boundaries cannot migrate unless the precipitates first become unstable. In fact, 12Cr-1MoVW steel similarly irradiated in HFIR at 300-500°C shows stability of both the as-tempered subgrain and carbide Structures? an opposite effect of irradiation relative to the 9Cr-1MoVNb steel, but consistent with precipitates preventing boundary migration. Thus, initial instability of the as-tempered carbides ($M_{23}C_6$ in particular) in the 9Cr-1MoVNb steel appears to be a root cause for the other microstructural changes observed during irradiation at 300-500°C.

In contrast to the radiation-induced aspects of microstructural evolution directly observed in 9Cr-1MoVNb steel irradiated in HFIR at 300-500°C, the noticeable absence of both fine VC and coarser Laves phase precipitation suggests that irradiation has retarded these thermal phenomena. However, the failure of these dominant thermal precipitates to occur during irradiation can also be related indirectly to the instability of as-tempered carbides during irradiation. The last observation that seems intuitively strange is the increase in matrix dislocation concentration in aged compared to irradiated material. However, even this result can be explained in part by loop nucleation that is very strongly dependent on temperature combined with thermal dislocation network recovery processes occuring at an enhanced rate during irradiation of the 9Cr-1MoVNb steel.

Microstructural evolution during irradiation is generally caused by several mechanisms acting in concert. including: a.) cascade damage and point-defect production, b.) annihilation, accumulation and/or migration of radiation-produced point defects, and c.) radiation-induced segregation (RIS) and radiation-enhanced diffusion, both of which are caused by the fluxes of radiation-produced point defects. Microstructural changes during thermal aging are usually driven by solute supersaturation and diffusion, and dislocation/boundary structure recovery processes.

It seems reasonable that the as-tempered microstructure established at high temperatures should be resistant to recovery during long-term aging at lower temperatures. The formation of fine VC carbides during aging below 600°C apparently indicates that the decrease in the carbon solubility with decreasing aging temperature produces a new carbon supersaturation (relative to that relieved by tempering), which then triggers additional carbide precipitation. The fine distribution of VC needles is consistent with nucleation on the increased number of dislocations available at the lower aging temperatures. The formation of Laves phase as films along grain boundaries or as crusts around carbide particles would indicate that localized carbon depletion triggers the formation of this carbon-free intermetallic phase.[28,29] The increase in the amount of Laves phase in the higher silicon heat of 9Cr-1MoVNb steel is consistent with silicon acting as a catalyst for the formation of that phase.[28,29]

Processes involving radiation-produced point defect are almost certainly the cause of the radiation-induced microstructural changes observed in 9Cr-1MoVNb steel, although several different mechanisms may be involved. While cascade-dissolution of precipitate particles cannot be ruled out, dissolution of coarser $M_{23}C_6$ while smaller MC particles survive would not suggest that this is the dominant mechanism. While RIS of chromium seems to be involved in the radiation-induced chromium enrichment of the MC phase,[24,27,30] it would not consistently explain the dissolution of Cr-rich $M_{23}C_6$ particles. One simple explanation for initial carbide dissolution during irradiation could involve the supersaturation of vacancies and their interaction with carbon atoms in the matrix. Binding of carbon atoms to the excess vacancies produced during irradiation would cause an apparent increase in the solubility of the matrix for carbon, similar to the case proposed recently for austenitic stainless steels.[30] Increased solubility without changing the instantaneous matrix carbon content would create a transient decrease in carbon activity which could then cause partial dissolution of pre-existing carbide particles, as is observed. The other aspects of the microstructural evolution in irradiated 9Cr-1MoVNb steel seem to support this simple mechanism. If depletion of carbon in the matrix below some critical concentration is a necessary condition for Laves phase precipitation, then any increase in the matrix carbon content due to the carbon atom-vacancy interaction would help to explain why Laves phase does not form during irradiation at 300-500°C. Carbide dissolution is certainly also a contributing factor to the instability of the subgrain boundary structure observed during irradiation, although

biased absorption of radiation-produced point defects (i.e., interstitials to compensate for the vacancy supersaturation) would ultimately drive continued boundary migration. The inverse temperature dependence of all of these coupled microstructural phenomena is certainly consistent with their dependence on the radiation-produced vacancy supersaturation, as the mechanism implies. In summary, explanations based on changes the residual carbon content of the matrix at 600°C and below, and differences during thermal aging and HFIR irradiation, help to provide a consistent interpretion of microstructural behavior in aged or irradiated 9Cr-1MoVNb steel.

Finally, two more questions should be answered: a.) are the microstructural data presented here consistent with similar data on comparable aged or irradiated martensitic/ferritic steels? b.) do these data or mechanistic insights have implications on the potential for further improvement of 9Cr-1MoVNb steel through alloy development? With regard to stress-free thermal aging, microstructural data on the same two heats of 9Cr-1MoVNb investigated in this work have been presented for 5000 h at 593 and 704°C, in conjunction with fatigue studies at the same temperatures.[31,32] Little change was observed in the as-tempered microstructure at 593°C, but subgrain structure and carbide coarsening was observed at 704°C. consistent with our data. Laves phase forms abundantly during aging of 9Cr-1Mo steels at 500-550°C for 20,000 h [13], and its formation along grain and subgrain boundaries has been related to impact embrittlement at lower temperatures [14,15]. Laves phase tends to form at higher aging temperatures in modified 12Cr-1Mo steels (600°C in FV 448 (12Cr-1MoVNb) and CRM-12 (12Cr-1MoV) [33], 500-700°C in 12Cr-1MoVW [34]), and even more abundantly in similar steels with more molybdenum (500-600°C in JMFS (10Cr-2MoVNb) [35], 550-650°C in 13Cr-2MoNbV [18]). Laves can even form after only 1 h at 730°C in a modified 10Cr-6Mo steel [36]. There is very little aging data at temperatures below 500°C or for times beyond 20.000 h. Although some fine VC needles have been observed to form during tempering in CRM-12 [33], our data on the abundant, fine formation of VC needles during aging at lower temperatures appears to be unique.

With regard to irradiated steels, the HFIR data on precipitation in 9Cr-1MoVNb steel irradiated at 300-600°C is also unique. Direct comparison of the same heats of 9 and 12Cr steels irradiated in HFIR and in FFTF (an LMFBR) at 400°C indicates there is little difference in the precipitate microstructure produced in either reactor. Consistent with our results, Laves phase has generally not been observed in most 9-12Cr steels irradiated in LMFBR's below 600°C (EM-10 (9Cr-1Mo) and EM-12 (9Cr-2MoVNb) [10], HT-9 [8, 24, 27], FV 448 [33] or 13Cr-2MoNbV [18]). Laves phase has been observed at 615°C in CRM-12 (with radiation-produced composition modification) [33], and at 650°C in EM-12 [8] during LMFBR irradiation. Only Suzuki et al. [36] found Laves phase below 600°C. in the 10Cr-2MoVNb steel irradiated in HFIR at 500°C to 34 and 57 dpa. In this case, however, the Laves phase composition was highly modified by RIS during irradiation relative to the thermal phase composition. Our observations of instability of the as-tempered microstructure and the radiation-produced compositional modification of the MC phase in 9Cr-1MoVNb irradiated at 300-500°C appear to be new findings.

With regard to further alloy development, new applications of 9Cr-1MoVNb today as either a core material in new modular, inherently-safe advanced reactors,[37] or as the first-wall material in a MFR. or as boiler tubing in fossil power plants' all go beyond those for which this steel was initially developed and optimized.[38,39] Furthermore, there is considerable effort in the United States'[40,41] and in Japan',[42] to develop steels that have reduced long-term radioactivity after exposure in a fusion reactor, but are metallurgically equivalent to conventional 7-9Cr martensitic steels (i.e., 9Cr-2WVTa or 8Cr-2WVTa). For non-nuclear, high-temperature applications of 9Cr-1MoVNb, loss of tensile strength, and creep-rupture and fatigue resistance above 550°C appear related to microstructural instability. Laves phase precipitation after long-term exposure at 450-550°C can cause impact embrittlement at lower temperatures and may also lead to structure recovery and softening due to molybdenum depletion. Alloying to further stabilize the carbide precipitate structure (particularly the MC carbides) could improve the high-temperature strength, while both minor compositional variations (lower Si, more C or B[28,29]) or changes in tempering conditions (higher tempering temperatures and/or shorter times for more residual carbon in the matrix) could reduce Laves phase precipitation during aging. A major concern for the application of 9-12Cr martensitic/ferritic steels in fusion reactors is the increase in their DBTT caused by irradiation at lower temperatures (<450-500°C).[44,45] Although such hardening-induced embrittlement may ultimately be related to point-defect and dislocation types of radiation damage in these steels, radiation-induced coarsening of the as-tempered structure does not help; better unirradiated toughness properties are often related to finer rather than coarser grain/subgrain structures. Stability of the as-tempered carbide during irradiation may be related to alloying changes that either produce more precipitation during tempering or alter the mixture of carbide phases or their compositions (i.e., $M_{23}C_6$/MC ratio, VC/NbC ratio, V/Cr ratio in MC phase) for better resistance to dissolution. The microstructural differences observed between aged and neutron-irradiated specimens of 9Cr-1MoVNb steel suggest that different optimization strategies will be needed for nuclear and non-nuclear applications.

CONCLUSIONS

1. Microstructural evolution in 9Cr-1MoVNb steel was significantly different during long-term thermal aging as compared to HFIR irradiation at 600°C and below.

2. During thermal aging for up to 25,000h, the as-tempered microstructure remained stable at 482-593°C, and coarsened at 650 and 704°C.

3. Thermal aging produced abundant amounts of coarse Laves phase and fine VC needles at 482-593°C. The higher silicon heat of steel contained more Laves phase.

4. HFIR irradiation to 37-39 dpa produced "black-dot" dislocation loops only at 300°C, and detectable helium bubbles and voids only at 400°C. No new precipitate phases were observed at 300-600°C.

5. The lath/subgrain boundary structure after irradiation at 300 and 400°C was considerably coarser than that found in as-tempered condition, whereas the subgrain structure after irradiation at 600°C was similar to the as-tempered structure.

6. Some dissolution of $M_{23}C_6$ particles and coarsening of MC particles was observed after irradiation at 300-500°C, but not at 600°C. Substantial modifications of the MC phase composition (increased Cr, decreased V) were also observed 300-500°C.

Acknowledgments

Research sponsored by the Office of Fusion Energy, US. Department of Energy, under Contract DE-ACOS 84OR21400, with Martin Marietta Energy Systems, Inc. We would like to thank Dr. V. Sikka at ORNL for supplying the thermally aged steel specimens. We would like to thank N. Rouse for expert thinning of the HFIR irradiated TEM specimens, and W. Jones for thinning and preparing replicas on the aged steel specimens.

REFERENCES

1. G.W. Cunningham, P. Patriarca and E.E. Hoffman, Ferritic Steels for High-Temperature Applications, A.K. Khare, Ed., American Society for Metals, Metals Park, OH, 1983, p. 3.

2. H. Haneda, F. Masuyama, S. Kaneko and T. Toyoda, Advances in Materials Technoloav for Fossil Power Plants, R. Viswanathan and R.I. Jaffee. ASM International, Metals Park, OH, 1987, p. 231.

3. J. Pelabon and F. Pellicani, Advances in Materials Technoloav for Fossil Power Plants, R. Viswanathan and R.I. Jaffee, ASM International, Metals Park, OH, 1987, p. 243.

4. C.E. Jaske and R.W. Swindeman, Advances in Materials Technoloav for Fossil Power Plants, R. Viswanathan and R.I. Jaffee, ASM International, Metals Park, OH, 1987, p. 251.

5. G.C. Bodine and R. E. McDonald, Ferritic Steels for High-Temperature Applications, A.K. Khare, Ed., American Society for Metals, Metals Park, OH, 1983, p. 9.

6. V.K.Sikka, C.T. Ward, and K.C. Thomas, Ferritic Steels for Hiah-Temperature Applications, A.K. Khare, Ed., American Society for Metals, Metals Park, OH, 1983, p. 65.

7. K.Q. Bagley, E.A. Little, V. Levy, A. Alamo, K. Ehrlich, K. Anderko, and A. Calzabini, Materials For Nuclear Reactor Core Applications, Bristol Meeting, Oct. 1987. Vol. 2, British Nuclear Energy Society, London, 1988, p. 37.

8. D.S. Gelles and L.E. Thomas, Proceedinas of a Topical Conference on Ferritic Allovs for Use in Nuclear Energy Technoloaies. J.W. Davis and D.J. Michel. Eds.. The Metallurgical Society of American Institute of Mining, Metallurgical and Petroleum Engineers. New York, 1984, p. 559.

9. D.S. Gelles, J. Nucl. Mater. 148 (1987) 136.

10. D. Gilbon, J. Seran, R. Cauvin, A. Fissolo, A. Alamo. F. Le Naour, and V. Levy. Effects of Radiation on Materials: 14th International Symposium, Vol. I, ASTM STP 1046, N.H. Packan, R.E. Stoller and S. Kumar, Eds.. American Society for Testing and Materials, Philadelphia, 1989, p. 5.

11. R.L. Klueh and M.P. Tanaka. J. Metals 37 (Oct. 1985) 16.

12. E.E. Bloom and D.L. Smith, Proceedinas of Conference on Materials for Future Enerav Svstems. held in Washington, D.C. May 1-3, 1984, American Society for Metals, Metals Park, OH, 1985, p. 253.

13. J.M. Titchmarsh, M. Wall, and B.C.Edwards, Analytical Electron Microscopy, D.B. Williams and D.C. Joy, Eds., San Francisco Press, San Francisco, CA, 1984. p. 247.

14. J.A. Hudson, S.G. Druce, G. Gage, and M. Wall, J. Theoretical and Applied Fracture Mechanics. 10 (1988) 123.

15. M. Wall, Temper Embrittlement in 9% Chromium Steel, Ph. D. thesis submitted to University of London, AEA Technology Harwell - AERE-R12812, Harwell Laboratory. Oxfordshire. England, August 1985.

16. W.L. Hu. and D.S. Gelles, Influence of Radiation on Materials Properties; 13th International Symposium (Part II), ASTM STP 956, F.A. Garner, C.H. Henager and N. Igata, Eds., American Society for Testing and Materials, Phildelphia. PA, 1987, p. 83.

17. J.M. Vitek, W.R. Corwin, R.L. Klueh, and J.R. Hawthorne, J. Nucl. Mater. 141-143 (1986) 948.

18. V.S. Agueev. V.N. Bykov, A M. Dvoryashin. EA. Golovanov. E.A. Medvedeva. V V. Romaneev, V.K. Sharnardin. and A.N. Vorobiev, Effects of Radiation on Materials: 14th International Symposium. Vol. I, ASTM STP 1046, N.H. Packan. R.E. Stoller and S. Kurnar. Eds.. American Societv for Testing and Materials, Philadelphia, 1989, p. 98.

19. R.L. Klueh and P.J. Maziasz, Effects of Radiation on Materials: 14th International Svmposium, Voi. I, ASTM STP 1046, N.H. Packan, R.E. Stoller and S. Kurnar. Eds.. American Society for Testing and Materials, Philadelphia, 1989, p. 246.

20. R.L. Klueh and D.J. Alexander, in: Proceedinas of the 4th International Conference on Fusion Reactor Materials (ICFRM-4), Tokyo, Japan, Dec. 1-4, 1989; to be published in Journal of Nuclear Materials in 1990.

21. N.J. Zaluzec, Introduction to Analvtical Electron Microscopy, J.J. Hren, J.I. Goldstein. and D.C. Joy, Eds.. Plenum Press, New York, 1979, p. 121.

22. P.J. Maziasz and G.A. Odette, Proceedinas of the 41st Annual EMSA Meeting, G.W. Bailey. Ed., San Francisco Press, San Francisco, 1983, p. 198.

23. E.A. Kenik and P.J. Maziasz, Analvtical Electron Microscopy - 1984, D.B. Williams and D.C. Joy, Eds., San Francisco Press, San Francisco, 1984. p. 231.

24. P.J. Maziasz and R.L. Klueh, Effects of Radiation on Materials: 14th International Svmposium. Vol. I, ASTM STP 1046, N.H. Packan, R.E. Stoller and A.S. Kumar, Eds., American Society for Testing and Materials. Philadelphia, 1989. p. 35.

25. J.M. Viek and R.L. Klueh, Proceedinas of a ToDical Conference on Ferritic Allovs for Use in Nuclear Enerav Technoloaies, J.W. Davis and D.J. Michel. Eds., The MetallurgicalSociety of American Institute of Mining, Metallurgicaland Petroleum Engineers, New York, 1984, p. 551.

26. P.J. Maziasz and V.K. Sikka, ADIP Semiannu. Proa. Rept. DOE/ER-0045/15 ending Sept. 30, 1985. U.S. Dept. of Energy, (Feb.,1986) p. 102.

27. P.J. Maziasz. R.L. Klueh. and J.M. Viek. J. Nucl. Mater. 141-143 (1986) 929.

28 P J Maziasz. M.Con '86 Optimizat on of Processing. Properties ana Service PerformanceThro.ugh Microstructura Control. ASTM STP 979. Amer can Society for Testing and Mater a.s. Pniadeipnia PA, 1988, p 116

29. P.J. Maziasz. J. Minerals. Metals and Materials (JOM), 41, no. 7 (1989) 14.

30. P.J. Maziasz, J. Nucl. Mater. 169 (1990) 95.

31. S. Matsuoka. S. Kim, and J.R. Weertman. Proceedinas of a ToDical Conference on Ferritic Allovs for Use in Nuclear Enerav Technoloaies. J.W. Davis and D.J. Michel. Eds., The Metallurgical Society of American Institute of Mining, Metallurgical and Petroleum Engineers, New York. 1984, p. 507.

32. S. Kim and J.R. Weertman, Metal. Trans. A, 19A (1988) 999.

33. L.P. Stoter and E.A. Little, Advances in the Physical Metallurgy and Applications of Steels. The Metals Society. London, 1981, p. 369.

34. P.S. Chen and R.C. Wilcox, Effects of Radiation on Materials: 14th International Symposium, Vol. I, ASTM STP 1046, N.H. Packan, R.E. Stoller and A.S. Kumar, Eds., American Society for Testing and Materials, Philadelphia. 1989, p. 114.

35. M. Suzuki. A. Hishinuma. P.J. Maziasz, and T. Sawai, J. Nucl. Mater. 170 (1990) 270.

36. K. Farrell and E.H. Lee, Scripta Met. 17 (1983) 791.

37. "PRISM Makes Progress." Nuclear Enaineerina International, September, 1988, p. 32.

38. P. Patriarca, Proceedinas of a Topical Conference on Ferritic Allovs for Use in Nuclear Enerav Technologies. J.W. Davis and D.J. Michel, Eds., The MetallurgicalSociety of American Institute of Mining, Metallurgicaland Petroleum Engineers, New York. 1984, p. 107.

39. V.K. Sikka. M.G. Cowgill, and B.W. Roberts, Proceedinas of a Topical Conference on Ferritic Allovs for Use in Nuclear Enerav Technologies. J.W. Davis and D.J. Michel, Eds., The Metallurgical Society of American Institute of Mining, Metallurgical and Petroleum Engineers, New York, 1984, p. 413.

40. R.L. Klueh and P.J. Maziasz, J. Nucl. Mater. 155-157 (1988) 602.

41. D.S. Gelles, Reduced Activation Materialsfor Fusion Reactors, ASTM STP 1047, R.L. Klueh, D.S. Gelles, M. Okada and N.H. Packan, Eds., American Society for Testing and Materials, Philadelphia PA, 1990, p. 113.

42. M. Tamura. H. Hayakawa, A. Yoshitake, A. Hishinuma. and T. Kondo, J. Nucl. Mater. 155-157 (1988) 620.

43. F. Abe, T. Noda. H. Araki, and M. Okada. Reduced Activation Materials for Fusion Reactors, ASTM STP 1047. R.L. Klueh. D.S. Gelles, M. Okada and N.H. Packan. Eds., American Society for Testing and Materials, Philadelphia PA, 1990, p. 130.

44. J.M. Viek, W R. Corwin, R.L. Klueh. and J.R. Hawthorne, J. Nucl. Mater. 141-143 (1986) 948.

45. R.L. Klueh and P.J. Maziasz, Effects of Radiation on Materials: 14th InternationalSymposium, Vol. I, ASTM STP 1046 N.H. Packan, R.E. Stoller and A.S. Kumar, Eds.. American Society for Testing and Materials, Philadelphia, 1989, p. 246.

MICROSTRUCTURE AND PROPERTIES OF WELDED W, V, and Ta MODIFIED FERRITIC STEELS WITH FAST INDUCED-RADIOACTIVITY DECAY - C. A. WANG and B. A. CHIN (Auburn University).

OBJECTIVE

The objective of this study is to characterize the microstructures and mechanical properties of welded W, V, and Ta modified low activation ferritic steels for fusion reactor structural applications.

SUMMARY

Sheet specimens of W, V, Ta modified low activation ferritic steels were welded using the gas tungsten arc welding (GTAW) process. Autogenous bead-on-plate welds were produced on samples of 2¼CrV, 2¼Cr-1WV, 2¼Cr-2W, 2¼Cr-2WV, 5Cr-2WV, 9Cr-2WV, 9Cr-2WVTa and 12Cr-2WV. Sound autogenous welds were obtained in all low activation 2¼% Cr bainitic steels and the 5% Cr martensitic steel. Bend tests of the welds yielded insufficient toughness at the fusion zone in the low activation 9 and 12% Cr martensitic steels. A post-weld heat treatment is recommended for the 9 and 12% Cr low activation steels to restore toughness.

PROGRESS AND STATUS

Introduction

A series of femtic steels patterned on the chromium-molybdenum alloys, 2¼Cr-1Mo, 9Cr-1MoVNb and 12Cr-1MoVW, were tested for weldability. The modified steels possess a fast induced-radioactivity decay rate and hence they are sometimes referred to as low activation steels. These steels are being developed as candidates for the first wall and blanket structures of fusion reactors. The use of these materials will minimize long-term radioactive hazards associated with disposal after service. In these low activation alloys, elements which become activated during irradiation with long half lives (Mo and Nb) are replaced. The major changes include the replacement of molybdenum with tungsten, the addition of vanadium in 2¼% Cr steels, and the replacement of niobium in the 9% Cr steel with tantalum.[1,2] These replacement elements radically modify both the mechanical properties and weldability of the alloys. In this study, the effect of the alloy modifications on the microstructure and the mechanical properties of the welds is investigated. Bainitic steels (2¼Cr%) usually exhibit good weldability, while the martensitic steels (5, 9 and 12 Cr%) are susceptible to embrittlement in the heat affected zone (HAZ).[3] The objective of this study was to characterize the welded microstructures and mechanical properties of these low activation alloys. Autogenous bead-on-plate welds were produced using the gas tungsten arc welding (GTAW) process to explore the weldability of the steels.

Experimental Procedures

Eight heats of low activation femtic steels, patterned after commercial chromium-molybdenum steels (prepared by Combustion Engineering, Inc.), were investigated in this study. The nominal chemical compositions are shown in Table 1. The as-received steels were heated at 700°C in an argon atmosphere followed by hot rolling to the final thickness of 0.76 mm. The as-rolled materials were heat-treated prior to testing and welding to obtain properties of a standard reference condition. All heats except heat 3787 were austenitized at 1050°C for 0.5 h, then water quenched. Heat 3787 was heated at 900°C for 0.5 h then quenched. Higher austenitization treatments were used for all steels, except heat 3787, to ensure that the vanadium carbides present were dissolved.[4-8] Tempering was performed for 1 h at 700°C for all heats. Autogenous bead-on-plate welds were produced using the GTAW process to evaluate the weldability of all low activation steels. Welds were produced in a protective argon atmosphere under a fully constrained condition. This restraint simulates anticipated conditions that will be encountered in the maintenance and repair of structural components. The welding conditions used were 10 V-dc, 38 A at a torch speed of 4.6 mm/s. The W electrode size was 1/16 in. diameter which resulted in a heat input of 82.6 J/mm. This heat input produced a full penetration weld with a 2.5 mm wide fusion zone perpendicular to the rolling direction.

Microstructures were observed using an optical microscope associated with an image analysis system to measure the ferrite volume fractions present. In order to ascertain microstructure-property relationships, traverse diamond pyramid microhardness (dph) measurements were made across the weld regions. A diamond pyramid indenter was used with a load of 50 g for a duration of 12 s. The specimen weld reinforcements were mechanically ground to be flush with the surface of the base metal and then electropolished prior to subsequent testing. The three-point guide-bend test was used as one index to evaluate weld integrity. Specimens used in this test had dimensions of 0.76 mm x 8 mm x 43 mm. As-electropolished specimens

Table 1. Chemical Composition of Low Activation Ferritic Steels

Alloys	Chemical Composition,[a,b] wt %						
	Cr	W	V	Ta	C	Mn	Si
3785	2.36		0.25		0.11	0.40	0.17
3786	2.30	0.93	0.25		0.10	0.34	0.13
3787	2.48	1.99	0.009		0.11	0.39	0.15
3788	2.42	1.98	0.24		0.11	0.42	0.20
3789	5.00	2.07	0.25		0.13	0.47	0.25
3790	8.73	2.09	0.24		0.12	0.51	0.25
3791	8.72	2.09	0.23	0.075	0.10	0.43	0.23
3792	11.49	2.12	0.23		0.10	0.46	0.24

[a] P = 0.014–0.016, S = 0.005–0.006, Co = 0.005–0.006, Cu = 0.02–0.03, N = 0.02–0.03, Ni < 0.01, Mo < 0.01, Nb <0.01, Ti < 0.01, B < 0.001.
[b] Balance iron.

were etched to aid in identifying the fracture location. The initial three-point bend was made at a speed of 0.508 mm/min over a 25 mm span distance to produce a 100° angle at the fusion zone. The final 180° bend was performed with a 1.5 mm thick space bar placed in between the two ends of the specimen. Testing was performed until the specimen broke into two pieces or laterally contacted the space bar (i.e., a 180° bend).

Tensile test specimens were cut perpendicular to the weld bead and had a reduced gage section of 12.7 mm length by 3.175 mm width by 0.76 mm thickness. In this study, tensile tests were performed at a speed of 0.508 mm/min which resulted in a strain rate of 6.67 x 10^{-4} s^{-1}. All tests were conducted at room temperature. The fracture surface examinations were carried out with a scanning electron microscope (SEM) to investigate the fracture mechanisms of the weld bend tested specimens. All the observations were conducted at a 15 kV accelerating voltage.

Results

The metallography examinations show that the as-welded microstructure consists of three distinct regions: fusion zone, heat-affected zone, and unchanged base metal. Experimental results reveal that all the steels are free of cracks and readily weldable. Microhardness measurements for each heat across the weld with corresponding microstructures are presented in Figs. 1-8. Optical micrographs show that 2¼Cr steels are basically bainitic steels with different amounts of proeutectoid polygonal ferrite in the base metal depending on the chemical composition. 2¼Cr-V steel contains 8-12% polygonal ferrite with the rest being bainite, while 2¼Cr-1WV steel consists of 5-10% ferrite. With an increase in tungsten content, 2¼Cr-2WV steel has a lower ferrite content of 3-8%. Without the vanadium addition, 2¼Cr-2W steel is fully bainite and possesses a finer grain structure as compared to the other 2¼Cr steels. The 5 and 9% Cr steels consist of a completely martensitic structure. A dual phase structure is observed in 12 Cr-2WV consisting of 12-17% delta ferrite and martensite. Table 2 lists the microstructures observed in the base metal for all the steels.

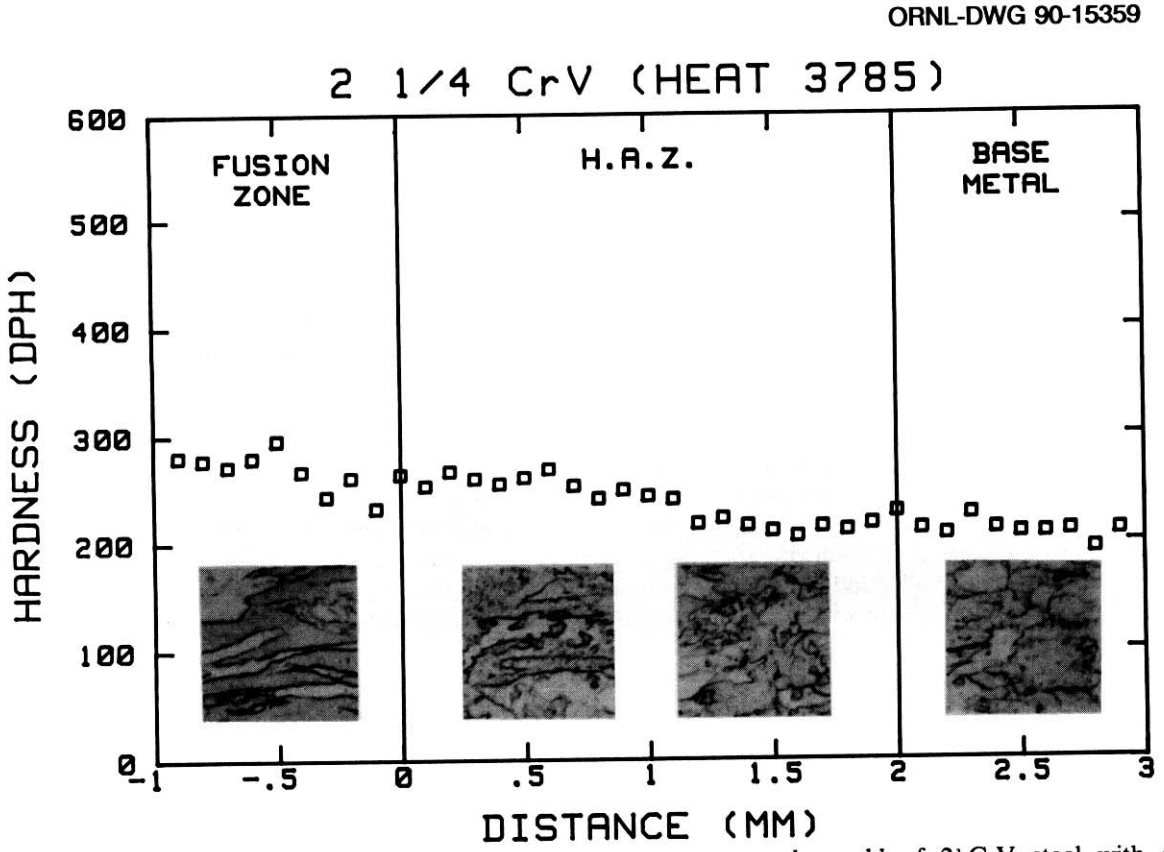

Fig. 1. Diamond pyramid microhardness measurements across the weld of 2¼CrV steel with corresponding microstructures.

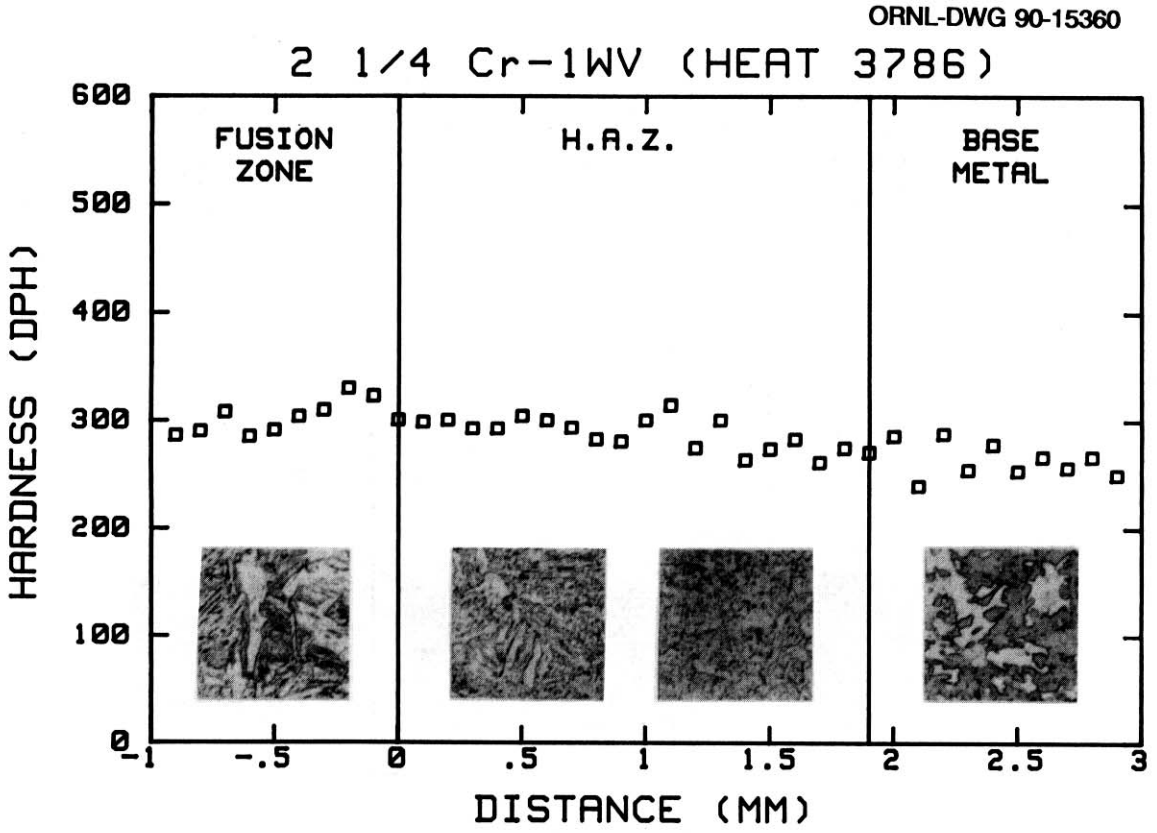

Fig. 2. Diamond pyramid microhardness measurements across the weld of 2¼Cr-1WV steel with corresponding microstructures.

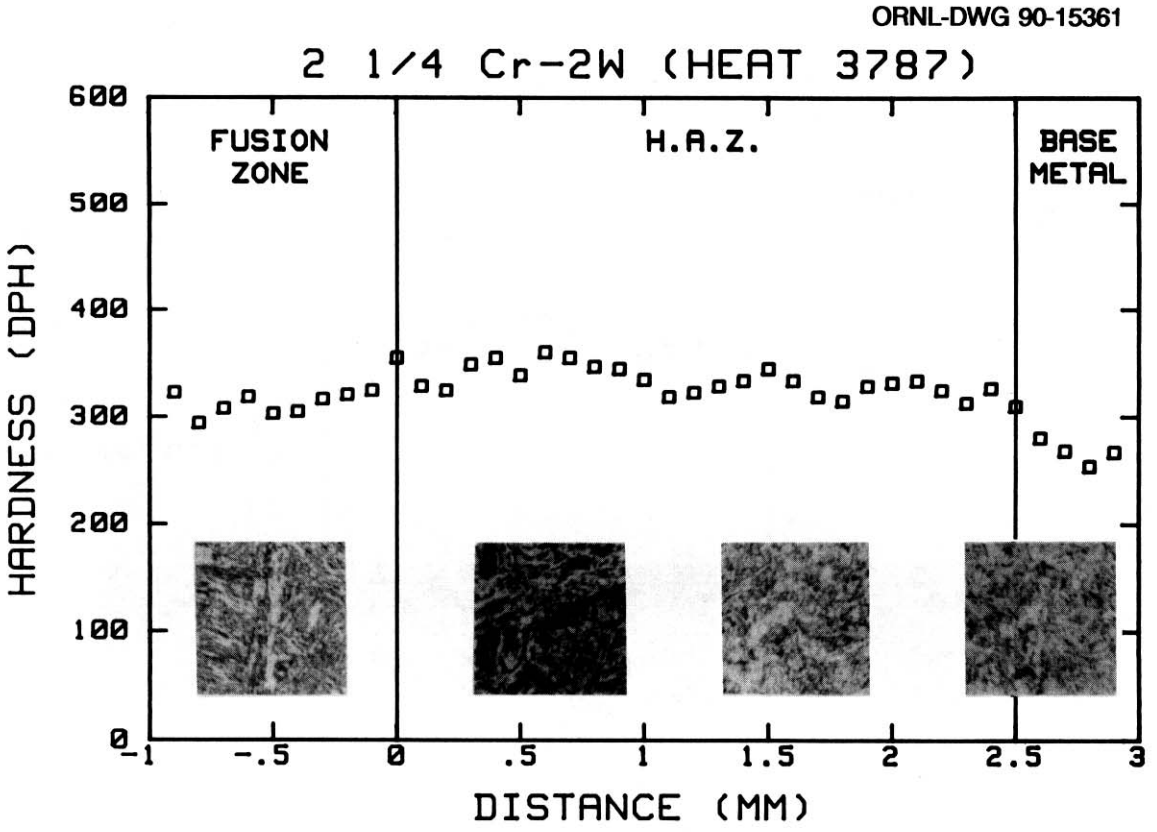

Fig. 3. Diamond pyramid microhardness measurements across the weld of 2¼Cr-2W steel with corresponding microstructures.

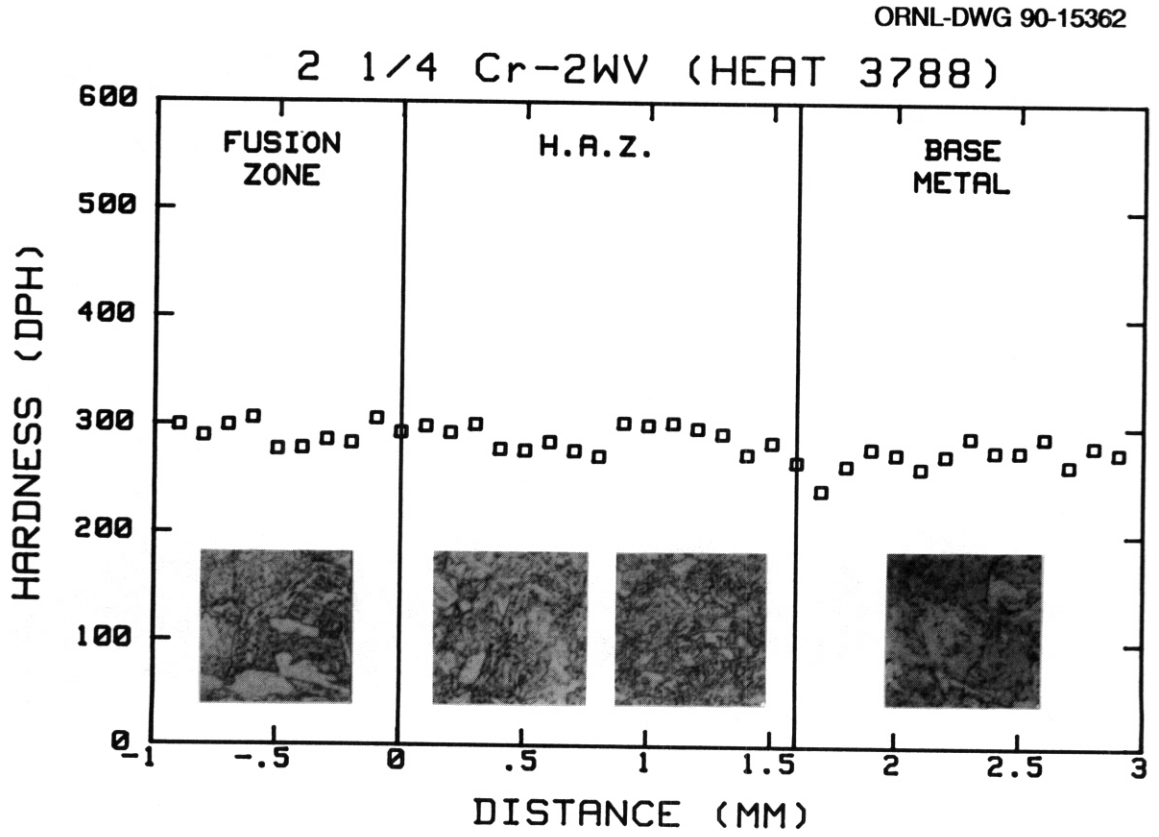

Fig. 4. Diamond pyramid microhardness measurements across the weld of 2¼Cr-2WV steel with corresponding microstructures.

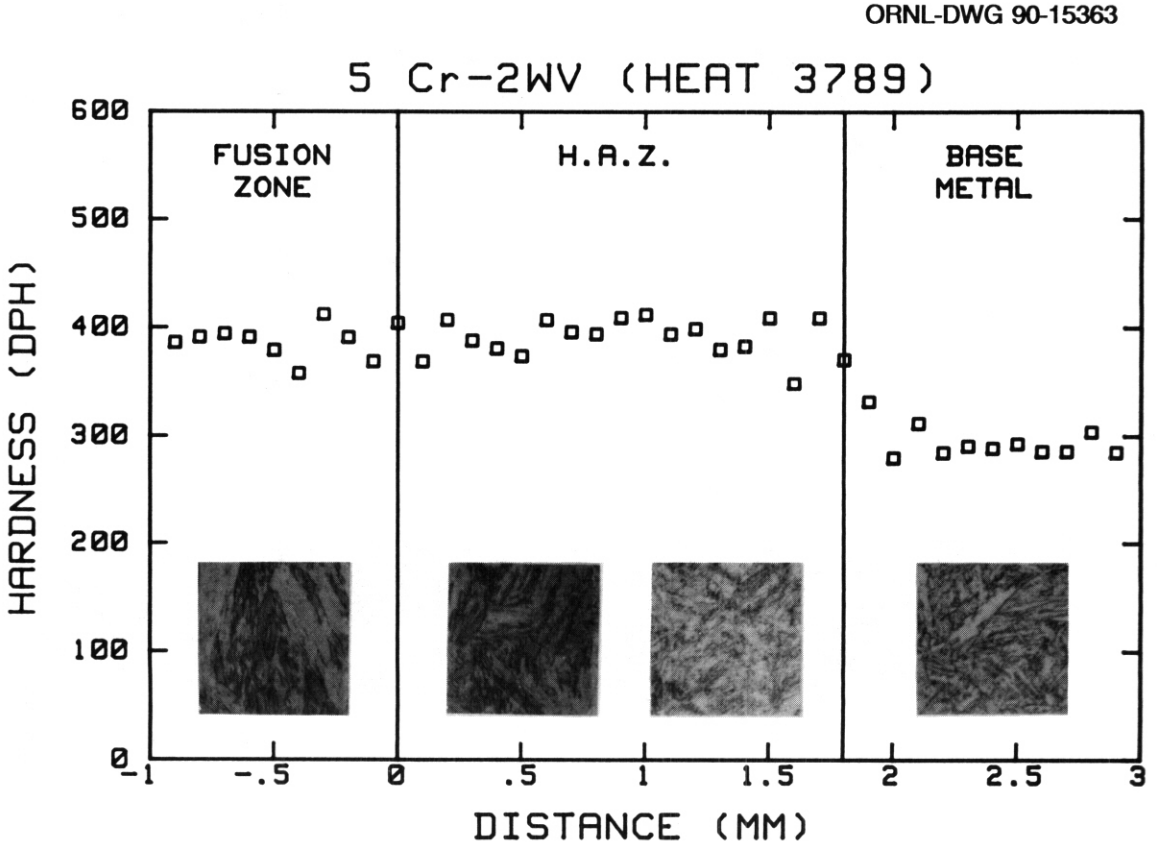

Fig. 5. Diamond pyramid microhardness measurements across the weld of 5Cr-2WV steel with corresponding microstructures.

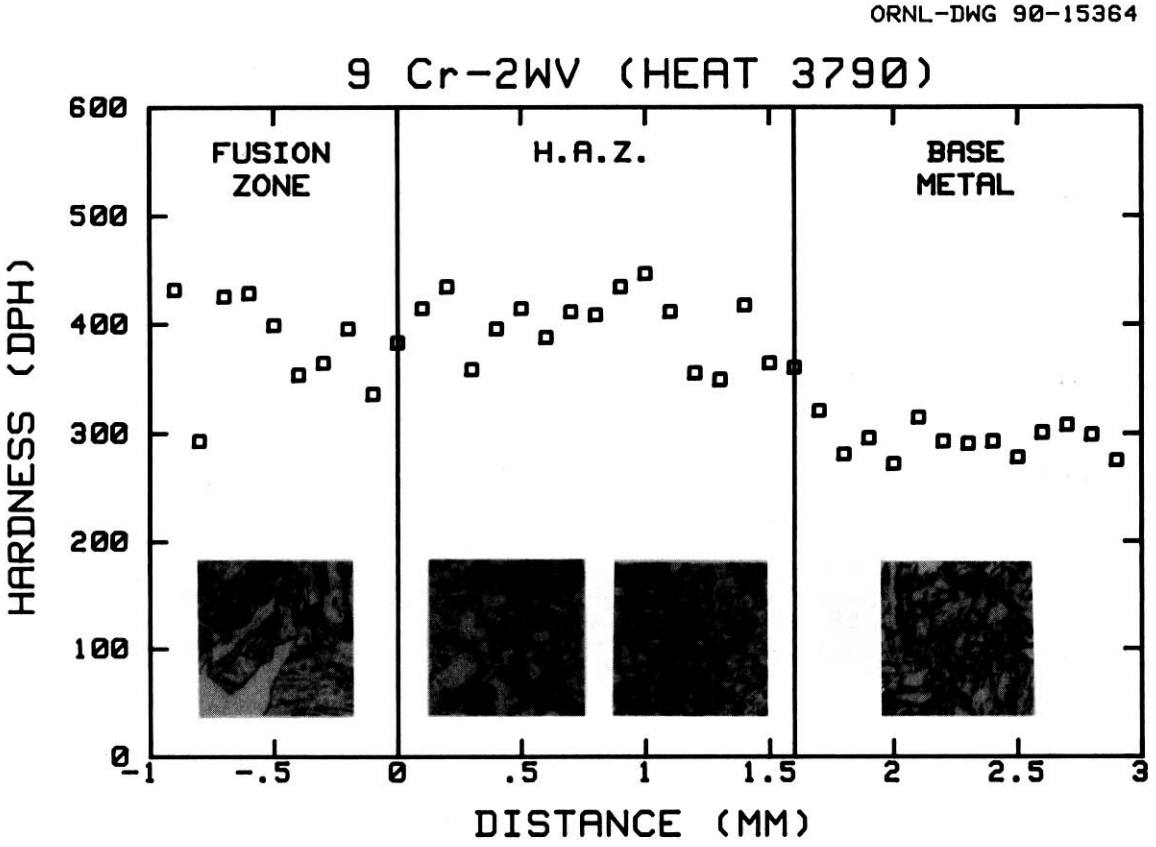

Fig. 6. Diamond pyramid microhardness measurements across the weld of 9Cr-2WV steel with corresponding microstructures.

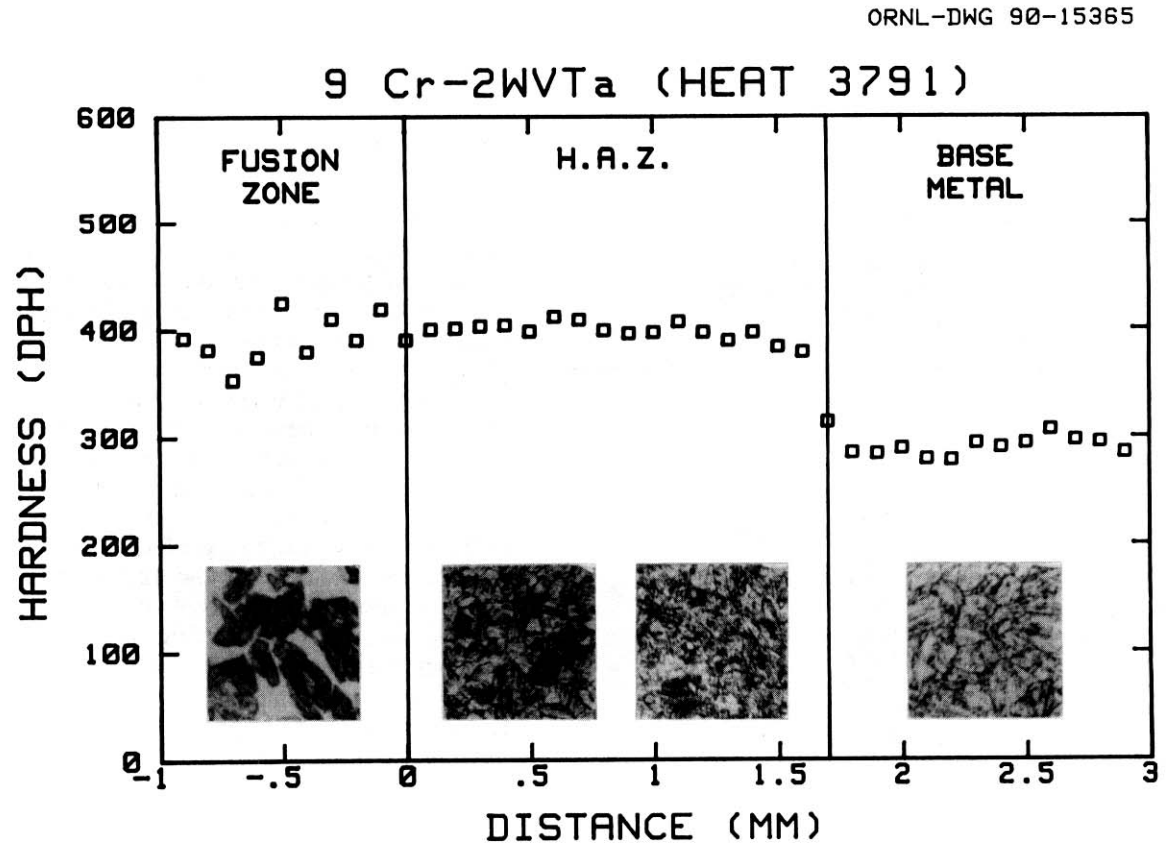

Fig. 7. Diamond pyramid microhardness measurements across the weld of 9Cr-2WVTa steel with corresponding microstructures.

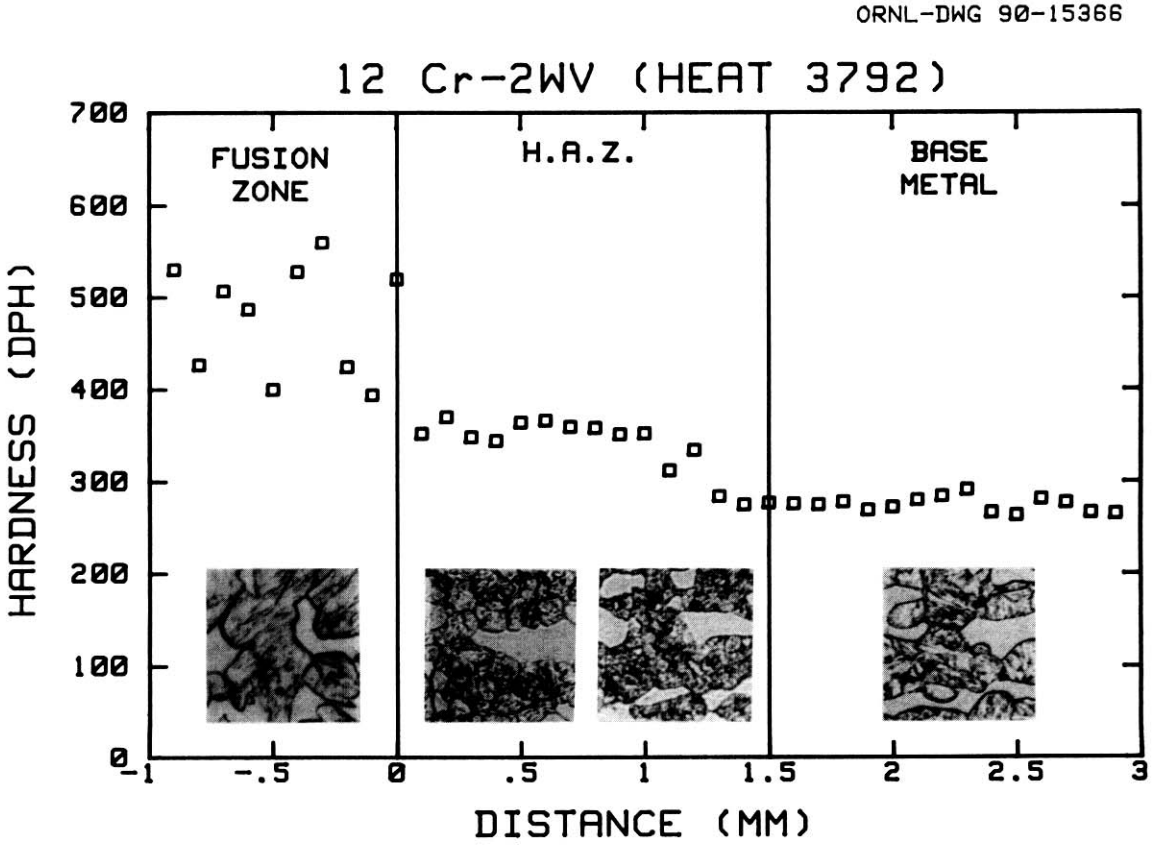

Fig. 8. Diamond pyramid microhardness measurements across the weld of 12Cr-2WV steel with corresponding microstructures.

Table 2. Microstructure of Low Activation Ferritic Steels

2¼Cr-V	8–12% polygonal ferrite + bainite
2¼Cr-1WV	5–10% polygonal ferrite + bainite
2¼Cr-2W	Fully bainite structure
2¼Cr-2WV	3–8% polygonal ferrite + bainite
5Cr-2WV	Fully martensite structure
9Cr-2WV	Fully martensite structure
9Cr-2WVTa	Fully martensite structure
12Cr-2WV	12–17% δ-ferrite + martensite

Table 3. Results of Weld Bend Test

2¼Cr-V	Satisfactory
2¼Cr-1WV	Satisfactory
2¼Cr-2W	Satisfactory
2¼Cr-2WV	Satisfactory
5Cr-2WV	Satisfactory
9Cr-2WV	Failed at fusion zone
9Cr-2WVTa	Failed at fusion zone
12Cr-2WV	Failed at fusion zone

Experimental results of weld bend soundness tests are shown in Table 3. The specimens were free of cracks for all control steels under quenched and tempered conditions. The 2¼ and 5% Cr welded steels exhibited adequate toughness in both initial and final bending tests. This is satisfactory. The welded 9% Cr steels show adequate ductility in initial bend test but failed at the fusion zone during the final bend test sequence. As expected, the welded 12% Cr steel has poor properties in weld bend response. All 12 Cr-2WV steel samples failed at the fusion zone during either the initial three point bend or the final 180° bend. Figure 9 shows the load-deflection curve for one of the 12 Cr-2WV steels which failed in the initial three point bend test. The material failed at a deflection of between 1.6 to 2.0 mm. This result suggests that the toughness and ductility are very low for the 12 Cr-2WV steel weld. Brittle failures were observed in the 9-12% Cr steel fracture surfaces as shown in Fig. 10. Both 9% Cr steels are dominated by brittle cleavage fracture with a small amount of dimple rupture at the rim around the fracture facets. A transgranular fracture mode was observed in the fracture surfaces of 12 Cr-2WV steel.

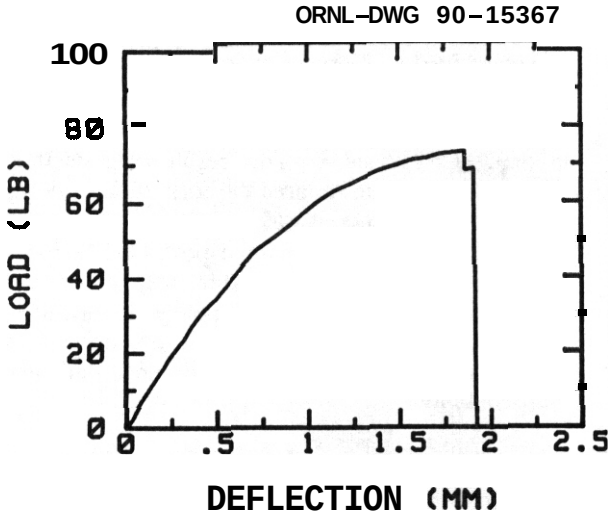

Fig. 9. Load deflection curve for the 12Cr-2WV steel during three-point bending.

Results of tensile tests are shown in Table 4. The 2¼Cr-2WV steel have both the highest ultimate tensile strength and 0.2% offset yield stress of the 24% Cr steels for both control and as welded conditions. The lowest value of strength was found in 2¼Cr-2W. This is consistent with microhardness observations. The 2¼Cr-1WV steel shows a slightly lower strength than 2¼Cr-2WV but a much greater strength than 2¼Cr-V steel. To quantify ductility, uniform elongation was used instead of the total elongation. Highly localized deformation and stretching are often observed after a major crack initiates. The highest uniform elongation is found in 2¼Cr-V steel while 2¼Cr-2WV steel appears to have the lowest ductility of the 24% Cr steels. Failures occurred either in the base metal or heat-affected zone (HAZ)/base metal interface for all 2¼% Cr steels.

The 9Cr-2WVTa steel has the highest tensile strength of all heats for both the control and welded conditions. This steel also possesses a relatively high uniform elongation. The 5 Cr-2WV steel shows the lowest values of both strength and elongation for the 5-12% Cr steels. Even though the 12 Cr-2WV steel has only slightly lower strength than the 9 Cr-2WV steels, it shows the highest ductility in uniform elongation of the 5-12% Cr steels. Base metal failures were observed for all the 5-12% Cr steels in tensile tests. It was found that the mechanical properties of these low activation femtic steels were degraded after gas tungsten arc welding. The area under the stress-strain curve, a measure of toughness, also decreased for all heats of the 5-12 Cr steels after welding while the Young's modulus remains the same.

Discussion

Experimental results show that the welds in all steels tested were free of defects. The low carbon content in all steels tested contributes to this excellent weldability. Steels with a higher carbon-equivalent will have greater hardenability and

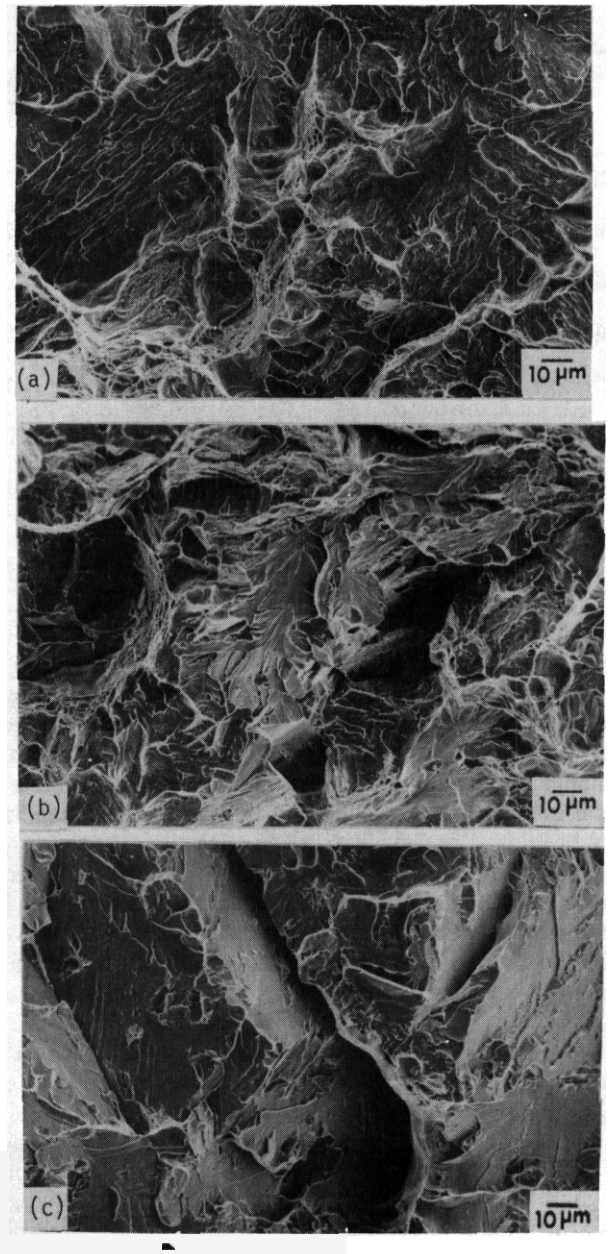

Fig. 10. SEM fracture surface photographs after bending test for (a) 9Cr-2WV steel (b) 9Cr-2WVTa steel, and (c) 12Cr-2WV steel.

therefore be more susceptible to HAZ cracking due to martensitic transformations. Results from GTA welding are satisfactory for all steels in this study, especially for the 12 Cr-2WV steel. The commercial 12 Cr-Mo steels crack extensively in the HAZ when no preheating is provided.[1] This low susceptibility to HAZ cracking is believed to be a result of the delta femte present in the microstructure of the modified alloys.

The alloying additions were found to have a significant effect on the base metal microstructure of 2¼% Cr steels. The 2¼% Cr steels are typically

Table 4. Results of Room-Temperature Tensile Test for Low Activation Ferritic Steels

Steel		Strength, MPa		Elongation, %	
		UTS	0.2% YS	Uniform	Total
2¼Cr-V	Control	516	428	7.2	18.0
	Weld	443	326	6.5	15.0
2¼Cr-1WV	Control	719	550	7.2	14.5
	Weld	686	524	5.8	8.8
2¼Cr-2W	Control	441	368	7.0	17.8
	Weld	403	330	6.9	17.6
2¼Cr-2WV	Control	727	588	6.6	11.4
	Weld	719	567	5.7	9.4
5Cr-2WV	control	806	535	7.1	13.5
	Weld	783	526	5.4	8.8
9Cr-2WV	Control	842	595	7.2	12.2
	Weld	786	572	5.7	10.5
9Cr-2WVTa	Control	874	615	8.1	11.6
	Weld	864	586	6.7	11.4
12Cr-2WV	Control	832	578	9.4	13.2
	Weld	802	556	6.4	11.2

composed of a bainitic structure. Without tungsten additions, 2¼Cr-V steel contains 8-12% proeutectoid polygonal ferrite. As tungsten is added, 2¼Cr-1WV has 5-10% polygonal ferrite and 3-8% ferrite is observed in the 2¼Cr-2WV steel. No polygonal ferrite was observed in the 2¼Cr-2W steel. This result suggests that the addition of tungsten reduces the formation of polygonal ferrite. Nevertheless, it was experimentally found that the 2¼Cr-2WV steel contained polygonal ferrite. This phenomenon probably resulted from vanadium carbides present in the steel not completely dissolving during austenitization. Vanadium carbide ties up carbon that would normally be in solution and hence decreases the hardenability.[4-10]

A martensitic structure is observed in the 5-12% Cr steels. This result implies that chromium effectively promotes martensite formation instead of bainite. The 5-9% Cr steels are fully martensite whereas the 12 Cr-2WV steel contains 12-17% δ-ferrite. The reason for the ferrite presence is insufficient austenite-stabilizing elements such as carbon, nickel and manganese. Both ferrite and austenite exist in the microstructure at the austenitizing temperature due to insufficient austenite forming elements. Austenite transforms to martensite upon cooling whereas ferrite remains as it is. This ferrite is referred to as delta-ferrite.[11,13] Unfortunately, carbon is restricted to 0.1% to ensure sound welding while nickel is not favored from a low activation point of view. Therefore, composition modification with manganese is one of the remaining choices to promote a fully martensitic structure in the 12% Cr steel.[10] On the other hand, it is known that chromium and tungsten, ferrite-stabilizers. tend to promote delta-ferrite formation.

In the 9 Cr-2WVTa steel, a finer martensitic structure is found than in the other 9 Cr steels. This is attributed to the addition of tantalum which considerably decreases the prior austenite grain size. Tantalum behaves similar to niobium in the commercial 9 Cr-Mo steels. Tantalum exists in 9 Cr-2WVTa steel in the form of carbide precipitates with a high melting point. During the austenitization process, tantalum carbide precipitates dissolve slowly or even remain in the solid form and act as pinning particles to confine grain growth. Therefore, a finer structure is obtained after solidification.

Since hardness of martensite is not sensitive to the cooling rate,[14] a comparison can be made to investigate the effect of chromium on hardenability. By comparing all the steels, it is obvious that chromium contributes greatly to hardenability. The higher the Cr content, the higher the hardness. The lower hardness in the heat-affected zone for 12 Cr-2WV steel compared to others is a result of the presence of delta ferrite. The scattering of microhardness values at the fusion zone is also attributed to the ferrite presence. Tantalum additions in the 9% Cr steels do not have much influence on the hardness but does significantly reduce the grain size hy the carbide-pinning process. The high microhardness of the fusion and heat-affected zones is attributed to untempered martensite. A very high dislocation density is a result of nonequilibrium solidification during fast cooling from high temperatures. With tempering, dislocations are recovered which alleviates the hardness and brittleness to some extent.

Results from the weld bend tests show that all 25% Cr steels have excellent ductility in the welds. No failure was observed in these steels. The microstructure of these steels consists of a bainite structure which has high strength and excellent toughness. Similar properties were obtained for the 5 Cr-2WV steel despite its martensite structure. It was found that the 5% Cr steel shows an intermediate toughness between 2t and 9% Cr content steels. This is attributed to the medium hardenability of the 5% Cr steel. The failures observed in the 9% Cr steels are inherent in welds of materials with a martensitic structure. The constituents in the fusion zone consist of untempered martensite and polygonal ferrite. The untempered martensite is hard and brittle in nature. The ductility is relatively low in the as-welded condition. Carbide precipitates will form when steels are subjected to the tempering process and thus will toughen the material.

Fusion zone failures in initial three point bend tests show that the 12 Cr-2WV steels display poor ductility in the weld region. Two reasons can be given for the deterioration of the 12% Cr steel. First, the high Cr content effectively increases the hardenability. The weld is cooled at a very high cooling rate from the melting point. The untempered martensite is hard and brittle and deformation is restricted. Second, the presence of delta ferrite reduces the toughness substantially.[15] Anderko et al. also concluded that elements which suppressed the formation of delta ferrite produced lower DBTT than elements, such as Cr, that promote delta ferrite formation.[16] The nonuniformity in structure and strength easily leads to crack formation. Fracture surfaces of the weld bend test specimens show that brittle fracture is predominant in the 9% Cr steels with a

transgranular cleavage mode. Some dimple rupture can he seen near the rim of the brittle cleavage facets in both steel fracture surfaces. This dimple structure **is** referred to as the ductile fracture mode. This is probably where the soft ferrite phase is located. The brittle fracture mode in 12Cr-2WV steel is attributed to its high hardenability and the presence of delta ferrite as discussed above.

Without vanadium addition, tempered 2¼Cr-2W steel appears to have the lowest strength hut possesses excellent ductility. Locally extensive deformation **is** observed during tensile tests after cracks initiate in the 2¼Cr-2W steel as seen in the total elongation data. Tempered 2¼Cr-V steel has a strength greater than 2¼Cr-2W steel. Extensive elongation **is** also observed for the 2¼Cr-V steel. This difference in strength suggests the V has a greater effect on improving the tensile properties than W does.

Tensile property results indicate that a large additive effect occurs in steels containing both W and V. The combined use of W and V in these steels results in high tensile strength, accompanied by excellent ductility. The 2¼Cr-1WV steel has a much greater tensile strength than both the 2¼Cr-V and 2¼Cr-2W steels but the tensile strength is slightly lower than the 2¼Cr-2WV steel. Observations reveal that coarser carbide precipitates are found in 2¼Cr-V steel and increases in W content decrease the size of carbide precipitates.'? The transformation temperature is effectively decreased by W additions and therefore finer precipitates are observed. Finely dispersed precipitates significantly impede the dislocation motion and increase the strength. However, the addition of W or V alone does not give satisfactory strength. The steel with tungsten additions, 2¼Cr-2W, has **a** coarser carbide precipitate distribution than that of steels without tungsten, 2¼Cr-V, or steels containing V, 2¼Cr-2WV. This explains why the lowest strength is found in 2¼Cr-2W steel and shows the remarkable additive effect of W and V.

The effect of chromium content on the tensile properties can he obtained by comparing the steels containing **2%** W and *0.25%* V. The tensile test results show that strength increases with increasing chromium content. However, a different result **is** presented by Klueh et al. They concluded that chromium had a nonlinear strengthening effect on these steels and showed a minimum strength in 5 Cr-2WV steel due to the coarser carbide distribution! The lower strength in the 12 Cr-2WV steel **is** attributed to the large amount of delta ferrite present in the microstructure. The presence of delta ferrite increases the nonuniformity of steel and hence the instability in deformation. However, the ductility remains adequate because of the soft ferrite. With tantalum additions, the grain size of 9 Cr-2WVTa is effectively reduced by the precipitate pinning process and strength, therefore, **is** increased.

Conclusions

From the results of this study, the following conclusions were drawn:

1. Sound autogenous welds can he achieved hy conventional gas tungsten arc welding in 21 and **5%** Cr low activation ferritic steels.
2. Post-weld heat treatment **is** necessary in the 9-12% Cr low activation steels to restore toughness.
3. Chromium, vanadium and tungsten additions strengthen **all** steels tested. V and **W** show significant additive effects.
4. Tantalum effectively refines the grain size and strengthens the steel presumably by a precipitate-pinning process.

REFERENCES

1. E. E. Bloom et al., "Low Activation Materials for Fusion Applications", Proc. of the third Topical Meetine on Fusion Reactor Materials, September 19-22, 1983, Albuquerque, New Mexico, USA, pp. 17-26.

2. R. L. Klueh and W. R. Corwin, "Impact Behavior of Cr-W Steels", J. Mater. Ener., 11, No. 2 (1989) 169-175.

3. **H.** T. Lin and B. A. Chin, "Properties of Welded Low Activation Ferritic Steels", Fusion Reactor Materials Semiannu. Proe. Rep., Mar. 31, 1987, DOE/ER/0313/2, pp. 135-150, Office of Fusion Energy.

4. R. L. Klueh and E. E. Bloom, "Alloy Development for Fast Induced-Radioactivity Decay for Fusion Reactor Applications", pp. 11-20 in ADIP Semiannu. **Proe.** Rev., Sep. 20, 1983, DOE/ER/0045/11, U. S. DOE, Office of Fusion Energy.

5. R. **L.** Klueh, 'The Development of Ferritic Steels for Fast Induced-Radioactivity Decay", ADIP Semiannu. Proe. Reo., Mar. 1986, DOE/ER/0045/16, pp. 109-113, Office of Fusion Energy.

6. R. L. Klueh, 'The Development of Ferritic Steels for Fast Induced-Radioactivity Decay", Fusion Reactor Materials Semiannu. Prog. Reo., Mar. 31, 1987, DOE/ER/0313/2, pp. 151-161, Office of Fusion Energy.

7. R. L. Klueh and P. J. Maziasz, "The Development of Ferritic Steels for Fast Induced-Radioactivity Decay", Fusion Reactor Materials Semiannu. Prog. Rep., Sep. 1987, DOE/ER/0313/3, pp. 161-169, Office of Fusion Energy.

8. R. L. Klueh, P. J. Maziasz and W. R. Corwin, "Development of Ferritic Steels for Fusion Reactor Applications", ORNL-6472, Oak Ridge National Laboratory, Oak Ridge, TN, 1988.

9. E. J. Vineberg, T. Wada, T. B. Cox and C. C. Clark, "Weldability of Duplex Structure 12Cr-(Mo,W) Steels", Conference Proceedings on Welding in /energy Related Projects, Welding Institute of Canada, 1984, pp. 235-245.

10. K. E. Thelning, Steel and its Heat Treatment, Buttenvorths, London, 1984

11. Edgar C. Bain and Harold W. Paxton, Alloying Elements in Steel, ASM, Metals Park, OHIO, 1961

12. R.W.K. Honeycombe, Steels-Microstructure and Prouerties, Edward Arnold Ltd. and ASM, Metals Park, OHIO, 1982.

13. W. W. Cias, Phase Transformation Kinetics and Hardenability of Medium-Carbon Alloy Steels. Climax Molybdenum Co., Greenwich, Conn., 1972.

14. W. C. Lesile, The Physical Metallurgy of Steels, McGraw-Hill book company, New York, 1981

15. B. A. Chin and R. C. Wilcox," The Effect of Heat Treatment on the Impact Properties of a 12Cr-1Mo-V-W Steel", Proc. of Touical Conference on Ferritic Alloys for use in Nuclear Energy Technology, TME/AIME, June 19-23,1983, Snowbird, Utah, pp.347-356.

16. K. Anderko, K. David, W. Ohly, M. Schirra, and C. Wassilew, "Optimization Work on Niobium Stabilized 12% CrMoVNb Martensitic Steels for Breeder and Fusion Reactor Applications, ibid. ref. [15], pp.299-306.

17. R.W.K. Honeycombe, Structure and Streneth of Alloy Steels, Climax Molybdenum Company, London, 1974.

6.2 Austenitic Stainless Steels

IRRADIATION EFFECTS OF GRAIN BOUNDARY CHEMISTRY OF MANGANESE STABILIZED MARTENSITIC STEELS - A. Kimura (Muroran Institute of Technology), L. A. Charlot, D. S. Gelles, D. R. Baer and R. H. Jones (Pacific Northwest Laboratory[a])

OBJECTIVE

The objective of this work is to investigate the effects of irradiation on the grain boundary chemistry of Mn stabilized reduced activation martensitic steels which exhibit irradiation-induced embrittlement and transition from transgranular cleavage to intergranular fracture.

SUMMARY

The effect of neutron irradiation (10 dpa at 638K, FFTF/MOTA) on solute segregation to the grain boundaries in reduced-activation 9Cr-1W-2Mn and 12Cr-1W-6Mn martensitic steels was investigated using Auger electron spectroscopy (AES). The AES spectrum obtained from the grain boundaries in both martensitic steels was influenced by neutron irradiation. Neutron irradiation caused marked increases in the amount of intergranular segregation of Si in 9Cr and Mn in 12Cr steel, respectively, while no significant increase in S and/or P segregations were found in either steel. Large shifts in DBTT to high temperatures caused by neutron irradiation observed in these two martensitic steels are interpreted in terms of site competition between C and Si resulting from irradiation-induced/enhanced segregation of Si in 9Cr steel and weakening of grain boundary strength by irradiation-induced/enhanced segregation of Mn in 12Cr steels, respectively.

PROGRESS AND STATUS

Introduction

Martensitic steels are being considered as structural materials for fusion first wall application in part because of better swelling and creep resistance properties than austenitic steels in the temperature range between 400 to 600°C. However, the low temperature toughness of martensitic steels such as 9Cr-1W-2Mn steel and 12Cr-1W-6Mn steel showed marked increases in ductile-brittle transition temperature (DBTT) following neutron irradiation up to only about 10 dpa in FFTF/MOTA.[1] Although it has been reported that the increase in DBTT was directly related to the amount of Mn in steels (namely, an increase in Mn concentration caused the proportional increase in irradiation induced shifts in DBTT[2]) the mechanism is still unclear. A transmission electron microscopy (TEM) study of manganese-stabilized 12Cr-1Mo martensitic steel irradiated up to 10 dpa at 800K in FFTF/MOTA suggested that chi-phase at grain boundaries might cause the intergranular embrittlement.[3] However, the cause of preferential formation of chi-phase at grain boundaries is still unknown. In his AES study, Kameda reported that neutron irradiation caused the intergranular segregation of S and/or P in iron.[4]

The report describes the results of AES work showing the irradiation-induced changes in grain boundary chemistry and proposes the mechanism of irradiation-induced intergranular embrittlement of Mn-stabilized reduced activation martensitic steels.

Exoerimental Details

The materials used were reduced-activation 9Cr-1W-2Mn (L8-VO2268-WHC/PNL) and 12Cr-1W-6Mn (L9-VO2269-WHC/PNL) martensitic steels. Notched plate specimens (12 x 2.5 x 5 mm^3) were broken at temperatures ranging from 110 to 150K in the vacuum (3 x 10^{-10} Torr) chamber of the AES, both before and after irradiation in FFTF/MOTA to a nominal fluence of 3 x 10^{22} n/cm^2 or 10 dpa at 638K, . In order to obtain an intergranular fracture surface on unirradiated specimens, specimens were cathodically charged with hydrogen[5] at room temperature for 16 hr in 1N sulfuric acid solution doped with a small amount of arsenic trioxide. To prevent escape of hydrogen, the hydrogen-charged specimens were kept in liquid nitrogen until AES tests were carried out. AES analyses were performed on selected areas of individual grain facets on the fractured surface with a primary beam size of 0.1 μm operated at 3 keV and 10 keV. Auger signal peak heights of several elements such as Si-92, P-120, S-152, Mn-589, Mn-636 and Fe-703 were measured by setting a window in a specific energy range for each element.

(a) Pacific Northwest Laboratory is operated for the U.S. Department of Energy by Battelle Memorial Institute under Contract DE-AC06-76RLO 1830.

Results and Discussion

Scanning electron micrographs on the fracture surface of irradiated (a and c) and unirradiated but hydrogen-charged (b and d) 9Cr and 12Cr steel are shown in Figures 1 and 2 respectively. Although both materials fracture in the transgranular cleavage mode before irradiation,[6] both neutron irradiation and hydrogen charging promoted intergranular cracking, which allows the grain boundary chemistry to be compared for both the unirradiated and irradiated conditions. Typical examples of Auger spectra obtained from smooth grain boundary facets in unirradiated and irradiated 9Cr and 12Cr steel are shown in Figures 3 and 4, respectively. As clearly shown in these figures, a marked enrichment of Si in 9Cr steel and Mn in 12Cr steel was induced by neutron irradiation, while no significant increase in P and/or S segregation was observed. The nitrogen peak in the Auger spectrum of irradiated 12Cr steel comes from the adhesive used to keep the two halves of the sample attached following fracture in the AES. No adhesive was used for 9 Cr steel. Results were obtained on selected area AES analyses for segregated Si, P, S and Mn on individual grain boundary facets of these two materials. The histograms plotted from 20-32 data points (individual grain boundary facets) represent the variation of solute segregation from facet to facet. In both materials, little significant effect of irradiation on segregation behavior of P and S was observed. However, the Si histogram in 9Cr steel (Figure 5) and the Mn histogram in 12Cr steel (Figure 6) were influenced markedly by neutron irradiation; irradiation induced/enhanced intergranular segregation of Si in 9Cr steel and Mn in 12Cr steel is apparent. However, no direct evidence was obtained from AES data as to whether Si and Mn were in the elemental form at the grain boundaries.

The following mechanisms are considered: 1) segregation of Si in elemental form decreases the grain boundary strength; 2) segregation of Si in elemental form enhances formation of Laves phase, which may cause intergranular embrittlement; 3) Si compounds such as SiO_2 at grain boundaries cause the embrittlement.

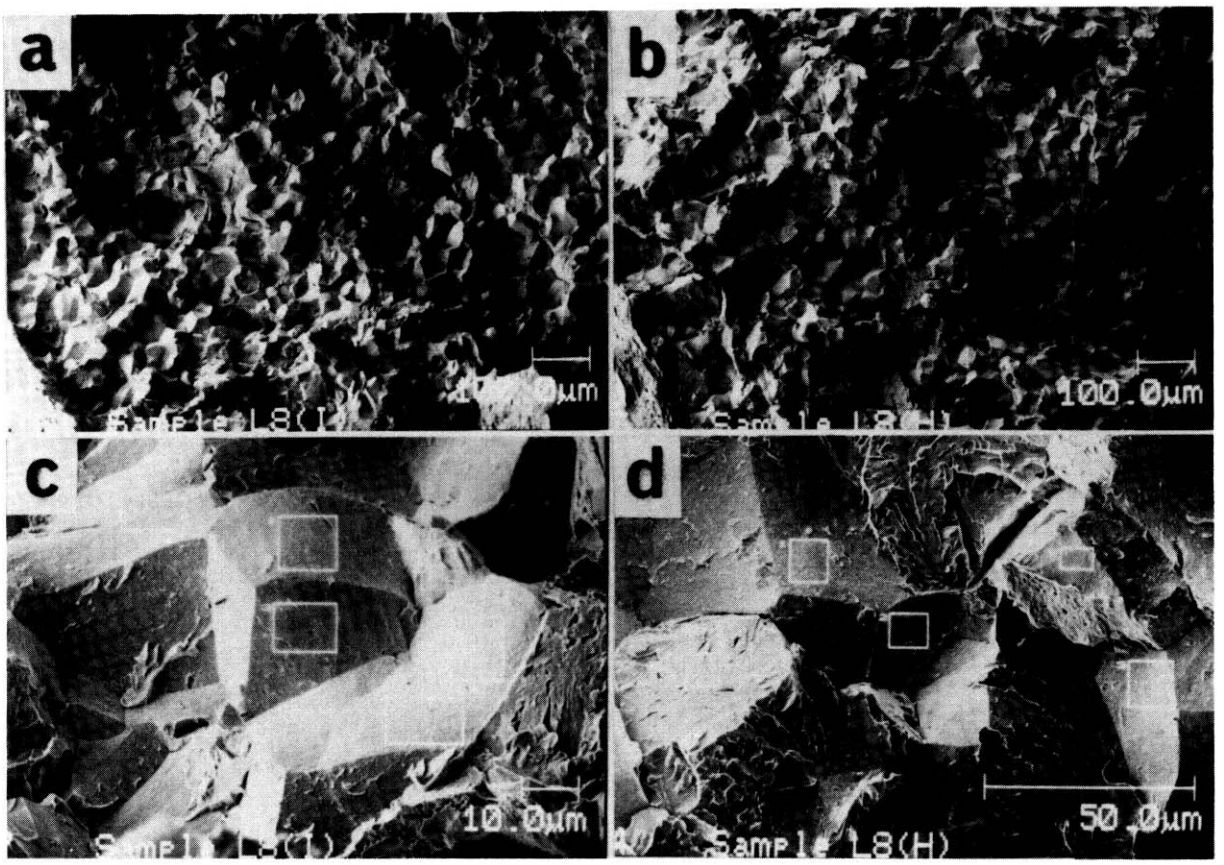

Figure 1. Scanning electron photographs of fracture surfaces of neutron-irradiated (a and c) and unirradiated but hydrogen charged (b and d) 12Cr-1W-6Mn steel. The squares in c and d define selected area analysis zones.

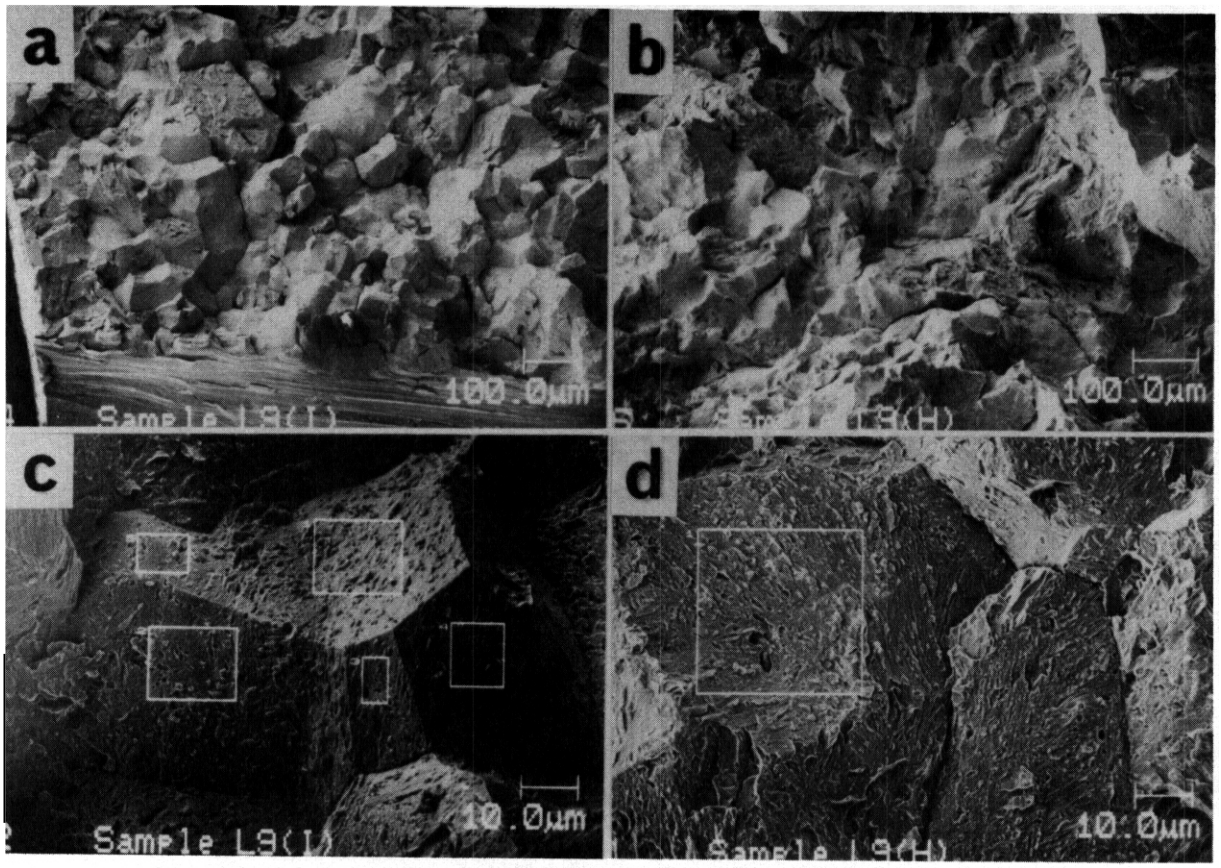

Figure 2. Scanning electron photographs of fracture surfaces of neutron-irradiated (a and c) and unirradiated but hydrogen charged (b and d) 9Cr-1W-2Mn steel.

It is well known that an increase in Si concentration in steel causes a shift of DBTT to high temperature brittle transgranular cleavage fracture. This shift has been interpreted in terms of an increase in the general yield stress caused by solid solution hardening by Si. More recently, it has been revealed that an addition of Si caused the enhancement of intergranular segregation of boron and carbon by repulsive interaction, resulting in a change in fracture mode from intergranular cracking to transgranular cleavage fracture.[6] Thus, the effect of Si in solid solution on the intergranular fracture toughness is beneficial rather than detrimental. However, it is also expected that Si at grain boundaries results in a decrease in carbon segregation at the grain boundary (site competition) and causes intergranular cracking. It has been reported that Laves phase (Fe_2W) was observed in both irradiated and unirradiated 8-9Cr-W steels.[7-9] The nucleation rate of Laves phase in 9Cr-1Mo steel (Fe_2Mo) was reported to be markedly influenced by an addition of Si; Laves phase nucleated two orders of magnitude faster in 0.7Si steel than in 0.01Si steel. Although it is unknown whether Si interacts in the same manner with W as with Mo, it is possible that Si segregation enhances the preferential formation of Laves phase at grain boundaries. However, no significant increase in the segregation of W was observed in the irradiated specimen. According to the previous TEM observation, some SiO particles were observed in irradiated 9Cr-0.5V containing 0.3Si steel. As the steel used in this work contains 0.1Si, it is expected that the Si peaks observed on the grain boundaries in irradiated 9Cr-1W steel came from the SiO_2 particles. However, the Si peak usually shifts to lower energy (less than 80 eV) when Si is present in the form of SiO_2. So it is not likely that Si is present as SiO_2. Thus, only the site competition mechanism is likely in 9Cr-1W-2Mn steel.

An increase in Mn segregation in elemental form may explain the irradiation-induced increase in DBTT of 12Cr-1W-6Mn steel. The addition of Mn has been reported to have two effects with regard to temper embrittlement. One effect is due to its interaction with phosphorus: 1) Mn accelerates the diffusion of P to the boundaries" and 2) P segregation promotes Mn segregation." Another is due to Mn itself, which is a potent element for intergranular embrittlement.[12] In this study, little increase in P segregation was observed in the irradiated 12Cr steel, suggesting that Mn by itself is a potent embrittling element. Another

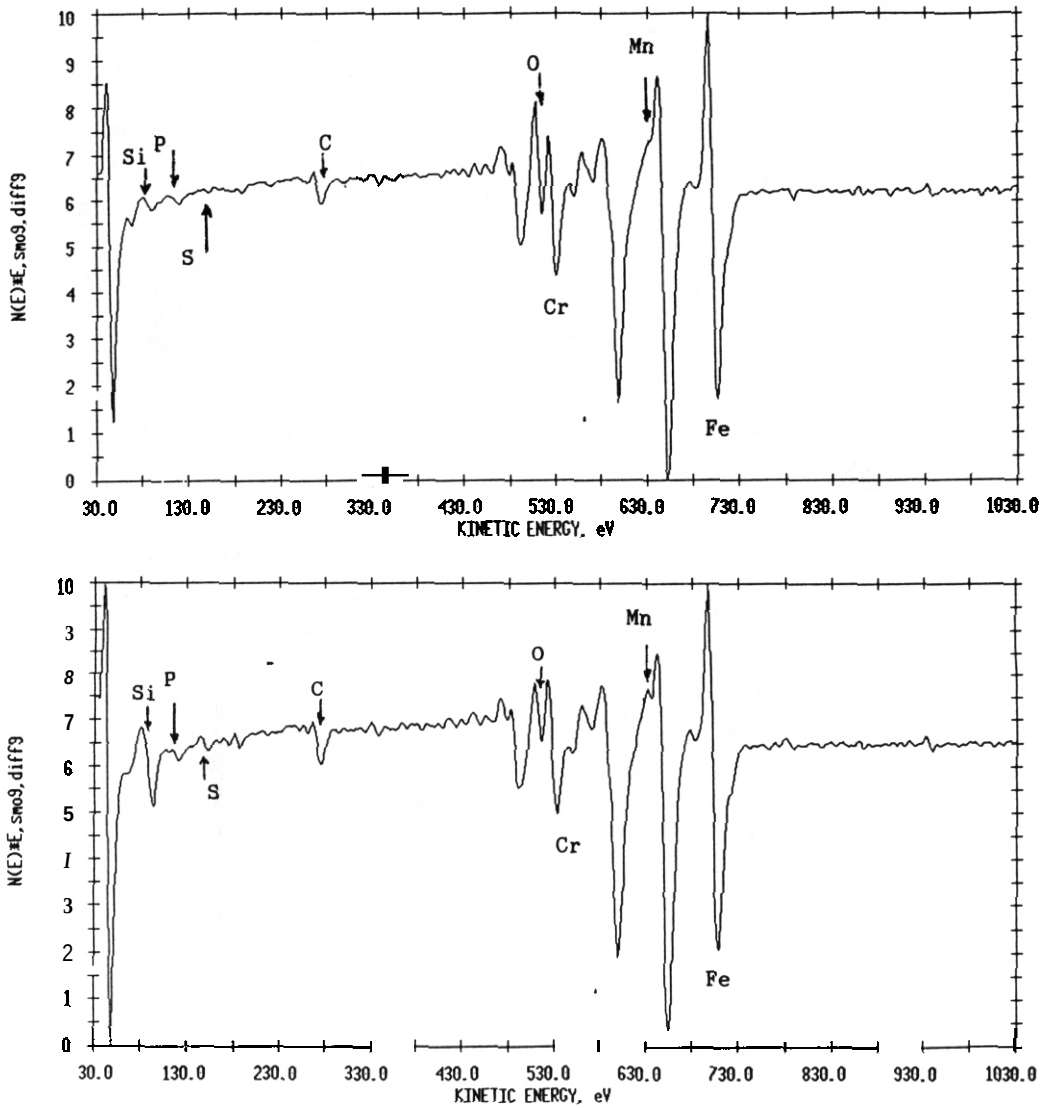

Figure 3. Typical Auger spectra of unirradiated [top] and irradiated (bottom) 9Cr-1W-2Mn steel

possibility is that segregated Mn enhances the formation of chi-phase at the grain boundaries,[3] which may cause intergranular embrittlement.

CONCLUSION

The mechanism of neutron irradiation-induced embrittlement accompanied by the transition in the fracture mode from transgranular cleavage to intergranular clacking was investigated by means of the chemical analysis on the intergranular fracture surfaces using high spatial resolution AES. AES analysis for grain boundary chemistry of both irradiated and unirradiated specimens revealed that irradiation (10 dpa) induced/enhanced intergranular Si and Mn segregation in 9Cr-1W-2Mn and 12Cr-1W-6Mn steel. It is proposed that intergranular segregation of Si decreases C segregation at grain boundaries by site competition mechanism (repulsive interaction), resulting in the intergranular embrittlement of 9Cr-1W-2Mn steel. In 12Cr-1W-6Mn steel, it is proposed that the segregation of Mn reduced the grain boundary strength in elemental form and/or by formation of chi-phase preferentially at grain boundaries.

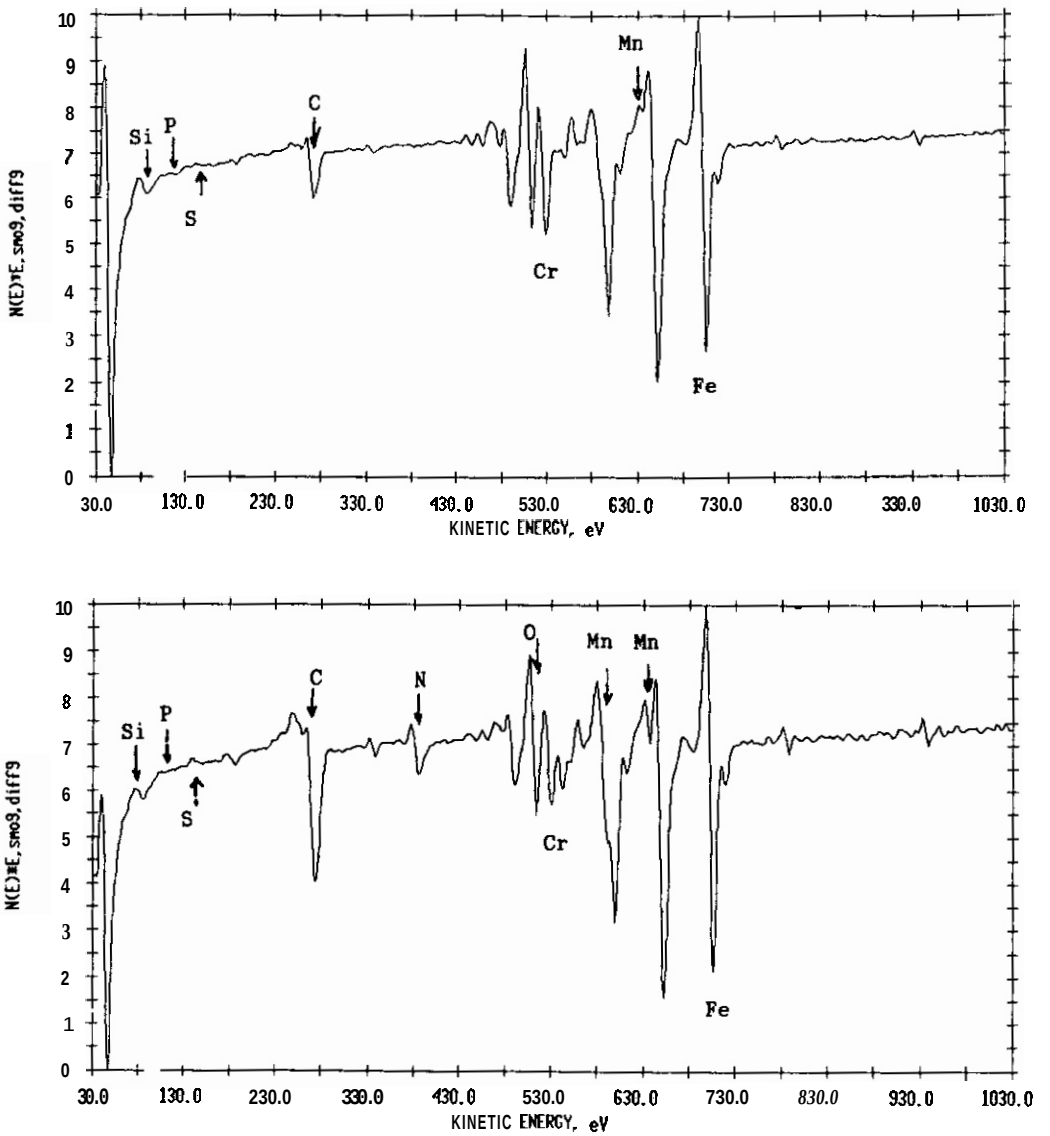

Figure 4. Typical Auger spectra of unirradiated (top) and irradiated (bottom) 12Cr-1W-6Mn steel

FUTURE WORK

In order to clarify the effects of Mn additions on the grain boundary toughness in 12Cr steel, further AES and x-ray photoelectron spectroscopy work should be performed on the materials doped with different concentrations of Mn.

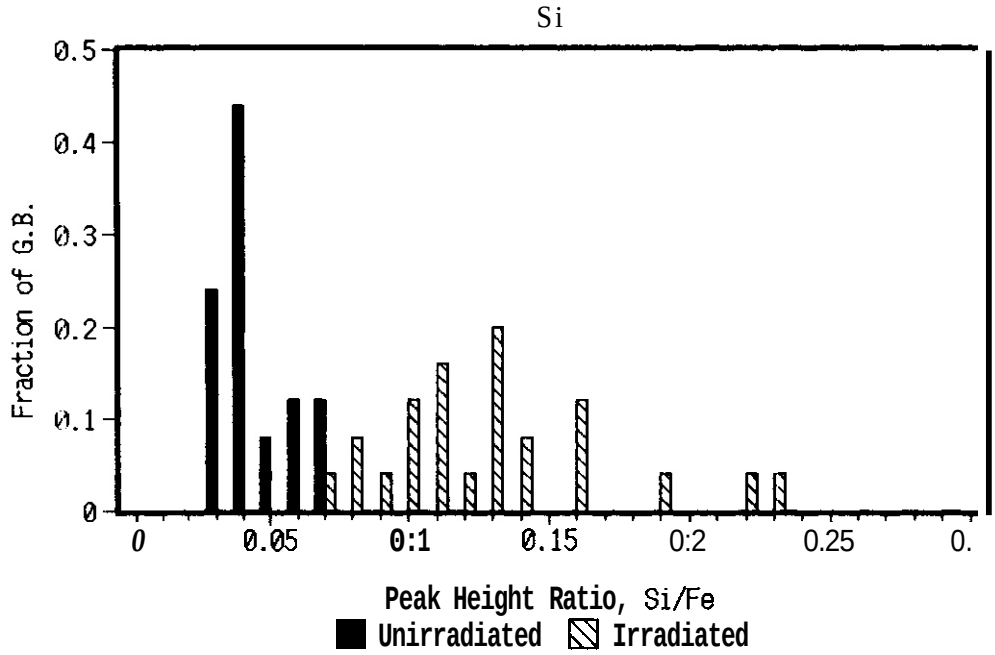

Figure 5. Distribution of intergranular segregation of Si in unirradiated and irradiated 9Cr-1W-2Mn steel.

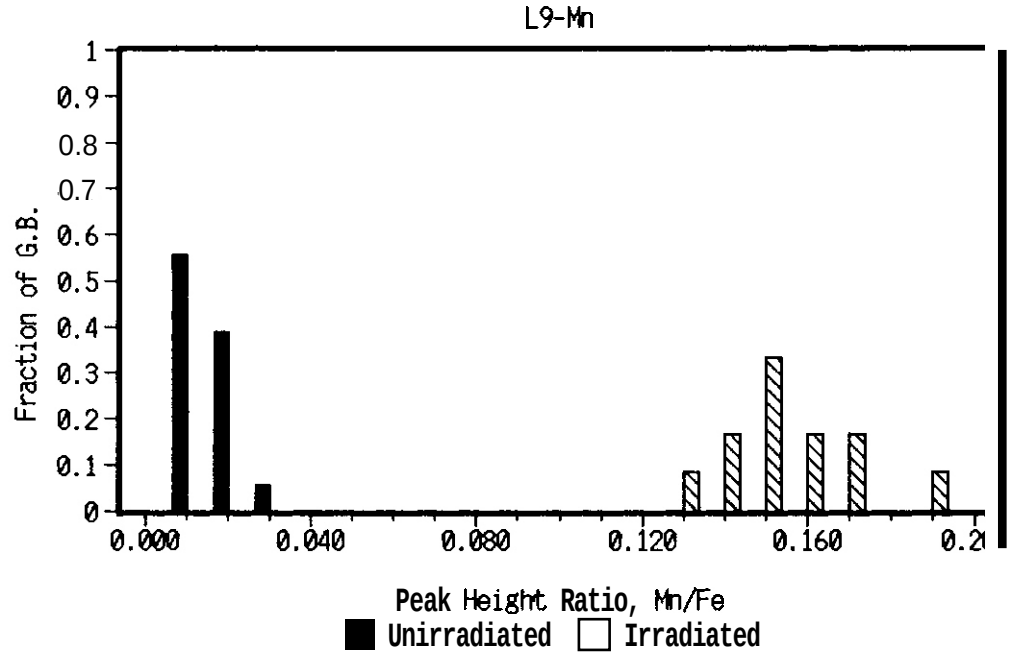

Figure 6. Distribution of intergranular segregation of Mn in unirradiated and irradiated 12Cr-1W-6Mn steel

REFERENCES

1. D. S. Gelles and N. S. Cannon, Fusion Reactor Materials DOE/ER-0313/4 March (1988) 95.

2. N. S. Cannon and D. S. Gelles, 4th International Conference on Fusion Reactor Materials (ICFRM-4) (1989), Kyoto, Japan.

3. D. S. Gelles and W. L. Hu, Fusion Reactor Materials DOE/ER-0313/1 September (1986) 242.

4. J. Kameda and A. J. Bevolo, Acta Met., 37 (No. 12) (1989) 3283.

5. A. A. Kimura, H. Kayano and M. Narui, ICFRM-4 (1989), Kyoto, Japan.

6. H. Kimura, unpublished research

7. F. Abe, H. Araki, T. Noda and M. Okada, J. of Nucl. Mater., 155-157 (1988) 656.

8. M. Tamura, H. Hayakawa, A. Yoshitake, A. Hishinuma and T. Kondou, J. of Nucl. Mater., 155-157 (1988) 620.

9. D. S. Gelles Fusion Reactor Materials, DOE/ER-0313/4 March (1988) 78.

10. H. J. Grabke, K. Hennesen, R. Moller and W. Wei, Scripta Met., 21 (1987) 1329.

11. C. J. McMahon, Jr., W. Yu-qing, M. J. Morgan and M. Menyard, Grain Boundary Structure and Related Phenomena, Proceedings of JIMIS-4 (1986), Suppl. to Trans. of the Japan Inst. of Metals, 27 (1986) 383.

12. W. Yu-qing and C. J. McMahon, Jr., ibid, 27 (1986) 579,

SWELLING BEHAVIOR OF AUSTENITIC STAINLESS STEELS IRRADIATED AT 400°C IN ORR MFE-7J CAPSULE BY SPECTRALLY TAILORED NEUTRONS — T. Sawai [Japan Atomic Energy Research Establishment (JAERI)], H. Kanazawa (JAERI), P. J. Maziasz (Oak Ridge National Laboratory), and A. Hishinuma (JAERI)

OBJECTIVE

The objective of this work is to evaluate the swelling susceptibility of various Japanese austenitic stainless steels, including weld specimens, in an irradiation environment with a fusion-relevant He:dpa ratio.

SUMMARY

Several Japanese austenitic stainless steels, including specimens taken from the electron beam (EB) welds, have been irradiated in the Oak Ridge Research Reactor (ORR) in special spectrally tailored experiments. The first batch of specimens have been retrieved at the damage level of 7.4 dpa and helium level of 102 appm in a type 316 stainless steel, and 130 appm He in JPCA with 16 wt % Ni. This irradiation produced significant alloy-to-alloy differences in swelling at 400°C. One low-carbon steel and an experimental ternary alloy have shown higher values of swelling. Irradiation in HFIR of the same set of alloys caused very high levels of void swelling only at 500°C and above. Metallurgical efforts to suppress such swelling (i.e., cold working and/or increased carbon level) were effective at this temperature range. The present results suggest that appropriate care also needs to be taken for the fusion application of this kind of alloy at lower temperatures like 400°C. Welds in this experiment showed no measurable degradation in swelling resistance compared to their base metals.

PROGRESS AND STATUS

Introduction

Austenitic stainless steels are one of the most promising candidates for use as structural materials for fusion reactors. The relatively high susceptibility to void swelling is, however, among the problems anticipated in its fusion application. Because of the lack of fusion-relevant irradiation data, swelling behavior of austenitic stainless steels has been studied using various kinds of irradiation facilities. The advantage of mixed-spectrum fission reactors for irradiation of austenitic stainless steel is that neutrons can simultaneously produce helium and displacement, similar to the effect that 14 MeV fusion neutrons will have on all types of material. In mixed-spectrum fission reactors, the two-step transmutation of ^{58}Ni by thermal neutrons' is employed to generate helium. Helium is generated from ^{59}Ni which is only available from the neutron absorption of ^{58}Ni. Therefore, helium production rate is relatively low at the initial stage of irradiation as the amount of ^{59}Ni builds up from transmutation reactions. Beyond a certain dose, ^{59}Ni is abundant and helium generation becomes quite high. Spectral tailoring is a method of controlling this natural nonlinearity in He:dpa ratios and keeping the He:dpa ratio approximately linear and close to a fusion-relevant level during the course of the irradiation. The ratio of thermal and fast neutrons is changed during irradiation by introducing material around the experiment subassembly that absorbs thermal neutrons, thus hardening the neutron energy spectrum.

Although there is good evidence that the co-generated helium affects the microstructural evolution under irradiation, the quantitative effect of constant irradiation near the fusion He:dpa on void swelling has been only recently demonstrated.[2] At low He:dpa ratios, void swelling is increased by helium assisting void nucleation, while when the He:dpa ratio is too high, void swelling decreases because too many helium bubbles act as the dominant point defect sinks.[3,4]

ORR irradiation using spectrally tailored neutrons is one of the three irradiation programs being conducted by the U.S./Japan collaborative research program between ORNL and JAERI. Japanese specimens loaded into ORR capules have two major characteristics. First, they have a wide variety of heats of austenitic stainless steels with varying composition. They include JPCA, 316R, 316W, C, K, and HP heats of austenitic stainless steels or alloys. JPCA, 316R, C, and K alloys were included in the previous HFIR phase I irradiation experiments of the collaborative program. Second, the Japanese ORR matrix includes welded specimens, which are also a major objective of the Japanese test matrix in the HFIR phase II irradiation program. The postirradiation examination (PIE) of welds of JPCA and 316W has been already completed and reported.[5] Further details on specimen loading and objectives are given elsewhere.[6]

This is a report on the transmission electron microscopy (TEM) of the first specimens retrieved from spectral tailoring ORR experiment. Duplicate specimens irradiated in ORR will be further irradiated in the spectrally tailored HFIR RB* positions.

Experimental procedure

Metallurgical Variables

Transmission electron microscopy disks of six different austenitic stainless steels were included in the ORR-MFE-7J capsule. They are JPCA, 316W, 316R, C, K heats of steel and the HP alloy. Chemical compositions of materials used are given in Table 1, thermal and mechanical treatment in Table 2. JPCA is a Japanese version of the primary candidate alloy for fusion application with slightly higher B and P levels than the U.S. counterpart, and is expected to be highly swelling resistant. 316R is a standard type 316 steel. Two low-carbon stainless steels, C and K, are Ti and/or Nb modified exploratory alloys selected for water-cooled systems, with special consideration given to their corrosion resistance in water. 316W is slightly modified for swelling resistance and welded specimens were included; HP is an experimental high-purity alloy. Specimens are also made from the EB weld portions of JPCA and 316W material. Details of these weld and specimen preparation are given elsewhere.' TEM specimens were loaded into tubes and the entire loading matrix of this experiment is already reported with a detailed description of their objectives.[6]

Table 1. Chemical compositions of used materials

	C	Si	Mn	P	S	Ni	Cr	Mo	Nb	Ti	B	N
JPCA	0.06	0.50	1.77	0.027	0.005	15.6	14.2	2.3	--	0.24	.0031	.0039
316R	0.06	0.61	1.80	0.028	0.003	13.5	16.8	2.5	--	0.005	--	--
316W	0.06	0.75	1.5	0.020	0.004	16.4	13.9	2.3	0.06	0.08	--	,0084
C	0.02	0.51	1.56	0.017	0.007	15.6	15.4	2.4	0.08	0.25	--	,0018
K	0.02	0.48	1.46	0.015	0.005	17.6	18.0	2.6	--	0.29	--	,004
HP	.005	.005	--	--	--	11.8	17.1	--	--	--	--	.020

JPCA	PS2	1100 C SA	C	CS1	1100 C SA
	PC1	PS2 t 10% CW		CC1	CS1 t 20% CW
316R	SS1	1050 C SA	K	KS1	1050 C SA
	SC1	SS1 + 20% CW		KC1	KS1 + 20% CW
316W	SW	1050 C SA	HP	HP1	1200 C SA

Irradiation Parameters

Irradiation of the ORR-MFE-6J/7J experiments began in April 1985, with the corepiece filled with water. The accumulated irradiation with this core configuration was 389.8 full-power-days (FPD) at 30 MW (ref. 8). On December 6, 1986, the irradiation spectrum was tailored by replacing the hollow aluminum core piece with a solid aluminum one. This phase of the experiment was terminated on March 26, 1987, accumulating total irradiation of 474.7 FPD at 30 MW (ref. 9). The average dpa rate was 5.91 dpa per full-power year by the initial softer spectrum and 7.16 dpa per full-power year by the harder one.[9] The total damage level was estimated to be 8.0 dpa (ref. 9) by neutronics analysis, and the actual analysis of dosimetry wires showed a slightly lower value of 7.4 dpa at the location of maximum neutron fluence (close to the middle of the experiment).[10] Dosimetry indicated that type 316 stainless steel with 12 to 13 wt % Ni contained about 70 appm He, and that JPCA with about 16 wt % Ni contained about 130 appm He.

PIE and Specimen Status

Two TEM disk tubes were retrieved from the 400°C portion of ORR-MFE-7J capsule at this irradiation level, tubes J7 and J9. Immersion densitometry" was first carried out for selected disks, with some control (unirradiated) disks. For the first time in this collaboration, one of the Japanese assignees (H. Kanazawa) observed the measurements and carefully monitored the condition of the densitometer. Measurement was rerun whenever the densitometer showed less stability.

To prepare irradiated TEM foils, disks were electropolished using a modified Tenupol jet polishing system. The polishing conditions are given in Table 3. Seventeen irradiated disks have been electropolished so far, and identification numbers for these are listed in Table 4. This table also includes a qualitative description of their polishing conditions and film numbers. As shown in Table 4, one specimen (0813 of SA-JPCA) remains to be examined. An analytical electron microscope (AEM), JEM-2000FX, operated at 200 kV was used for the microstructural observation. Most radioactive specimens are routinely examined in a single tilt holder for easier loading and less radiation exposure to the researcher; while this does limit selection of diffracting conditions for imaging, usually g_{111} or g_{200} orientations are easy to obtain.

Table 3. Electropolishing conditions for the Tenupol

Electrolyte	CH_3CH_2OH (7 vol) + H_2SO_4 (1 vol)
Temperature	−15°C
Voltage	-14 V
Current	140 mA
Flow Rate	1

Two more TEM tubes irradiated at 330°C were also retrieved from the ORR-MFE-7J experiment. They were tubes J1 and J3. The swelling at 330°C is expected to be less than at 400°C, and it could be still less than the detection limit of the Precision Densitometer [0.1% (ref. 12)]. These specimens are currently being examined by TEM. Several specimens from both 400°C and 330°C are being used for Electrochemical Potentiokinetic Reactivation (EPR) tests.[13] These activities are currently in progress, so results are not included in this report.

ALLOY	CONDITION	NAME	ID#	POLISH	NEGA #
JPCA	SA 1100 C	PS2	OB11 OB13	A ? ')	J16478-87
	PS2 + CH 20%	PC3	OF12 OF13	X ◎	no nega. J16941-72
C	SA 1100 C	CS1	OG13	◎	J16439-77
	SA + CW 20%	CC1	OH11	○	J16656-72
K	SA 1050 C	KS1	OT12	◎	J16398-738
	SA + CW 20%	KC1	OJ12	△	J16488-503
316R	SA 1050 C	SS1	OK14	◎	516172-221
	SA + CW 20%	SC1	OL11	◎	J16234-62
HP	SA 1200 C	HP1	TXZZ	◎	J16348-97
316W	base metal	SW1	RQ08	Θ	J15611-65 516923-40
	weld metal	SW4	RS56 RS57	A A	J15839-63 J15265-80
JPCA	bare metal	PW1	RT10	O	J15476-501
	weld metal	PH4	RU56 RU60	A A	J15864-92 J15419-74

Results

The immersion densitometry data are given in Table 5. The swelling values of base metals are summarized in Fig. 1. Cold work (CW) has effectively suppressed void swelling in all alloys relative to the solution annealed (SA) condition. In the SA condition, the base metals showed differences in their swelling resistance related to differences in alloy composition. The highest swelling value of 0.7% was obtained for the HP alloy, while JPCA showed good swelling resistance even in the SA condition. The two base metals used in the weld effects experiment were sufficiently resistant to swelling that no measurable swelling was detected by densitometry. Moreover, the welding did not degrade their swelling resistance within the detection limits of the densitometry data.

Microstructural observations were consistent with the densitometry results. Few fine cavities were observed in CW materials, which produces very little measurable swelling. In six SA alloys, however, cavity formation was different, as shown in Fig. 2. The size distributions of these cavities are given in Fig. 3, showing a typical bi-modal distribution. The cavity statistics of the SA alloys are shown in Fig. 4, with those after HFIR irradiation to 33 dpa at 400°C (refs. 14,15). The averaged swelling values of immersion densitometry are also included in this figure. The swelling values of TEM and immersion densitometry show quantitatively good agreement. In the case of SA JPCA and SA 316W, where immersion densitometry could not detect measurable swelling, the swelling values obtained from TEM were less than 0.1%, below the detection limit of the densitometer. The highest swelling values were observed for HP and K alloys. The swelling behavior and TEM disks of these alloys varied so much that the ratio of highest and lowest swelling values exceeds 10.

Precipitates of MC type were also observed in titanium-containing alloys (JPCA, 316W, C, K), using Moire' fringes obtained with dynamical contrast imaging conditions (Fig. 5). MC precipitates were Observed both in SA material and CW material, but the specimen of CW alloy K was not suitable for MC imaging. Although no quantitative analysis of MC precipitates was done, it could be easily seen in the micrographs that alloy C contained much more precipitation than either PCA or alloy K.

Microstructural observation of weld specimens[5] did not show any degradation of swelling resistance in JPCA or 316W relative to the base metal behavior. The cavity formation in weld metals was quite similar to their base metals, and no heterogeneous cavity formation was observed. The cellular dislocation/subcell structure present in the as-welded metal remained after irradiation.

Table 5. Results of immersion densitometry

Base metals of austenitic stainless steels

ALLOY	H. ID	H. DEN	C. ID	C. DEN	AV. C	SWELL
PS1	OA13 OA12	7.9057 7.9039	A17	7.9166 7.9178	7.9172	0.15 0.17
PS2	OB1: OB1·	7.9224 7.9132	OBX1	7.9159	7.9159	-0.08 0.03
PS3	OC12 OC15	7.9167 7.9175	C17	7.9186 7.9171	7.9179	0.02 0.01
PC1	OD12 OD14	7.9178 7.9257	D29	7.9157 MISSIN	7.9157	-0.03 -0.13
PC3	OF11 OF15	7.9150 7.9184	F29	7.9144 7.9142 7.9162	7.9149	0.00 -0.04
PA1	OM11 OM14	7.9160 7.9128	M29	7.9206 7.9262	7.9234	0.09 0.13
SS1	OK15 OK13	7.8788 7.8761	OKX1	7.8877 7.8897	7.8887	0.13 0.16
SC1	OL14 OL15	7.8899 7.8957	L29	7.8966 7.8940	7.8953	0.06 -0.01
CS1	OG13 OG15	7.9044 7.8986	OGX1	7.9125 7.9163	7.9144	0.13 0.19
CC1	OH11 OH15	7.9308 7.9268	H12	7.9140 7.9203	7.9172	-0.17 -0.12
CS1	OT12 OT13	7.8647 7.8681	T30	7.9037 7.9111	7.9074	0.54 0.50
C1	OJ12 OJ14	7.9047 7.9035	J15	7.9000 7.9016	7.9008	-0.05 -0.03
N1	TX12 TX11	7.8753 7.8115	TX96	7.9015 7.8952	7.8984	0.29 0.34
P1	TX22 TX23 TX25	7.8396 7.8607 1.8347	TXX1	7.9032 7.9013	7.9023	0.80 0.53 0.86

Weld joints of austenitic stainless steels

ALLOY	H. IO	H. DEN	C. ID	C. DEN	AV. C	SWELL
SW1	RQ09 RQ10	7.8792 7.8769	RQ22	7.8805 7.8866	1.8836	0.06 0.09
SW2	RQ56 RQ60	7.8847 7.8862	RQX1	1.8873 7.8818	7.8876	0.04 0.02
SW3	RS06 RS07	7.8829 7.8895	RS21	7.8886 7.8828	7.8857	0.04 -0.05
SW4	RS59 RS61	7.8871 7.8715	RUX1	7.8877 7.8932	7.8905	0.04 0.24
PW1	RT06 RT07 RT08	7.9215 7.9168 7.9182	RT22	7.9203 7.9131	7.9167	-0.06 0.00 -0.02
PW2	RT57 RT59	7.9159 7.9171	RTX1	7.9216	7.9216	0.07 0.06
PW3	RU06 RU07	7.9213 7.9138	RU24	7.9196 7.9218	7.9207	-0.01 0.09
PW4	RU58 RU59	7.9215 MISSIN	RU74	7.9157 7.9237	7.9197	-0.02

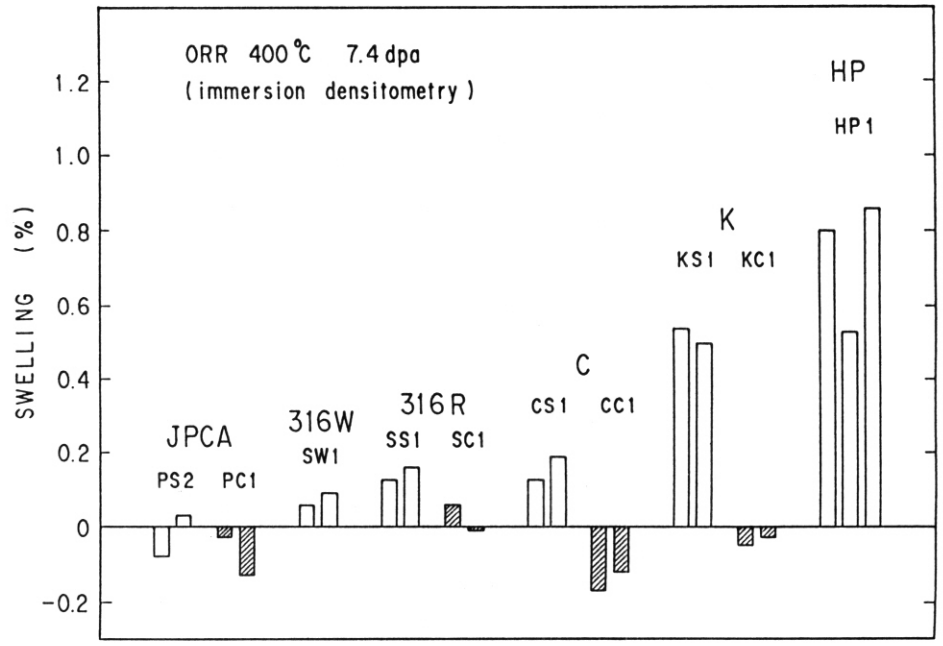

Fig. 1. Void swelling of various austenitic stainless steels measured by immersion densitometry.

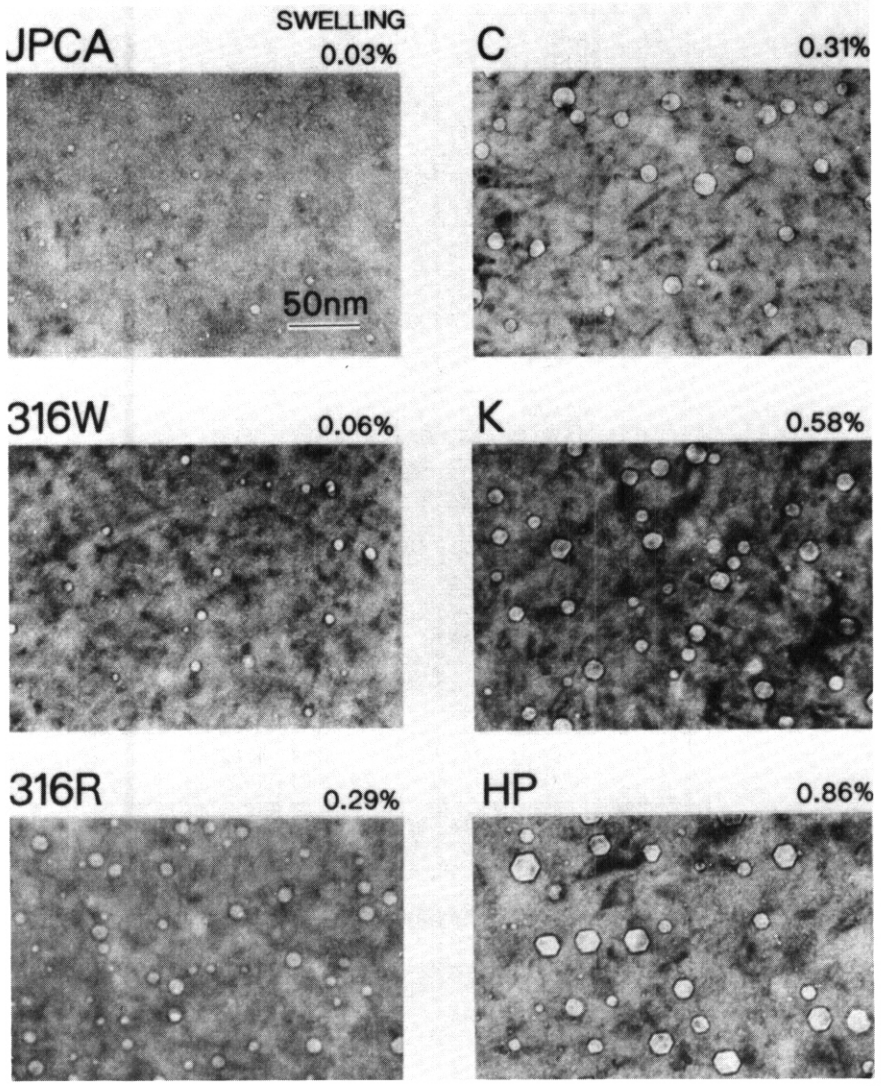

Fig. 2. Cavity microstructure of solution annealed alloys and cavity swelling by microscopy.

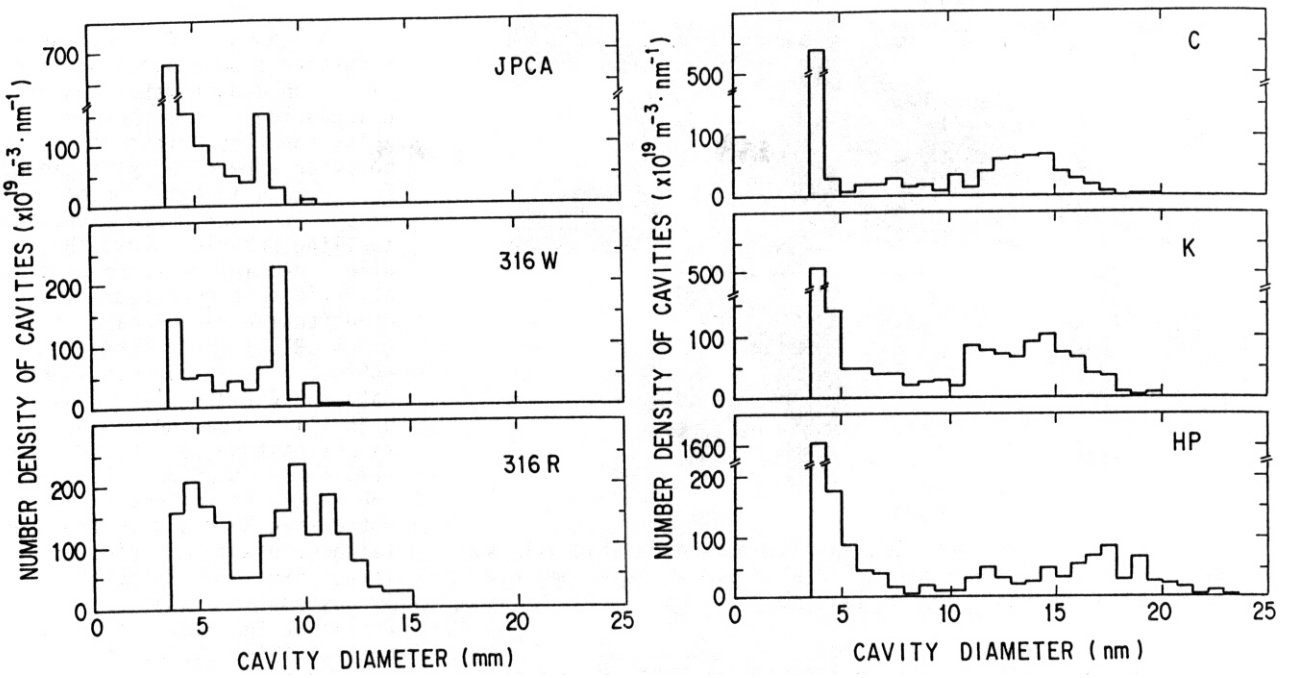

Fig. 3. Cavity size distribution of solution annealed alloys.

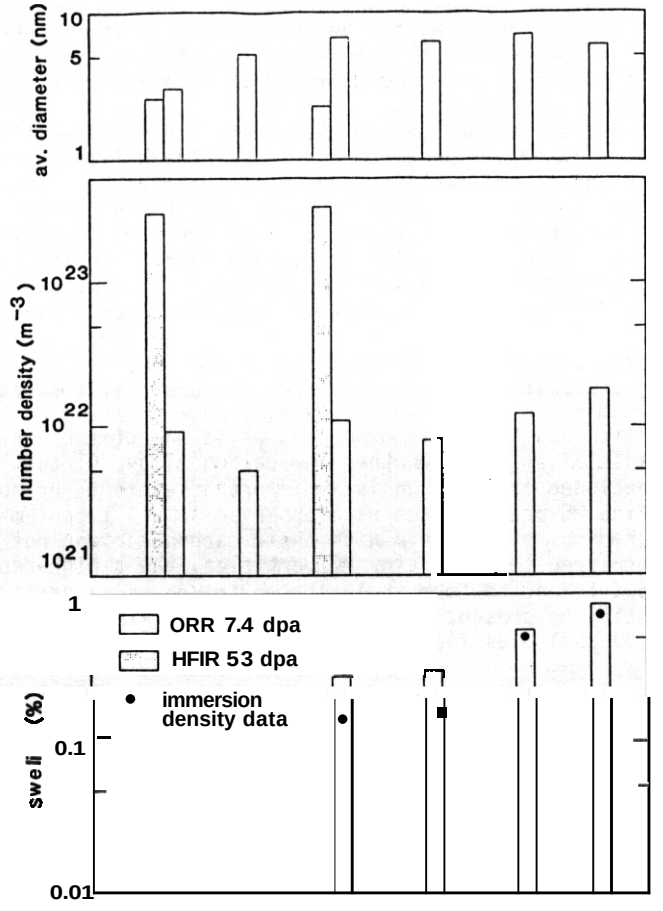

Fig. 4. Cavity statistics of solution annealed alloys. This figure includes also that of HFIR irradiation [33 dpa, 400°C (refs. 13, 14)] and swelling values observed by imnersion densitometry.

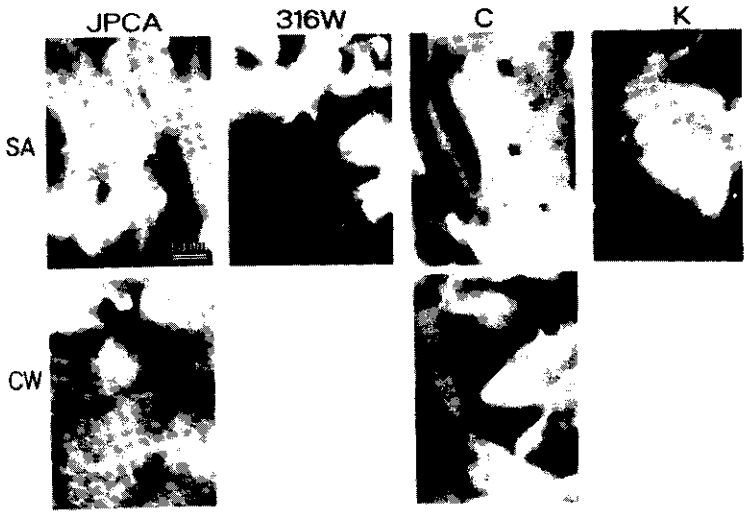

Fig. 5. MC precipitates in titanium-containing alloys. Specimen of CW 316W was not irradiated and the specimen of CW K was not suitable for MC imaging.

DISCUSSION

As shown in Fig. 4, the swelling behavior of SA materials observed in immersion densitometry and microstructural observation coincides very well. Marked alloy-to-alloy differences in swelling behavior were clearly distinguished. During HFIR irradiation of the same set of alloys, the temperature dependence of swelling behavior shows that a substantial alloy-to-alloy difference is only observed at 500°C or higher temperature.[14-16] The quantitative cavity data of two alloys (JPCA, 316R) irradiated in HFIR at 400°C[14,15] are included in Fig. 4. Cavity data for C and K alloys have not yet been quantified, but the micrographs show no significant degradation in their swelling resistance compared with JPCA or 316R.[16] The He:dpa ratio behavior is quite different during HFIR and during spectrally tailored ORR irradiation. During HFIR irradiation, the He:dpa becomes very high in austenitic stainless steels only after the first few dpa. At 33 dpa, the lowest dose of this U.S.-Japan HFIR phase I irradiation, the amount of generated helium in JPCA reaches 2500 appm, and thus the final He:dpa ratio was 75 appm/dpa. At 400°C, this causes nucleation of many fine helium bubbles which then provide a very high sink strength for recombination of both vacancies and interstitials. As shown in Fig. 4, the cavity number density after HFIR irradiation is much higher than that found after ORR irradiation. The microstructural evolution of HFIR irradiation was dominated by the helium bubbles acting as neutral sinks so that the void swelling of various alloys was suppressed.[2-4] Nevertheless, the relative swelling resistance shown in the present ORR experiment is the same as observed during HFIR irradiation at 500 and 600°C.

Although SA alloys irradiated in ORR showed different values of swelling, their cavities have similar bi-modal size distributions (Fig. 3). The average size of bias-driven voids (the larger portion of the distribution) tends to increase as the swelling resistance decreases. The nominal average diameter of cavities given in Fig. 4 does not adequately reflect this because there are so many small bubbles. As for the cavity number density, the difference is smaller than that observed in cavity size. Two niobium-containing alloys, 316W and C, showed slightly lower values of cavity number density, while the HP alloy showed more cavities. The alloy-to-alloy difference of swelling behavior is, however, mainly due to the difference in cavity size distribution, which would reflect changes in the critical cavity size.

In this experiment, some alloys included titanium as the swelling inhibitor. Titanium is expected to form MC precipitates along dislocations, preventing the preferential absorption of interstitial atoms by dislocations. These titanium-containing alloys, however, showed different levels of swelling resistance. JPCA showed the best swelling resistance, as expected, while one of the low-carbon alloys, K, showed poor swelling resistance. Because alloy K and another low-carbon alloy, C, both showed relatively poor swelling resistance, it could be concluded that carbon is an important element for suppressing void swelling at these irradiation conditions. Fine MC precipitates were observed in all titanium-containing alloys (JPCA, 316W, C, and K), but the amount had no relationship with their carbon content nor their swelling resistance. Moiré fringe technique, employed to image tiny MC particles, has a high-resolution capability, but still requires a particle size sufficient to form at least two fringes in a particle. Smaller particles, undetectable by TEM, could still be present and change the strain field around a dislocation, and thus contribute to the effect on the overall bias factor of the system.

According to the first spectrally tailored experiment in ORR (MFE-4A/4B), the swelling of SA-USPCA after 13 dpa reaches 0.35% at 400°C (ref. 2). Assuming the similar irradiation response in both U.S. and Japanese PCAs, the dose dependence of swelling would be accelerated. This is consistent with the established swelling behavior of neutron-irradiated austenitic stainless steel that a low-swelling transient period is followed by an acceleration to a regime of near-linear swelling.[4] Another effect could superimpose upon this dose dependence -- the delay of helium generation. Even in this spectrally tailored experiment, the initial generation rate of helium is relatively low. For example, the helium generation in type 316 stainless steel irradiated in this experiment is estimated to be only 31 appm at the damage level[17] of 3.7 dpa. This He:dpa ratio of 8.4 is almost a factor of 2 less than the value of 13.8 achieved at higher dose (= 102 appm/7.4 dpa). This could also affect the initial nucleation of cavities and could have delayed the cavity evolution. At the current damage level, one low-carbon steel, K, showed an unexpectedly high swelling rate value (0.08%/dpa). It is possible that this rate would be even higher at a higher damage level from the above consideration.

The weld metal specimens showed no heterogeneous cavity formation,[5] although the cellural microstructure formed during solidification of weld remained unchanged in the irradiated specimens. The same welded specimens did show heterogeneous void formation after electron irradiation.' In the case of electron irradiation, such differences in cavity evolution suggest that nucleation is also different relative to neutron irradiation, where helium is available to stabilize cavity embryo. Further analysis will be given elsewhere.[5]

CONCLUSIONS

Austenitic stainless steels were irradiated in the ORR-MFE-7J capsule at 400°C to 7.4 dpa, with co-generated helium and dpa at fusion-relevant He:dpa ratios. Imnersion densitometry and microstructural observation revealed the following:

1. CW materials showed good swelling resistance, but there was significant alloy-to-alloy variation of swelling behavior in SA materials.
2. In SA materials, the relative ranking of various alloys with regard to swelling resistance observed in ORR irradiation at 400°C was the same as observed during HFIR irradiation at 500°C or above.
3. Samples with higher swelling showed a bi-modal size distribution and the difference of swelling resistance reflected the average size of larger bias-diven voids. The difference of cavity number density plays a minor role in explaining the relative difference in swelling resistance in these alloys. Critical cavity size and void growth rates are more important factors.
4. MC precipitates were observed in all of the titanium-containing alloys, but the amount of detectable MC precipitates had no relationship to their carbon content nor their swelling resistance.
5. Low-carbon steels showed relatively higher swelling in the SA condition, even when they contained titanium as a solid-solution swelling inhibitor. Carbon is obviously another important element to suppress swelling.
6. Swelling resistance is still an important factor to be considered for fusion application of austenitic stainless steel at 400°C.
7. Welding did not degrade the swelling resistance in any of the alloys irradiated in these low-dose experiments.

REFERENCES

1. A. A. Bauer and M. Kangilaski, J. Nucl. Mater. 42 (1972) 91.
2. R. E. Stoller, P. J. Maziasz, A. F. Rowcliffe, and M. P. Tanaka, J. Nucl. Mater. 155-157 (1988) 1328.
3. R. E. Stoller and G. R. Odette, "The Effect of Helium on Swelling in Stainless Steel: Influence of Cavity Density and Morphology," p. 275 in Effect of Radiation on Materials: 11th Conf., ASTM STP 782, ed., H. R. Brager and J. S. Perrin, American Society for Testing and Materials, Philadelphia, 1982.
4. P. J. Maziasz, J. Nucl. Mater. 122&123 (1984) 472.
5. T. Sawai, P. J. Maziasz, and A. Hishinuma, J. Nucl. Mater. 176 (1990) (in press).
6. J. L. Scott et al., Second Annual Progress Report on United States-Japan Collaborative Testing in the High Flux Isotope Reactor at the Oak Ridge Research Reactor for the Period Ending September 30, 1985, ORNL/TM-10102.
7. T. Sawai, K. Fukai, S. Hamada, K. Suzuki, and A. Hishinuma, J. Nucl. Mater. 141-143 (1986) 444.
8. I. I. Siman-Tov, FRM Semiannu. Prog. Rep., March 31, 1987, DOE/ER-0313/2, USDOE, Office of Fusion Energy, p. 18.
9. R. A. Lillie, FRM Semiannu. Prog. Rep., Sept. 30, 1987, DOE/ER-0313/3, USDOE, Office of Fusion Energy, p. 28.
10. L. R. Greenwood, FRM Semiannu. Prog. Rep., March 31, 1989, DOE/ER-0313/6, USOOE, Office of Fusion Energy, p. 23.
11. R. A. Buhl and L. J. Turner, Oak Ridge National Report, ORNL/TM-10378 (to be published).
12. H. Kanazawa, T. Sawai, and L. J. Turner, FRM Semiannu. Prog. Rep., March 31, 1990, DOE/ER-0313/8, USDOE, Office of Fusion Energy, p. 17.
13. T. Inazumi and G.E.C. Bell, FRM Semiannu. Prog. Rep., March 31, 1989, DOE/ER-0313/6, USOOE, Office of Fusion Energy. p. 373.
14. M. P. Tanaka, P. J. Maziasz, A. Hishinuma, and S. Hamada, J. Nucl. Mater. 155-157 (1988) 801.
15. S. Hamada, P. J. Maziasz, M. P. Tanaka, M. Suzuki, and A. Hishinuma, J. Nucl. Mater. 155-157 (1988) 838.
16. S. Hamada, JAERI, private comnunication, 1990.
17. R. A. Lillie, FRM Semiannu. Prog. Rep., March 31, 1986, DOE/ER-0313/16, USDOE, Office of Fusion Energy, p. 12.

DETERMINATION OF CREEP-SWELLING COUPLING COEFFICIENTS FOR IRRADIATED STAINLESS STEELS - M. B. Toloczko, Univ. of California at Berkeley, F. A. Garner, Pacific Northwest Laboratory,(a) and C. R. Eiholzer, Westinghouse Hanford Company

OBJECTIVE

The objective of this effort is to provide irradiation creep data and design correlations for application to fusion reactor design.

SUMMARY

Irradiation creep data at ~400°C were analyzed for two 20% cold-worked titanium-modified type 316 stainless steels. One of these steels was the fusion prime candidate alloy designated PCA. The analysis was based on the assumption that the $B_o + DS$ creep model applies to these steels at this temperature. This assumption was found to be valid. A creep-swelling coupling coefficient of $D \approx 0.6 \times 10^{-2}$ MPa^{-1} was found for both steels, which is in excellent agreement with the results of earlier studies conducted using annealed AISI 304L and also 10% and 20% cold-worked AISI 316 stainless steels. There appears to be some enhancement of swelling by stress, leading to an apparent but misleading nonlinearity of creep with respect to stress. The dependence of the creep-swelling coupling coefficient on irradiation temperature for temperatures greater than 400°C has not yet been established.

PROGRESS AND STATUS

Introduction

In a number of recent reports the creep-swelling relationship has been investigated for annealed AISI 304L[1] and various thermomechanical treatments of AISI 316 stainless steel.[2-6] These studies were conducted in EBR-II and showed a remarkable consistency in results, indicating that irradiation creep at most temperatures of interest could be described as consisting of several minor contributions (precipitation-related dimensional changes and transient relaxation of cold-work-induced dislocations) and two major contributions.[6] The major contributions were associated with the creep compliance, B_o, a quantity unrelated to void swelling, and a swelling-driven creep component. While swelling itself is very sensitive to a large variety of material and environmental variables, the instantaneous creep rate appears to be proportional only to the applied stress and the instantaneous swelling rate. As discussed in other publications,[7-9] the instantaneous creep rate can therefore be written in the form

$$B = \dot{\bar{\epsilon}}/\bar{\sigma} = B_o + D\dot{S}, \qquad (1)$$

providing that the material is annealed and does not develop any significant phase-related strains or density changes. In this equation, $\dot{\bar{\epsilon}}$ is the effective strain rate per unit stress, $\bar{\sigma}$ is the effective stress ($\sqrt{3}/2\ \sigma_{hoop}$), B_o is the creep compliance, D is the creep-swelling coupling coefficient and $\dot{S}$ is the instantaneous volumetric swelling rate.

Experimental Details

In this study the fusion prime candidate alloy [designated PCA (heat K280)] and another titanium-modified type 316 steel [designated 09 (heat 83508)] were irradiated in FFTF/MOTA. For PCA, 2.24-cm-long helium-pressurized tubes were used with outer and inner diameters of 4.57 mm and 4.17 mm, respectively. The 09 tubes were somewhat larger, with a length of 2.82 cm, and 5.84 and 5.08 mm outer and inner diameters. The compositions of these steels are shown in Table 1. The specimens were removed periodically from the reactor and their diameters measured at five equidistant positions using a noncontacting laser system.[10] The three middle measurements were averaged to calculate the diametral strain. During any one irradiation interval the temperature is actively controlled within ±5°C. The 09 tubes were placed in positions in MOTA that operated at slightly higher (~20°C) temperatures and neutron fluxes than experienced by the PCA tubes. For each set of tubes there were small cycle-to-cycle variations in temperature that arose as the tubes were placed at somewhat different reactor levels during each MOTA reconstitution (see Table 2).

Results and Discussion

Figure 1 shows the total diametral strain for six nominally identical PCA tubes irradiated side-by-side for six irradiation cycles at ~400°C. These tubes varied only in their internal gas pressure, which yielded

---

(a) Pacific Northwest Laboratory is operated for the U.S. Department of Energy by Battelle Memorial Institute under Contract DE-AC06-76RLO 1830.

Table 1
Composition (wt%) of Stainless Steels Used in this Study

	Fe	Ni	Cr	Mo	Mn	Si	C	P	Ta	Zr
PCA	BAL	16.63	14.31	1.95	1.83	0.52	0.048	0.014	--	--
D9	BAL	15.77	13.70	1.65	2.03	0.80	0.039	t0.005	<0.01	<0.01

	S	V	Nb	Ti	Co	Cu	Al	B	N
PCA	0.025	0.04	0.02	0.31	0.04	0.02	0.05	0.001	0.008
D9	0.003	0.01	..	0.34	t0.01	<0.01	<0.01	0.0005	0.004

Table 2
Temperatures of Individual Irradiation Sequences

	MOTA-1A	MOTA-1B	MOTA-1C	MOTA-1D	MOTA-1E	MOTA-1F
PCA						
Temperature, °C	405	401	396	386	384	386
Neutron fluence, n cm^{-2} (E>0.1 MeV)	4.6×10^{22}	6.6×10^{22}	11.9×10^{22}	15.4×10^{22}	19.2×10^{22}	24.3×10^{22}
Cumulative dpa	20.4	29.3	50.2	65.3	81.1	106.8
D9						
Temperature, °C	427	431	420	404		
Neutron fluence, n cm^{-2} (E>0.1 MeV)	6.0×10^{22}	9.2×10^{22}	16.7×10^{22}	21.9×10^{22}		
Cumulative dpa	27.8	42.6	77.2	101.2		

hoop stresses ranging from 0 to 200 MPa. Note that these data are plotted versus the estimated neutron exposures expressed in units of dpa. An earlier report contained these data as a function of neutron fluence for energies greater than 0.1 MeV.[11] Both the neutron fluence and dpa values have been upgraded recently and are reported in Table 2.

The diameter changes of the zero stress tube represents primarily the contribution of void swelling. but there may also be some secondary contribution from precipitation-related strains. The strains of the stressed tubes include additional contributions from irradiation creep and possibly the stress-enhanced portion of swelling

Figure 2 shows the total diametral strains for a similar set of D9 tubes that were irradiated at somewhat higher fluxes and temperatures (~420°C). Although the total neutron exposure is nearly the same, only four irradiation cycles were completed compared to the six completed for the PCA tubes. The D9 tube at 200 MPa failed in the last irradiation cycle, and therefore only three cycles are shown for this stress level.

In order for the creep data to fit the $B_0 t DS$ model, it is necessary for creep to be proportional to the first power of stress and to increase directly in proportion to the instantaneous swelling rate. If we calculate the midwall creep strains and divide them by the stress level, the validity of these assumptions can be checked. First, as shown in Figure 3, the creep strains are separated by subtracting the zero stress swelling strains. Figure 4 presents a comparison of the stress-normalized midwall strains for each steel, and Figure 5 presents a comparison of the range of the normalized creep strains and the stress-free swelling. The latter figure shows that each of the steels exhibits accelerated creep rates that coincide with the onset of accelerated swelling, while Figure 4 shows that the stress-normalized creep strains appear not to be completely linear with applied stress. However, this appearance may be misleading, with the slight but steady increase in normalized creep strain arising from a somewhat incorrect assumption that swelling is not affected by stress. In general, increasing the stress levels progressively shortens the incubation period of swelling in cold-worked austenitic steels.[12-14] It appears that there is a small but persistent effect of stress on the swelling incubation period and also that the effect of stress occurs relatively late in the irradiation.

The PCA alloy at the lower displacement rate and irradiation temperature is clearly swelling and creeping at rates comparable to that of the D9 alloy, but the onset of accelerated strain rates occurs with a delay of ~10 dpa relative to that of D9. This delay cannot be attributed to compositional differences alone, but probably arises from both compositional and environmental differences (displacement rate and temperature). It may also reflect some differences in production methods associated with the two tubes sizes.

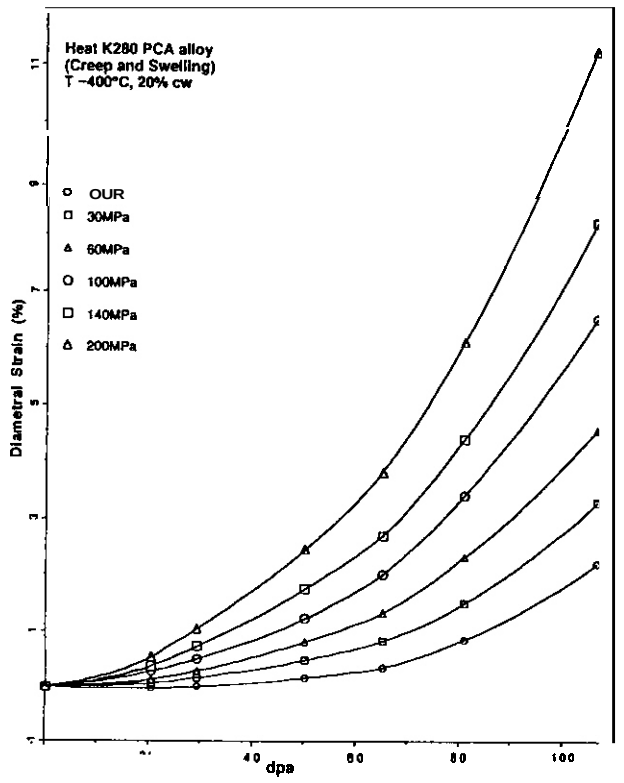

Figure 1. Total diametral strains observed in pressurized tubes of 20% cold worked PCA irradiated at ~400°C in FFTF/MOTA.

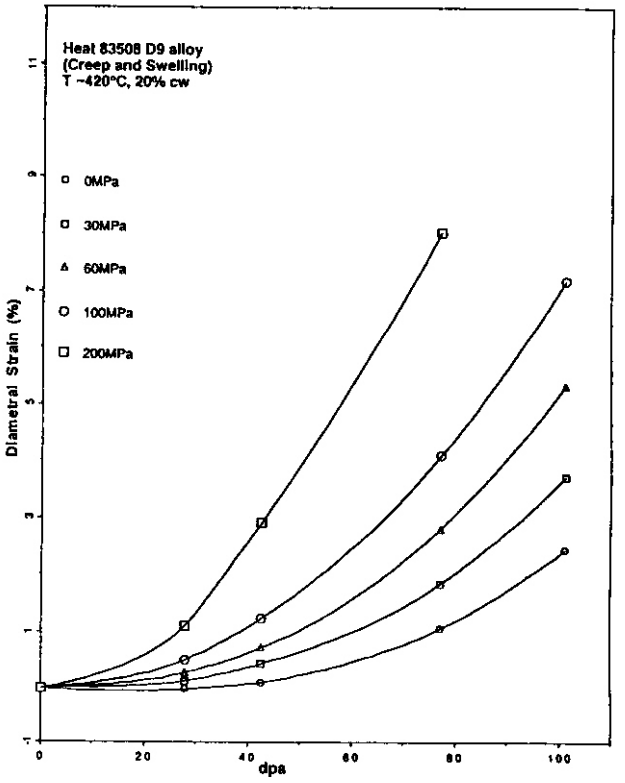

Figure 2. Total diametral strains observed in pressurized tubes of 20% cold worked D9 irradiated at ~420°C in FFTF/MOTA.

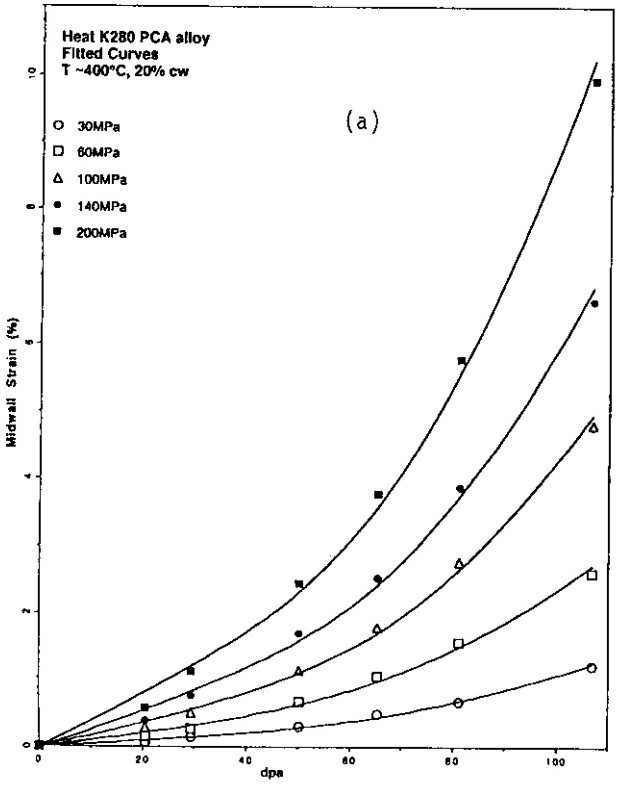

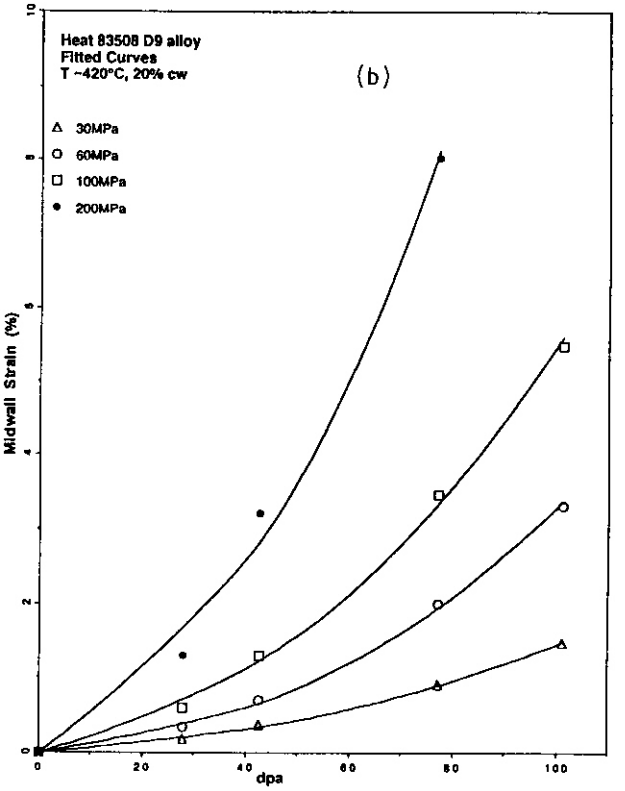

Figure 3. Comparison of midwall strains observed in (a) PCA and (b) D9 pressurized tubes. The curve-fits shown are those used in the creep analysis.

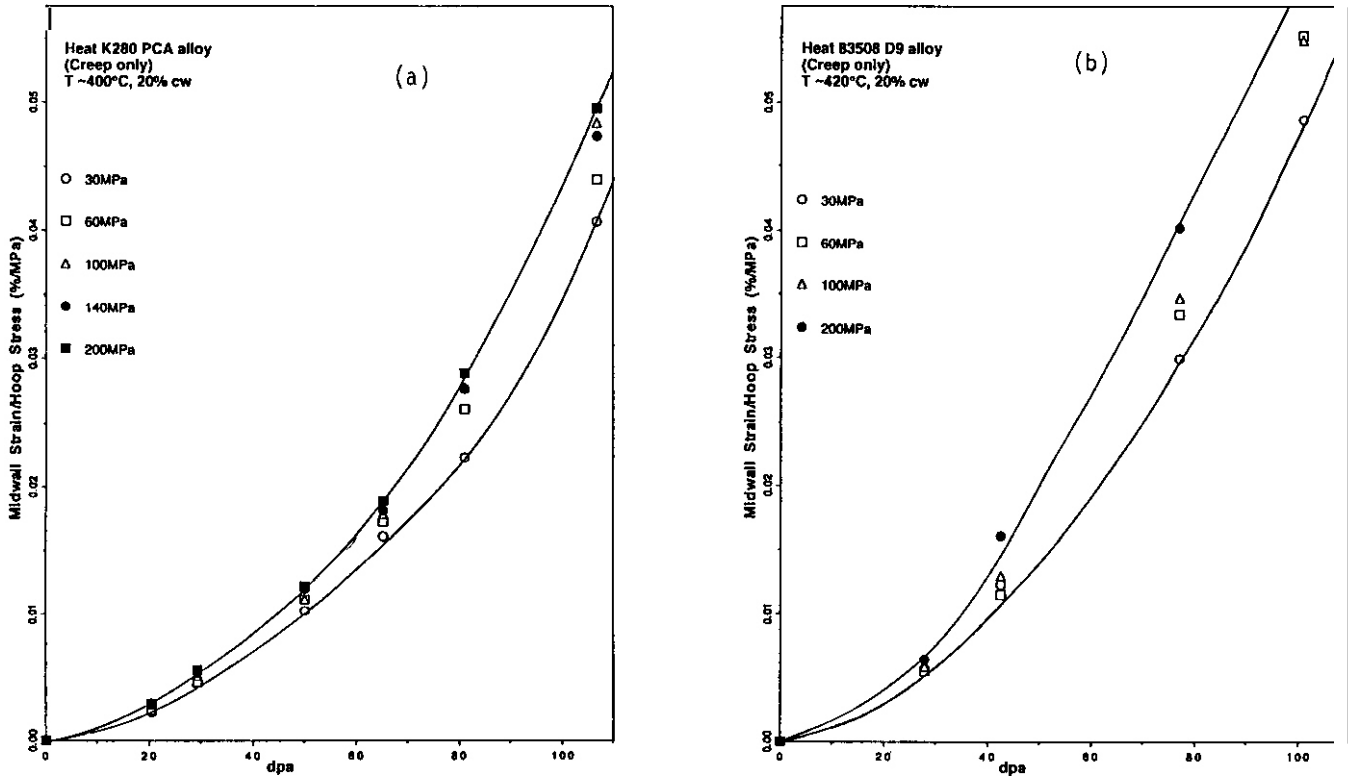

Figure 4. Stress-normalized midwall strains observed in (a) PCA and (b) D9 pressurized tubes. Gradual increases in the normalized strain with increasing stress level is thought to occur as a consequence of stress-enhanced swelling.

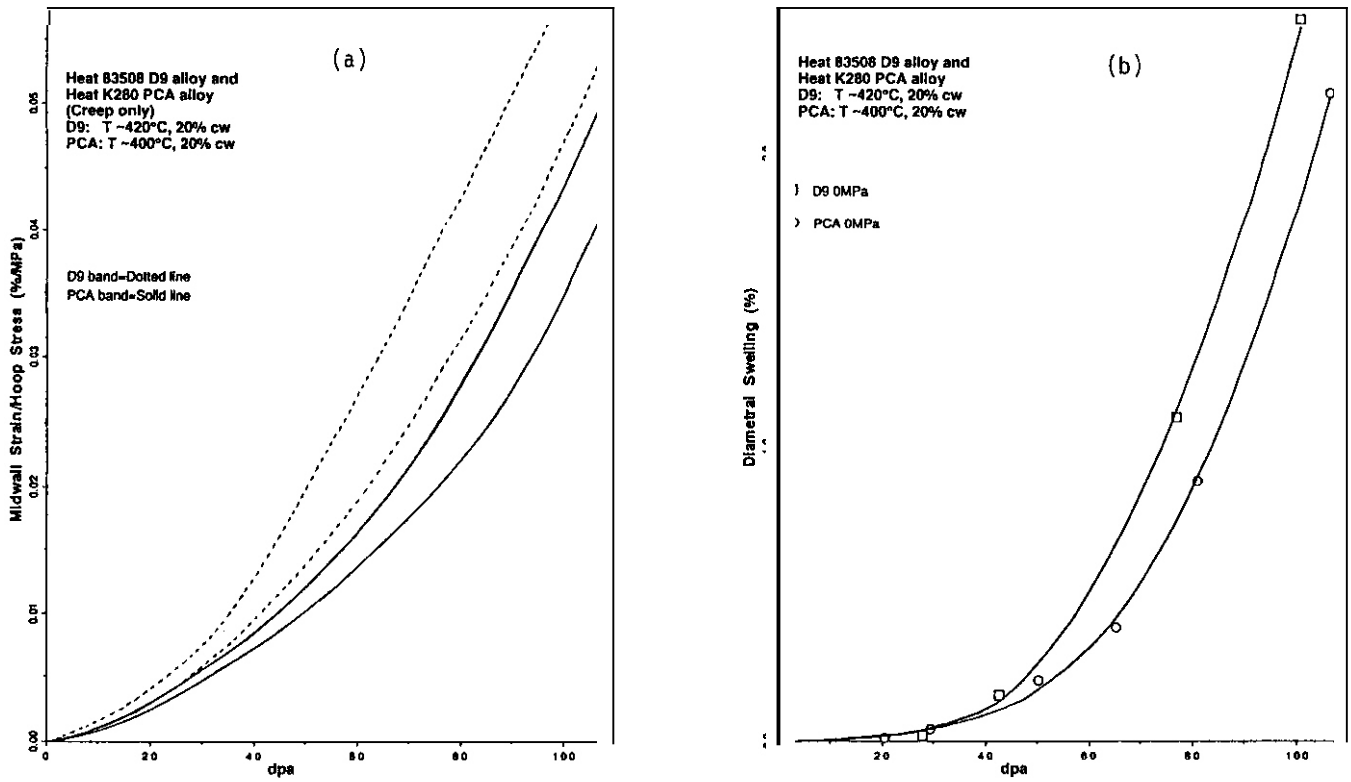

Figure 5. Comparison of (a) range of normalized strains with the stress-free swelling strains for both steels. The curve fits used in the analysis for stress-free swelling are also shown.

If both the small effect of stress on swelling and the possibility of precipitation-related strains are ignored, one can calculate a first order estimate of the B_o and O coefficients, using a least-squares fitting procedure. The first step is to fit the stress-free linear swelling strain (S_L) curve with an equation of the form

$$S_L = \frac{a}{c} \log \left[\frac{(b + e^{-cx})}{(1 + b)\, e^{-cx}} \right], \tag{2}$$

were x is the dose in dpa, a is the steady-state swelling strain rate, b is the incubation parameter and c is a parameter controlling the rate of curvature between the incubation and steady-state regimes.

The second step is to fit each creep strain curve in Figure 3 with an equation of the form

$$\epsilon = q\, x + \frac{r}{c} \log \left[\frac{(b + e^{-cx})}{(1 + b)\, e^{-cx}} \right] \tag{3}$$

Note that it is assumed that the incubation and curvature parameters are identical for both creep and swelling. This is a reasonable assumption if the B_o t DS model is correct. The degree of fit to the creep strain curves in Figure 3 appears to confirm the validity of this assumption.

Upon integrating equation (1) with respect to X

$$\bar{\epsilon}/\bar{\sigma} = B_o x \text{ t } DS + K, \tag{4}$$

where $S \simeq 3S_L$ for small S. The parameter K = 0, since $\epsilon(0) = 0$ and $S(0) = 0$. When expressed in terms of midwall strain and hoop stress, σ_H, equation (4) becomes

$$\epsilon/\sigma_H = 3/4\ [B_o \text{ t } OS]. \tag{5}$$

Substituting equations (2) and (3) into equation (4) yields

$$\frac{qx}{\sigma_H} + \frac{r}{c\sigma_H} \log \left[\frac{(b + e^{-cx})}{t\ b)} \right] = \frac{3}{4} B_o x + \frac{9Da}{4c} \log \left[\frac{(b + e^{-cx})}{(1 + b)\, e^{-cx}} \right]. \tag{6}$$

Solving for B_o and D gives

$$B_o = \frac{4q}{3\sigma_H} \text{ and } D = \frac{4r}{9a\sigma_H} \tag{7}$$

The least-squares fitting routines used to determine q, r, a, b and c starts from an initial graphical estimate of these values. Table 3 shows that the first-order estimates of B_o and D are -3×10^{-6} MPa^{-1} dpa^{-1} and -0.6×10^{-2} MPa^{-1} for the D9 alloy. For the PCA alloy, the coefficients were found to be -2×10^{-6} MPa^{-1} dpa^{-1} and -0.6×10^{-2} MPa^{-1}. The value of 0.6×10^{-2} MPa^{-1} for O agrees with that observed in 304 and 316 stainless steels at ≃400°C, but the B_o values found here are somewhat higher than the usually assumed value

Table 3
Calculated Values of Creep Coefficients

Alloy	Stress Level, MPa	B_o MPa^{-1} dpa^{-1}	O MPa^{-1}
PCA	30	2.1×10^{-6}	0.50×10^{-2}
	60	2.2×10^{-6}	$\mathbf{0.57} \times 10^{-2}$
	100	$\mathbf{2.3} \times 10^{-6}$	$\mathbf{0.64} \times 10^{-2}$
	140	2.4×10^{-6}	0.60×10^{-2}
	200	2.4×10^{-6}	$\mathbf{0.64} \times 10^{-2}$
D9	**30**	3.1×10^{-6}	0.46×10^{-2}
	60	$\mathbf{2.8} \times 10^{-6}$	$\mathbf{0.63} \times 10^{-2}$
	100	$\mathbf{3.3} \times 10^{-6}$	$\mathbf{0.57} \times 10^{-2}$
	200	$\mathbf{3.7} \times 10^{-6}$	$\mathbf{0.75} \times 10^{-2}$

of -1 X 10^{-6} MPa^{-1} dpa^{-1}. The larger values of B_o found here are thought to be a possible consequence of ignoring the effect of stress on swelling. It is therefore significant that the largest value of B_o was found in the D9 steel, which possesses the shortest incubation period and the largest effect of stress, both of which would tend to yield overestimates of B_o.

Analysis of Data at Higher Temperatures

Irradiation creep and thermal creep data are available for both of these steels at temperatures above 400°C. A preliminary analysis shows, however, that it may *be* difficult to extract meaningful values of B_o and D from these data. An overtemperature event in MOTA-10 resulted in a programmatic decision to terminate the irradiation of many of the high-temperature tubes. At the lower fluence levels, swelling strains are often too low to provide measurable DS contributions. Also, many of the high-temperature specimens failed during the overtemperature event. In addition, thermal creep becomes a large contributor to the strain at the higher temperatures and tends to obscure the DS contribution to total strain.

An attempt is currently being made to extract an estimate of B_o and D from other high-temperature data sets that involved higher swelling levels.

CONCLUSIONS

Based on the results of this and other studies on various austenitic stainless steels irradiated at ≈400°C in either EBR-II or FFTF, it appears that the B_o + DS model of irradiation creep is valid for application as a design equation. This model can be applied to both PCA and austenitic steels in general, providing the effect of stress on swelling is relatively small and occurs relatively late with respect to the onset of rapid swelling. At 400°C the value of D in the 300 series of steels appears to be -0.6 x 10^{-2} MPa^{-1}, relatively independent of both composition and thermomechanical condition. Unfortunately, the data available on the two titanium-modified steels at higher irradiation temperatures are insufficient at present to establish the dependence of the creep-swelling coefficient at higher temperatures.

ACKNOWLEDGEMENTS

M. B. Toloczko gratefully acknowledges support from the U.S. Department of Energy, Division of University and Industry Programs, Office of Energy Research, as a Science and Engineering Research Semester program participant at Pacific Northwest Laboratory.

REFERENCES

1. D. L. Porter, F. A. Garner and G. D. Hudman, "Irradiation Creep and Swelling of Annealed 304L Stainless Steel at ≈390°C and High Neutron Fluence," Fusion Reactor Materials Semiannual Progress Report DOE/ER-0313/7 (1989) 133-139.

2. F. A. Garner, D. L. Porter and B. J. Makenas, J. Nucl. Mater. 148 (1987) 279-287.

3. D. L. Porter and F. A. Garner in Influence of Radiation on Material Properties, ASTM STP 956, Eds. F. A. Garner, C. H. Henager, Jr. and N. Igata (1987) 11-21.

4. F. A. Garner and D. L. Porter, J. Nucl. Mater. 155-157 (1988) 1006-1013.

5. D. L. Porter and F. A. Garner, J. Nucl. Mater. 159 (1988) 114-121.

6. R. W. Clark, A. S. Kumar and F. A. Garner, J. Nucl. Mater. 155-157 (1988) 845-849.

7. F. A. Garner, J. Nucl. Mater. 100 (1984) 459-471.

8. F. A. Garner and D. S. Gelles, J. Nucl. Mater. 159 (1988) 286-309.

9. K. Ehrlich, J. Nucl. Mater. 100 (1981) 149.

10. E. R. Gilbert and B. A. Chin in "Effects of Radiation on Materials," Tenth Conference, ASTM STP 725, Eds. D. Kramer, H. R. Brager and J. S. Perrin American Society for Testing and Materials, Philadelphia, (1981) 665-679.

11. F. A. Garner and R. J. Puigh, "Irradiation Creep of PCA Observed in FFTF/MOTA," Fusion Reactor Materials Semiannual Progress Report DOE/ER-0313/7 (1989) 140-144.

12. F. A. Garner, E. R. Gilbert and D. L. Porter, in Ref. 10 pp. 680-697.

13. T. Lauritzen, S. Vaidyanathan, W. L. Bell and W. J. S. Yang in "Radiation-Induced Changes in Microstructure," 13th International Symposium (Part I) ASTM STP 955, F. A. Garner, N. H. Packan and A. S. Kumar, Eds., American Society for Testing and Materials, Philadelphia, 1987, pp. 101-103.

14. D. L. Porter, M. L. Takata and E. L. Wood, J. Nurl. Mater. (1983) 272-276.

6.3 Refractory Metal Alloys

FFTF/MOTA IRRADIATION OF REFRACTORY ALLOYS UNDER CONSIDERATION AS PLASMA FACING COMPONENTS - F. A. Garner, Pacific Northwest Laboratory[a]

OBJECTIVE

The objective of this effort is to provide data on the radiation response of refractory alloys being considered for short-term applications such as the ITER project and also for long-term fusion goals.

SUMMARY

A refractory alloy irradiation series involving four discharges of the Materials Open Test Assembly (MOTA-1B through MOTA-IE) has been completed. This experiment contains pure Mo, Mo-41Re, TZM and Nb-1Zr. Irradiation temperatures in this experiment ranged from 404 to 730°C with neutron exposures yielding 0.1 to 110.8 dpa. Measurement of density changes and disk bend testing are planned to begin shortly.

PROGRESS AND STATUS

Introduction

Dispersion-strengthened copper and several refractory alloys are now under consideration as possible candidates for applications as plasma facing structural components for the ITER project. The refractory alloys are Mo-(5-10)Re, Mo-(41-50)Re, and Nb-1Zr. For ITER applications, the fluences currently envisioned are fairly low (~3 dpa) at temperatures of 50-700°C. Long-term applications might require much higher exposure levels, depending on the level of emphasis placed on low activation. Neither Nb, Mo, or Cu currently qualify as low activation materials.

A refractory alloy irradiation sequence involving four discharges from MOTA-18, 1C, 1D, and 1E has been completed. It contains pure Mo, Mo-41Re and Nb-1Zr, each in two different heat treatments (see Table 1). All specimens are in the form of TEM disks. There are two specimens of each alloy in each packet. In most cases there are two identical packets for each set of irradiation conditions. Thus in most cases there are four specimens for each set of alloy and irradiation condition. The refractory alloy TZM was also included in a small subset of packages. Only one dose level at each irradiation temperature is available for TZM. The dose levels for TZM range from 52.6 to 61.5 dpa, with the exception of the 431°C series, which reached 110.8 dpa.

Table 1
Specimen Identity

Identification Code	Group Designation[a]	Alloy	Heat Treatment[b]
AN	A	Pure Molybdenum	HTB
AM	B	Pure Molybdenum	HTA
AO	B	Mo-41Re	HTA
AP	B	Mo-41Re	HTB
AT	A	Nb-1Zr	HTB
AR	B	Nb-1Zr	HTA
AK	C	TZM	HTA

(a) All alloys except TZM were irradiated in packets containing subsets of specimens designated either group A or B. Group C (TZM) was irradiated along with some subsets of group B. See Table 2, column 2 for details.
(b) HTA = solution annealed
HTB = 20% cold worked.

(a) Pacific Northwest Laboratory is operated for the U.S. Department of Energy by Battelle Memorial Institute under Contract DE-AC06-76RLO 1830.

The irradiations, with one exception in MOTA-ID, were conducted with active temperature control to ±5°C. (An overtemperature event of approximatly 1-h duration occurred in MOTA-1D, with varying impact on the packet temperature, depending on the target temperature of each specimen packet.) The irradiation and specimen matrix are shown in Table 2.

Those specimens retrieved from the MOTA-10 discharge received doses ranging from 0.7 to 15.0 dpa and will provide a conservative estimate of the behavior required for the ~3 dpa ITER application. Data at higher dpa levels can be used not only for long-term fusion goals, but also to extrapolate back to fluence levels below the 0.7 to 15.0 dpa range, i.e., those relevant to the ITER project.

Table 2
Irradiation Conditions for Refractory Alloy Experiment in FFTF-MOTA

		MOTA-10		MOTA-1C		MOTA-ID		MOTA-1E		
Packet	Contents[a]	Temperature, °C	dpa[b]	Temperature, °C	dpa	Temperature, %	dpa	Temperature, %	dpa	Total dpa
MAEZ	A	431	15.0	--	--	--	--	--	--	15.0
NAEZ	A	431	15.0	420	35.3	--	--	--	--	50.3
N6EZ	O	431	14.1	420	33.1	--	--	--	--	47.2
P6EZ	O	431	13.0	420	32.2	404	24.0	--	--	70.0
R6EZ	B	431	13.0	420	32.2	404	23.3	414	32.8	102.1
M6EZ	B,C	431	14.5	420	33.9	404	24.5	414	32.8	105.7
PAEZ	A	431	15.0	420	35.3	404	25.5	414	35.0	110.8
RAEZ	A	431	15.0	420	35.3	404	25.5	414	35.0	110.8
MAE1	A	471	11.4	--	--	--	--	--	--	11.4
NAE1	A	471	11.4	470	26.0	--	--	--	--	30.2
N6E1	B	471	9.6	470	22.6	--	--	--	--	32.2
P6E1	B	471	0.7	470	20.3	470	14.7	--	--	43.1
R6E1	O	471	8.7	470	20.3	470	14.7	--	--	43.7
M6E1	B,C	471	10.4	470	24.5	470	17.7	--	--	52.6
PAE1	A	471	11.4	470	26.8	470	19.4	--	--	57.6
RAE1	A	471	11.4	470	26.8	470	19.4	--	--	57.6
MAE7	A	569	11.5	--	--	--	--	--	--	11.5
NAE7	A	569	11.5	550	27.0	--	--	--	--	38.5
N6E7	O	569	12.2	550	20.6	--	--	--	--	40.8
P6E7	O	569	12.7	550	29.7	549	21.5	--	--	63.9
R6E7	O	569	13.1	550	30.0	549	22.3	--	--	66.2
M6E7	B,C	569	12.2	550	20.6	549	20.7	--	--	61.5
PAE7	A	569	11.5	550	27.0	549	19.6	--	--	58.1
RAE7	A	569	11.5	550	27.0	549	19.6	--	--	50.1
MAE5	A	645	11.5	--	--	--	--	--	--	11.5
NAE5	A	645	11.5	652	27.0	--	--	--	--	30.5
N6E5	B	645	12.2	652	28.6	--	--	--	--	40.0
P6E5	O	645	12.7	652	29.7	650	21.5	--	--	63.9
R6E5	O	645	12.7	652	30.0	650	22.3	--	--	65.0
M6E5	B,C	645	12.2	652	28.6	650	20.1	--	--	61.5
PAE5	A	645	11.5	652	27.0	650	19.6	--	--	58.1
RAE5	A	645	11.5	652	27.0	650	19.6	--	--	58.1
MAE6	A	722	11.5	--	--	--	--	--	--	11.5
NAE6	A	722	11.5	730	27.0	--	--	--	--	38.5
N6E6	O	722	12.2	730	28.6	--	--	--	--	40.8
P6E6	B	722	12.7	730	29.7	730	21.5	--	--	63.9
R6E6	B	722	13.1	730	30.0	730	22.3	--	--	66.2
M6E6	B,C	722	12.2	730	20.6	730	20.7	--	--	61.5
PAE6	A	722	11.5	730	27.0	730	i9.6	--	--	58.1
RAE6	A	722	11.5	730	27.0	730	19.6	--	--	58.1

(a) Group A contains Mo (HTB) and Nb-1Zr (HTB). Group O contains Mo-41Re (both HTA and HTB) and Mo (HTA) and Nb-1Zr (HTA). Group C contains only TZM (HTA).
(b) dpa values calculated for stainless steel.

Post-Irradiation Examination

Specimen packets from MOTA-16, -1C, and -lE are currently available in the fusion hot cell for removal and sorting of specimens. Specimen packets from MOTA-ID have been requested for transfer from long-term storage to the fusion hot cell. Density change measurements have been scheduled, with priority placed on the lower fluence ITER-relevant specimens. Disk bend tests are also under consideration to examine the possibility of radiation-induced embrittlement.

FUTURE WORK

This effort will continue focusing on post-irradiation examination of existing specimens and on the possibility of including minitensile specimens in MOTA during cycle 12 of FFTF.

SWELLING DEPENDENCE OF NEUTRON-IRRADIATED VANADIUM ALLOYS ON TEMPERATURE, NEUTRON FLUENCE, ANI) THERMOMECHANICAL TREATMENT – B. A. Loomis (Argonne National Laboratory). K. Abe (Tohoku University), L. J. Nowicki (Argonne National Laboratory). H. Chung (Argonne National Laboratory). and D. L. Smith (Argonne National Laboratory)

OBJECTIVE

The objective of this research is to determine the composition of a vanadium-base alloy with the optimal combination of swelling resistance, corrosion resistance. and mechanical properties in the environment of a magnetic fusion reactor.

SUMMARY

Swelling of vanadium alloys was determined after irradiation at 420 and 600°C to neutron fluences ranging from 0.3 x 10^{27} neutrons/m^2 (17 dpa) to 1.9 x 10^{27} neutrons/m^2 (114 dpa). Binary and ternary vanadium alloys with Cr, Ti, Mo, W, Ni, Fe. Zr, and Si additions were irradiated in either the fully annealed, partially annealed, or 10% cold-worked condition. Upon irradiation at 600°C, the swelling of vanadium to which Cr had been added was greatly exacerbated, whereas the swelling of vanadium to which Ti, Mo, W. and Ni (3-20%) had been added was not significantly affected. Swelling of V-Cr alloys upon irradiation at 600°C was substantially reduced (<0.1% per dpa) by the addition of Ti (1-15%). Upon irradiation at 420°C, the swelling of the vanadium alloys was <0.2% per dpa. Partial annealing or 10% cold-working had no significant effect on swelling of the alloys.

PROGRESS AND STATUS

Introduction

The swelling of vanadium-base alloys with Cr, Ti, Mo, W, Ni. Fe, Zr, and Si additions on neutron irradiation at 420 and 600°C to 77-84 dpa in the Materials Open Test Assembly (MOTA) of the Fast Flux Test Facility (FFTF) has been reported by Loomis and Smith.'-3 These swelling results, obtained from determinations of the density of the unirradiated and irradiated materials. have shown that the swelling of vanadium alloys upon neutron irradiation can be effectively minimized by the presence of >3% Ti in the alloy. In this report, we present (1) some additional data on the swelling (density change) of unalloyed vanadium and binary and ternary vanadium-base alloys with Cr, Ti, Mo, W, Ni. Fe, Zr, and Si additions that were irradiated at 420 and 600°C to damage levels ranging up to 114 dpa in the FFTF-MOTA and (2, microstructures of alloys observed by transmission electron microscopy (TEM) after irradiation at 420°C to 114 dpa and 600°C to 84 dpa.

.MATERIALS AND PROCEDURES

Vanadium alloys with the compositions listed in Table 1 were obtained in the form of 50% cold-worked sheets. Disk-shaped specimens –3.0 mm in diameter and ≈0.3 mm thick were obtained from the cold-worked sheets for the swelling determinations. The cold-worked specimens were annealed at either 1125. 950, or 850°C for 1 h in an ion-pumped vacuum system with a typical pressure of 1.3 x 10^{-6} Pa. Spenmens annealed at 1125°C had an average recrystallized grain diameter of 0.020 mm. In this paper, specimens that were annealed at 950 and 850°C are termed "partially annealed." In addition to the annealed and partially annealed specimens, annealed specimens with 10% cold-work were also prepared. The specimens were irradiated in the FFTF-MOTA. They were contained in sealed. Li^7-filled, TZM Mo capsules during irradiation to prevent contamination by oxygen, nitrogen, and carbon impurities in the Na coolant of the FFTF. The specimens were irradiated at 420. 520, and 600°C to neutron fluences (E >0.1 MeV) ranging from 0.3 x 10^{27} neutrons/m^2 (17 dpa) to 1.9 x 10^{27} neutrons/m^2 (114 dpa) during Cycles 7-10 of the PFTF-MOTA. The irradiated specimens were removed from the Li-filled TZM Mo capsules by immersion of the opened capsules in liquid ammonia and subsequent immersion of the specimens in a mixture of 50% ethanol and 50% methanol.

The swelling. S, of an irradiated specimen was obtained from a determination of the density of an unirradiated specimen, D_{ann}, and the density of an irradiated specimen, D_{irr}, by immersion in carbon tetrachlonde. i.e., $S = (D_{ann}-D_{irr})/D_{irr}$. Specimen density was determined with a precision of ±0.1% from three to six separate determinations on each specimen.

Table 1. Composition of Vanadium and Vanadium Alloys Used in this Study[a]

ANL ID	Nominal Allov Composition (wt.%)	Concentration (ppm) O	N	C	Si	Al
BL–1	V–4Mo	230	73	90	110	<100
BL–2	v – 9w	300	150	120	59	<100
BL–3	V–12Ni	490	280	500	405	<100
BL–4	V–10Cr	530	76	240	<50	1190
BL–5	B–14Cr	330	69	200	<50	2/40
BL–10	V–15Ti–7.5Cr	1110	250	400	400	30
BL–11	V–5Ti	1820	530	470	220	115
BL–12	V–10Ti	1670	390	450	245	<100
BL–13	V–14Ti	1580	370	440	205	<100
BL-15	V–18Ti	830	160	380	480	33
BL–16	V–20Ti	390	530	210	480	–
BL–20	V	570	110	120	325	<100
BL–24	V–15Cr–5Ti	1190	360	500	390	40
BL–25	V–14Cr–0.3Ti	390	64	120	<50	3270
BL–26	V–14Cr–1Ti	560	86	140	<50	3090
BL27	V–3Ti–1Si	210	310	310	2500	160
BL-28	Vanstar–7[c]	275	540	740	–	–
BL-34	V–9Ti	990	180	420	290	<100
BL-35	V–10Cr	340	45	120	<50	1450
BL–36	V	810	86	250	<50	<100
BL–42	V–3Ti–1Si	580	190	140	5400	290
BL–43	V–10Cr–5Ti	230	31	100	340	140

[a]Chemical analyses of these materials were performed by the Analytical Department of the Teledyne Wah Chang Albany Company, Albany, OR. komplete composition of these materials is presented in Ref. 6.
[c]V-9Cr-3Fe-1Zr.

Irradiated specimens were prepared for TEM by electrochemical thinning to perforation in a solution of 14% sulfuric add-72% methanol-13% butyl cellosolve at -5°C. Microstructures were examined with a JEOL 100CX electron microscope operating at 100 KeV.

EXPERIMENTAL RESULTS

Density Change (Swelling) Data

The dependence of density change (i.e., swelling) on Ti concentration of vanadium-base alloys after irradiation at 420°C to 114 dpa and at 600°C to 77-84 dpa is shown in Figs. 1 and 2, respectively. Of the alloys, V-3Ti-1Si alloy showed the highest swelling upon irradiation at 420°C to 114 dpa. Even so, swelling of all the alloys at 420°C to 114 dpa was <0.02% per dpa (Fig. 1). The addition of 0.3% Ti to the V-14Cr alloy reduced swelling of this alloy from 39% to 14% upon irradiation at 600°C to 84 dpa (Fig. 2). An increase of Ti concentration to 5% reduced swelling of the V-14Cr alloy further to <10%. The data presented in Figs. 1 and 2 suggest that swelling of V-Ti and V-Cr-Ti alloys is relatively independent of Ti concentration in the range of 3-20%.

Addition of either 9% W, 4% Mo, or 12% Ni to vanadium slightly decreased the swelling of vanadium on irradiation at 420°C to 114 dpa and at 600°C to 84 dpa. The Vanstar-7 alloy exhibited 7-10% swelling upon irradiation at 600°C to 77 dpa.

The dependence of swelling of vanadium and V-Ti alloys on irradiation damage (dpa) at 420°C is shown in Fig. 3. These results show that vanadium and V-3Ti-1Si exhibit maximum swelling (–3%) at 60-80 dpa, whereas swelling of V-(5-20)Ti alloys is relatively independent of irradiation damage.

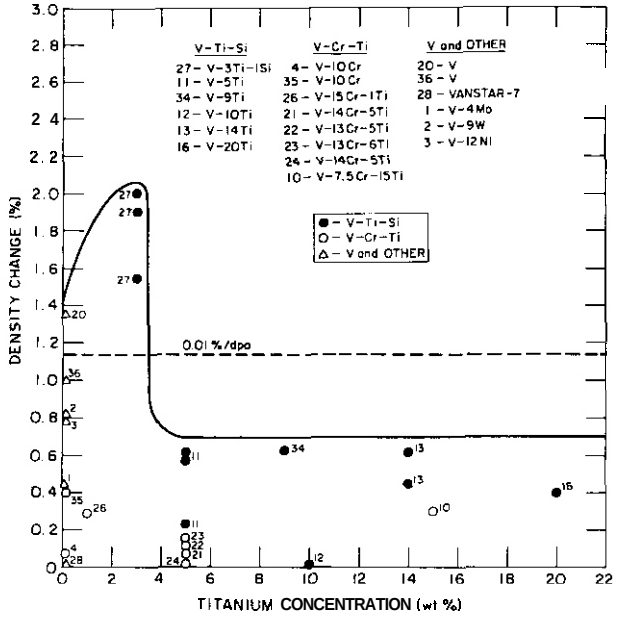

Fig. 1. Dependence of density change (swelling) on titanium concentration for vanadium alloys irradiated at 420°C to 114 dpa.

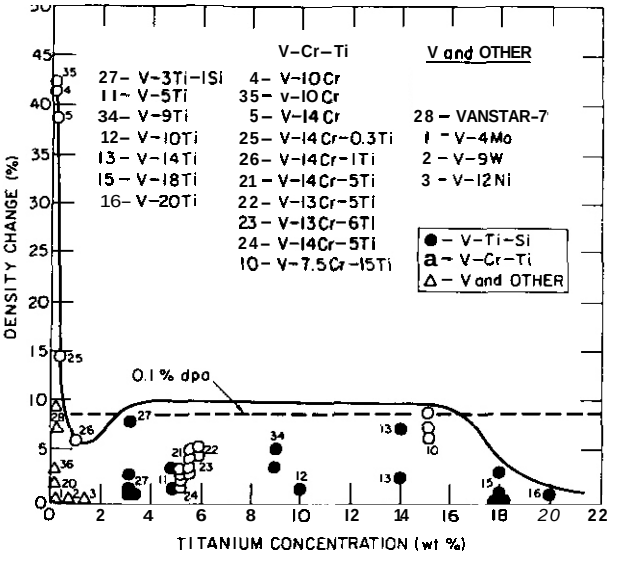

Fig. 2. Dependence of density change (swelling) on titanium concentration for vanadium alloys irradiated at 600°C to 77–84 dpa.

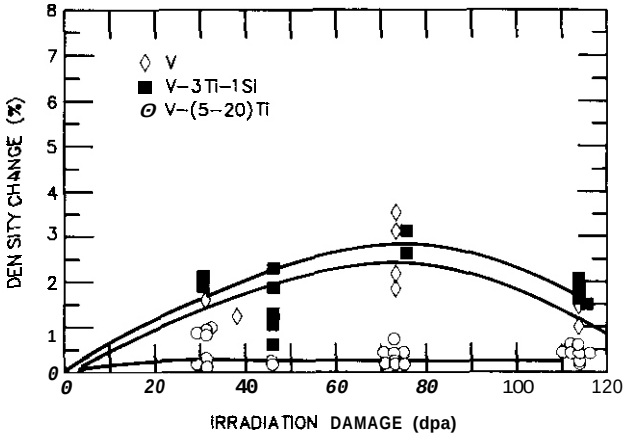

Fig. 3. Dependence of density change (swelling) on irradiation damage (dpa) for V and V-Ti alloys irradiated at 420°C.

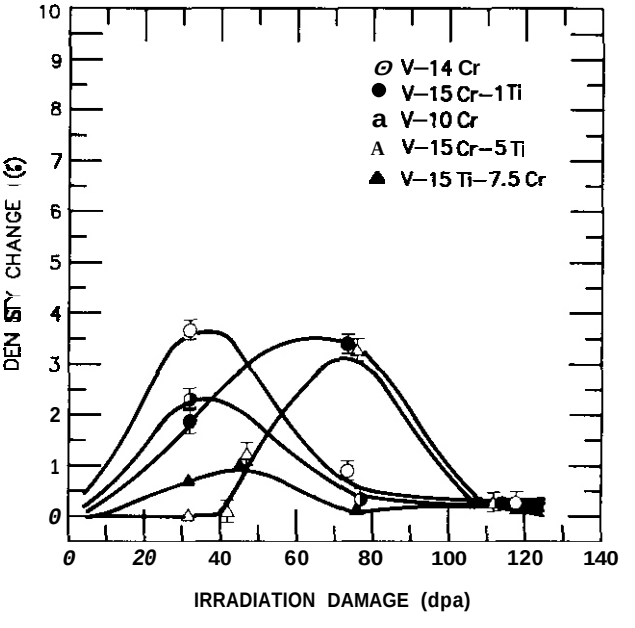

Fig. 4. Dependence of density change (swelling) on irradiation damage (dpa) for V-Cr-Ti alloys irradiated at 420°C.

The dependence of swelling of V-Cr-Ti alloys on irradiation damage at 420°C is shown in Fig. 4. These results show that upon irradiation at 420°C, V-Cr binary alloys exhibit maximum swelling at ≈30 dpa, whereas V-15Cr-(1-5)Ti alloys exhibit maximum swelling at 60-80 dpa.

The dependence of swelling of V-15Ti-7.5Cr, V-15Cr-5Ti, V-10Cr-5Ti, V-3Ti-1Si, and V-20Ti alloys on irradiation damage at 600°C is shown in Fig, 5 (from Ref. 3). Swelling data obtained by TEM of the irradiated alloys are also shown in Fig. 5. On the basis of these data, the swelling of V-15Ti-7.5Cr, V-15Cr-5Ti, V-10Cr-5Ti, V-3Ti-1Si, and V-20Ti alloys upon irradiation at 600°C to 84 dpa is 0.10, 0.03, 0.03, 0.01, and 0.01% per dpa, respectively.

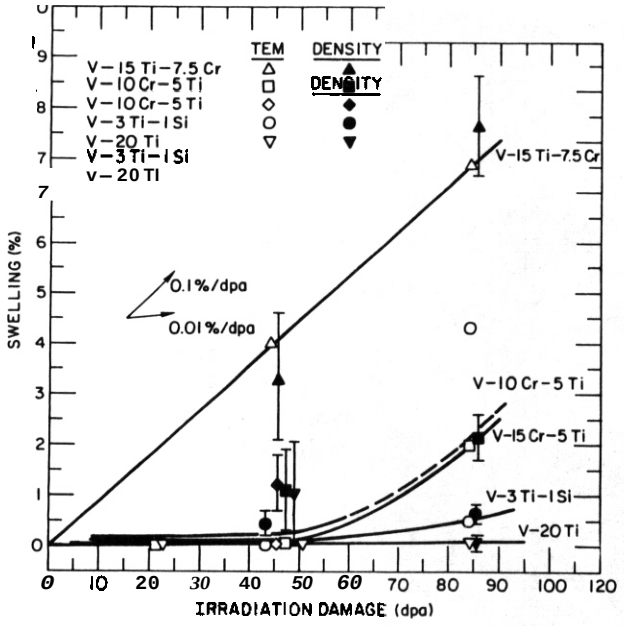

Fig. 5. Dependence of swelling of vanadium alloys at 600°C on irradiation damage.

Swelling of the partially annealed and 10% cold-worked V-Ti and V-Ti-Cr alloys does not significantly differ from the swelling of annealed alloys.

TEM Microstructures

The microstructures obtained by TEM for unalloyed V, V-10Cr, V-3Ti-1Si, V-20Ti, V-15Cr-1Ti, and V-15Cr-5Ti after irradiation at 420°C to 114 dpa are shown in Fig. 6. The swelling values determined by TEM agree well with the swelling (density change) data presented in Fig. 1, i.e., swelling of V-3Ti-1Si > V > V-10Cr > V-20Ti > V-15Cr-1Ti > V-15Cr-5Ti. For comparison, the microstructures obtained by TEM of V-15Cr-5Ti, V-15Ti-7.5Cr, V-20Ti, V-3Ti-1Si after irradiation at 600°C to 84 dpa (from Ref. 3) are shown in Fig. 7.

CONCLUSIONS

Swelling of V-Cr-Ti alloys upon neutron irradiation at 600°C is strongly dependent on Ti concentration. V-Cr-Ti alloys with >3% Ti exhibit greater resistance to irradiation-induced swelling. Swelling of V-Ti and V-Cr-Ti alloys is nearly independent of Ti concentration in the range of 3-20% Ti. Swelling of V-15Ti-7.5Cr, V-15Cr-5Ti, V-10Cr-5Ti, V-3Ti-1Si, and V-20Ti alloys upon neutron irradiation at 600°C to 84 dpa is 0.10, 0.03, 0.03, 0.01, and 0.01% per dpa, respectively. Swelling of the vanadium alloys on irradiation at 420°C to 114 dpa is <0.02% per dpa.

Partial annealing and 10% cold-work have no significant effect on swelling of the vanadium alloys.

FUTURE WORK

The swelling, precipitate composition, and precipitate crystallographic structure for vanadium-base alloys after irradiation at 420,520, and 600°C to 21-114 dpa will be determined by TEM, Energy Dispersive X-ray Spectroscopy, and Electron Energy Loss Spectroscopy.

REFERENCES

1. B. A. Loomis and D. L. Smith, "Swelling of Neutron-Irradiated Vanadium Alloys," Fusion Reactor Materials Semiannual Progress Report for Period Ending March 31, 1989, DOE/ER-0313/6, Oak Ridge National Laboratory, Oak Ridge, TN (August 1989) pp. 339-345.

2. B. A. Loomis, D. L. Smith, and F. A. Garner, "Swelling of Neutron-Irradiated Vanadium Alloys", Proceedings of the Fourth International Conference on Fusion Reactor Materials, December 4-8, 1989, Kyoto, Japan.

3. B. A. Loomis and D. L. Smith, in: Fusion Reactor Materials Semiannual Progress Report for Period Ending March 31,1990, DOE/ER-0313/8, Oak Ridge National Laboratory, Oak Ridge, TN (August 1990) pp. 225-235.

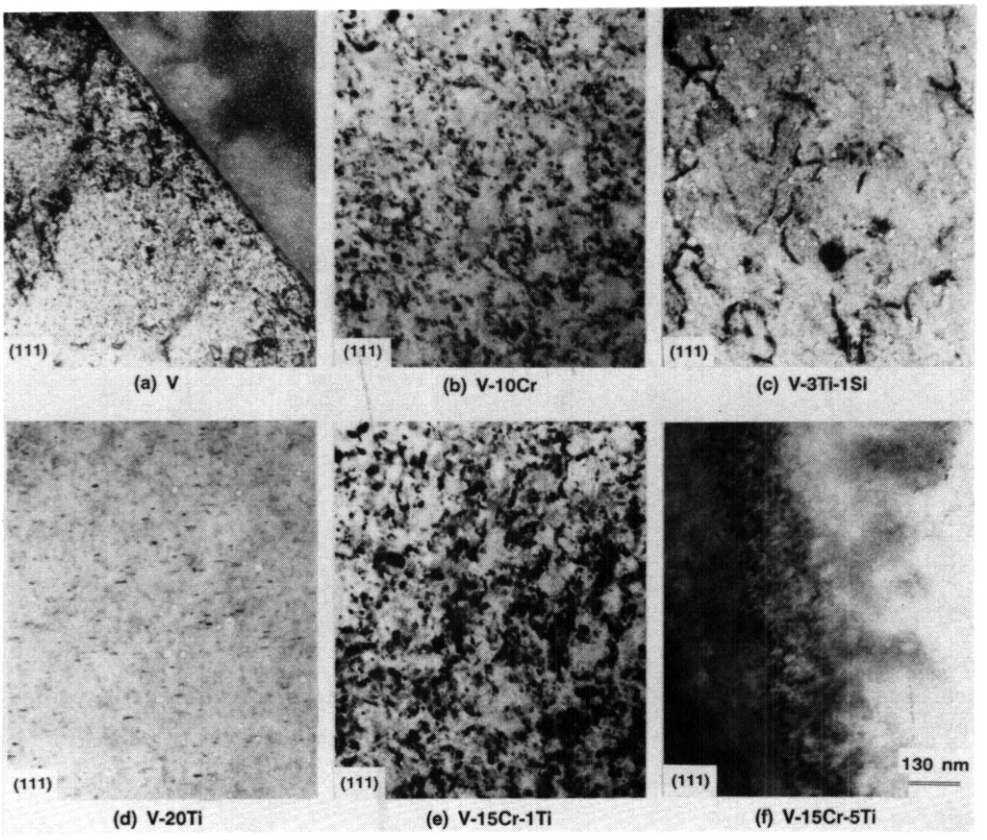

Fig. 6. Microstructures of vanadium alloys after irradiation at 420°C to 114 dpa in the FFTF-MOTA.

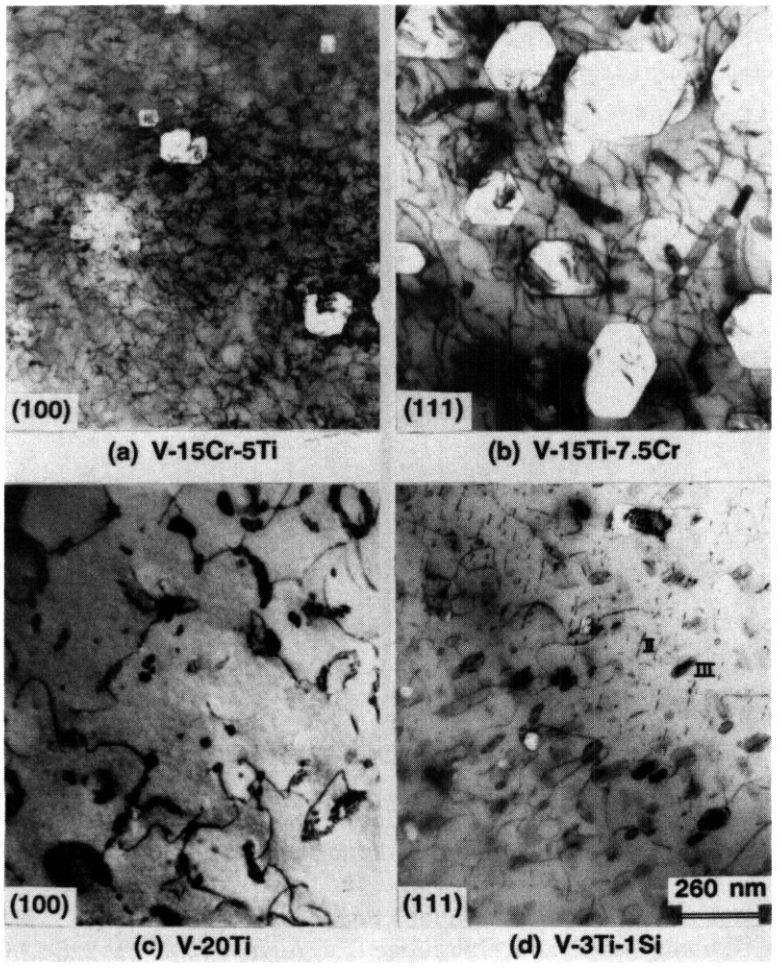

Fig. 7. Microstructures of vanadium alloys after irradiation at 600°C to 84 dpa in the FFTF-MOTA.

6.4 Copper Alloys

MECHANICAL PROPERTY CHANGES AND MICROSTRUCTURES OF DISPERSION-STRENGTHENED COPPER ALLOYS AFTER NEUTRON IRRADIATION AT 411, 414, AND 529% - K. R. Anderson (University of Illinois, F. A. Garner, M. L. Hamilton (Pacific Northwest Laboratory),[a] and J. F. Stubbins (University of Illinois)

OBJECTIVE

The objective of this effort is to identify suitable copper alloys for high heat flux applications in fusion reactors.

SUMMARY

Dispersion strengthened copper alloys have shown promise for certain high heat flux applications in both near term and long term fusion devices. This study examines mechanical properties changes and microstructural evolution in several oxide dispersion strengthened alloys which were subjected to high levels of irradiation-induced displacement damage. Irradiations were carried out in FFTF to 34 and 50 dpa at 411-414°C and 32 dpa at 529°C.

The alloys include several oxide dispersion-strengthened alloys based on the Cu-A1 system, as well as ones based on the Cu-Cr and Cu-Hf systems. Of this group, certain of the Cu-A1 alloys, those produced by an internal oxidation technique to contain alumina weight fractions of 0.15 to 0.25% outperformed the other alloys in all respects. These alloys, designated CuAl15, CuAl20, and CuAl25, were found to be resistant to void swelling up to 50 dpa at 414°C, and to retain their superior mechanical and physical properties after extended irradiation. The major factor which controls the stability during irradiation was found to be the dispersoid volume fraction and distribution.

The other alloys examined were less resistant to radiation-induced properties changes for a variety of reasons. Some of these include dispersoid redistribution by ballistic resolution, effects of retained dissolved oxygen, and nonuniformity of dispersion distribution. The effect of laser welding was also examined. This joining technique was found to be unacceptable since it destroys the dispersoid distribution and thereby the resistance of the alloys to radiation-induced damage.

PROGRESS AND STATUS

Introduction

Severe radiation and thermal environments are foreseen in advanced nuclear reactor applications. These conditions require the development of new radiation resistant materials which are also immune to thermally induced problems, such as thermal shock, thermal fatigue, irradiation and thermal creep, and thermally induced static stresses. Many of these problems can be minimized by using high strength materials with high thermal conductivity. Copper-base alloys appear to fill this need. A significant number of scoping studies have identified one specific class of copper alloys as showing exceptional potential for use in these demanding nuclear applications: oxide-dispersed copper alloys.[1-16]

This study evaluates a wide variety of oxide-dispersed alloys and identifies the factors that influence their microstructure and mechanical property changes during irradiation. This evaluation, coupled with conductivity measurements, provides the basis for judging the suitability of specific oxide-dispersed alloys for fusion applications.

Experimental Procedure

Zone-refined, Marz-grade copper and four different types of oxide-dispersed copper alloys were neutron irradiated in sealed helium-filled capsules in the Materials Open Test Assembly of the Fast Flux Test Facility to 34 displacements per atom (dpa) at 414°C, 50 dpa at 411°C, and 32 dpa at 529°C, Table 1. Irradiation temperatures were actively controlled to ±5°C. Two alloys were irradiated in the laser-welded condition in order to determine the viability of this fabrication technique in nuclear service. Thermal aging was also performed at 420°C or 521°C for 1026 hours to assess alloy thermal stability.

The four types of oxide-dispersed alloys examined are shown, along with their composition and final processing condition, in Table 2. These alloys include three commercially available copper alloys strengthened by varying quantities of aluminum oxide (CuAl15, CuAl20, and CuAl25), one alloy strengthened by chromium oxide (CuCr), one alloy strengthened by hafnium oxide (CuHf), and two castable oxide-dispersed alloys. The grain sizes of these alloys prior to irradiation are provided in Table 3. More specific information

---

(a) Pacific Northwest Laboratory is operated for the U.S. Department of Energy by Battelle Memorial Institute under Contract DE-AC06-76RLO 1830.

Specimen Irradiation Conditions

Alloy	MOTA IE Material Code	MOTA ID 411°C 50 dpa	MOTA ID 414°C 34 dpa	529°C[a] 32 dpa
Marz cu	RO	d/t[b]	d/t	d[c]
CuAl25	R4	d/t		--
CuAl25 (welded)	3N	d/t	--	--
CuAl20	UX	d/t	d/t	d/t
CuAl15 +B	V0	d	d/t	d
ODS-1	3F	d/t	--	--
ODS-1 (welded)	3H	d/t		--
ODS-4	3M	d/t		--
CuCr	3A	d/t		--
CuHf	3B	d/t		--

(a) Overtemperature of 201°C for 50 minutes and 2 undertemperatures.
(b) d/t = TEM discs t tensiles.
(c) d = TEM discs.

TABLE 2

Composition and Final Processing Conditions of Copper Alloys

Alloy	Code	Composition (wt%)	Final Processing Condition[a][b]
Marz Cu	RO	99.999% Cu	Annealed
CuAl25	R4	0.25% Al as Alumina, bal. Cu	50% CW
CuAl25	3N	0.25% Al as Alumina, bal. Cu	50% CW t welded
CuAl20	UX	0.20% Al as Alumina, bal. Cu	20% CW
CuAl15+B	V0	0.15% Al as Alumina, < 200 ppm Boron, bal. Cu	Annealed
CuCr	3A	3.5% Cr Oxide, bal. Cu	20% CW, 1/2 hr 450°C, Air Cooled
CuHf	3B	1.1% Hf Oxide, bal. Cu	20% CW, 1/2 hr 450°C, Air Cooled
ODS-1	3F	0.25% Mg, 1% Alumina, bal. Cu	40% CW
ODS-1	3H	0.25% Mg, 1% Alumina, bal. Cu	40% CW t welded
ODs-4	3M	0.5% Mg, 1% Alumina, bal. Cu	40% CW

(a) All heat treatments in argon
(b) CW =.cold worked.

Grain Size in Plane of Rolling Direction

Material	Material Code	Average Grain Diameter (microns)	Approximate ASTM Grain Size
Marz Cu	(RO)	120	3
CuAl25	(R4)	elongated 0.6 x 2.4	NM[a]
CuAl25 welded	(3N)	elongated 0.6 x 2.4	NM
CuAl20	(UX)	elongated 0.45 x 3.0	NM
CuAl15+B	(VO)	elongated 0.5 x 3.0	NM
CuCr	(3A)	1.0 - 11.5[b]	NM
CuHf	(3B)	1.0 - 11.5[b]	NM
ODS-1	(3F)	210	2
ODS-1 welded	(3H)	210	2
ODs-4	(3M)	100	1

(a) Not meaningful.
(b) Exhibited highly deformed, randomly shaped grains that could not be adequately characterized. Approximate size 1.0 to 11.5 microns.

regarding the sources and processing of these alloys is given elsewhere.[17] All specimens in this study were in the form of 3 mm TEM discs and miniature tensile specimens, the dimensions of which are given elsewhere.[18,19]

The tensile properties of unirradiated, thermally aged, and irradiated miniature tensile specimens were determined at room temperature using a precision horizontal tensile testing frame.[17] The 0.2% offset yield strength, ultimate tensile strength, fracture strength, uniform elongation, and total elongation were determined. Specimen thicknesses were measured with a micrometer prior to testing. All testing was performed at room temperature (24°C) at a crosshead velocity of 2.413 x 10^{-6} m/sec (9.5 x 10^{-5} in./sec), which corresponds to a strain rate of 4.7 x 10^{-4} sec^{-1}.

Fractography was performed with a JEOL JSM 35C scanning electron microscope (SEM). A JEOL 840 SEM with a Link Systems energy-dispersive x-ray spectroscopy (EDS) and image analysis system was also used. Fracture surfaces required examination soon after tensile testing due to rapid formation of an oxide layer that obscured detail at magnifications over approximately 1000X. Examination of the bulk microstructure was carried out with a JEOL JEM 100CX transmission electron microscope (TEM) operated at 100 kV.

Results

The results of room temperature tensile tests are given in Table 4. The yield and ultimate tensile strengths generally showed the same behavior with respect to specimen condition. The trends in the yield and ultimate tensile strengths, and uniform and total elongations, are compared in Figure 1 for alloys irradiated at 411°C to 50 dpa. Data for Marz copper are included for comparison.

Tensile properties were sensitive to several types of microstructural changes during irradiation and, to a lesser extent, changes during thermal aging. The alloy dimensional stability under irradiation, primarily influenced by void swelling, is shown in Figure 2. That and other microstructural changes are discussed subsequently.

Discussion

The discussion of alloy performance is best grouped into four classes: copper-alumina alloys, the CuCr alloy, the CuHf alloy, and castable copper ODS alloys. It is clear, however, that the performance of all of these materials is linked to dispersoid stability under irradiation and to the level of retained cold work.

TABLE 4

Average Tensile Properties from Copper and Copper Alloy Miniature Specimens

Material Code	Alloy	Yield (0.2% offset) Strength		Ultimate Tensile Strength		Fracture Strength		Uniform Elongation	Total Elongation	Number of Specimens
		MPa	(ksi)	MPa	(ksi)	MPa	(ksi)	(%)	(%)	
RO	Man Cu									
	Unirradiated	14.7	(10.8)	170.6	(24.7)	4.5	(0.6)	23.2	29.0	2
	Aged 420°C, 1016 hrs.	70.5	(10.2)	170.6	(24.7)	2.1	(0.3)	16.7	20.8	1
	Irr. 34 dpa, 414°C	64.0	(9.3)	116.1	(16.8)	103.4	(15.0)	9.7	10.1	1
	Irr. 50 dpa, 411°C	63.0	(9.1)	131.2	(19.0)	119.7	(11.4)	14.7	15.0	2
VO	CuA115									
	Unirradiated	274.4	(19.8)	359.3	(52.1)	266.2	(18.6)	12.4	15.5	3
	Aged 420°C, 1026 hrs.	301.7	(43.8)	391.4	(56.8)	106.3	(44.4)	13.4	18.3	2
	Irr. 34 dpa, 414°C	295.1	(42.8)	172.1	(54.0)	302.6	(43.9)	12.1	11.1	1
UX	CuAl20									
	Unirradiated	471.2	(68.9)	499.8	(72.5)	405.1	(58.8)	1.3	1.6	7
	Aged 420°C, 1026 hn.	422.7	(61.3)	444.1	(64.5)	387.1	(56.1)	3.5	5.9	2
	Aged 521°C, 1026 hrs.	392.9	(17.0)	425.9	(61.8)	156.8	(51.8)	5.6	8.3	2
	Irr. 34 dpa, 414°C	177.1	(54.7)	411.1	(59.6)	345.6	(50.1)	7.9	9.9	2
	Irr. 50 dpa, 411°C	176.1	(54.5)	196.5	(17.5)	353.4	(11.2)	11.1	14.1	2
	Irr. 12 dpa, 529°C	188.4	(56.3)	440.9	(61.9)	378.4	(54.9)	10.6	14.7	2
R4	CuAl25									
	Unirradiated	501.0	(72.7)	556.1	(80.7)	462.7	(67.1)	1.5	4.1	4
	Aged 420°C, 1026 hrs.	471.1	(68.6)	501.6	(72.8)	425.4	(61.7)	4.3	8.4	2
	Irr. 10 dpa 411°C	461.2	(66.9)	481.0	(69.8)	414.2	(60.1)	8.3	11.5	2
IN	CuAl25 Laser Welded									
	Unirradiated	145.U	(21.01	201.8	(29.6)	14.6	(2.1)	8.6	13.6	3
	Aged 420°C, 1026 hrs.	70.8	(10.3)	202.1	(29.3)	95.0	(13.8)	21.4	30.9	2
	Irr. 50 dpa, 411°C	72.9	(10.6)	142.Y	(20.7)	119.7	(20.3)	13.0	13.1	2
3A	CuCr									
	Unirradiated	158.8	(23.0)	299.7	(41.5)	219.9	(31.9)	22.0	30.1	2
	Aged 420°C, 1026 hrs.	148.9	(21.6)	294.9	(42.8)	202.8	(29.4)	22.6	11.0	2
	Irr. 50 dpa, 411°C	161.0	(23.6)	108.0	(44.7)	295.1	(42.8)	18.8	19.8	2
3B	CuHf									
	Unirradiated	378.1	(54.8)	461.6	(66.9)	317.0	(46.0)	4.2	8.7	1
	Aged 420°C, 1026 hrs.	154.0	(22.3)	110.0	(41.0)	204.9	(29.1)	20.9	21.6	2
	Irr. 50 dpa, 411°C (upper)	326.8	(47.4)	320.5	(46.5)	251.1	(36.4)	16.3	20.5	2
	(lower)	305.4	(44.3)							
IF	OOs-I									
	Unirradiated	312.0	(45.3)	344.6	(50.0)	171.9	(25.8)	08	3.7	2
	Aged 420°C, 1026 hrs.	62.2	(9.0)	218.1	(31.6)	75.7	(11.0)	33.8	39.8	2
	Irr. 50 dpa, 411°C	87.0	(12.6)	111.5	(22.0)	92.1	(13.4)	8.4	9.3	2
3H	ODS-1 Laser Welded									
	Unirradiated	190.6	(27.6)	228.9	(33.2)	132.9	(19.3)	15	1.5	3
	Aged 420°C, 1026 hrs.	141.5	(20.8)	224.4	(32.5)	11.5	(11.2)	2.3	4.7	2
	Irr. 50 dpa, 411°C	123.1	(17.9)	125.9	(18.3)	119.4	(17.3)	0.4	0.4	2
3M	ODS-4									
	Unirradiated	178.3	(40.4)	352.6	(51.1)	214.8	(31.2)	0.8	3.8	2
	Aged 420°C, 1026 hm.	55.2	(8.0)	227.1	(32.9)	150.6	(21.8)	37.1	40.9	2
	In. 50 dpa, 411°C	19.5	(11.5)	167.9	(13.6)	45.1	(6.5)	13.3	14.5	2

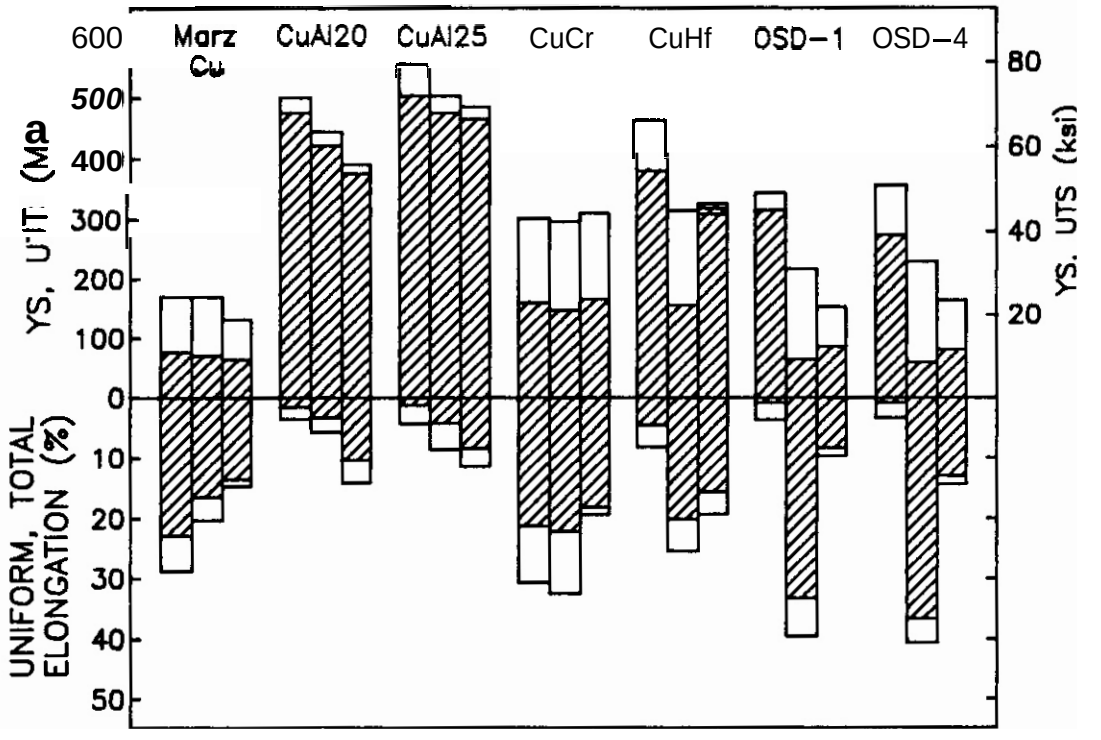

Figure 1. Tensile properties of the oxide-dispersed alloys compared with zone-refined Marz copper.

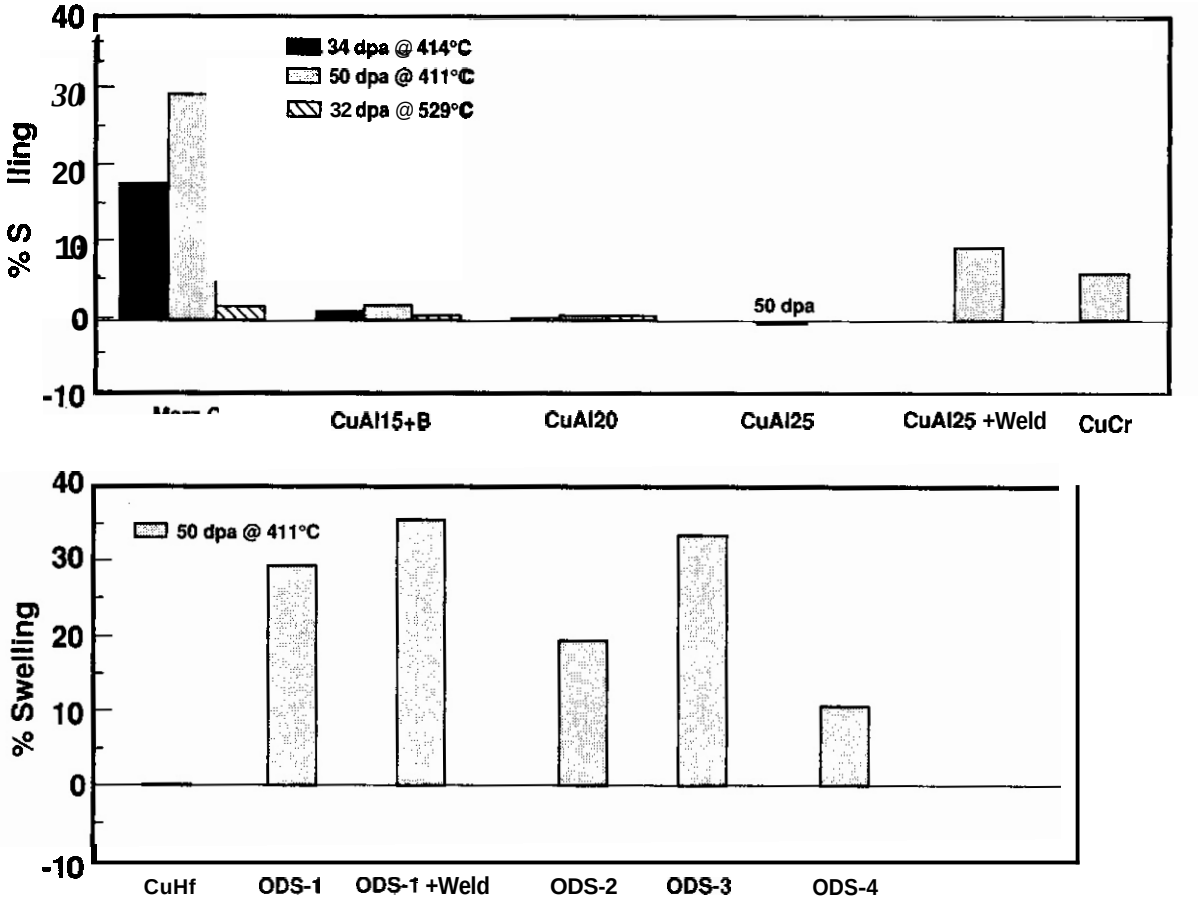

Figure 2. Swelling levels as measured by immersion density.

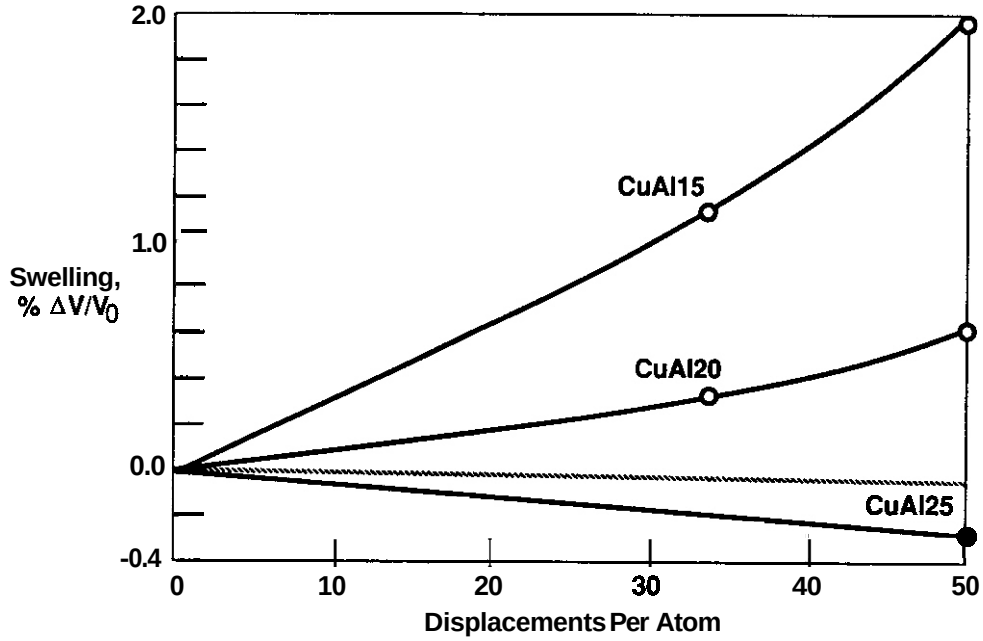

Figure 3. Swelling in copper-alumina alloys irradiated at 411 to 414°C as a function of dose.

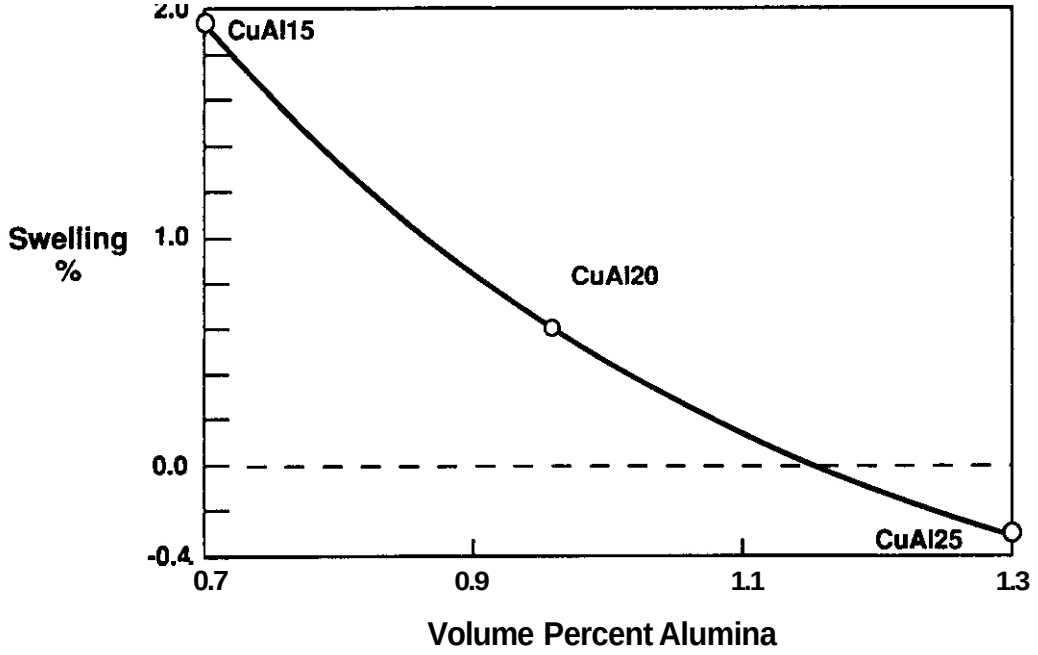

Figure 4. Swelling in copper-alumina alloys irradiated to 50 dpa at 411°C as a function of alumina volume fraction.

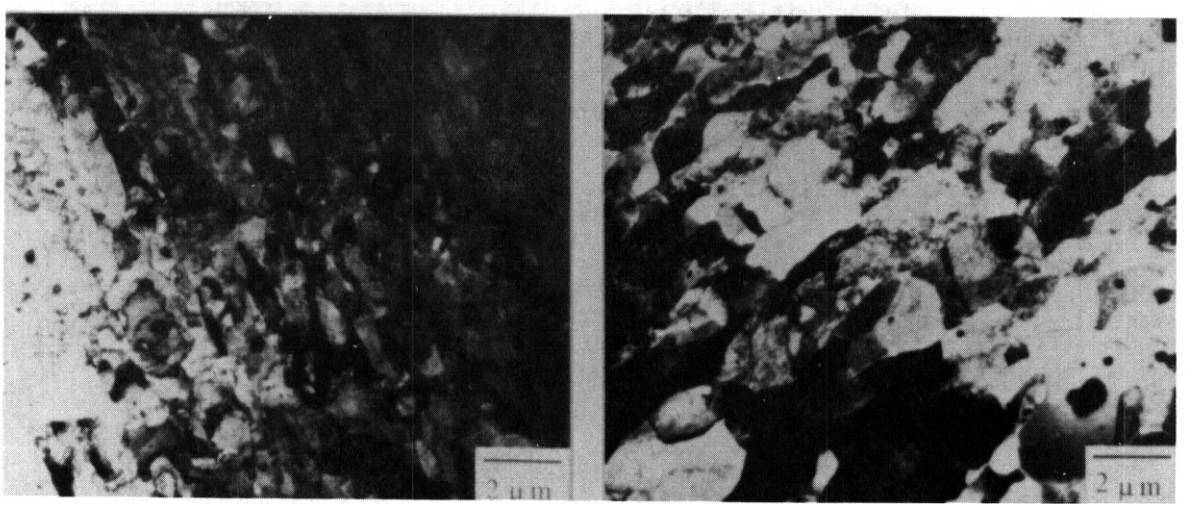

Figure 5. TEM micrographs of CuAl15, (a) unirradiated and (b and c) irradiated to 50 dpa at 411°C. Total recrystallization following irradiation is evident in (b), and the development of damage structure in areas of low dispersion density is seen in (c).

Copper-Alumina Alloys

The three copper-alumina alloys in this study, CuAl15, CuAl20, and CuAl25, were produced using powder metallurgical, internal oxidation techniques by SCM Metal Products, Inc. under the trade name of Glidcop.[20] Their Universal Numbering System designations are C15715, C15720, and C15725. The alloys were produced from Cu powder containing small amounts of aluminum in solid solution. The powder was subjected to an elevated temperature oxidizing atmosphere where the aluminum was preferentially oxidized. The powder was then consolidated by rolling at elevated temperature between thin sheets of OFHC copper. The copper cladding, which served to reduce wear of the rolls and extrusion dies, was removed by sanding. The respective volume fractions of alumina in CuAl15, CuAl20, and CuAl25 are 0.7%. 1.0%, and 1.3%. Although the difference in alumina content is not the only variation between these alloys, it is by far the most important.

The aluminum oxide phase was determined by electron diffraction to be primarily gamma alumina, in agreement with the work of Livak et al.[10] Particle diameters ranged from 2 nm to 1 μm with an average of approximately 7 nm. This average particle size is close to the 12 nm particle size that provides maximum theoretical strengthening for alumina in copper.[21] Electron diffraction also revealed the presence of a significant quantity of Cu_2O in the matrix, as would be expected from this alloy production technique. A trace quantity of alpha aluminum oxide and a relatively non-stoichiometric aluminum oxide were also observed in isolated regions of TEM foils. The oxide dispersions are not completely uniform; however the uniformity is the best available from commercial practice. The fine dispersion of gama alumina not only serves to provide substantial Orowan strengthening, but also provides excellent retention of cold work at elevated temperature.[20]

The volumetric swelling of all three copper-alumina alloys was low, as shown in Figure 3. The swelling level was found to decrease with increasing volume fraction of alumina (Figure 4). While the three alloys had different levels of cold work, the amount of cold work has a minimal influence on swelling in these alloys. This was established from annealed, 20%. and 80% cold worked CuAl20 irradiated to 34 dpa at 414°C, which swelled -0.22, 0.31, and 0.30%, respectively.

A careful TEM through-focus series on several CuAl15, CuAl20, and CuAl25 specimens irradiated to 50 dpa revealed no void formation. However, in limited regions of foils where a low dispersoid density was present, a minimal yet distinct damage structure was observed. An example of this damage structure in CuAl15 irradiated to 50 dpa is shown in Figure 5. Frank loops ranging in size from 4.0 to 12 nm in diameter were present. Both of these structures are often considered to be precursors to void formation. A small quantity of helium bubbles measuring 3.2 to 20 nm in diameter with an average diameter of 4.0 nm were also seen. No neutron irradiation study has found void formation in copper-alumina alloys; however, a high damage level ion irradiation study of CuAl60 by Spitznagel and Davis showed limited void formation in regions of low dispersoid density.[22] The helium bubbles are probably due to a $^{10}B\ (n,\alpha)\ ^{7}Li$ thermal neutron reaction with the 200 ppm (max) boron remaining in this CuAl15 alloy following deoxidation.[23] If this is the case, the boron must have been in solid solution rather than particulate form, since halos of helium and lithium, which form around boron-containing particles, were not observed.[24-27]

The room temperature tensile properties of these alloys in the unirradiated condition agree relatively well with those in the published industrial literature.[20] SEM fractography on broken tensile specimens, Figure 6, revealed the failure mechanism to be microvoid coalescence. Alumina particles of all sizes were observed to be sites for microvoid nucleation.

Room temperature tensile properties of these alloys following irradiation are dependent primarily on the amount of retained cold work. CuAl15, which was irradiated in the annealed condition, shows very small changes in the tensile properties following irradiation. However, recrystallization was observed following irradiation to 50 dpa at 411°C. Prior to irradiation, grains were elongated with an average grain size of 0.5 x 3.0 μm. Recrystallization during irradiation produced larger, more equiaxed grains measuring 1.4 x 2.5 μm on average. Despite recrystallization, significant decreases in Hall-Petch strengthening are not expected due to the small magnitude of this change and the decreased sensitivity of Hall-Petch strengthening at small grain sizes. In addition, the Hall-Petch strengthening for FCC metals is not as substantial as in BCC and HCP metals due to the larger number of slip systems and low critical stresses. The tensile failure morphology was microvoid coalescence, with fracture surfaces nearly identical in appearance to the fracture surfaces of unirradiated specimens, Figure 6.

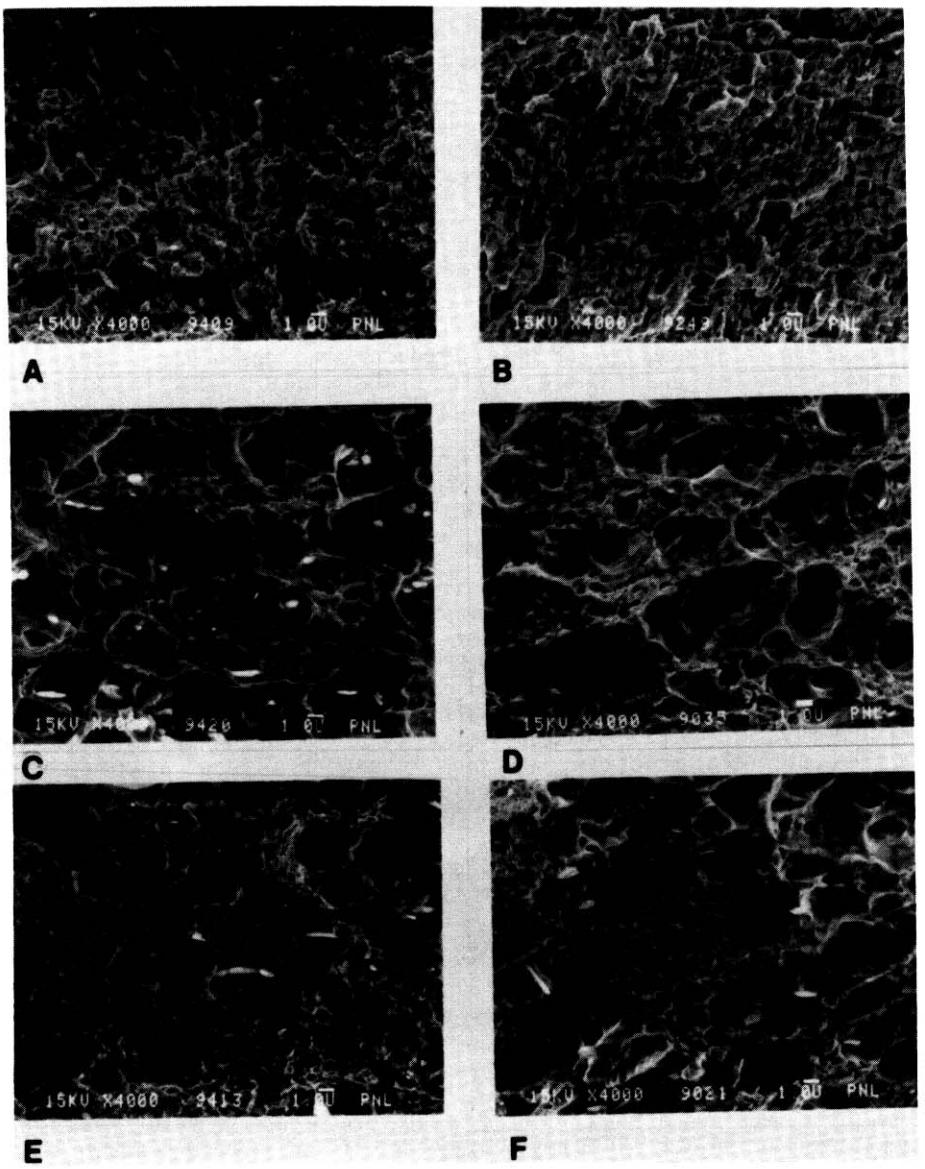

Figure 6. SEM fractographs of tensile failure surfaces for the CuAl alloys, (a,c,e) unirradiated and (b,d,f) irradiated. CuAl15 (a,b) was irradiated to 34 dpa at 414°C (b); CuAl20 (c,d) was irradiated to 50 dpa at 411°C (d); and CuAl25 (e,f) was irradiated to 50 dpa at 411°C (f).

The 20% cold worked CuAl20 exhibited significant reductions in strength and large increases in elongation for both the thermally aged and irradiated conditions. TEM examination of specimens irradiated to 50 dpa at 411°C revealed complete recovery and recrystallization. The average grain size prior to irradiation was 0.45 X 3.0 pm. Following irradiation to 50 dpa at 4112, grains were equiaxed with an average grain diameter of 0.7 μm. The failure morphology of both unirradiated and irradiated miniature tensile specimens was by microvoid coalescence, though fewer large alumina particles were found on the irradiated alloy fracture surfaces, Figure 6. The only prior neutron irradiation studies of this alloy showed no significant mechanical property or microstructure changes following irradiation.[7-13] However those studies examined substantially lower damage levels, 3 and 15 dpa.

CuAl25 was irradiated in the 50% cold worked condition to 50 dpa at 411°C. TEM examination of irradiated specimens showed the alloy to be approximately 40% recrystallized. Prior to irradiation, this heavily cold worked alloy had an average grain size of 0.6 X 2.5 μm. During irradiation, recovery and recrystallization produced regions with equiaxed grains with 1.0 μm average diameter. Recrystallized areas contained a lower density of alumina particles than the unrecrystallized, slightly polygonized areas. These microstructural changes resulted in decreased strengths and increased elongations. However, the changes were not as large as in the fully recrystallized CuAl20 alloy. The tensile fracture surfaces, Figure 6, show a microvoid coalescence failure morphology. A decrease in the quantity of large alumina particles on the irradiated alloy fracture surfaces was observed, similar to CuAl20.

Previous neutron irradiation studies of CuAl25 involved tensile testing of specimens irradiated to 16 dpa at 430°C.[1-3] This work revealed decreased strengths and increased elongations in agreement with the results here. However, no recovery or recrystallization and only minimal microstructural changes were observed by TEM examination. It is possible that recovery and recrystallization may have been present, but not revealed by limited sampling volume during TEM examination.

There is substantial evidence for ballistic redistribution (recoil dissolution) of the alumina dispersion in these alloys by neutron irradiation. This evidence arises from three sources: immersion density measurements, SEM examination of fracture surfaces, and electron diffraction patterns. Neutron-induced recoil dissolution of particles, at its simplest, is a process where the atoms composing a particle are ballistically ejected by impinging neutrons.[27,28] Ballistic dissolution of the alumina dispersion was first considered after noting the densification of CuAl25 at 50 dpa. Commonly, densification is due to phase changes or phase modifications. In this simple, fully dense alloy, one change that could provide densification is dissolution of alumina. SEM fractography of CuAl20 and CuAl25 tensile specimens revealed a reduced quantity of large alumina particles following irradiation. (Only a very few large alumina particles were observed in the CuAl15 alloy prior to irradiation; therefore, no definitive statement can be made about dissolution in this alloy.) Densification may also arise from the formation of solid transmutants, primarily nickel and zinc. This possibility is being explored.

The best evidence for ballistic redistribution is taken from the electron diffraction patterns of CuAl20 and CuAl25 before and after irradiation. The characteristic ring patterns from the fine dispersion of particles in the unirradiated material decreased substantially in intensity following irradiation. In addition, the ring resolution became less distinct, suggesting radiation damage of the dispersoid itself. Figure 7 shows a larger alumina particle in CuAl15 for both the unirradiated and irradiated to 50 dpa at 411°C conditions, where a distinct damage structure in the irradiated alumina particle can be seen.

None of the previous neutron irradiation studies involving copper-alumina alloys have noted ballistic dissolution of the alumina dispersion. However, high energy ion irradiation of CuAl60 at 250 and 500°C to20 dpa did cause dissolution and amorphization of the alumina particles.[22,28] Such recoil dissolution of particles has also been predicted theoretically.[29,30]

The dissolution phenomenon may have severe canseouences. At higher damage levels, the alloy may become more susceptible to volumetric swelling by void formation due to both a decreasing amount of alumina and an increase in dissolved oxygen. This will also affect electrical and thermal conductivity. Furthermore, strength levels may suffer both due to the loss of particulate strength and the concomitant inability to retain cold work.

Laser welding was found to be an ineffective joining method for alumina-dispersed copper alloys. Laser butt welding of CuAl25 substantially reduced the quantity of alumina in the weld section. This loss of dispersion caused irradiation-induced swelling and tensile property changes similar to those of Marz copper.[19]

The overall swelling of CuAl25 laser-welded TEM discs was approximately 9% due to void formation solely in the weld region. Unirradiated tensile strengths of welded specimens were slightly greater than for pure copper, but with nearly identical fracture surfaces. Following irradiation, similar results were found, however, the grain structure was columnar along the direction of welding and not equiaxed.

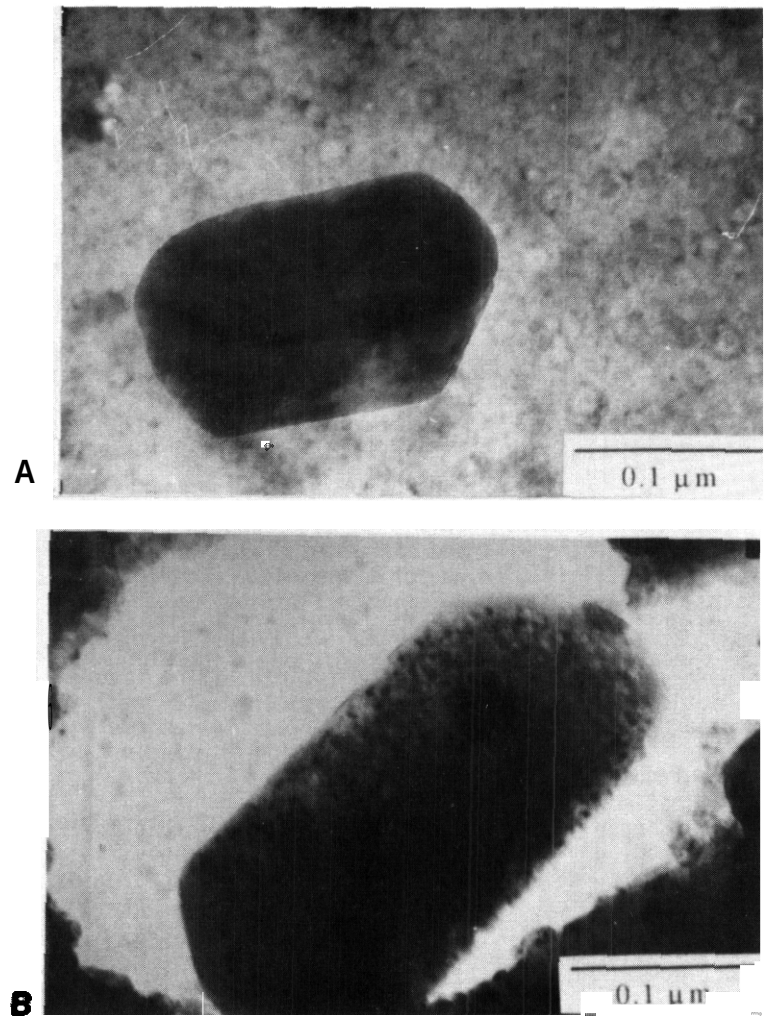

Figure 7. Large alumina particles in CuAl15, (a) unirradiated and (b) irradiated to 50 dpa at 411°C.

Copper-Chromium Oxide

The copper-chromium oxide alloy was produced by hot extrusion of a mixture of OFHC copper and chromium oxide powders. TEM and SEM examination revealed a range of chromium oxide particle sizes from 0.012 to 0.7 µm in diameter, with an average diameter of 0.05 µm. Electron diffraction also indicated the presence of a small quantity of Cu_2O in the matrix. Fractography of unirradiated tensile specimens revealed several large, irregularly shaped inclusions. The appearance and electrical charging of these inclusions during SEM examination suggests that they are ceramic. Windowless EDS chemical analysis showed varying quantities of calcium, magnesium, aluminum, and oxygen. These elements are the same as those commonly found in ceramic refractories, indicating that these inclusions were possibly pieces of ceramic furnace lining or slag in the original OFHC copper powder.

The volumetric swelling of this alloy was approximately 6% following irradiation to 50 dpa at 411°C, primarily due to void formation and dissolution of the refractory inclusions. SEM tensile fractography following irradiation revealed both voids and the presence of other cavities containing only trace remnants of the refractory inclusions, Figure 8.

As in the case of the copper-alumina alloys, evidence of ballistic redistribution of the oxide dispersion was found. TEM examination of unirradiated material revealed large, relatively spherical chromium oxide particles, Figure 9. Following irradiation, these large particles were seen to be redistributed into smaller, less distinct particles with sizes ranging to below 2 nm in diameter, Figure 9. The redistribution of the oxide dispersion in this alloy is more prominent than in the copper-alumina alloys, probably due to the lower thermodynamic stability of chromium oxide compared to aluminum oxide.

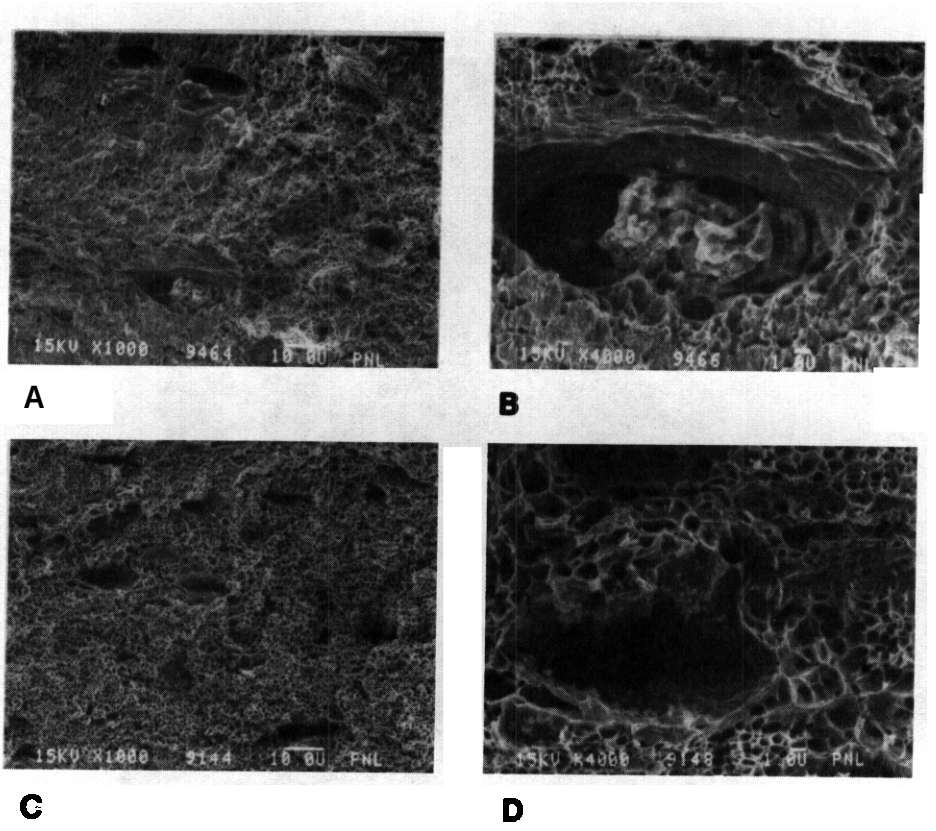

Figure 8. SEM fractographs of CuCr tensile fracture surfaces, (a,b) unirradiated and (c,d) irradiated to 50 dpa at 411%. The influence of large inclusions on the fracture morphology can be noted.

Prior to irradiation, this alloy exhibited a moderate tensile strength and an elongation comparable to that of zone-refined copper. The failure morphology was transgranular by microvoid coalescence, Figure 8. The yield and ultimate strengths of this alloy changed only slightly following irradiation to 50 dpa at 411°C, even though TEM examination revealed substantial microstructural evolution. This is due to the competing influences of several strengthening mechanisms. The initial 20% cold work was completely recovered during irradiation. Recrystallization produced a grain size that was too large to be measured using TEM; high radioactivity precluded optical measurement. The reduction in cold work and grain size strengthening were offset by increased Orowan strengthening from a finer, redispersed particulate distribution and a slight contribution from voids, Figure 9.

The reduced total elongation in the irradiated alloy is a direct conseauence of a limited reduction of area promoted by voids and cavities. Just as in zone-refined copper, voids acted as sites for failure by microvoid coalescence, reducing the ability of this alloy to undergo localized deformation. Cavities, which were previously occupied by inclusions, also acted as sites for crack nucleation and propagation, Figure 8.

Comer-Hafnium Oxide

The copper-hafnium oxide alloy was produced by a hot extrusion of a mixture of OFHC copper and hafnium oxide powders. SEM examination revealed large rounded hafnia particles ranging in diameter from 0.05 to 0.65 μm with an average of 0.25 μm. TEM bright and dark field imaging also revealed many smaller, less distinct hafnia particles, as small as 2.5 nm in diameter. A small quantity of Cu_2O was seen and many small unidentified particles also were manifested in the diffraction pattern as widely scattered spots.

Volumetric swelling of 0.15% was measured by density change following irradiation to 50 dpa. However, TEM examination found no signs of voids. Helium bubbles, Frank loops, and other precursors to void formation also were not observed.

TEM examination revealed extensive redistribution of the dispersion, again most probably by a ballistic mechanism. This was evidenced by a reduced quantity of the large, rounded hafnia particles as well as many smaller polygonal particles which were not present prior to irradiation. These particles measured an average of 0.1 μm in diameter and are shown in Figure 10. A significant quantity of new particles, averaging 5 nm in diameter, of the same structure as the larger polygonal particles are also seen. SAD indicated that these particles are most probably monoclinic HfO_2.

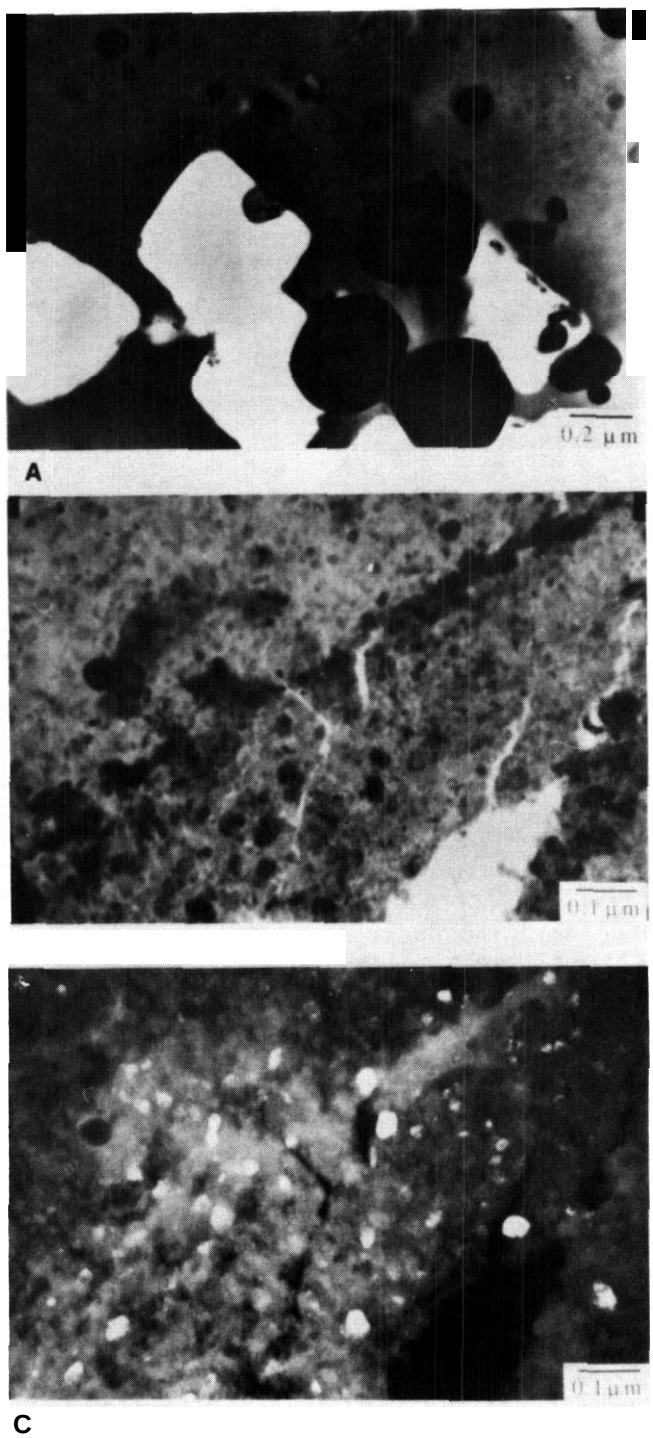

Figure 9. TEM micrographs of CuCr, (a) unirradiated and (b,c) irradiated to 50 dpa at 411%. The irradiated material is shown in a bright field (b) and dark field (c) pair.

This alloy exhibited good tensile strength and reasonable elongation in the unirradiated condition. The failure morphology was transgranular by microvoid coalescence, Figure 11. Thermal aging for 1026 hours at 420°C promoted a substantial reduction in tensile strength and increase in elongation, probably due to recovery of cold work.

The influence of the redistribution of the oxide dispersion was dramatically illustrated in the tensile properties of this alloy following irradiation to 50 dpa at 411°C. A prominent yield point drop was observed. This yield point phenomenon, commonplace in ferritic steels and other BCC metals, is highly unusual in

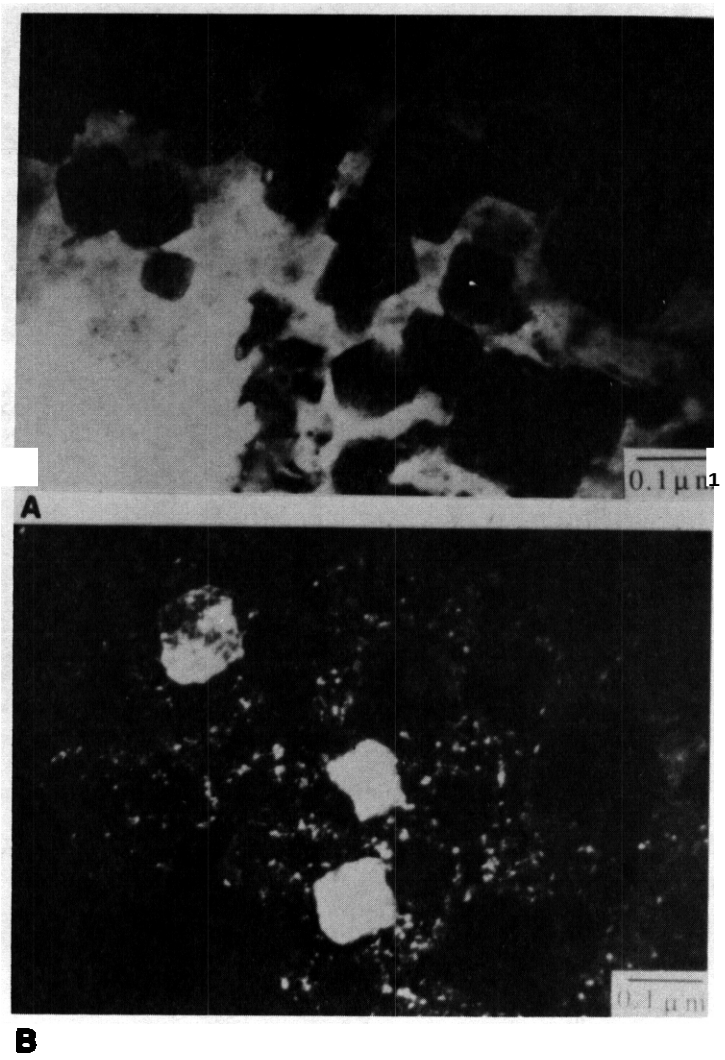

Figure 10. TEM micrographs of CuHf irradiated to 50 dpa at 411°C. A bright field (a) and dark field (b) pair is shown where two distinct particle distributions can be seen.

FCC metals. Figure 12 shows tensile curves for this alloy in the unirradiated, thermally aged, and irradiated conditions. The irradiation-induced yield point is of approximately of the same maqnitude as the ultimate tensile strength of this alloy. Following this yield drop, the tensile curve was wavy, becoming smoother at higher strains.

In addition to extensive redistribution of the oxide dispersion, TEM examination revealed total recovery and recrystallization during irradiation. Pinning of a low density of dislocations by redistributed hafnium is directly responsible for the unique tensile properties. There is some doubt as to the form of the redistributed hafnium. There is a large size difference (23%) between copper and hafnium.[31] Thus, despite arguments for the lack of a shear component in the substitutional atom strain field and a consequent inability to pin screw dislocations, it may be that the large size difference would nevertheless cause such an effect here. Alternatively, dislocations may act as sites for preferential hafnium oxide reformation during irradiation, effectively pinning them with small hafnia particles. It was not possible to distinguish between these possibilities by TEM examination techniques.

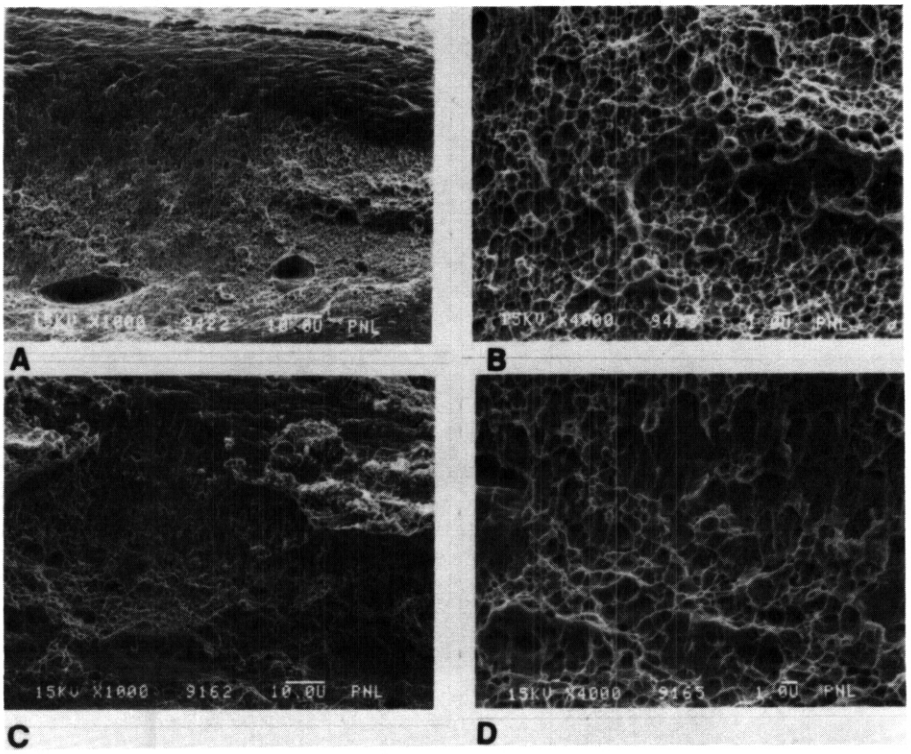

Figure 11. SEM fractographs of tensile fracture surfaces of CuHf, (a,b) unirradiated and (c,d) irradiated to 50 dpa at 411°C.

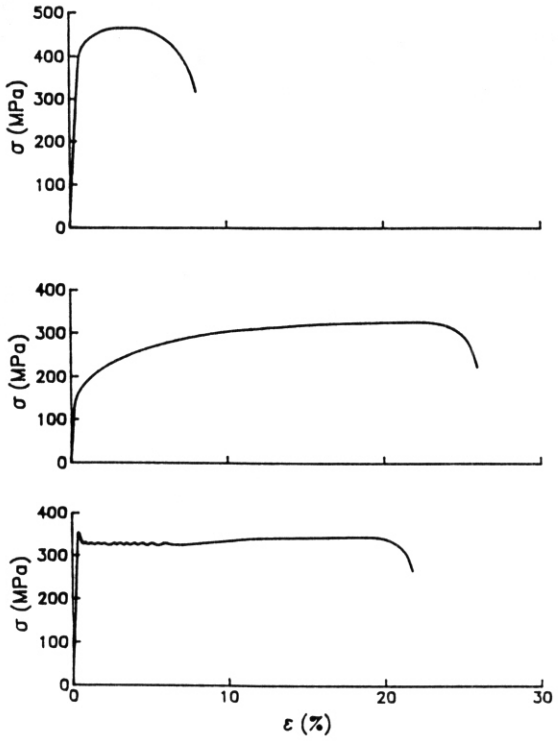

Figure 12. Tensile curves of CuHf in the unirradiated, thermally aged, and irradiated to 50 dpa at 411°C conditions. The upper and lower yield phenomenon in the irradiated condition is notable.

Fractography revealed no apparent change of failure mechanism following irradiation. Failure was seen to occur by transgranular microvoid coalescence, as also shown in Figure 11.

Castable ODS Comer Allovs

These alloys were cast from a melt composed of a fine dispersion of copper-coated colloidal oxide particles added to magnesium-bearing OFHC copper. Magnesium should promote effective incorporation and retention of the dispersed oxide during casting. One goal of the alloy design was to create a castable oxide-dispersed alloy that could also be welded.

These alloys showed extremely poor swelling resistance following irradiation to 50 dpa at 411°C: 10.75% for ODS-4 and 29.4% for ODS-1. The swelling level of ODS-1 was the same as pure copper under these irradiation conditions.

The unirradiated alloys exhibited minimal uniform tensile elongations due to microporosity, Figure 13. The microporosity was in the form of planar arrays of bubbles along cold rolling directions. Laser-welded ODS-l had spherical microporosity in the melted and undeformed weld region. Thermal aging at 420°C for 1026 hours promoted substantial decreases in strength and increases in elongations, verifying the poor thermal stability of these alloys.

Poor tensile properties following irradiation were due not only to poor thermal stability but also to substantial void formation. The failure morphology was identical to that observed in irradiated copper: transgranular by microvoid coalescence with surfaces often lying parallel to but not on the grain boundaries, Figure 13.[19]

The poor irradiation performance of these alloys is most probably attributable to a supersaturation of dissolved oxygen introduced during the casting process. However, it was not possible to obtain a measurement of the matrix oxygen concentration independent of the dispersed oxide to verify this postulate. Nevertheless, the microporosity found on fracture surfaces of unirradiated material supports this conclusion. Several researchers have shown that dissolved oxygen is highly efficient in promoting void formation in copper,[14-16,32] such as found here. Studies of electrolytic tough pitch copper irradiated in EBR-II to 13.5 dpa at 400°C found swelling of 34% or ~2.5%/dpa.[14-16] These results indicate that stringent oxygen-free casting practices must be observed when producing not only these alloys, but possibly other copper alloys. With such practice, it is possible that these castable ODS alloys would possess acceptable radiation resistance.

CONCLUSIONS

Zone-refined copper and several oxide-dispersed copper alloys were neutron irradiated to 34 dpa at 414°C, 50 dpa at 411°C, and 32 dpa at 529°C and a wide range of irradiation response was observed. The most important conclusions from this study are as follows:

1. The chemical composition of the dispersed oxide has a significant influence on the radiation resistance of oxide-dispersed alloys. Aluminum oxide-dispersed alloys were much more stable than either chromium or hafnium oxide-dispersed alloys. A highly unusual yield point phenomenon was observed in hafnium oxide-dispersed copper due to extensive redistribution of the oxide dispersion during irradiation.

2. All oxide-dispersed alloys showed some dissolution and restructuring of the dispersion by ballistic recoil during irradiation.

3. The radiation resistance of aluminum oxide-dispersed alloys (CuAl15, CuAl20, and CuAl25) was found to be directly dependent on the amount of dispersed oxide in the matrix. Volumetric swelling decreased as the amount of dispersed oxide increased, though it was small in all cases. No voids were found in these alloys.

4. The tensile properties of the aluminum oxide-dispersed alloys (CuAl15, CuAl20, and CuAl25) following irradiation were dependent on the amount of retained cold work, which was also related to the alumina content.

5. CuAl25 was found to be the most radiation-resistant alloy in terms of swelling, tensile properties, and conductivity.[32] It appears to be the best copper alloy for elevated temperature, neutron environment exposure.

6. Laser welding was found to be an ineffective joining method for oxide-dispersed alloys. A substantial loss of the dispersion in the weld region led to irradiation performance nearly identical to the poor performance observed in pure copper.

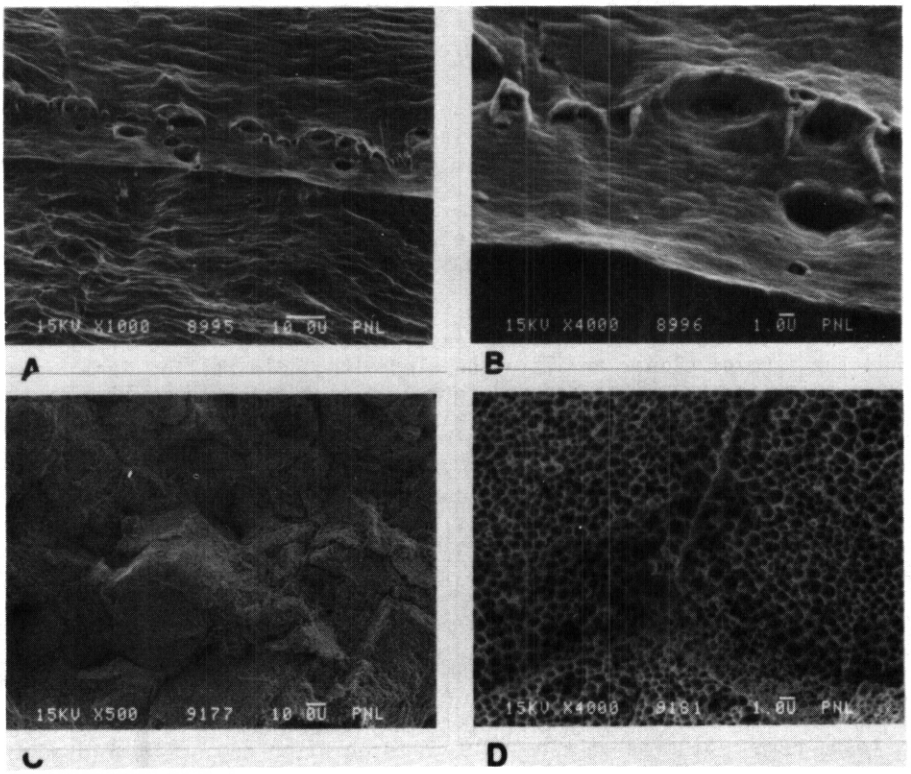

Figure 13. SEM fractographs of the tensile fracture surfaces of the ODS-1 alloy, (a,b) unirradiated and (c,d) irradiated to 50 dpa at 411°C. The strong influence of the void structure on the tensile fracture behavior is clearly evident in the irradiated material.

7. Oxygen contamination during casting must be prevented for copper alloys in nuclear service since oxygen promotes extensive radiation-induced void formation. Dissolved oxygen may become a concern even in the presence of oxide particles if ballistic dissolution places significant amounts of oxygen into solution.

FUTURE WORK

Analysis of specimens irradiated to 100 and 150 dpa will be performed.

ACKNOWLEDGEMENTS

The participation of K. R. Anderson and J. E. Stubbins was supported by the Northwest College and University Association for Science.

REFERENCES

1. Brager, H. R., H. L. Heinisch, and F. A. Garner, J. Nucl. Mater. 133 & 134 (1985) 676-679.

2. Brager, H. R., J. Nucl. Mater. 141-143 (1986) 163-168.

3. Brager, H. R., J. Nucl. Mater. 141-143 (1986) 79-86.

4. Brager, H. R., and F. A. Garner, in Fusion Reactor Materials, DOE/ER-0313/3 (1987), 254-259.

5. Brager, H. R., and F. A. Garner, in Effects of Radiation on Materials: 14th International Symposium (Volume II), ASTM STP 1046, N. H. Packan, R. E. Stoller and A. S. Kumar, eds., American Society for Testing and Materials (1990), pp. 599-604.

6. Garner, F. A., H. R. Brager and K. R. Anderson, "Neutron-Induced Changes in Density and Electrical Conductivity of Copper Alloys at 16 to 98 dpa and 430°C," to be published in J. Nucl. Mater. 176 (1990).

7. Livak, R. J., T. G. Zocco, and J. C. Kennedy, in ADIP Semiannual Progress Report, DOE/ER-0045/14 (1985), 152-160.

8. Frost, H. M., and J. C. Kennedy, in ADIP Semiannual Proaress Report, DOE/ER-0045/14 (1985), 161-167.

9. Livak, R. J., L. S. Leinson, and E. K. Opperman, Trans. ANS 49 (1985) 106.

10. Livak, R. J., T. G. Zocco, and L. W. Hobbs, in Damaae Analysis and Fundamental Studies, DOE/ER-0046/24 (1986), 94-99.

11. Livak, R. J., H. M. Frost, T. G. Zocco, J. C. Kennedy, and L. W. Hobbs, J. Nucl. Mater. 141-143 (1986) 160-162.

12. Frost, H. M., and J. C. Kennedy, J. Nucl. Mater. 141-143 (1986) 169-173.

13. Livak, R. J., T. G. Zocco, and L. W. Hobbs, J. Nucl. Mater. 144 (1987) 121-127.

14. Ames, M., G. Kohse, T. S. Lee, N. J. Grant, and O. K. Harling, J. Nucl. Mater. 141-143 (1986) 174-178.

15. Lee, T. S., L. W. Hobbs, G. Kohse, M. Ames, O. K. Harling, and N. J. Grant, J. Nucl. Mater. 141-143 (1986) 179-183.

16. Harling, O. K., N. J. Grant, G. Kohse, M. Ames, T-S Lee, and L. W. Hobbs, J. Mater. Res. 2(5) (1987) 568-579.

17 Anderson, K. R., PhD Thesis, University of Illinois at Urbana-Champaign, Department of Materials Science and Engineering (1990).

18. Panayotou, N. F., S. D. Atkin, R. J. Puigh, and B. A. Chin, "Design and Use of Nonstandard Tensile Specimens for Irradiated Materials Testing," in The Use of Small-scale Specimens for Testing Irradiated Materials, ASTM STP 888 (1986), 201-219.

19. Anderson, K. R., F. A. Garner, and J. F. Stubbins, "Unusual Tensile and Fracture Behavior of Pure Copper at High Levels of Neutron-Induced Swelling," DOE/ER-0313/8 (1990), 243.

20. Glidcop, SCM Metal Products, Inc., 11000 Cedar Avenue, Cleveland, Ohio 44016, U.S.A. (1988).

21. Kupcis, O. A., B. Ramaswami, and O. T. Woo, Acta Met 21 (1973) 1131.

22. Spitznagel, J. A., and J. W. Davis, in ADIP Semiannual Proaress Report, DOE/ER-0045/14 (1985), 168.

23. Zinkle, S. J., in Fusion Reactor Materials, DOE/ER-0313/6 (1989).

24. Hishinuma, A., Y. Katano, and K. Shiraishi, J. Nucl. Mater. 52 (1974) 103-111.

25. Gelles, D. S., and F. A. Garner, J. Nucl. Mater. 85-86 (1979) 689.

26. Vela, P., J. Hardy, and 8. Russel, J. Nucl. Mater. 26 (1968) 129.

27. Kumar, A. S., and F. A. Garner, Rad. Effects 82 (1984) 61-72.

28. Spitznagel, J. A., N. J. Doyle, W. J. Choyke, J. G. Greggi, Jr., J. N. McGruer, and J. W. Davis, Nucl. Instr. and Meth. in Phys. Res. B16 (1986) 279-287.

29. Frost, H. J., and K. C. Russell, Acta Met. 30 (1982) 953-960.

30. Russell, K. C., Progress in Mat. Sci. *28* (1984) 229-434.

31. Wert, C. A., and R. M. Thomson, Phvsics of Solids, Second Edition, McGraw-Hill, New York, 1970, p. 23.

32. F. A. Garner, K. R. Anderson and T. Shikama, "Radiation-Induced Changes in Electrical Conductivity of a Wide Range of Copper Alloys, also in this semiannual report.

BRAZING OF COPPER-ALUMINA ALLOYS - B. A. Chin, C. K. Lee and R. C. Wilcox, Auburn University, Auburn, AL 36849.

OBJECTIVE

The objective of the research is the development of an induction brazing process for GLIDCOP Al-15 using a silver-based brazing alloy. This objective centers on minimizing the time required at elevated temperatures during the brazing process in order to eliminate the problems of furnace brazing.

SUMMARY

An induction braze has been developed to join copper-alumina alloys. This brazing technique is proposed to replace current furnace brazing methods that have yielded poor results because of silver ingression along the fine grain boundaries of the copper-alumina alloys. The induction braze (because of the short braze time) severely restricts silver ingression along the grain boundaries of the alloy. Tensile tests of induction brazed lap joints fail in the base material rather than the braze indicating good braze properties.

PROGRESS AND STATUS

Introduction

The GLIDCOP A1-15 alloy (CDA alloy 15715) for use in tokamak fusion reactors. This choice was made because of the alloy's high heat carrying capacity, high electrical conductivity, and the ability to retain a cold worked structure at elevated temperatures. Specific uses of the alloy are as a structural material in diverter and limiter assemblies and as magnets. However, the successful use of this alloy depends on the ability to join the alloy during fabrication without destroying its properties such as the high heat carrying capacity, and electrical conductivity. Thus, a brazing process that does not alter the alloy's structure or properties is highly desirable for the design of these devices and their Successful application in tokamak reactors.

The development of an induction brazing process for GLIDCOP A1-15, a cold worked copper-0.15 aluminum alloy, will eliminate 3 major problems associated with furnace brazing of GLIDCOP Al-15:

1. Plating the joining surfaces prior to brazing if a material (braze alloy) is used.
2. Using an inert cover gas or a vacuum pump to prevent excessive oxidation.
3. Lowering of the yield and ultimate tensile strength by approximately 20% due to recovery of the matrix.

Experimental Procedure

Brazed joints will be produced by using a 50 Kw induction furnace with an oval shaped helical coil. The samples will be electrically insulated from the coil by means of a quartz tube. Very fine copper wire is to be wound about the joint that is to be brazed to hold the 0.076 mm thick BAg-5 brazing alloy in place and to keep the two metal strips straight. A range of braze times and power settings for consistent brazing have been developed.

Microhardness measurements will be made both lengthwise and across the brazed section. Measurements will be made at a number of places in the brazed section and at 1 mm intervals from the brazed region into the base metal.

Rectangular strips of constant cross-sectional area are to be machined into tensile specimens from a brazed single overlap joint. A pin loaded single-lap shear test specimen (Figure 1) according to the AMERICAN WELDING SOCIETY STANDARD is to be used for evaluating the strength of brazed joints in shear. Additional mechanical testing will be done using miniature tensile specimens (Figure 2). Strain data for the miniature specimens will be obtained using a LASERMIKE 162-100 Laser Scanner with a LASERMIKE 1010 Processor. The processor will be interfaced with a plotter.

Fatigue specimens of constant cross-sectional area will be produced by butt brazing thick plates. Miniature fatigue specimens will then be machined from this butt joint. Transmission electron microscopy size (3 mm diameter) fatigue specimens also will be made. These later specimens will be used for determination of the effects of stress cycling on the structure of the alloy.

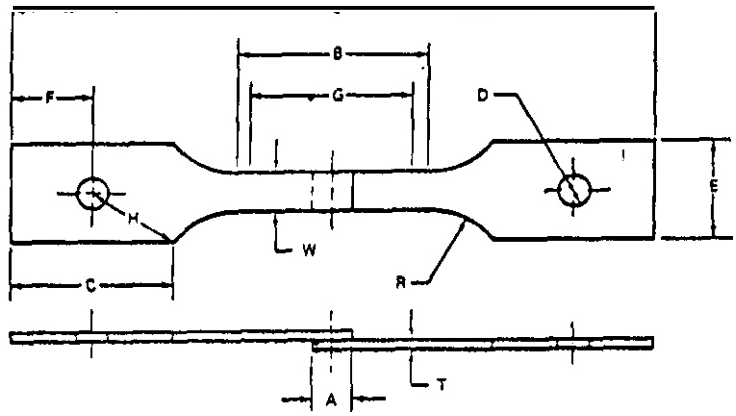

Descriution - Modified Standard

G - gage length ..... 12.2 mm
W - width ..... 3.2 mm
T - thickness ..... 0.7 mm
R - radius of fillet, min. .....3.2 mm
L - overall length, min. .....48.8 mm
B - length of reduced section, min. .....13.7 mm
C - length of grip section, min. ....12.2 mm
E - width of grip section approx. ....7.6 mm
D - diameter of hole for pin .....3.2 mm
F - edge distance from pin, approx. ..... 6.4 mm
A - joint overlap ..... 7.1 mm

Figure 1. AWS standard Pin Loaded Single-Lap Shear Test specimen

Description - Miniature

G - gage length ..... 5.1 mm
W - width ..... 1.0 mm
T - thickness ..... 0.7 mm
R - radius of fillet, min. .....1.6 mm
L - overall length, min. .....12.7 mm
E - width of grip section approx. ....2.5 mm
A - joint overlap .....2.0 - 2.8 mm

Figure 2. Miniature Tensile Specimen Dimensions

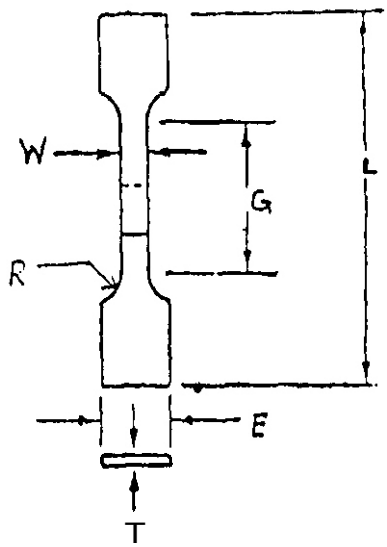

Recent Results

Preliminary results of induction brazing of GLIDCOP Al-15 using the BAg-5 alloy have been obtained by varying the heating time and power used. The best brazing results were obtained using a power setting of 45 to 50 for the pin-loaded specimens and a setting of 55 for the miniature samples. The greater power requirements of the miniature samples was the result of fabrication of a large specimen from which the miniatures were machined. The minimum brazing time required to produce mechanically sound joints was 4 to 5 seconds using a 50 Kw induction furnace and a tightly wound oval-shaped helical coil. Both the miniature and the pin loaded specimens required this amount of brazing time. For times less than 4 seconds, the filler metal did not completely melt resulting in incomplete bonding. At a brazing time of 6 seconds the base copper alloy had a tendency to distort (wrinkle). The alloy started to melt in 7 to 8 seconds.

Table 1 shows some typical values of yield strength for pin loaded samples along with the overlap length and the furnace power settings. For the pin-loaded specimens with an overlap of slightly over 6.4 mm, the yield strength was generally of the same order as that of the unbrazed material. This would indicate that little degradation of the alloy occurred during induction brazing under the given conditions.

Table 1. Yields strength of induction brazed pin-loaded GLIDCOP A1-15 joints. (Braze time - 4 seconds).

Yield Strength (MPa)	Overlap length (mm)	Power Setting (unitless)
328	6.91	55
228	7.72	55
313	6.86	50
324	7.85	50
365	7.24	45
316	6.73	45
ORNL yield strength data at room temperature for unbrazed GLIDCOP Al-15		
315		
325		

Calculations were performed to study the extent of diffusion of silver from the brazing alloy into the GLIDCOP Al-15 base material. Such calculations could help to determine the possible damage caused by diffusion of silver to both the microstructure and properties of the joint as a result of induction brazing. The following assumptions were made in these calculations.

1. Silver content in the braze filler (BAg-5) was 45%
2. Solvent: copper
   Impurity: silver
   Diffusion coefficient of silver in copper: 0.63 cm^2/sec [1]
   Activation energy for volume diffusion: 46.5 Kcal/mole.
   Activation energy for surface and grain boundary diffusion was assumed to be one-half of that for volume diffusion: 23.3 Kcal/mole.

The resulting data on the diffusion of silver into copper are listed in Table 2.

Table 2. Amount of silver diffused into copper as a function temperature and depth of penetration.

Depth of Penetration into copper (mm)	Percentage of Silver Present Temperature 1273°K	1173°K	1073°K
Volume Diffusion			
0.025	0.0	0.0	0.0
0.0025	5.4	0.0	0.0
surface and Grain Boundary Diffusion			
0 025	39	36	32
0 0025	45	45	45

TO verify these calculations, EDX analysis was performed on various types of joints and on the filler material. The filler alloy BAg-5 has a nominal composition of 45 Ag, 30 Cu and 25 Zn by weight. EDX analysis showed a composition of 44.3 Ag, 30.2 Cu and 25.1 Zn. Several furnace brazed lap joint specimens were produced for comparison with the induction brazed samples. The Standard Ticusil Cycle [2] was used for furnace brazing. This cycle was chosen because the composition of the Ticusil filler alloy is 68.8 Ag, 26.7 Cu and 4.5 Ti which is the closest to the BAg-5 composition. The furnace brazing cycle used was as follows:

1. 25°K per minute to 1088°K, hold at 1088°K for 20 minutes
2. 5°K per minute to 1143°K, hold for 5 minutes
3. Cool at 2.5°K per minute to room temperature.

EDX analysis of the furnace brazed joint using the BAg-5 filler alloy showed two major results. First, the zinc in the filler material decreased from 25% to 1.7% or less. Second, a measurable amount of silver was found at about 0.37 mm below the external surface of the lap joint (Fig. 3) indicating considerable diffusion of the filler material into the copper alloy. The thickness of the copper was only 0.76 mm.

Induction butt joints and lap joints did not have such change in composition of the filler material during brazing. A decrease in zinc from 25 to 218 did occur in butt joints for an increase in brazing time of 5 to 14 seconds. The longer time permitted a higher temperature to be reached. Lap joints suffered a greater decrease in zinc to about 10.5% for a 4 second braze. The loss of zinc during brazing is time-temperature dependent. The lap joints are heated to a higher temperature than the butt joints because of the smaller mass of material to be heated. A loss of about 50% of the silver during induction brazing also was noted. However, this might be the result of thinner joints and thus picking up more copper from the base alloy during the EDX analysis.

Examination of the microstructure of the brazed lap joints indicated that the brazing procedure produced virtually no diffusion zone at the copper-silver interface (Figure 4). Also, no indication of recrystallization was found in the GLIDCOP alloy after brazing. The size of microhardness indentations showed little or no difference along the length of the alloy after brazing or between the alloy and the brazing alloy.

Twelve miniature tensile specimens with brazed joints have been made and six have been tensile tested (Table 3). Miniature samples were made by machining small specimens from a larger overlap joint. Machining was tedious and time consuming. The brazing operation produced inconsistent samples because the filler metal thickness could not be controlled in the large overlap. The filler metal had a tendency to melt and run with gravity producing a thickness variation. Some of the filler tended to be extruded from the joints and bonded to the Glidcop outside of the overlap. This produced locally thickened sections. This local thickening will be difficult to correct when dealing with specimens of such dimensions. In

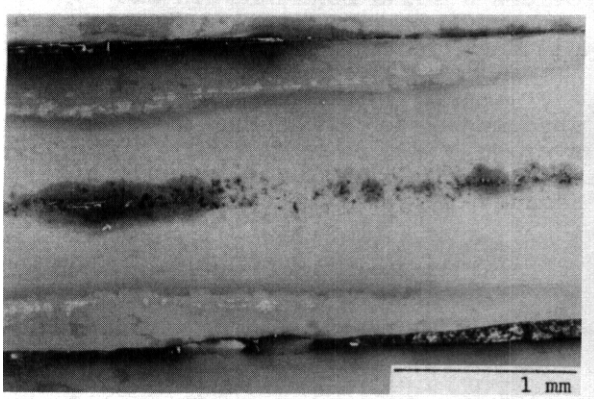

Fig. 3. SEM photomicrographs of a furnace brazed joint showing the amount of diffusion of the brazing alloy with the joint at the center.

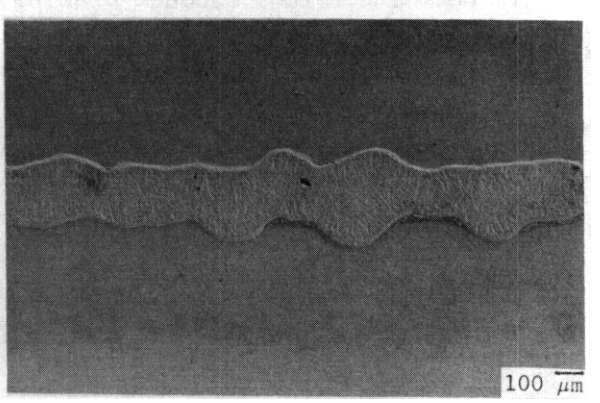

Fig. 4. SEM photomicrographs of a pin-loaded brazed joint showing the joint at the center.

Table 3. Miniature tensile specimen joint dimensions

Width (mm)	Overlap Thick-ness (mm)	Overlap Length (mm)	Filler Thick-ness (mm)	Yield Strength MPA	Tensile Strength MPA	Fracture Relative to Brazed Area
0.94	1.57	2.16	0.20			
0.89	1.35	2.79	0.03			
1.12	1.40	2.67	0.08			
1.09	1.35	2.67	0.03	270	316	outside
1.12	1.52	2.03	0.20			
1.14	1.50	2.03	0.18	192	266	outside but w/cracking in brazed region
0.99	1.35	2.67	0.03	153	198	outside
1.02	1.42	2.03	0.10			
0.98	1.42	2.54	0.10			
1.08	1.37	2.41	0.05	260	307	outside
1.02	1.57	2.16	0.05	300	300	inside
1.02	1.60	2.16	0.08	230	288	inside

addition, since the sheet thickness of the Glidcop alloy remains the same, the change in thickness of the filler metal would now be large relative to the width of the joint. These specimens contained varying overlap lengths and joint thicknesses.

The small size of these miniature specimens made fabrication more difficult than for that of the larger specimens. Also, the bending moment due to eccentric loading during tensile testing is more significant with the miniature specimens than with the other samples. This probably resulted in incorrect strain measurements obtained during tensile testing of the six miniature specimen in Table 3. In addition, small imperfections are relatively larger compared to the sample dimensions and all measurements must be made with greater precision.

Discussion

The initial results indicate that a satisfactory induction brazing process using BAg-5 can be achieved. The 4 to 5 seconds brazing cycle provides a sound bond between the filler and the Glidcop alloy without the use of a wetting agent (flux). Additionally, very little oxidation occurred even though neither a flux or a protective atmosphere were used. Minimal secondary cleaning will be required.

The average yield strength of the pin-loaded specimens was 329.2 MPa with an average deviation of 14.3 MPa. (The room temperature average yield strength from ORNL data of unbrazed Glidcop was 325 MPa). No significant loss in yield strength was incurred during the brazing process. The 228 MPa value was discarded because of premature failure resulting from improper joint fabrication.

REFERENCES

1. C. Tomizuka, quoted by D. Lazarus, Solid State Physics, Vol. 10, p. 117, Academic Press, Inc., New York, 1960

2. J.J. Stephens and D.T. Schmale, "The Effect of High Temperature Braze Thermal Cycles on Mechanical Properties of a Dispersion Strengthened Copper Alloy," Sand87-1296.

A BRIEF REVIEW OF CAVITY SWELLING AND HARDENING IN IRRADIATED COPPER AND COPPER ALLOYS --

S. J. Zinkle (Oak Ridge National Laboratory)

OBJECTIVE

The purpose of this report is to assess the current understanding of radiation effects in copper and copper alloys.

SUMMARY

The literature on radiation-induced swelling and hardening in copper and its alloys is reviewed. Void formation does not occur during irradiation of copper unless suitable impurii atoms such as oxygen or helium are present. Void formation occurs for neutron irradiation temperatures of 180 to 550°C, with peak swelling occurring at ~320°C for irradiation at a damage rate of 2 x 10^{-7} dpa/s. The post-transient swelling rate has been measured to be ~0.5%/dpa at temperatures near 400°C. Dispersion-strengthened copper has been found to be very resistant to void swelling due to the high sink density associated with the dispersion-stabilized dislocation structure.

Irradiation of copper at temperatures below 400°C generally causes an increase in strength due to the formation of defect clusters which inhibit dislocation motion. The radiation hardening can be adequately described by Seeger's dispersed barrier model, with a barrier strength for small defect clusters of $\alpha \approx 0.2$. The radiation hardening apparently saturates for fluences greater than ~10^{24} n/m² (~0.1 dpa) during irradiation at room temperature due to a saturation of the defect cluster density. Grain boundaries can modify the hardening behavior by blocking the transmission of dislocation slip bands, leading to a radiation-modified Hall-Petch relation between yield stength and grain size. Radiation-enhanced recrystallization can lead to softening of cold-worked copper alloys at temperatures above 300°C.

PROGRESS AND STATUS

Introduction

Copper and its alloys have been the subject of numerous radiation damage studies, dating back to the 1950s.[1,2] Most of these studies were fundamental in nature and employed low damage levels. A large amount of our present understanding of the properties of point defects in metals, along with more applied aspects such as dispersed barrier strengthening in metals (radiation hardening), can be attributed to these early copper irradiation studies. Radiation effects in copper are also of technological interest because its high thermal and electrical conductivity make it useful for applications such as fusion reactors.

This report reviews the current state of knowledge on radiation-induced swelling and hardening in copper and its alloys. The extensive literature on radiation-modified solute segregation and precipitation[1-4] will not be addressed directly. The effects of irradiation on the electrical properties of copper are also well studied,[5] but will not be covered here. There have been numerous fundamental studies on radiation hardening conducted on copper and its alloys. This paper will concentrate on irradiation-induced changes in the tensile properties. Very little is known about the effects of irradiation on creep[5-7] or fatigue of copper.

There have been relatively few investigations on the performance of copper and copper alloys in high neutron irradiation environments. Figure 1 summarizes the temperatures and doses investigated for copper irradiated to neutron damage levels greater than 1 displacement per atom (dpa) (refs. 8-20). It is worth noting that essentially all of these high fluence studies have been performed within the last five years. The most extensive investigation of copper at high damage levels was conducted by Brager and Garner and coworkers,[14-18] where the microstructure, density changes, electrical resistivity. and tensile properties of copper and a range of solid solution, precipitation- strengthened, and dispersion-strengthened copper alloys were measured at temperatures >400°C. The temperature dependence of void swelling and defect cluster formation over the temperature range of 182through 500°C has been determined by Zinkle and coworkers[19,20] There is a strong need for higher fluence data at irradiation temperatures ≤350°C, where most of the applications occur for copper in high irradiation environments.

VOID SWELLING IN COPPER AND COPPER ALLOYS

It was noticed shortly after the discovery of void swelling in irradiated metals by Cawthorne and Fulton[21] that impurii gases. in particular oxygen and helium, could exert a significant influence on void formation.[22,23]

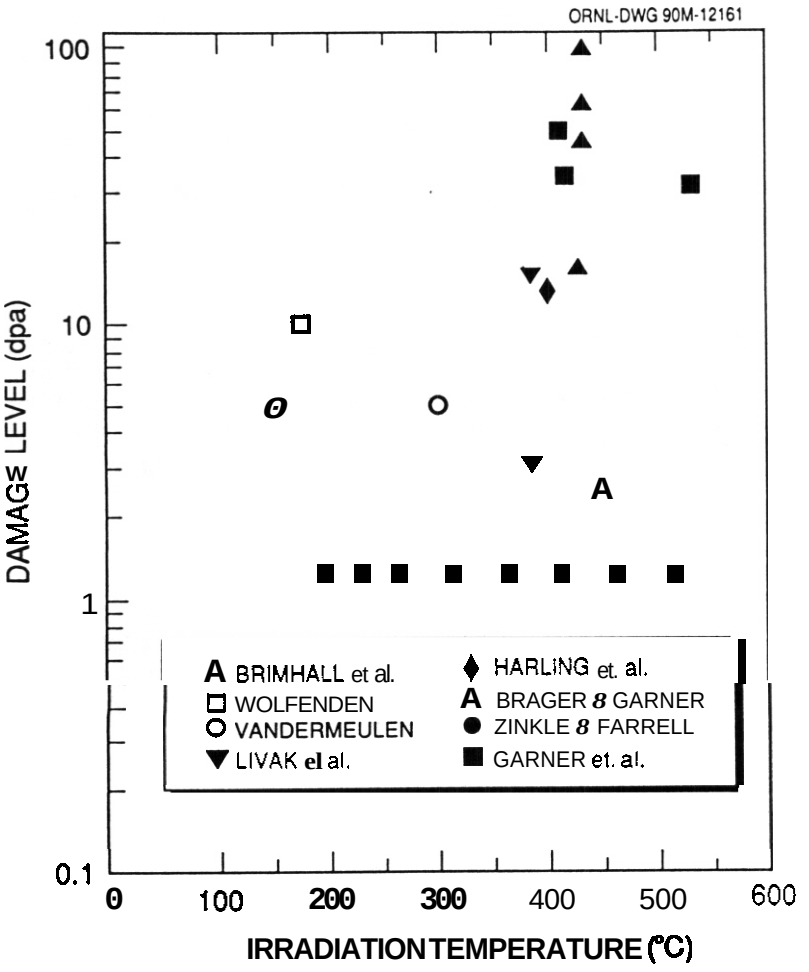

Fig. 1. Summary of high dose neutron irradiation experiments on copper and copper alloys.[8-20]

Oxygen effects on void formation

A series of neutron, ion and electron irradiation experiments by a group of French scientists[pm] demonstrated that preimpianted or residual impurity oxygen could have a dramatic effect on void swelling in copper. Void formation was not observed in "degassed copper foils subjected to ion[24,26] or electron" irradiation at 450°C, and void annealing studies on oxygen preimplanted specimens showed that the surface energy could be reduced to nearly half of the pure copper value for oxygen contents of ~100 wt ppm (ref. 27).

Several recent studies have confirmed and quantified the influence of small concentrations of oxygen on void formation in copper.[28-30] In a high fluence ion irradiation study,[28] void formation was not observed in high-purity. low-oxygen copper over the broad temperature range of 100 through 500°C. Figure 2 shows the low-magnification microstructures of some of the irradiated copper specimens from this study. Conversely. ion irradiation of copper containing 360 appm O (introduced by annealing high-purity copper in inert gas containing a trace amount of impurii oxygen) resulted in copious void formation at 375 and 475°C.[29] Figure 3 shows an example of the void formation observed in ion irradiated oxygen-bearing copper. Theoretical analyses — have found that the void is generally not thermodynamically stable in pure copper in comparison with the vacancy loop or stacking fault tetrahedron (SFT). A model based on oxygen chemisorption on void nuclei surfaces (which causes a reduction in surface energy and hence can stabilize void formation) is in reasonable agreement with experimental observations on the effect of oxygen on void formation.[29] Figure 4 shows a quantitative comparison of the predicted and observed effect of oxygen on void formation (open symbols indicate void formation was observed, and filled symbols indicate no void formation occurred).

The charged particle studies have proved to be important for understanding the importance of impurii atoms on void formation. It is clear that impurities such as oxygen need to be controlled in order to minimize the propensity of copper for void swelling. The strong role of impurity oxygen has also been recently demonstrated in a neutron irradiation experiment" on electrolytic tough pitch (ETP) copper, which was of nominally high purity but contained about 300 wt ppm O (1200 appm O). The oxygen-bearing ETP copper swelled at a rate that was four times larger than that of oxygen-free copper (34% vs. 8% swelling after 13.5 dpa at 400°C).

Helium effects on void formation

There have been several experimental studies on the effects of helium on cavity formation in copper,[20,24,26,33-41] but further information is needed at fusion-relevant conditions (~7 appm Heldpa). Most of these studies either preinjected helium[24,26,33,34,41] or produced helium via thermal reactor irradiation of boron-doped copper using very large Heldpa ratios.[20,36-40] Both methods are unsatisfactory for determining the effect of helium in fusion reactor environments. Figure 5 shows an example of substantial cavity swelling that occurred during simultaneous irradiation of copper with helium and heavy ion beams." Void formation was not observed in specimens that were not exposed to the helium beam. According to experimental results and theoretical calculations. the amount of helium needed to stabilize cavity formation in pure oxygen-free copper is very small—on the order of <1 appm He (refs. 26,42).

YE-14469

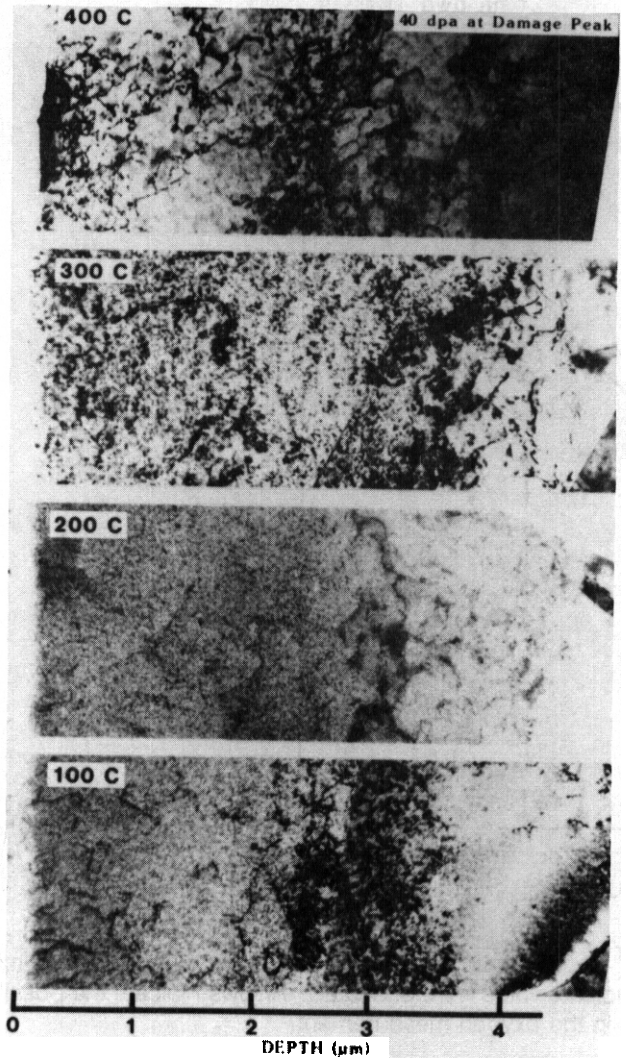

Fig. 2. Cross section microstructure of pure copper following 14-MeV Cu^{3+} ion irradiation to a peak damage level of 40 dpa at 100 through 400°C.[28] The original surface lies to the left in all of the micrographs, and the measured ion damage range was about 3.5 μm.

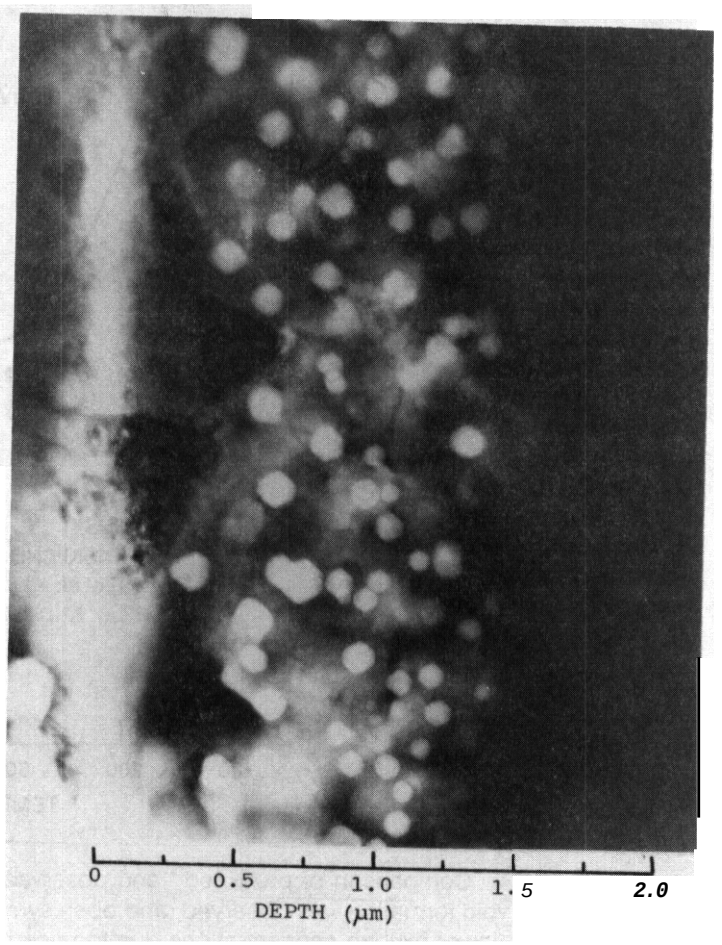

Fig. 3. Cross-section microstructure of copper containing 360 appm O following 3.8 MeV Fe^{++} ion irradiation to a peak damage level of 17 dpa at 475°C.[29] The ion damage range was about 1.3 μm. The very small circular and large triangular features are due to surface contamination of the TEM foil.

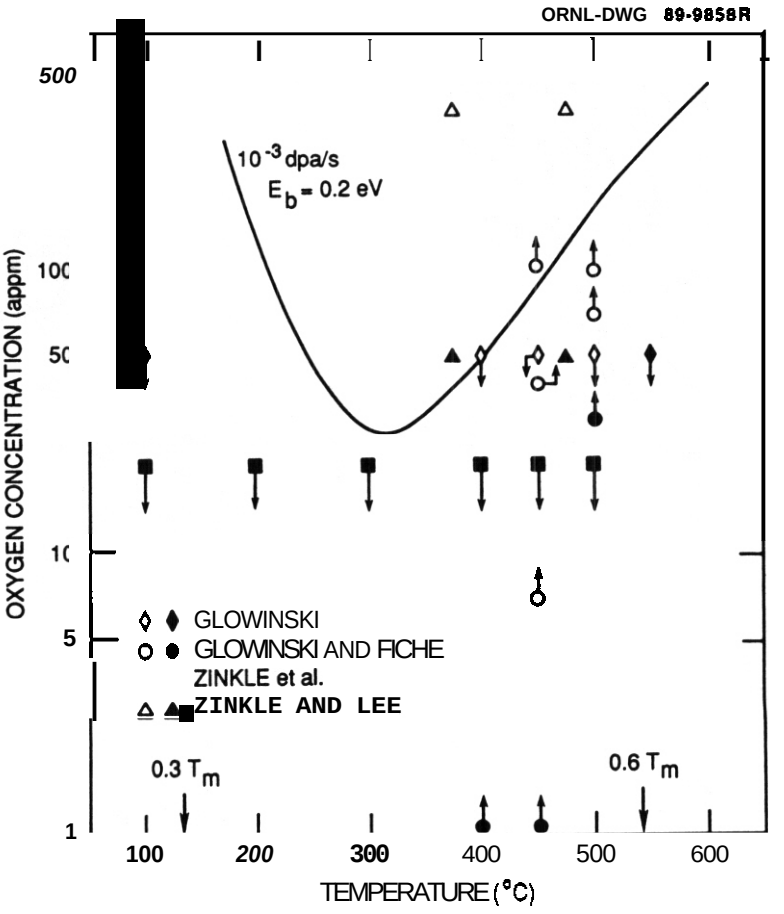

Fig. 4. Comparison of predicted[27] and observed[25,26,28,29] void formation in oxygen-bearing copper. Filled symbols indicate no void formation was Observed, and open symbols indicate voids Were observed. Arrows indicate the possibility of higher or lower oxygen concentrations due to uncertainties in the oxygen measurement.

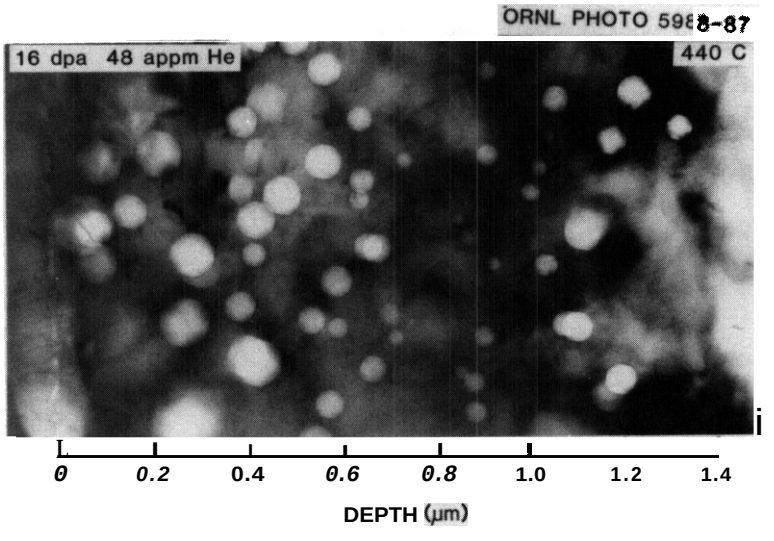

Fig. 5. Cross-section microstructure of copper following simultaneous dual beam irradiation at 440°C with 4 MeV Fe^{++} ions and 200 to 400 keV He^{+} ions. The peak irradiation damage level was 16 dpa at a depth of about 1 μm, and a uniform He concentration of 48 appm was injected at depths of 0.5 to 1.1 μm.[35] The calculated damage level at a depth of 0.5 μm was ~10 dpa. and the cavity swelling was ~3.5%.

Several researchers have irradiated dilute Cu-B alloys in order to probe helium bubble formation in neutron-irradiated copper.[20,36-40] The reaction $^{10}B(n,\alpha)^{7}Li$ produces both helium and lithium during irradiation in a thermal neutron environment, both of which are essentially insoluble in copper. It has been observed that the cavity formation in boron-doped copper is due to the helium produced by the (n,α) reaction (as opposed to the lithium).[36] These studies have provided useful information on the thermal stability of helium bubbles and on the conversion of bubbles to voids.

Preinjection of small amounts of helium (up to 100 appm) enhances void formation in pure copper during irradiation to moderate damage levels (~20 dpa).[33] However, preinjection of large amounts of helium (2000 appm) apparently overstimulates void nucleation and suppresses observable cavity swelling.[40] As discussed later, there is relatively little information available on helium effects in swelling-resistant copper alloys.

Effects of temperature and fluence on swelling

Copper has been found to contain voids following neutron irradiation at temperatures between 160 and 550°C (0.33 to 0.60 T_m).[1,8,9,11-20,23,43-52] The temperature dependence of the cavity swelling of copper following low dose neutron irradiation[19,23,45,46] is similar to that observed in many other metals: The void size increases gradually with increasing temperature while the cavtty denstty decreases rapidly, which results in a swelling peak at intermediate temperatures (~300 to 325°C for copper). Figure 6 shows the measured swelling as a function of irradiation temperature for copper irradiated to a damage level of ~1 dpa.[19,20] The measured temperature-dependent cavity swelling was similar for both pure copper and a helium-containing dilute Cu-B alloy. This is interpreted as evidence for a very small incubation fluence for void swelling due to the presence of large amounts of impurity oxygen in both materials (according to conventional radiation damage theory, helium has only a minor effect on the post-transient cavity swelling rate).

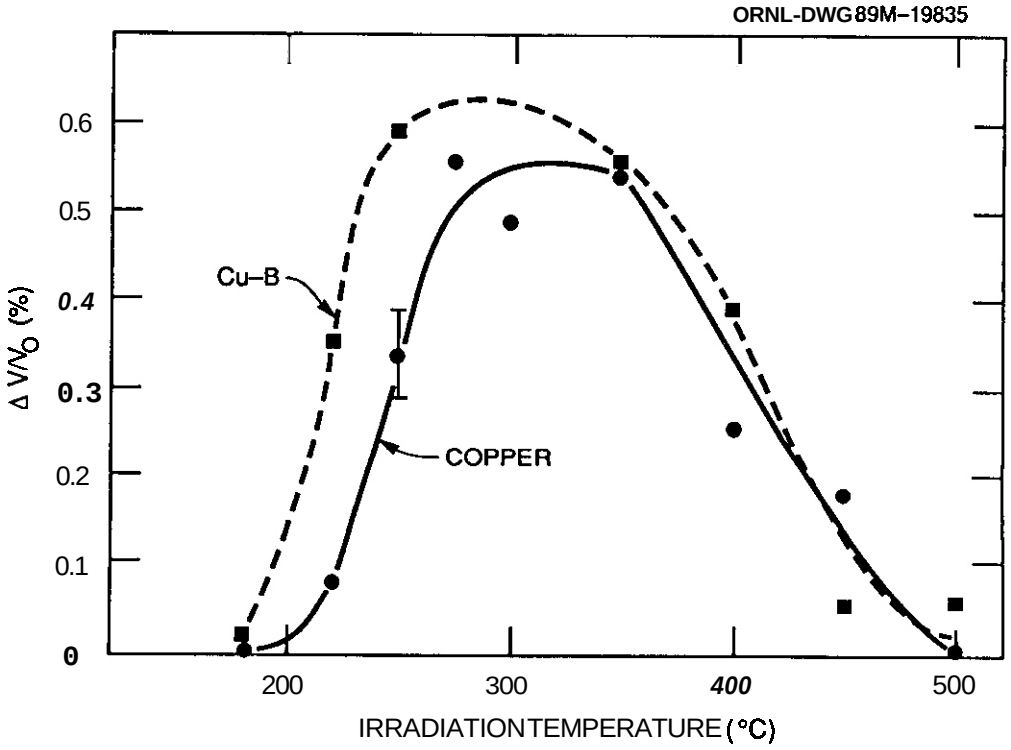

Fig. 6. Temperature-dependent cavity swelling in copper and Cu-18 wI ppm ^{10}B following fission neutron irradiation at a damage rate of ~2×10^{-7} dpa/s.[19,20] The irradiation produced ~100 appm He in the Cu-B alloy.

The primary effect of a variation in the damage rate on swelling is to shift the peak swelling temperature. An order of magnitude decrease in the neutron flux (from 2×10^{-7} to 2×10^{-8} dpa/s) decreased the location of the peak swelling temperature by ~20°C.[45,46] The peak swelling temperature shift between neutron (2×10^{-7} dpa/s) and ion (1×10^{-3} dpa/s) irradiated copper is ~165°C.[24,25]

Voids have been detected in copper following irradiation to fluences as low as 1×10^{21} n/m² (refs. **48.49).** The swelling behavior at low doses (<0.2 dpa) is often nonlinear, and transient swelling rates in excess of 1%/dpa have been

observed in some studies of neutron-irradiated copper.[44,49] The void formation is often very heterogeneous for these low dose irradiations.[48,49,52] Higher dose neutron and electron irradiation studies have found that a steady state void swelling rate of 0.4 to 0.9%/dpa eventually occurs, with no evidence for saturation up to swelling levels in excess of 60% (refs. 11-16,33,53,54). Some of the electron irradiation studies[33,54] suggest that the steady state swelling rate is temperature-dependent,[33,54] but these observations might also be attributable to thin foil effects. Figure 7 shows the fluence-dependent swelling observed in copper following neutron irradiation at ~420°C (refs. 14,15). The transition fluence for void swelling in irradiated pure copper is apparently very small, ~1 dpa (refs. 14,15,33,41,53).

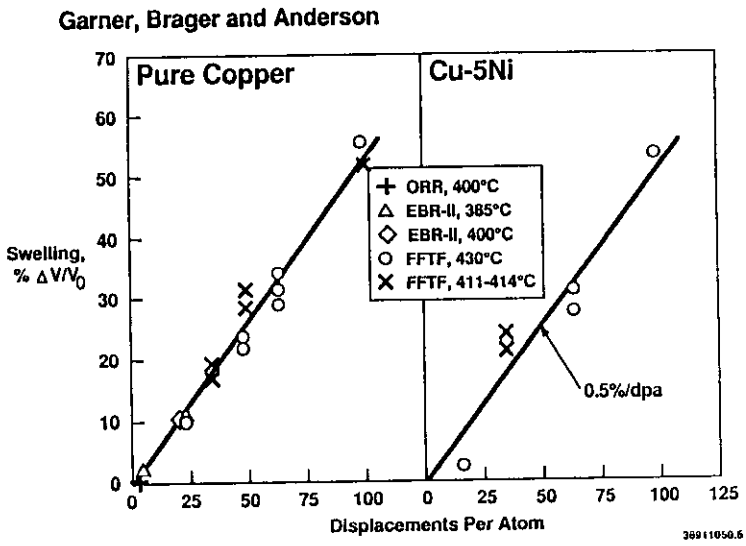

Fig. 7. Comparison of the swelling behavior of copper and a solid-solution Cu-5% Ni alloy following fast reactor irradiation at temperatures near 400°C (refs. 14-16).

Influence of nongaseous solutes on void swelling

With the notable exceptions of Ag, Al, and Cd,[33,41,55] the addition of alloying elements to copper generally results in a reduction of void swelling. The primary influence of solute additions appears to be an extension of the transient regime of void swelling (as opposed to a reduction in the steady state swelling rate)[14,15] although further studies are needed to confirm this finding. Reduced swelling compared to pure copper has been reported for solute additions of Au, Be, C, Fe, Ge, In, Mg, Ni, Pt, Sb, and Si.[14,15,23,26,33,34,41,45,48,54-58] Figure 7 compares the fluence-dependent swelling behavior of Cu-5%Ni with pure copper following neutron irradiation near 420°C (refs. 14-16). It can be seen that the addition of nickel suppressed swelling at low doses (16 dpa), but had little effect on the swelling behavior at high doses.

Several potential physical mechanisms have been proposed to explain the observed suppression or enhancement of void swelling in solid solution copper alloys. Radiation-induced segregation of the solute atoms toward or away from void embryos could modify the surface energy of the void nuclei, and thereby enhance or suppress void swelling. Solute trapping effects could enhance the recombination rate of point defects and thereby suppress void swelling, but most substitutional solutes are not effective interstitial traps at temperatures above 100 K (refs. 60,61). On the other hand, interstitial solutes could impede the migration of irradiation-produced interstitials and thereby increase the probability of vacancy-interstitial recombination. Reductions in stacking fault energy due to solute additions should in principle make other vacancy cluster morphologies favorable compared to the void.[23,30,45,48] However, experimental results on copper alloys of low stacking fault energy do not show a direct correspondence with a reduction in void swelling.[59] Further study in this area would be obviously worthwhile, but solid solution alloying does not appear to be useful for preventing cavity swelling at high doses in copper.

Void Swelling in Precipitation- and Dispersion-Strengthened Copper

The presence of a second phase in copper results in better swelling resistance compared to pure copper and solid solution copper alloys. Irradiation studies have been performed on aged Cu-Co, Cu-Be, Cu-Fe, Cu-Cr, Cu-Ti, and Cu-Zr binary alloys along with more complex alloys such as Cu-Cr-Zr, Cu-Be-Ni, Cu-Ni-Sn, and Cu-Ni-Ti.[11-18,41,53,62-66] Good swelling resistance (<2% swelling) has been observed in Cu-2%Be and Cu-3.5%Ti during fast reactor irradiation near 420°C to doses of 34 to 50 dpa.[14-16] All four of the ternary alloys studied to date show reasonable swelling resistance during high-fluence fast reactor[11-16,18] or dual-ion[64] irradiation, although the results are dependent on the initial thermomechanical treatment. For example, Cu-Ni-Be has been shown to be very swelling resistant during dual-ion[64] irradiation to 20 dpa at 250 to 500°C (30 appm He/dpa) and during fast reactor irradiation at 410°C to 34 dpa.[16-18] Conversely, fast reactor irradiation to 48 dpa at 430°C produced swelling in excess of 12% for cold-worked and aged Cu-Ni-Be.[14,15] Lower swelling levels were observed in an annealed and aged Cu-Ni-Be alloy. Tensile[15] and TEM[66] measurements revealed that recrystallization along with precipitate coarsening had occurred in the cold-worked alloy during irradiation at 430°C, and this led to the swelling instability.

Several studies have demonstrated that oxide dispersion-strengthened copper alloys containing inert particles of Al_2O_3, TiO_2, HfO_2 or ZrO_2 are swelling resistant.[11-16,18] Dispersion-strengthened Cu-Cr_2O_3 has poor swelling resistance relative to Cu-Al_2O_3, etc.,[16] and has poor strength at elevated temperatures.[13] The Cu-Al_2O_3 dispersion-strengthened alloys have

received particular attention due to their excellent swelling resistance during high-fluence fast reactor irradiation at temperatures of 365 to 530°C (refs. 11-16,18) and during dual ion beam irradiation.[64] Substantial void swelling has been observed in one series of commercial oxide dispersion-strengthened copper alloys following high-fluence neutron irradiation due to the presence of excess oxygen in the matrix.[16,18]

It appears that the swelling suppression in precipitation- and dispersion-strengthened copper is partly due to point defect trapping at the precipitate-matrix interface, but is primarily due to the presence of a high dislocation density. The swelling resistance is generally best in alloys that contain a stabilized cold-worked structure due to the additional point defect sink strength supplied by the dislocations. During high fluence ion[64] or neutron irradiation,[15] void formation is initiated in regions of the matrix that have recrystallized (leaving a low defect sink density). A large part of the swelling resistance of dispersion-strengthened alloys can be attributed to their superior resistance to recrystallization (precipitate overaging does not occur since the dispersion is inert in the copper matrix). Figure 8 summarizes the swelling behavior of three grades of a commercial dispersion-strengthened copper, GlidCop, following neutron irradiation near 410°C (ref. 15). The swelling resistance of the GlidCop alloys improved with increasing dispersoid content and cold-work level.

There is a strong need for irradiation data on swelling-resistant copper alloys at fusion-relevant He/dpa ratios. Fission reactor irradiation of copper generates only ~0.2 appm He/dpa, which is more than one order of magnitude smaller than the DT fusion first wall generation rate for copper of ~7 appm He/dpa. Spitznagel et al.[64] found that dispersion-strengthened copper had about five times higher swelling following dual-beam irradiation at 30 appm He/dpa as compared to specimens irradiated without helium coimplantation. On the other hand, Cu-Ni-Be specimens did not exhibit observable cavtty swelling after either dual-beam or single ion-beam irradiation to 20 dpa. The relatively high swelling that was observed in the GlidCop Al-15 alloy compared to the Al-20 and Al-25 alloys following neutron irradiation (Fig. 8) may have been partially enhanced by the presence of a small amount of residual boron (<200 wt ppm) remaining from a preirradiation deoxidation treatment. A boron content of 100 wt ppm would transmute during high-fluence fast reactor irradiation to produce ~100 appm He when fully burned up.

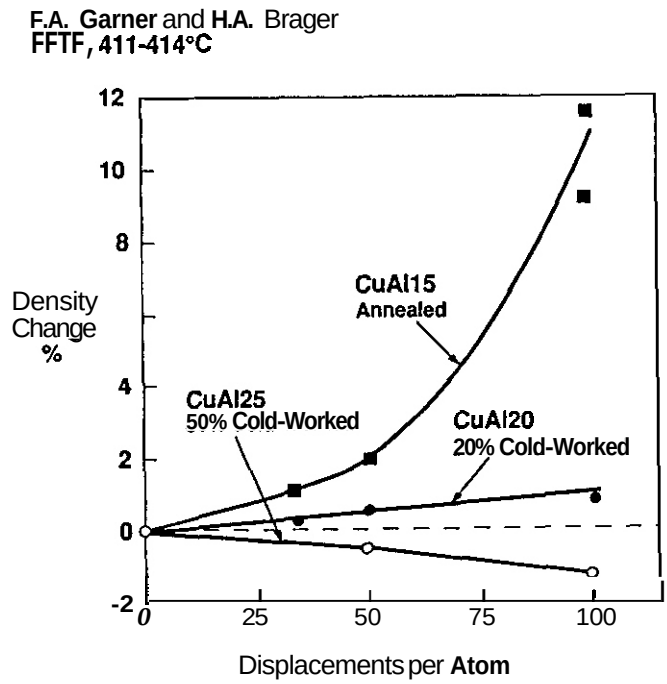

Fig. 8. Swelling behavior of three commercial dispersion-strengthened copper alloys following fast-reactor irradiation at 411 to 414°C (ref. 15). The alloys contained 0.15, 0.20, and 0.25 wt % Ai in the form of Al_2O_3 particles. The Cu-Al15 alloy contained <200 wt ppm B due to a preirradiation boron deoxidation treatment.

RADIATION HARDENING

Radiation Hardenino in Pure Comer

Numerous fundamental studies on radiation hardening have been conducted on pure copper over the past 40 years.[67-75] Significant amounts of hardening occur in annealed copper for irradiation temperatures <350°C. It has been demonstrated[71,73] that the strength increase is due to "black spot" formation (small dislocation loops and SFT). The yield strength increase is described by Seeger's[71] dispersed barrier model,

$$\Delta\tau = \alpha G b \sqrt{Nd} \qquad (1)$$

$$\Delta\sigma_y = \bar{M}\Delta\tau \qquad (2)$$

where G is the shear modulus, b is the magnitude of the dislocation Burgers vector ($a_0/\sqrt{2}$ for copper), N and d are the density and mean diameter of the defect clusters, α is the barrier strength coefficient, and $\bar{M}$ is the Taylor factor ($\bar{M} = 3.06$ for fcc polycrystals) which describes the relationship between shear stress ($\Delta\tau$) and polycrystalline yield stress ($\Delta\sigma_y$) (ref. 75). Various experimental and theoretical studies have found that the barrier strength coefficient for defect clusters formed during room temperature neutron irradiation of copper is α = 0.2 to 0.25 [73,75,76].

The fluence dependence of radiation hardening in copper was the subject of a long-standing controversy,[**] with different research groups claiming that the strength increase was proportional to the one-third power of Ruence[**] or the square root of fluence with a saturation term.[****] It was also recently suggested that the hardening was best described by a one-fourth root dependence over an extended Ruence range.[****]

Part of the cause of the controversy can be resolved by examination of recent TEM studies on the fluence dependence of the defect cluster density in neutron-irradiated copper. Figure 9 shows that the defect cluster density in copper irradiated near room temperature — is initially proportional to fluence up to $\phi t \sim 5 \times 10^{20}$ n/m^2. This produces a strength increase proportional to $\sqrt{\phi t}$ in this fluence regime since the defect cluster size was essentially independent of fluence [Eq. (1)]. The fluence dependence of the cluster density at higher fluences is strongly dependent on the purity wntent of the irradiated copper (in particular interstitial impurities).[**] Several studies on high-purity copper and other fcc metals have demonstrated that there is a substantial fluence range where the defect cluster density is proportional to $(\phi t)^{1/2}$ (refs. 77,80,87,88), which would produce a one-fourth root dependence of hardening on fluence [Eq. (1)]. This has been interpreted as evidence for the interaction of freely migrating defects with defect clusters from surrounding displacement cascades, causing shrinkage and annihilation of some clusters. Simple theoretical models predict a square root dependence on fluence for the defect cluster density when migrating defect interactions with defect clusters are occurring.[60,77 80,87] Copper containing moderate amounts of interstitial impurities does not show a deviation from the linear accumulation of defect clusters until $\phi t > 5 \times 10^{21}$ n/m^2. This suggests that the impurities are blocking migration of the freely migrating interstitials. Hence, irradiation of nominally pure copper specimens containing differing amounts of interstitial impurities will produce differing radiation hardening rates over certain fluence ranges.

For defect cluster densities > 10^{23}/m^3, there is an increasing probability of cascade overlap events, i.e., a displacement cascade occurs in the vicinity of an existing defect cluster and causes its annihilation with the result that there is no net increase in defect cluster density. The TEM measurements (Fig. 9) suggest that the maximum defect cluster density in copper irradiated with neutrons near room temperature is ~10^{24}/m^3. Higher fluence studies are needed to confirm the saturation density of defect clusters. A saturation in the radiation hardening on neutron-irradiated copper has similarly been observed[89-92] at fluences ~10^{24} n/m^2 (~0.1 dpa). Figure 10 shows the yield strength of neutron irradiated copper as a function of fluence.[**] In this study[**] an apparent saturation in hardening already occurred at a fluence of 10^{23} n/m^2 (E > 1 MeV). A similar saturation in hardening also has been observed in ion-irradiated copper.[93]

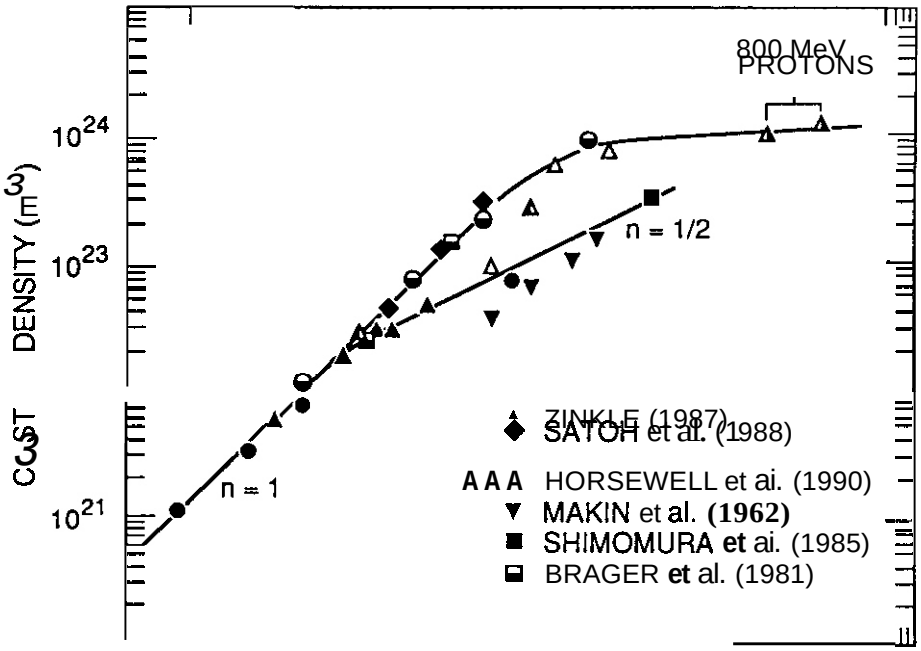

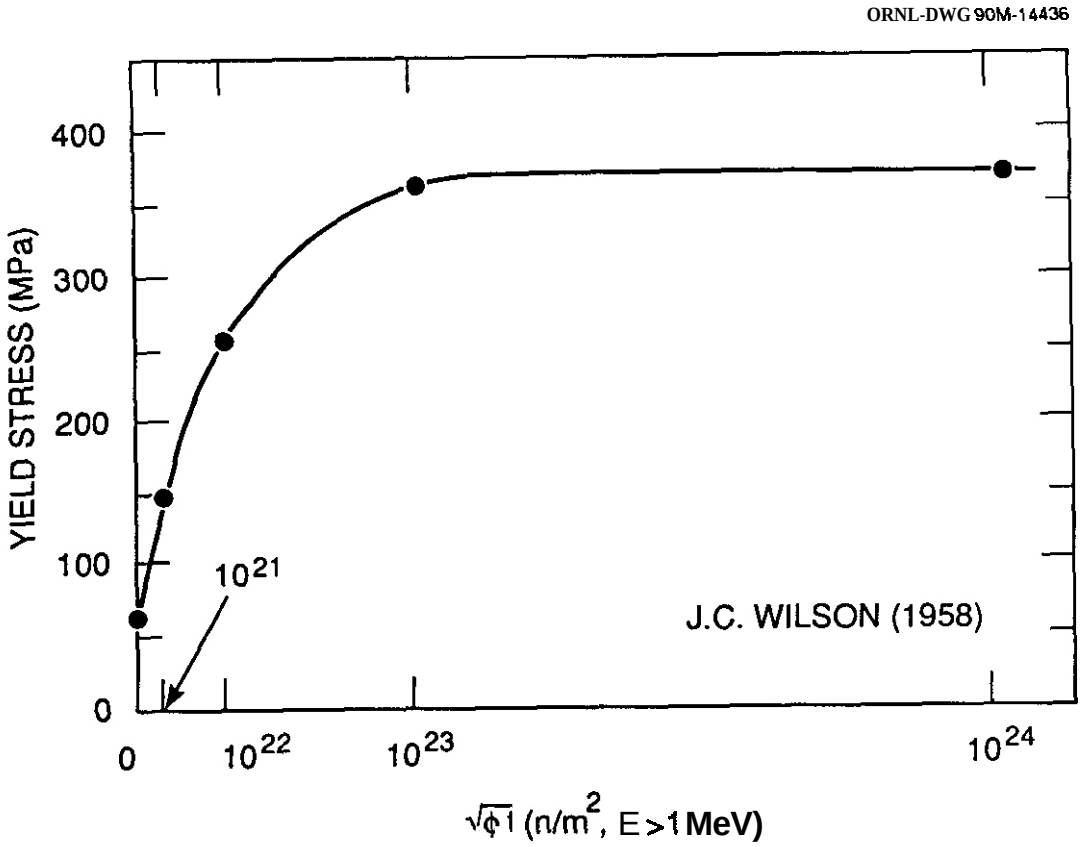

Fig. 10. Measured yield strength of polycrystalline copper following fission reactor irradiation near room temperature.[89]

An interesting observation that is deserving of further study concerns the effect of grain size on the radiation hardening rate. Several studies have shown that the strength increase as a function of fluence is higher for small-grained compared to large-grained copper.[70,94] Figure 11 shows an example of the dependence of yield strength on grain size for neutron-irradiated copper.[70] It has been suggested that this effect is due to grain boundaries blocking the transmission of slip bands." It is not clear whether this grain size-dependent radiation hardening rate continues at higher fluences.

TemDerature Dependence of Radiation Hardening

There have been extensive studies on the temperature dependence of radiation hardening in pure copper utilizing isochronal and isothermal annealing.[70,71,73] The flow stress in irradiated copper decreases with increasing irradiation temperature due to two factors. First, the barrier for dislocations to shear defect clusters is thermally activated. In addition, the defect clusters responsible for the radiation hardening of copper are thermally unstable at elevated temperatures. Figure 12 shows the temperature-dependent defect cluster density observed in copper following ion irradiation to a damage level of 10 dpa.[28] Similar results have been obtained in other studies of neutron-[48,95] and ion-irradiated[96] copper. The room temperature strength of ion-irradiated copper also shows a similar dependence on irradiation temperature.[93]

The defect cluster density that is produced during irradiation at elevated temperatures is shown in more detail in Fig. 13 (ref. 20). The defect cluster density decreases by over three orders of magnitude between the irradiation temperatures of 182 and 450°C. The results demonstrate that the defect clusters responsible for radiation hardening are highly sensitive to irradiation temperatures >182°C. The decreased cluster density at elevated temperatures is a further indication that the defect clusters are thermally unstable, although additional factors such as the temperature dependence of the production of defect clusters directly in displacement cascades may also be playing a role.

At high fluences. some hardening from cavity formation is expected to occur." However, experimental results indicate that the yield strength of irradiated copper decreases when void swelling becomes very high, due to a lack of load-bearing area.[98]

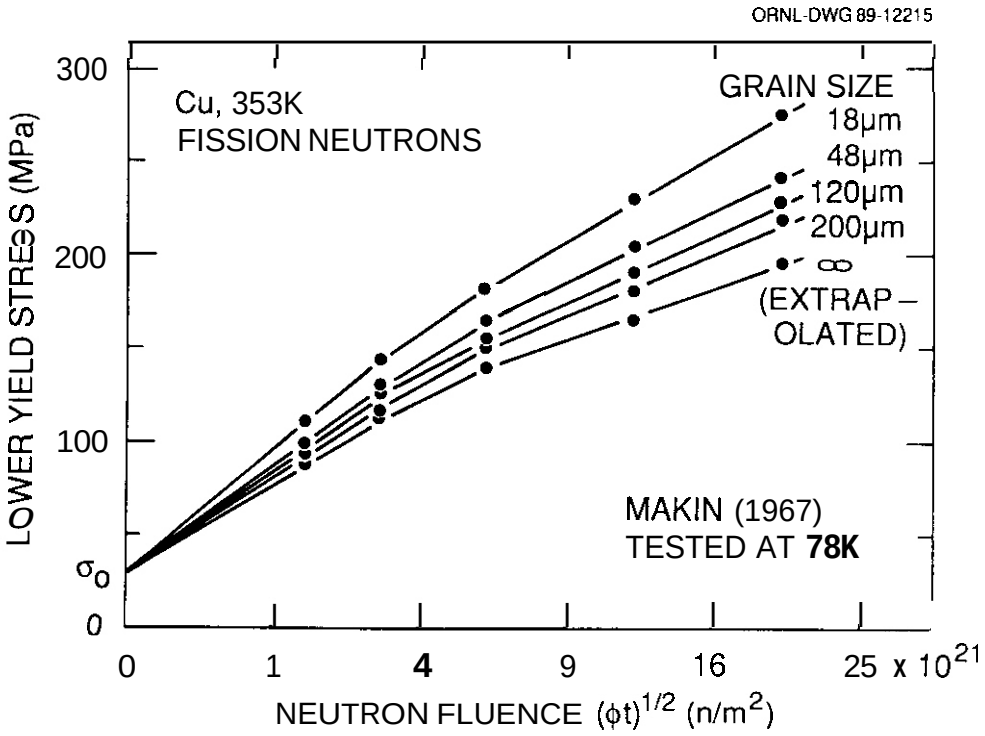

Fig. 11. Measured yield strength of polycrystalline copper versus the epithermal fission reactor fluence showing enhanced hardening rates for small-grained material." The fast (E > 1 MeV) neutron fluence was ~10% of the epithermal fluence.

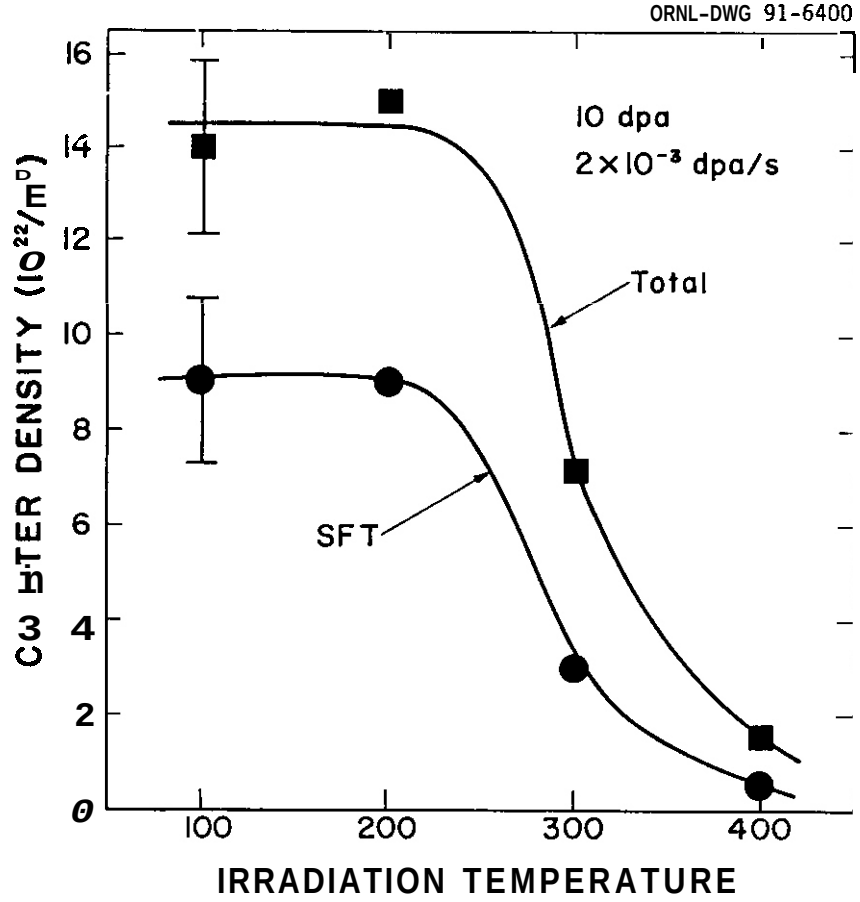

Fig. 12. Measured defect cluster density in 14-MeV Cu^{3+} ion-irradiated copper as a function of irradiation temperature.[28]

A loss of ductility is associated with radiation hardening. Figure 14 shows the total elongation of annealed copper is rapidly reduced by neutron irradiation." and that cold work shortens the Ruence required to reach the embrittled state (e <2%). Confirmation of this cold-work effect on radiation embrittlement is needed.

Other studies have shown that copper becomes severely embriiled in the presence of large cavities, introduced by the tritium trick[99,100] or neutron irradiation.[98] Helium embrittlement effects have also been suggested in some Cu-B irradiation studies," but more data are needed.

Alloying Effects on Radiation Hardening

High-strength copper alloys are desirable for several applications in fusion reactors. Their strength is generally achieved by classical precipitation hardening. or by pinning a dislocation structure with precipitates or an inert dispersed phase such as Al_2O_3 particles. Radiation-enhanced recrystallization is an important phenomenon in cold worked copper alloys at irradiation temperatures $\geq$300°C.[10,12,64,65,101,102] The enhanced diffusion associated with irradiation can accelerate the dislocation recovery and grain recrystallization processes, particularly if the dislocation structure is not pinned effectively. A substantial loss of strength associated with the recrystallization generally occurs in alloy systems whose strength is derived from a cold-worked structure that is stabilized by precipitates.[103] In addition. established phenomenon such as radiation-enhanced precipitate overaging or loss of coherency"" in classic precipitation hardened systems such as Cu-Be should cause a large strength decrease. These softening effects are offset to a certain degree at low irradiation temperatures (<300°C) by the increased hardening associated with defect cluster formation.[10,65,101,102]

The most promising radiation-resistant copper alloy system from both a cavity swelling and retained strength perspective is dispersion-strengthened copper. The commercial dispersion-strengthened alloys GlidCop Cu-Al_2O_3 have been found to be resistant to radiation-enhanced recrystallization for irradiation temperatures as high as 420 to 530°C and doses as high as 100 dpa.[13,14,17,18,66] (However. one study" reported *that* neutron irradiation at 410°C to 50 dpa caused substantial recrystallization in two GlidCop Cu-Al_2O_3 alloys.) The resistance to recrystallization may be attributed in large part to the

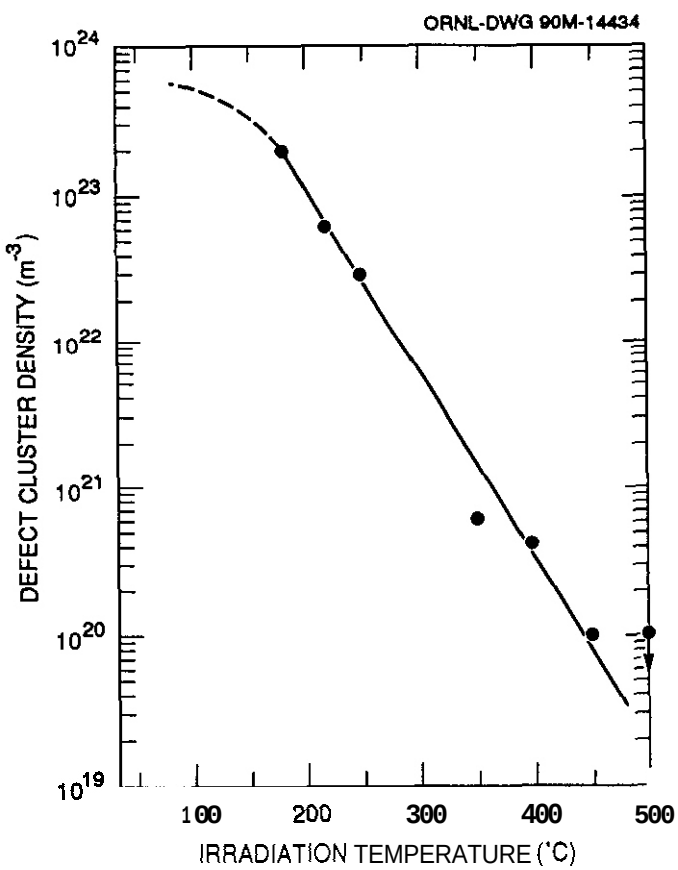

Fig. 13. Temperature-dependent defect cluster density observed in Cu-18 wt ppm ^{10}B following fission neutron irradiation to a damage level of ~1.2 dpa (ref. 20).

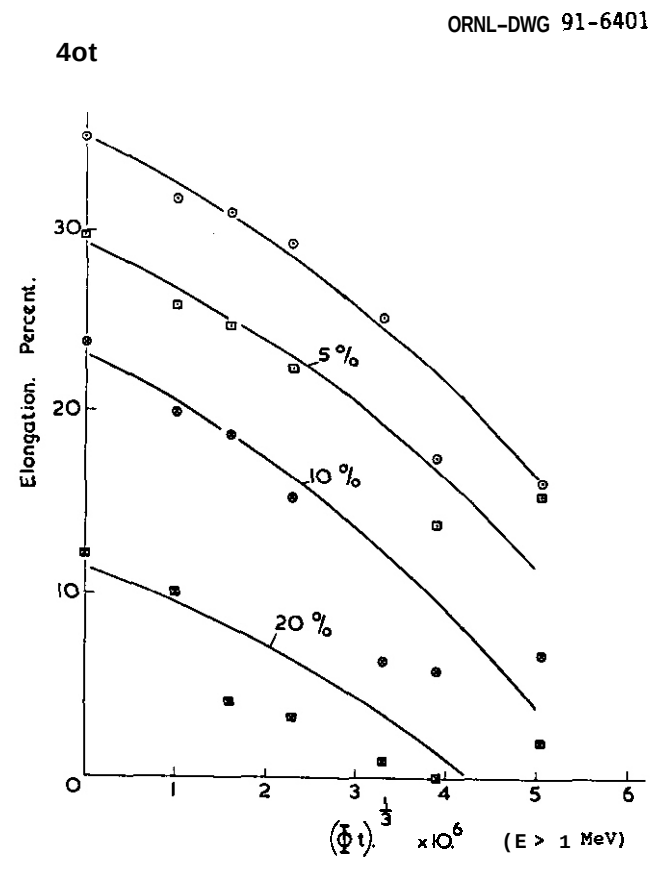

Fig. 14. The effect of extension prior to irradiation on the dose dependence of elongation to fracture of fission neutron-irradiated copper tested at 20°C (ref. 70).

chemical inertness of the Al_2O_3 particles, along with a high dislocation barrier strength for the particles that inhibits particle shearing. One concern is the possibility of radiation-induced dissolution of the Al_2O_3 particles during high-fluence irradiation due to displacement cascade effects (ballistic dissolution) as observed by Spitznagel et al.[64] However, several experimental[12,63,66,104] and theoretical[105,106] studies on Cu-A1203 and other copper alloys have found that particles of sizes appropriate for dispersion strengthening ($d \geq 10$ nm) are stable during irradiation. Since the particle dissolution rate is dependent on temperature, dose rate and displacement cascade size, further study is warranted.

CONCLUDING **REMARKS**

Examination of the existing data base for irradiated copper shows that the irradiation temperature determines whether cavity swelling or radiation hardening effects will occur. Figure 15 shows in schematic form the temperature regimes that are important for cavity swelling and radiation hardening of neutron-irradiated copper. Radiation hardening effects are significant for temperatures <300°C, and the saturated defect cluster density is nearly constant for temperatures <180°C. The decrease in the defect cluster density at temperatures >180°C allows cavity growth to become appreciable due to the decrease in sink density. The amount of void swelling becomes small at temperatures >500°C due to thermal annealing of voids.

The strength of copper and copper alloys can be either increased or decreased by irradiation, depending on the cold-work level of the material and the irradiation temperature. Strengthening due to defect cluster formation is appreciable for irradiation temperatures <300°C. The strength increase associated with defect cluster formation in copper apparently saturates during neutron irradiation near room temperature at a dose of ~0.1 dpa. Radiation-enhanced recrvstallization and accelerated precipitate overaging can lead to a decrease in strength in cold-worked or precipitation-hardened systems for irradiation temperatures **1300°C.**

Cavity swelling during irradiation is of concern chiefly for irradiation temperatures of 200 to 500°C. Small amounts of swelling may occur at temperatures as low as 180°C and as high as 550°C. The swelling peak at low doses occurs at ~320°C. It is apparent that small amounts of impuriiies (either gaseous or solid) are essential for the formation of cavities during irradiation. Only a small amount of oxygen (~10 appm) or helium (~1 appm **He)** is needed to stabilize cavities in pure copper. Deleterious matrix solutes such as oxygen should be minimized through careful control of the manufacturing process in order to produce materials suitable for high radiation environments.

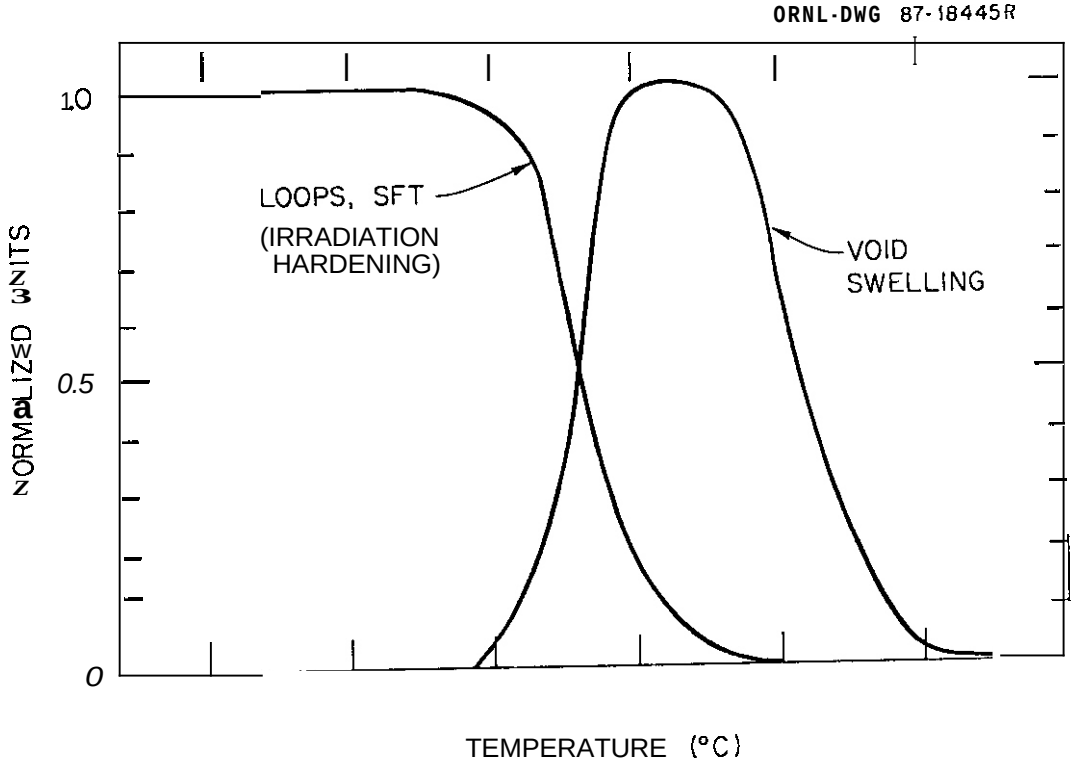

Fig. 15. Schematic temperature dependence of radiation hardening and void swelling regimes in neutron-irradiated copper.

There is a strong need for high fluence studies on copper alloys at irradiation temperatures $\leq$350°C in order to generate data on tensile property changes, cavity swelling resistance, and microstructural changes. Additional low dose studies would be useful for understanding the details of the dose dependence of the defect cluster density (including impurity effects) and other matters of fundamental interest, including the effect of grain size on radiation hardening. In addition, irradiation data are required on fatigue and creep behavior, and the effects of irradiation on brazed or welded joints. Data are needed on the influence of helium on cavity swelling in swelling-resistant materials such as dispersion-strengthened Cu-Al_2O_3 alloys. From a design standpoint, it is not particularly useful to study He effects in pure copper, since He should have little influence on the swelling behavior of materials that swell readily in the absence of helium.

Dispersion-strengthened alloys such as GlidCop Cu-Al_2O_3 are the most promising class of commercially available copper alloys in terms of radiation resistance. The radiation resistance of this material can be attributed to its very high sink density (dislocations plus Al_2O_3 particles). Unlike precipitates, the high density ($10^{22}/m^3$) of small (d ~ 10 nm) inert Al_2O_3 particles are resistant to overaging and thermal dissolution effects during irradiation. Additional high-dose studies are needed to confirm the absence of appreciable displacement cascade dissolution of particles in dispersion-strengthened copper. Similar dispersion-strengthened alloys based on other alloy systems (e.g. Fe or Ni matrix) would be worthy of further investigation for fusion reactor structural applications. Precipitation-strengthened alloys such as Cu-Cr-Zr or Cu-Ni-Be may be suitable for high-fluence applications at temperatures where radiation-enhanced recrystallization is not of concern (<300 to 350°C).

ACKNOWLEDGMENTS

The author thanks E. A. Kenik and R. L. Klueh for their technical comments on the manuscript.

REFERENCES

1. Zinkle, S.J. and Knoll, R.W., "A Literature Review of Radiation Damage Data for Copper and Copper Alloys," Univ. Wisconsin Fusion Technology Institute Report UWFDM-578. June, 1984, 94pp.

2. Corbett, J.W., Electron Radiation Damaae in Semiconductors and Metals, Solid State Physics Supplement 7, Academic Press, 1966.

3. Adda, Y., Beyeler, M., and Brebec, G., Thin Solid Films. Vol. 25, 1975, pp. 107-156.

4. Russell, K.C., "Phase Stability under Irradiation", Prog. in Mat. Sci., Vol. 28, No. 34, 1985, pp. 229-434.

5. Buckley, S.N., "Irradiation Growth and Irradiation Enhanced Creep in FCC and BCC Metals", in Proc. Symp. on The Interactions Between Dislocations and Point Defects, Vol. II, Part III, AERE-R5944, 1968, Harwell, Berkshire, England, pp. 547-565.

6. Jung, P. and Ansari, M.I., "A Correlation Between Irradiation Creep Strength and Yield Stress of FCC Metals and Alloys", J. Nucl. Mater., Vol. 138, 1986, pp. 40-45.

7. Ibragimov. S.Sh., Atkhozhin. E.S.. and Pyatiletov, Y.S.. "Radiation-Induced Creep of Aluminum and Copper", Influence of Radiation on Material ProDerties: 13th Int. Symp. (Part II), ASTM STP 956, F.A. Garner et al., Eds., ASTM, Philadelphia, 1987. pp. 5-10.

8. Brimhall, J.L., Kissinger, H.E., and Kulcinski, G.L., in Radiation-induced Voids in Metals, J.W. Corbett and L.C. Ianniello, Eds., U.S. Atomic Energy Commision Symp. Series No. 26, CONF-710601, 1972, pp. 338-362.

9. Wolfenden, A., "High Fluence Neutron Irradiation Damage in Copper-10 wt % Aluminum and Copper", Radiation Effects, Vol. 15, 1972, pp. 255-258.

10. Vandermeulen. W., Massaut. V.. Van de Velde, J., and Hendrix, W., "The Effect of Irradiation at 150 and 300°C on the Tensile Properties of Cu and CuCrZr", in 14th Symp. on Fusion Technology. Sept. 1986, Avignon. France, Comm. Europ. Communities, Pergamon Press, 1986. pp.1031-35.

11. Livak, R.J., et al., "Promising Copper Alloys for High Heat Load Applications in Neutron Environments", J. Nucl. Mater., Vol. 141-143, 1987. pp. 160-62.

12. Livak, R.J., Zocco, T.G., and Hobbs, L.W., "Neutron Damage Microstructures of High-Conductivity Copper Alloys", J. Nucl. Mater., Vol. 144. 1987, pp. 121-27.

13. Harling. O.K., Grant, N.J., Kohse. G., Ames, M., Lee, T-S., and Hobbs, L.W.. "Neutron Irradiation Scoping Study of Twenty-Five Copper-Base Materials", J. Mater. Res., Vol. 2, 1987. 568-579.

14. Brager. H.R. and Garner, F.A.. "Effects of Neutron Irradiation to 98 dpa on the Swelling of Various Comer Alloys", Effects-of Radiation *on* Materials: 14th Int. Symp. (Vol. II), ASTM STP 1046, N.H. Packan et al., Eds., ASTM, Philadelphia, 1990, pp. 599-604.

15. Garner, F.A., Brager. H.R., and Anderson, K.R., "Neutron-Induced Changes in Density and Electrical Conductivity of Copper Alloys at 16 to 98 dpa and 420°C", J. Nucl. Mater., in press 1990 (ICFRM-4, Kyoto).

16. Garner, F.A.. Brager, H.R., and Anderson, K.R., "Density Changes of Generation 1.5 and 2.0 Copper Alloys Irradiated at 411-414 C and 529 C in FFTF-MOTA. Fusion Reactor Materials Semiannual Progress Report DOE/ER-0313/7, Sept. 30, 1989, pp. 223-231.

17. Anderson, K.R., Garner, F.A., Hamilton, M.L.. and Stubbins, J.F.. Tensile Properties and Fracture Behavior of Dispersion-Strengthened Copper Alloys Irradiated in FFTF-MOTA, Fusion Reactor Materials Semiannual Progress Report DOE/ER-0313/7, Sept. 30, 1989, pp. 213-19.

18. Anderson, K.R., Garner, F.A., Hamilton, M.L.. and Stubbins, J.F.. "Behavior of Copper-Base High Heat Flux Candidate Alloys During Neutron Irradiation at 412 and 529 C , J. Nucl. Mater., in press 1990 (ICFRM-4, Kyoto).

19. Zinkle, S.J. and Farrell, K., "Void Swelling and Defect Cluster Formation in Reactor-Irradiated Copper", J. Nucl. Mater., Vol. 168, 1989, pp. 262-67.

20. Zinkle. S.J.. Farrell. K., and Kanazawa, H., "Microstructure and Cavity Swelling in Reactor-Irradiated Dilute Copper-Boron Alloy", J. Nucl. Mater., Vol. 176, 1990, in press.

21. Cawthorne. C. and Fulton, E.J., "Voids in Irradiated Stainless Steel", Nature, Vol. 216, 1967, pp. 575-76.

22. Norris, D.I.R.. Rad. Effects, Vol. 15. 1972. PP. 1-22.

23. Adda, Y., in Radiation-Induced Voids in Metals, J.W. Corbett and L.C. Ianniello, Eds.. U.S. Atomic Energy Commision Symp. Series No. 26, CONF-710601. 1972, pp. 31-83.

24. Glowinski, L., Fiche, C., and Lott. M.. J. Nucl. Mater., Vol. 47, 1973, pp. 295-310.

25. Glowinski, L.D.. J. Nucl. Mater., Vol. 61, 1976, pp. 8-21.

26. Glowinski, L.D., and Fiche, C., J. Nucl. Mater., Vol. 61, 1976. pp. 29-40.

27. Felsen. M.F. and Regnier. P.. "Influence of some Additional Elements on the Surface Tension of Copper at Intermediate and High Temperatures", Surf. Sci., Vol. 68, 1977, pp. 410-418.

28. Zinkle, S.J., Kulcinski, G.L. and Knoll, R.W.. J. Nucl. Mater. Vol. 138, 1986. pp. 46-56.

29. Zinkle, S.J. and Lee, E.H., "Effect of Oxygen on Vacancy Cluster Morphology in Metals". Met. Trans. A, Vol. 21A. 1990, pp. 1037-51.

30. Zinkle, S.J., Seitzman, L.E., and Wolfer, W.G., "Stability of Vacancy Clusters in Metals", Phil. Mag. A, Vol. 55, 1987, pp. 111-125.

31. Sabochick. M.J.. Yip, S., and Lam, N.Q., "Atomistic Simulation Study of Large Vacancy Clusters in Copper", J. Phys. F: Met. Phys., Vol. 18, 1988, pp. 349-361.

32. Kapinos, V.G.. Osetskii. Yu.N., and Platonov, P.A., Sov. Phys. Solid State, Vol. 28, 1986, pp. 2031-34.

33. Barlow, P., "Radiation Damage in Pure FCC Metals and Alloys in HVEM", Ph.D. thesis, University of Sussex, England, 1977

34. Mazey, D.J. and Menzinger, F., J. Nucl. Mater., Vol. 48, 1973, pp. 15-20.

35. Zinkle, S.J.. "Dual-Ion Irradiation of Copper", Fusion Reactor Materials Semiannual Progress Report DOE/ER-0313/3, Sept. 30, 1987, pp. 86-89.

38. Vela. P. and Russell, B., J. Nucl. Mater., Vol. 19, 1966, p. 327.

37. Vela, P., Hardy, J.. and Russell, B.. "The behavior of elemental boron particles in copper during neutron irradiation", J. Nucl. Mater., Vol. 26, 1968, pp. 129-31.

38. Carpenter, G.J.C. and Nicholson, R.B., in Radiation Damaae in Reactor Materials, Vol. 2, IAEA, Vienna. 1966, p. 383.

39. Barry, D.E., Phil. Mag., Vol. 23, 1971, p. 495.

40. Viswanathan, B., Amarendra, G., and Gopinathan. K.P.. "Helium bubbles in neutron-irradiated copper-boron studied by positron annihilation", Rad. Eff.. Vol. 107, 1989, pp. 121-137.

41. Makin, M.J., in Voids Formed by Irradiation of Reactor Materials, S.F. Pugh, et al., Eds., British Nucl. Eng. Soc., 1971, pp. 269-271.

42. Zinkle. S.J., Wolfer, W.G.. Kulcinski. G.L.. and Seitzman, L.E., " Stability of vacancy clusters in metals II: Effect of oxygen and helium on void formation in metals", Phil. Mag. A, Vol. 55, 1987, pp. 127-140.

43. Brimhall. J.L. and Mastel. B., J. Nucl. Mater., Vol. 29, 1969, pp. 123-25.

44. Brimhall, J.L. and Kssinger. H.E., Rad. Effects, Vol. 15, 1972, pp. 259-272.

45. Labbe. M. and Poirier. J.P., J. Nucl. Mater., Vol. 46, 1973, pp. 86-98.

46. Labbe, M., Brebec, G.. and Poirier, J.P., J. Nucl. Mater., Vol. 49, 1973/74, pp. 232-34.

47. Adamson, R.B.. Bell, W.L., and Kelly, P.C., J. Nucl. Mater., Vol. 92, 1980, pp. 149-154.

48. English, C.A., J. Nucl. Mater.. Vols. 108&109, 1982, pp. 104-123.

49. English, C.A., Eyre, B.L., and Muncie, J.W., Phil. Mag. A, Vol. 56, 1987, p. 453.

50. Eldrup, M., Evans, J.H., Mogensen, O.E., and Singh. B.N., Rad. Effects, Vol. 54, 1981. pp. 65-80.

51. Yoshida. N.. Kitajima, K. and Kuramoto, E., J. Nucl. Mater., Vols. 122&123, 1984. pp. 664-68.

52. Singh. B.N., Leffers, T., and Horsewell, A., Phil. Mag. A, Vol. 53, 1986, p. 233.

53. Takeyama, T.. Ohnuki, S., and Takahashi, H., J. Nucl. Mater., Vol. 89, 1980, pp. 253-262.

54. Leffers, T.. Singh, B.N., Buckley, S.N., and Manthorpe, S.A., J. Nucl. Mater., Vol. 118, 1983, pp. 60-67.

55. Takeyama, T.. in Proc. Conf. on New Trends in Atom Resolution, Materials Science and Biology, H. Hashimoto et al., Eds., Science Press, Beijing, China, **1982,** pp. **78-86.**

56. Leister, K-H, "Influence of solutes on heavy ion induced void swelling in binary copper alloys", Ph.D. Thesis, Kernforschungszentrum Karlsruhe Report KfK **3499,** May **1983.**

57. Venker, H.. Giesecke. P.. and Ehrlich. K.. "The influence of fast diffusing substitutional elements on the swelling behaviour of Ni- and Cu-alloys", in Radiation Effects in Breeder Reactor Structural Materials, M.L. Bleiberg and J.W. Bennett, Eds., TMS-AIME, **1977.** PP. **41520.**

58. Leffers, T., Singh, B.N., and Barlow, P., Research Establishment Riso Report Riso-M-1937, Roskilde, Denmark, May, **1977;** also Singh, B.N. et al., in 5th Int. Conf. on HVEM, Kyoto, Japan, Aug., **1977,** pp. **581-84.**

59. Hashimoto, M. et al., "HVEM study of void swelling in concentrated Ag-base and Cu-base alloys", in Proc. XIth Int. Cong. on Electron Microscopy, Kyoto, **1986,** pp. 1103-4.

60. Dworschak. F., Lennartz, R., and Wollenberger, H., "Interstiial trapping and detrapping in electron irradiated dilute copper alloys", J. Phys. F: Metal Phys., Vol. **5, 1975,** pp. **400-418.**

61. Maury. F., et al., Rad. Effects, Voi. **51,** 1980, pp. **57-68.**

62. Takeyama, T., Ohnuki, S., and Takahashi. H., Scripta Met., Vol. **14,** 1980, pp. **1105-1110.**

63. Knoll, R.W., "Effects of heavy ion irradiation on the phase stability of several copper-base alloys", Ph.D. Thesis, Univ. of Wisconsin-Madison, 1981.

64. Spitznagel, J.A., et al., "Ion irradiation effects of high strength, high conductivity copper alloys", Nucl. Instr. Methods B, Vol. 16, **1986,** pp. 279-287.

65. Zinkle, S.J., Dodd, R.A., and Kulcinski. G.L.. "Ion irradiation of high strength, high conductivity copper alloys at fusion-relevant temperatures", J. Nuci. Mater., Vols. **133&134, 1985,** pp. 680-684.

66. Brager, **H.R.,** J. Nucl. Mater., Vols. **141-143, 1986, pp.163-168.**

67. Seeger, A.K., in 2nd U.N. Conf. on Peaceful Uses of Atomic Energy, Vol. 6, **1958,** pp. 250-273.

68. Blewitt, T.H., Coltman, R.R., Jamison, R.E.. and Redman, J.K., J. Nucl. Mater., Vol. **2, 1960,** p. **277.**

69. Rukwied. A. and Diehl. J., Z. Metallkunde, Vol. 55, **1964,** p. **266;** Rukwied, A., ibid., p. **146.**

70. Makin, M.J., "Radiation Damage in Face Centered Cubic Metals and Alloys", in Radiation Effects, W.F. Sheely. Ed., Gordon and Breach Science Publ., New York, **1967,** pp. 627-669.

71. Diehl. J. and Seidel, G.P.. "Effect of alloying and cold work on the neutron irradiation hardening of metals", in Radiation Damaae in Reactor Materials, Vol. I, IAEA, Vienna, **1969,** pp. 187-214.

72. Makin, M.J.. Minter, F.J., and Manthorpe, S.A., Phil. Mag., Vol. **13, 1966,** pp. **729-39.**

73. Koppenaal, T.J. and Arsenault, R.J., "Neutron-irradiation strengthening in fcc single crystals", Metallurg. Rev., Vol. **16, 1971,** pp. 175-196.

74. Mitchell, J.B., Van Konynenburg, R.A., Parkin, D.M.. and Echer, C.J.. "DT fusion neutron radiation strengthening of copper and niobium", in Radiation Effects and Tritium Technology for Fusion Reactors, Vol. 11, J.S Watson and F.W. Wiffen. Eds., CONF **750989, 1975,** pp. 172-208.

75. Kojima, S. and Zinkle, S.J., "Radiation hardening in neutron irradiated polycrystalline copper", J. Nucl. Mater., Vol. **176, 1990,** in press **1990** (ICFRM-4, Kyoto)

76. Fleischer, R.L., J. Appl. Phys.. Vol. **33, 1962,** p. **3504.**

77. Zinkle. S.J. and Kulcinski. G.L.. J. Nucl. Mater., Vols. **122&123, 1984.** pp. **449-454.**

78. Zinkle, S.J. and Kulcinski, G.L., "Low-load microhardness changes in 14-MeV neutron irradiated copper alloys", in The Use of Small-Scale Specimens for Testina Irradiated Material, ASTM STP 888, W.R. Corwin and G.E. Lucas. Eds., ASTM, Philadelphia, **1986,** pp. 141-160.

79. Heinisch. H.L.. J. Nucl. Mater., Vols. **155-157, 1988.** pp. **121-129;** also H.L. Heinisch et al., ibid., pp. 1159-63.

80. Zinkle, S.J., J. Nucl. Mater., Vol. **150, 1987,** pp. 140-58.

81. Makin. M.J., Whapham, A.D., and Minter, F.J., Phil. Mag., Vol. **7, 1962,** p. **285.**

82. Brager, H.R.. Garner, F.A.. and Panayotou. N.F.. J. Nucl. Mater., Vols. **103&104, 1981,** pp. 955-59.

83. Shimomura, Y., et al., J. Nucl. Mater., Vols. **1338134, 1985,** pp. 385-89.

84. Yoshida. N., Akashi, Y., Kitajima, K., and Kiritani, M.. J. Nucl. Mater., Vols. **1338134, 1985.** pp. **4059.**

85. Satoh, Y.. Ishida. I., Yoshiie, T., and Kiritani, M.. J. Nucl. Mater., Vols. **155-157, 1988.** pp. 443-48.

86. Horsewell. A.. et al., "Defect structures in copper and gold irradiated with fast neutrons, 14-MeV neutrons and 600 to **800** MeV protons", J. Nucl. Mater., Vol. 176, **1990,** in press, **1990** (ICFRM-4, Kyoto)

87. Kiritani, M., Mat. Sci. Forum, Vols. 15-18, **1987,** pp. 1023-46.

88. Kiritani. M., J. Nucl. Mater., Vols. **155-157, 1988,** pp. 113-120.

89. Wilson, J.C.. in 2nd U.N. Int. Conf. on Peaceful uses of Atomic Energy, Vol. **5, 1958,** pp. 431-445.

90. El-Shanshoury, I.A., J. Nucl. Mater., Vol. **45,** 1972/73, pp. 245-57.

91. Mohamed. H.G., Hammad, A.M., and Hammad, F.H., Trans. Ind. Inst. Metals, Vol. **35,** No. **3, 1982,** pp. 258-**62.**

92. Kruglov, A.S., Bykov, V.N., El-Shanshuri, I., and Gabor, Kh., Sov. Atomic Energy, Vol. 26, **1969,** pp. 582-84.

93. Didyk. A.Yu., Regel, V.R., Skuratov, V.A., and Mikhailova, N.Yu., Sov. Phys. Tech. Phys.. Vol. **34, No.5, 1989.** pp. 563-565.

94. Adams, M.A. and Higgins, P.R.B.. Phil. Mag., Vol. 4, 1959, p. 777.
95. Muncie, J.W., Eyre, B.L., and English, C.A., Phil. Mag. A, Vol. 52, 1985, pp. 309-331.
96. English, C.A., Eyre, B.L.. and Summers. J., Phil. Mag., Vol. 34, 1976, pp. 603-14.
97. Kulcinski. G.L., Mastel, B., and Kissinger, H.E., Acta Met., Vol. 19, 1971. pp. 27-36.
98. Anderson. K.R.. Garner. F.A.. and Stubbins. J.F., "Unusual tensile and fracture behavior of pure copper at high levels of neutron-induced swelling", 15th Int. Symp. on' Effects of Radiation on Materials, June, 1990, these Droceedinas. R.E. Stoller et al., Eds.. ASTM
99. Goods, S.H., Scripta Met., Vol. 20, 1986, pp. 565-69.
100. Goods, S.H.. in 14th Int. Symp. on Effects of Radiation on Materials, Vol. I, ASTM STP 1046, N.F. Packan et al., Eds., ASTM, Philadelphia, pp. 340-352.
101. Zinkle, S.J.. Kulcinski, G.L.. and Mansur, L.K., J. Nucl. Mater., Vols. 141-143, 1986. pp. 188-192.
102. Appello. M. and Fenici, P.. J. Nucl. Mater., Vol. 152, 1988, pp. 348-50.
103. Zinkle. S.J., Plantz, D.H., Bair. A.E., Dodd. R.A. and Kulcinski, G.L., J. Nucl. Mater., Vols. 133&134, 1985, pp. 685-89.
104. Piercy. G.R.. J. Phys. Chem. Solids, Vol. 23, 1962, pp. 463-77.
105. Chou. P.. and Ghoniem, N.M., J. Nucl. Mater., Vol. 117, 1983, pp. 55-63.
106. Wollenberger, H., Rad. Effects, Vol. 113, 1990, pp. 161-64.

6.5 Environmental Effects on Structural Alloys

ELECTROCHEMICAL AND MICROSTRUCTURAL CHARACTERIZATION OF AN AUSTENITIC STAINLESS STEEL IRRADIATED BY HEAVY IONS AT 515°C - G. E. C. **Bell** (Oak Ridge National Laboratory), T. Inazumi (Japan Atomic Energy Reasearch Institute, assigned to ORNL) and E. A. Kenik (Oak Ridge National Laboratory)

OBJECTIVE

The objective of this work is to evaluate radiation-induced sensitization of austenitic stainless steels under simulated fusion reactor conditions by the electrochemical potentiokinetic reactivation (EPR) test technique.

SUMMARY

The electrochemical and microstructural behavior of a solution-annealed, heavy-ion-irradiated, austenitic stainless steel, designated LS1A, have been investigated at 515°C after doses of 1, 10, and 30 displacements per atom (dpa). Changes in electrochemical properties due to radiation induced segregation in thin radiation-affected layers of the material were detected by the electrochemical potentiokinetic reactivation (EPR) technique using transmission electron microscopy (TEM) disk specimens. At all doses, the Flade potential and reactivation charge were greater than those measured for thermally-aged control specimens. Flade potentials increased with increasing dpa while the reactivation charge did not increase beyond 10 dpa. Grain face etching, similar to that found on EPR-tested neutron-irradiated austenitic stainless **steels,** was observed on all specimens after testing. Grain boundaries were etched after doses of 10 and 30 dpa. The extent of grain face etching increased with increasing dose. Duplicate heavy-ion-irradiated specimens were also examined by high resolution analytical electron microscopy (AEM). The 1-dpa specimen showed only a high density of small faulted dislocations (−10 nm), and no grain boundary precipitation was observed nor was any grain boundaty segregation detected. AEM confirmed chromium depletion at grain boundaries as measured by EPR for the 10- and 30-dpa specimens. Depletion widths of approximately 10 nm and grain boundary chromium compositions of **less** than 10% by weight were found. Molybdenum was also depleted near the boundary, whereas nickel, silicon, and iron were enriched for the 10- and 30-dpa irradiations. Precipitation of G and eta phases and larger dislocation loops (−60 nm) were observed in the 10- and 30-dpa specimens.

PROGRESS AND STATUS

Introduction

The dose rate (dpa/s) in material bombarded by heavy ions is between 2 and 6 orders of magnitude higher than that in both fission and fusion reactors. As such, heavy ion irradiation is often used as an accelerated method for investigating radiation-induced segregation (RIS) and the evolution of microstructures in materials during neutron irradiation. Although irradiation by heavy ions does not induce radioactivity in the material and simplifies handling and testing as compared with neutron-irradiated materials, the penetration distance of the heavy ions is small (on the order of 1 μm) and the volume of affected material is correspondingly small. However, analytical techniques which sample small volumes of material, such as analytical electron microscopy (AEM),[1,2] or electrochemical techniques which detect changes in surface properties are well suited for **use** with heavy-ion-irradiated material. Examination by AEM allows characterization of **the** radiation-produced microstructure and microchemistry while electrochemical methods yield information about the effect of these microstructural changes on the corrosion properties of the material. Correlation between the microstructural and electrochemical results gives insight into radiation-assisted corrosion phenomena, such as irradiation-assisted stress corrosion cracking (IASCC). In this research, we investigated the changes in electrochemical properties, as measured by the electrochemical potentiokinetic reactivation (EPR) method,[3] of an austenitic stainless steel irradiated by heavy ions at 515°C to doses of 1. 10, and 30 dpa. Surface morphology after testing was examined using scanning electron microscopy (SEM). The radiation-produced microstructures and grain boundary microchemistry of duplicate specimens were examined by AEM.

Experimental

Specimen Material. Irradiation. and Preparation Conditions - The material investigated was an experimental austenitic stainless steel alloy, similar to type 316 stainless **steel,** designated LS1A (Fe-16.4Cr-13.7Ni-1.0Si-2.0Mn-1.7Mo-0.15Ti-0.08C, wt %). Complete details of the specimen preparation and heavy ion irradiation were reported elsewhere.2 A detailed diagram of the specimen radiation damage region and the electrochemically tested areas is shown in Fig. 1. Disk specimens of 3 mm diam suitable for both electrochemical testing4 and evaluation by AEM were punched from 0.25-mm-thick sheet stock and solution annealed at 1150°C for 1 h before irradiation. The specimens were mounted on a thermal-control block during irradiation and the temperature of the specimens was measured using an infrared pyrometer. The center 2.5-mm-diam region of the disks was subjected to a normally incident beam of 4 MeV Ni^{++} ions with a beam current of ~0.6 amps/cm^2, which produced a peak damage profile at approximately 0.7 μm below the original surface at a dose rate of approximately 1.2×10^{-4} dpa/s. The nickel ions came to rest

approximately 1 μm below the incident surface and the bombarding ions produced a peak nickel enrichment of approximately 0.1% nickel by weight per dpa. Control specimens of the solution-annealed material were thermally aged at 515°C for 9 h in vacuum to simulate the thermal history of the most heavily irradiated specimens.

Prior to EPR testing, the surface of the specimens was sectioned to 0.5 μm below the original surface by electropolishing near -10°C in a 10:6:1 methanol:betyl cellusolve:perchloric acid solution. In this way, the peak damage region is exposed during electrochemical testing while any changes in alloy composition due to ion implantation should be minimized. The specimens were then rinsed in alcohol and stored in acetone until just prior to testing. In preparation for electrochemical testing, the specimen surface was masked with silicon rubber and vinyl tape such that only the central 2-mm-diam (0.0314 cm^2) region of the heavy ion irradiated surface was exposed to the electrochemical testing solution.

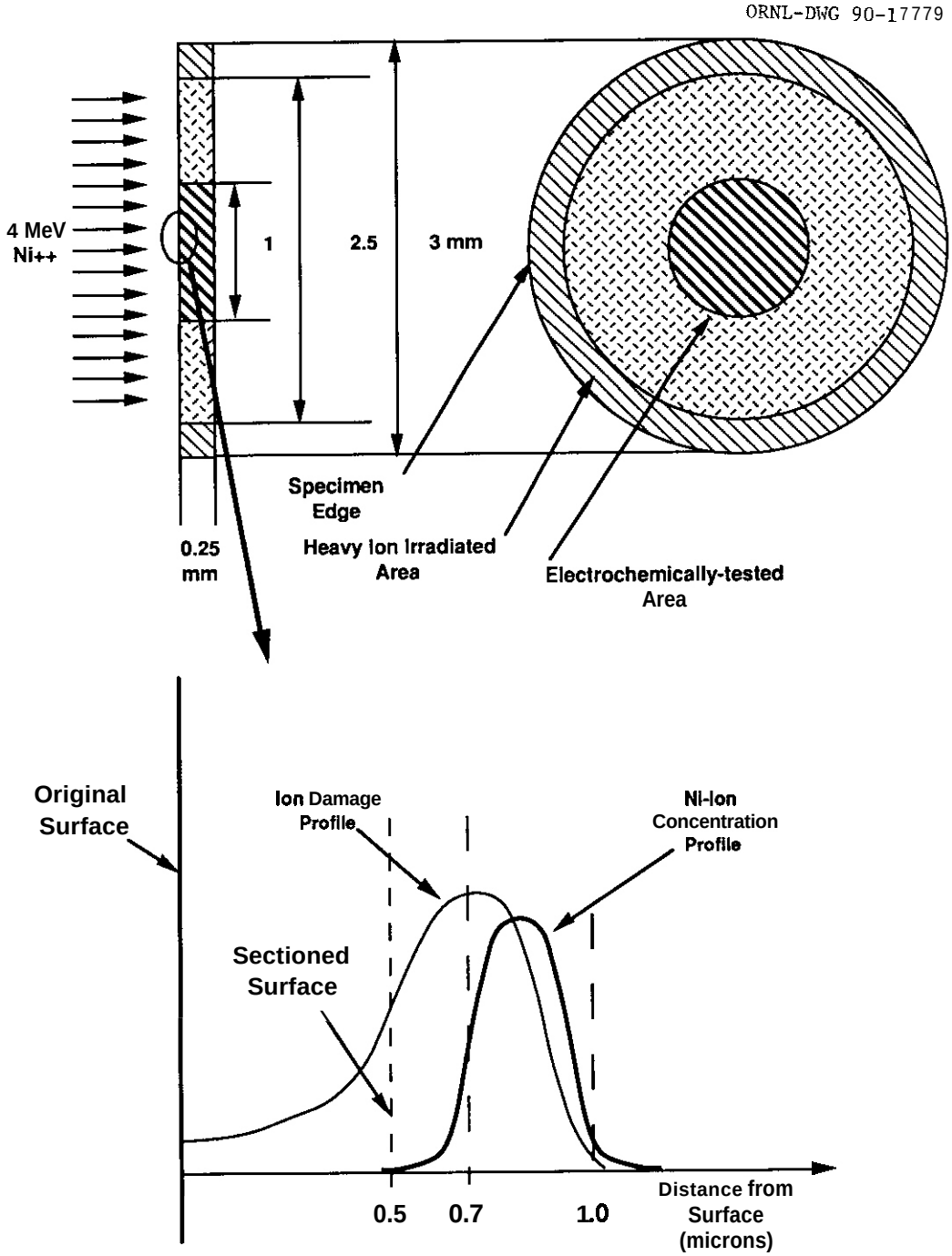

Fig. 1. Detailed schematic of heavy-ion-irradiated specimen.

Single-Loop EPR - The details of the EPR method and experimental apparatus has been described in detail elsewhere.[3,4] The conditions for the single-loop EPR tests are summarized in Table 1. In the case of radiation-induced segregation, chromium is depleted at grain boundaries and other microstructural defects without precipitation of a chromium-rich phase via the reverse-Kirkendall effect5 and has been detected by electrochemical methods for neutron irradiated material.[6] By comparing the dissolution charge (integral of the dissolution current) and film breakdown potential (Flade potentials) of control and heavy-ion-irradiated materials, the degree of sensitization attributable to the heavy ion irradiation damage can be quantified. More positive Flade potentials and higher dissolution charges are indications of less stable passive films and increased susceptibility to localized corrosion. The Flade potential, E_F, was defined as the first inflection point of the potential versus current curve during the controlled cathodic potential scan. Since the potential scan rate is constant and applied potential is proportional to time, the total reactivation charge, Q_R^{Total}, was calculated by integrating the potential versus current curve from (initial passivating) +200 mV vs saturated Calomel electrode (SCE) to free-corrosion potential. SEM examination was performed after EPR testing using either a Joel JSM-35GF or Hitachi 8000.

Analytical Electron Microscopy - Duplicate specimens were sectioned to the peak damage region by electropolishing near -10°C in a 10:6:1 methanol:betyl cellusolve:perchloric acid solution. Analytical electron microscopy was performed in a Philips EM400T/FEG microscope. Analyses were performed in the scanning TEM mode with a probe ~2 nm in diameter. Details for high spatial resolution X-ray microanalyses at boundaries and defects have been given elsewhere.'

Table 1. Summary parameters for single-loop electrochemical potentiokinetic reactivation tests.

Test Parameter	Condition
Potentiostat	Princeton Applied Research model 273/342
Test Solution	0.5 M H_2SO_4 +0.01 M KSCN
Solution Temperature	30 ± 1 °C
Surface Preparation	Electropolishing
Surface Conditioning	-600 mV vs. SCE for 120 s
Pre-test Delay	-600 s to stabilize E_{corr}
Initial Passivation Conditions	+200 mV vs SCE for 120 s
Reactivation Scan Rate	6 V/h
Final Potential	E_{corr} - 50 mV vs. Saturated Calomel Electrode (SCE)

Results

Electrochemical - The EPR results for the heavy ion irradiated and thermal control specimens are shown in Fig. 2 and Table 2. The thermal control specimen (515°C for 9 h) behaved similar to a solution-annealed specimen and did not exhibit a reactivation peak or Flade potential, indicating that no electrochemically detectable thermal sensitization (precipitation) had occurred even during the longest heavy ion irradiation (30 dpa). Irradiation by heavy ions at 515°C to 1 dpa was sufficient to cause the occurrence of a Flade potential and corresponding reactivation peak. Irradiation to 10 dpa increased the reactivation charge by more than 2 orders of magnitude. Similar reactivation charges (EPR curves) were obtained for the 10- and 30-dpa specimens. In general, the Flade potential increased with increasing dose while the reactivation charge did not increase beyond 10 dpa.

Post-EPR Surface Morphology - Scanning electron micrographs of the post-EPR test heavy ion irradiated surfaces are shown in Fig. 3. [Note magnification difference between (a) and (b) and (c)]. The thermal control specimen was not etched or pitted during the EPR test and is not shown. Light, grain face pitting (etching) of the 1-dpa specimen was found and accounted for the existence of a Flade potential and reactivation peak (charge). No grain boundary etching was observed for the 1 dpa specimen. The 10- and 30-dpa specimens were similar in appearance to each other and showed etching of both grain boundaries and grain faces after EPR testing. The 30-dpa specimen was more heavily etched at grain boundaries (~0.5 to 1 μm width), as compared to the 10-dpa specimen (~0.1 to 0.3 μm width) and the etching of the grain face coarsened with increasing dose.

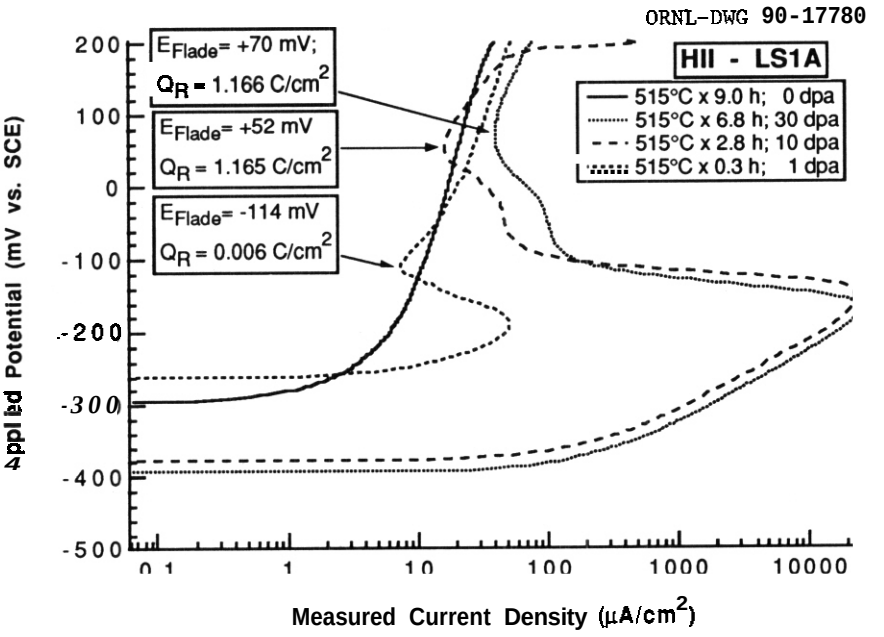

Fig. 2. Single-loop EPR results for heavy-ion-irradiated and thermal control specimens of LS1A, 515°C.

Table 2. Summary of Flade potentials and reactivation charges for thermally-aged and heavy ion irradiated at 515°C.

Temperature T (°C)	Time at T (h)	Dose (dpa)	Flade Potential, E_F (mV vs SCE)	Reactivation Charge, q_R (C/cm^2)
515	**9.0**	**0**	**N/A**	**N/A**
515	0.3	1	-114	0.006
515	2.8	10	+52	1.165
515	6.9	30	+70	1.166

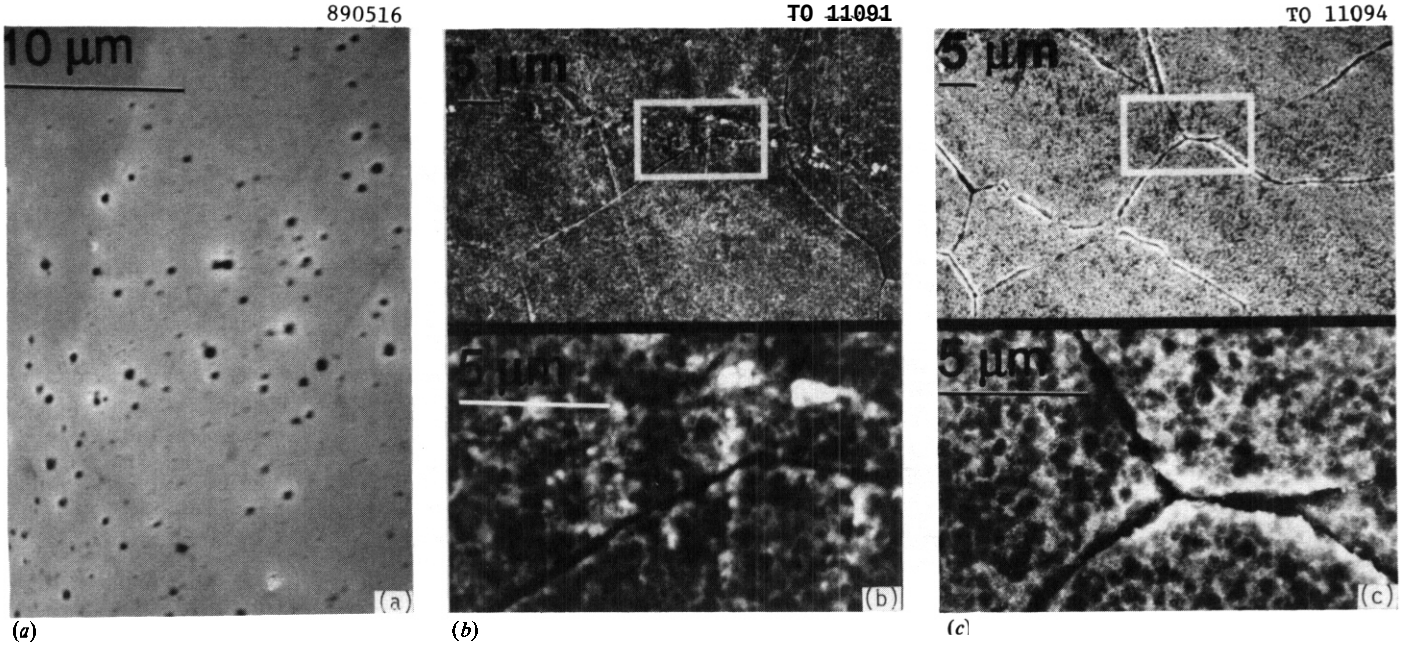

(a) (b) (c)

Fig. 3. SEM micrographs of post-EPR test LS1A 515°C heavy-ion-irradiated surfaces. (a) 515°C; 1 dpa. (b) 515°C; 10 dpa. (c) 515°C; 30 dpa.

Microstructural (AEM) Results - After a dose of 1 dpa at 515°C, only a high density (~5 x 10^{20} m^{-3}) of small defects (~10 nm diam) were observed [Fig. 4(a)]. Their contrast behavior was consistent with that for faulted dislocations. No grain boundary precipitation was observed, nor was any grain boundary segregation detected. With the 10-dpa material, both faulted dislocation loops (~60 nm diam) and similarly sized precipitates were observed [Fig. 4(b)]. The precipitates were enriched in silicon and nickel and had large interplanar spacings consistent with G and eta phase silicides. Both G and eta phase were identified at the grain boundaries from X-ray microanalysis and electron diffraction. The two phases were distinguished via the chromium level in the precipitate relative to the matrix (G phase contains ~5 wt % Cr, whereas eta phase contains ~30 wt % Cr).[8] Figure 5(a) shows a grain boundary with a G phase precipitate. X-ray microanalysis indicated RIS at the boundary [Fig. 5(b)]. Chromium was depleted from a region ~10 nm wide near the boundary with a minimum value of 10 wt % Cr. Molybdenum was also depleted near the boundary, whereas nickel, silicon, and iron were enriched near the boundary.

In the material irradiated to 30 dpa. precipitates of G and eta phase dominated the matrix with dislocation segments and some faulted loops [Fig. 4(c)]. No voids or cavities were observed in either material or after irradiation to 70 dpa at 515°C. G and eta phases were also observed at grain boundaries. X-ray microanalysis was performed on a similar alloy with lower silicon which was irradiated to 30 dpa at the same time. Figure 6 shows the grain boundary composition profiles typical for that specimen. Similar to the 10-dpa specimen, the chromium was depleted in an ~10-nm-wide region at the boundary with a minimum value of 11 wt % Cr. Whereas iron was locally depleted at the grain boundaty, a region approximately 4 to 20 nm on either side of the boundary was enriched in iron with respect to the surrounding matrix. A similar but less pronounced enrichment was observed for chromium. Molybdenum was also depleted at the grain boundary, whereas enrichment of silicon (~2 wt %) and nickel (~25 wt %) occurred in a narrow band at the grain boundary. Just outside of that region a depletion of silicon and nickel relative to the matrix was observed.

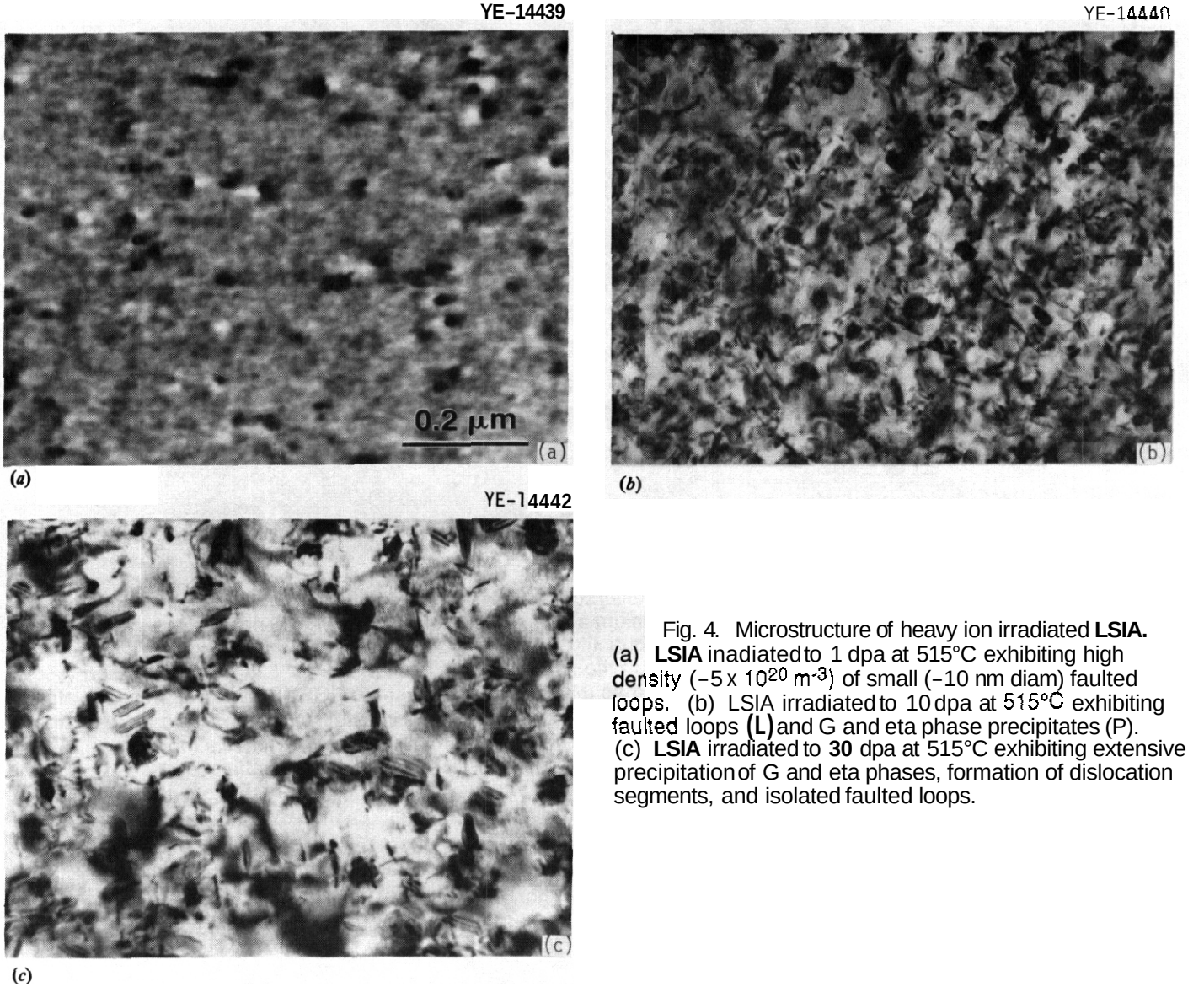

Fig. 4. Microstructure of heavy ion irradiated LSIA. (a) LSIA inadiated to 1 dpa at 515°C exhibiting high density (~5 x 10^{20} m^{-3}) of small (~10 nm diam) faulted loops. (b) LSIA irradiated to 10 dpa at 515°C exhibiting faulted loops (L) and G and eta phase precipitates (P). (c) LSIA irradiated to 30 dpa at 515°C exhibiting extensive precipitation of G and eta phases, formation of dislocation segments, and isolated faulted loops.

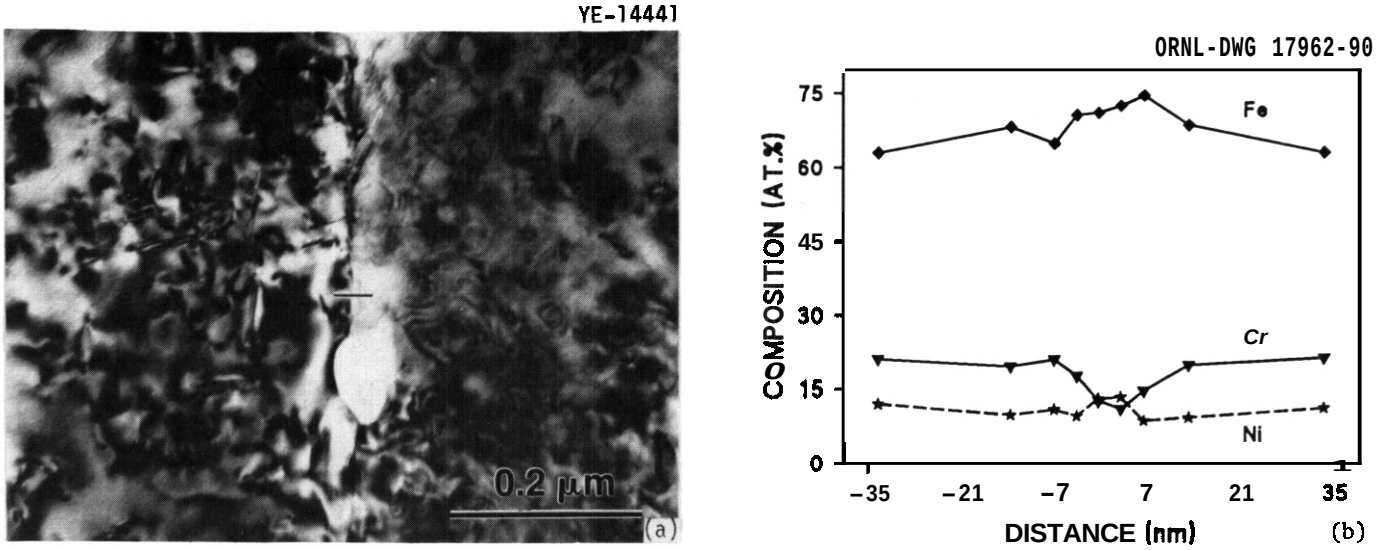

Fig. 5. Microstructural and compositional analysis of heavy-ion-irradiated LSIA. (a) Grain boundary in LSlA irradiated to 10 dpa at 515°C exhibiting a G phase precipitate. Hole on boundary is probable site of second precipitate which has fallen out. Line indicates region of X-ray microanalysis. (b) Iron, chromium, and nickel profiles at grain boundary in (a).

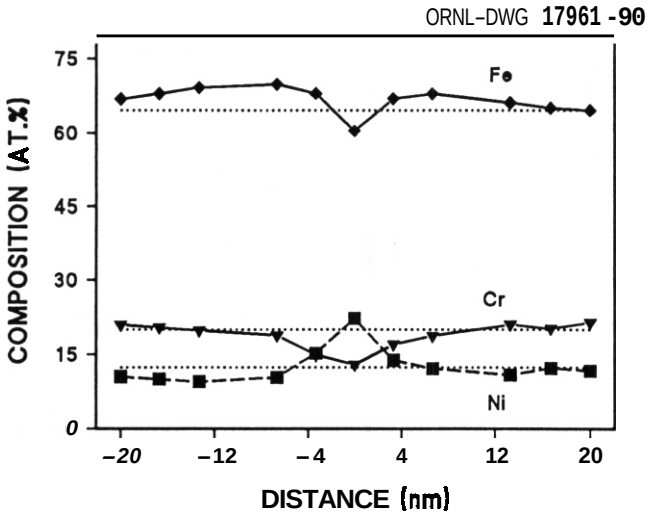

Fig. 6. Iron, chromium, and nickel profiles at grain boundary in stainless steel similar to LSIA irradiated to 30 dpa at 515°C under same conditions as in Fig. 4(c). Dotted lines indicate matrix composition away from boundaries.

Discussion

Susceptibility of austenitic stainless steels to intergranular stress corrosion cracking (IGSCC) has been termed sensitization and is attributed to the depletion of chromium at grain boundaries when $M_{23}C_6$ precipitates in the boundaries. The EPR test method was developed to quantify the susceptibility of austenitic stainless steels to IGSCC in aqueous environments due to thermal sensitization in the heat-affected zones of welds. Chromium depletion via radiation-induced segregation has also been proposed as a possible mechanism for IGSCC observed in light-water reactors and the phenomena has been called IASCC.[9] Recently, we have successfully applied EPR to the detection of chromium depletion in an austenitic stainless steel via RIS.[6,10] In thermally sensitized material, only grain boundaries are etched during EPR testing; grain faces of thermally sensitized material are unaffected. However, grain face etching and pitting was observed in this study on heavy-ion-irradiated material similar to that previously observed on EPR-tested neutron-irradiated austenitic stainless steels.[7,8] It is possible that chemical changes in the nitrogen-deaerated EPR test solution via γ-radiolysis could have caused the etching of grain faces for neutron-irradiated material. However, since grain face etching has been observed for both heavy-ion- and neutron-irradiated austenitic stainless steels, it does not appear to be the result of chemical changes in the EPR test solution due to γ-radiolysis. As a corollary, grain face etching during EPR testing in the present work does not appear to be attributable to changes in alloy chemistry due to implantation of a major alloy element (nickel).

The results of post-EPR SEM examination of the specimens correlated with the AEM results. No grain boundary etching was observed after 1 dpa dose and, correspondingly, no segregation (chromium depletion) was observed at grain boundaries. On the other hand, for both 10- and 30-dpa specimens, very clear grain boundary and chromium depletion via RIS was detected with AEM. It is apparent from these results that EPR is able to resolve very thin chromium depleted zones (~10 nm); however, the width of the resulting post-EPR grain boundary etching could not be directly related to the measured RIS chromium depletion width. Once the passive film in the chromium-depleted region at the boundary breaks down, dissolution occurs not only in the chromium-depleted region but also beneath the surface and then over a wider region during the active portion of the EPR test.

It should be noted that, as a result of the narrow width of the RIS profiles relative to the excited volume for X-ray microanalysis, the AEM measured profiles differ from the actual profiles. The measured profiles represent a convolution of the actual profiles with a "broadening" function related to the size of the excited volume. As a result, the measured chromium profile underestimates the actual chromium depletion at the grain boundaries. Therefore, actual chromium levels at the grain boundaries are well below the 12 wt % chromium required to maintain the stainless character of the alloy. Further, sensitization via RIS, as measured by EPR, is exacerbated by the simultaneous depletion of molybdenum, which also helps form a passive film, from the grain boundary region.

We previously reported[7,8] that the presence of grain face etching tends to obscure the quantitative interpretation of EPR results relative to determining the susceptibility of the irradiated material to IGSCC or IASCC because current flows from both the grain boundaries and the grain faces. However, the results of EPR on neutron-irradiated surfaces can be correlated to RIS at microstructural boundaries (e.g., grain boundaries, dislocations, and voids).[8] We feel that the grain face etching of both heavy-ion- and neutron-irradiated materials was the result of RIS (chromium depletion) at dislocations and/or precipitates in the irradiated material.[1,8] The extent or coarseness of the grain face etching paralleled the increased size of the microstructural defects and may be an indication of RIS at these defects.[1,8]

Irradiation by heavy ions did not significantly increase the measured reactivation charge beyond 10 dpa. This is in agreement with Bruemmer et al.[11] who reported that chromium depletion profiles at grain boundaries in similar austenitic stainless steels heavy ion irradiated at 500°C were fully developed by 5 dpa, and chromium-depletion widths on either side of a grain boundary were 10 nm. Because the distance between defects is much smaller than grain diameters, RIS profiles at other defect sinks in the bulk material were also probably fully developed by 5 dpa near 500°C.

Grain boundary etching was deeper for 30-dpa specimens as compared to the 10-dpa specimens although the reactivation charges were nearly equal. The total reactivation charge is the sum of the contributions due to the grain boundaries and that of the grain faces:

$$Q_R^{Total} = Q_R^{GB} + Q_R^{GF} = q_R A_{Total} , \quad (1)$$

$$\frac{Q_R^{Total}}{A_{Total}} = q_R = q_R^{GB} \frac{A_{GB}}{A_{Total}} + q_R^{GF} \frac{A_{GF}}{A_{Total}} , \quad (2)$$

where q_R, q_R^{GB}, and q_R^{GF} are the reactivation charges per unit tested specimen area, grain boundary area, and grain face area, respectively; and A_{Total}, A_{GB}, and A_{GF} are the associated areas. Since the total grain boundary area is small compared to the grain face, $\frac{A_{GB}}{A_{Total}} << \frac{A_{GF}}{A_{Total}}$, the measured q_R should be relatively insensitive to changes in q_R^{GB}, corresponding to deeper grain boundary etching

Although it was not evident from the measured reactivation charges, electrochemical changes continued to occur beyond 10 dpa. Flade potentials increased with total dose to 30 dpa, with a significantly larger change occurring between 1 and 10 dpa, as compared with that between 10 and 30 dpa. The Flade potential is a measure of the inherent stability of the passive film on the stainless steel (i.e., higher Flade potentials imply less stable or thinner passive films). This increased instability may be due to compositional variations (e.g., chromium depletion) in the film or locally higher diffusivities of cation vacancies in the film and/or the metal substrate due to dislocations as suggested by Chao et al.[12] and later Urquidi-Macdonald and Macdonald.[13] However, dislocations produced by cold working do not Significantly affect the results of EPR and do not per se produce grain face etching for austenitic stainless steels of similar composition.8 Therefore, the grain face etching observed appears to be due to RIS of chromium at dislocations. The higher Flade potential of the 30-dpa specimen may also account for the deeper etching at the grain boundaries because the passive film tends to first break down at grain boundaries and these regions of the specimen would be in the active region for a longer time at a fixed scan rate.

The results of our research with heavy-ion-irradiated materials are very similar to those which we have obtained with neutron-irradiated materials.[8] It appears that heavy ion irradiation is a useful method for simulating and investigating the effects of radiation-produced microstructure on the electrochemical and subsequent corrosion properties of materials.

CONCLUSIONS

The following conclusions can be drawn from these results:

1. Grain face etching in both heavy-ion- and neutron-irradiated materials was the result of radiation damage to the material. Grain face etching is due to chromium depletion via RIS at dislocations and not due to enhanced vacancy diffusion through the passive film. The coarseness of grain face etching increased with increasing defect size and density.

2. The Flade or passive film breakdown potential of LS1A increased with increasing radiation dose to 30 dpa. indicating decreased passive film stability or thickness with increasing radiation dose. A large change occurred between 1 and 10 dpa with a smaller, but detectable, change occurring between 10 and 30 dpa.

3. Reactivation charge did not increase significantly beyond 10 dpa, although deeper grain boundary etching was observed in the 30-dpa specimen. Reactivation charge was relatively insensitive to depth of grain boundary attack during EPR testing for irradiated materials because the total reactivation charge is dominated by the grain face reactivation charge, Q_R^{GF}.

4. AEM showed that chromium was depleted from a region ~10 nm wide near grain boundaries and reached a minimum value of 10 wt % Cr for both the 10- and 30-dpa specimens. Molybdenum was also depleted near the boundary, whereas nickel, silicon, and iron were enriched near the boundary. Chromium depletion at grain boundaries was not measurable in the 515°C, 1-dpa material. The width of the resulting post-EPR grain boundary etching is not directly related to the RIS chromium depletion width.

5. It appears that heavy ion irradiation is a useful method for simulating and investigating the effects of radiation-produced microstructure on the electrochemical and subsequent corrosion properties of materials.

REFERENCES

1. E. A. Kenik. "Measurement of Equilibrium and Nonequilibrium Segregation by X-ray Microanalysis," p. 209 in Mater. Res. Symp. Proc., Vol. 62, Material Science Research Society, Pittsburgh, Penn.. 1986.

2. E. A. Kenik, Scr. Metall. **10** (1976) 733.

3. W. E. Clarke, V. M. Romero, and J. C. Danko, Detection of Sensitization in Stainless Steel Using Electrochemical Techniques, GEAP-21382, General Electric Company, 1976.

4. T. Inazumi, G. E. C. Bell, and K. Kiuchi, J. Nucl. Mater. **198** (1990)

5. P. R. Okamota and L. E. Rehn. J. Nucl. Mater. 83 (1979) 2-23.

6. T. Inazumi et al., accepted for publication in Corrosion (October 1990)

7. E. A. Kenik. Scr. Metall. 21 (1987) 811-816.

8. E. A. Kenik and E. H. Lee, p. 234 in Proc. 41st Annual Meeting of Electron Microscopy Society of , ——— San Francisco Press, San Francisco, Calif., 1983.

9. R. N. Duncan, Stainless Steel Failure Investigation Program. Final Summary Report, GEAP-5530, General Electric Company, 1968.

10. T. Inazumi, G. E. C. Bell. and A. Hishinuma, "Evaluation of Radiation-Induced Sensitization Using Electrochemical Potentiokinetic Reactivation Technique for Austenitic Stainless Steels," Paper No. 507, CORROSION/90, Las Vegas, Nev., April 23-27, 1990.

11. S. A. Bruemmer, L. A. Charlot, and E. P. Simonen, "Grain Boundary Chemistry Effects on Irradiation-Assisted Stress Corrosion Cracking," Paper No. 506, CORROSION/90, Las Vegas. Nev., April 23–27, 1990.

12. Y. Chao, L. F. Lin, and D. D. Macdonald, J. Electrochem. Soc. 128 (1981) 1187

13. M. Urquidi-Macdonald and D. D. Macdonald, J. Electrochem. Soc. 134 (1987) 41.

ENVIRONMENTAL EFFECTS ON AQUEOUS STRESS CORROSION OF CANDIDATE AUSTENITIC STEELS FOR ITER STRUCTURAL APPLICATIONS – A. B. Hull, M. R. Fox, J. W. Pascoe, and T. F. Kassner (Argonne National Laboratory)

OBJECTIVE

The corrosion resistance of the structural material to be used in an aqueous environment characteristic of candidate first wall/ blanket systems in the International Thermonuclear Experimental Reactor (ITER) has not been quantified. Information obtained on the stress corrosion cracking (SCC) susceptibility of several candidate stainless steels under ITER-relevant conditions will help to identify an optimal combination of structural materials, coolant chemistry, and operational conditions for the ongoing ITER design work. The objective of this task is to provide baseline information on the SCC susceptibility of these candidate stainless steels in high-purity oxygenated water that simulates many important parameters anticipated in ITER first wall/ blanket systems.

SUMMARY

Susceptibility of Types 316NG, 316, and 304 stainless steel to SCC was investigated at several temperatures between 50 and 150°C in slow-strain-rate-tests (SSRTs) in oxygenated water that simulates important parameters anticipated in first-wall/blanket systems. The water chemistry was based on a computer code that yielded the nominal concentrations of molecular radiolytic species produced in an aqueous environment under conditions likely to be found in the ITER. To be conservative, however, the SSRTs were performed in a less benign, more oxidizing reference environment.

Predominantly ductile fracture was observed in crevice specimens of Type 316 stainless steel (SS) strained to failure in a reference ITER water chemistry. The failure behavior of Type 304 SS crevice specimens heat-treated to yield sensitization values of 2, 3, or 20 C/cm^2 by electrochemical potentiokinetic reactivation (EPR) demonstrated that degree of sensitization had a dramatic effect on intergranular SCC (IGSCC) susceptibility. Type 304 SS specimens sensitized to the highest value exhibited shorter failure times, lower maximum stresses, and lower reduction in area values than did less-sensitized Type 304 SS or Type 316NG SS specimens. Scanning electron microscopy showed minimal evidence of SCC in the Type 316NG and solution-annealed Type 316 SS but clear evidence of IGSCC in moderately sensitized (EPR = 20 C/cm^2) Type 304 SS specimens in these environments.

Ranking for resistance to SCC in simulated ITER water by electron microscopy and SSRT parameters (e.g., total elongation, ultimate strength, and reduction in area) is: 304 SS (EPR = 20 < 2 C/cm^2) < 316NG SS.

PROGRESS AND STATUS

Introduction and Background

The ceramic breeder with a beryllium multiplier has been selected as the first option for the ITER driver blanket, with the Pb-Li breeder as an alternative. The first wall and shield are integrated with the blanket, and all concepts utilize water cooling; austenitic stainless steel is used for the structure. Research and development needs[1] for ITER with respect to aqueous corrosion include establishing a reliable data base on the following parameters:

- Reference materials (Types 316, 316L, and 316NG SS; solution-annealed/cold-worked).
- Water chemistry (high-purity water with stable radiolysis/electrolysis products, e.g., dissolved O_2, H_2O_2, H_2 (at ppm levels) and flow rate < 5 m/s.
- Temperature (nominally 60-150°C) with periodic increases to 250°C (conditioning) or 350°C (bakeout).
- Stress conditions to simulate high thermal stresses (exceeding yield), static and cyclic operation (ITER $\approx 10^4$ cycles), and tensile residual stresses.
- Coolant channel geometry/material microstructure, including weldments (both diffusion and fusion welds) and crevice/notch sensitivity.
- Radiation type (gamma, electron, neutron), dose (fast neutron fluence to 5 x 10^{22} nvt), and effects (up to 2500 appm hydrogen generation).

Earlier work[2,3] focused on developing criteria to define the simulated ITER water chemistry and establish the experimental protocol. Interim results from a series of experiments to evaluate SCC susceptibility of Types 316NG, 316. and 304 SS have been reported previously.4 No indication of SCC was observed in testa conducted at a strain rate of 3 x 10^{-7} s^{-1} in oxygenated water with sulfate additions (0.1-1.0 ppm) at temperatures of 95 and 150°C. The results described in the present report are from additional tests5 on these steels under more severe conditions, namely lower strain rates and with the addition of hydrogen peroxide to the oxygenated water.

Experimental Procedures

Cylindrical tensile specimens with a 6.35-mm diam. and a 36.0-mm gage length were fabricated from Types 316NG, 316, and 304 SS and then heat treated.[4,5] The heat treatments given to Type 316NG SS did not produce sensitization.6 For comparison with tests on Type 316NG SS (Tables 1 and 2), analogous SSRTs were performed on crevice specimens of sensitized Type 304 SS, which are expected to exhibit greater sensitivity to SCC in oxygenated water. Tables 3 and 4 give details of the degree of sensitization produced in Type 304 SS, as determined by electrochemical-potentiokinetic-reactivation (EPR).[7] Crevice specimens (Fig. 1) were created by drilling two small-diameter (≈0.8-0.9 mm) through holes in the gage section of the specimen and placing a corresponding austenitic stainless steel pin in the top hole to form a tight crevice; the bottom hole was left open.5 Reference SSRTs were performed in air with an Instmn Model 1125 tensile testing machine at strain rates of >10^{-5} s^{-1}; additional air tests and SSRTs at lower strain rates were conducted in small-diameter autoclaves with a once-through water system. Water chemistry was established by bubbling a 20% O_2-80% N_2 gas mixture though deoxygenated/deionized feedwater (conductivity<0.2 μS/cm) contained in a 130–L stainless steel tank. Hydrogen peroxide and/or sulfuric acid (0.1 or 1.0 ppm) was added to the feedwater before sparging with the gas mixture to ensure adequate mixing. An external silver/silver chloride (0.1M KCl) reference electrode, a thermocouple, and platinum and Type 304 SS electrodes were located at the autoclave outlet to establish the redox and open-circuit potential, respectively. The electrochemical potentials (ECPs) measured during the experiments were converted to the standard hydrogen electrode (SHE) scale by using the thermocell and liquid junction potentials.[8]

Tests were either carried to failure or interrupted at <20% strain. Tests to failure were characterized by time-to-failure, total strain, maximum stress, and fracture surface appearance. Interrupted tests were employed to reduce loading severity and help avoid artifacts associated with very high plastic strains. The load applied to each specimen was recorded continuously as a function of time, and an engineering-stress-vs-strain curve was produced for each specimen. Total elongation and reduction in area were determined by measuring the fractured specimen. In all cases, the fracture surfaces of the specimens strained to failure were examined by both optical and scanning electron microscopy (SEM) to determine the fractions of the reduced cross-sectional

Table 1. Influence of Temperature and Water Chemistry on SCC Susceptibility of Type 316NG SS Crevice Specimens

								SSRT Parameters						Potentials	
			Strain	Feedwater Chemistry[a]				Yield	Fail.	Max.	Total	Reduct.			
Test	Heat	Temp.	Rate	H_2O_2	O_2	Cond.	pH at	Stress	Time	Stress	Elong.	in Area	Fracture	304 SS	Pt
No.	No.	(°C)	(s^{-1})	(ppm)	(ppm)	(μS/cm)	25°C	(MPa)	(h)	(MPa)	(%)	(%)	Morphology[b]	mV(SHE)	mV(SHE)
3	467958	95	3x10^{-7}	--	7.2	0.97	5.68	267	195	457	21	60	0.9 D, 0.1 T	346	449
42	P91576	95	3x10^{-7}	7.0	7.1	0.81	5.76	140	281	469	30	54	1.0 D	413	473
6	590019[c]	95	3x10^{-7}	--	7.2	8.6	4.72	164	250	436	27	60	0.9 D, 0.1 T	428	559
30	467958	105	2x10^{-7}	5.3	7.6	0.94	5.73	191	358	463	26	61	1.0 D	499	414
29	P91576	105	2x10^{-7}	6.1	7.9	0.90	5.72	151	400	424	29	60	1.0 D	489	392
14	467958	150	1x10^{-7}	7.0	6.9	0.92	5.71	177	661	441	24	59	0.9 D, 0.1T	418	380
13	P91576	150	3x10^{-7}	5.7	7.0	0.92	5.60	137	252	400	27	61	0.9 D, 0.1 T	431	410

[a] Conductivity and pH were adjusted by addition of H_2SO_4; pH values of 4.7 and 5.7 correspond to 1.0 and 0.1 ppm of acid.

[b] Ductile (D) and transgranular (T) in terms of fraction of cross-sectional area. Characterization of fracture surface morphologies is in accordance with illustrations and definitions in Refs. 9 and 10.

"Heat No. 590019 is *Type* 316 SS, not *Type* 316NG SS, and was hydrogen-charged before straining.'

Table 2. Failure Behavior of Type 316NG SS Crevice Specimens in Air

Test No.	Heat No.	Temp. (°C)	Strain Rate (s^{-1})	SSRT Parameters: Yield Stress (MPa)	Failure Time (h)	Max. Stress (MPa)	Total Elong. (%)	Reduction in Area (%)	Metallographic Characterization
7	467958	92	1×10^{-5}	272	5.8	478	21	59	0.9D, 0.1T
41b	P91576	95	3×10^{-7}	158	--	--	17	18	--
46	P91576	105	2×10^{-7}	150	401	424	29	57	0.9 D, 0.1T
20	467958	150	1×10^{-5}	204	7.0	435	25	63	0.9D, 0.1T
19	P91576	150	1×10^{-5}	158	7.2	400	26	62	0.9D, 0.1T

[a] Ductile (D) and transgranular (T) in terms of fraction of cross-sectional fracture surface area. Characterization of fracture surface morphologies is in accordance with illustrations and definitions in Refs. 9 and 10.
[b] Interrupted test.

Table 3. Influence of Temperature, Water Chemistry, and Degree of Sensitization on SCC Susceptibility of Type 304 Crevice Specimens[a]

Test No.	EPR (C/cm^2)	Temp. (°C)	Strain Rate (s^{-1})	Feedwater Chemistry[b]: H_2O_2 (ppm)	O_2 (ppm)	Cond. (µS/cm)	pH at 25°C	SSRT Parameters: Yield Stress (MPa)	Fail. Time (h)	Max. Stress (MPa)	Total Elong. (%)	Reduct. in Area (%)	Metall.[c] Charact.	Potentials: 304 SS mV(SHE)	Pt mV(SHE)
21	2	150	3×10^{-7}	6.0	7.3	0.95	5.63	159	249	426	27	61	0.95 D, 0.05 T	437	418
24	2	150	3×10^{-7}	6.0	7.6	0.94	5.79	170	173	368	19	42	0.9 I, 0.1 T	424	418
2	3	95	3×10^{-7}	-	7.4	9.5	4.15	151	280	424	29	58	0.9 D, 0.1 T	394	549
27	20	52	3×10^{-7}	7.0	7.3	1.03	5.71	213	259	495	28	42	1.01	580	445
23	20	95	3×10^{-7}	5.9	7.8	0.83	5.78	185	247	469	27	49	1.01	415	331
31	20	105	2×10^{-7}	7.2	7.6	0.92	5.73	210	334	463	24	41	1.0 I	493	406
32[d]	20	105	2×10^{-7}	6.7	7.0	0.93	6.10	205	..	..	21	13	NA	526	505
22	20	150	3×10^{-7}	1.0	6.7	0.99	5.73	157	124	323	13	37	1.01	426	417
28[d]	20	150	3×10^{-7}	6	7	0.9	5.7	178	..	..	8	6.6	IC	..	..

[a] Specimens of *Type* 304 SS (Heat No. 30956) were sensitized to EPR values of 2 to 20 C/cm^2 and were exposed to environments for ≈ 10 h before straining.
[b] Conductivity and pH were adjusted by addition of H_2SO_4; pH values of 4.7 and 5.7 correspond to 1.0 and 0.1 ppm of acid.
[c] Ductile (D), transgranular (T), and intergranular (I) in terms of fraction of cross-sectional area. Characterization of fracture surface morphologies is in accordance with illustrations and definitions in Refs. 9 and 10. In interrupted tests 32 and 28, incipient cracks (IC) in hole or crevice regions were observed, or characterization results were not available (NA).
[d] Interrupted teats; a micrometer was used to measure the gage section before and after straining.

area with ductile, transgranular, and intergranular morphologies.[9,10] The crevice and hole regions of the specimens subjected to interrupted tests were sectioned parallel to the line of tension by electrical discharge machining. The sections were then examined by SEM to ascertain the existence of incipient cracking. The chemical compositions of materials used for this study and the experimental methods have been fully described in previous papers.[5,6,11,12]

Cracking susceptibility can be assessed from SSRTs by using various parameters. Total elongation, reduction in area, and maximum stress are often used, as are fracture surface morphology and maximum crack length present (either on the fracture surface or on the sectioned surface after test interruption). Because of the

Table 4. Failure Behavior of Type 304 SS Crevice Specimens in Air

Test No.	EPR[a] (C/cm^2)	Temp. (°C)	Strain Rate (s^{-1})	SSRT Parameters: Yield Stress (MPa)	Total Elong. (%)	Reduction in Area (%)	Metallographic Characterization
43	2	150	3×10^{-7}	168	16	7.5[b]	NA
38	20	95	3×10^{-7}	181	18	21[b]	NA
44[d]	20	105	3×10^{-7}	192	32	41	0.6 D, 0.4 I
39	20	150	3×10^{-7}	174	17	18[b]	NA

[a]Type 304 SS (Ht. 30956) sensitized to EPR values of 2 and 20 C/cm^2.
[b]Interrupted test; gauge section measured by micrometer after straining.
[c]Incipient cracks (IC) in hole (IC_h) or crevice (IC_c) region of interrrupted–test specimens; NA refers to characteriztion results not yet available. Ductile (D) and intergranular (I) in terms of fraction of fracture surface area (Refs. 9, 10).
[d]Run to failure; thus, No. 44 was also characterized by failure time 297 h) and ultimate strength (464 MPa).

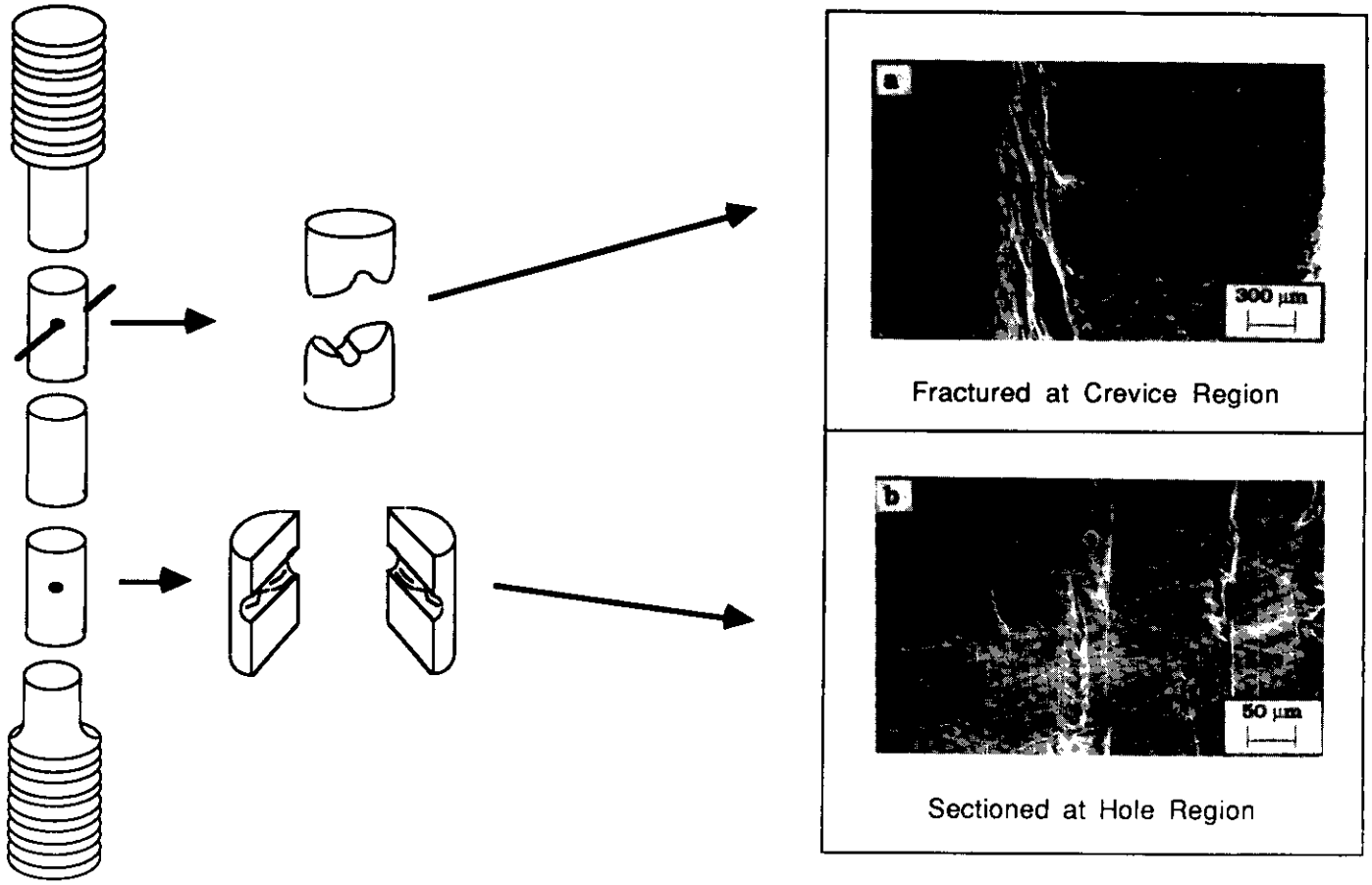

Fig. 1. SSRT crevice specimen and typical sectioning to reveal shallow cracks in hole region after specimen failed at crevice region. SEM photographs show that Types 316NG and lightly sensitized 304 SS exhibit predominantly ductile fracture.

high SCC resistance of Type 316NG SS relative to that of sensitized Type 304 SS, it is difficult to quantify the SCC behavior of Type 316NG SS in terms of crack growth rate[11] from SSRT results. An alternative, employed here, is evaluation of SCC susceptibility in terms of the load-carrying ability of geometrically identical specimens in air and in water.

Ultimate strength, total elongation, and reduction in area are shown graphically in Tables 2-4. For Type 316NG SS, there is relatively little variation in SSRT parameters from air to water. Variation in the strength of two heats of Type 316NG SS is most apparent from the ultimate strength of the crevice specimens in both air and water, i.e., it is apparent that Heat 467958 is stronger than Heat P91576. This can perhaps be attributed to the higher Si concentration in the former heat.5

The maximum stress of Type 316 SS is less than that of either of the two Type 316NG SS heats, which again may be attributable to the bulk composition of the steels (Table 1). Type 316 SS has 0.05% C and 0.01% N, whereas Type 316NG SS has 0.02% C and 0.10% N.5

The ultimate strength of Type 316NG SS is consistently higher than that of sensitized Type 304 SS at corresponding temperatures (Fig. 2). With the moderately sensitized Type 304 SS, there are significant differences between tests in air and the water environment in which intergranular cracking was observed on the fracture surfaces (Tables 3 and 4). Degree of sensitization had a large effect on total elongation of the more highly sensitized material at 95 and 150°C (Fig. 3b); for example, total elongation was only about 13% at 150°C.

As determined by reduction in area (Fig. 4), Type 304 SS with a moderate degree of sensitization exhibited greater SCC susceptibility than either the Type 316NG or the lightly sensitized Type 304 SS. Totally intergranular failure occurred even at 52°C (Table 3). This work substantiates earlier results[13,14] indicating that to prevent SCC in near-term fusion reactors operating at temperatures of < 100°C, it is imperative to control sensitization in the steel. Temperature does not have a large effect on SCC of the lightly sensitized specimens. Although heat treated identically, SSRT specimens 21 and 24 exhibit remarkably different SCC susceptibility, particularly as judged by fracture morphology (Table 3). The degree of sensitization produced by heat treatment at low temperatures can be strongly dependent on intergranular carbide spacing; thus, wide variation can occur in the amount of chromium depletion from boundary to boundary,[15] perhaps resulting in effectively variable sensitization. This phenonemon may contribute to some of the variability exhibited in these lightly sensitized (EPR = 2 C/cm^2) specimens.

The difference in morphology exhibited by a moderately sensitized Type 304 SS after failure in air and in water is shown in Fig. 5. Although some evidence of intergranular fracture surface is seen in the air-tested specimen (Fig. 5a and b), it is much more pronounced in the specimen tested in water (Fig. 5c and d).

CONCLUSIONS

Susceptibility of Types 316NG, 316, and 304 SS to SCC was investigated at several temperatures between 50 and 150°C in SSRTs in oxygenated water that simulates important parameters anticipated in first-wall/blanket systems. The water chemistry was based on a computer code that yielded the nominal concentrations of molecular radiolytic species produced in an aqueous environment under ITER-type conditions. However, to be conservative, SSRTs were performed in a less benign, more oxidizing reference environment containing ~7 ppm oxygen, 6 ppm hydrogen peroxide, and 0.1 ppm sulfuric acid.

Predominantly ductile fracture was observed in crevice specimens of Type 316 SS strained to failure in a reference ITER water chemistry. The failure behavior of Type 304 SS crevice specimens heat treated to yield sensitization values of 2, 3, or 20 C/cm^2 by electrochemical potentiokinetic reactivation demonstrated that the degree of sensitization had a dramatic effect on IGSCC susceptibility. Type 304 SS specimens Sensitized to the higher value exhibited shorter failure times, lower maximum stresses, and lower reduction in area values than did less-sensitized Type 304 SS or Type 316NG SS specimens.

Scanning electron microscopy showed minimal evidence of SCC in the Type 316NG and solution-annealed Type 316 SS, but clear evidence of IGSCC in moderately sensitized (EPR = 20 C/cm^2) Type 304 SS specimens. Ranking for resistance to SCC in simulated ITER water, as determined by electron microscopy and SSRT parameters (e.g., total elongation, ultimate strength and reduction in area), is: 304 SS (EPR = 20 <2 C/cm^2) < 316NG SS.

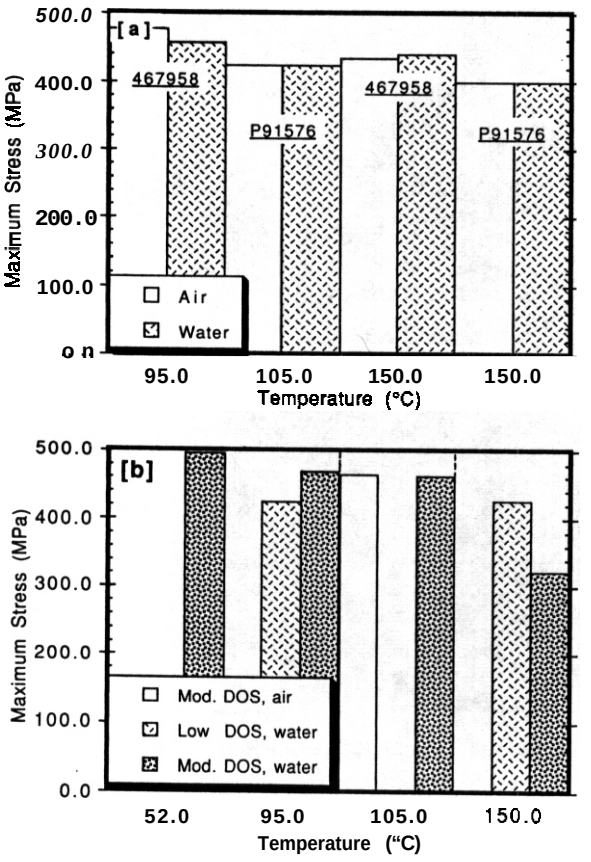

Fig. 2. Ultimate strength of (a) Types 316NG and (b) sensitized 304 SS in oxygenated water and reference air environments (DOS = degree of sensitization).

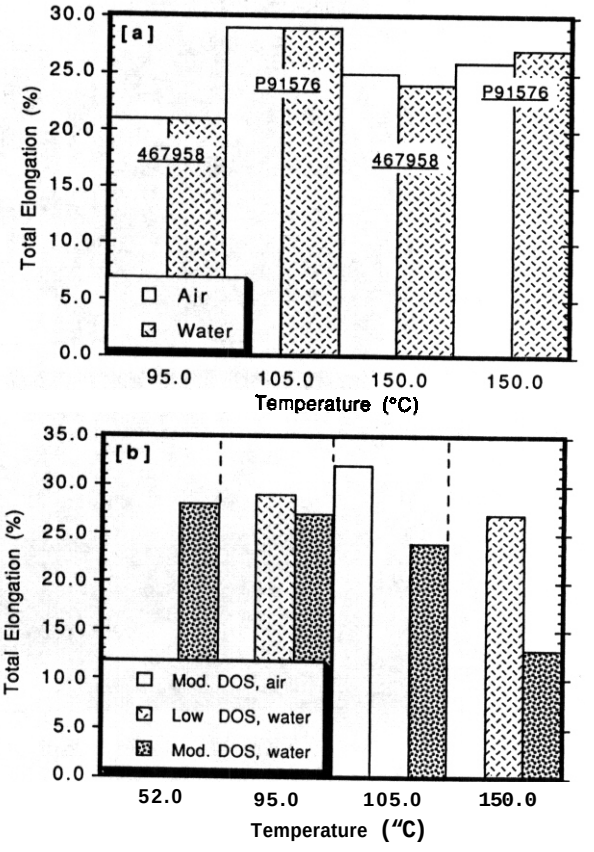

Fig. 3. Total elongation of (a) Types 316NG and (b) sensitized 304 SS in oxygenated water and reference air environments (DOS = degree of sensitization).

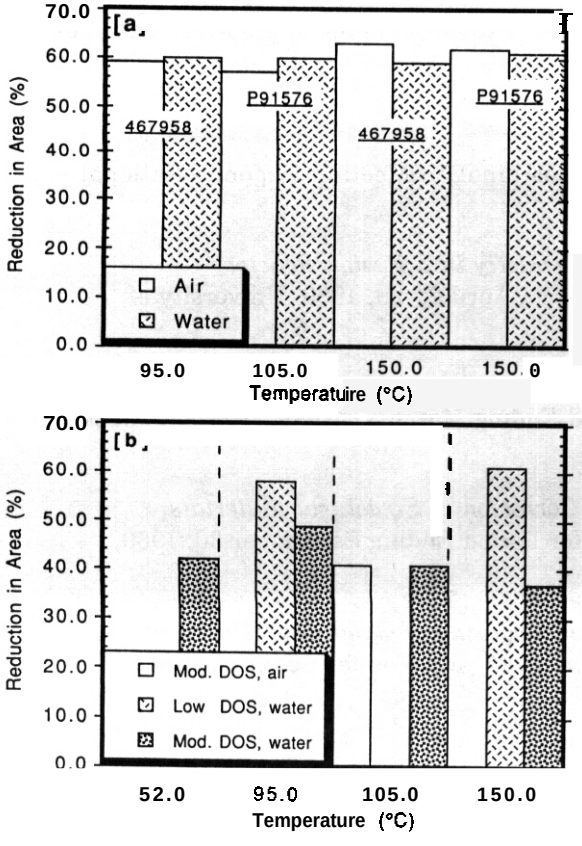

Fig. 4. Reduction in area of (a) Types 316NG and (b) sensitized 304 SS in oxygenated water and reference air environments (DOS = degree of sensitization).

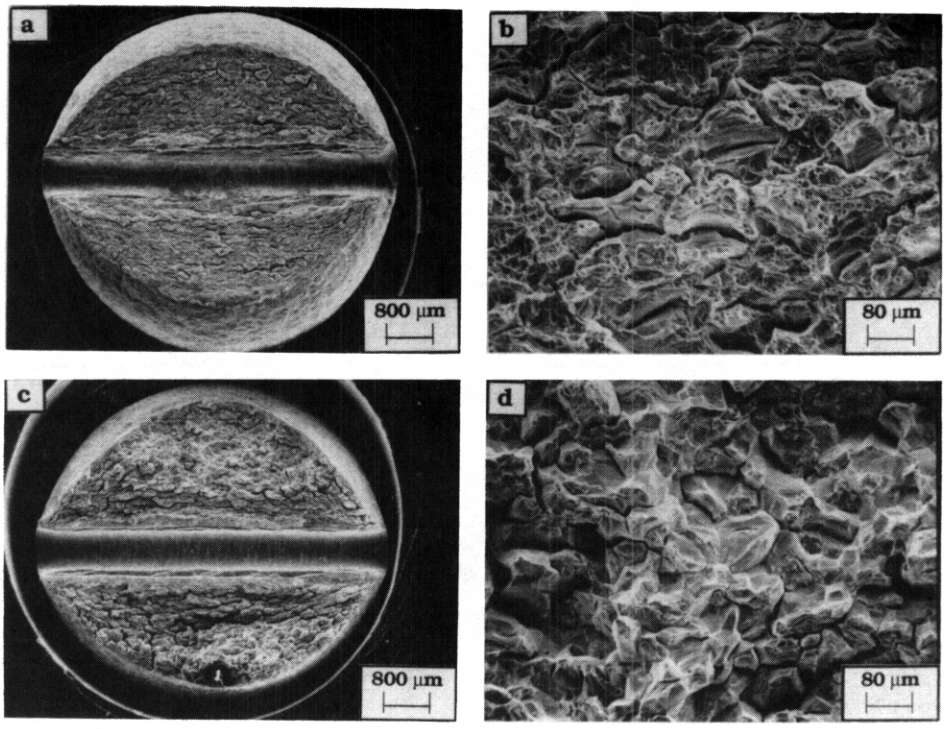

Fig. 5. SEM photomicrographs of fracture surface of Type 304 SS (EPR = 20 C/cm^2) crevice specimens in (a,b) air at 105°C and (c,d) oxygenated water at 105°C. Strain rate = 3 x 10^{-7} s^{-1}.

FUTURE WORK

Experiments will be continued to investigate the SCC susceptibility of selected austenitic steels (such as Types 316, 316L, and 316NG SS) in the solution-annealed, solution-annealed and cold-worked, and solution-annealed and moderately sensitized conditions of interest to ITER applications. The existing data base will be extended to ≈300°C. SSRTs will be performed on weldment specimens to examine the appropriateness of different welding options.

REFERENCES

1. D. Smith, *Aqueous Corrosion Task for ITER R&D*, U.S. Coordination Meeting, Argonne National Laboratory, August 6, 1990.

2. H. G. Khalak, *Computer Simulation of Water Coolant Chemistry in a Fusion Reactor*, Proceedings Third National Conference on Undergraduate Research, April 27-29, 1989, University of North Carolina, Asheville, p. 287.

3. H. Khalak, A. B. Hull, and T. F. Kassner, *Aqueous Stress Corrosion of Austenitic Steels*, Sixth Fusion Reactor Materials Semiannual Progress Report for Period Ending March 31, 1989, DOE/ER-0313/6, Oak Ridge National Laboratory, p. 379.

4. A. Patel, A. B. Hull, and T. F. Kassner, *Aqueous Stress Corrosion of Structural Materials*, Seventh Fusion Reactor Materials Semiannual Progress Report for Period Ending September 30, 1989, DOE/ER-0313/7, Oak Ridge National Laboratory, p. 250.

5. M. R. Fox, A. B. Hull, and T. F. Kassner, *Stress Corrosion Cracking of Candidate Structural Materials under Simulated First-Wall/ Aqueous Coolant Environments*, accepted for publication in Fusion Technology, May 1991.

6. P. S. Maiya, *Plastic Strain, Environmental, and Crevice Effects on SCC Initiation and Propagation in Types 316NG and 304 Stainless Steel,* Corrosion, 45, 11, p. 915 (1989).

7. W. L. Clarke, *The EPR Method for the Detection of Sensitization in Stainless Steels,* NUREG/CR-1095, GEAP 24888 (General Electric Co., 1981).

8. D. D. Macdonald, A. C. Scott, and P. Wentrcek, *External Reference Electrodes for Use in High Temperature Aqueous Systems,* J. Electrochem. Soc., 126, 6, p. 908 (1979).

9. H. D. Solomon, *Transgranular, Granulated, and Intergranular Stress Corrosion Cracking in AISI 304 SS,* Corrosion, 40, 9, 493 (1984).

10. V. Kerlins, Modes *of Fracture,* Metals Handbook, 9th Ed., ASM Metals Park, Ohio 44073 (1987).

11. W. E. Ruther, W. K. Soppet, and T. F. Kassner, *Effect of Temperature and Ionic Impurities at Very Low Concentrations on Stress Corrosion Cracking of AISI 304 Stainless Steel,* Corrosion, 44, p. 791 (1988).

12. P. S. Maiya, W. J. Shack, and T. F. Kassner, *Stress Corrosion Cracking of Candidate Materials for the Nuclear Waste Containers,* Paper No. 511, Corrosion/90, Las Vegas, April 23-27 (1990).

13. R. H. Jones, *Assessment of Stress-Corrosion Cracking for Near-Term Fusion Reactors,* Fourth Fusion Reactor Materials Semiannual Progress Report for Period Ending March 31, 1988, DOE/ER-0313/4, Oak Ridge National Laboratory, p. 184.

14. R. H. Jones and S. M. Bruemmer, *Assessment of Stress-Corrosion Cracking in a Water-Cwled ITER,* Sixth Fusion Reactor Materials Semiannual Progress Report for Period Ending March 31, 1989, DOE/ER-0313/6, Oak Ridge National Laboratory, p. 389.

15. T. M. Devine, *The Mechanism of Senzitization of Austenitic Stainless Steel,* Corrosion Science, SO, 2/3, pp. 135-151 (1990).

SEGREGATION IN THERMALLY AGED TYPE 304L ALLOYS FOR THE ICG-IASCC ROUNO ROBIN -- E. A. Kenik (Oak Ridge National Laboratory)

OBJECTIVE

Comparative studies of segregation produced both by thermal aging and by irradiation are under way utilizing analytical electron microscopy for comparison with the propensity toward irradiation-assisted stress corrosion cracking in austenitic stainless steels.

SUMMARY

Grain boundary segregation in thermally aged type 304 stainless steels has been investigated by X-ray microanalysis. In one commercial alloy sensitized at low temperature, narrow (<10 nm) zones depleted of chromium, silicon, and molybdenum have been observed along with enrichment of phosphorus and nickel. For high purity alloys doped with either sulfur or phosphorus. no significant segregation of either impurity was detected. In a second Commercial alloy which exhibited no grain boundary precipitation, segregation of phosphorus, chromium, and molybdenum to boundaries was observed along with a corresponding depletion of iron. The occurrence of phosphorus segregation in the two commercial alloys and absence in the high purity, phosphorus-doped alloy seems to indicate some synergism of phosphorus segregation with either chromium or carbon segregation or with the precipitation of $M_{23}C_6$ at the grain boundaries.

PROGRESS AND STATUS

Introduction

The International Cooperative Group on Irradiation-Assisted Stress Corrosion Cracking (ICG-IASCC) is concerned with the possibility of irradiation-enhanced sensitization and stress corrosion cracking in commercial nuclear power reactors. While IASCC is a current materials problem for fission reactors, it has ramifications for proposed water-cooled fusion instruments, such as the International Thermonuclear Experimental Reactor (ITER). One of the concerns is that radiation-induced segregation (RIS) could result in sensitization and stress corrosion cracking of austenitic stainless steels. The relation of grain boundary chemistry and the propensity toward IASCC is being studied. The analytical techniques being applied to the measurement of near-grain boundary chemistry include analytical electron microscopy, Auger electron spectroscopy (AES), and atom probe field ion microscopy. Grain boundary chemistry of both thermally aged and irradiated materials will be studied. The current report is based on the preliminary X-ray microanalysis study of several of the aged materials.

Experimental Procedure

Table 1 gives the compositions of the alloys studied. Most of the alloys were received in the as-aged condition (650°C. 50 h). The AJ9139 type 304L material received a complex heat treatment aimed at producing narrow chromium-depleted zones at the grain boundaries (621°C, 24 h; 850°C, 50 h; 400°C, 100 h). Analytical electron microscopy was performed on a Philips EM400T/FEG in the scanning transmission electron microscopy mode with a probe diameter of <2 nm (ref. 1). Subtraction of "in-hole" spectra from the measured EOS spectra corrected for l) the normal "in-hole" counts associated with uncollimated radiation from the microscope illumination system. A liquid nitrogen cooled specimen holder was employed for X-ray

Table 1. Alloy Composition (wt %)

Heat	Cr	Ni	Si	Mn	Mo	S	P	N	C	Comments
AJ9139	18.37	8.13	0.47	0.93	0.25	0.028	0.026	0.048	0.066	Commercial
V946B	18.68	8.90	<0.01	1.06	<0.005	0.019	<0.005	0.0034	0.0015	UHP + S
BPV603	19.06	9.02	0.02	1.15	<0.005	0.0055	0.05	0.0022	0.0015	UHP + P
BPV604	19.14	9.02	0.46	1.16	<0.005	0.0043	<0.005	0.0022	0.0011	UHP + Si
BPV606	18.25	8.61	<0.01	1.16	<0.005	0.0067	<0.005	0.110	0.0026	UHP + N
K34043	17.23	10.7	0.40	1.61	2.06	0.015	0.022	0.072	0.016	Comnercial

microanalysis in order to minimize contamination under the focussed spot. However, many of the alloys had M_S, martensite start, temperatures between 0 and —130°C and transformed during cooling. This was especially true for the high purity alloys with their low carbon levels. The presence of the magnetic martensite made specimen tilting and correcting the astigmatism of the STEM probe difficult. In some cases the stresses generated by the transformation cracked the thin area of the specimen and fractured some of the grain boundaries. The quoted compositions are in weight percent as measured, and no attempt has been made to deconvolute the effect of excited volume size on the actual composition or profiles.

Results

The aged AJ9139 material exhibited heavy grain boundary precipitation of $M_{23}C_6$. Some boundaries contained a continuous or nearly continuous film of $M_{23}C_6$, whereas others contained discontinuous, blocky $M_{23}C_6$. Three boundary regions were analyzed with EDS and measurements in the matrix and on the boundaries are summarized in Table 2. Figure 1(a,b) shows composition profiles for the major and minor alloying elements at a portion of boundary GB#1 ~40 nm from a large $M_{23}C_6$ precipitate. Chromium was depleted over a region ~9 nm wide (FWHM) to a minimum value of ~12 wt %. The second set of values given for GB#1 in Table 2 were masured ~100 nm from the same precipitate. Nickel was slightly enriched at the boundaries. Trace amounts (0.2 and 2.0 wt %) of molybdenum were detected in the alloy bulk and in the GB precipitates. As far as the minor alloying elements are concerned, phosphorus was enriched and silicon was depleted at the boundaries with a FWHM of ~9 nm. The phosphorus segregation to grain boundaries in other aged type 304L steels has been reported previously.[2] Though there was a local minimum for molybdenum at the boundary, there was a region 3 to 7 nm from the boundary that appeared enriched in molybdenum. No segregation of sulfur to boundaries was detected; however, the Mo L peak overlaps the S K peak and could mask a small amount of sulfur. The influence of this overlap could be reduced by calculating the intensity of Mo L X rays based on the observed Mo Ka X ray intensity and the Mo L/Mo Ka ratio observed for type 316 steel. After this correction, no statistically valid sulfur enrichment was detected at the boundaries.

Table 2. Composition (wt %)

Location	Si	P	Cr	Fe	Ni	Mo
Matrix	0.51	0.006	17.84	72.62	8.73	0.24
GB #1						
40 nm from $M_{23}C_6$	0.46	0.44	11.83	77.57	9.53	0.17
100 nm from $M_{23}C_6$	0.57	0.35	12.35	76.81	9.61	0.31
GB #2	0.50	0.30	12.19	77.26	9.74	0.00

For the high purity alloys, only limited results on grain boundary compositions are available-as a result of the martensitic transformation. In the sulfur and phosphorus doped alloys (V9468 and BPV603, respectively), no statistically significant segregation of either element was detected. While a slight silicon enrichment (0.17 wt %) and a corresponding decrease in chromium level at the boundary were indicated, these differences are near the standard deviation for repeated analyses. No useable grain boundaries have been observed in the silicon-doped alloy (BPV604); the nitrogen-doped alloy (BPV606) was not examined, as only X-ray microanalysis was available.

In the second commercial alloy (K3403), significant grain boundary enrichment of phosphorus to ~1.0 wt %, of chromium to ~22 wt %, and of mlybdenum to ~9 wt % were observed along with a corresponding decrease in iron to ~59 wt %. Similar results indicating cosegregation of phosphorus and chromium have been observed in other type 304 alloys.[2] No sulfur segregation was detected, even after correction for the S Kα/Mo L overlap. Detection of sulfur by X-ray microanalysis was harder in this alloy as a result of the high molybdenum content (2 wt %). No grain boundary precipitation was observed in K3403.

Discussion and Conclusions

It is possible to produce narrow chromium-depleted zones similar to those produced by RIS by appropriate thermal treatment. However, the silicon and nickel enrichments typical of RIS are not duplicated. In addition, the aging treatment used for AJ9139 results in copious and nearly continuous precipitation of $M_{23}C_6$ on grain boundaries. While analytical electron microscopy and atom probe field ion microscopy would still be able to measure the depleted zone. AES analysis would have difficulty separating the effects of the precipitates and the depleted zones, unless the spacing of the $M_{23}C_6$ was significantly coarser.

In both commercial alloys, segregation of phosphorus to grain boundaries was observed. In contrast, no significant phosphorus segregation was observed in the high purity alloys. One possible explanation is a synergism between segregation of phosphorus and that of either chromium or carbon at the grain boundaries. A second possible origin is an interaction between the formation and growth of $M_{23}C_6$ and phosphorus segregation. While the K3403 alloy annealed at 650°C exhibited no precipitates at the grain boundaries, enrichment of chromium and molybdenum was observed which would be a required precursor to the formation of $M_{23}C_6$.

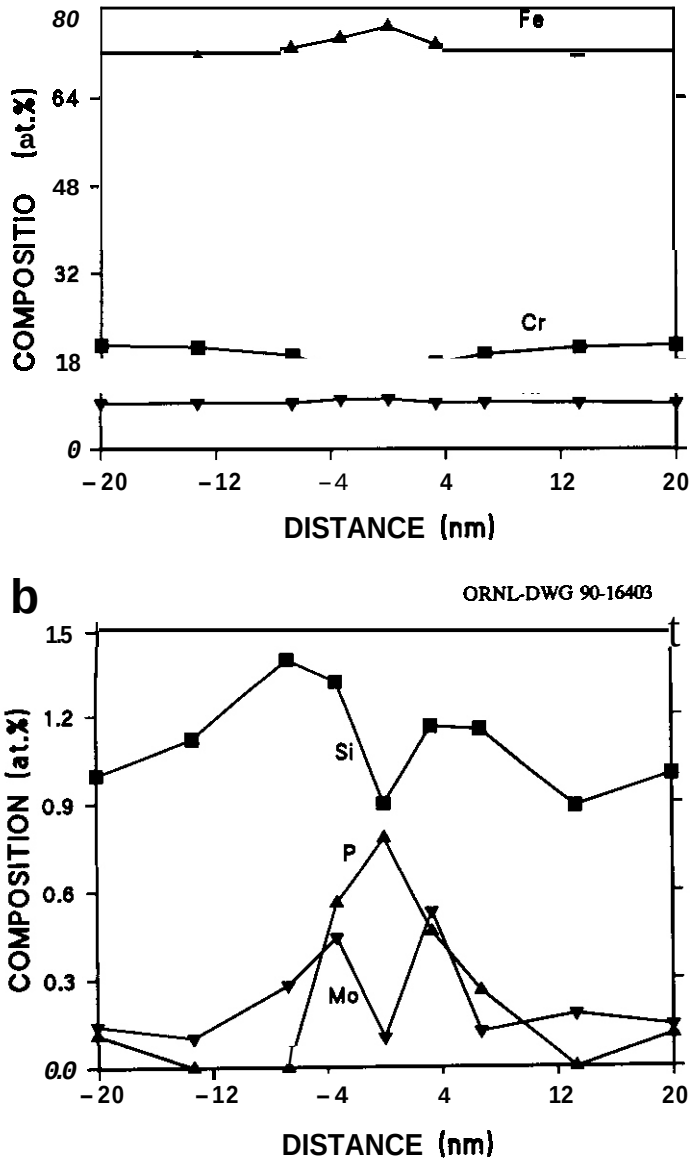

Fig. 1. Composition profiles at a grain boundary for (a) major and (b) minor alloying elements in type 304L alloy AJ9139 which was aged at 621°C, 24 h; 850°C, 50 h; 400°C, 100 h to produce narrow zones depleted of chromium. X-ray microanalysis was performed between grain boundary $M_{23}C_6$ precipitates.

another commercial type 304 alloy annealed at 600°C for 15 h. Significant formation of grain boundary $M_{23}C_6$ was observed. While the grain boundary regions and the $M_{23}C_6$ precipitates exhibited no significant phosphorus enrichment, the matrix-precipitate interface exhibited ~0.3 wt % P, more than a fourfold increase over the matrix, grain boundary, and precipitate levels. It is not clear if the phosphorus segregates to the matrix-

The absence of detectable sulfur segregation to boundaries as measured by X-ray microanalysis is somewhat surprising, especially in the light of indications of sulfur segregation by AES analysis.[3] The overlap of S Kα and Mo L X rays complicates the detection of sulfur in the commercial alloys which contain molybdenum. However, this problem has been partially remedied by using known Mo L/Mo Ka ratios to correct the apparent sulfur intensity. In addition, the high-purity alloy doped with sulfur did not exhibit any sulfur segregation. There are two possible reasons for the differing results between X-ray and AES microanalysis. If the sulfur is in the form of sulfides or sulfur-enriched precipitates at the grain boundaries, AES analysis would indicate sulfur segregation, whereas X-ray microanalysis which avoids precipitates when analyzing boundaries would not indicate any segregation. Secondly, it is not unusual for sulfur to diffuse to free surfaces during AES analysis and for repeated analyses of the same region to indicate an increasing sulfur content with analysis time.

FUTURE WORK

Some additional X-ray microanalysis will be performed on the thermally aged materials, especially the high-purity alloys doped with either silicon or nitrogen. Radiation-induced segregation (RIS) will be studied in two neutron-irradiated type 304 stainless steels for comparison with segregation observed in the thermally aged materials. These results will be combined with atom probe field ion microscopy and AES analysis for structure-property correlations on the irradiation-assisted stress corrosion cracking (IASCC) of the irradiated materials. From this correlation, the materials parameters critical in IASCC are to be identified.

REFERENCES

1. E. A. Kenik, Materials Problem Solving with the Transmission Electron Microscope, vol. 62, eds. L. W. Hobbs, K. H. Westmacott, and D. B. Williams, Materials Research Society, Pittsburgh, PA, 1986, p. 209.
2. E. A. Kenik, Met. Trans. (In Press).
3. P. A. Andresen, General Electric Research and Development Center, private comnunication (1989).

MEASUREMENT OF RADIATION-INDUCED SEGREGATION IN NEUTRON-IRRADIATED AUSTENITIC STAINLESS STEELS --
E. A. Kenik (Oak Ridge National Laboratory), K. Hojou (Japan Atomic Energy Research Institute, assigned to ORNL), and J. Bentley (Oak Ridge National Laboratory)

OBJECTIVE

Radiation-induced segregation (RIS) to various point defect sinks has been measured in irradiated USPCA and EP838 stainless steels by X-ray microanalysis. The application of parallel electron energy loss spectroscopy (PEELS) to such measurements is demonstrated and compared to that of X-ray microanalysis.

SUMMARY

X-ray microanalysis of RIS to grain boundaries and large dislocation loops in neutron-irradiated USPCA has indicated enrichment of silicon and nickel and depletion of chromium and iron. However, there are numerous artifacts which can lead to erroneous results and must be recognized and avoided. Some of these effects include surface films, preferential etching, overlapping RIS profiles from different defects, as well as the more obvious hole count and induced radioactivity of neutron-irradiated material. For irradiated EP838, silicon, nickel, and iron are enriched at boundaries, whereas manganese replaces chromium as the strongly depleted element. Preliminary measurements of RIS profiles at grain boundaries by parallel electron energy loss spectroscopy (PEELS) are discussed. The relative advantages and disadvantages of EDS and PEELS for such measurements are considered.

PROGRESS AND STATUS

Introduction

The effects of radiation-induced segregation (RIS) are manifold and include phase instability in the matrix or at grain boundaries, the influence of phase instability on subsequent swelling, and irradiation-assisted stress corrosion cracking. Energy dispersive X-ray microanalysis in an analytical electron microscope has been one of the primary techniques applied to such measurements. In a majority of the studies on irradiated austenitic stainless steels, enrichment of silicon and nickel and depletion of chromium and iron has been reported at grain boundaries, dislocation loops, and voids.[1-4] However, there are some reports of enrichment of chromium and titanium with nickel depletion at small dislocation loops.[5] The current study is directed at measurements of RIS profiles at both grain boundaries and dislocation loops in two neutron-irradiated austenitic stainless steels, USPCA and EP838.

Electron energy loss spectroscopy (EELS) can also provide elemental microanalysis similar to that provided by energy dispersive X-ray spectroscopy (generally referred to as EDS). With the advent of parallel detection systems for EELS (PEELS), the acquisition times for useable PEELS spectra can be significantly less than those for X-ray microanalysis. In addition the induced radioactivity of the specimens does not interfere with PEELS analysis as it does with X-ray microanalysis. A direct comparison of RIS profiles masured with bath PEELS and EDS at a grain boundary in a non-radioactive, ion-irradiated stainless steel will be discussed.

Experimental Procedure

Standard 3-mm-diam TEM disks of solution-annealed USPCA and 25% cold-worked EP838 were used. Specimens had been irradiated in MOTA/FFTF to a nominal dose of 15 dpa at 520°C. Analytical electron microscopy was performed on a Philips EM400T/FEG in the scanning transmission electron microscopy mode with a probe diameter of <2 nm.[4] Subtraction of "in-hole" spectra from the measured EDS spectra corrected for 1) the normal "in-hole" counts associated with uncollimated radiation from the microscope illumination system and 2) radiation associated with the induced radioactivity of the specimen by neutron irradiation (predominantly Mn K X rays). The quoted compositions are in atomic percent as measured, and no attempt has been made to deconvolute the effect of excited volume size on the actual composition or profiles. The PEELS data was quantified by a ratio technique in which effective cross sections were chosen to set the measured compositions away from the grain boundary to that measured by EDS.

Results

A curved grain boundary in the irradiated USPCA steel is shown in Fig. 1(a). From the high local curvature of the boundary and the lower dislocation density to the right of the boundary, it is concluded that this grain boundary had migrated during the irradiation. Figure 1(b) shows the RIS profiles measured at this boundary. In the region swept relatively clear of dislocations, nickel is enriched and chromium is depleted as a result of RIS to the migrating boundary. There is a narrow region ~70 nm wide to the left of the boundary which is both slightly depleted of nickel and enriched in chromium. The observed depletion of nickel in this zone arises from RIS of nickel to the boundary from the left, whereas chromium rejected from the boundary region diffuses ahead of the migrating boundary.

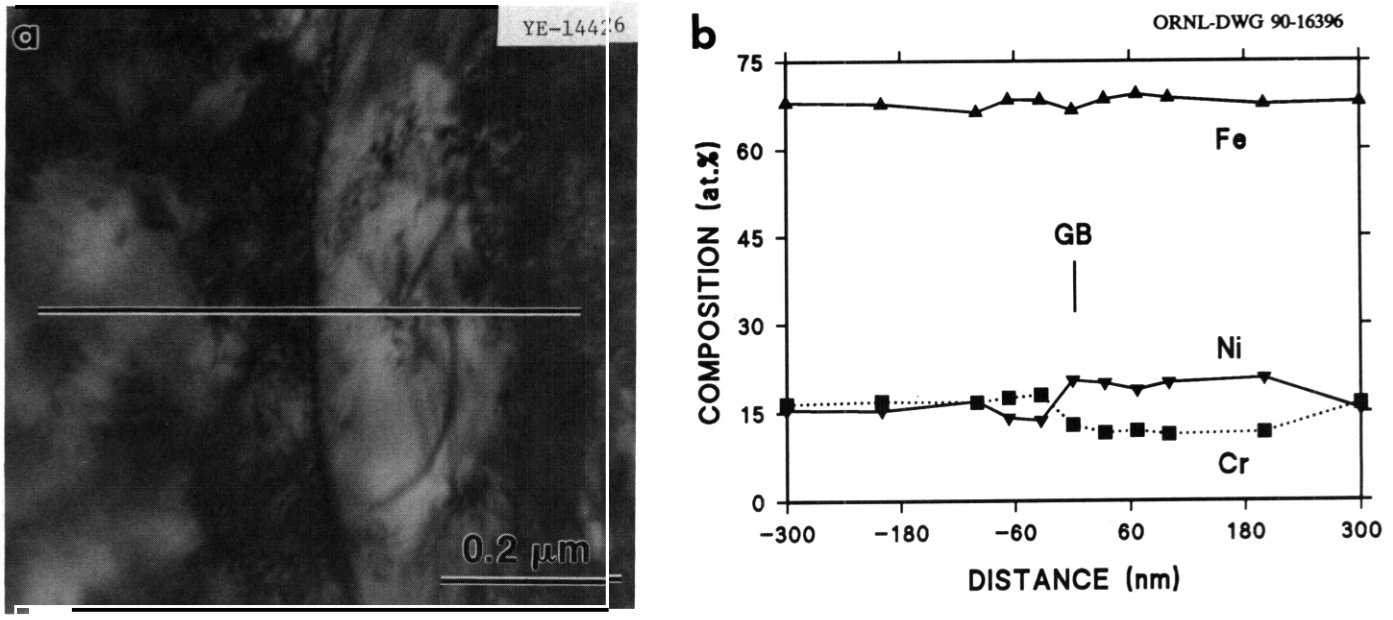

Fig. 1. (a) Curved, migrating grain boundary in USPCA stainless steel irradiated in MOTA/FFTF to a nominal dose of 15 dpa at 520°C. (b) RIS profiles measured at this boundary by X-ray microanalysis.

Figure 2(a) shows four nearly edge-on dislocation loops (A-D) in the irradiated USPCA steel with different sizes, approximately 100, 50, 25, and 25 nm in diameter, respectively. From their relative sizes, it is assumed that loop A nucleated first, followed by loop B, and then loops C and D formed. As such, loop B grew in the three-dimensional RIS profile of loop A. The observed elemental distribution is determined by the flow of point defects to sinks over the entire irradiation. Profiles were measured perpendicular to loops A and B at their center [Fig. 2(b, c)]. For loop A, nickel and silicon are highly enriched at the loop, whereas chromium and iron are depleted. The magnitude of the composition change at the fault plane induced by RIS is noteworthy — nickel exceeds iron as the major constituent. However, as the distance from the loop increases, the magnitude of the segregation decreased and somewhere between 30 and 50 nm actually changes sign relative to the unperturbed matrix composition far from the loop. This effect is especially obvious to the right of loop A where the RIS profiles are not disturbed by RIS to other defects. The origin of this reversal in segregation is twofold; the conservation of solute and limited diffusion distances. Solute which segregates to the boundary must be removed from the adjacent matrix producing a depleted zone just beyond the enriched zone. The opposite effect occurs for solute removed from the vicinity of the boundary. This effect has been noted in other studies of RIS to defect sinks.[1,2,4]

The asymnetry of the RIS profile at loop A seen in Fig. 2(b) is a result of the modification of the point defect fluxes by the presence of loops B-D to the left of loop A. Conversely, loop B nucleates and grows in the pre-existing RIS profile of loop A. The RIS profile for loop B is given in Fig. 2(c). Though the composition at loop B is depleted of silicon and nickel and enriched in iron relative to the unperturbed matrix composition, silicon exhibits a local maximum at the fault plane of loop B. The general trend in Fig. 2(c) is for silicon and nickel to increase and for chromium and iron to decrease as one moves to the right and approaches loop A. As loop B is ~40 nm from loop A, it is growing in the zone composition change associated with loop A. Similar effects are observed for loop C. The RIS profiles measured near loop B are in part determined by the point defect fluxes to loop A. As such, loop A perturbs the matrix composition out at least 100 nm from the fault plane. Often it is difficult to estimate the spatial extent of the RIS modified volume, especially when unobserved defects above or below the volume preserved in the current TEM specimen may interfere with the RIS profiles for the defect of interest.

Figure 3(a,b) indicates the RIS profiles measured with EDS at a migrating boundary in the irradiated EP838 steel. The asymmetry of the profiles is the result of the motion of the boundary from right to left. At the boundary, manganese is strongly depleted and there is a slight depletion of chromium and molybdenum, whereas nickel, silicon, and iron are enriched. The local RIS zone at the boundary is ~10 nm (FWHM) in width. In the region swept by the migrating boundary, similar depletions or enrichments to those at the boundary are observed, though at reduced levels.

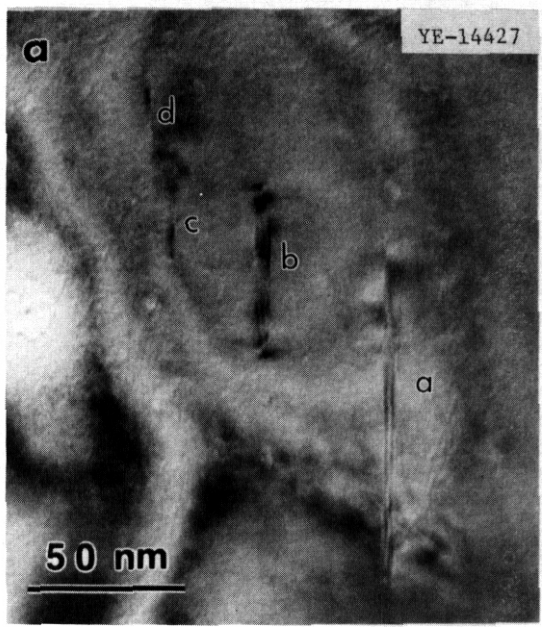

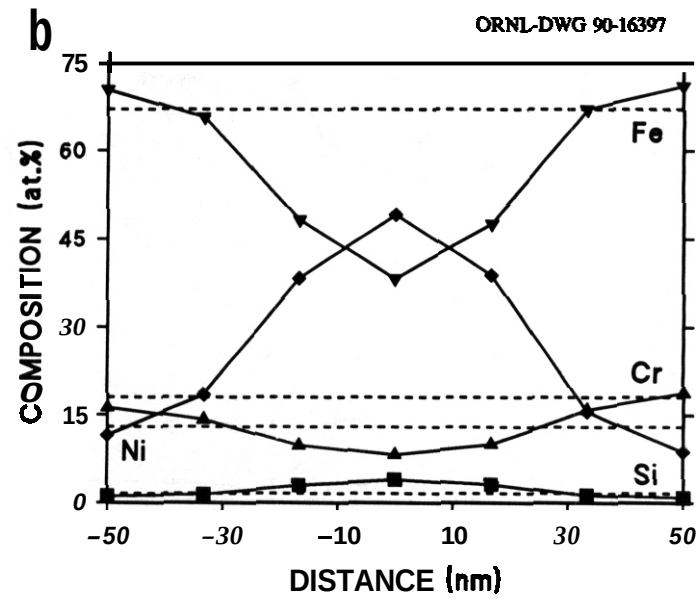

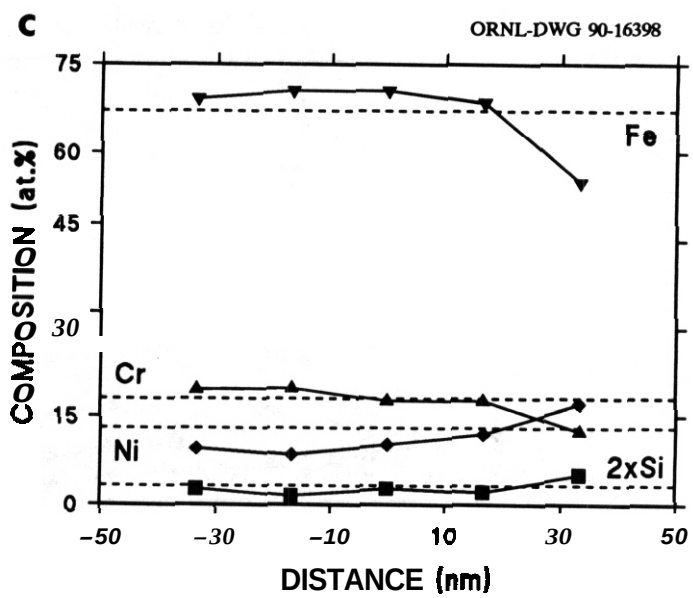

Fig. 2. (a) Four nearly-edge-on dislocation loops (A-D) in USPCA stainless steel irradiated in MOTA/FFTF to a nominal dose of 15 dpa at 520°C. Loops are of different sizes, approximately 100, 50, 25, and 25 nm In diameter, respectively. (b) RIS profiles measured perpendicular to loop A by X-ray microanalysis. (c) RIS profiles measured perpendicular to loop B by X-ray microanalysis.

For highly irradiated materials, the induced radioactivity may be too high for X-ray microanalysis to be a viable technique to measure RIS. The induced radioactivity can result in high background or in hole spectra, high deadtime, increased peak width, and ultimately detector saturation. Reducing the amount of activated material or Increased shielding of the X-ray detector can extend the useful range of this technique. In contrast, PEELS is relatively insensitive to the induced radioactivity of the specimen as a result of the location of the detector (<1000 mm from the specimen as opposed to ~20 mm for typical EDS detectors). Preliminary measurements of RIS profiles at a grain boundary have been made with both EDS and PEELS for a non-radioactive, ion-irradiated specimen. Figure 4 shows the chromium RIS profiles masured by these two techniques. The agreement is good as both techniques give similar profiles and the width of the depleted zone is comparable (~20 nm FWHM). The PEELS measurements indicate a slightly lower chromium level at the boundary (~10.7 at. % Cr) than that indicated by EDS (~11.6 at. % Cr). This is consistent with PEELS being less influenced by beam broadening effects than is X-ray microanalysis. Beam broadening results in averaging composition over a larger volume and results in the higher chromium level observed by EDS.

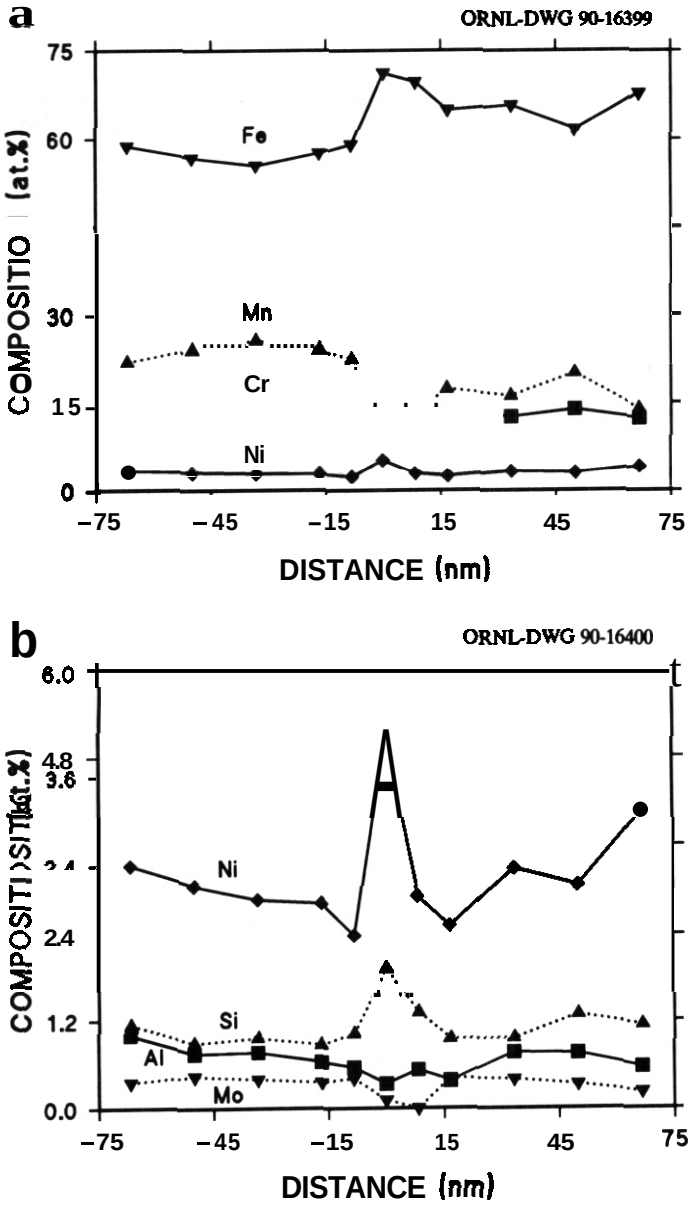

Fig. 3. (a,b) RIS profiles measured by x-ray microanalysis at a migrating boundary in EP838 stainless steel irradiated in MOTA/FFTF to a nominal dose of 15 dpa at 520°C.

There are several difficulties in applying PEELS to RIS measurements in austenitic stainless steels. The major problem is reproducibly defining the form of the rapidly decreasing background at each elemental edge. This is complicated by the presence of a thin oxide layer on the surface of the specimen, the proximity of the Cr, Mn, Fe, and Ni L edges, and the extended structure of these edges. In addition, the proximity of the Cr and Mn L edges makes quantification of the manganese content relatively imprecise. However, X-ray microanalysis of manganese in an irradiated stainless steel is also impaired by the emission of a Mn K x ray by the irradiation-produced ^{55}Fe. Surface films of differing composition from the matrix can affect measurements in thin films for both EOS and PEELS analysis alike. The last problem for PEELS is that the cross sections for the Cr, Fe, and Ni L edges decrease as a function of atomic number with the cross section for chromium being one-third to one-quarter of that for chromium, reducing the accuracy of nickel analysis.

Discussion and Conclusions

For grain boundaries and relatively large dislocation loops (>50-nm-diam) in irradiated USPCA austenitic stainless steel, it has been shown that RIS results in the enrichment of silicon and nickel and deoletion of chromium and iron. There are several effects which can interfere with the accurate assessment of RIS profiles associated with smaller dislocation loops. These include 1) reduced segregation at small loops (which will be discussed later), 2) reduced spatial extent of loop and associated RIS zone relative to the foil thickness and excited volume, enriched in a particular solute, another region must exist that is depleted in that solute. If the distance seoarating these two regions is smaller than the volume analyzed, little or no segregation will be detected.

The degree of RIS to a dislocation loop is determined by its stress field. The stress field for small loops decreases as 1/distance^3, whereas a 1/distance dependence applies to an infinite straight dislocation. As a dislocation loop grows, it passes from one regime to the other and the volume influenced by the loop increases dramatically. For a small dislocation loop, both the strength of the interaction with point defects and the small interaction volume reduces the amount of RIS. As long as a loop continues to attract point defects, RIS will continue and will tend to increase the degree of composition change. From these effects it can be seen that RIS at small loops should be significantly less than that at larger loops. Though the dislocation climbs away from the segregated region. the climb rate is proportional to the difference in the self-interstitial and vacancy fluxes, whereas RIS is proportional to the individual fluxes. In addition, back-diffusion of the segregated solutes occurs at slower rates more typical of thermal diffusion. These two effects in part explain why significant compositional changes are detected at both the dislocation and across the entire fault plane of the loop,[2] though RIS takes place to the dislocation.

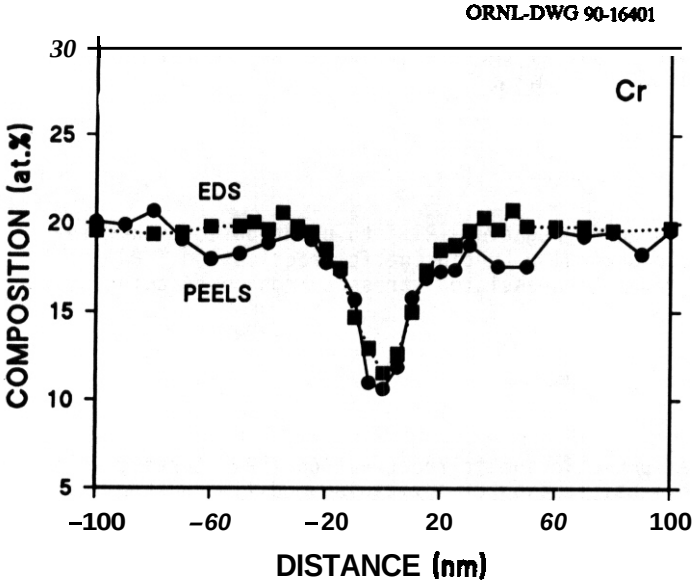

Fig. 4. Chromium RIS profiles in a modified type 316 stainless steel ion-irradiated at 675°C to 1 dpa as measured by X-ray microanalysis (EDS) and by parallel electron energy loss spectroscopy (PEELS).

In the high manganese austenitic stainless steel, EP838, manganese is the primary solute depleted at boundaries by RIS. This is an interesting result in that chromium is not strongly depleted and as such the alloy may be more resistant to irradiation-assisted stress corrosion cracking. In addition, the stability of the austenite may not be seriously compromised by the manganese depletion as a result of the nickel enrichment at the boundary.

The preliminary results comparing EDS and PEELS measurements of RIS indicate that PEELS is a viable alternative to X-ray microanalysis. PEELS offers similar sensitivity for major constituents, shorter acquisition times, possibly better spatial resolution, and the ability to analyze highly radioactive specimens. Data analysis is more labor-intensive than X-ray microanalysis and reliable, reproducible background fitting routines are critical.

FUTURE WORK

Microanalysis of RIS to dislocation loops in irradiated EP838 will be performed for comparison with that observed at grain boundaries. The application of PEELS to moderately activated USPCA, where EDS analysis is still possible, will be performed to further validate the technique. At that point PEELS will be applied to detect RIS at grain boundaries and other defects in highly radioactive material, where X-ray microanalysis is not possible.

REFERENCES

1. D.I.R. Norris, C. Baker, and J. M Titchmarsh, Radiation-Induced Sensitisation of Stainless Steels, Proc. CEGB Symposium, ed. D.I.R. Norris, 1987. p. 86.

2. E. A. Kenik. Materials Problem Solving with the Transmission Electron Microscope, vol. 62, eds. L. W. Hobbs, K. H. Westmacott, and D. B. Williams, Materials Research Society, Pittsburgh, PA, 1986, p. 209.

3. L. Lenauor, M Voillon, and V. Levy, Effects of Irradiation on Materials: 11th Conf., eds. H. R. Brager and J. S. Perrin, ASTM STP-782, American Society for Testing and Materials, Philadelphia, PA, 1982, p. 310.

4. E. A Kenik. T. Inazumi, and d. L. c. Bell, "Radiation-Induced Grain Boundary Segregation and Sensitization of a Neutron-irradiated Austenitic Stainless Steel," thic progress report; Submitted to J. Nucl. Mater.

5. K. Hojou., S. Jitsukawa. M. Suzuki, S. Hamada, and A. Hishimuna, Proc. 4th International Conference on Fusion Reactor Materials (ICFRM-4), to be published in J. Nucl. Mater.

RADIATION-INDUCED GRAIN BOUNDARY SEGREGATION AND SENSITIZATION OF A NEUTRON-IRRADIATED AUSTENITIC STAINLESS STEEL -- E. A. Kenik (Oak Ridge National Laboratory), T. Inazumi (Japan Atomic Energy Research Institute), and G.E.C. Bell (Oak Ridge National Laboratory)

OBJECTIVE

Comparison of X-ray microanalysis of radiation-induced segregation (RIS) to point defect sinks in irradiated USPCA stainless steel with results of electrochemical potentiokinetic reactivation (EPR) testing has been made to aid in the understanding of irradiation-assisted stress corrosion cracking (IASCC).

SUMMARY

Analytical electron microscopy and electrochemical potentiokinetic reactivation (EPR) testing were applied to the radiation-induced segregation (RIS) and sensitization of a titanium-modified austenitic stainless steel irradiated to 9 dpa at 420°C in the Materials Open Test Assembly (MOTA) of the Fast Flux Test Facility (FFTF). The EPR testing of both solution annealed (SA) and 25% cold-worked (CW) materials indicated a significant increase in the reactivation charge (P_a). Both optical and scanning electron microscopy of the specimen surface after EPR testing indicated preferential attack at grain boundaries, indicative of sensitization. In addition, localized attack of the matrix was observed. Though precipitates were occasionally present on grain boundaries, they were not chromium-rich $M_{23}C_6$, but nickel- and silicon-enriched G phase. Faulted loops, fine γ' precipitates, and isolated cavities were observed in the matrix. X-ray microanalysis indicated significant RIS at high-angle boundaries in both materials. Depletion of chromium to apparent levels of 10 at. % was observed in the irradiated SA material. The boundaries were enriched in nickel, silicon, and titanium (up to 28. 6, and 1 at. % respectively) and depleted of iron and mlybdenum (as low as 54 and 0.7 at. %, respectively). The width of the segregation zone was very narrow (<6 nm). Similar grain boundary RIS was observed in the cold-worked material. There was also evidence for boundary migration in the cold-worked material (boundary facetting and asymnetric composition profiles). Voids and faulted dislocation loops in the SA material also exhibited similar RIS.

PROGRESS AND STATUS

Introduction

Irradiation-assisted stress corrosion cracking (IASCC) of austenitic stainless steels neutron-irradiated at low temperatures (~300°C) has become a major concern for water-cooled nuclear power systems.[1-4] It is also of concern in the design of proposed magnetic fusion devices. IASCC has been reported in type 304 stainless steel at fast neutron fluences (E > 1 MeV) above ~5×10^{20} neutrons/cm^2. While there are parallels with intergranular stress corrosion cracking (IGSCC) of thermally sensitized materials, there are still questions about the exact origin of IASCC. The relative importance of radiation-enhanced precipitation versus radiation-induced-segregation (RIS) is of concern, as is the magnitude and spatial extent of segregation and identity of the segregating species. In some studies RIS of silicon and/or phosphorus to grain boundaries has been indicated as the dominant origin of IASCC,[5,6] whereas other studies question the role of phosphorus and indicate that RIS-induced chromium depletion is responsible.[7,8] The current work combines electrochemical potentiokinetic reactivation (EPR) testing for sensitization with subsequent analytical electron microscopy of RIS in a neutron-irradiated austenitic stainless steel, the prime candidate alloy (PCA) developed for fusion reactors. The one-to-one correlation of sensitization and segregation is aimed at further understanding of the IASCC problem.

Experimental Procedures

The alloy studied was a titanium-modified, austenitic stainless steel, PCA, developed by the U.S. Department of Energy Fusion Materials program. The composition of PCA is given in Table 1. The main difference between PCA and a commercial Type 316 stainless steel is the lower chromium level (15 at. %) and the addition of 0.28 at. % Ti in PCA. The material was prepared in the as-solution-annealed (SA) at 1100°C for 0.5 h (SA) and as-25%-cold-worked (CW) conditions. The specimens (3-mm-diam, 0.25-mm-thick disks) were irradiated in the Materials Open Test Assembly (MOTA) of the Fast Flux Test Facility (FFTF) at 420°C to 9 dpa. Control specimens were aged at 420°C for 5000 h to simulate the thermal history of the irradiated specimens.

Electrochemical characterization was performed on TEM disks by single loop EPR testing in an apparatus designed for radioactive materials, which has been described previously.[9] Conditions for EPR testing and the use of the normalized reactivation charge (P_a) to indicate the degree of sensitization followed

Table 1. PCA Alloy Composition

Element	Weight %	Atomic %
Fe	65.00	65.03
Ni	16.20	15.42
Cr	14.00	15.05
Mo	2.30	1.34
Mn	1.80	1.83
Si	0.40	0.80
Ti	0.24	0.28
C	0.05	0.23
P	0.01	0.02
S	0.003	0.005

suggestions by Clarke et al.[10] The specimen surface after EPR testing was observed with both optical and scanning electron microscopy Subsequently each specimen was prepared for analytical electron microscopy (AEM) by electropolishing at ~10°C in 10:6:1 methanol:butyl cellusolve:perchloric acid. X-ray microanalysis was performed in a Philips EM400T/FEG in the scanning transmission electron microscopy mode with a probe diameter of <2 nm.[11] Subtraction of "in-hole" spectra from the measured spectra corrected for 1) the normal "in-hole" counts associated with uncollimated radiation from the microscope illumination system[12] and 2) radiation associated with the induced radioactivity of the specimen from neutron irradiation (predominantly Mn K X rays). The quoted compositions are in atomic percent and are as measured, and no attempt has been made to deconvolute the effect of excited volume size on the actual composition or profiles.

Results

Reactivation curves for the irradiated and thermally aged control specimens are shown in Fig. 1. The peak in reactivation current density occurred at approximately –120 mV referenced to a saturated calomel electrode (SCE) for all specimens. In both SA and CW conditions, the peak current densities for the irradiated materials were approximately a thousand times higher than those for the control specimens. The individual curves were quite reproducible when the initial surface conditions were duplicated (i.e., electropolishing to remove surface oxideletching from previous EPR testing, followed by passivation at +200 mV vs SCE for 2 min). There was only a slight difference in the reactivation curves for the SA and CW materials. The Flade potential (that potential at which the current density starts increasing) was substantially higher for the irradiated specimens (increasing by approximately 75 and 125 mV for the SA and CW conditions, respectively).

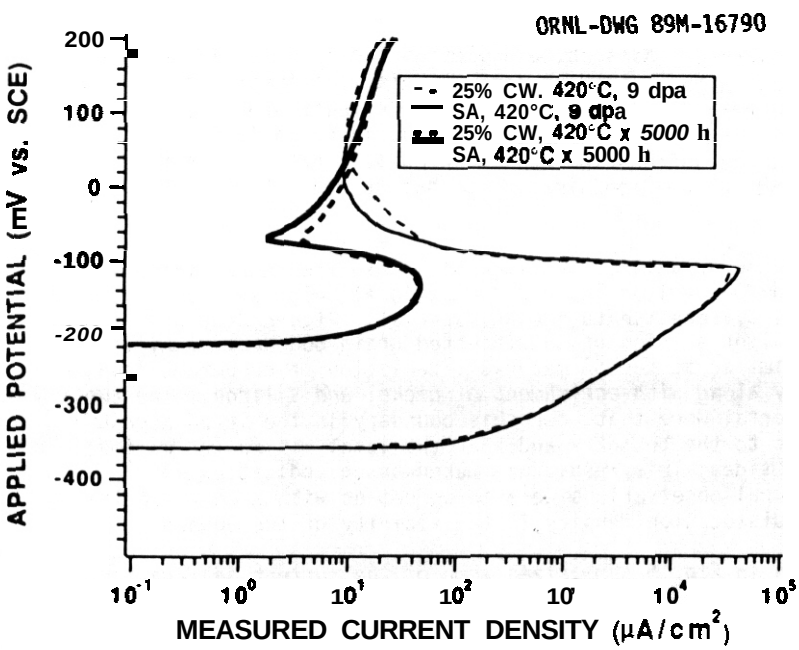

Fig. 1. Reactivation curves for both thermally aged and irradiated specimens of SA and CW PCA.

The reactivation charge is the integral of the charge associated with the current density peaks in Fig. 1. The reactivation charge normalized by the grain boundary area [P_a (coulombs/cm^2)] (ref. 9) was calculated for each specimen. The average P_a values for the irradiated specimens (62 and 54 coulombs/cm^2 for the SA and CW conditions, respectively) were over two-orders-of-magnitude higher than those for the thermally aged controls (0.14 and 0.24 coulombs/cm^2 for the SA and CW conditions, respectively). The differences in the SA and CY conditions were not significant. The P_a values for two different specimens for each condition were in good agreement.

Optical micrographs of the surface of the thermally aged control and irradiated SA specimens after EPR testing are shown in Figs. 2(a) and 2(b), respectively. The control SA specimen exhibited very little etching; whereas the irradiated SA specimen exhibited both preferential grain boundary attack and fine, uniform etching in the matrix. The maximum width of the grain boundary etching was approximately 1 μm. Similar microstructures were observed for the CW materials. The irradiated CW material also exhibited preferential attack at shear bands.

Figure 3(a) shows the microstructure of the irradiated SA material. A high density of fine faulted loops (–50-nm-diam) is observed in the matrix along with a low density of voids. At the grain boundaries, occasional precipitates are observed along with a 70-nm-wide zone denuded of voids. Little or no denuded zone for faulted loops is observed. Figures 3(b) and 3(c) give measured composition profiles near the grain boundary in Fig. 3(a) for the major and minor alloying elements. In a zone ~5 nm wide (full width, half maximum - FWHM) at the boundary, iron and chromium are depleted and nickel, silicon. and titanium are enriched. Molybdenum is depleted over a wider zone (~13 nm FWHM). Outside this near-boundary zone is a

ORNL-PHOTO 3723-90

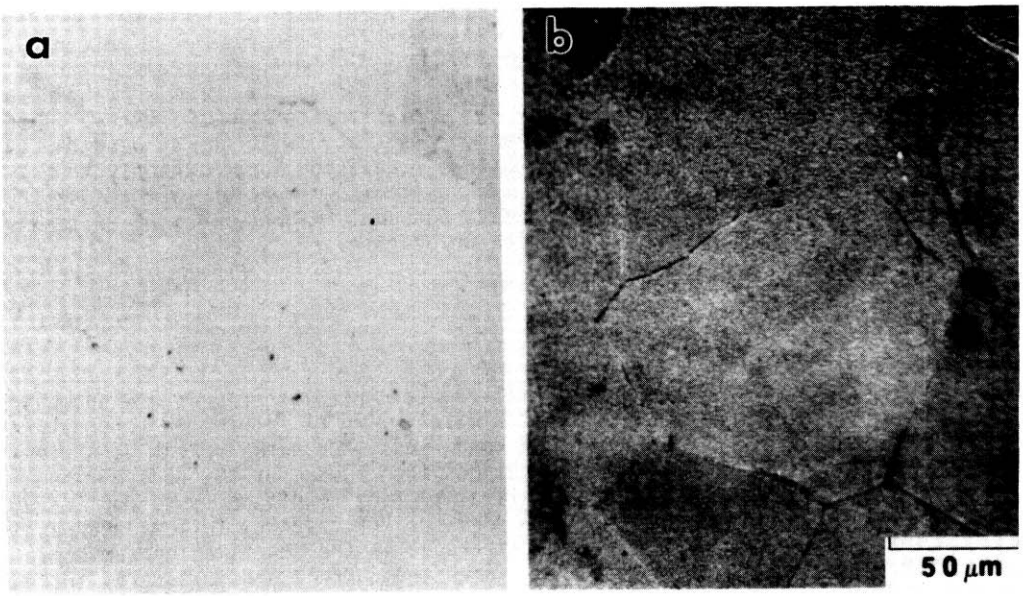

Fig. 2. Optical micrographs of SA PCA after EPR testing. (a) Material aged at 420°C for 5000 h. (b) Neutron-irradiated material.

second zone where the sign of the segregation is reversed. As such, a depletion (enrichment) in the boundary zone results in a slight enrichment (depletion) in the secondary zone. This is illustrated in Fig. 3(b) for iron where the composition far from the boundary is indicated. Similar effects are observed for chromium, nickel, and silicon. For the SA material, the local minima (or maxima) in composition was always found at the position of the grain boundary. No segregation was detected at coherent twin boundaries; whereas incoherent twin boundaries exhibited segregation similar to that at grain boundaries, though at a slightly reduced level.

Figure 4(a) illustrates the microstructure of the irradiated CW material. Amid the dense dislocation network remaining from cold-working, fine (~40-nm-diam) faulted loops and occasional voids were observed in the matrix, though at a significantly lower density relative to the SA material. Figure 4(b) and 4(c) give measured composition profiles near a long straight section of the facetted grain boundary in Fig. 4(a) for the major and minor alloying elements. Similar to the SA material, depletion of chromium, iron, and molybdenum was observed near the grain boundary along with enrichment of nickel and silicon. The two differences relative to the results for the SA material were that, for this boundary in the irradiated CW material, the profiles were asymmetric with respect to the boundary and that the local minima (or maxima) was not at the boundary position, but ~3 nm to one side. This result was taken as an indication for migration of that boundary. Two other microstructural observations were in agreement with such a conclusion; the facetting of the boundary and the lower dislocation density in the vicinity of the boundary.

The histogram of measured compositions given in Fig. 5 summarizes some of the current segregation results. The matrix composition corresponds to 1.2 Si, 0.3 Ti, 16.6 Cr, 65.5 Fe, 15.3 Ni, and 1.2 Mo (at. %). Grain boundaries in both the SA and CW materials are depleted of chromium, iron, and molybdenum, but are enriched in silicon and nickel. The degree of RIS appears to be more pronounced in the SA material relative to the CW material. However, insufficient boundaries have been analyzed to clarify whether there is an actual difference in RIS for the two materials or if the effect may simply reflect a boundary-to-boundary variation in RIS. The chromium level observed at grain boundaries ranged from 10.5 to 12.5 at. % Cr for the SA material and 13 to 15 at. % Cr for the CW material. The lower chromium level was observed for the facetted boundary in Fig. 4, which appeared to have migrated during irradiation. The lower dislocation density adjacent to this boundary may be the reason for the similarity of its RIS profiles to that of the boundaries in the SA material.

Only semi-quantitative analysis of the grain boundary precipitates in the SA material was possible as a result of their small size and resultant excitation of the adjacent matrix. The average measured composition was 46 Fe, 31 Ni, 12 Cr, 9 Si, 1 Ti, and 1 Mo (at. %). The composition of these precipitates

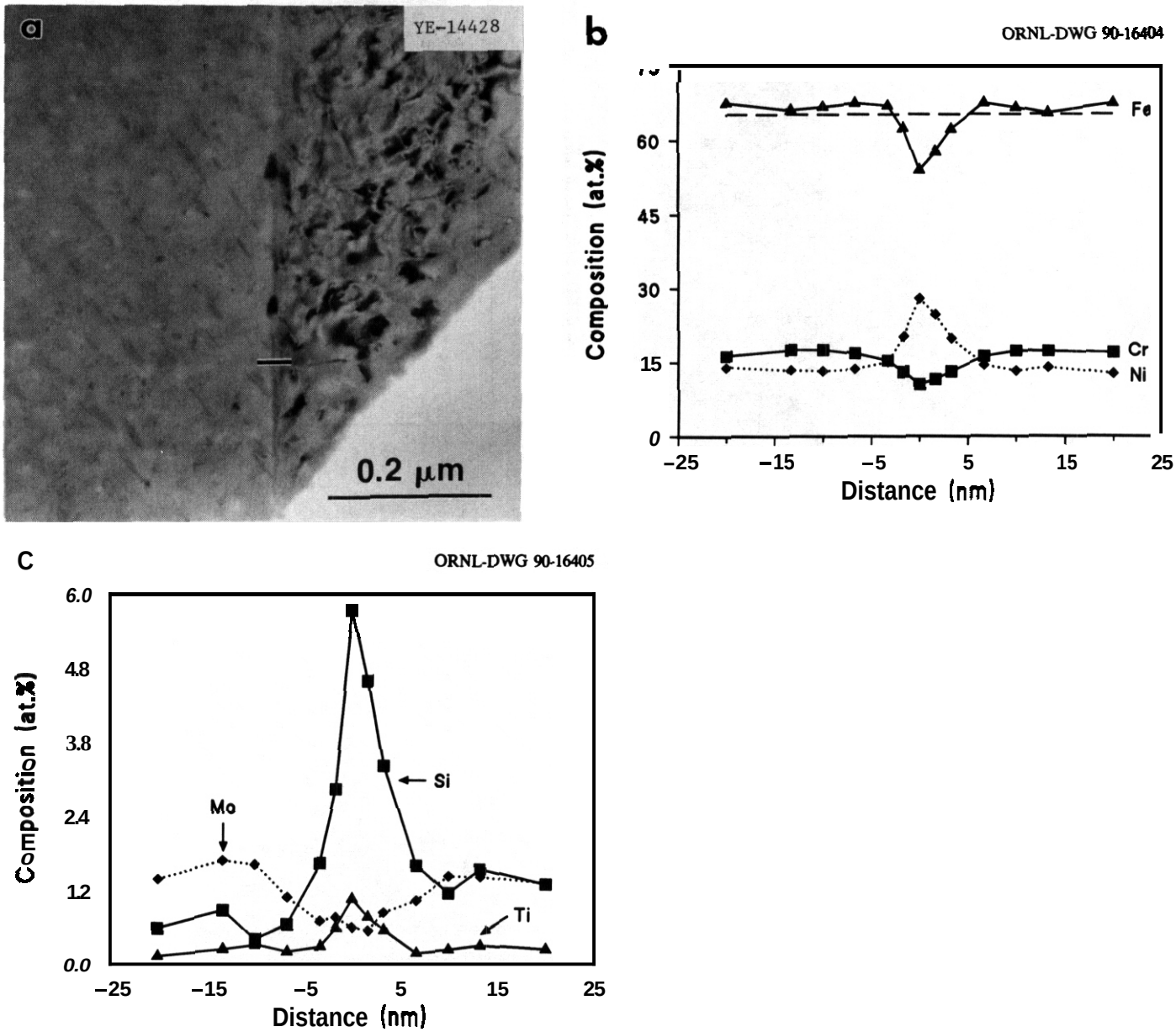

Fig. 3. (a) Microstructure of irradiated SA material. Note faulted loops, voids, and zone denuded of voids at grain boundary. (b,c) Elemental profiles across boundary in region indicated by line in Fig. 3(a). Dashed line indicates average iron composition in matrix away from segregation zone.

relative to the matrix is presented in Fig. 5. The precipitates are depleted in iron, chromium, and molybdenum relative to the matrix, whereas they are enriched strongly in silicon and nickel and slightly in titanium. Electron diffraction patterns were consistent with a cubic phase with a lattice parameter of 1.1 nm. The precipitates were identified as G phase, a nickel-rich silicide, and not chromium-rich $M_{23}C_6$. A similar nickel/silicon enriched phase, η, was eliminated as it contains roughly equal levels (~30 at. %) of chromium and nickel.[13] On the basis of their composition relative to the matrix, the formation of the grain boundary precipitates is not the cause of the observed composition changes at grain boundaries but is rather the result of RIS at the boundary. In contrast to the SA material, the CW material did not exhibit grain boundary precipitation. This indicates that the magnitude of RIS was reduced by the high sink strength associated with the dislocation network in the CW material.

In an attempt to understand the fine matrix etching observed after EPR testing, X-ray microanalysis of two types of matrix defects, voids and faulted loops, was performed in order to check for RIS. For the SA material, regions containing a void exhibited average compositions of 3.6 Si, 12.9 Cr, 60.8 Fe, 21.8 Ni and 0.7 Mo; whereas faulted loops exhibited average compositions of 2.2 Si, 15.8 Cr, 62.2 Fe, 18.5 Ni, and 1.0 Mo (at. %). As such, RIS to both voids and faulted loops is similar to that at grain boundaries,

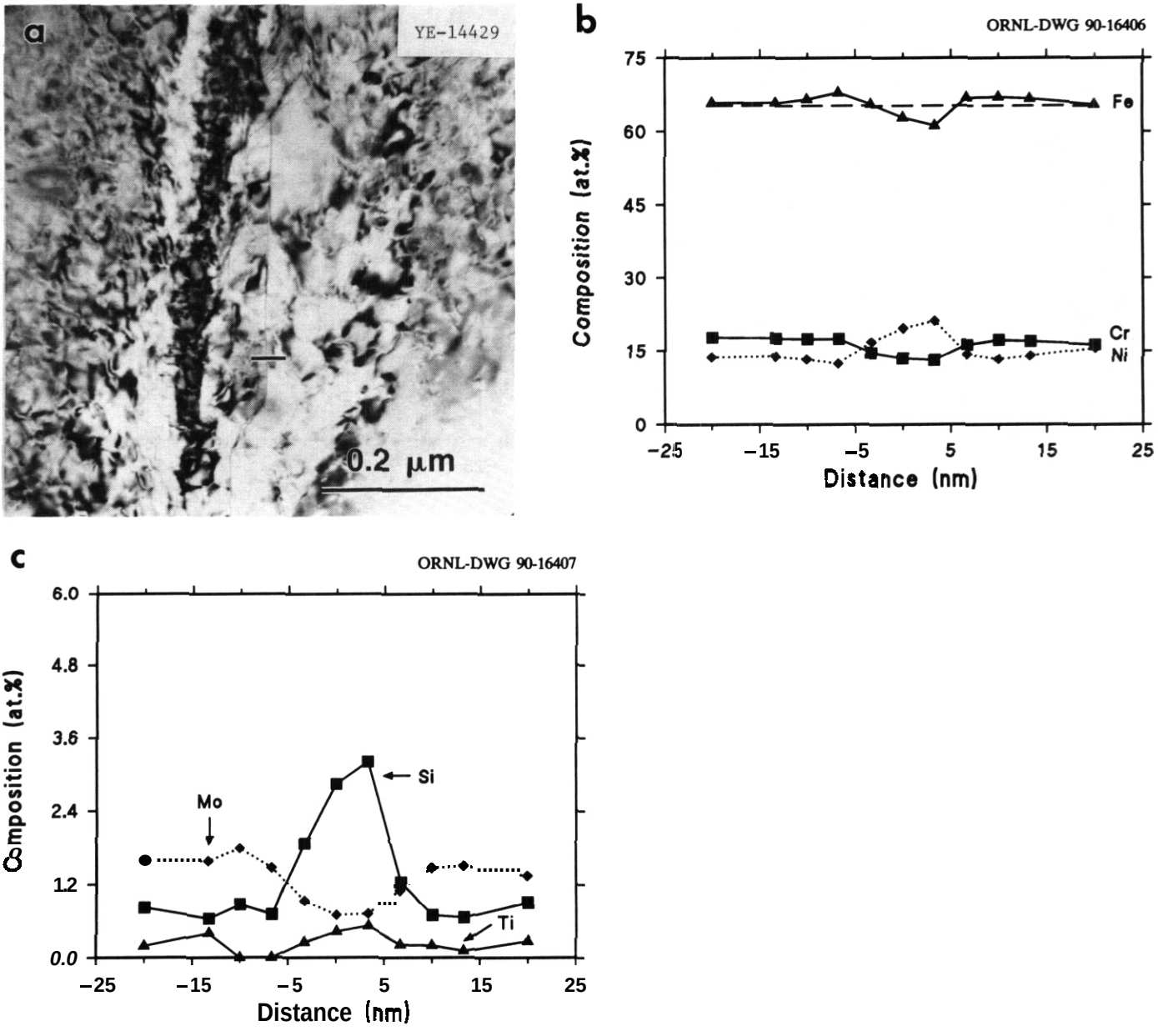

Fig. 4. (a) Microstructure of irradiated CW material. Note dislocation network, occasional faulted loops and voids, and region of lower dislocation density near the facetted grain boundary. (b,c) Elemental profiles across boundary in region indicated by line in Fig. 4(a). Dashed line indicates average iron composition in matrix away from segregation zone.

though possibly at a reduced level. However, the measured compositions are biased toward the matrix composition as a result of the defects not extending through the foil thickness and the finite size of the excited volume associated with incident probe size and beam broadening. Therefore, *segregation at voids* and loops may be similar in magnitude to that at grain boundaries. Such similarity of RIS has been observed for larger faulted loops and grain boundaries in ion-irradiated stainless steel.[14] Composition profiles in the matrix have indicated periodic fluctuations in composition with chromium- and iron-enriched (nickel- and silicon-depleted) regions alternating with chromium- and iron-depleted regions. The chromium fluctuated ~3 at. % Cr with a period of ~60 nm. Such a wavelength is much too small to be associated with the low density of voids, and a one-to-one correlation with the faulted loop structure could not be discerned. The origin of these composition fluctuations will be discussed further at a later point.

Figures 6(a,b) show electron diffraction patterns from the matrix that indicate the presence of precipitates. Besides spots which are consistent with the γ' (Ni_3Si) phase, extra spots near the 1/2 {311} type positions were observed at <112> and <130> zones. These extra spots did not shift significantly with

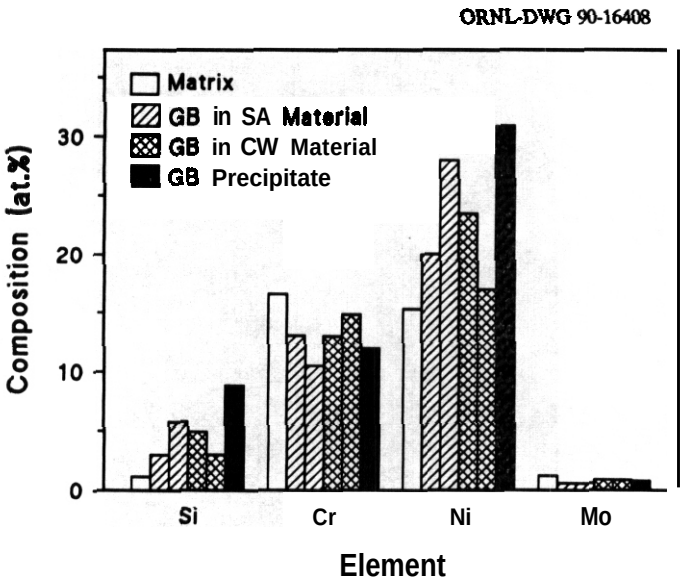

Fig. 5. Composition histogram for matrix, two grain boundaries in SA material, two grain boundaries in CW material, and grain boundary precipitates in the SA material. Iron levels can be estimated by difference from 100%.

tilt. As the extra 1/2 {311} spots and those presumed to arise from γ' form a two-dimensional net, the possibility that a single non-γ' precipitate phase is present had to be addressed. Figures 6(c,d) show dark-field images of the same area using a 1/2(113) reflection and a presumed (001) reflection for γ', respectively, near the [211] orientation. These two images demonstrate that the 1/2{311} type reflections arise from the nearly face-on faulted loops, whereas the other reflections arise from fine (~6-nm-diam) matrix precipitates consistent with γ' phase.

Detailed consideration of the geometry for the reciprocal lattice of a faulted fcc material for both orientations in Fig. 6 has shown that a 111 relrod will appear at the exact 1/2(113) position when the matrix (113) reflection is strongly diffracting. In addition, the position of the 111 relrod intersection is relatively insensitive to slight specimen tilts as the relrod is nearly perpendicular to the zero order Laue zone (19° to the [211]).

The spacing of the larger γ' particles in Fig. 6(b) is ~40 nm, similar to the wavelength of the periodic composition fluctuations observed by X-ray microanalysis of the matrix. The presence of fine γ' (Ni_3Si) would result in composition fluctuations of the type observed (chromium- and iron-enriched regions versus nickel- and silicon-enriched regions).

Discussion

The large values of the normalized reactivation charge, P_a, and the preferential grain boundary attack observed after EPR testing for the irradiated materials indicates that both the SA and CW materials have been sensitized. However, the validity of P_a as an indicator for the degree of sensitization is questionable. The occurrence of matrix etching and the associated current results in anomalously high values of P_a. If the reactivation charge for the irradiated materials is normalized by the entire surface area EPR tested, rather than by the grain boundary area, the values are 18 and 15 for the SA and CW materials, respectively. The actual values of P_a for the grain boundary regions must be higher than this average value, as preferential attack of the boundaries was observed. As such, the reactivation charge for the grain boundaries is probably equal to or greater than the 2 coulombs/cm^2 indicated by Clarke et al.[10] as the critical value for IGSCC of thermally sensitized Type 304 stainless steel.

X-ray microanalysis indicates similar RIS at grain boundaries, voids, and faulted dislocation loops. Chromium, iron, and molybdenum are depleted at these point defect sinks, whereas silicon and nickel are enriched. These results can be explained by either the solute size/interstitial mechanism[15] or the vacancy inverse Kirkendall mechanism.[16] In general, the undersized andlor slow diffusing solutes (e.g., Ni and Si) move toward point defect sinks; whereas oversized and/or fast diffusing solutes (e.g., Cr and Mo) move away from sinks. However, titanium is an oversized solute, but was observed to segregate to boundaries in the SA material. One possible explanation for such behavior has been suggested by Marwick et al.[17] They postulated the diffusion of a vacancy-titanium atom complex in order to explain the reversal of titanium segregation at temperatures below 400°C. Migration of such a complex would result in titanium enrichment at point defect sinks. No segregation of phosphorus to grain boundaries was observed in either SA or CW material. However, PCA has a low phosphorus content (0.02 at. %), and the titanium present in the alloy would getter what little phosphorus was present.

Both chromium and molybdenum are critical in the formation of protective passive films for Type 316 stainless steels. A nominal chromium content of ~13 at. % (12 wt %) is required for an austenitic stainless steel to maintain its corrosion resistance. X-ray microanalysis revealed that chromium levels at or below 13 at. % were observed at grain boundaries of both irradiated materials. Molybdenum levels were reduced nearly twofold to 0.7 at. % at the boundaries. As the measured compositions represent the average composition of the excited volume, the actual chromium and molybdenum levels are below that measured. These depletions result in the local breakdown of the passive film and subsequent preferential attack of grain boundaries. As the grain boundary precipitates observed were not chromium or molybdenum enriched relative to the matrix, the observed composition changes and the associated sensitization must

CONCLUSIONS

The increased reactivation charge and grain boundary etching observed after EPR testing indicates radiation-induced sensitization. Matrix etching of the irradiated materials suggests similar RIS at matrix defect sinks. The reactivation charge (P_a) normalized by the grain boundary area cannot be used as an index for comparison to thermal sensitization, as a result of the charge associated with the matrix etching. If the reactivation charge is normalized by the total area, the P_a values are close to 2 coulombs/cm^2 which is the critical level determined for IGSCC of thermally sensitized Type 304 material. There were no significant differences in the EPR results between the irradiated SA and CW materials.

X-ray microanalysis indicates RIS depletes chromium, iron, and mlybdenum and enriches silicon and nickel at high-angle grain boundaries, voids, and faulted dislocation loops. No phosphorus segregation was observed in either material. Whereas RIS was detected at incoherent twin boundaries, none was detected at coherent twin boundaries. Segregation of titanium, an oversized solute, to grain boundaries was observed in the SA material. Grain boundary precipitates observed *in* the SA material were identified as G phase silicide, which cannot contribute to the observed chromium depletion. The formation of fine γ' precipitates was observed in the matrix and contributed in part to a periodic fluctuation in composition observed in the matrix.

REFERENCES

1. A. J. Jacobs and G. P. Wozadlo, Proc. Int. Conf. on Nuclear Power Plant Aging, Availability Factor, and Reliability Analysis, ASM, Metals Park, OH, 1985, p. 173.

2. D.I.R. Norris, ed. Proc. Symp. Radiation-Induced Sensitization of Stainless Steels, Berkeley Nuclear laboratory, CEGB, 1986.

3. H. Hanninen and I. Aho-Mantila, Proc. Third Int. Symp. on Environmental Degradation of Materials in Nuclear Power Systems - Water Reactors, eds. G. J. Theus and J. R. Weeks, The Metallurgical Society, Warrendale, PA, 1988, p. 77.

4. P. L. Andresen, F. P. Ford, S. M. Murphy, and J. M. Perks, Proc. Fourth Int. Symp. on Environmental Degradation of Materials in Nuclear Power Systems - Water Reactors, NACE (in press).

5. R. H. Jones, Proc. Second Int. Symp. on Environmental Degradation of Materials in Nuclear Power Systems - Water Reactors, American Nuclear Society, La Grange Park, IL, 1985, p. 173.

6. K. Fukuya, S. Nakahigashi, S. Ozaki, M. Terasawa, and S. Shima, ibid., ref. 1, p. 665.

7. P. L. Andresen and C. L. Briant, ibid., ref. 1, p. 371.

8. D.I.R. Norris, C. Baker, and J. M Titchmarsh, ibid., ref. 3, p. 86.

9. T. Inazumi, G.E.C. Bell, and K. Kiuchi, J. Nucl. Mater. (ICFRM-4) (in press).

10. W. L. Clarke, R. L. Cowan, and W. L. Walker, Intergranular Corrosion of Stainless Alloys, ASTM STP 656, 1978, p. 99.

11. E. A. Kenik, Scripta Metal. 21 (1987) 811.

12. J. Bentley, N. J. Zaluzec, E. A. Kenik, and R. W. Carpenter, Scanning Electron Microscopy/1979, II, SEM, Inc., AMF O'Hare, IL, 1979, p. 581.

13. E. H. Lee, A. F. Rowcliffe, and E. A. Kenik, J. Nucl. Mater. 83 (1979) 79.

14. E. A. Kenik. Materials Problem Solving with the Transmission Electron Microscope, vol. 62, eds. L. W. Hobbs, K. H. Westmacott, and D. B. Williams, Materials Research Society, Pittsburgh, PA, 1986, p. 209.

15. R. A. Johnson and N. Q. Lam. Phys. Rev. B13 (1976) 4364.

16. A. D. Marwick, J. Phys. F 8 (1979) 1849.

17. A. D. Marwick, R. C. Piller. and P. M. Sivell, J. Nucl. Mater. 83 (1979) 35.

DEVELOPMENT OF CERAMIC COATINGS FOR LIQUID METAL BLANKET APPLICATIONS – D. Y. Wang (Dept. Mech. Engr., National Chung Hsing University, Taichung, Taiwan), A. B. Hull, M. R. Fox, and C. E. Campbell (Argonne National Laboratory)

OBJECTIVE

Two major concerns for liquid metal blankets in magnetic fusion reactor designs are the corrosion resistance of the structural material and the magnetohydrodynamic (MHD) force and its subsequent influence on thermal-hydraulics and corrosion. The objective of this study is to develop stable, corrosion-inhibiting ceramic coatings at the liquid metal/structural material interface with an emphasis on electrically insulating coatings that prevent adverse MHD-generated currents from passing through the structural walls.

SUMMARY

Based on a preliminary survey of more than 15 oxides and nitrides, four materials (CaO, MgO, Y_2O_3, and BN) were identified as candidates for insulator coating development. Additionally, Cr_2O_3, V_xO, and $(V,Ti)_xN$ were included for study because of their chemical stability in liquid lithium and their potential as corrosion inhibitors. These ceramic compounds were fabricated by a variety of techniques and exposed to flowing lithium at 400°C to assess chemical compatibility. Preparation technologies included hot-press-sintering of MgO, CaO, and Y_2O_3; diffusion coating of Cr_2O_3; oxidation of vanadium; and reactive sputtering of BN. Among the three hot-press-sintered materials, only Y_2O_3 displayed acceptable corrosion resistance when exposed to high purity lithium. A ferritic substrate alloy (HT-9, coated with a 1-μm-thick BN layer) was immersed in flowing lithium at 400°C for 1 h, after which its physical stability and chemical compatibility were determined to be unacceptable. Chromized V-20Ti and oxidized V-20Ti immersed in flowing lithium at 410°C for 100 h showed greater potential for further development than did the BN insulator coating. Preliminary work has begun in the development of in-situ-formed insulator coatings. The first step has been to examine the characteristics of $(V,Ti)_xN$ reaction product layers formed after exposure of V-Ti specimens to flowing lithium. Work is also in progress to test a self-regenerating $CaO{\cdot}V_2O_5$-type insulator coating on a vanadium substrate.

PROGRESS AND STATUS

Introduction and Background

Liquid lithium is an attractive material for both the coolant and tritium breeder in fusion blankets. However, its use presents some unique compatibility problems. One possible way to combat these problems is through the use of ceramic coatings. The lithium is also subject to MHD forces as it flows through the high magnetic fields present in fusion reactors. These forces will alter the flow profiles of the lithium, produce additional stresses in the structure, and result in higher pumping power requirements. The net result is a limitation on heat removal capability.[1] Because of these MHD effects, a high-electrical-resistance ceramic coating is preferred. By placing such a coating at the liquid metal/structure interface, heat transfer related to MHD turbulence will be enhanced in two ways: (1) the insulating coatings will diminish the induced currents and thus suppress turbulence, and (2) higher flow velocities will be facilitated and thus create higher Reynolds numbers and lower interaction parameters.[2] Besides reducing the MHD effects, the insulating wall has the potential to reduce interstitial impurity transport and protect vanadium from the formation of V_2O_5 in the system outside the liquid-metal blanket. The major concerns for insulator coatings are compatibility with liquid metals, thermal stresses and cycling behavior, and long-term effects of irradiation.[3] The conceptual basis for the fabrication of selected thin insulator coatings on the surface of the conducting wall or a laminated insulator with a thin metallic layer over an insulator on the wall has been discussed previously.[4] A similar approach for developing a low Z coating to face the hydrogen plasma in tokamaks is described elsewhere.[5] The objectives are different but the coating methodology is similar. Other studies have investigated the engineered formation[6] of diffusion coatings in liquid metal systems and the suitability of various in-situ coating technologies.[7]

Experimental Procedures and Results

1. Screening Tests of Candidate Ceramic Insulators

Based on a preliminary survey[4] of more than 15 oxides and nitrides, four insulators (CaO, MgO, Y_2O_3, and BN) were identified as the candidate materials for insulator coating development. Screening criteria included

electrical resistivity, thermodynamic stability in contact with liquid lithium, radiation stability, mechanical integrity, fabricability, activation, and cost. Experimental results[8] from studies of the corrosion resistance of ceramics in static lithium for 100 h at 816°C were also considered in finalizing the candidate ceramic materials.

2. Coating Fabrication

Three types of coating processes (additive, reactive, and autogenous) are being investigated to meet both sets of criteria, imposed by both first wall and liquid-metal blanket conditions. Additive processes that have been examined in our laboratory include plasma vapor deposition and reactive RF-sputtering. Reactive processes that have been explored include diffusion coating and oxidization. Autogenous processes that have been experimentally examined include in-situ coating of calcium vanadate and a V-Ti-N reaction product layer formed in 410°C flowing lithium.

Reactive Magnetron Sputtering: BN. Cubic boron nitride coatings on HT-9 alloy (Fe-12Cr) were produced by reactive sputtering.[9] Plasma was generated from a pure boron target, without reverse bias, in an atmosphere containing an N_2/Ar mixture in the ratio of 1:4. A 1-μm-thick BN film was successfully grown on the surface of HT-9 in 4 h. Microhardness tests showed a significant hardness increase over noncoated HT-9, and electrical resistivity was orders of magnitude higher than the required 10^2 Ωm (Table 1).[10] Figure 1a is a scanning electron microscopy (SEM) photograph of the cross section of the BN coating on HT-9.

Hot-Press Sintering: MgO, CaO, Y_2O_3. MgO, CaO, and Y_2O_3 were fabricated as bulk specimens (Table 2) due to the lack of suitable target materials for sputtering and source powders for thermal spraying. Ceramic powders were ball-milled to ~1-3 μm in size before sintering. Solid ceramic disks were produced in a hot-press-sintering furnace. Densified transparent MgO disks (95% theoretical density) were formed at 1500 psi at 1200°C for 1 h. Because higher densification could be expected at the center portion of the disk, only this region was cut into the final specimens. Y_2O_3 was cold pressed for 1 min at 3000 psi and then hot pressed at 1280°C for 1.5 h at 3690 psi. CaO was formed by cold pressing for 5 min under 2100 psi and then sintered in air at 1200°C for 24 h.

Diffusion Coating: Cr_2O_3. Because Cr_2O_3 is one of the most commonly applied coating materials for high-temperature protection in oxygen- and/or sulfur-containing environments,[12,13] a vanadium alloy (V-20Ti) coated with chromium was included in the test matrix. The objective was to grow a diffusion layer of chromium on V-20Ti, to serve as a source of chromium for Cr_2O_3 formation in the lithium environment and to provide strong diffusionbonding against spalling of the in-situ-formed oxide layer. A 20-μm-thick diffision layer grew after 16 h in an argon environment at 1000°C with a cementation pack consisting of 60 wt.% Cr, 36 wt.% Al_2O_3, and 4 wt.% NH_4Cl. Because Cr is a strong oxygen getter, the chromized vanadium alloy formed a thin and stable oxide layer at the surface during exposure to the liquid metal environment. To examine the compatibility between the Cr_2O_3 and liquid lithium, a second set of chromized specimens were preoxidized at 800°C for 30 min before the exposure. The surface layers of both the as-chromized and the chromized and preoxidized V-20Ti samples can be seen in Fig. 2.

Table 1. Compatibility of Bulk Ceramic Specimens with 410°C Flowing Lithium

	Specimen Characteristics		Response to Lithium Exposure		
Compound	Fabrication Technique	Electrical Resistance at 600°C[a] (Ωm)	Time (h)	Weight Loss (%)	stability
Cao	Sintering	10^9	140	42.72	Heavily corroded
MgO	Hot–press sintering	10^9	61	64.65	Heavy disaolution
Y_2O_3	Hot–press sintering	10^7	140	0.04	No visible corrosion
Si_3N_4	--	10^6	61	1.92	Unstable, cracked

[a]Source: Ref. 10.

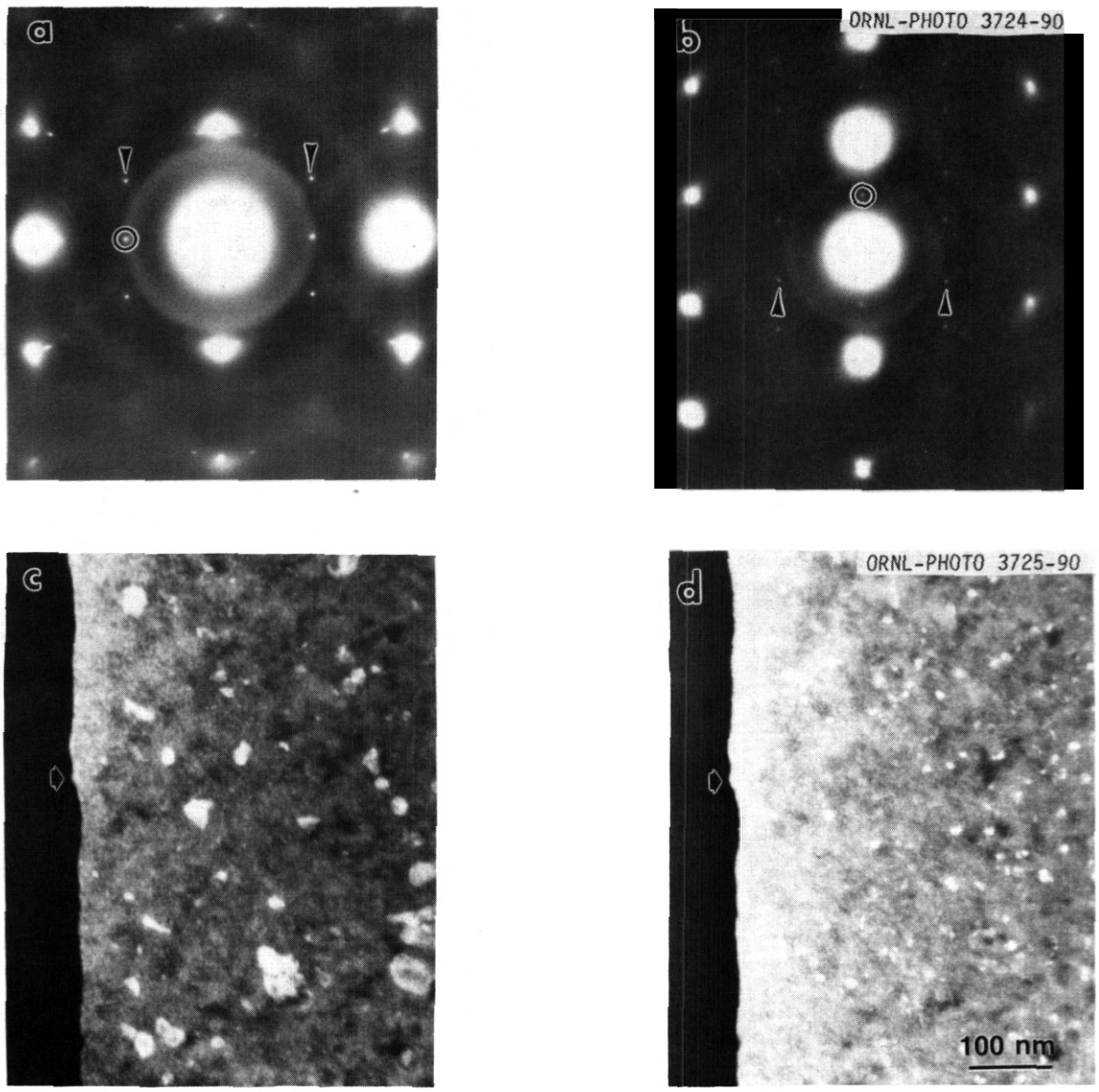

Fig. 6. (a,b) Electron diffraction patterns indicating extra spots at {011} and ½{113} positions in [211] aid [130] zones, respectively. (c) Dark-field image taken with a ½{113} reflection near the [211] zone. (d) Dark-field image taken with a (011) reflection near the [211] zone.

result from RIS at the boundaries and not from the radiation-induced precipitation. The mechanism responsible for sensitization under irradiation differs from that under thermal aging, where the formation of chromium-rich $M_{23}C_6$ precipitates results in the observed chromium depletion.

The matrix etching observed after EPR testing indicates localized composition changes in the matrix, presumably the result of RIS at some point defect sink. Regions containing voids exhibit measured chromium depletions sufficient to cause local passive film breakdown. However, the CW material exhibits significantly lower void density than the SA material, whereas the matrix etching is similar. Faulted loops also exhibit chromium depletion induced by RIS. The formation of fine γ' (Ni_3Si) would also result in local variations in composition. Periodic composition fluctuations (3 at. % Cr) have been observed in the matrix with wavelengths of ~60 nm. The actual chromium levels are less than those measured as a result of the relative size of the excited volume, foil thickness, and defect size for either loops or γ' precipitates. While the spacing of the larger γ' precipitates is ~40 nm, close to the wavelength of the composition oscillations, it is not clear which of these defects, voids, faulted dislocation loops, or γ' precipitates, is responsible for the localized matrix attack.

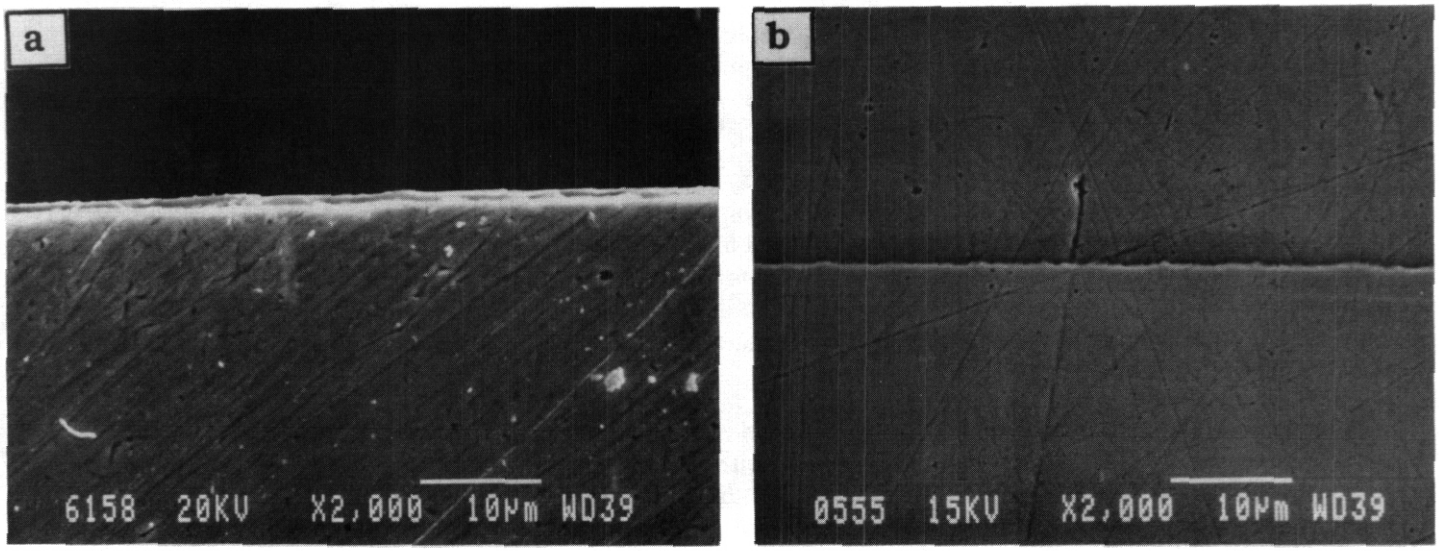

Fig. 1. SEM cross sections of as–coated BN on HT–9 substrate (a) before and (b) after exposure to flowing lithium at 410°C for 100 h.

Table 2. Compatibility of Ceramic Coatings and Underlying Substrates with 410°C Flowing Lithium

		Insulator Coating Characteristics				Response to Lithium Exposure			
Ceramic Compound	Metallic Substrate	Fabrication Technique	Elect. Resist. at 600°C[a] (Ωm)	Weight (g)	Thickness (µm)	Time (h)	Weight Loss (g)	Weight Loss (%)	Compatibility
V_xO	V	Oxidation	0.3[b]	0.0020	10	140	0.0008	0.154	Good
V_xO	V	Oxidation	0.3	0.0019	10	140	0.0009	0.160	Good
Cr_2O_3	V-20Ti	Diffusion coating	1	0.0107	20	100	0.0001	0.016	Excellent
Cr_2O_3	V-20Ti	Diffusion coating[c]	1	0.0109	20	100	0.0052	1.101	Unacceptable
--	V-20Ti[d]	--	--	--	--	100	--	0.09	--
BN	HT-9	Reactive RF-sputtering	5×10^9	0.0009	1	100	0.0015	0.064	Ext. dissolution
BN	HT-9	Reactive RF-sputtering	5×10^9	0.0009	1	1	0.0017	0.072	Ext. dissolution
--	HT-9[d]	--	--	--	--	100	--	0.02	--

[a]Magnitudes are given in Refs. 10 and 11.

[b]V_2O_5 at 660°C.

[c]Pre-oxidized.

[d]Uncoated HT-9 and uncoated V-20Ti were also included in the lithium exposure as standards.

Oxidation Coating: V_xO. Pure vanadium was exposed to air at 600°C for 4 h to form an 8-µm-thick oxide layer (Fig. 3A). Analysis by X-ray diffraction (XRD) and energy-dispersive spectrometry (EDS) before lithium exposure revealed that the layer consisted mainly of V_3O_5, $VO_{0.9}$, V_7O_{13}, and V_6O_{11}.[14]

Autogenous Coating: $CaO\text{-}V_2O_5$. Thermodynamic analysis[15] suggests that a $CaO\text{-}V_2O_5$ -type coating can form on vanadium where the oxygen is derived from that present in the vanadium and the calcium is supplied by the calcium-enriched lithium. Calcium vanadate is an attractive candidate for an in-situ-formed coating because of its intrinsically high electrical resistivity.[16] The concept was experimentally tested by immersing oxidized

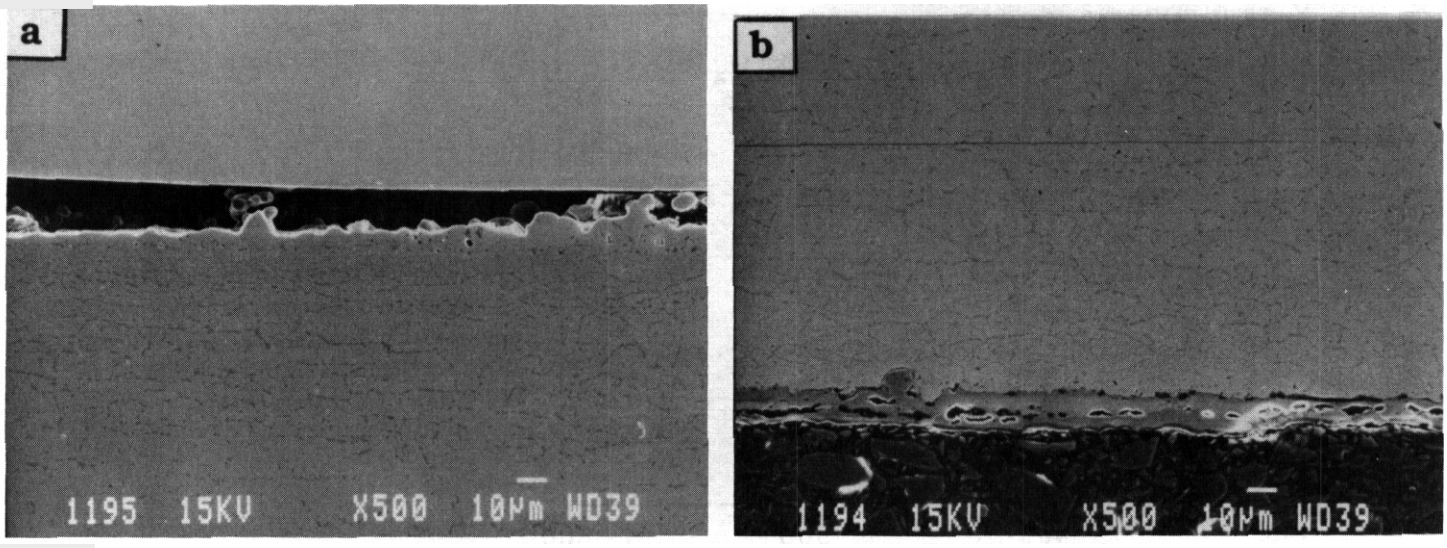

Fig. 2. SEM cross sections of (a) chromium diffusion layer on V–20Ti and (b) chromized and preoxidized coalting on V–20Ti.

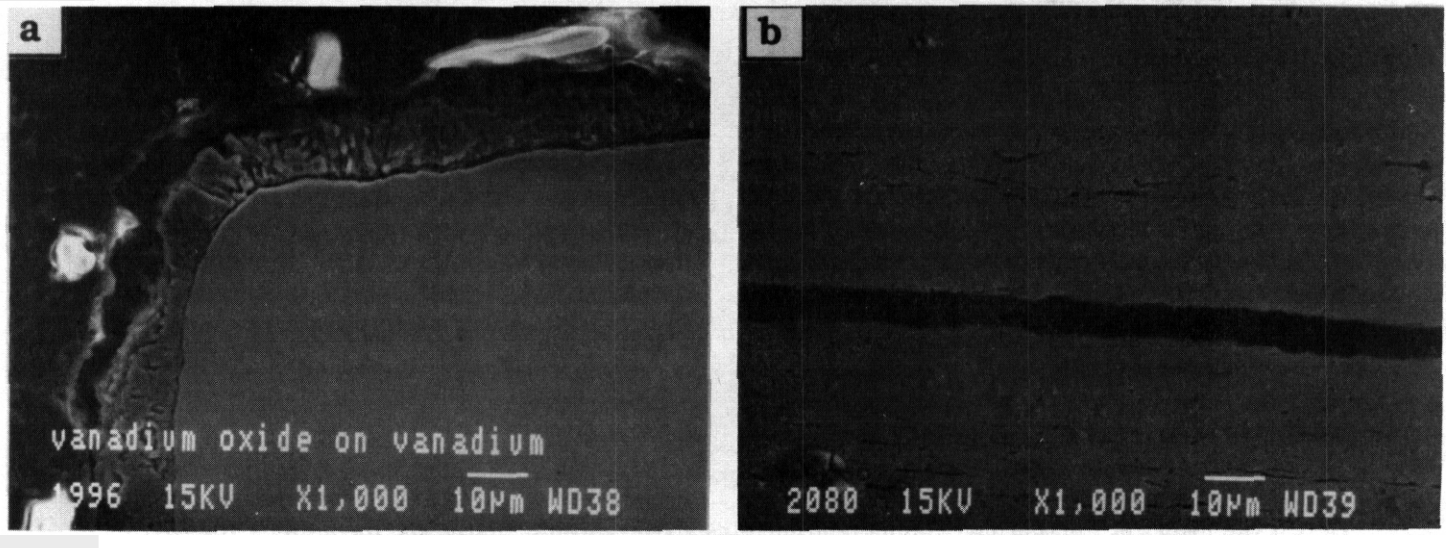

Fig. 3. **SEM** cross sections of V_xO coating on vanadium (a) before and (b) after exposure to flowing lithium 410°C for 100 h.

vanadium coupons in 400°C flowing lithium containing >250 ppm calcium. After a **100-h** lithium exposure, there was no XRD or EDS evidence of a ternary calcium vanadate. Future studies will be conducted with preformed calcium vanadate to examine the chemical stability and electrical resistivity of this material after exposure to liquid lithium.

3. Compatibility with Lithium

Figure 4 is a plot of the standard free energy of formation of the oxide and nitride compounds in our experiments, along with the chemical potentials of dissolved oxygen and nitrogen in liquid lithium at concentrations of 10^{-3}, 1, and 10^{3}. [9,15,17] The two nitride candidates (BN and Si_3N_4) have thermodynamic stabilities descending in that order. BN *can* be expected to be stable in lithium with 100 ppm N (Fig. 5), whereas Si_3N_4 requires increased N for optimal stability. The four oxides (CaO, MgO, Y_2O_3, and Cr_2O_3) exposed to liquid lithium have thermodynamic stabilities descending in that order. Although the oxygen level in the flowing lithium had not been evaluated, earlier studies in the same test facility demonstrated that the exposure of yttrium to relatively high-purity lithium (400-600°C) resulted in formation of a uniform adherent film.[18]

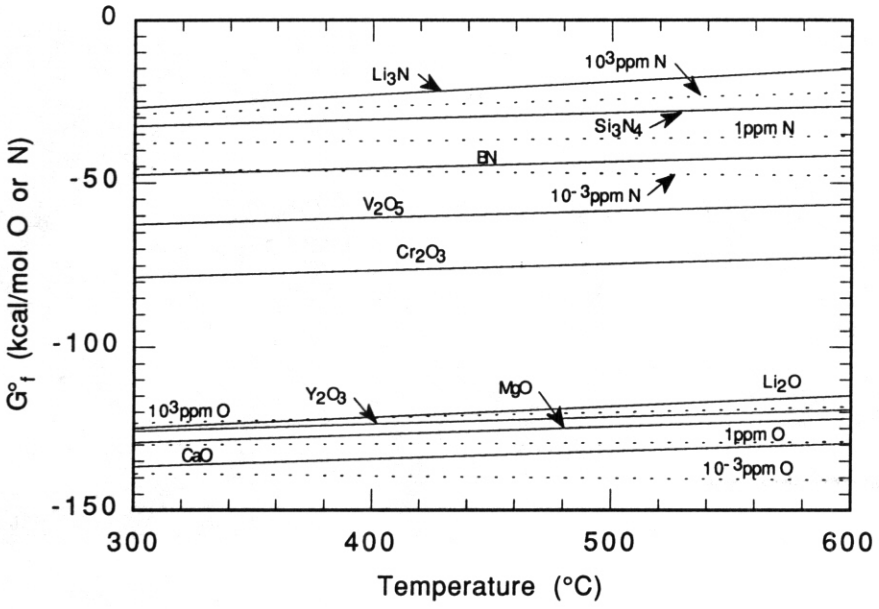

Fig. 4. Stability diagram showing variation of standard free energy of formation of several ceramics and the chemical potentials of dissolved oxygen and nitrogen in liquid lithium as a function of temperature.

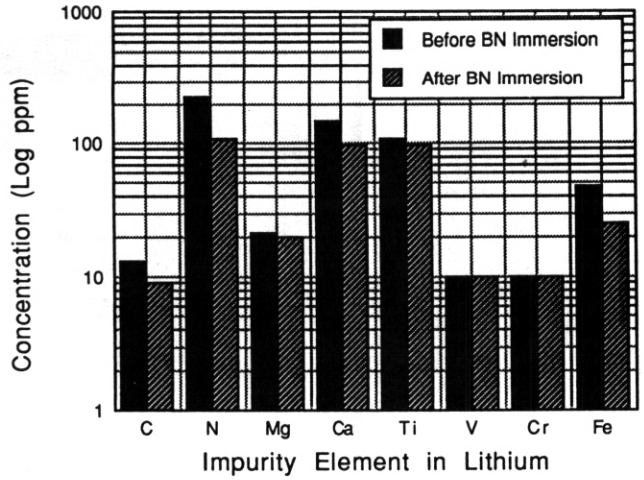

Fig. 5. Impurity levels of lithium in FFTL–3 test facility before and after exposure of HT–9 specimens coated with BN electrical insulator.

To test the utility of the thermodynamic relationships above, ceramic materials, including a BN coating on HT-9 (Fe-12Cr), bulk ceramic specimens of Si_3N_4, MgO, CaO, and Y_2O_3, oxidized vanadium, and chromized V-20Ti specimens were exposed to flowing lithium at 400°C with the lithium impurity levels shown in Fig. 5. Results of the tests are shown in Tables 1 and 2. A description of the FFTL-3 lithium test facility and characterization of chemical impurities in lithium were presented previously.[19]

BN was found to be unstable in high-purity lithium subjected to short-term exposure (≤100h). The reaction was so fast that the BN film on HT-9 dissolved completely after a 1-h exposure (Fig. 1b). The samples with the BN coating did not undergo a large relative weight loss (Fig. 6), but the entire coating dissolved. Although BN can be expected to be thermodynamically stable in lithium containing 100 ppm nitrogen (Fig. 4), defects in the film may have contributed to the poor adhesion to the HT-9 (Fe-12Cr) substrate. Further experiments will be made on bulk BN specimens or BN-coated vanadium coupons in static lithium capsules.

Based on a tensile stress criterion for cracking, BN, MgO, and CaO are unlikely to develop cracks because they are expected to be in compression on the metallic substrate.[17] However, Si_3N_4 had one of the highest calculated tensile stresses. The proclivity of Si_3N_4 to cracking was borne out in experimental testing. After a 61-h exposure in 410°C flowing lithium, Si_3N_4 cracked extensively, probably augmented by lithium penetration into the Si_3N_4 lattice.

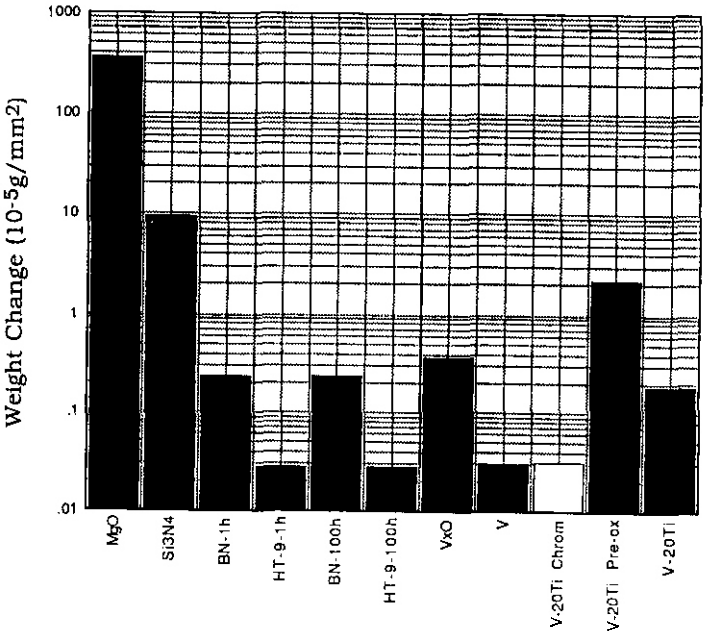

Fig. 6. Weight change summary of BN, HT–9, Si_3N_4, MgO, V_xO, V, Cr–(V–20Ti), and V–20Ti after exposure to flowing lithium. Black columns signify weight loss and white column signifies weight gain.

The compatibility of the oxide materials with the flowing lithium was rather puzzling in the context of expected thermodynamic stability. A bulk specimen of MgO was heavily corroded after a 61-h exposure in flowing lithium. After a 100-h exposure, a CaO specimen had lost nearly one-half of its mass, but a Y_2O_3 specimen showed no signs of corrosion. Therefore, further investigations of electrical insulators in high-purity lithium will emphasize Y_2O_3. An important concern about the use of yttrium is its high affinity for hydrogen.[20] Perhaps the incorporation of Y_2O_3 into a very thin surface region of the vanadium-base alloy may suffice as an electrical insulator[21] and prevent the possibility of hydrogen embrittlement of the structural material.

Among the corrosion-resistant alloys, both the as-chromized V-20Ti and the oxidized vanadium showed promising results. Cross sections of the V_xO layer after exposure can be seen in Fig. 3b. Although the as-chromized V-20Ti sample showed a slight weight gain, it should have gained more weight from stoichiometric pickup of oxygen than was observed (Fig. 6). The V-20Ti specimen with a preformed Cr_2O_3 scale showed greater weight loss, possibly because of defects in film, as shown in Fig. 2b. Spalling of Cr_2O_3 could occur by penetration of lithium through the pores and cracks. The preoxidation procedure will be conducted in a low-pO_2 environment to reduce the porosity of the oxide layer.

4. Development of In-Situ-Formed Insulator Coatings

For the complex geometries and high-temperature operating environments of interest, in-situ-formed self-healing coatings appear to offer the most reasonable solution. Excellent-quality diffusion coatings on metals and alloys have been obtained when the diffusing element has been introduced via a liquid metal, e.g., lithium.[6]

Formation of the nitride (V-Ti)N on V-base alloys has been observed in various experiments (Table 3). This nitride surface layer has been associated with limited diffusion of nonmetallic impurities in the liquid lithium/structural materials systems: more specifically, a retarded carbon transfer phenomena[22] was observed in V-20Ti alloys. Adelhelm et al.[23] observed that corrosion rates of V-3Ti-1Si were minimized with 30 wppm nitrogen in liquid lithium and attributed this to the protective effect of a $(V,Ti)_xN$ reaction layer with x = 1.55-1.67. The thickness of this layer was dependent on nitrogen concentration, not time. Chopra and Smith[24] also observed a nitride layer on vanadium-base alloys exposed to liquid lithium. Although no uniform scale was observed in alloys with a low titanium content (<5%), a uniform, mixed nitride layer formed on V-(15,20)Ti. The thickness increased with temperature, not time, with values of about 1.5, 2.5, and 6.0 μm at 427, 482, and 583°C, respectively. However, the layer was brittle and could spall under thermal stresses. Votinov et al.[25] found that titanium, being a more reactive element, caused nitrides to form closer to the surface, and these nitrides limited further diffusion. Similar reaction products were also found in other lithium compatibility studies.[26-29]

Table 3. Summary of Reported Observations of Reaction Product Layer Formed on V-base *Alloys* after Li-Exposure[a]

Observed Reaction Product	V-base Alloy Substrate	Test Condltlons Temp. (°C)	Time (h)	Lithium Impurities (wppm) N	O	C	Surface Layer Characterization Thickness (μm)	Observations[b]
V_3N, VN, Li_7VN_4	V	--	--	--	--	--	--	--[26]
VN	V	477	..	140	--	--	--	Reaction products Insoluble in Li[27]
Li_7VN_4	V	477	--	23,400	--	--	--	Reaction products insoluble In Li[27]
Mixed nitrides	V-(15, 20)Ti	427-538	>700	20-50	--	8-12	1.5-6.W	Uniform brittle scale[24]
TIN	V-(15, 20)Ti	482	>1600	20-50	--	8-12	IO	Decreased N &Tam Increased hardness[c]
Nitrides	V-(5-30)Ti	700	500	3633	580	19,000	20	Dense scale. restricted impurity diffusion[25]
Nitrides	V-(5-30)Ti	700	500	13.524	1400	35,000	15-40	Dense scale. restricted Impurity diffusion[25]
$(V,Ti)_xN$[d]	V-3Ti-1Si	533-550	>362	8-64	..	0.3-2	2-5	Density of scale a N content[c],[28]
Fe. Cr. Ni enriched	V	800	1000	200-2000	<250	<50	10	Film formed In V/Fe system in static Li[29]

[a]Limited to open literature: more observations are reported verbally or *in* Informal documents.
[b]More information Is given In the cited references.
[c]Surface layer thickness Increased with temperature and dld not form on alloys with 5%Ti or Less.
[d]Where $1.55 < x < 1.67$.

Ongoing experiments focus on characterization of the nitride layer on the V-20Ti and titanium specimens exposed to flowing lithium at Argonne National Laboratory and on measurements of electrical conductivity to quantify insulation properties.

CONCLUSIONS

Based on a series of scoping studies, diffusion and in-situ-formed coatings appear to exhibit the most potential for good corrosion resistance and high electrical resistivity in a lithium environment. However, preliminary experimental studies indicate that the actual stability of BN, MgO, and CaO in lithium is unsatisfactory in high purity lithium containing low concentrations of nitrogen and oxygen. The only electrical insulator material that was compatible on the basis of these preliminary tests was Y_2O_3. Because some of these results are not consistent with expected thermodynamic relationships, more tests are warranted. Among the structural materials, both oxidized vanadium and chromized V-20Ti showed promising results, but more work is required to develop a suitable preformed Cr_2O_3 layer.

FUTURE WORK

Additional efforts will focus on the development of self-regenerating diffusion coatings and corrosion-resistant layers that have adequate electrical insulation properties with liquid lithium. If the original coating cracks or spalls, a new coating would form to maintain the required properties.

Emphasis will be placed on completing the compatibility studies of Y_2O_3 in lithium at higher temperatures and for longer exposure periods (>1000 h). Work is also in progress to evaluate the appropriateness of $CaO{\cdot}V_2O_5$, Al_2O_3, AlN, $Y_3Al_5O_{12}$, and $MgAl_2O_4$ as possible electrical insulator coatings For use in flowing lithium.

A critical examination of the stability, corrosion resistance, and electrical resistivity of the vanadium-titanium-nitride surface reaction layer formed on V-Ti alloys during exposure in lithium will be made.

Successful completion of the coating fabrication and compatibility tests will enable selection of an appropriate electrical insulator coating. Because the life span of the insulator coating will depend on its mechanical integrity during service, especially under the influence of neutron irradiation, a series of mechanical and irradiation tests will begin.

REFERENCES

1. H. Tas, S. Malang, F. Reiter, and J. Sannier, *Liquid Breeder Materials*, J. Nucl. Mater., **155-157**, 178 (1988).

2. T. Q. Hua, J. S. Walker, B. S. Picologlou, and C. B. Reed, *Three-Dimensional Magnetohydrodynamic Flows in Rectangular Ducts of Liquid-Metal-Cooled Blankets*, Fusion Tech., **14**, 1389 (1988).

3. G. P. Pells, *Radiation Effects and Damage Mechanisms in Ceramic Insulators and Window Materials*, J. Nucl. Mater., **155-157**, 67 (1988).

4. Y. Y. Liu and D. L. Smith, *Ceramic Electrical Insulators for Liquid Metal Blankets*, J. Nucl. Mater., **141-143**, 38 (1986).

5. M. J. Davis, *Material Surface Modification for First Wall Protection*, J. Nucl. *Mater.*, **85 & 86**, 1063 (1979).

6. V. F. Shatinskii and O. M. Zboshnaya, *The Impregnation of 1Kh18N9T by Beryllium and the Corrosion Resistance of the Coating in Molten Lithium*, Fiziko-Khimicheskaya Mekhanika Materialov, **8**, 59 (1972).

7. K. Obara, K. Kawasaki, H. Hiratsuka, T. Kuroda, K. Ohta, Y. Miyo, M. Ohkuho, and M. Ohta, *In-Situ Coating Device for JT-60*, JAERI-M **88-117** (1988).

8. J. O. Cowles and A. D. Pastemak, *Lithium Properties Related to Use as a Nuclear Reactor Coolant*, UCRL-50647 (1980).

9. D. Y. Wang, A. B. Hull, and D. L. Smith, *Preliminary Study of Ceramic Insulator Coating for Liquid Metal Blanket of Fusion Reactor*, Presented at TMS 1990 Annual Meeting, Anaheim, CA., February 19-23, 1990.

10. W. D. Kingery et al., *Introduction to Ceramics*, 2nd Ed., John Wiley and Sons, New York (1976).

11. P. Kofstad, *Nonstoichiometry, Diffusion, and Electrical Conductivity in Binary Metal Oxides*, Robert E. Krieger Publishing Co., Inc., New York (1983).

12. D. Y. Wang, *Corrosion Behavior of Chromized and/or Aluminized 21/4Cr-1Mo Steel in Medium-BTU Coal Gasifier Environments*, Surface and Coatings Technology, **36**, 49-60 (1988).

13. D. Y. Wang and K. Natesan, *Corrosion Performance of High-Chromium Weldments in Simulated Medium-BTU Coal Gasifier Enuironments*, Preprint for Corrosion/90, Las Vegas, April 23-21 (1990).

14. C. E. Campbell, *Fabrication of Ceramic Insulator Coatings for Liquid Metal Blanket Inuestigation*, ANL Student Research Participation Program Final Report (1990).

15. D. Ehst, et al., *Tokamak Power Systems Studies - FY 1986: A Second Stability Power Reactor*, Argonne National Laboratory Report ANL/FPP/86-1 (1986).

16. A. F. Grandin de l'Eprevier and R. C. Buchanan, *Preparation and Properties of $Ca_2V_2O_7$ Single Crystals*, J. Electrochem. Soc., **129**, 2562 (1982).

17. C. C. Baker, et. al., *Tokamak Power Systems Studies FY 1985*, Argonne National Laboratory Report ANL/FPP-85-2 (December 1985).

18. D. L. Smith, R. H. Lee, and R. M. Yonco, *Investigation of Nonmetallic Element Interactions in Vanadium-Alloy/Lithium Systems*, Pmc. 2nd Intl. Conf. on Liquid Metal Technology in Energy Production, U. S. Dept. of Energy Report CONF-800401-P1 (1980), p. 272.

19. O. K. Chopra and D. L. Smith, *Corrosion of Ferrous Allays in a Flowing Lithium Enuironment*, J. Nucl. Mater., **133 & 134**, 861 (1985).

20. A. B. Hull, O. K. Chopra, B. Loomis. and D. Smith, *Compatibility between Vanadium-base Allays and Flowing Lithium: Partitioning of Hydrogen at Elevated Temperatures,* Eighth Fusion Reactor Materials Semiannual Progress Report for Period Ending March 31, 1990, DOE/ER-0313/8, Oak Ridge National Laboratory, p. 257.

21. D. L. Smith et al., *Blanket Comparison and Selection Survey - Final Report,* Argonne National Laboratory Report ANL/FPP/84-1, Vol. 2 (1984).

22. O. K. Chopra and A. B. Hull, *Influence of Carbon and Nitrogen Impurities on the Corrosion of Structural Materials in a Flowing-Lithium Environment,* Fus. Tech., 15, 308 (1989).

23. Ch. Adelhelm, H. U. Borgstedt, and J. *Konys, Corrosion of V-3Ti-1Si in Flowing Lithium,* Fus. Tech., *8,* 541 (1985).

24. O. K. Chopra and D. L. Smith, *Corrosion Behavior of Vanadium Alloys in Flowing Lithium,* J. Nucl Mater., 155-157,683 (1988).

25. S. N. Votinov, L. I. Gomozov, A. I. Dedyrin, R. I. Bobyk, and E. M. Lyutyi, *Questions of the Corrosion Resistance of Vanadium Alloys as a Possible Thermonuclear Reactor Constructional Material, Sov.* Mater. Sci., 23,559 (1987).

26. M. G. Barker, S. A. Frankham, P. G. Gadd, and D. R. Moore, *Chemical Aspects of the Corrosion Behavior of Type 316 Stainless Steel in Liquid Lithium and Liquid Sodium,* Material Behavior and Physical Chemistry in Liquid Metal Systems, 113 (1982).

27. P. Hubberstey and P. G. Roberts, *Corrosion Chemistry of Vanadium in Liquid Lithium Containing Dissolved Nitrogen, J.* Nucl. Mater., 165-157,694 (1988).

28. H. Borgstedt, M. Grundmann, J. *Konys,* and Z. Peric', *A Vanadium Allay for the Application in a Liquid Metal Blanket of a Fusion Reactor,* J. Nucl. Mater., 155-157,690 (1988).

29. V. A. Evtikhin, V. B. Kirillov, A. Ya. Kosukhin, and I. E. Lyublinskii, *Influence of Nonmetallic Impurities on the Compatibility of Vanadium With Liquid Lithium, Sov.* Mater. Sci., 22,478 (1986).

7. SOLID BREEDING MATERIALS

LITHIUM MASS TRANSPORT IN CERAMIC BREEDER MATERIALS

P. E. Blackburn and C. E. Johnson (Argonne National Laboratory)

OBJECTIVE

The objective of this activity is to measure the lithium vaporization from lithium oxide breeder material under differing temperature and moisture partial pressure conditions.

SUMMARY

The transport of lithium by vaporization of LiOH(g) from lithium ceramics, particularly $Li_2O(s)$, poses a constraint on the maximum operating temperature of the blanket. Experimental measurements have shown that, depending on temperature, moisture pressure, and proximity of structural steels, the lithium transport process is complex. For conditions wherein the $Li_2O(s)$ is "free standing." the lithium vaporization is controlled by the Li_2O/H_2O system themdynamics that are already well established. Simply stated lithium transport as LiOH(g), increases with increasing temperature and higher partial pressures of moisture. In the proximity of stainless steel there is an added chemical potential driving force due to formation of Li_2CrO_2, $LiFeO_2$ and $LiNiO_2$. The transport of LiOH(g) to the stainless steel is driven by the concentration gradient of LiOH(g) from that at the $Li_2O(s)$ surface and that at the steel surface. This gas-solid reaction may become important for blanket designs where the structural steel is very close to the $Li_2O(s)$ ceramic.

PROGRESS AND STATUS

Lithium ceramics are being investigated for use as tritium breeding materials. The lithium is readily converted to tritium after reacting with a neutron. With the addition of 1000 ppm H_2 to the He purge gas, the bred tritium is readily recovered from the blanket as HT and HTO above 400°C. Within the solid, tritium may also be found as LiOT which may transport lithium to cooler parts of the blanket. This process may cause loss of lithium from the blanket, blocking of flow paths, and increase of the tritium inventory. Laboratory studies have established the pressure of LiOH(g) for reaction of $Li_2O(s)$ with water vapor,

$$0.5\ Li_2O(s) + 0.5\ H_2O(g) = LiOH(g). \qquad (1)$$

The purpose of this work is to investigate the transport of LiOH(g) from the blanket material.

Experimental

A fixed bed system was assembled that enabled good contact between the purge gas and the lithium oxide at high gas velocities. In this fixed bed arrangement, a silver lined quartz tube was used to hold seven cylindrical Li_2O pellets 8 mm long by 5.3 mm diameter arranged in a close-packed configuration. A platinum sieve was located at the downstream end to hold the pellets in place. The space through which the gas flows is divided into three different regions: a single region bounded by two concentric silver cylinders, six triangular regions bounded on two sides by Li_2O and on a third side by silver, and six small triangular regions bounded by Li_2O on all three sides. The quartz tube assembly was heated in a clam shell furnace. Chromel-alumel themcouples provided temperature measurement and temperature control. Helium flowed through two rotometers, one line through a water saturator and the other line directly from the high purity tank helium. Needle valves on the rotometers were adjusted to reduce the water content to 5×10^{-4} atm. Total flow rates as high as 7000 cc/min (STP) permitted gas velocities as high as 2600 cmlsec at 850°C.

The furnace was heated to 850°C and held for experimental times ranging from 40 to 300 minutes followed by cooling to room temperature. After cooling, the silver tube was soaked in water to dissolve the condensed LiOH. The LiOH solution was added to a 100 mL volumetric flask along with 20 mL of 1-N HCl to produce the 0.2-N HCl solution required for lithium analysis.

The pressure of LiOH was calculated from the lithium analysis and the ideal gas law,

$$P\ (LiOH,g) = nRT/V \qquad (2)$$

where n is the number of moles of lithium transported per minute, R is the gas constant, T is the absolute room tenperature, and V is the volume flow of helium per minute (STP) corrected for the fraction of helium gas (55.9%) flowing over the $Li_2O(s)$.

The gas velocity was calculated from the total volume and the total effective areas of the three regions. For this calculation the effective diameters were computed from,

$$d_{eff} = 4A/P_w, \qquad (3)$$

This work supported by the U.S. Department of Energy, Office of Fusion Energy, under contract no. W-31-109-Enq-38.

where d_{eff} is the effective diameter, A the geometric area, and P_w the length of the perimeter. The effective area is $0.1655 cm^2$ as calculated from equation (4).

$$A_{eff} = \pi d_{eff}^2 / 4 \quad (4)$$

The decrease in the pressure of LiOH(g) was correlated with increase in flow velocity assuming that the process is diffusion controlled. The formation of LiOH(g) from reaction of $H_2O(g)$ with $Li_2O(s)$ is a two-step process: first, water vapor diffuses from the flowing helium to the lithium oxide surface, and second, the reaction of $H_2O(g)$ with $Li_2O(s)$ produces LiOH(g) which diffuses into the flowing helium. The two simultaneously occurring processes can be calculated from the product of the fractional saturation of each process. The fractional saturation of each process may be calculated from tables and equations of L. S. Darken[2] where the fractional saturation is given as a function of Dt/L^2. D is the diffusivity of LiOH(g) or $H_2O(g)$ in helium, t is the time in seconds, and L is the half-thickness if the gas volume flowing past the lithium oxide. LiOH(g) originates primarily from the six triangular regions bounded by silver on one side and $Li_2O(s)$ on the two other sides and these regions were treated as six slabs. Since one side of each of these six regions is silver, the value for L is the full thickness. L was estimated from the root of the product of the diameter of the geometric area and the effective diameter. L is equal to 0.191 $\pm$ .077 cm. The diffusivities of LiOH(g) and $H_2O(g)$ gas in helium were estimated using equation (5) from R. E. Treybal,[3]

$$D_{AB} = \frac{(0.00107 - 0.000246 \sqrt{1/M_A + 1/M_B}) T^{1.5} \sqrt{1/M_A + 1/M_B}}{P_t (r_{AB})^2 [f(kT/e_{AB})1} \quad (5)$$

where D_{AB} is the diffusivity of LiOH(g) (or $H_2O(g)$) in He, M_A and M_B are the molecular weights of LiOH (or H_2O) and He, T is the absolute temperature, P_t is the total pressure, r_{AB} is the molecular separation at collision, and $f(kT/e_{AB})$ is the collision function given graphically in R. E. Treybal.

The time for the reaction was calculated from the gas velocity and the length of the Li_2O cylinders (8 mm). The fractional saturation equation for short times is given by equation (6).

$$F = 1.128 \frac{\sqrt{Dt}}{L} \quad (6)$$

The fractional saturation equation for long times is given by equation (7).

$$F = 1 - e^{-a \left(\frac{\frac{Dt}{L^2} + 0.0851}{0.4052} \right)} \quad (7)$$

At 1123 K, the diffusivities (D) calculated with equation (5) are 6.22 and 6.98 cm^2/sec for LiOH(g) and $H_2O(g)$ respectively. Fractional saturations for LiOH(g) and $H_2O(g)$ were calculated with equations (6) or (7). These fractional saturations apply to a single step process. The two-step process is assumed to be the product of F_{H_2O} and F_{LiOH},

$$F_{prod} = F_{H_2O} \cdot F_{LiOH} \quad (8)$$

Values for the product are given in column 6 of Table 1. The calculated fractional saturation may be compared to the measured saturation in column 5 of Table 1. Figure 1 shows a plot of the log of the measured saturation against the log of the calculated saturation.

Table 1

Calculation of LiOH Fractional Saturation[a]

P_{LiOH} atm x10^6	Vol cc/sec at Temp	Velocity cm/sec	Residence Time sec	P_{LiOH}/P^o	Frctnl Saturtn	Log_{10} P/P^o	Log_{10} Frctnl Saturn
32.3	8.3	50.2	0.016	1.90	0.999	0.278	-0.0006
12.9	8.7	52.7	0.0152	0.75	0.998	-0.123	-0.0009
16.2	15.8	95.7	0.0084	1.05	0.961	0.020	-0.017
3.39	297	1794	0.00045	0.20	0.103	-0.706	-0.987
20.9	12.3	74.4	0.0107	1.24	0.986	0.092	-0.006
12.6	11.2	67.9	0.0118	0.74	0.991	-0.131	-0.004
6.92	49.8	301	0.0027	0.41	0.612	-0.390	-0.213
4.90	98.6	596	0.0013	0.29	0.309	-0.542	-0.510
2.19	220	1332	0.00060	0.13	0.138	-0.887	-0.859
1.26	433	2618	0.0003 1	0.074	0.070	-1.128	-1.154

(a) The temperature was 1123 K, D_{LiOH} was 6.22 cm^2/sec, D_{H2O} was 6.98 cm^2/sec, and L was assumed to be 0.19 cm. P^o_{LiOH} is 1.70E-5 atm.[1]

Data were derived from Noda's paper4 to calculate the degree of LiOH(g) saturation when helium and 500 ppm water were flowed through a cylinder packed with 5 mn spheres of Li_2O, The cylinder was 2 cm in diameter and 10 cm high. The log of the pressure of LiOH(g) measured by Noda divided by that calculated from Tetenbaum and Johnson is plotted against the log of the calculated fractional saturation in Fig. 1. Noda's residence time was over 10 times greater than ours for the same gas velocity. Noda's measurements and our calculation of his data, plotted in Fig. 1, agree that his helium was fully saturated with LiOH(g).

This work established conditions for calculating LiOH(g) undersaturation in helium as a function of the velocity of the purge gas. It has been assumed that fractional saturation of two-step interdependent reactions can be treated as the product of each fractional saturation. The measured and calculated fractional saturation agree within experimental uncertainties.

Measurements of the effect of stainless steel on LiOH(g) transport.

Preliminary experiments were carried out to determine what effects the placement of structural stainless steel near the $Li_2O(s)$ could have on the transport of LiOH(g) fmm the $Li_2O(s)$ blanket material. In this study, a silver boat was used to hold $Li_2O(s)$ with a stainless steel sheet placed at desired distances above the $Li_2O(s)$. The boat and plate were placed inside a silver lined quartz tube and the quartz tube assembly was heated in a clam shell furnace. Helium flowed through two rotometers, one line through a water saturator and the other line directly from the high purity helium tank. In some measurements the helium contained about 1% hydrogen. The two helium streams were mixed and flowed into the silver lined quartz tube containing the boat and lithium oxide. Needle valves were adjusted to reduce the water content within the range 0.001 to 0.01 atm. The furnace was heated to 750°C for this set of measurements. Most of the LiOH(g) produced from water vapor and $Li_2O(s)$ deposited on the stainless steel plate. The remaining LiOH(g) condensed in cooler downstream regions of the silver tube.

After each experiment, the boat was removed and the silver tube was soaked in water to remove the condensed LiOH, for chemical analysis. The deposit on the stainless steel was dissolved in nitric acid for lithium chemical analysis. The pressure of LiOH(g) was calculated from the lithium analysis of the condensed LiOH in the silver tube and the ideal gas law.

Six experiments were carried out at 750°C. In experiments 21, 22, and 26 He flow was 10 cc/min and water pressure was about 9000 ppm; in experiments 23-25 He flow was 100 cc/min and water pressure was about 1200 ppm. With the exception of experiment 21 all measurements were made with 303 stainless steel plates above the $Li_2O(s)$ fixed bed. The results of experiments are sumnarized in Table 2. In column 6 of table 2, the measured LiOH(g) pressure was determined, assuming all the lithium condensed in the silver tube was entrained as LiOH(g) in the flowing helium. This was not the case in experiments 21, 22 and 26 where the apparent pressures were an average of nine times greater than those calculated from Tetenbaum[1]. This was verified when the flow rate was increased to 100 cc/min and apparent LiOH(g) pressures decreased to within a factor of two of that calculated from Tetenbaum's work. The LiOH(g)

condensed in the silver tube by two mechanisms: 1) transport by entrainment in flowing helium: 2) thermal migration from the flowing helium in the hot zone to cooler regions of the silver tube, driven by the temperature gradient. As the velocity of the helium flow decreases, the ratio of thermal migration to entrainment increases toward infinity.

Table 2
Diffusion driven LiOH(g) reaction with stainless steel

Run No	He Flow cc/min	Ratio meas/Tet	$P(H_2)$ atm	$P(H_2O)$ atm	P(LiOH) atm meas	P(LiOH) atm* Tet
21	10	9.02	.0000	.00875	1.14E-4	1.26E-5
22	10	13.3	.0000	.00799	1.59E-4	1.20E-5
23	100	2.14	.0097	.00120	9.93E-6	4.44E-6
24	100	1.64	.0097	.00125	7.77E-6	4.75E-6
25	100	1.85	.0097	.00120	8.64E-6	4.67E-6
26	10	5.00	.0097	.00986	6.66E-5	1.33E-5

*Calculated from ref. 1.

Steady state diffusion

In our experiments the $Li_2O(s)$ and the stainless steel sheet are separated by distances of five millimeters to less than a millimeter. During the experiment the LiOH(g) transports to the stainless steel surface, driven by the diffusivity of LiOH(g) in helium and the LiOH(g) pressure gradient, and deposits on the stainless steel.

The LiOH(g) pressure decrease may be caused by reaction of LiOH(g) with the steel to form Li_2CrO_2, or Li_2FeO_2, or Li_2NiO_2. For example, the chromate may be produced by the reactions,

$$Cr + 3/2\ H_2O(g) = 1/2\ Cr_2O_3 + 3/2\ H_2(g), \quad (9)$$

and,

$$LiOH(g) + 1/2\ Cr_2O_3 = LiCrO_2 + 1/2\ H_2O(g). \quad (10)$$

The LiOH(g) pressure at the lithium oxide interface with water concentration of 93 ppm at the three temperatures used in the compatibility studies by Chopra et al.,[6,7] and the temperature of our experiments are given in Table 3 for reactions (10 and 11),

$$1/2\ Li_2O + 1/2\ H_2O(g) = LiOH(g) \quad (11).$$

The LiOH(g) pressure at the stainless steel interface for reaction (11) in equilibrium with Cr_2O_3, $LiCrO_2$, and 93 ppm $H_2O(g)$ are given in Table 3. The LiOH pressure at the stainless steel interface will depend on the composition of the corrosion layer on the steel surface. The composition depends on time, temperature. and gas composition. In all cases, this pressure will be substantially lower than that at the $Li_2O(s)$ surface.

Table 3

Equilibrium LiOH(g) pressures (atm) as a function of the temperature (K) at the surfaces of $Li_2O(s)$ and stainless steel where $Cr_2O_3/LiCrO_2$ and 93ppm H_2O control the LiOH(g) pressure.

	723	823	923	1023
Li_2O	4.08E-10	1.15E-8	1.59E-7	1.31E-6
Stainless steel	7.90E-17	1.25E-14	5.45E-13	1.24E-11

The LiOH(g) pressures in table 3 are based on Tetenbaum's[1] pressures in equilibrium with $Li_2O(s)$ and water vapor. The LiOH(g) pressures at the steel surface are 2E-7 to 9E-6 times lower than the pressures at the $Li_2O(g)$ surface. The LiOH(g) formed at the $Li_2O(s)$ surface is influenced by the pressure gradient and diffusivity of LiOH(g) in the gap between $Li_2O(s)$ and the stainless steel. In this steady state diffusion process, the flux of LiOH(g) is given by,

$$N_A = \frac{D_{AB} P_t}{RTz} \left[P_{A1} - P_{A2} \right] \qquad (13)$$

where N_A is the flux of LiOH(g) in He in g mol/sec/cm^2, D_{AB} is the diffusivity in cm^2/sec of LiOH(g) in He, P_t is the total pressure in atm, P_{A1} and P_{A2} are the LiOH(g) pressures at the $Li_2O(s)$ and stainless steel surfaces respectively, R is the gas constant (cc-atm/deg/mol), T is the absolute temperature, and z is the distance, in cm, between the $Li_2O(s)$ and the stainless steel. The flux of LiOH(g) varies inversely with the separation distance z, rising rapidly as z decreases.

CONCLUSIONS

These studies have shown that the transport of LiOH(g) can be strongly influenced by the proximity of a stainless steel surface to the $Li_2O(s)$. The pressure of LiOH(g), in equilibrium with $Li_2O(s)$, is proportional to the square root of the $H_2O(g)$ pressure and increases exponentially with temperature. The transport of LiOH(g) to the stainless steel is driven by the concentration gradient of LiOH(g) from that at the $Li_2O(s)$ surface and that at the steel surface. At the stainless surface the LiOH(g) pressure is likely to be in equilibrium with either $LiCrO_2$, or $LiFeO_2$, or $LiNiO_2$. Experiments of this type must be run for extended periods to assess the importance of this interface complexity.

REFERENCES

1. M. Tetenbaum and C. E. Johnson, Nucl. Mater, 120 (1984) 213.

2. L. S. Darken and R. W. Gurry, "Physical Chemistry of Metals," New York, McGraw-Hill, p 447, 1953.

3. R. E. Treybal, "Mass-Transfer Operations", Second Edition, McGraw-Hill Book Company, New York, 1968, p. 25.

4. K. Noda, "Mass transfer and compatibility of lithium oxide," presented at ITER Specialist's Meeting on Materials Data Base, F. R. G., August 22-26, 1988

5. Robert E. Treybal, "Mass-transfer operations," second edition, Mcgraw-Hi11 Book Company, New York, 1968, p 22.

6. O. K. Chopra, T. Kurasawa, and D. L. Smith, "Compatibility of Ferritic Steels with Sintered Li_2O Pellets in a Flowing Helium Environment," pp. 209-214 in Proc. Topical Conf. on Ferritic Alloys for Use in Nuclear Energy Technologies. eds. J. W. Davis and D. J. Michel. AIME. NEW YOAK. 1984.

7. O. K. Chopra and D. L. Smith, "Compatibility of Li_2O in a Flowing Helium Environment'. Argonne national Laboratory

8. M. C. Billone, personal communication, Argonne National Laboratory, June 15, 1990.

DESORPTION CHARACTERISTICS OF THE $LiAlO_2$-$H_2O(g)$ SYSTEM

Albert K. Fischer and C. E. Johnson (Argonne National Laboratory)

OBJECTIVE

The objective of this study is to describe the energetics and kinetics of desorption of $H_2O(g)$ and $H_2(g)$ from the surface of ceramic breeders with data that allow predictions of the characteristics of tritium release.

SUMMARY

The energetics and kinetics of the evolution of $H_2O(g)$ and $H_2(g)$ from $LiAlO_2$ are being studied by the temperature programed desorption technique. The concentrations of H_2, H_2O, N_2, and O_2 in a helium stream during a temperature ramp are measured simultaneously with a mass spectrometer. The amount of H_2 adsorption/desorption is small compared to the amount of H_2O adsorption/desorption. After prolonged treatment with helium containing 990 ppm H_2 at 400°C, H_2O evolution into the He-H_2 stream was observed during 473 to 1023 K (200 to 750°C) ramps at rates of 2 or 5.6 K/min. The different peak shapes reflecting this process were deconvoluted to show that they are composites of only 2 or 3 reproducible processes. The activation energies and pre-exponential terms were evaluated. The different behavior originates in the differences anmng different surface sites for adsorption. The interpretation of higher temperature peaks (above 873 K (650°C)) must still consider the possibility of contributions from interactions with the steel walls.

PROGRESS AND STATUS

Introduction

Recent work has shown that multiple desorption processes contribute to the evolution of $H_2O(g)$ from ceramic oxides that are candidates for tritium breeders in fusion reactors.[1] These processes differ in several respects: the type of desorption, whether chemisorption or physisorption, and the different degrees of coverage by OH- groups on the various types of surface sites from which desorption occurs. The distinctions in sites involve defects, impurities, and differences in the physical-chemical nature of ions on different crystallographic planes exposed to the gas phase. It is possible to regard these sites, with various activation energies of desorption, as kinds of surface "traps" for tritium.

It is important to have accurate, independently measured values of activation energies for the constituent processes so that the data for tritium release from complex irradiation tests can be interpreted properly. If the species released from the surface in irradiation tests can be considered to be dominantly in the oxidized form (HTO or T_2O), measurements of the activation energy for desorption of $H_2O(g)$ are especially important for the application of tritium release models. The appearance of HT is often ascribable to post-release interactions of $HTO(g)$ with the metallic walls or exchange with H_2. A useful experimental technique for measuring desorption activation energies, as well as other kinetic data like the reaction order and the preexponential terms in the rate equations, is temperature programmed desorption (TPD).[2]

TPD measurements have been made for some limited conditions to provide data that describe the kinetics of desorption of $H_2O(g)$ and $H_2(g)$ from $LiAlO_2(s)$. Complexity in the adsorption of $H_2O(g)$, in the form of differently activated adsorption processes, has already been revealed.3 However, the apparent ability of H_2 in the gas stream to enhance the rate of release of tritium in various tests of breeder performance under irradiation conditions makes it important to understand the interaction of both, H2O and H_2, with the breeder substrate. (Under some conditions, the possibility for interactions with the tube walls also needs to be considered.[4]) This information can then be used to define the optimum purge gas chemistry for a balance between the amount of H_2 added as a tritium release promoter to the helium purge gas and the amount of protium that must be separated from tritium in processing the recovery stream. With its focus on $H_2O(g)$, this study, emphasizing the kinetics of desorption, a non-equilibrium process, complements the earlier study[3] on adsorption isotherms, which relates to surface inventory at equilibrium.

Experimental

A quadrupole mass spectrometer was used for the continuous detection of gaseous species, H_2O, H_2, O_2, and N_2. In addition, the H_2O level in the gas stream was monitored with an electrolytic moisture analyzer. The mass spectrometric data were recorded and processed digitally. The gas-carrying lines of the all-stainless-steel apparatus were heated to minimize holdup of $H_2O(g)$. High-temperature chromatographic valves enabled gas streams to be changed very quickly with a sharp concentration profile. A prograimnable temperature controller provided linear heating rates.

This work supported by the U.S. Department of Energy, Office of Fusion Enerav. under contract no. W-31-109-Ena-38.

The thermocouple measuring the temperature was immersed directly in the ceramic sample, which weighed 0.52 g. The γ-$LiAlO_2$ sample was from a batch prepared at CEN, Saclay. France, for the EXOTIC V experiment.5 The specific surface area was 6.6 m^2/g and the mean grain diameter was 0.28 or 0.35 μm, depending on whether it is calculated from the porosity and the pore radius or from the surface area and density. In its preparation it had been sintered at 1373 K (1100°C), and before being bottled for the present study it was heated at 1073 K (800°C) for 1 hr.

After a preliminary drying, six TPD runs (Table 1 and Figures 1 through 6) were performed with temperature ramps from 473 to 1023 K (200 to 750°C); for 5 of the 6 runs, the ramp rate was 5.6 K/min; for one (number 5) it was 2.0 K/min. Between runs, the sample was kept at 673 K (400°C), while a stream of helium with 990 ppm H_2 passed through it. This soaking period ranged from 20 hours to 264 hours: the duration for each run is indicated in the caption for each figure. Just before starting a run, the temperature was reduced quickly to 473 K (200°C) while maintaining the flow of helium-990 ppm H_2. Then the gas was switched to pure helium if a desorption into pure helium was planned (runs 1 and 2) or the flow of helium-990 ppm H_2 was maintained for desorptions into H_2-containing sweep gas. The tqerature ramp was started at 473 K (200°C) 5 minutes later.

Table 1. Kinetic Parameters
First Order Desorption of H_2O
from A, B, and C sites on $LiAlO_2$

			Sweep Gas: Helium			
Run No.	ν_A	E_{dA}	ν_B	E_{dB}	ν_C	E_{dC}
1	0.090	17.8	0.28	23.0		
2	0.072	17.5	0.28	23.0		
			Sweep Gas: Helium + 990 ppm H_2			
Run No.	ν_A	E_{dA}	ν_B	E_{dB}	ν_C	E_{dC}
3	0.078	17.0	0.39	22.9	1.74	28.5
4	0.017	15.7	0.13	23.0		
5	0.025	16.3	0.20	22.7	0.62	27.5
6	0.022	16.0	0.15	22.6		

Results and Discussion

For desorption into pure helium, runs 1 and 2, the H_2 trace remained at essentially the baseline level until a temperature of approximately 873 K (600°C) was reached. This result suggests that the amount of H_2 absorbed at 673 K (400°C) in the period before the run is small or negligible, or incapable of being desorbed. The rise in evolved H_2 at higher temperature is most likely the result of interaction of the evolved H_2O with the stainless steel tube wall, as shown by earlier work, and/or the evolution of H_2 dissolved in the steel during the pretreatment with H_2.

The spectra were deconvoluted, using Lotus 1-2-3 software, with the finding that they are the sums of 2 (in four cases) or 3 (in two cases) sub-peaks. The sub-peaks are identified as the A, B, and C peaks and are taken to correspond to desorption processes involving three different types of sites on the surface of the $LiAlO_2$, designated as types A, B, and C. The overall rate of desorption of $H_2O(g)$ expressed by the measured curves and comprised of the sum of desorption from the individual types of sites identified by subscript i for the A, B, and C sites is given by:

$$r = \Sigma \nu_i \theta_i \exp(-E_{di}/RT)$$

This is the functional form used in the deconvolution. θ_i is the individual fractional surface coverage for each of the types of sites at a given moment.6 Total fractional coverage is $\theta_T = \Sigma\theta_i$. The preexponential term, ν_i, is in units of mol/min-m^2 where m^2 refers to total BET surface area. The activation energy for desorption, E_{di} is in units of kcal/mol. The sub-peaks are for first order desorption. Attempts to reproduce the curves as a mixture of first and second order or as completely second order processes did not yield as good fits to the data. The θ values for the A, B, and C peaks were in the range of approximately 0.01 and 0.02.

In comparing the A and B peaks with and without H_2 in the sweep gas. one sees that the B peak is substantially smaller than the A peak in the absence of H_2 (Figures 1 and 2) but comparable to or larger than the A peak in the presence of H_2 (Figures 3-6). In the absence of H_2, the B peak contributes to the overall curve as a shoulder, whereas in the presence of H_2 it is a distinct second or dominant peak. The frequently reported enhancement of tritium release attending the use of H_2 in the sweep gas might be related, therefore, to enhanced population of B sites and to the emerging participation of C sites which apparently were not involved in the runs without H_2. It is also apparent from Table 1 that the activation energies and pre-exponential terms for a given type of site are reproducible, showing that the seemingly disparate TPD spectra are unified in reflecting mixtures of common processes.

As far as the numerical values for these kinetic parameters for the A and B sites are concerned, the effect of 990 ppm H_2 in the sweep gas is small. There appears to be a small decrease in the activation energy for the A sites in the presence of 990 ppm H_2, but this is compensated by by a small decrease in the pre-exponential term. Considering that the conditioning of the $LiAlO_2$ with H_2 was at a relatively low temperature in the context of operation of solid breeders, 673 K (400°C), the small effect of the H_2 addition observed here is consistent with the results from tritium residence time measurements in at least two release experiments. In the TEQUILA experiment,[7] the tritium residence times in 0.15 μm grain size $LiAlO_2$ were equal at approximately 750 K (477°C) for helium gas purges containing either 1% or 0.1% H_2, or a mixture of 50 vppm H_2 and 100 vppm H_2O. That is, there was no effect from the H_2 additions at this temperature. However, the additions to the purge gas became increasingly effective at higher temperatures. A similar conclusion was reported in the study by Tanaka et a1.[8] on the residence times for tritium release from $LiAlO_2$. They found that the residence time was shortened by a factor of 6.8 at 973 K (700°C) and by a factor of only 3.8 at 803 K (530°C) when the H_2 concentration in the sweep gas was changed from 10 ppm to 1000 ppm. These result suggest that smaller effects would be expected at lower temperatures, e.g., 673 K (400°C).

Comparison of Figures 3, 4, and 6, for which the ramp rate was constant and for which the duration of pretreatment with 990 ppm H_2O increased monotonically, reveals a trend for increasing amplitude of the A and B peaks as duration of pretreatment increased. This suggests that the buildup of surface OH- was time dependent and aided by the H_2. It also suggests the process is slow because the pretreatment periods were of the order of days. It appears reasonable that at higher temperature the buildup processes would be faster; future work should inquire into whether the peaks increase in amplitude for higher pretreatment temperatures.

Observation of first order kinetics deserves consideration in view of the generally accepted proposition that desorption of H_2O which is chemisorbed as OH-, even in the presence of H_2.[8] The observation of first order kinetics for a bimolecular process can be understood in terms of a theory originated by Lindeman.[10] If the surface is represented by s and the surface-bonded OH- groups are s - OH and the transition state is s - H_2O*, then the stepwise process can be visualized as the bimolecular step:

$$s - OH + s - OH \rightleftharpoons s - H_2O^* + s - O$$

with rate constants k_2 to the right and k_{-2} to the left followed by the unimolecular step:

$$s - H_2O^* \rightarrow H_2O(g) + s$$

with rate constant k_1. Development of the Lindeman theory lead to the final expression,

$$\frac{d[H_2O(g)]}{dt} = \frac{k_1 k_2 [s - OH]^2}{k_{-2}[s - OH] + k_1}$$

If $k_{-2} \gg k_1$, then

$$\frac{d[H_2O(g)]}{dt} \approx \frac{k_1 k_2 [s - OH]}{k_{-2}}$$

which is a first order expression relating to a bimolecular process and provides the conceptual rationale for the observations of first order kinetics. The condition $k_{-2} \gg k_1$ implies that the reversal of the bimolecular step is faster than the evolution of $H_2O(g)$, and that increasing the concentration of s - OH, will increase the evolution of $H_2O(g)$ according to the rate equation. Higher temperatures could alter the relationship between the rate constants so that if $k \gg k_2$ the observed kinetics would become second order, though the total mechanism would still involve a bimolecular step followed by a unimolecular one. This point needs further study.

It was indicated earlier[9] that formation of surface OH- together with F^+ centers can result from adsorption of H_2. Surface space charge layer effects attending H_2 adsorption were also discussed as contributors to increased surface OH- concentrations.

Even if apparently only weakly adsorbed, H_2 can still be understood to be sufficiently present and active on the surface from the following consideration. The rate of impingement of H_2 molecules on the surface at 820 K from a gas with 990 ppm H_2 is, from kinetic theory calculations, 6.4×10^{20} molecules-cm^{-2}-sec^{-1}. By comparison, the rate of evolution of H_2O at one of the peak heights is of the order of 8×10^{9} molecules-cm^{-2}-sec^{-1}. Therefore, the H_2 impingement rate exceeds the H_2O departure rate by a factor of approximately 10^{11}. This implies that even if H_2 is weakly adsorbed, and implying brief residence times on the surface, the high impingement rate can compensate.

In interpreting the C peaks, it is still uncertain whether the $H_2O(g)$ released at these higher temperatures reflects only desorption from the surface, or whether diffusion from the bulk is increasingly augmenting the surface OH- concentration, or if there are interactions between H_2 and the steel surface. These questions require further study. When it appeared, evolution from the C sites was comparable in magnitude to the evolution from the A and B sites. Possibly, the soaking temperature of 673 K (400°C) was only marginally adequate to activate chemisorption of H_2 to populate the C sites.

The 28 kcal/mol value for the activation energy for the C peaks is close to the 29.5 kcal/mol reported by Kudo for the activation energy of decomposition of LiOH, a process of $H_2O(g)$ evolution.[11] In Kudo's case, the decomposing LiOH produced a Li_2O surface with scattered OH- groups. The apparent similarity between the two cases suggests that the C sites on $LiAlO_2$ resemble sites on Li_2O in their H_2O-evolving behavior, but there remains also the question of possible steel surface effects in the work with LiOH.

FUTURE WORK

The next phase of TPD measurements will center on Li_2O in order to provide data that are of current interest for ITER blanket designs.

REFERENCES

1. J. P. KOPASZ, A. K. FISCHER, and C. E. JOHNSON, Proceedings of the Second International Symposium on the Fabrication and Properties of Lithium Ceramics (American Ceramic Society, Indianapolis, April 1989), in press.

2. J. L. FALCONER and J. A. SCHWARTZ, "Temperature Programmed Desorption and Reaction: Applications to Supported Catalysts," Catal. Rev. - Sci. Eng., 25, 141 (1983).

3. A. K. FISCHER and C. E. JOHNSON, "Measurements of Adsorption in the $LiAlO_2$-$H_2O(g)$ System," Fusion Tech. 15, 1212 (1989).

4. A. K. FISCHER and C. E. JOHNSON, "Desorption of H_2O and H_2 from Steel and $LiAlO_2$ by Temperature Programmed Desorption," J. Nucl. Mater. 176, in press (1990) and "Desorption Characteristics of the $LiAlO_2$-H_2-H_2O System, Fusion Reactor Materials Semiannual Progress Report for Period Ending March 31, 1990, DOE/ER-0313/8, 286 (1990).

5. H. KWAST, R. CONRAD, L. DEBARBERIS, A. J. FLIPOT, P. KENNEDY, and J. D. ELEN, "Tritium Release from the Various Solid Breeder Materials Irradiated in EXOTIC Experiments, 1, 2, and 3," J. Nucl. Mater. 155-157, 558 (1988).

6. D. O. HAYWARD and B. M. W. TRAPNELL, "Chemisorption," 2nd edition, Butterworths, 1984, Chapter IV.

7. M. BRIEC, J. KOPASZ, S. CASAOIO, and H. WERLE, "In-Pile Tritium Release from Lithium Ceramics and Influence of Surface Processes," Proceedings of the September 1990 SOFT Meeting, in press.

8. S. TANAKA, A. KAWAMOTO, M. YAMAWAKI, T. TERAI, Y. TAKAHASHI, H. KAWAMURA, and M. SAITO, 'In-Situ Tritium Release Experiments from Solid Breeding Materials (TTTEx) - Tritium Diffusion Coefficients and Surface Reaction on Lithium Aluminate," Fus Eng. Des. 8, 155 (1989).

9. A. K. FISCHER and C. E. JOHNSON, "Tritons and Tritides as the Solute and Diffusing Species in Ceramic Tritium Breeders," Proceedings on Fabrication and Properties of Lithium Ceramics', American Ceramic Society, Pittsburgh, 1987, Advances in Ceramics, 25, 29 (1989).

10. W. J. MOORE, "Physical Chemistry,' 3rd ed., Prentice-Hall, 1962, p. 278.

11. H. KUDO, "Rates of Thermal Decomposition of LiOH(s), LiOD(s), and LiOT(s)," J. Nucl. Mater. 87, 185 (1979).

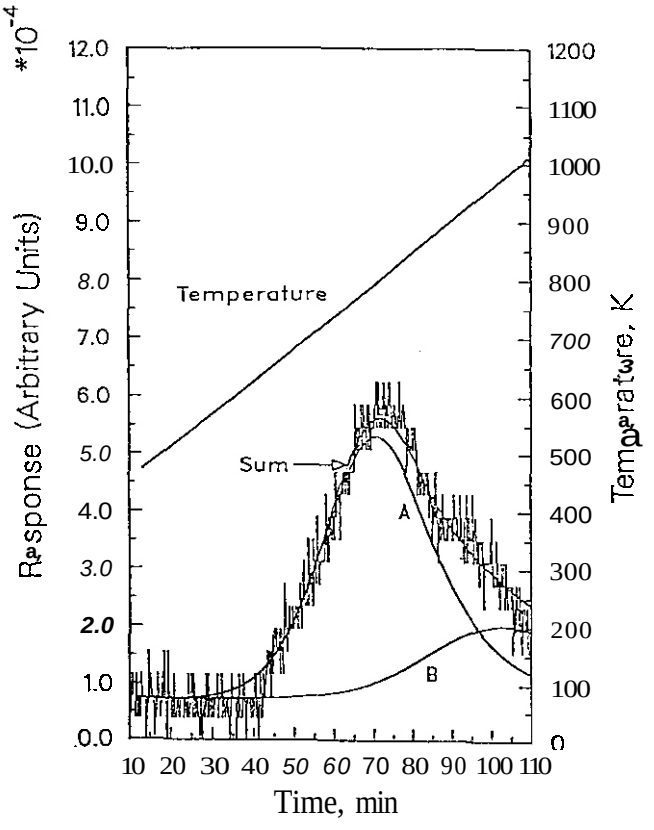

Fig. 1. Desorption of H_2O into pure helium after 264 hours pretreatment with 990 ppm H_2 in helium at 673 K. Ramp rate is 5.6 K/min.

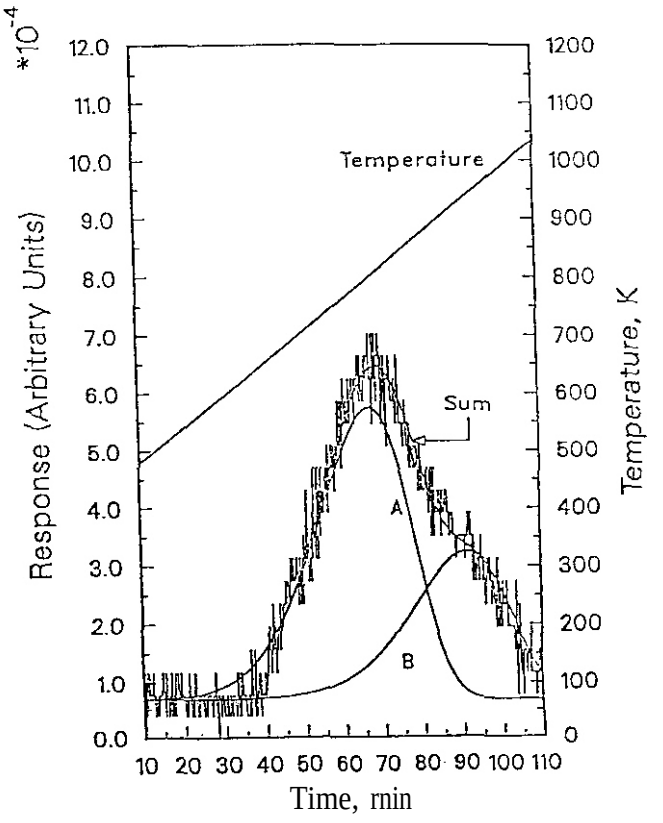

Fig. 2. Desorption as in Fig. 1, but after 120 hours pretreatment.

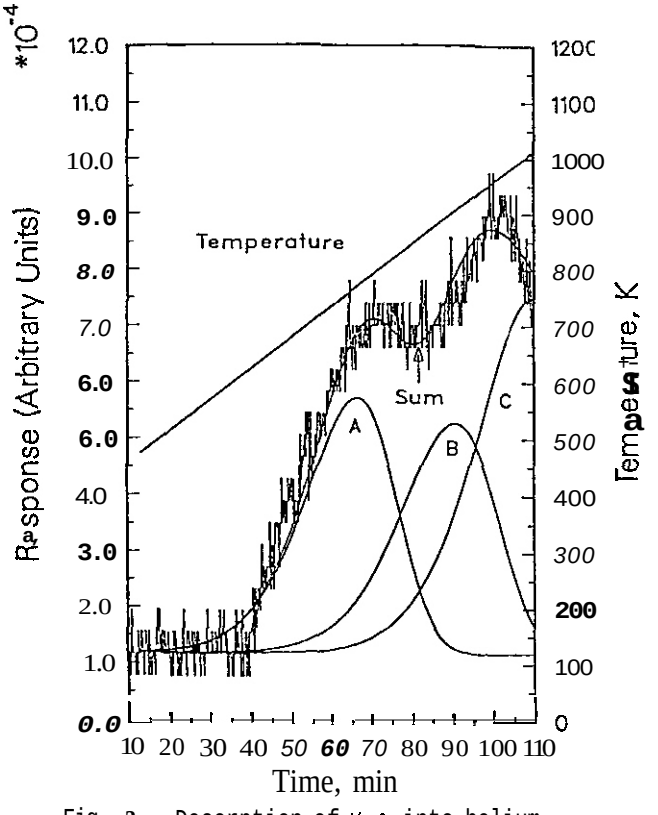

Fig. 3. Desorption of H_2O into helium containing 990 ppm H_2 after 20 hours pretreatment with 990 ppm H_2 in helium at 673 K. Ramp rate is 5.6 K/min.

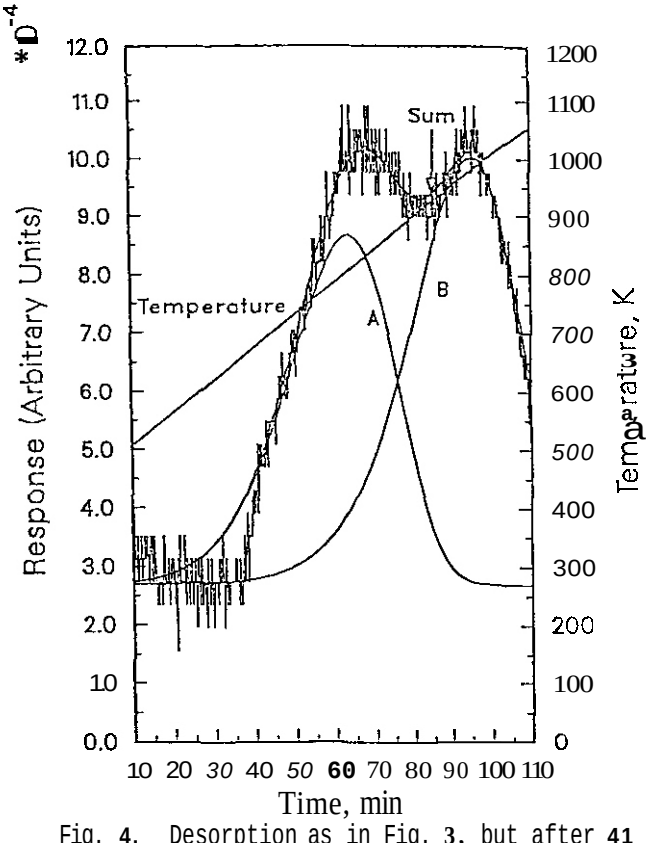

Fig. 4. Desorption as in Fig. 3, but after 41 hours preptreatment.

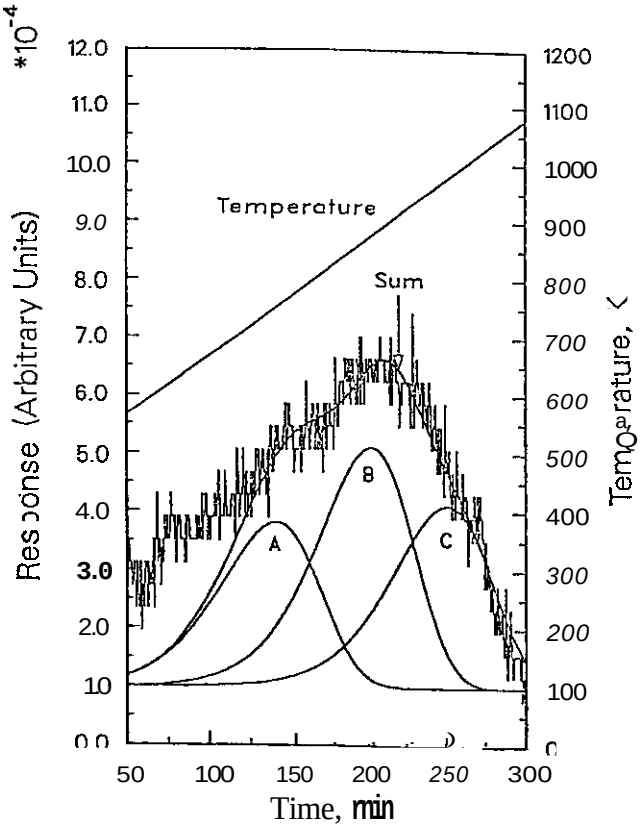

Fig. 5. Desorption as in Fig. 3, but after 66 hours pretreatment. Ramp rate is 2.0 K/min.

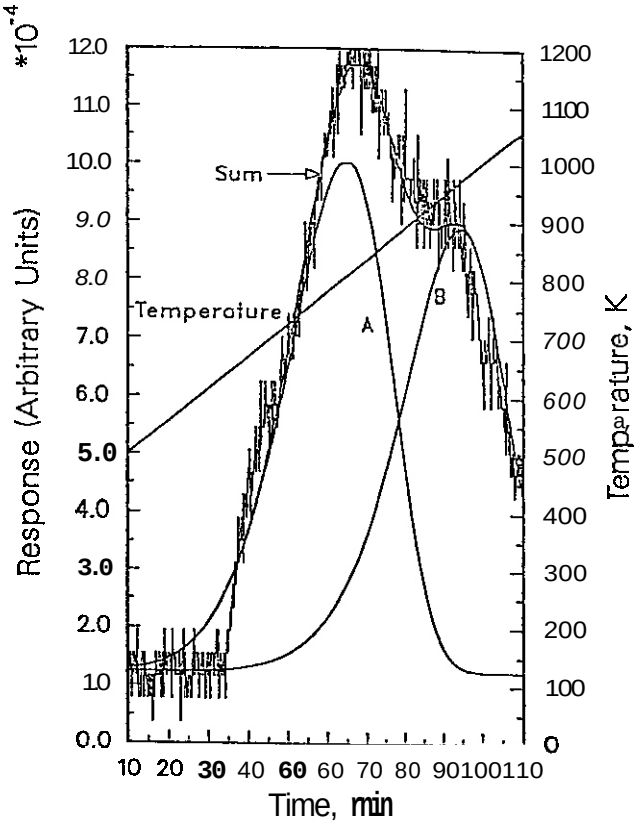

Fig. 6. Desorption as in Fig. 3, but after 210 hours pretreatment. Ramp rate is 5.6 K/min.

TRITIUM RELEASE FROM LITHIUM CERAMICS

J. P. Kopasz (Argonne National Laboratory), M. Briec (CEA/CEN Grenoble. France), S. Casadio (ENEA/CRE, Cassaccia. Italy), and H. Werle (Karlsruhe, Germany)

OBJECTIVE

The objective of this effort was to improve the current understanding of tritium transport in ceramic breeder materials and to assist CEA staff (Saclay, France) in analysis of their in-situ tritium recovery experiments.

SUMMARY

Recent in-pile tritium extraction experiments from lithium ceramics have investigated the effects of temperature, material microstructure, purge gas composition, and tritium generation rate on the kinetics of tritium release. The relationship between the tritium release characteristics and sample microstructure indicates desorption is the dominant mechanism controlling tritium release for the conditions investigated. Literature results indicate that this desorption step may be second order and the activation energy of desorption may vary significantly with surface coverage. The changes in inventory with variations in the key parameters mentioned above were investigated to determine the applicability of these reports to in-pile tritium release. The results suggest tritium release is first order, and that the desorption activation energy is dependent on the surface coverage.

PROGRESS AND STATUS

Introduction

A large amount of data are available for in-pile tritium recovery experiments which have investigated the effects of the generation rate, sample microstructure, purge gas composition and temperature on tritium release. The results have led to a qualitative understanding of the dependence of tritium inventory and release on these factors: however, a detailed interpretation of the results leading to an understanding of the rate controlling mechanisms is not always straightforward. One model which has been widely used to interpret the results is the diffusion-desorption model.[1] This model treats the desorption as pseudo first order in tritium and generally considers the desorption occurring with one activation energy. Other work has suggested that the desorption step is second order in tritium or that the desorption may be occurring with different activation energies.[2] Using data from experiments carried out at the Centre d'Etudes Nucléaires de Grenoble we have examined the effects of the key parameters mentioned above on tritium release and inventory and have compared the magnitude of these effects with those predicted from various tritium release models.

Key Parameters Affecting Tritium Release

The tritium release kinetics are dependent on the tritium generation rate, temperature, microstructure of the ceramic, and composition of the purge gas. The tritium residence time (defined here as the ratio of the tritium inventory to the tritium generation rate) is a convenient indicator of the release kinetics. The tritium residence time should be independent of the generation rate if a diffusion or first order desorption mechanism is the rate controlling step while the tritium residence time will be dependent on the generation rate if a second order desorption mechanism is rate controlling.

The sample microstructure is a crucial factor affecting tritium release kinetics. For a diffusion mechanism the tritium residence time is given by:

$$t = a^2/15D \qquad (1)$$

and the inventory increases as the square of the grain radius. For a desorption mechanism, the residence time is given by the sample volume divided by the product of the surface area times the desorption rate constant. For a sphere, this leads to:

$$t = a/3h \qquad (2)$$

For other geometries an effective radius a', defined as three times the ratio of the sample volume to the specific surface area, can be used to calculate the residence time. The residence time will be proportional to this effective radius if desorption is the rate controlling mechanism.

The composition of the purge gas has been demonstrated to have a substantial effect on the tritium residence time. It is obvious that the surface processes are influenced by the purge gas chemistry. However, the bulk properties may also be affected by the purge gas. For example, water addition to the purge gas may be expected to increase the desorption of tritium from the surface. Addition of water in the purge gas may also lead to a hydrogen concentration in the bulk which exceeds the solubility limit, causing the precipitation of a second phase of LiOH/LiOT, thereby changing the bulk properties including diffusivity (this is likely to occur for Li_2O at temperatures below 450°C where the hydrogen solubility is low).

RESULTS AND DISCUSSION

Effect of Generation Rate

In an effort to clarify the order of the desorption reaction, tests were performed with different thermal neutron fluxes and, consequently, different tritium generation rates. For a desorption mechanism which is first order in tritium, the tritium residence time will be independent of the aeneration rate while for a desorption mechanism which is second order in tritium, the tritium residence time will be inversely proportional to the square root of the generation rate. Transient tenperature changes were performed on Li_4SiO_4 samples with He + 0.1% H_2 as the purge gas for two thermal neutron fluxes, 0.4 and **0.93** x 10^{17} nlm^2s. The tritium residence times obtained are shown in table 1. The values at a given temperature are identical, within the error of the calculations, for the two fluxes, indicating the rate determining step is not second order in tritium. Other factors indicate desorption is rate controlling for these samples, so we can conclude desorption is first order in tritium under these conditions.

Effect of Microstructure

The effect of sample microstructure on tritium inventory was investigated in the TEQUILA experiment. Temperature transient runs were performed on samples of $LiAlO_2$ with different microstructures. Results for experiments with He + 0.1% H_2 purge gas and for two different microstructures are given in table 2. The results indicate that tritium residence time decreases with decreasing grain size. This was also observed in the LILA III[4] experiment.

Table 1. Tritium residence time (in hours) versus thermal neutron flux Li_4SiO_4 sample. He + 0.1% H_2 as purge gas.

neutron flux	temperature	tritium residence time
10^{17} n/m^2s	°C	h
0.93	450	$17.5 < \tau < 27$
	500	$4 < \tau < 4.2$
0.40	450	26.5
	500	4.1

It follows from equation (1) that for diffusion controlled release, the tritium .residence time will increase in proportion to the square root af the grain size which means that a ratio of 600 is expected for the tritium residence times of the two samples with 6 and 0.15 μm grain sizes. The observed ratios, >10.8 at 670°C, >16.3 at 620°C, >26.6 at 560°C and >14.4 at 510°C are much lower, indicating that diffusion is not rate limiting for these temperatures and grain sizes. Likewise if desorption is rate limiting the tritium residence time will increase in proportion to the effective grain radius calculated from the specific surface area which means that a ratio of 13.3 is expected for the tritium residence times of the two samples with 6 and 0.45 μm effective grain radii (a^*). The observed values (see table 1) are of the same order of magnitude as expected for the desorption controlled release, suggesting that desorption is the controlling factor determining tritium residence time for these materials. Any variation from the expected ratios suggests other processes may be playing a minor role in determining the tritium residence time.

Table 2. Effect of microstructure on tritium residence time.

grain size a μm	a* calc. from spec. surf. area μm	Temperature ^oC	Tritium residence time, τ	τ/τ a = 0.15
0.15	0.45	670	0.95	1
6	6		> 10.3	> 10.8
0.15	0.45	620	1.3	1
6	6		> 21.2	> 16.3
0. 15	0.45	560	3.9	1
6	6		>103.8	> 26.6
0.15	0.45	510	9.7	1
6	6		>140.2	> 14.4

Effect of Purge Gas Composition

It is obvious that the surface processes (desorption of tritium or tritiated water) are influenced by the purge gas chemistry. It has been shown repeatedly that addition of hydrogen to the purge gas improves the tritium release rate.[4,5] It seems reasonable to assume that water addition will also improve the tritium release rate.

In the TEQUILA experiment, three purge gas compositions were investigated: He + 0.1% H_2, He + 1.0% H and He + 50 vppm H_2 + 100 vppm H_2O. The results for samples with grain radius of 0.15 pm are iflustrated in figure 1 as plots of the natural log of tritium residence time versus the inverse temperature.

The tritium residence times obtained in TEQUILA indicate that for small grain radius samples, tritium release is better for a purge gas containing 1.0% H_2 than for one containing 0.1% H_2. This conclusion is supported by the tritium release observed for a change in purge gas from He t 0.1% H_2 to He + 1.0% H_2 which shows a decrease in tritium inventory. The TEQUILA results also indicate that tritium release was better for a purge of He + 0.1% H_2 than for He + 50 vppm H_2 + 100 vppm H_2O at high temperatures (> 510^{o}C), while at low temperatures (460^{o}C) release was better for the purge gas containing water than for those without water.

In TEQUILA, for small grain samples, the desorption activation energies were the same for purge gases of He + 0.1% H_2 and He + 1.0% H_2 (within the experimental errors), while the desorption activation energy for He + 50 vppm H_2 + 100 vppm H_2O was substantially lower. This observation suggests that the activation energy may be dependent on the hydrogen (OH groups) surface coverage. The degree of hydrogen gas adsorption on $LiAlO_2$ is certainly less than that for water, and therefore it is not surprising that the desorption activation energy is smaller when water is added to the purge gas. In addition, since H_2 adsorption is expected to be dissociative, the hydrogen surface coverage would be expected to vary as the square root of the hydrogen pressure. This suggests the hydrogen surface coverage for He + 1%H_2 is of the same order of magnitude as for He + 0.1% H_2 and therefore one would expect the desorption activation energies to be similar.

Effect of Temperature

The effect of temperature was investigated by performing temperature transient tests. Generally the tritium inventory and tritium time constant decreases with increasing temperature. The tritium time constants, however, exhibit an interesting phenomenon. In some cases the time constant (defined as the tine for a temperature transient peak to decay to 35% of its maximum value) determined for a temperature increase from temperature T1 to temperature T is different than the time constant determined for a temperature decrease from temperature T2 to the same final temperature (table 3, TEQUILA experiment).

For a pure first order desorption process or a pure diffusion process, the time constant is independent of the previous temperatures while for a second order desorption process the time constant will depend on the previous temperature. In the case of mixed diffusion-desorption the mathematics are less straight forward and it is not obvious whether the time constant are dependent on or independent of the previous conditions. To solve this problem, calculations were performed using the DISPL Code6 for diffusion with a first order desorption boundary condition in spherical geometry. The results indicate that in the mixed diffusion-desorption regime the time constant

Table 3. Time constants of tritium release: dependence on temperature history gamma-$LiAlO_2$ samples. He + 0.1% H_2 as purge gas

grain size μm	temperature °C	previous temperature °C	time constant h
12	620	670	10.75
		570	5.5
bimodal 0.2-5		670	11
		570	3.7

is dependent on the previous conditions, but as the ratio ah/D increases toward diffusion controlled release or decreases toward desorption controlled release, this dependence disappears. This suggests tritium release is in the mixed diffusion-desorption regime at the temperature when the time constants for temperature increases and temperature decreases are unequal or desorption is second order in tritium in these cases, however separate tests on Li_4SiO_4 indicate desorption is first order.

CONCLUSION

Tritium extraction experiments performed at CEN Grenoble have determined the effects of tritium generation rate, sample microstructure, purge gas composition and temperature on tritium release from ceramic tritium breeding materials. These results have also provided some insight into the rate limiting mechanism. The relationship between the tritium residence time and the sample microstructure indicate that desorption is the dominant mechanism in tritium release for the conditions investigated. The importance of surface processes is further illustrated by the effect of the purge gas composition on tritium release. The presence of different activation energies for the rate limiting process for the different purge gases indicate that a simple desorption model with a single activation energy is inadequate and a model with multiple desorption activation energies or mechanisms is necessary to account for the variations in inventory with different purge gas compositions.

Some data also suggest a second mechanism contributes to the tritium inventory. Diffusion is the most likely candidate, and a diffusion-desorption model is able to account for the observed differences in time constants for temperature increases and temperature decreases to the same final temperature. An alternative explanation is a second order desorption mechanism which would account for the differences in time constants but separate tests on Li_4SiO_4 have indicated the tritium release is independent of the generation rate, and therefore not second order.

REFERENCES

1. J. Kopasz. S. W. Tam and C. E. Johnson, J. Nucl. Hater. 155-157 (1988) 500.

2. A. K. Fischer and C. E. Johnson, Fusion Technology, 15 (1989) 1212.

3. H. L. Gruber, J. Phys. Chem. 66 (1962) 48.

4. S. Tanaka, T. Terai, H. Mohri and Y. Takahashi. J. Nucl. Hater. 155-157 (1988) 533.

5. M. Briec, J. J. Abassin, C. E. Johnson, M. Masson, N. Roux and H. Watanabe, Fusion Technology, Proc. 15th SOFT (1988) 1105.

6. G. K. Leaf, M. Minkoff, ANL-84-56, Argonne National laboratory (1984).

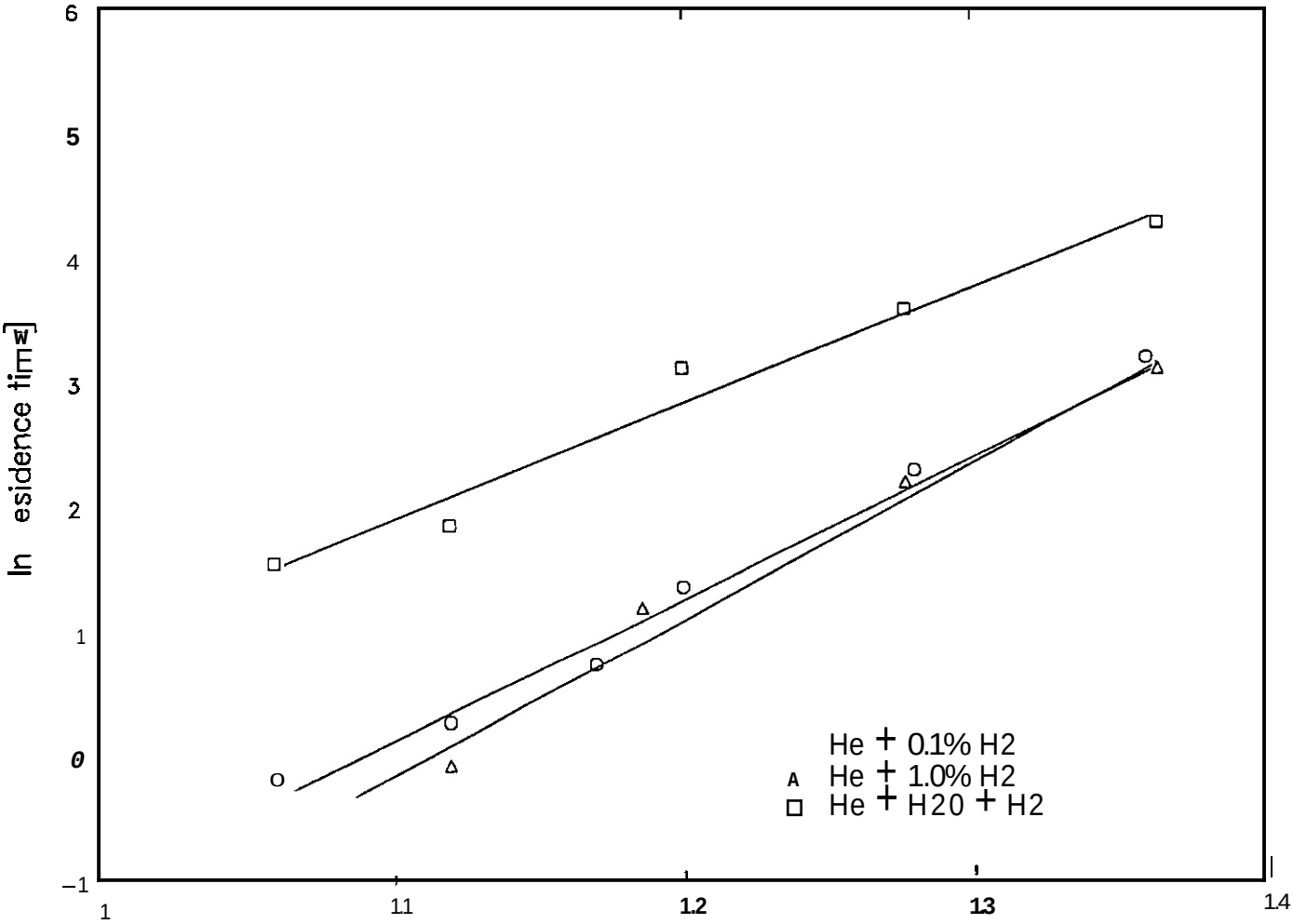
6
5
4
3
2
1
0
−1
1
1.1
1.2
1.3
1.4
ln esidence tim
He + 0.1% H2
He + 1.0% H2
He + H20 + H2

IN-SITU TRITIUM RECOVERY FROM Li_2O IRRADIATED IN FAST NEUTRON FLUX - BEATRIX-II INITIAL RESULTS -

T. Kurasawa, Japan Atomic Energy Research Institute, O. O. Slagle and G. W. Hollenberg, Pacific Northwest Laboratory,[a] R. A. Verrall, AECL Research, Chalk River Laboratories

OBJECTIVE

The purpose of this work is to evaluate the performance of candidate ceramic breeding materials for use in a fusion blanket. This evaluation is specifically aimed at characterizing the behavior of materials in a neutron flux.

SUMMARY

The BEATRIX-II experiment in FFTF is an in-situ tritium recovery experiment to evaluate the tritium release characteristics of Li_2O and its stability under fast neutron irradiation to extended burnups. This experiment includes two specimens: a thin annular ring specimen capable of temperature transients and a larger temperature gradient specimen.

During the first 85 days of the operating cycle of the reactor, the tritium recovery rate of a temperature transient capsule was examined as a function of temperature, gas flow rate, gas composition and burnup. Temperature changes in the range from 500 to 650°C resulted in decreasing tritium inventory with increasing temperature. Lower gas flow rates resulted in slightly lower tritium release rates while gas composition changes affected the tritium release rate significantly, more than either flow rate or temperature changes. Three different sweep gases were used: He-0.1% H_2, He-0.01% H_2, and pure He. Decreasing the amount of hydrogen in the sweep gas decreased the steady-state release rate by as much as a factor of two.

A temperature gradient capsule is more prototypic of the conditions expected in a fusion blanket and was designed to provide data that can be used in evaluating the operational parameters of a solid breeder in a blanket environment. The operation of this canister during the first 85 EFPD cycle suggests that Li_2O is a viable solid breeder material.

PROGRESS AND STATUS

Introduction

BEATRIX-II is an International Atomic Energy (IEA) sponsored irradiation experiment to evaluate the tritium release characteristics of Li_2O and its stability under fast neutron irradiation to extended burnups[1,2]. It is an in-situ tritium release experiment being carried out in the Fast Flux Test Facility (FFTF). The participants in this experiment are the Japan Atomic Energy Research Institute (JAERI), the Atomic Energy of Canada, Ltd. (AECL), and the United States Department of Energy (US/DOE). Results from the first 85 effective full power days (EFPD) of operation are described in this paper.

The experiment includes two capsules containing different Li_2O specimens each with a separate sweep gas and tritium measurement system. One specimen is in the form of a thin annular ring operating at a nearly uniform temperature capable of temperature transients while the other specimen is a solid cylinder of pellets operating under a temperature gradient. A sophisticated tritium gas handling system, that both monitors the release of tritium from the two solid breeder specimens and recovers the tritium in specially designed getter beds,[3] was designed and built.

Experiment Design

The ring specimen was designed to operate in a manner similar to previous tritium recovery experiments, e.g., TRIO,[4] VOM,[5] CRITIC,[6] while the solid specimen provides performance data on Li_2O irradiated in a temperature gradient. Each gas stream is instrumented for continuous monitoring of the flow rate, total moisture, tritium concentration, and the form of the tritium. The total tritium concentration and form of the tritium is determined in a manner similar to the VOM experiment[5] and uses a Ceramic Electrolysis Cell (CEC) to reduce the water vapor.[6] A more complete description of the system is given in References 1 to 3 and the operation of the system is described in Reference 3.

The specimen description and the irradiation conditions are given in Table 1. The ring specimen has a wall thickness of 0.16 cm with thermocouples located at the inner and outer surfaces. During irradiation, the temperature difference across this specimen is 40°C. The temperature of the ring specimen is controlled by changing the type of gas in the thermal gap of the canister.[1,2] Temperature transients imposed on the specimen occur in times less than 15 seconds. The solid specimen is not temperature controlled and has an edge temperature of 450°C and a center temperature of 1000°C. Although the outer dimensions are nearly the same, the solid specimen is a factor of 2.9 larger by weight. Both specimens are exposed to similar levels

Table 1

Materials and Environmental Conditions for BEATRIX-II

Specimen Characteristics	Ring	Solid
Length (cm)	8.90	8.92
Outer dia. (cm)	1.84	1.70
Inner dia. (cm)	1.51	0.27
Weight (g)	11.95	34.31
Density (%TD)	79.3	84.5-92.6
Grain Size (microns)	5.5	46
^6Li (at %)	61	61
Temperature (°C)		
Center	540-640	1000
Edge	500-600	450
Tritium Generation Rate (10^{-6} Ci/s)		
Calculated	47	124
Measured	58	143
Total Generation:		
300 EFPD (Ci)	1500	3700

of neutron flux in the Materials Open Test Assembly (MOTA). Because of the weight difference, the solid specimen generates 150% more tritium during irradiation. The goal burnup for a 300 EFPD irradiation is 4% of the total lithium far bath specimens.

Exoerimental Test Plan

This paper describes the first series of experiments carried out during a recent operational cycle equivalent to 85 EFPO. The first part of the irradiation was devoted to conditioning the specimens and adjusting the instrument parameters to optimize the data. The reference condition was selected to be an inner thermocouple reading of 6502, a sweep gas of He-0.1 $\%H_2$, and a flow rate of 100 mL/min. This corresponds to a specimen outer surface temperature of 600°C and an inner surface temperature of 640°C. The inner thermocouple temperature is used to designate the temperature of the ring specimen.

The tritium recovery rate from the temperature transient capsule was examined as a function of temperature, gas flow rate, gas composition, and burnup. The first series of tests, designed to determine the effect of temperature transients and sweep gas flow rates on the tritium recovery rates, is described in Table 2. Runs 1 to 6 and 14 to 20 are a series of temperature transients between 650, 600, and 550°C to characterize the temperature dependence at reference flow and gas composition. In Runs 6 to 14, the effect of 50, 100 and 200 mL/min sweep gas flow rates and temperature transients between 550 and 650°C at 50 and 200 mL/min were investigated. A series of runs to characterize the effect of gas composition and burnup is given in Table 3. In Runs 21 to 33 the sweep gas composition was varied along with the temperature. Three different sweep gases were used: He-0.1% H; He-0.01% H_2, and pure He. Runs 33 to 38 are a series of temperature transients with the reference sweep gas that will be repeated later in the experiment to determine the effect of burnuo.

RESULTS AND DISCUSSION

A primary purpose of this experiment, and vented-tests in general, is to determine the viable operating parameters of a solid breeder blanket and the associated tritium inventories. To date, no attempt has been made to determine tritium inventories for the Li_2O in this 85 EFPD cycle of the experiment, but observations of steady-state tritium recovery rates and the shape of recovery peaks permit general comments.

In general, an indication of "acceptable" operating conditions can be defined if steady-state tritium recovery is established within a reasonable amount of time, such as one day after a change in a specific operating parameter. A "true" steady-state recovery rate implies that the recovery rate is equal to the tritium generation rate in the ceramic. However, under many experimental conditions the "apparent" steady-state recovery rate is not the generation rate. In these circumstances, the tritium inventory is steadily increasing (or decreasing). Given a sufficiently long time, the "apparent" steady-state recovery rate should approach the true steady-state release rate, i.e., the generation rate. The results obtained to date, in many cases, relate to "apparent" steady-state recovery rates and the critical questions as to the time for establishing true steady-state release rates and the equilibrium inventory have not yet been determined for these experimental results.

Table 2

Experimental Test Plan for the Ring Specimen to Determine the Effect of Temperature Changes and Flow Rate Using He-0.1%H_2 Sweep Gas

	Temperatures °C			Flow Rate (mL/min)		
Run ID	550	600	650	50	100	200
1			X		X	
2	X				X	
3			X		X	
4	X				X	
5		X			X	
6			X		X	
7			X			X
8	X					X
9			X			X
10			X		X	
11			X	X		
12	X			X		
13			X	X		
14			X		X	
15		X			X	
16	X				X	
17		X			X	
18			X		X	
19	X				X	
20			X		X	

generation rate. In these circumstances, the tritium inventory is steadily increasing (or decreasing). Given a sufficiently long time, the "apparent" steady-state recovery rate should approach the true steady-state release rate, i.e., the generation rate. The results obtained to date, in many cases, relate to "apparent" steady-state recovery rates and the critical questions as to the time for establishing true steady-state release rates and the equilibrium inventory have not yet been determined for these experimental results.

TemDerature Change Effects

Typical tritium recovery peaks associated with temperature transient tests performed in He-0.1% H_2 sweep gas are shown in Figure 1. In agreement with results from other in-situ tests,[6] temperature increases result in recovery peaks associated with decreasing the tritium inventory of the specimen; the opposite occurs for temperature decreases. The double recovery peaks, associated with the temperature increase tests (Run 3 in figure 1), are not generally seen in other in-reactor tests but are typical for this experiment. Also noteworthy is the variation in the apparent tritium recovery rate following the transients and the relatively small peak sizes relative to steady-state recovery (less than 10%). The very small tritium recovery peaks associated with the temperature change tests in He-0.1%H_2 sweep gas indicate that the tritium inventory is very small under these conditions.

Temperature changes performed during the initial phases of the system conditioning and parameter adjustment (not shown) produced small "reverse" tritium recovery peaks preceding the normal peaks. That is, for a temperature decrease, there was initially a small increase in the tritium concentration prior to the normal decrease. These "reverse peaks" occurred when the specimen was taken to temperatures higher than previous exposure. Subsequent tests performed at the same or lower temperatures did not result in the small reverse peaks. For this reason, these peaks appear to be related to specimen conditioning. Reverse peaks were also observed in CRITIC-I.[6]

Form of the Released Tritium

The tritium recovery curves associated with the temperature increases are characterized by an initial sharp peak followed by a broader long term peak. By comparing the difference between the total tritium concentration and the concentration of the elemental tritium, this second broader peak can be correlated with tritiated water recovery. The association of these peaks with water can also be seen by comparing them with curves of sweep gas moisture from the specimen. In Figure 2 the sweep gas moisture for the ring specimen is

Table 3

Experiment Test Plan for the Ring Specimen to Determine the Effect of Gas Composition Changes and Burnup. Sweep gas flow rate is 100 mL/min.

	Temperatures °C			Gas Composition %H_2 in Helium		
Run ID	550	600	650	0	0.01	0.1
21			X			X
22			X		X	
23			X	X		
24		X		X		
25		X				)
26		X			X	
27		X		X		
28		X				)
29	X					)
30	X				X	
31	X			X		
32			X	X		
33			X			)
34		X				)
35	X					)
36			X			)
37	X					X
38			X			X

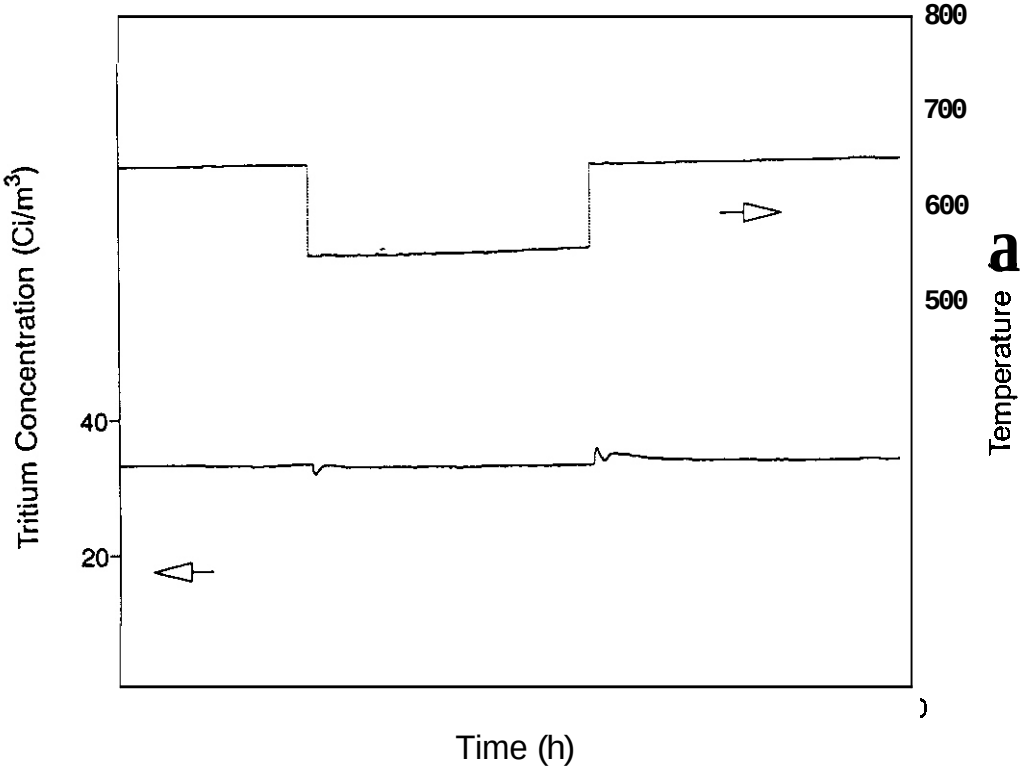

Figure 1. Tritium recovery and temperatures for the series of temperature transients (runs 1-3)

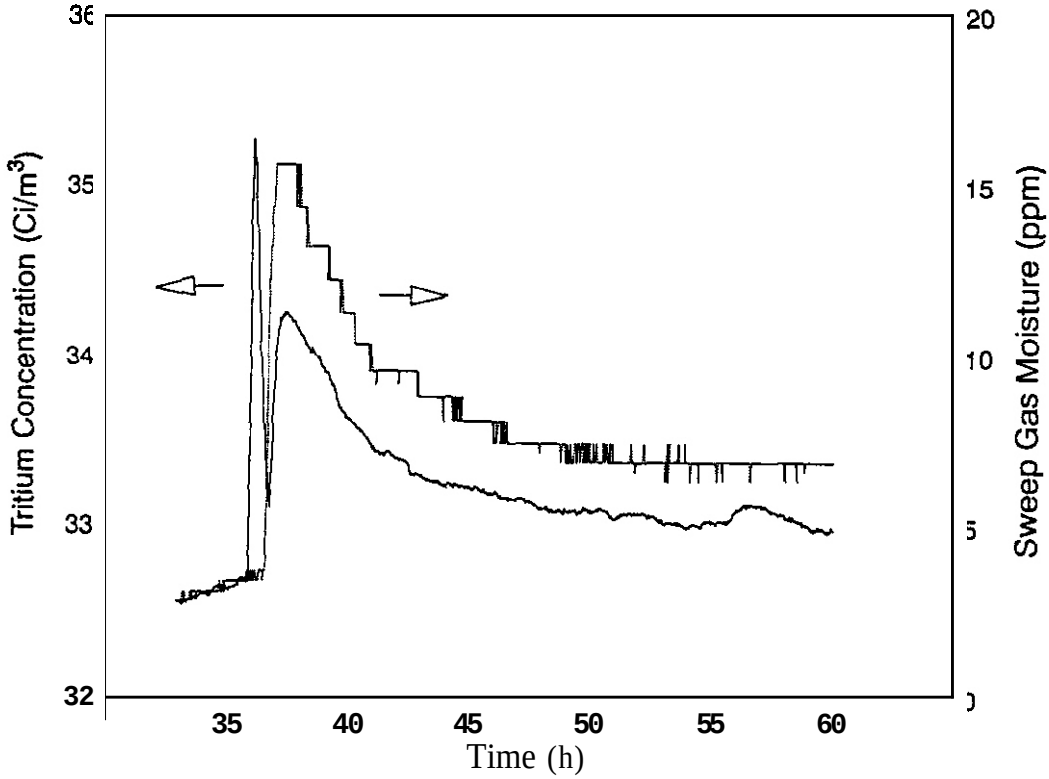

Figure 2. Tritium recovery and sweep gas moisture for temperature transients from 550-650°C (runs 2-3)

compared with the recovered tritium concentration during the thermal transient in Run 3. There is very good correlation between the sweep gas moisture and the secondary peaks in the recovered tritium concentration.

The first sharp peak of tritium recovery after a thermal transient appears to be associated with the change in the recovery rate of elemental tritium. The most likely source of this tritium is the surface of the Li_2O ceramic, but another possible source is the surface of the capsule components which change temperature. More important is the question as to whether this first peak was released from the specimen as elemental tritium or whether it resulted from reduction of the tritiated water by the capsule components.

The separation of the two peaks in Figures 1 and 2 also has several possible explanations. One explanation is that the tritium is released from the specimen both as elemental and as water; the elemental form is released in a short time period following the transient while the water form is released over a longer time period. An alternative explanation for the separation, is that the delay results because of an interaction of the water vapor with the sweep gas lines to give a "drag" or time delay in the movement of the tritiated water from the specimen to the tritium measurement system.

Although the present results do not differentiate between the processes involved in the tritium release from the specimen during the thermal transient, there is reason to believe that both elemental and hydrated tritium are being released from the specimen. For the BEATRIX-II experiment under normal reference conditions, with He-0.1% H_2 sweep gas, 95% of the recovered tritium is in the elemental form. If it is assumed that this is due to a reduction by the capsule components, then because of the small size of the thermal transient tritium recovery peaks relative to the steady-state recovery rate, the thermal transient peaks should also have 95% of the tritiated water reduced to HT and an HTO peak would not be observed. The fact that the total tritium recovered as water after a thermal transient is often larger than the amount recovered as elemental tritium shows that the system is not reducing 95% of the tritiated water to elemental tritium. Therefore, it is reasonable to assume that a significant proportion of the 95% recovered elemental tritium under reference conditions is released in the elemental form. This suggests that for the case of H_2 doped sweep gas, isotopic exchange at the surface of the specimen plays a significant role in the release of tritium from the solid breeder material.

Sweep Gas Composition Effects

Sweep gas composition [the amount of H_2 in the He) has a major effect on the observed steady-state recovery rates, and therefore on the tritium inventories. The test plan included measuring both the effect of changing gas composition at constant temperature and the effect of gas composition on tritium recovery during a thermal transient.

Figure 3 is a plot of the variation in sweep gas tritium concentration for a change in sweep gas composition at 600%. In general, the recovery rate decreases as the H_2 decreases from 0.1 H_2 to 0.01 H_2 to He with transient release peaks observed when the composition is changed from He to 0.1% H. The observed steady-state tritium recovery rate for the different gas compositions at the 550, 600 and 650°C are compared in Table 4. The recovery rates are compared relative to the case of He-0.1% H_2 at 550°C. The recovery rate does not appear to be strongly dependent on temoerature but for a chanae in sweep gas composition varies in the ratio of 1 : 2/3 : 1/2 for 0.1% H_2 : 0.01% H_2 : He. To a smaller extent, this effect was observed in the VOM experiment.[5] In the CRITIC-1 test on Li_2O[6], this effect was not seen directly, but was inferred from a buildup in the tritium inventory over long periods of time using low H_2 concentrations in the sweep gas.

Within experimental error, the steady-state recovery rate established with He-0.1% H_2 is thought to approach the true steady-state. Such observations have potentially important ramifications on acceptable sweep gas compositions in a blanket.

The other type of behavior considered is the effect of gas composition on tritium recovery during a thermal transient. Figure 4 is a comparison of the recovered tritium concentration during a thermal transient from 550°C to 650°C in He versus He-0.1% H. The difference is dramatic, with the initial transient recovery in helium being much larger than that for the case of He-0.1% H. The small recovery peak resulting from temperature change tests in He-0.1%H_2 sweep gas versus that in He indicate that the tritium inventory for He-0.1% H_2 is much smaller than for He at these temperatures. The low apparent steady-state recovery rate using He sweep gas also suggests an increasing tritium inventory. Another way of interpreting this is that an increasing inventory leads to a longer time between generation of the tritium in the ceramic and the release.

The recovery peaks for the temperature transients in He-0.1% H have large secondary tritium concentration peaks typically associated with water release. Also shown in Figure 4 is a comparison of the moisture peaks for the two different sweep gases. The moisture release is approximately 10 times larger for the case of He-0.1% H_2 than for He.

Sweep Gas Flow Rate Effects

The effect of changing sweep gas flow rates (200, 100 and 50 mL/min) on the tritium recovery rates (Ci/s) is shown in Figure 5. The width of the recovery peaks can be expected to increase for lower flow rates because of the delay time for the sweep gas to pass through the system. However, there can also be an effect associated with the time to establish steady-state release rates from the specimen.

The results shown in Figure 5 indicate an apparent difference in the steady-state recovery at the different flow rates. On the left side of the figure, before the flow-rate changes were made, the difference between the maximum and minimum recovery rate is 8%. Recovery rates decrease with decreasing flow rate so that 50 mL/min gave the lowest recovery rate, etc. However, after the flow-rate changes were made, the difference in recovery rates increased to 20%, and were no longer ordered as well as before. At 100 mL/min, two different recovery rates differing by 15% were established in two different tests.

The data indicate that there may be an effect of sweep gas flow rate on recovery rate. However, whether this is related to the dynamical interaction between sweep gas flow rate and the specimen or is due to permeation losses through the cladding cannot be determined at this time. The peculiarities in the peak shape, as well as the reason for the variation in the steady-state release levels, are not well understood at present. Tritium holdup on 30 to 40 m of unheated sweep gas piping may be a contributing factor. Buildup of a background signal on the ion chambers due to tritium contamination is another possibility. Background shifts during the first 85 EFPD of operation have amounted to 9% (3.33 Ci/m^3) of the generation rate for the ring specimen and to 5% (4.27 Ci/m) for the solid specimen.

Solid Specimen

The experiment test plan on the solid specimen has been limited during the first cycle of irradiation. Changes in sweep gas flow rate and gas composition have been carried out, and the tritium recovery characteristics caused by those changes are in agreement with the behavior exhibited by the ring specimen. At the start of the test, the temperature at the center of the solid specimen was approximately 1000°C. During the first cycle, the temperature slowly decreased approximately 20°C. This decrease in temperature is in agreement with the drop in flux expected for this position in the reactor due to fuel burnup and the change in control rod configuration. The important conclusion is that under the current operating conditions no gross changes are indicated that would limit the use of Li_2O as a tritium breeder in a fusion blanket application.

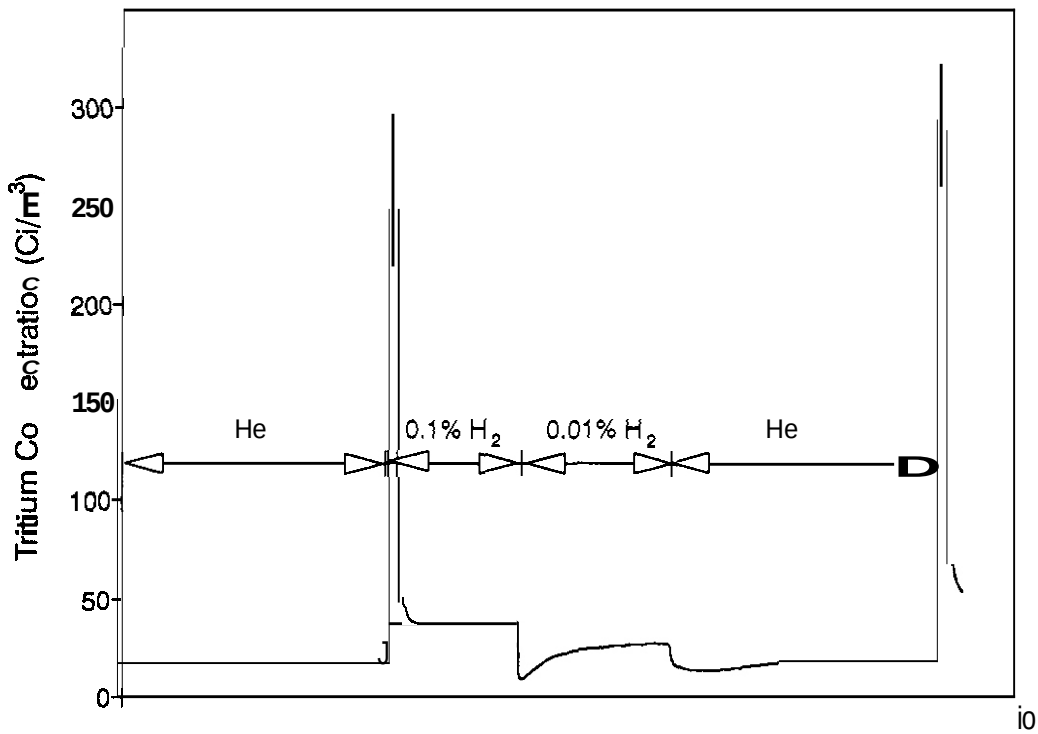

Table 4

Effects of Sweep Gas Composition on the Tritium Recovery from the Ring Specimen. Recovery rates are relative to the "apparent" steady-state recovery rate at 550" in He-0.1% H_2

TemDerature	Sweep Gas Comoosition He	0.01%	0.1%
550°C	0.45	0.59	1.00
600°C	0.53	0.73	1.01
650°C	0.46	.63	0.93

CONCLUSIONS

The BEATRIX-II experiment has provided an excellent opportunity for international collaboration on the design, fabrication, operation and analysis of an in-situ tritium recovery experiment on ceramic solid breeder materials. All systems are performing as expected and the test is continuing. The results from the first 85 EFPD of operation of the experiment can be summarized in the following conclusions:

1. Varying the sweep gas composition resulted in larger changes in the tritium recovery rates than did changes in either the flow rate or temperature. Decreasing the amount of hydrogen in the reference gas composition of He-0.1% H_2 to pure helium decreased the apparent tritium recovery rate by as much as a factor of 2.

2. Temperature changes in the range of 650 to 500°C resulted in a slightly decreasing/increasing tritium inventory with increasing/decreasing temperature. This indicates that the apparent recovery rate at 650 - 500°C in He-0.1% H_2 approximates the generation rate.

3. A double tritium recovery peak is observed following a temperature transient. The first, sharper peak is hypothesized to be associated with elemental tritium while the second peak which is delayed in time and broader is thought to be associated with tritium recovered as water.

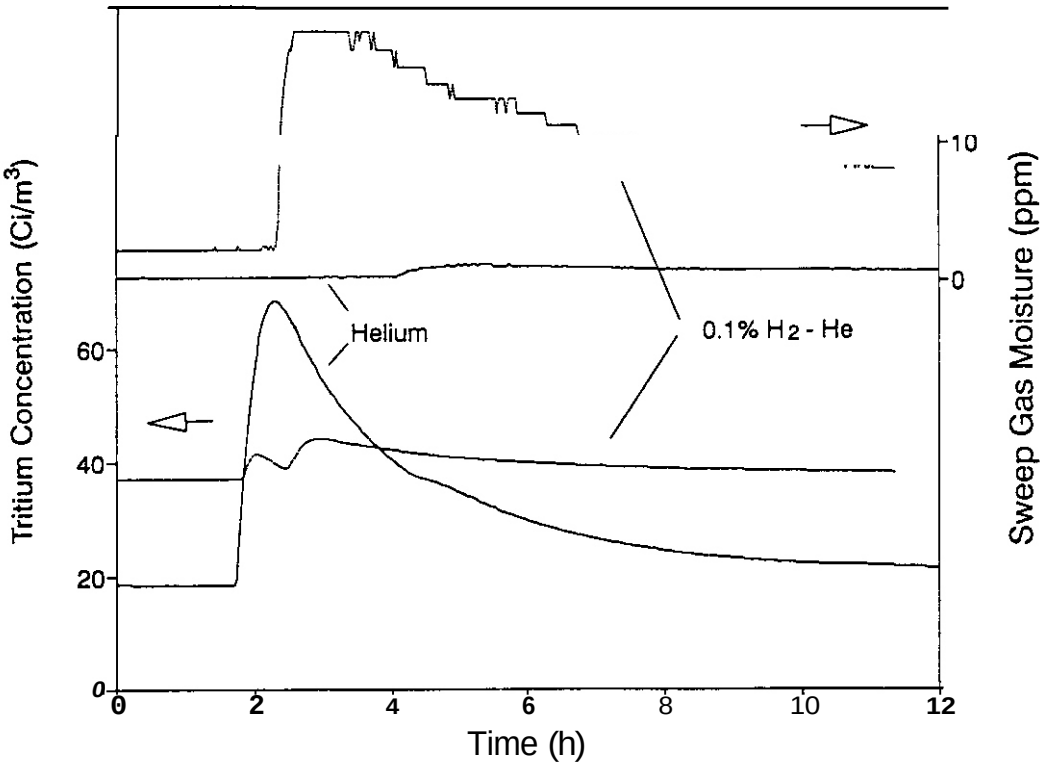

Figure 4. Tritium recovery for temperature transients between 550 and 650°C made in He-0.1% H_2 (runs 35-36) and in He (runs 31-32)

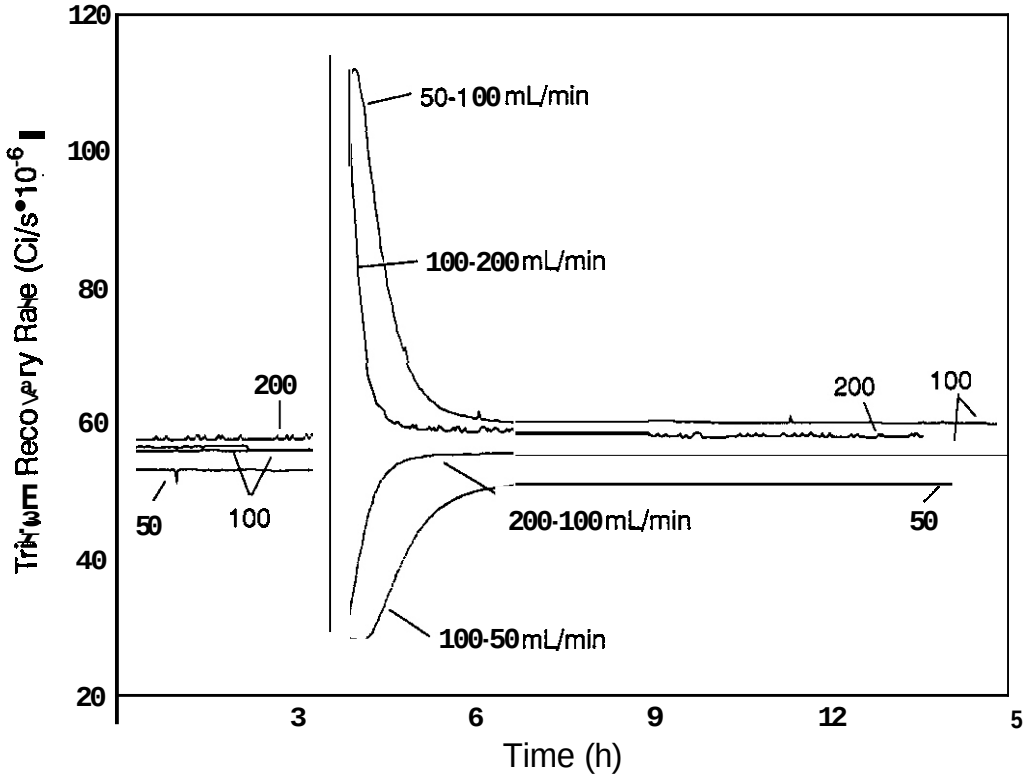

Figure 5. Tritium recovery rates during sweep gas flow rate changes at reference temperature and gas composition. Increasing flow rates are from tuns 6-7 and 13-14 and decreasing flow rates are from runs 9-10 and 10-11.

4. The effect of sweep gas flow rates on tritium recovery indicates that lower flow rates may lead to lower recovery rates. This type of data is useful in establishing optimum flow rates both for this experiment and in blanket applications.

5. The solid Li_2O specimen, with a surface to center temperature gradient of 450-1000°C has exhibited excellent thermal stability and tritium release characteristics throughout the first cycle of operation.

FUTURE WORK

BEATRIX-II Phase I is continuing through the reminder of FFTF Cycle 11, which has an approximate duration 300 EFPD. The test plan is directed towards further defining the tritium recovery as a function of sweep gas composition, temperature, and flow rate. The effects of neutron irradiation damage and burnup will be determined by comparing the present results with results from later cycles.

REFERENCES

1. G. W. Hollenberg, T. Kurasawa, S. E. Berk, I. J. Hastings and D. E. Baker, "A Fast Neutron, In situ Tritium Recovery Experiment on Solid Breeder Materials", Fusion Technology ,15, 1349-1354 (1989).

2. R. J. Puigh, G. W. Hollenberg, T. Kurasawa, H. Watanabe, I. J. Hastings, J. M. Miller, S. E. Berk, R. E. Bauer, and D. E. Baker, "BEATRIX-II: In-Situ Tritium Recovery from a Fast Neutron Irradiation Of Solid Breeder Materials", In Proceedings of the 15th Symoosium on Fusion Technology, edited by AM Van Inger, A. Nigsen-Vis, and HP Kippel, pp 1282-1286, September 19-23, 1988, Utrecht, The Netherlands. Elsevier, Netherlands.

3. D. E. Baker, T. Kurasawa, J. M. Miller, and O. D. Slagle, "BEATRIX-II: In Situ Tritium Test Operation" Presented at the Ninth Topical Meeting on the Technology of Fusion Energy Oak Brook, Ill, October 7-11, 1990.

4. R. G. Clemmer, et al., "The TRIO-1 Experiment: In-Situ Tritium Recovery Results", J. Nucl. Mater., 122-123, 890 (1984).

5. T. Kurasawa et al, "The Time Dependence of In-Situ Tritium Release from Lithium Oxide and Lithium Aluminate (VOM-22H Experiment)", J. Nucl. Mater., 141-143, 265 (1986).

6. R. A. Verrall, J. M. Miller, D. S. MacDonald, and S. R. Bokla, "CRITIC-1 Irradiation of Lithium Oxide", J. Nucl. Mater., 155-157, 553-557 (1988).

7. S. Konishi, H. Yoshida, H. Ohno, Y. Naruse, D. O. Coffin, C. R. Walthers and K. E. Binning, "Experiments on a Ceramic Electrolysis Cell and a Palladium Diffuser at the Tritium Systems Test Assembly", Fusion Technology, 8, 2042-2047 (1987).

8. CERAMICS

IEA WORKSHOP ON IN-SITU MEASUREMENT OF ELECTRICAL PROPERTIES OF IRRADIATED CERAMICS -- F. W. Clinard, Jr. (Los Alamos National Laboratory)

OBJECTIVE

This meeting was held to review the status of studies in the area of transient changes in electrical properties of ceramic insulators while under irradiation, to plan future work, and to make recommendations to designers of fusion devices.

SUMMARY

This International Energy Agency workshop was held in Los Alamos, NM June 27-29, 1990. In attendance were 14 participants representing fusion ceramics programs in Spain, the U.K, Japan and the U.S. The workshop was divided into four sessions: Background, Current In-Situ Work, Plans and Goals for Future Work, and Recommendations. Informal discussion sessions on various subjects were also included in the workshop.

Studies of in-situ electrical properties have accelerated since the last gathering of this group, with recent findings demonstrating that dielectric breakdown as well as enhanced conductivity can be induced by concurrent irradiation. Based on present knowledge, recommendations were made to designers of NET and ITER on materials selection and anticipated performance, as well as on design-related considerations.

INTRODUCTION

This workshop was the fourth in a series for the ceramic insulator community. The first was held near Madrid, Spain in 1986, the second in Karlsruhe, FRG in 1987, and the third in Garching, FRG in 1989. These earlier meetings, all of which were held under the auspices of IEA Working Group - Task Annex II, were dedicated to general reviews of fusion insulator needs, the status of the various national programs, and plans for future work.

In contrast the the first three meetings, the Los Alamos workshop involved discussion of a specific scientific and technological issue: in-situ degradation of electrical properties of irradiated ceramics. This problem area involves transient changes in such properties as resistivity and loss tangent during irradiation rather than afterwards. Put another way, the materials problems are primarily flux-dependent rather than fluence-dependent, although as discussed below the damage state of the material (a fluence effect) has also been shown to be important.

The earlier workshops in this series have been recorded in Proceedings reports issued by the International Energy Agency. Such a report for the Los Alamos meeting is in preparation as of this writing.

HIGHLIGHTS OF THE WORKSHOP

Background

G. P. Pells (AEREIHarwell) and E. Hodgson (CIEMAT/Madrid) reported that they are involved in ongoing consultations with NET designers on materials choices and anticipated problems for insulating ceramics in that machine. It is recognized that such discussions are also relevant to insulator needs for ITER.

The situation with respect to the various insulator applications for NET can be sumnarized as follows:

Toroidal current breaks - NET will employ metallic breaks, and so this application is not relevant to that machine. However, it was noted that ITER designers are planning for current breaks made of insulating ceramic.

ICRH insulators - These insulators are required to support the coaxial feeder line and to act as tritium barriers. A loss tangent of 10^{-3} may be adequate.

LHRH insulators - A large number of small windows in clustered waveguides will be required, along with thin ceramic sheets between waveguide modules to stop formation of current loops during disruptions. The windows will be recessed and water cooled, and should have a loss tangent less than 10^{-4}. Contamination on the window surfaces is expected to present difficulties. The windows must serve as retaining barriers for tritium from the plasma and SF_6 dielectric gas in the waveguide. For NET a maximum lifetime dose of 10^{18} n/cm^2 is expected.

ECRH insulators - The waveguides and their windows are currently being designed. A loss tangent less than 10^{-6} is required; it is hoped that this specification can be met by operating the window at 20 K with periodic warmups that can result in annealing of some of the irradiation damage. A dose of 10^{18} n/cm^2 is anticipated.

Neutral beam injector insulators - The NBI modules will be located 40 meters from the torus; nevertheless, radiation from neutron streaming and other sources is of concern. Very large, high-quality water-cooled ceramic insulators capable of holding off 10-20 kV/cm are required for this application.

Insulators for copper coils - Water-cooled ceramic insulators are required for the vertical stabilizing coil and for divertor coils; both applications involve high neutron fluxes. Electric fields will be on the order of 5 kV/cm.

Insulators for diagnostic applications - Insulator applications of concern include optical windows, insulators for particle counters and detectors, and fiber optic cables. Specific component designs are not yet available for review.

Current In-Situ Work

H. Ohno (JAERI/Tokai) reported on initial findings using gamma radiation from a ^{60}Co source and a frequency range from 5 Hz to 13 MHz. Test materials included ZrO_2-10% Cr_2O_3 and Al_2O_3 single crystals, plus Sic-2 wt% BeO polycrystalline material. Only slight, dose-dependent changes in ac conductivity were noted at 723 K to 1023 K with dose rates of approximately $1x10^3$ Rad/s.

E. Hodgson, (CIEMAT/Madrid) reviewed his studies over the past several years, plus work in progress. All experiments have been carried out using a 2 MeV electron accelerator. Test ceramics include MgO and Al_2O_3.

Results to date show that transient or radiation-induced conductivity (RIC) will be a problem from the onset of operation of any D-T fusion device. The basic phenomena (generation of charge-carrying electrons and holes, trapping, and recombination) are well-understood theoretically and have been measured, although over relatively short times on the order of one hour.

Recent work shows that at longer times electrical breakdown occurs, and this is considered to present severe technological problems. Breakdown occurs only with concurrent ionization and displacement damage, and irradiation with an applied electric field is essential. Subsequent examination under optical microscopy reveals the formation of precipitates.

Breakdown appears to result from radiation-enhanced electrolysis, in which impurity aggregation and colloid production probably play important roles. Since breakdown occurs at 50 Hz as well as under dc conditions, the phenomenon cannot involve a polarization effect.

G. P. Pells (AERE/Harwell) reported on studies that he and S. Buckley have carried out using proton beams. Work on polycrystalline alumina using 3 MeV protons has shown that at 60 MHz transient dearadation of loss tangent (i.e., a flux effect) does not occur; however, an increase in lossiness due to damage buildup was seen at doses as low as 10^{-3} dpa. A post-irradiation effect (namely decay of damage-induced degradation) was also noted, indicating that fluence-dependent changes should be measured promptly for most meaningful results. Applied electric fields were low for this work.

DC studies employing 18 MeV protons showed transient degradation of resistivity; however, at 10^4 Gyls (about that expected at the first wall of a D-T-burning device) degradation below 600 C was not excessive

N. Itoh (Nagoya University) described work with K. Tanimura, J. Valbis and C. Itoh on the behavior of transient point defects under electron irradiation. Properties measured were luminescence, optical absorption, and volume change. Results for a number of ceramics showed that (1) defects having relatively long lifetimes are generated under irradiation, (2) the contribution of transient defects to loss tangent is not yet clear, and (3) time change of loss tangent and conductivity after an intense pulse of electrons can reveal the nature of the defects responsible for loss tangent changes.

R. Stoller (ORNL) presented the research plan that he, S. Zinkle, and R. Goulding have developed for the study of RIC effects. Measurements of loss tangent will be carried out at 100 MHz in an ionizing radiation field using the HFIR spent core facility. It is also planned to measure the same property at 50-500 MHz in combined ionizing and displacive radiation fields using the University of Illinois TRIGA reactor. Variables for this work include dose rate, rf power levels, and ratio of ionizing to displacive radiation. Tests will conducted on single-crystal and polycrystalline Al_2O_3.

NOTE: Post-workshop experimental results from this project are reported elsewhere in this volume.

T. Shikama (Tohoku University, Oarai Branch) reported on RIC studies carried out with M. Narui, A. Ochiai, H. Kayano and Y. Endo. This work involved measurement of electrical conductivity of single-crystal Al_2O_3 in the JMTR fission reactor. The gamma dose rate ranged from $1.5x10^2$ Gyls at shutdown to $1.4x10^4$ Gyls at full power, while the neutron flux under power was $3.4x10^{18}$ n/m^2s (fast) and $1.8x10^{18}$ n/m^2s (thermal).

Test frequencies employed were in the range 100 Hz to 100 kHz, and some data were obtained as a function of temperature despite a noise problem from the sample heater. RIC was observed, but only below 10 kHz.

Conductivity values at 350 C ranged from 3×10^{-8} to $6\text{-}15 \times 10^{-6}$ $(\text{ohm-m})^{-1}$ at reactor shutdown and full power, respectively. A time-dependent rise in conductivity was noted, implying a fluence effect.

W. Unruh (LANL) described an irradiation testing capability that he, F. Clinard, J. Kennedy, W. Sommer, and C. Kise developed to study radiation-induced breakdown for another, now-defunct program. The phenomenon of concern here involves classical electrolysis (polarized motion of ions in a DC field leading in time to runaway conduction, dielectric breakdown, and often structural failure), with contributing effects from simultaneous irradiation.

This work involved development and testing of an environmental capsule designed for irradiation with spallation neutrons at the LAMPF beam stop area (LASREF). Target fluxes and fluences were 4×10^{13} n/cm^{2}s and 2×10^{20} n/cm^2 respectively. The capsule was designed to accommodate a large number of samples, both with and without guarded electrodes and with and without exposure to a continuous dc field, at elevated temperatures in a helium gas atmosphere.

Initial tests were conducted out of the neutron irradiation field but at the design temperature of 825 C and with an applied electric field of 1000 V/cm, during a continuous run of 75 days. Test materials were single-crystal Al_2O_3, both undoped and with 150 wppm Ti, and equivalent polycrystalline samples. Measured conductivity values ranged from 10^{-11} $(\text{ohm-cm})^{-1}$ for undoped sapphire to 10^{-9} $(\text{ohm-cm})^{-1}$ for doped alumina. The test capsule exhibited some shortcomings, so that an improved design was subsequently developed. The project is currently at a standstill, but could be reactivated if required for fusion studies.

Future Plans

H. Ohno reported that gamma irradiation studies at his laboratory will continue, and in the near future in-situ measurements will be initiated using the JRR-3 fission reactor. Beginning in 1993, tests will be carried out utilizing a triple-beam ion accelerator facility now under construction.

E. Hodgson described planned future work in the areas of bulk breakdown and degradation, including studies of the effect of radiation spectrum, temperature and dose rate, voltage, impurities, and test frequency. Other work will include studies of surface breakdown and radiation-enhanced diffusion.

G. P. Pells reported that funding restrictions necessitate dropping in-situ RIC measurements from the Harwell program. Future work will involve measurement of swelling during irradiation at cryogenic temperatures using a capacitance method. Plans also include post-irradiation studies of high-frequency dielectric properties of ceramics at 20 K after fission reactor irradiation.

N. Itoh presented a plan to use intense pulses of electrons to study transient defects produced by electronic excitation. Measurements will include optical absorption, volume change, and electrical conductivity or loss tangent.

S. Zinkle described planned studies in three areas: (1) electrical conductivity of SiC and other ceramics, (2) ICRF dielectric properties of several ceramics in gamma and neutron irradiation fields, and (3) microstructural examination of electric field effects during irradiation. The first two study areas will involve electrical measurements, while the last will include post-irradiation examination by TEM and XPS.

Dr. Shikama described upcoming work on in-situ electrical property measurements to be conducted in Japanese fission reactors. This will include studies of both insulating ceramics and graphite, at 200 to 800 C. It is also planned to attach a 400 keV TEM to a 2 MeV Van de Graaff accelerator for concurrent damage studies.

E. Farnum reported on plans to carry out in-situ measurements using a 2-3 MeV proton beam. Test materials will include single-crystal sapphire as well as Al_2O_3 samples that have previously been damaged by neutron irradiation. Test frequencies will range from near dc to frequencies relevant to RF heating applications.

NOTE: A more extensive description of this experiment is given elsewhere in this volume

Discussions

The following are some of the highlights of the discussion sessions:

1. This community must continue and expand its efforts to support reactor designers, both with respect to materials choices and to recommended design changes.

2. Although this workshop focused on in-situ electrical properties, it was recognized that in-situ changes in structural and thermal properties as well as diffusional effects also need attention, and should be part of the fusion ceramics program.

3. As new irradiation facilities such as IFMIF are conceived and planned, the fusion insulator community must supply input with respect to (1) radiation environment (e.g., ionizing radiation levels and neutron energy spectra) and (2) access for in-situ studies.

4. International collaboration in the areas of standard and reference materials and in round-robin testing is progressing well. Consideration should be given to exchange of personnel where appropriate.

5. Hodeling of electronic and ionic mobility as well as radiation effects could be most helpful in interpreting and explaining observed RIC phenomena.

6. There was a persistent theme during the workshop that long-term basic studies are needed to understand in-situ degradation mechanisms.

RECOMHENDATIONS

The workshop participants made the following recommendations to designers, based on the present state of knowledge, with respect to the six insulator applications for NET/ITER. (Design and operating conditions for the ITER toroidal current break were not known, and so no recommendations could be made for that application.)

ICRH insulators. The recommended material is 99.5% pure Al_2O_3.

LHRH insulators. The material of choice is again 99.5% Al_2O_3, selected for lowest loss tangent. Further data on RIC effects is needed, and tritium permeation may be a problem.

ECRH insulators. A cooled single-crystal material such as sapphire should be used. Even low-dose damage may present difficulties; irradiation testing to appropriate damage levels should be carried out, and under cyclic temperatures that approximate expected operating conditions.

Neutral beam injector insulators. Current leakage and dielectric breakdown at surfaces may present a problem. Fabrication of large insulators with the requisite strength is another issue. The radiation environment requires further specification.

Insulators for copper coils. The vertical stabilizing coil insulators present serious problems, given the expected high electric fields, irradiation fluxes, and fluences. The form of the insulator (e.g., solid vs. powder) and its composition must be carefully chosen, and an electrical resistivity as low as 10^6 ohm-m (reduced to that value by RIC) must be anticipated.

Insulators for diagnostic applications. Further information on materials needs and operating conditions is required. The use of IR windows necessitates development of an acceptable mounting technique. With respect to optical fibers, irradiation-induced degradation of the polymeric coatings will present a serious problem.

IN-SITU MEASUREMENT OF RADIATION INDUCED CONDUCTIVITY IN CERAMICS—E. H. Farnum. H. M. Frost and F. W. Ciinard (Los Alamos National Laboratory)

OBJECTIVE

The objective of this work is to develop a data base and understanding of radiation-induced changes In the electrical properties of ceramic insulators, and then use this information to identify or design new ceramic materials that will improve the performance of magnetic fusion machines.

SUMMARY

This report describes our experimental plan and schedule for measuring the radiation induced conductivity (RIC) in ceramics while being irradiated with 3 MeV protons. In the Initial experiments, dielectric constant and loss will be measured in pure and in Ti-doped sapphire. The measurements will be made at room temperature. at frequencies between 100 Hz and 10 MHz, with and without an applied DC bias. and as a function of radiation flux and fluence. The Ion Beam Materials Laboratory (IBML) ion source at Los Alamos will be used with beam currents up to 1 micro-ampere. We expect initial results to be available lor the *next* semi-annual Progress Report.

PROGRESS AND STATUS

Introduction

The fact that penetrating radiation reduces the electrical reslstivity of ceramics has been known for some time (1-4) and has been measured in a number of candidate fusion reactor insulator materials. This effect, called radiation-Induced conductivity (RIC), has been shown to reduce the predicted lifetime of reactor windows to unacceptable levels (5.6). The effect has been measured as a function of flux and fluence with fast and thermal neutrons (1,4,7), with gamma rays (2,7,8) , and with accelerated charged particles (9,10,11). These measurements were made by subjecting the material to the irradiation at a fixed temperature and subsequently measuring the change from the pre-inadiated conductivity. Recently, Hodgson in Spain (10.12) and Peils in England (13) measured the RIC in-situ during irradiation with electrons and with protons respectively. Both of these experiments showed higher RIC than would be expected from post-irradiation measurements. Further. they then applied a DC electric field to the material during the irradiation and observed an even greater RIC effect (12,13). Their experiments showed for the first time that even in-situ experiments may be insufficient for predicting the behavior of insulators in fusion applications. Since in plasma heating applications at ECRH. LHRH and ICRH frequencies the insulator is used for very hlgh power transmissions, high electric fields at the applied frequencies will be coincident with neutron and gamma irradiation. Therefore, to simulate a real fusion reactor environment, radiation and electric fields must be applied simultaneously. Our experiments will attempt to simulate the fusion environment as closely as possible.

Experimental Plans

Neutron and gamma radiation from the fusion reactor produce both ionizing and displacive damage in ceramics. High energy protons also cause both ionizing and dispiacive damage and have been used to simulate fusion reactor conditions (13). Advantages of protons as a radiation source include the ability to adjust the beam energy, to achieve very high fluxes and to control the irradiation environment. Three-MeV protons have a range in aluminum oxide of 49 um, and nearly all of the protons stop in the last few um of path. in irradiating insulators it is necessary to assure that the protons pass through the sample and stop in a metal backing layer. Otherwise the build-up of space charge would destroy the sample. Therefore we have chosen a sample thickness of 25um and a guard-ring capacitor configuration with thin gold top electrodes as shown in Fig. 1. Protons that are incident on the top electrode with 3 MeV energy. enter the alumina with 2.92 MeV and enter the gold backing layer with 1.92 MeV. Thus each proton loses 1.0 MeV in the alumina. Of this, 999.4 keV is lost to ionization reactions and 0.6 keV is lost to coilisions that cause displacements. A plot of energy absorption is shown in Fig 2. Because most of the absorbed energy is ultimately converted to heat, the metal backing also serves as a heat sink to keep the sample near room temperature, initial experiments will focus on low frequencies (< 10 MHz) and will explore the effect of flux and DC bias on in-situ RIC. The experimental configuration is shown schematically in Fig 3. Samples will be held at constant temperature near 25 ^{o}C by controlling the backing plate temperature. Proton flux will be varied between 1.3 nA (10^{3} Gy/s) and 1.3 uA (10^{6} Gy/s). (Peak ionizing flux for the first wail of CIT is -1.67 x 10^{4} Gy/s.) The beam will be periodically turned off to compare in-situ RIC with post-irradiation values and to determine decay time (if greater than -1 s). A DC bias of 0 to 25 V, corresponding to 0 to 1000V/mm, will be applied during the irradiation. (In alumina irradiated at 450 ^{o}C, thermoelectric breakdown has been observed at 130 V/mm (13,14).) Initial in-situ RIC measurements will be made on both pure sapphire (Crystal Systems, Inc.; c-axis in plane of disk) and sapphire doped with 150 ppm Ti.

Experimental Schedule

We expect to put the first IBML proton beam on a sapphire sample in December. 1990. Initial results should be ready lor the March 1991 Progress Report.

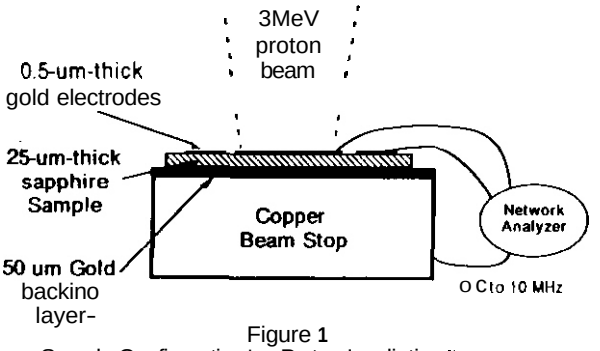

Figure 1
Sample Configuration lor Proton Irradiation Experiment

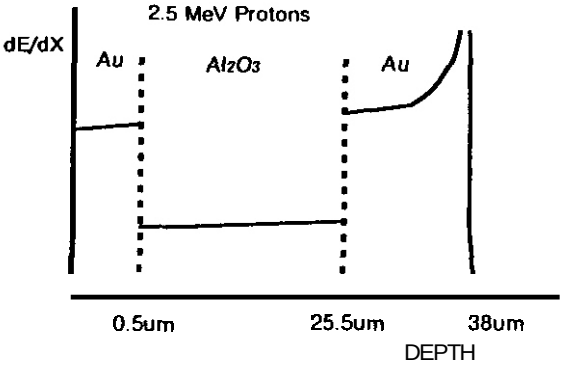

Figure 2
Proton Energy Deposition Rate *vs* Depth in a
gold / alumina/ gold Target

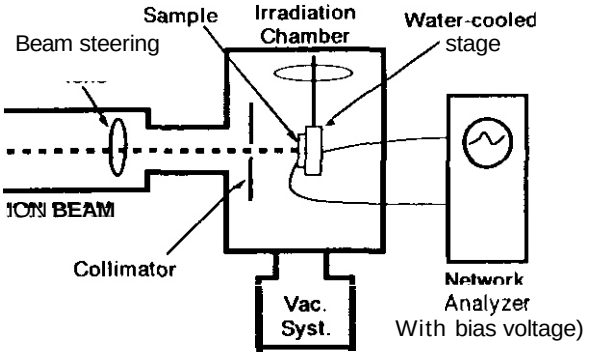

Figure 3
Schematic lor planned Proton Irradiation Experiment

REFERENCES

1. Frank W. Ciinard Jr. Physics of Radiation Effects in Crystals (Ed. R. A. Johnson and A. N. Orlov), Eisevier Science (1986).
2. G. P. Pells and G. J. Hill, J. Nucl. Mat. 141-143 (1986) 375-381.
3. E. R. Hodgson and S. Clement, J. Nuci. Mat. 155-157 (1988) 357-360.
4. H. M. Frost and F. W. Clinard Jr. J. Nucl. Mat. 155-157 (1988) 315318.
5. M. K. Ferber. H. D. Kimrey. P. F. Becher J. Mat. Sci. 19 (1984) 3767-3777 Part 1; and P. F. Becher, M. K. Ferber, Ibid. 3778-3785, Part 2.
6. H. M. Frost and F. W. Clinard Jr. Fusion Reactor Materials (Semiannual Progress Report lor Period ending March 31, 1988), *US* DOE, Office of Fusion Energy, *DOE/ER-0313/4*.
7. R. E. Stoller. R. H. Goulding and S. J. Zinkle, See this Progress Report.
8. H. Ohno, Y Katano and K Noda. IEA Workshop on In-Situ Measurement ot Electrical Prowrties of Irradiated Ceramics, (Los Alamos. NM, June 27-29, 1990) to be published.
9. R. W. Klaffkey, B. H. Rose, A. N. Goland and G. J. Dienes, Phvs. Rev. 21 (1980) 3610-3634.
10. E. R. Hodgson. Fourth International Conference on Fusion Reactor Materials, (iCFRM-4, Kyoto, Japan Dec. 4-8, 1989) To Be Published.
11. G. P. Pells *et.* al., Culham/EEC Fusion Technology Task MAT-I3 AERE R 13222. Materials Development Div. Harwell Lab., Oxfordshire OX11 0RA.
12. E. R. Hodgson. IEA Workshop in In-Situ Measurement of Electrical Prowrties of Irradiated Ceramics, Op. Cit.
13. G. P. Pells, Ibid.
14. C. Wu, Private communication.

MILLIMETER-WAVE TESTING OF ISOTOPICALLY ENRICHED ALUMINA

H. M. Frost, 111, J. C. Kennedy, 111, and T. N. Claytor (Los Alamos National Laboratory) and S. J. Zinkle (Oak Ridge National Laboratory)

OBJECTIVE

Evaluate the quality of isotopically enriched high-purity alumina made by closed-cycle processing, with application to a special irradiation experiment.

SUMMARY

In a special fusion-neutron irradiation simulation experiment, ^{17}O has been substituted for ^{18}O in 99.5% alumina to be neutron-irradiated in the High Flux Isotope Reactor (HFIR) at Oak Ridge for raising the potentially deleterious helium gas yield to levels closer to those expected from the neutrons of deuterium-tritium (D-T) fusion reactions. Earlier, we reported values of complex dielectric constant k^* measured at Los Alamos at millimeter-wave (MMW) frequencies for conventional (unenriched) 99.5% alumina test specimens[1]. These specimens were made under the same conditions applying to the present report of k^* measured for ^{17}O-enriched specimens based on the same alumina system. The present alumina has lower dielectric losses than that reported in the earlier work. Furthermore, we corroborate the earlier finding that k^* is a sensitive nondestructive measure of the quality of alumina being considered for rf-window use -- and the overall quality of high-purity ceramics in general.

PROGRESS AND STATUS

Introduction

While neutron-irradiation studies have been carried out on electrically insulating or mechanically strong ceramics such as alumina, the high fluences reached of 1×10^{22} n/cm^2 or greater have been achieved only in fission reactors whose 'fast neutrons' (E > 0.1 MeV) are slower than the 14 MeV neutrons expected from D-T fusion reactions. When D-T neutrons were available from the Rotating Target Neutron Source (RTNS-II) at Lawrence Livermore National Laboratory, the corresponding fluences, as limited by irradiation scheduling and aperture constraints, were below 5×10^{18} n/cm^2.

Fission reactors can simulate the extent of displacement and ionization damage expected from 14 MeV neutrons in ceramics such as alumina, but generally not the extent of that type of damage linked to transmutation production of gases such as helium and hydrogen. When produced, these gases are initially atomically dispersed, but are subject to subsequent diffusion and segregation effects. Lack of sufficient levels of transmuted gas occurs under the usual materials irradiation conditions of a hard neutron spectrum (E > 0.1 MeV) and normal isotopic abundances for the test specimen elements involved (e.g., Al and O in alumina). Gas levels produced by fission neutrons in a test specimen can be boosted, however, through isotopic substitution within the material to be irradiated and inclusion of thermal as well as fast neutrons. The effect of this is to increase the cross section of the desired (n,α) reaction, which in our case is $^{17}O(n,\alpha)^{14}C$.

ExDerimental Drocedureg

1. Processing

Hard, nearly theoretically dense (> 99.5% TD), isotopically adjusted alumina samples of 99.5% purity were made through dissolving an organic precursor (aluminum isopropoxide) in isopropyl alcohol and then hydrolyzing in ^{17}O-enriched water followed by removal of the alcohol, calcining, mixing with MgO (sintering aid), milling, and sintering.[2] The resulting maximum ^{17}O fraction in the total oxygen content was about 25%. The flexural strength resulting from the closed-cycle processing involved was 280 MPa. Average grain sizes were 10 μm.

2. Dielectric measurements

The dielectric constant, k, and loss tangent, tanδ, contribute to the complex dielectric constant via $k^* = k(1 - j\tan\delta)$. These properties were measured at room temperature by means of a computer-operated, swept-frequency MMW scalar network analyzer system operating at an average frequency of about 95 GHz on specimens inserted within single-moded waveguide. Further details on this technique are reported elsewhere, as well as on data-reduction software needed when spatial inhomogeneities (e.g., pores or inclusions) are present in the test specimens.[1,3] From four to ten repeat measurements were made on each specimen available. Specimens were machined from sintered alumina blocks (12 per block).

Experimental results

The values of k and tan6 are given in Table 1, along with the number of specimens in the statistical sample involved.

Table 1. Dielectric properties of sets of unenriched and enriched alumina specimens from blocks no. 3 and 8, respectively.

DESCRIPTOR/Statistic	Unenriched (block #3)	Enriched (block #8)	Standard
DIELECTRIC CONSTANT			
Mean:	10.05	9.86	9.84
Standard deviation:	0.016	0.044	0.022
Fractional deviation:	0.16%	0.45%	0.22%
LOSS TANGENT			
Mean:	5.1×10^{-4}	5.2×10^{-4}	4.2×10^{-4}
Standard deviation:	0.17×10^{-4}	0.64×10^{-4}	0.51×10^{-4}
Fractional deviation:	3.4%	12.%	12.%
No of specimens in statistical sample:	8	5	(1)

Values of the dielectric properties were extracted from 'channel spectra' consisting of plots of transmission loss as a function of frequency swept from 90 to 100 GHz. For obtaining reliable values, a subjective but repeatable selection process was used for accepting or rejecting channel spectra for subsequent data reduction. This process involved a comparison of important features of each plot with those for the plot expected from electrodynamics theory. Differences between the expected and observed spectra are due to either specimen-related or measurement-related effects, such as cracks and inclusions producing spurious MMW scattering within the specimen or multimoding due to imperfect specimen and waveguide geometries.

Each average value given in Table 1 is actually a mean of the means. Repeat measurements on a specific specimen were averaged before subsequent averaging of measurements over several specimens. For 13 of the total of 17 specimens represented in this report, the rounded off values of the 'intra-specimen' standard deviations for k fell in the range of 0.04 to 0.06, with the other four values above (2) and below (2) this range. These typical values essentially overlap those for the 'inter-specimen' standard deviations of 0.02 to 0.05 (rounding off to one significant figure). This overlap condition was basically mirrored in the intra-specimen and inter-specimen standard deviations for tanδ as well.

The "standard" alumina featured in Table 1, with a density of 95% TD, is a Coors AD-995 (99.5 %) alumina control specimen used in an earlier EBR-II irradiation experiment [3,4]; the mean and standard deviation of its k and tan6 values were estimated through repeat measurements alone. "Fractional deviation" is the ratio in percent of the (n-1) weighted standard deviation divided by the mean and multiplied by 100.

Acceptable dielectric data were also obtained on specimens from other (enriched) blocks (#7 and #10). Only two specimens per block were available in these cases, though, so inter-specimen variafions could not be evaluated. For block no.7, k and tan6 were 9.95 and 4.2×10^{-4}, respectively; for block no.10, they were 9.85 and 4.3×10^{-4}. The dielectric losses were the same as for the 'standard' alumina.

Test specimens were examined by acoustic microscopy for their defect contents. This method involves "B-scan" imaging of internal structure by an ultrasound transducer operated in a pulse-echo mode and mechanically scanned under computer control over the test specimen immersed within a coupling medium (water).[1,5] Acoustic microscopy probes the entire volume of each test specimen, as opposed to the limited sampling capabilities of optical and electron microscopy. Images obtained by both acoustic and optical microscopy revealed internal and surface-connected defects which usually correlated in a predictable manner with the quality of the associated channel spectra. In the MMW measurements, it was also observed, however, that this quality was sensitive to the varying 'specimen to waveguide' gaps presumably resulting during repeat measurements on a given specimen.

Discussion

Our earlier report[1] of the sensitiveness of fractional deviation in the dielectric constant (k) to material quality is borne out in the present work as well -- that is, the greater this deviation, the worse the quality. Results from microscopy indicate that specimens cut from block no.3 are much more free of defects than those block no.8, especially those defects with sizes of the order of the specimen width (0.100 in = 2.5 mm). Corresponding examination of Table 1 indicates that the fractional deviation of k for block no.8 is almost three (2.8) times larger than is the case for k from block no.3.

The corresponding means of k for the two different blocks are different and this difference appears to be statistically significant. That is, these means are separated by much more than the sum of their probable errors (assuming a Gaussian distribution), as given by $0.6745(s.d._3 + s.d._8)$, where "s.d." stands for standard deviation. However, the tan6 values are nearly equal (to within 3%) -- and are roughly 25% larger than the value for the "standard" alumina used in our earlier work. As reported in that work, the measurable losses in the standard specimen probably arose from absorption only, e.g., not scattering from inclusions or pores. That is probably also the case here: The densities of the experimental aluminas are within a small fraction of one percent of the theoretically dense value, so that porosity is low and scattering losses unimportant. Thus, the present alumina has an excess dielectric absorption of *25%* more than in the standard alumina.

One possible explanation for excess absorption (in block nos. 3 and 8) and larger dielectric constant (in block no.3) involves electric polarization on the interfaces between the matrix and the inclusion materials revealed by acoustic microscopy. The charge carriers and/or electric dipoles involved in this 'interfacial polarization' would have to be essentially free or unbound for this effect to be important at MMW frequencies and room temperature, however. Delocalized electronic states on the interface or electric dipole moments of relatively tightly bound cations associated with symmetry breaking bi- or tri-vacancies are possibilities. Presence of an effective, slightly viscous medium within which these charges move could give rise to the dielectric loss.

The (alumina-like) inclusion material itself may be a vestige of a small amount of the organic precursor that remained as particulate matter during solubilization in alcohol during synthesis of the alumina powder. One speculation is that the inclusion material is alumina itself that calcined and sintered at a different rate and to a lower density than the matrix alumina.

In our earlier report on the MMW dielectric properties of the same alumina system featured (except for lack of enrichment), the tanδ values reported there were 7.5×10^{-4} and 13.1×10^{-4} (for specimen sets no. 4 and 3, respectively). The lower value had been attributed entirely to absorption losses, so the alumina featured in the present report has a substantially improved transparency as a MMW window.

One possible explanation for the differences in k* between the experimental aluminas vs. the standard alumina involves the residual carbon content resulting from incomplete burnoff of the organic precursor used for making the powder. During a planned irradiation in HFIR, transmuted carbon will also be produced at boosted levels by the nuclear reaction $^{17}O(n,\alpha)^{14}C$ intended for producing helium gas. For comparison, typical MFE conditions of 1 MW/m^2 fusion-neutron loading of natural isotope abundance (99.76% ^{16}) alumina at the first wall would yield 624 appm of carbon.[6] Such material could affect the dielectric losses because of its relatively conductive nature, especially if segregated out, as on grain boundaries. Trace carbon analyses will thus be needed on both the control and irradiated samples.

The question of trace amounts of silicon also needs to be addressed. This is because the same thermal neutrons used to convert oxygen into helium (plus carbon) may also convert ^{27}Al into ^{28}Si. This question was raised in the 1960's[7] and was dealt with at greater length by Youngman fifteen years later[8], as noted in a recent review of radiation effects in non-metals.[9]

CONCLUSIONS

The present results, combined with those in our earlier report,[1] indicate that the fractional deviation -- equal to the mean divided by the standard deviation (and multiplied by 100) -- in the dielectric constant is a sensitive indicator of material quality, as substantiated by independent results from acoustic microscopy, which for our work here had a lateral resolution of about 0.1 mm.

From the standpoint of dielectric properties, alumina specimens cut from unenriched block no.3 have the highest quality of all the specimens we have examined *so* far in the fusion-neutron simulation experiment, and this quality is comparable to that for a commercially available high-purity alumina used for comparison purposes. The dielectric quality of specimens cut from block no.8 was somewhat lower than for block no.3, but still acceptable -- and comparable to that for specimens from "set no.4" featured in our earlier report.[1]

With MMW dielectric testing, the entire volume of the ceramic can be sensitively and nondestructively sensed for the presence of internal defects, and tested specimens can be archived for subsequent retesting at any time. Such advantages outweigh the disadvantage of the precision machining now required for preparation of test specimens which are inserted under tight tolerances into the waveguide section serving as the test fixture in MMW testing.

Acoustic microscopy is a valuable adjunct to MMW testing, and it probably will also be useful for improving the statistics of the four-point bend tests intended for measuring flexural strength. It indicates in straightforward manner those surface regions in each specimen to avoid when placing the test anvils on the specimen, so that the stress concentration effects of anvil and defect do not overlap to produce premature failure.

Because of the presence of thermal as well as fast neutrons in the anticipated irradiation in HFIR, trace amounts of carbon are expected from the transmutation of ^{17}O in the enriched alumina. Silicon may also be generated through transmutation of ^{27}Al into ^{28}Si through neutron capture. The electrical and dielectric properties may be changed significantly with these impurities either atomically dispersed or segregated on grain boundaries, for example.

FUTURE WORK

In the next phase of this work, various sets of ^{17}O-enriched and unenriched alumina specimens will be irradiated under various flux and temperature conditions in HFIR at Oak Ridge. When available, irradiated sets will be sent to Los Alamos for specimen preparation and subsequent post-irradiation MMW measurements. Assays of trace carbon in both irradiated and unirradiated alumina specimens will have to be added to the materials characterization planned.

ACKNOWLEDGEMENTS

We gratefully acknowledge the specimen preparation contributions of H. E. Kim and W. R. Allen (Oak Ridge). The original idea of simulating the transmutation gas effects of fusion neutron irradiation through isotopic substitution in alumina (and other materials) subsequently irradiated in a fission reactor is due to F. W. Clinard, Jr. (Los Alamos).

REFERENCES

1. H. M. Frost, K. C. Kennedy, T. N. Claytor, E. F. Brown, and S. J. Zinkle, "Ceramic Processing Aided by Millimter-Wave Testing," pp. 289-296 in Fusion Reactor Materials Semiannual Progress Report for Period Ending September 30, 1989, DOE/ER-0313/7, U. S. Department of Energy, Washington, DC, 1989.

2. S. J. Zinkle, H. E. Kim, and W. R. Allen, "Preparation and Characterization of Alumina Containing Enriched oxygen Isotopes," pp. 315-321 in Fusion Reactor Materials Semiannual Progress Report for Period Ending September 30, 1988, DOE/ER-0313/5, U. S. Department of Energy, Washington, DC, April 1989. Also, H E. Kim, S. J. Zinkle, and W. R. Allen, "Preparation and Characterization of "0-Enriched Al_2O_3 for Nuclear Fusion Damage Experiments", J. Am. Ceram. Soc. 73, 425-429 (90).

3. H. M. Frost and F. W. Clinard, Jr., "Dielectric Changes in Neutron-Irradiated RF Window Materials," J. Nucl. Mater. 155-157, 315-318 (1988).

4. H. M. Frost, "Millimeter-Wave Properties of Neutron-Irradiated ceramics for RF-Window MFE Applications," pp. 11-16 in DOE/ER-0113/5, Eighth Annual Progress Report on Special Purpose Materials for Magnetically Confined Fusion Reactors, U. S. Department of Energy, Washington, DC, March 1986.

5. T. N. Claytor, H. M. Frost, T. H. Feiertag, G. A. Sheppard, and P. D. Shalek, "Nondestructive Measurement of Microstructure Evolution in Ceramics," Mater. Eval. 47, 532-537 (89).

6. L. H. Rovner and G. R. Hopkins, "ceramic Materials for Fusion," Nucl. Technol. 29, 274-302 (1976).

7. P. P. Budnikov, F. G. Kerbe, and N. S. Xostyukov, "Influence of Irradiation by Thermal Neutrons on Certain Electrical Properties of Ceramics Made from Pure Aluminum Oxide," Izv. Akad. Nauk SSSR, Neorg. Mater. 3, 94-100 (1967) (English translation journal available).

8. R. A. Youngman, "Neutron Irradiated Damage to Ceramic Solids," Ph. D. thesis, Case Western Reserve University, 1982.

9. F. W. Clinard, Jr. and L. W. Hobbs, "Radiation Effects in Non-Metals," pp. 387-471 (Ch. 7) in Physics of Radiation Effects in Crystals, ed. by R. A. Johnson and A. N. Orlov, Elsevier Science Publishers B. V., 1986.

WORKSHOP ON CERAMIC MATRIX COMPOSITE MATERIALS FOR STRUCTURAL APPLICATIONS IN FUSION REACTORS - R. H. Jones, Pacific Northwest Laboratory,(") and G. E. Lucas, University of California.[b]

OBJECTIVE

The objective of the workshop was to assess the potential of ceramic matrix composites for structural applications in fusion reactors. This included identifying the critical issues regarding their use and data needs to comolete this assessment.

SUMMARY

The workshop to assess the potential application of ceramic matrix composites (CMCs) for structural applications in fusion reactors was held on May 21-22, 1990, at University of California, Santa Barbara. Participants included individuals familiar with materials and design requirements in fusion reactors, ceramic composite processing and properties and radiation effects. The primary focus was to list the feasibility issues that might limit the application of these materials in fusion reactors.

Clear advantages for the use of CMCs (i.e., SiC/SiC) are high-temperature operation, which would allow a high-efficiency Rankine cycle, and low activation. Limitations to their use are material costs, fabrication complexity and costs, lack of familiarity with these materials in design, and the lack of data on radiation stability at relevant temperatures and fluences.

Fusion-relevant feasibility issues identified at this workshop include:

- hermetic and vacuum properties related to effects of matrix porosity (10-15%) and matrix microcracking
- chemical compatibility with coolant, tritium, and breeder and multiplier materials, radiation effects on compatibility
- radiation stability and integrity
- ability to join CMCs in the shop and at the reactor site, radiation stability and integrity of joints.

It was suggested that a true feasibility assessment of CMCs for fusion structural applications could not be completed without evaluation of a material "tailored" to fusion conditions or at least to radiation stability. It was suggested that a follow-up workshop be held to design a tailored composite after further results of CMC radiation studies are available and the critical feasibility issues are more fully addressed.

Feasibility Issues for Use of Ceramic Matrix Comoosites for Fusion Structural Applications

The following issues were identified during the workshop. For each topical area, the first short list contains those issues deemed most critical and fusion-relevant. Many of the issues in the second list are generic to CMCs, and their outcome could not be affected by the limited fusion budget available for this activity. The issues are also listed by category, although it is recognized that there is considerable overlap among these categories.

I. PROCESSING

A. Critical Fusion Issues

CMCs with 30-40% continuous reinforcement contain 10-15% porosity, which may be interconnected. Also, CMCs exhibit matrix microcracking long before final failure and they may be utilized at stresses above the matrix microcracking stress. Therefore, it is important to evaluate the effect of the original porosity and matrix microcracking on the following:

- coolant and tritium containment
- vacuum integrity
- outgassing characteristics.

(a) Operated for the U.S. Department of Energy by Battelle Memorial Institute under Contract DE-AC06-76RLO 1830.
(b) University of California, Santa Barbara, California.

B. General Issues

1. What are the problems and potential for scale-up of CMC processing methods to produce fusion reactor-relevant components; i.e., size and shape?

2. What is the role of CMC processing in the variability of CMC properties and can this variability be controlled?

3. If CMC impurities impose low activation limitations, can the desired purity be achieved?

4. Are currently used fiber/matrix interface layers such as C and BN suitable for irradiation environments? If not, what materials might be suitable?

5. Is it possible to integrate quality control methodology into CMC processing?

6. Since the costs of CMCs are heavily dependent on processing method and the materials costs presently range from $1000 for material to $7000/lb for complex components, what is the potential for future reductions in materials costs and what are the impacts of these costs on reactor costs?

II. FABRICATION OF COMPONENTS

A. Critical Fusion Issues

Joining of CMCs is a relatively untested technology, although there are several methods for making ceramic/ceramic and ceramic/metal joints. Joining of CMCs will clearly be necessary because the fabrication of large components from a single piece is very difficult. Also, on-site joining will be necessary. Therefore, the following joining issues were identified:

- demonstration of joining CMCs
- on-site joining of CMCs (e.g., microwave or laser joining).

B. General Issues

1. What is the status of NDE for CMCs? Can critical fracture toughness-sized flaws (~0.2 mm) be distinguished from porosity, which can have similar dimensions?

2. Can net shape components be fabricated or will it be necessary to machine parts to final shape? What will be the impact of a machining process on fabrication costs?

3. How will the as-built integrity be assessed? Will it be necessary to proof-test or will NDE be adequately developed for composites in the future to ensure reactor integrity?

III. UNIRRADIATEO MATERIAL PROPERTIES

A. Critical Fusion Issues

1. The chemical compatibility of CMCs with the coolant, tritium, and breeder and multiplier materials is of major concern. Alkali elements alter the protectiveness of the SiO_2 layer that forms on SiC, so Li as a coolant or from the breeding material could induce corrosion. Also, oxygen reacts with SiC to form SiO_2. The SiO_2 forms as a protective layer but the growth rate as a function of time and temperature is important. Also, the compatibility of SiC and C with tritium is a concern at elevated temperatures.

B. General Issues

1. The inter-layer shear strength of composites[a] is generally very poor. This is a concern for the use of CMCs in fusion reactors because of the need to transfer load at fittings and couplings.

2. Can the variability of material properties from batch to batch and vendor to vendor be reduced and what is the impact of this variability on fusion design?

3. What is the proper specimen design for obtaining mechanical and physical properties data?

4. Is the matrix fracture stress the proper limiting stress for CMCs or is some value greater than this appropriate?

5. The design methodology for brittle matrix materials has not been proven and this will be necessary before reactor licensing. The effects of irradiation will complicate this. Will this methodology be in place for use of CMCs in fusion reactor construction?

6. What are the thermal and mechanical fatigue and creep properties of CMCs? Are they acceptable? For steady-state operation, creep properties will be most critical but cyclic stresses and strains will also occur with start-up/shut-down and non-steady-state operation.

IV. IRRADIATED MATERIAL PROPERTIES
(at relevant fluences and temperatures)

A. Critical Fusion Issues

1. Radiation stability: failure induced by differential dimensional changes of fiber and matrix.

2. Radiation effects on electrical and thermal conductivity and mechanical properties.

3. Radiation effects on chemical compatibility.

4. Stability and integrity of joints in an irradiation field.

B. General Issues

1. What is the activation level for commercial CMCs including the effects of impurities?

2. What are the effects of transmutants (solid and gaseous) on properties?

3. What is the life-limiting property?

4. What is the effect of plasma/material interactions on material performance?

5. Is there enough basic understanding about radiation damage (gas transport, defect migration and agglomeration) to adequately design radiation-resistant CMCs?

6. How does radiation affect the interfacial (fiber/matrix) properties of CMCs?

7. Are there flux- and rate-dependent properties which will impact the use of CMCs in ICFs?

8. Does radiation accelerate creep in CMCs as it does in metals?

9. What are the optimal reinforcement and reinforcement architecture for radiation resistance?

10. Is the dimensional stability of SiC/SiC independent of fluence as suggested by the limited data on SiC?

(a) The inter-layer shear strength of composites is generally a major concern for 2-dimensionally reinforced composites using organic matrix materials. The 2-D composites are manufactured using a resin that "glues" two sheets of fiber cloth together. This manufacturing approach results in a weak inter-layer shear strength. For ceramic matrix composites, however, the chemical vapor infiltration manufacturing approach generally avoids this shortcoming by using a 3-D weave. Otherwise, a non-reinforced layer of ceramic between layers of 2-D fiber-reinforced sheets would be susceptible to the same catastrophic failures as is bulk ceramic material. For ceramic matrix composite materials the issue of inter-layer shear strength is replaced by the issue of fiber/matrix interface strength.

V. OTHER ISSUES

A. Consideration of CMCs should be based on an evolutionary understanding of their behavior in a radiation environment, in that lessons learned in early irradiation testing should be used in conjunction with a fundamental understanding of the structure-property relations of these systems to tailor the structure for improved irradiation response. A feasibility assessment of CMCs may not be complete until at least one iteration has occurred in this development cycle.

B. It is possible that the final reactor design will not be all ceramic nor all metallic but a mixture of the two. What are the priority uses for CMCs and how do the feasibility issues relate to these uses?

VI. ON-GOING IRRADIATION STUDIES OF CMCs

A. ORNL: C/C, pitch and pan fibers, 600 and 900°C irradiation temperatures, fluence less than 32 dpa, evaluate dimensional change, microstructure, modulus, conductivity, strength (brittle ring).

B. PNL: Same materials as above, cycle 11 of FFTF MOTA.

C. PNL/KIST Tests: Large variety of C/C and SiC/SiC; 850 and 1500°C, 1.5-4.0 dpa. Dimensional change and fracture strength at irradiation temperature.

D. RPI/ORNL: SiC/Nicalon composite, 300°C, 2–24 dpa with neutrons; SiC/Nicalon 1→100 dpa, RT-900°C with C, He, H beams. Emphasis of work, will be to study radiation and gas production effects on interface. Radiation-induced conductivity measurements are also underway at RPI.

E. LANL will be commencing research on CMCs which will be partly dictated by the results of this workshoo.

FUTURE PLANS

A workshop report containing presentations and summaries will be published. A second workshop was recommended but a date for this follow-up workshop has not been set.

DEVELOPMENT OF THIN-SECTION PUSH-OUT TECHNIQUE FOR USE IN MEASURING RAOIATION-INDUCED MODIFICATION OF COMPOSITE INTERFACES — Lance L. Snead [Rensselaer Polytechnic Institute (RPI), assigned to Oak Ridge National Laboratory], Steven J. Zinkle (Oak Ridge National Laboratory), and Don Steiner (RPI)

OBJECTIVE

The possibility of using low-activation ceramic composites in fusion systems will depend not only on the radiation integrity of the composite fiber and matrix, but also on the interfacial structure inherent to such composites. The objective of this study is the development of a technique to directly measure interfacial mechanical properties of the fiber/matrix interface. Once this technique has been verified, the influence of radiation on the interface may be quantified and it may be used as a tool in the development of radiation hardened composites.

SUMMARY

A technique for measuring the interfacial properties for extremely thin composite sections is presented. The data shown is for a single composite section of 22 μm thickness. By employing a Nanoindenter microhardness tester, composite fibers were individually loaded and the debond and frictional sliding strength measured. It is shown that such a technique can discriminate between the debond and frictional components of the interfacial bond. The technique presented is a substantial improvement over previous techniques in both thickness of composite section, fiber loading accuracy, and percentage of fiber failures. Though the data presented is only for a single section, the results are typical of other sections tested. A statistical analysis of the data suggests that a Weibull treatment is more appropriate to interfacial data than the commonly used normal distribution.

PROGRESS AND STATUS

Introduction

The potential benefits of ceramics for use as structural materials in fusion systems have long been apparent. Their inherently low activation and afterheat are benefits for maintenance and disposal, their potentially higher operating temperatures offer the possibility of increased reactor thermal efficiencies, and the unusually high modulus and strength of some ceramics are attractive. However, ceramics are inherently brittle, which raises many practical objections to their use.

In recent years there has been a growing interest in ceramic composites. A composite offers the possibility to take advantage of the strong points of the monolithic material, and being a composite, a degree of "ductility* can be built in. A composite which offers the attractive features of a ceramic and possesses a degree of ductility is the SiC/SiC system. Through the incorporation of high-strength silicon carbide fibers into a chemically vapor-deposited matrix, along with a fiber/matrix interfacial layer, the ceramic no longer fails jn a catastrophic manner. Figure 1 shows the load/displacement behavior of such a composite made with varied thicknesses of a graphitic carbon interfacial layer. From the figure it is apparent that the composite with no interfacial coating failed at a relatively low load and in a brittle manner. As the interfacial layer becomes thicker, the failure appears to be more ductile with the ultimate strength of the composite dramatically increasing and passing through a maximum.

It is well known that the ceramic composite strength and fracture toughness are very sensitive to the type and magnitude of bonding at the fiber/matrix interface.[1,2] This interface has the dual roles of being strong enough to transfer load between matrix and fiber to take advantage of the high fiber strength and being compliant enough to inhibit crack propagation, thus adding toughness to an otherwise brittle composite. If ceramic composites are to be used as structural materials in fusion systems, a fundamental understanding of not only the radiation effects on the matrix and fibers will be required, but also effects on the composite interfacial structure.

Due to the fundamental importance of the composite interface and the newness of direct interfacial measurement techniques, there has been growing interest in this area. There have been several recent papers in which experimenters have employed microindentation testing techniques to measure interfacial strength.[3-6] The bulk of the work for ceramic fiber composites has been on the SiC/glass system which, due to the mismatch in thermal expansions and resulting debonding during process cooling, has a pre-cracked interface yielding only a frictional resistance to fiber sliding. Marshall[7,8] was the first to employ a microindentation technique to measure this interfacial frictional strength by using a Vickers pyramic indenter to apply load and push-down fibers oriented normal to a polished SiC(Nicalon)/lithium-alumina-silicate (LAS) glass surface. In the corresponding analysis, Poisson effects on the fiber end were neglected and the frictional resistance was taken to be proportional to the square of the applied force divided by the sliding distance of the fiber. Results of interfacial friction were shown to compare reasonably well with data taken using matrix crack-spacing measurements.

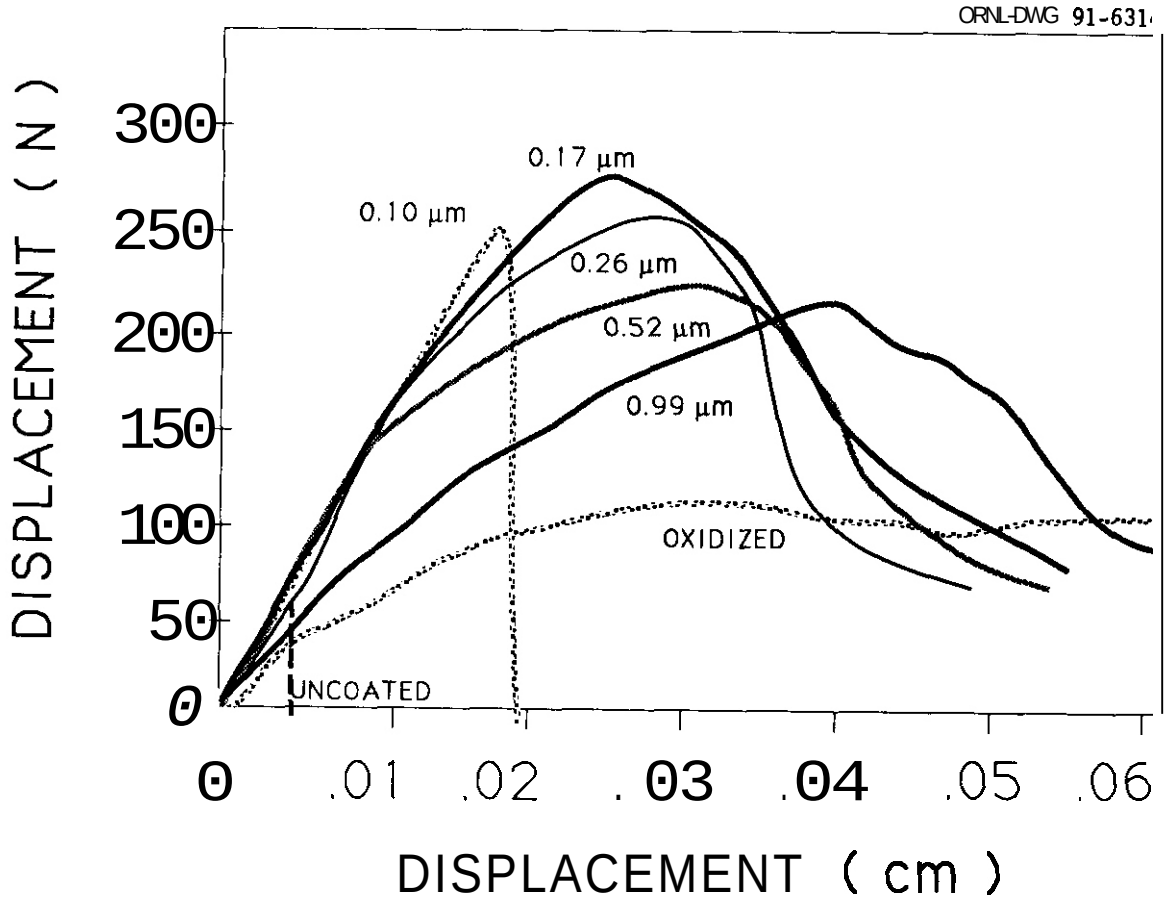

Fig. 1. Load-displacement curve showing effect of composite interfacial coating.

It is clear that for a fully bonded interface there will be at least two competing resistances to fiber sliding. First, there will be a minimum force required to initiate a crack in the interfacial chemical bond which may or may not then have the required energy to propagate along the length of the fiber. Second, there will be a frictional component to the resistance which is caused by the crack surfaces passing over each other as the fiber slides.

Marshall and Oliver[9] were the first to use a microindentation technique to attempt to separate the effects of bonding and frictional sliding in weakly bonded composites. In their experiments they heat treated as-processed, unbonded Si(Nicalon)/LAS composite in air and argon between 900 and 1250°C forming a carbon chemical bond at the interface. The Nanoindenter™ was used to apply load to fibers of thick sections of the as-processed and heat treated composite. Using the Nanoindenter, an accurate force-vs-displacement curve was generated and from the loading curve and the unload-reload hysteresis curves an estimate of the debonding and frictional resistance could be obtained.

Later researchers[10] employed a similar methodology with composite sections thin enough such that a small percentage of the fibers were "pushed-out" of the matrix, thereby simplifying analysis of the interfacial strengths. Bright et al.[5] applied the push-out technique to fully bonded SiC(AVCO)/reaction-bonded-silicon-nitride composites and measured both bonding and frictional interfacial strength for sections as thin as 0.5 mm, or a fiber diameter to thickness ratio of approximately 1/35. For fiber push-out experiments it is beneficial to have as large a fiber diameter-to-thickness ratio as possible while not altering the fiber/matrix interface in the thinning process. By doing this the calculation of the interfacial shear stress is simplified.

A characteristic of most ceramic fiber composite interfaces is the wide distribution of intersample interfacial strengths. There has been little statistical analysis of this variation to date, with some researchers assuming a normal distribution in strengths.[10]

The purpose of this report is to present interfacial bond and frictional strength obtained from push-out measurements for a very thin section of SiC(Nicalon)/SiC(CVD) composite material. Such a thin section technique is ideal for analyzing radiation modifications caused by displacements and the high helium gas generation intrinsic to this material. All results reported are for a single composite section of 22 μm, which corresponds to a Nicalon fiber diameter to sample thickness ratio approaching unity. While results represent a single composite section, they are typical of other sections tested. Finally, a methodology is presented for selecting between competing statistical distribution functions to describe interfacial strength data.

Experiments

The composite sample is a layered 30/60/90 weave of Nicalon cloth infiltrated with SiC using the ORNL Forced Chemical Vapor Infiltration process." The fiber/matrix interface contains a 1 μm layer of graphitic carbon which was deposited onto the fibers from a methane gas prior to SiC infiltration.

The composite was sliced into 250 μm sections with a low-speed diamond saw and mechanically thinned and polished with 6, 1, and 1/2 μm diamond paste to a final thickness of 22 μm. The sample was then mounted onto a polished aluminum holder such that the center of the sample was positioned over a groove of 200 μm in width. The composite section was then held rigidly to the mount and fixed to the surface with crystal bond mounting wax. Care was taken during the thinning and mounting procedure to prevent bending the sample in order to avoid pre-cracking the interface.

A load-controlled Nanoindenter microindentation hardness tester was used to apply a force to the fibers which lay normal to the composite surface. A good discussion of the Nanoindenter can be found elsewhere.[12] The Nanoindenter has an applied force and depth measurement sensitivity of 0.3 μN and 0.16 nm, respectively. The X-Y table has sub-micron accuracy to ensure loading near the center of fibers which have diameters ranging from 12 to 25 μm. A constant loading rate of 900 μN/s was used with a maximum loading capability of 0.12 N which corresponds to approximately 700 MPa for the average fiber. A Berkovitch-type pyramidal diamond indenter tip was used with an aspect ratio of 1:7.

Once the fibers were loaded to their debond load and pushed through the matrix (or to the maximum load of the machine while remaining intact), the sample was then demounted and turned over in the holder such that the debonded fibers again lay over the 200 μm groove. The positions of the fibers, which are seen as standing out of the matrix, were found and the load reapplied with the Nanoindenter so that the fibers passed through their original positions and out the opposite side of the composite section. By keeping track of the coordinates for the fibers in both directions, the debond strength and sliding resistance for each fiber could be compared. The individual fiber diameters were measured by utilizing the Nanoindenter optics and positioning.

Results

A total of 44 fibers were tested, of which 37 fibers debonded within the machine's maximum load of 0.12 N. All of the debonded fibers that were tested in reverse loading showed frictional sliding. Figure 2 shows the load displacement curve For a fiber that did not fail, which provides a measure of the specimen compliance. This can be crucial since, if there is appreciable specimen bending present, there may be a fiber pinching effect which would affect the results. It can be seen from Fig. 2 that the maximum diamond indenter depth corresponding to maximum machine load is 1.5 μm (marked A), of which 0.4 μm (marked B) is plastic deformation of the fiber.

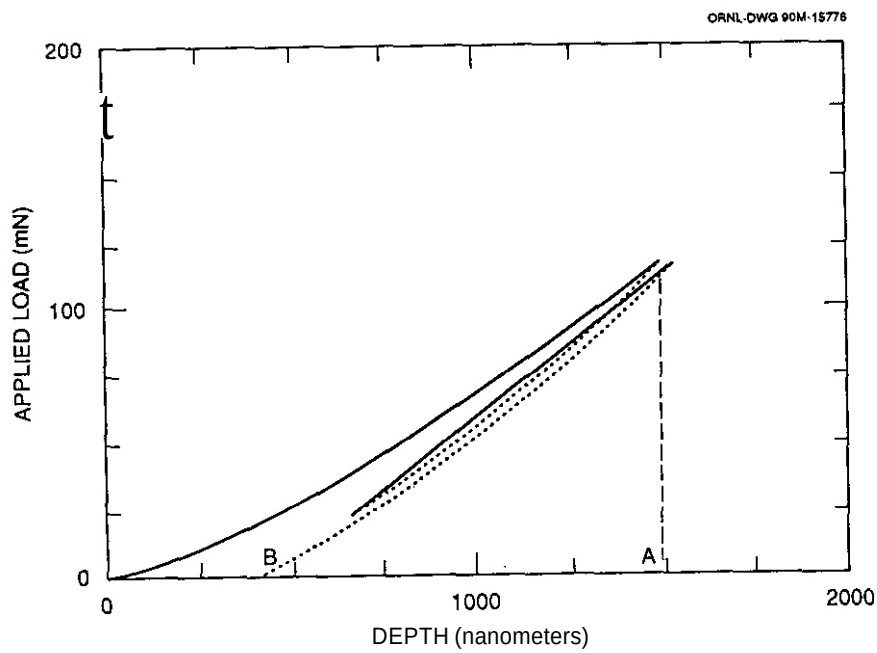

Fig. 2. Load displacement curve showing a non-yielding fiber.

Previous researchers have noted the problems of testing very thin composite sections.[5,8,13] The interfacial bonding and sliding friction strengths can be affected by precracking of the interface during thinning and by altering the interfacial stress state as the result of specimen compliance during testing. However, by careful mechanical thinning and polishing it is possible to overcome these problems with SiC composites. It is easily shown that the 1.1 μm displacement (in Fig. 2) of a large section suspended over a 200 μm groove will have a negligible effect on the results. Also, due to the fact that the matrix SiC becomes transparent for thicknesses less than (approximately) 50 μm, the absence of large matrix cracks was verified using a transmission optical microscope.

It is also seen from Fig. 2 that the load-displacement (and hysteresis) curve has the parabolic shape characteristic of indentation hardness measurements of monolithic materials, which indicates an absence of fiber interfacial failure. When fiber interfacial cracking occurs, followed by a fiber debonding, there will be a noticeable departure from the parabolic load curve. The bond failure can be either a partial or total debonding depending on whether the crack front has the energy to propagate the length of the fiber. The partial debonding is measured here as 2% departure from the parabolic load curve whereas the total fiber debond is measured as the stress at which the fiber is pushed out of the matrix. However, it was observed that a fiber could exhibit one, both, or neither of these failure mechanisms. Some fibers showed no parabolic deviation prior to the point of complete push-out, which would correspond to a very rapidly propagating crack front, whereas other fibers showed a deviation at a relatively low load and no push-out within the machine's maximum load, which is indicative of an arrested crack front.

Figure 3 shows an example of a bonding failure exhibiting distinct interfacial yielding followed by total debonding. As the fiber was loaded, there was a partial (2%) yield of the interface at approximately 65 mN (A) followed by a total debonding and fiber push-out at 80 mN (B). The fiber was pushed out of the composite section ~2.2 μm, at which point the indenter contacted the matrix surrounding the fiber. The matrix contact depth is seen in Fig. 3 at an indenter depth of 3000 nm. Both partial debonding (A) and the point of fiber push-out (B) are noted. The absence of data points between B and C is evidence of the rapid fiber failure indicative of the total interfacial debonding and push-out. The stress at failure is taken to be the load applied at the point of yielding divided by the interfacial area. This, however, is an oversimplification as the load is actually concentrated at the crack front itself and not spread over the entire interface.

The failure in the reverse loading situation is shown in Fig. 4. The frictional failure is characterized by a graceful departure from the normal loading curve. The frictional stress is obtained by dividing the sliding load by the fiber interfacial area. In this case, sliding occurred at 32.5 mN (A) and was pushed a total length of 4500 nm (B). With total fiber debonding, the applied load required to keep the fiber moving at a constant rate should remain constant or change slightly with the change in interfacial area as the fiber is pushed out. In Fig. 4, after the point (A) when the fiber started to slide, the force continues to increase until the diamond comes in contact (B) with the channel walls left behind by the sliding fiber. The load increase occurs because the Nanoindenter was programmed to produce a constant loading rate during the indentation. After the onset of fiber sliding the load continued to increase, accelerating fiber sliding which is demonstrated by the increased spacing between the data points A and B.

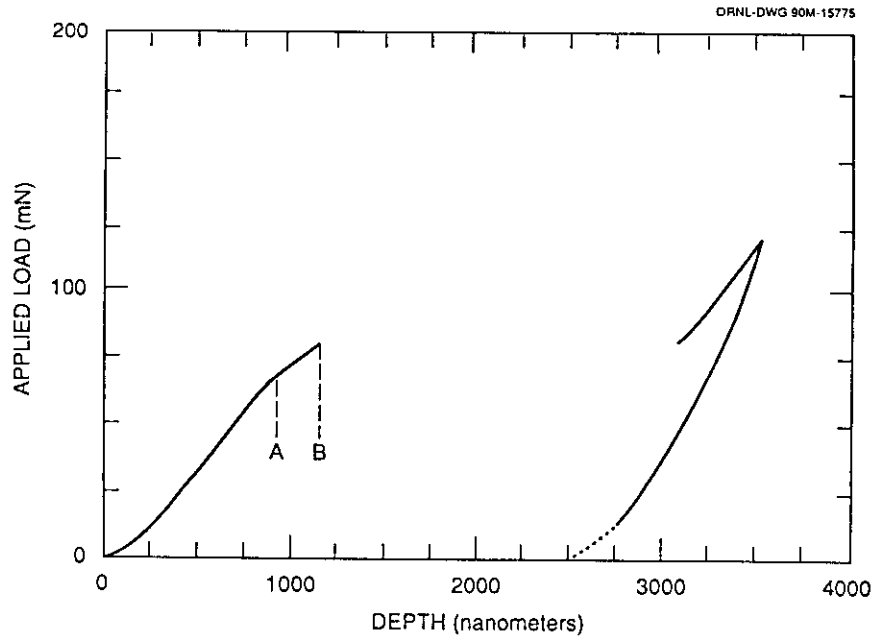

Fig. 3. Load displacement curve showing a fiber which yielded and then pushed out of the section.

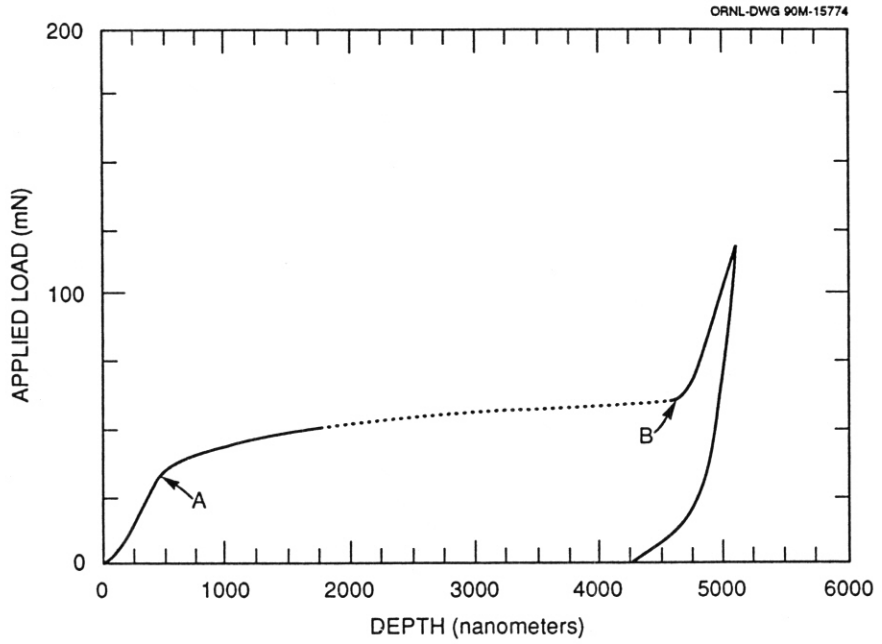

Fig. 4. Load displacement curve showing fiber sliding.

Figure 5 shows a scanning electron micrograph of a pushed-out fiber. The fiber pictured in the bottom portion of the micrograph is the fiber of Fig. 2, which did not yield, and has a large pyramid-shaped imprint resulting from plastic deformation of the Nicalon at the Nanoindenter's maximum load. Pictured above this is a debonded fiber which was pushed out and then reloaded and pushed in the opposite direction a total of 5 μm. Though the micrograph may suggest that a nearest neighbor effect may have been responsible for the adherence of the lower fiber, in the inspection of hundreds of failed fibers such a correlation was not found.

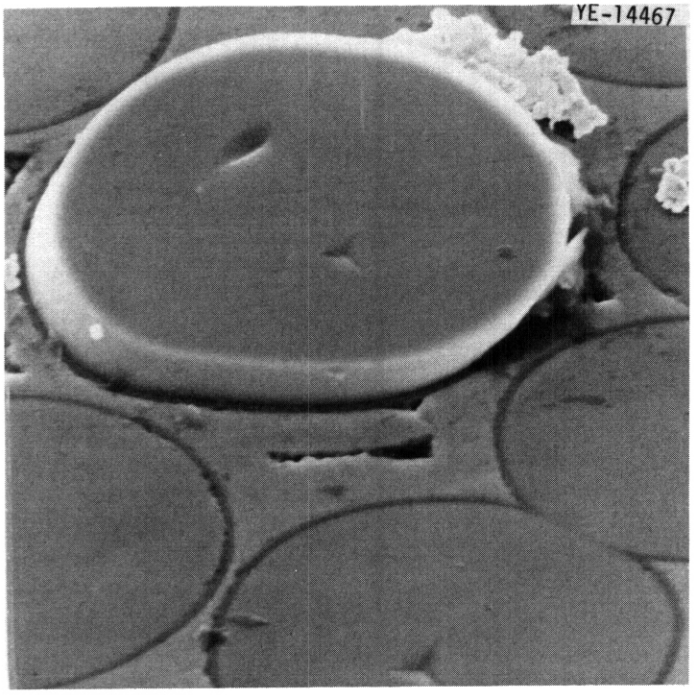

Fig. 5. SEM micrograph of bonded and pushed-out fibers.

Analysis of Results

Because of the large variation in interfacial strengths observed by other researchers,[10] the choice of the most appropriate distribution function to describe the data is of fundamental importance. While from a theoretical bases, no one distribution is better than any other, the choice of the best-fitting function will have a large impact on predicting such values as mean strengths from censored and non-censored data.

The possible probability density functions considered here are the lognormal, exponential, gamma, and Weibull distribution The functional forms for each are listed in Table 1. In order to discriminate between competing distributions, the formalism proposed by Dumonceaux and Antle[14] and Kent[15] has been adopted here. This method is based on the concept of a Maximum Likelihood Ratio (MLR) which is defined below. The ML function was used as the selection statistic to find the best-fitting distribution for the data.

Consider a set of data given by:

sample: y1, y2, ... yn ,

Table 1. Probability Distribution Functions

NAME	SYMBOL	PROBABILITY DISTRIBUTION FUNCTION
EXPONENTIAL	$E(\theta)$	$\theta^{-1} \exp^{(-x/\theta)} \cdot I(\theta,\infty)(x)\ \theta>0$
GAMMA	$G(\theta,\alpha)$	$\theta^{-\alpha}[\Gamma(\alpha)]^{-1} x^{\alpha-1} e^{(-x/\theta)}\ \theta>0,\ \alpha>0$
WEIBULL	$W(\theta,\beta)$	$\frac{\beta}{\alpha} \cdot \left(\frac{x}{\theta}\right)^{\beta-1} \cdot e^{[-(x/\theta)^{\beta}]} \cdot I(0,\infty)(x)\ \theta>0,\ \beta>0$
LOGNORMAL	$LN(\theta,\sigma)$	$\frac{1}{\sqrt{2\pi}\,\sigma x} \cdot e^{\left\{\frac{-[\ln(x/\theta)]^2}{2\sigma_0^2}\right\}} \cdot I(0,\infty)(x)\ \theta>0,\ \sigma>0$

with assumed distribution function given by:
distribution: Y1, Y2, ... Yn;
then the Likelihood Function, L, is:

$$L(y1, y2, \ldots yn;\theta) = \prod_{i=1}^{n} f(yi,\theta)$$

where θ is the ML parameter(s) and F is the distribution under consideration. For example, in the case of the lognormal distribution. the likelihood function would be:

$$L(y1, y2, \ldots yn;(\mu_0,\sigma_0^2)) = \frac{1}{\sqrt{2\pi}\sigma_0} e^{-\frac{1}{2}\left(\frac{y1-m}{\sigma_0}\right)^2} \cdot \frac{1}{\sqrt{2\pi}\sigma_0} e^{-\frac{1}{2}\left(\frac{y2-m}{\sigma_0}\right)^2} \cdots \frac{1}{\sqrt{2\pi}\sigma_0} e^{-\frac{1}{2}\left(\frac{yn-\mu}{\sigma_0}\right)^2} \cdot$$

If the derivative with respect to μ_0 (mean) and σ_0^2 (variance) is taken and equated to zero, the parameters yielding the maximum likelihood function are obtained and an associated MLR is calculated. The MLR then gives a measure of the correctness of the fit as given by the distribution. By calculating the ML parameters for each distribution under consideration, the best-fitting function is obtained by choosing the distribution with the least negative MLR.

For both fully bonded and unbonded interfaces, researchers have found a great variability in measured intersample interfacial strengths. The variability in the interfacial strengths had initially been treated as being best fitted by a lognormal distribution.[10] A normal plot reproduced from Weihs and Nix[10] showing the frictional resistance to sliding of Nicalon™ fibers in a LAS matrix is shown in Fig. 6. For this data the MLRs were obtained as given in Table 2 for the as-processed and annealed conditions. By inspection of the table, it is apparent that the Weibull distribution gives the least negative MLR value (thus the best fit) for the three composite conditions with the lognormal giving the most negative MLR values for two out of the three. This analysis suggests that the interfacial frictional sliding may be best described utilizing a Weibull treatment of the data.

Table 2. MRL values of interfacial friction measurements on SiC/LAS composite[10]

	Weibull	Gamma	Exponential	Lognormal
As-Processed	−77.5	−78.8	-83.0	-80.61
2-h Anneal	-87.3	-88.3	−91.1	−90.29
4-h Anneal	−66.2	66.2	−66.6	-66.34

Figure 7 shows a Weibull plot of the same data as Fig. 6. By comparison of Figs. 6 and 7, it would appear that the data is somewhat better represented by the Weibull in the tail regions where the two fitted curves would be expected to show the largest difference. It shoud be mentioned, however, that due to the limited number of data points, there is a minimum theoretically expected error with a MLR selection. According to Kent,[15] the probability for incorrectly choosing a Weibull distribution from lognormally distributed data for 20 observations is 26% (and for 30 observations 19%). However, the probability for incorrectly choosing the Weibull in all three cases is 0.26 cubed or 1.76%. This calculated error does not account for any experimental error in the data forcing an incorrect selection.

Results obtained for the SiC(Nicalon)/SiC composite system suggest also that a Weibull distribution is the most appropriate. Table 3 shows the MLR comparisons for the debond strength and frictional resistance to sliding for a 22 μm section. Again, the Weibull has the largest MLR values indicating the best fit to the data. The MLR values for the data presented do not drastically differ between distributions and in the case of the 2% debond yield data the values for the Weibull and gamma distributions are nearly identical. Such small differences are typical of an MLR analysis, however. By comparison of the exponential distribution with the other distributions, which have fundamentally different shapes, one would intuitively expect a large difference in goodness of fit statistic (for 5 not approaching unity). Though for an MLR analysis, this difference is typically less than 10%.

Table 3. MRL values for push-out of SiC/SiC

	Weibull	Gamma	Exponential	Lognormal
2% Debond Yield	−172.5	−173.0	−175.0	−175.0
Frictional Sliding	-89.9	−90.5	−98.8	−91.7

The two-parameter form of the Weibull probability distribution function is applied, given by:

$$P = \left(\beta\sigma^{\beta-1}/\theta^{\beta}\right) e^{-(\sigma/\theta)^{\beta}} ,$$

where β is the Weibull slope (shape parameter), θ is the size parameter, and σ is the applied variable stress. This can be written in the more convenient form of the cumulative failure distribution which would represent the total probability of fiber failure:

$$F = 1 - e^{-(\sigma/\Theta)\beta} .$$

The data for the debonding and frictional sliding of the composite fibers are plotted on standard Weibull paper in Fig. 8. Both the 2% deviation from the parabolic curve and the total debond (push-out) criteria for bond failure are plotted. From the figure, it appears that the 2% yield criterion for failure is the more attractive description of the debonding stress, giving an approximate Weibull modulus of 1 and shape parameter of 60 MPa for debond yield strength. The fiber frictional sliding data is seen to have a steeper slope (higher Weibull modulus) with a lower average strength. The optimized values of 5 and Θ are given on Fig. 9, which shows the cumulative distributions for debonding and frictional sliding. The average Weibull shear strengths are calculated to be 60.8 MPa for debonding and 16.5 MPa for friction.

Due to the relatively low values of the Weibull moduli, the probability distribution function for the debonding yield strength and the frictional sliding resistance is rather broad. Because of this, there will be noticeable overlapping of the probability functions which would become more pronounced as the average strengths of the two distributions approach each other. When the fibers are initially loaded, therefore, there will be some fraction of fibers (mathematically) which possess a higher frictional resistance to sliding than debond strength. Physically this means that the stress required to initiate and propagate a crack is less than the stress required to slide the fracture surfaces across each other. On the load curve of such fibers, the debonding is not noticeable and the gradual frictional-type failure would dominate.

Figure 10 shows the correlation between the debond yield strength and the frictional resistance to sliding. This plot simply shows the measured 2% debond strength and frictional resistance for each individual fiber tested. From this figure it is apparent that the two strengths are not independent of each other and that the higher bond strength fibers have a higher average frictional resistance. For each fiber with bond strength, σ_b, there should be a (Weibull type) scatter in possible values of the frictional strength, σ_f, around some mean value of frictional strength (σ_{fm}). The line fitted to the data of Fig. 10 represents such a mean value of frictional resistance. Because it is possible for very low bond strength fibers to have a significant frictional resistance to sliding this lines does not pass through the origin.

The increase in frictional strength with the more strongly bonded interfaces may simply be because the path which the crack front travels for the stronger bonds provides a more jagged surface for fiber sliding, thereby inducing a higher frictional resistance.

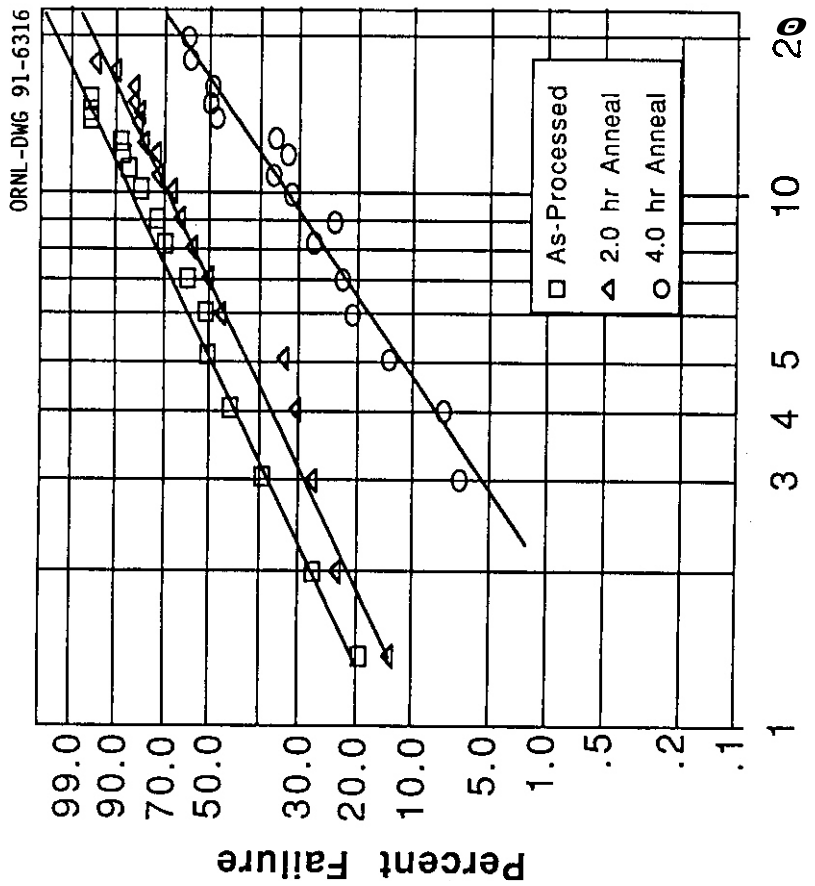

Fig. 7. Weibull Plot of the variation of frictional resistance in the SiC(AVCO)/LAS glass system.

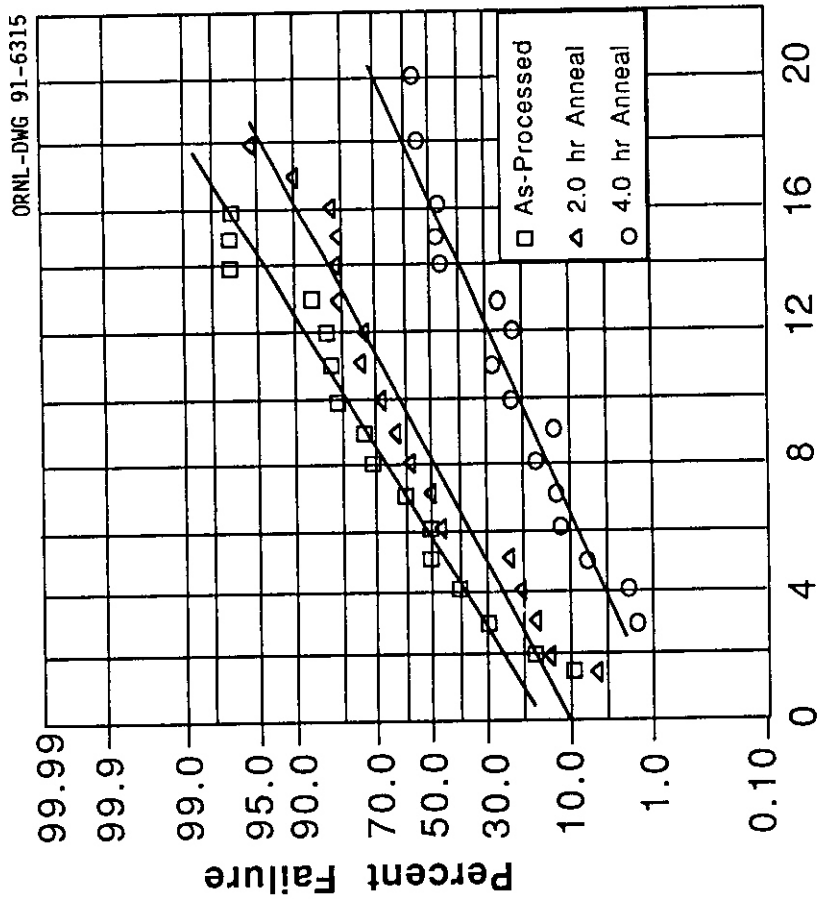

Fig. 6. Normal Plot of the variation of frictional resistance in the SiC(AVCO)/LAS glass system.

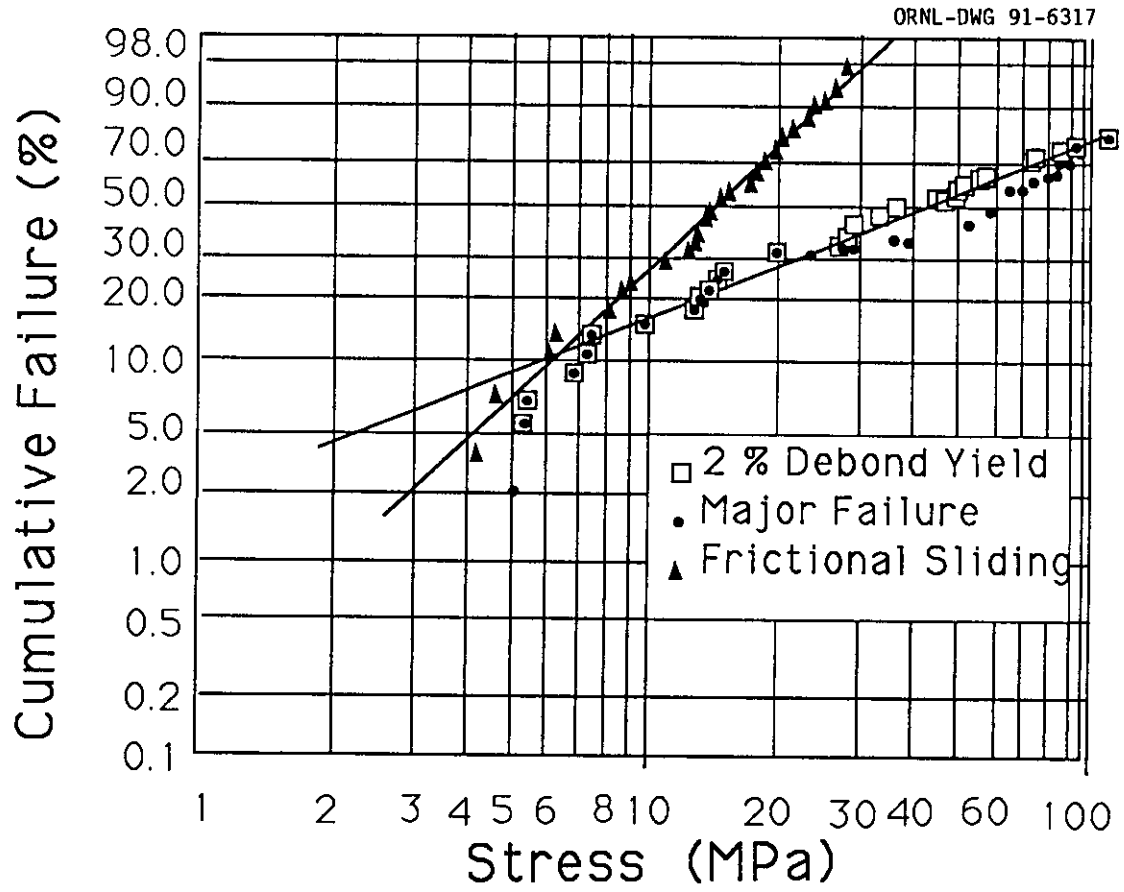

Fig. 8. Weibull plot of the variation of frictional and debond resistances in the SiC(Nicalon)/SiC system.

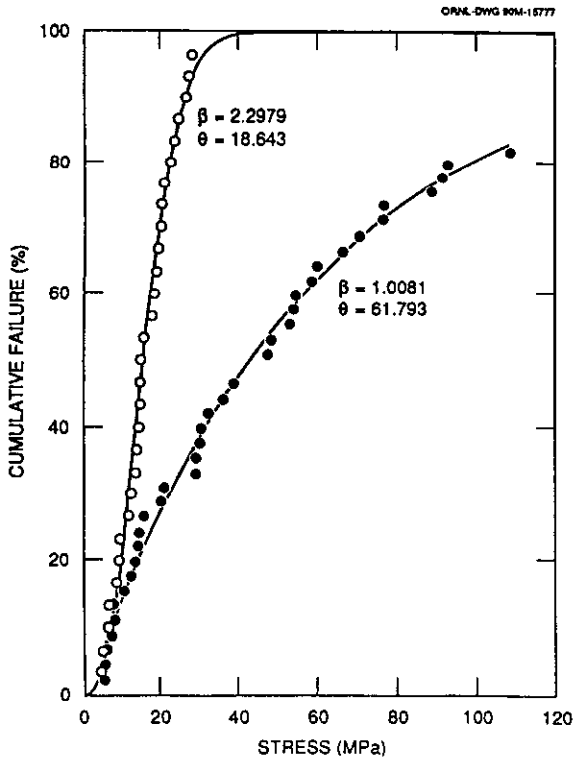

Fig. 9. Cumulative failure plot of variation of frictional and debond resistances in the SiC/Nicalon)/SiC system.

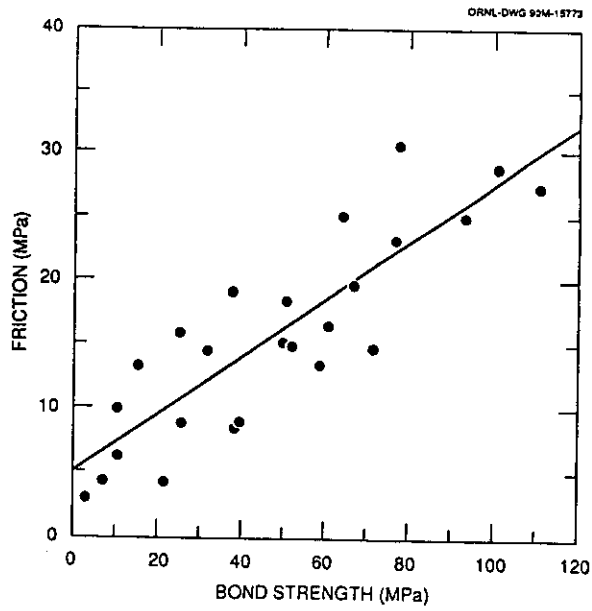

Fig. 10. Plot showing relationship between frictional resistance to sliding and interfacial debonding.

CONCLUSIONS

It has been shown that samples of SiC(Nicalon)/SiC composites can be thinned to a thickness approaching a fiber diameter (~20 μm) and push-out tests can be performed without sample compliance limitations or matrix cracking. Also, testing of such a thin section allowed a high percentage of interfacial failures of those fibers tested. The debond yield strength and fiber push-out strength for these small fibers can be obtained using a Nanoindenter. The frictional resistance to sliding can likewise be determined by reapplying the load to the opposite end of the pushed-out fiber. Such a technique is ideal for studying the interfacial effect of displacement damage and helium gas generation for either neutron or ion beam irradiated materials.

The debond yield, debonding push-out, and fiber sliding stress can be adequately separated by inspection of the load-displacement curve. The debonding is characterized by an abrupt failure while the fiber sliding is a more graceful failure.

A Maximum Likelihood Ratio technique has been used as a selection statistic to choose between competing distributions. Of the four distributions considered, the Weibull distribution appears to fit the data most appropriately.

The result of the analysis has shown that the interfacial frictional stress has a higher Weibull modulus than the debond stress, thus a less "brittle" failure.

A correlation between individual fiber debond strength and the fiber resistance to sliding has been shown. The results indicate that the fiber interfaces which possess a higher degree on bond strength also have a higher resistance to fiber sliding.

FUTURE WORK

This technique of measuring the interfacial debond yield strength and frictional resistance to sliding is being developed to be applied to composites modified by neutrons and ion beams. Specifically, the effect of neutron displacement damage will be studied on HFIR and FFTF irradiated samples with displacements of 2 and 30 dpa, respectively. Also, the effect of carbon beam displacements and helium bubble formation at the interface is being pursued in the displacement and temperature range of 1 to 30 dpa and 300 to 1100°C, respectively.

ACKNOWLEDGMENTS

The authors would like to thank Rick Lowden of Oak Ridge National Laboratory for providing the SiC/SiC composite material used and also K. B. Alexander for the scanning electron micrograph.

REFERENCES

1. A. G. Evans and D. B. Marshall, "The Mechanical Behavior of Ceramic Matrix Composites," Acta Met. 37(10) (1989) 2567–2583.

2. R. J. Kerans, R. S. Hay, N. J. Pagano, and T. A. Parthasarathy, "The Role of the Fiber-Matrix Interface in Ceramic Composites," Ceram. Bull. 68(2) (1989) 429–442.

3. D. B. Marshall and W. C. Oliver, "Measurement of Interfacial Mechanical Properties in Fiber-Reinforced Ceramic Composites," J. Am. Ceram. Soc. 70(8) (1987) 542–548.

4. T. P. Weihs and W. D. Nix, "Direct Measurement of the Frictional Resistance to Sliding of a Fiber in a Brittle Matrix," *Scripta* Met. 22 (1988) 271–278.

5. J. D. Bright et al., "Interfacial Bonding and Friction in Silicon Carbide (filament)-Reinforced Ceramic and Glass-Matrix Composites," J. Am. Ceram. Soc. 7(10) (1989) 1891–1898.

6. C. J. Yang, S. M. Jeng, and J. M. Yang, "Interfacial Properties Measurement for SiC Fiber Reinforced Titanium Alloy Composites," Scripta Met. 24 (1990) 469–474.

7. D. B. Marshall and A. G. Evans, "Failure Mechanisms in Ceramic-Fiber/Ceramic-Matrix Composites," J. Am. Ceram. Soc. 68(5)(1981) 225–231.

E. D. B. Marshall, "An Indentation Method for Measuring Matrix-Fiber Frictional Stresses in Ceramic Composites," J. Am. Ceram. Soc. 67(12) (1984) C-259–C-260.

9. D. B. Marshall and W. C. Oliver, "Measurement of Interfacial Mechanical Properties in Fiber Reinforced Ceramic Composites," J. Am. Ceram. Soc. 70(12) (1987) 542–548.

10. T. P. Weihs and W. D. Nix, "In Situ Measurements of the Mechanical Properties of Fibers, Matrices and Interfaces in Metal Matrix and Ceramic Matrix Composites," Mechanical and Physical Behavior of Metal and Ceramic Comp. (Proc. of Ninth Riso International Symposium on Metallurgy and Material Science, Sept. 5–9, 1988).

11. D. P. Stinton, A. J. Caputo, and R. A. Lowden, "Synthesis of Fiber-Reinforced SiC Composites by Chemical Vapor Infiltration," Ceram. Bull. 65(2) (1986) 347–350.

12. W. C. Oliver et al., "Measurements of Hardness at Indentation Depths as Low as 20 Nanometers," pp. 90–108 in ASTM Special Technical Publ. 889, Microindentation Techniques *Material Science and Engineering, ed., P. J. Blau and B. R. Lawn, American Society for Testing and Materials, Philadelphia (1985).

13. T. P. Weihs, C. M. Dick, and W. D. Nix, "The Frictional Resistance to Sliding of a SiC Fiber in a Brittle Matrix," pp. 247–252 in High-Temperature/High-Performance Composites, ed., F. D. Lemkey et al., Mat. Res. Soc. Symp., Vol. 120 (1988).

14. R. Dumonceaux and C. E. Antle, "Likelihood Ratio Test for Discrimination Between Two Models with Unknown Location and Scale Parameters," Technometrics *15 (1973)* 19–27.

15. C. P. Quesenberry and J. Kent, "Selecting Among Probability Distributions Used in Reliability," Technometrics 24(1) (1982) 59–65.

MEASUREMENT OF DIELECTRIC PROPERTIES IN ALUMINA UNDER IONIZING AND DISPLACIVE IRRADIATION CONDITIONS — R. E. Stoller, R. H. Goulding, and S. J. Zinkle (Oak Ridge National Laboratory)

OBJECTIVE

This work has been undertaken in support of the research and development needs of CIT and other near-term fusion devices.

SUMMARY

Several experiments have been completed in which the dielectric properties of alumina have been measured in the presence of ionizing and displacive irradiation. Spent fuel elements from the High Flux Isotope Reactor (HFIR) at the Oak Ridge National Laboratory were used to provide an intense source of ionizing irradiation for some of the measurements. The TRIGA reactor at the University of Illinois was used to provide an irradiation field that produced both ionization and atomic displacements. The results of these in situ measurements indicate that the dielectric properties of alumina are more severely degraded by displacive irradiation that was indicated by earlier, postirradiation measurements.

PROGRESS AND STATUS

Introduction

The motivation for this work was detailed in an earlier report.' The fact that ceramic materials are good electrical insulators is one reason why current reactor designs call for them to be used in the fabrication of many components. The applications for insulating ceramics range from simple dc voltage standoffs to components in microwave heating systems that operate at high frequencies. The critical dielectric parameter in these latter components is the so-called loss tangent. The loss tangent must be maintained at a low value because the microwave power absorbed is proportional to the loss tangent' and excessive heating due to rf power absorption could lead to early mechanical failure.[2,3] Typical values for the loss tangent in unirradiated ceramics of interest to the fusion program are from 10^{-4} to 10^{-3}. The maximum tolerable value of the loss tangent (tan δ) in ion cyclotron radiofrequency heating (ICRH) designs ranges from 10^{-2} for pulsed near-term machines such as the compact ignition tokamak (CIT) to 10^{-3} for steady-state operation.

The well-known phenomenon of radiation-induced conductivity at dc or low-frequency ac conditions[4] gives rise to some concern about whether the candidate materials will remain sufficiently insulating when exposed to a radiation field that is typical of their ultimate operating environment. Postirradiation measurements have shown that both ionizing (at low frequencies) and displacive irradiation can increase the value of the loss tangent.[5-9] There is also some evidence that the amount of the increase is dependent on the neutron spectrum.[5] However, there have been no relevant measurements of dielectric properties during irradiation and the validity of postirradiation measurements is called into question by data that show significant levels of recovery in the loss tangent at room temperature following proton irradiation.[8] A recent IEA workshop held to review the current understanding of radiation-induced conductivity and dielectric property changes emphasized the need for in situ property measurement.[10]

In order to begin addressing some of these concerns, a series of in situ irradiation experiments have been conducted to measure the dielectric properties of alumina and sapphire while they are exposed to either an ionizing irradiation field or a field that is both ionizing and displacive. Alumina and sapphire were chosen for this initial work because they are prime candidates for use in microwave heating systems.[10,11] Similar work has been proposed and is also under way by other workers.[12]

Materials

The experimental matrix included the use of oriented single-crystal sapphire and commercial-grade polycrystalline alumina. The commercial products were obtained from two different vendors. Since postirradiation measurements have shown a significant influence of impurities,[5,6] the commercial products include several different purity levels. The materials obtained for these initial experiments are listed in Table 1. Not all of the materials have been tested to date.

Irradiation Facilities

Two irradiation facilities have been used in this work. The first was the Gamma Irradiation Facility (GIF) of the High Flux Isotope Reactor (HFIR) at the Oak Ridge National Laboratory. The GIF uses spent HFIR cores as a source of gamma radiation. Decay of fission products in the spent cores provides an intense source of ionizing radiation. The damage rate in the HFIR-GIF on the day that it was used for this work was 1.25×10^7 rads/h. This is somewhat lower than that expected near the CIT first wall. The

Table 1. Materials obtained for in situ dielectric experiments

Material	Vendor	Grade
Single crystal (0001) orientation	Crystal Systems	Sapphire
Alumina	Coors Technical Ceramics	AD94 (0.94% purity), AD998 (0.998% purity)
Alumina	WESGO Oivision, GTE Corp.	AL300 (0.967% purity), AL995 (0.995%

influence of gamma heating in this facility was determined by using a thermocouple brazed to the specimen chamber. A temperature of 73°C was measured at steady state. The small increase in rf losses in the resonant cavity walls due to the temperature rise was taken into account in evaluating the experimental results. Since gamma irradiation does not produce stable displacements in Al_2O_3, this facility provided direct information on the effect of purely ionizing radiation on loss tangent changes at ICRH frequencies.

The TRIGA reactor at the University of Illinois was used to obtain data on the influence of a mixed (i.e., displacive plus ionizing) irradiation environment. When the TRIGA is operated in a pulsed mode, the displacement rate is comparable to that expected in the CIT. The ionizing damage rate is somewhat higher than CIT. The maximum temperature due to gama heating observed during the TRIGA irradiations was 33°C. The nominal peak damage rates are listed in Table 2, along with the value for the HFIR-GIF and the CIT values.

Table 2. Typical radiation damage rates in various facilities

Facility	Damage Rate		Gamma/Neutron Absorbed Dose Ratio
	Ionizing (rads/h)	Displacement (dpa/s)	
HFIR-GIF	up to 10^8	None	Not applicable
TRIGA			
$1.50 pulse	1.3×10^9 (Al_2O_3)	1.3×10^{-8} (Ni)	19 (Al_2O_3)
63.00 pulse	2.1×10^{10} (Al_2O_3)	1.8×10^{-7} (Ni)	19 (Al_2O_3)
CIT central cell			
Near first wall	3.7×10^9 (Si)	1.9×10^{-6} (Ni)	0.65 (Si)
Rear blanket	9.6×10^6 (Si)	4.6×10^{-9} (Ni)	1.2 (Si)

The values listed in Table 2 are based on information obtained in discussions with the staff at each facility. Since the damage rate is material dependent, representative values are quoted for the materials indicated in parentheses. The gamma ray to neutron damage ratio is calculated using the absorbed dose (rads) due to gamma rays and the absorbed dose due to neutrons. The fraction of the absorbed dose due to neutrons that leads to atomic displacements is a function of the neutron energy spectrum. For example, this fraction is 0.093 near the CIT first wall and increases to 0.15 in the rear blanket position. All of the values in Table 2 are approximate and more detailed dosimetry needs to be done to characterize both the anticipated fusion environment and the test reactor environments. This need for dosimetry is greater for measurements of radiation-induced changes in dielectric properties than for structural properties since current indications are that the response of insulators to radiation is more sensitive to the details of the irradiating particle spectrum.

Experimental Method

The dielectric measurements were made using a capacitively loaded resonant cavity. The details of the experimental method were reported previously' and a drawing of a prototype cavity is reproduced in Fig. 1. The resonant cavity method is well suited to measurement of the loss tangent because the power dissipation is maximized in the ceramic relative to the balance of the experimental apparatus. In addition, losses in the feed line can be accounted for without the need for prior calibration, which would be extremely difficult to accomplish in situ. The loss tangent is measured by determining the cavity quality factor, the ratio of the stored energy to the energy dissipated per rf field period. Relative changes in the dielectric constant can also be measured using the resonant cavity technique with an accuracy of 1/Q, or less than 1% at the highest values of the loss tangent measured here.

This initial set of experiments utilized cavities that were sized to permit the measurement of the loss tangent at 100 MHz. A copper cavity with the dimensions of the prototype shown in Fig. 1 was used for some of the measurements. This was the largest cavity that the dimensions of the HFIR-GIF would

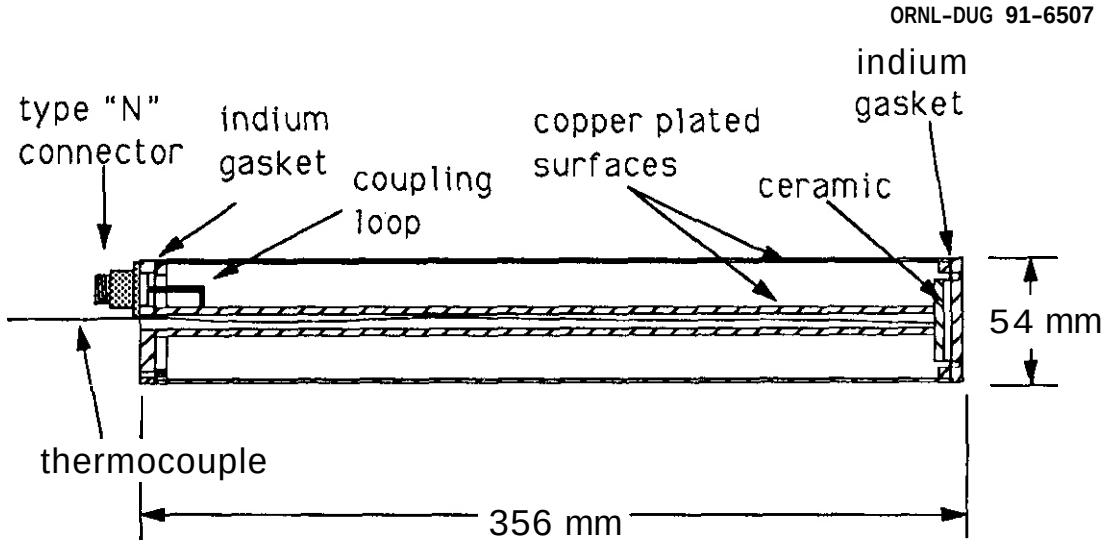

Fig. 1. Design of prototype resonant cavity for in situ dielectric measurements.

accommodate. This same cavity was also used in some of the TRIGA measurements to permit a direct comparison between the measurements obtained in the two facilities without introducing any uncertainties due to different cavities. However, a larger diameter cavity would yield a higher Q and hence improve the accuracy of the measurements. Therefore, two additional cavities were fabricated that had an inside diameter of 70 mm (with the same overall length), since the TRIGA beam tube would accommodate this larger device. In order to minimize the induced radioactivity in the larger cavities, they were constructed of aluminum rather than copper. A layer of copper about 25 μm thick was plated onto the aluminum cavity to ensure adequate electrical conductivity. Both the larger and the smaller cavities used disk-shaped specimens that were 35 mm in diameter and 3 mm thick. The larger cavities were also capable of being evacuated to determine whether there was any effect due to gas ionization in the cavity.

Results of Initial Experiments

The results of measurements in the HFIR-GIF indicated that purely ionizing radiation did not increase the loss tangent in either single or polycrystalline alumina (0.995 purity) at a dose rate 1.25×10^7 rads/h. The maximum exposure obtained in the GIF was 3.15×10^7 rads. However, substantial effects were observed in the case of experiments utilizing neutron and gama irradiation from the pulsed TRIGA reactor. As seen in Fig. 2, the loss tangent of a sample of AL995 irradiated by a pulse with a peak displacement rate of 1.8×10^{-7} dpa/s was observed to increase from 5×10^{-5} to 8×10^{-3}. This large increase in the loss tangent persisted for the duration of the radiation pulse, and then recovered to a value approximately twice the original value. It is not clear at this time whether or not this residual change is real, or an artifact caused by small temperature changes in the cavity after the pulse. As is also shown, the loss tangent was observed to peak 2 ms before the peak in the ion chamber signal. This effect was observed consistently, but is unexplained at the present time. A reduction in the real part of the dielectric constant of the ceramic was also observed during the radiation pulse, as shown in Fig. 3. A Smith chart plot showing the path followed by the cavity input impedance (with the coupling loop reactance subtracted off) during a typical pulse is shown in Fig. 4. Overlayed on this plot is the path that would be followed if there was a negative change in the real part of the dielectric constant equal in magnitude to the change in the imaginary part, that is, if we assume that

$$\Delta\varepsilon' = -\varepsilon' \tan\delta \quad .$$

It can be seen that this relationship agrees very well with the observed data. This type of behavior would typically be observed in a semiconductor, with $\varepsilon' \tan\delta$ and the change in ε' both proportional to the density of free electrons.

A complicating factor in these measurements was the presence in air in the resonant cavity, which becomes partially ionized during gamma irradiation, and can he ionized at low pressures by the rf electric field as well. Experiments to date at the GIF facility were carried out at atmospheric pressure, while the TRIGA measurements were carried out at pressures ranging from 12 Pa to atmospheric (10^5 Pa). The effect of the rf electric field on the TRIGA measurements was investigated by obtaining data at several rf

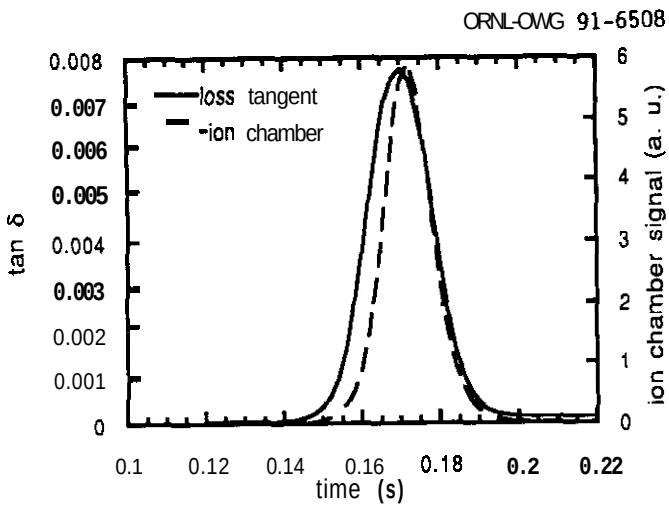

Fig. 2. Time scan comparing typical loss tangent measurements and the output from the TRIGA ionization chamber during a $3 pulse. Reactor power is proportional to the signal from the ionization chamber.

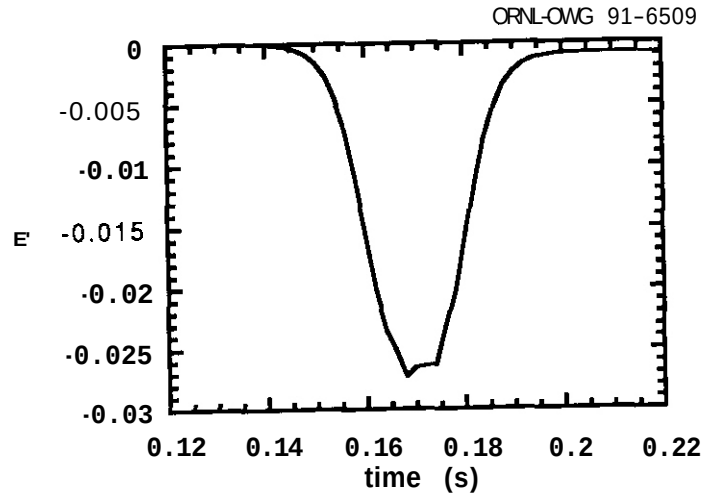

Fig. 3. Time scan showing changes in the real part of the dielectric constant for the same pulse as is shown in Fig. 2.

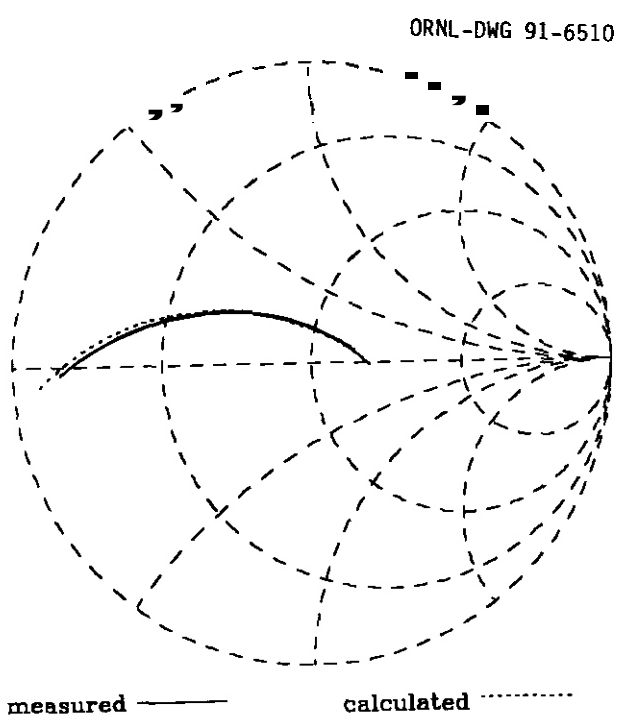

Fig. 4. Smith chart plot of the resonant cavity impedance comparing the path followed during an actual pulse with the path followed assuming tan6 increases from 5×10^{-5} to 8×10^{-3} with $\Delta\varepsilon' = \varepsilon' \tan\delta$.

power levels. At atmospheric pressure, no power dependence was observed, while at low pressure (12 to 22 Pa), no dependence was observed for rf power levels of < 1 mW. Most of the data shown here was obtained at a power level of 0.1 mW.

In order to examine the effects of ionization due to gammas accompanying the neutron pulse, the cavity pressure was varied, with the results shown in Fig. 5. It can be seen that there was no change in the observed loss tangent as the pressure was varied from 12 to 22 Pa (0.095 to 0.165 torr), but that the observed value decreased by an order of magnitude at atmospheric pressure. We are attempting to model this phenomenon, but feel that the lack of pressure dependence at low pressure indicates that air ionization has little effect on the results in this case. Experiments were also performed using an empty cavity, in which the capacitor gap was reduced so that the resonant frequency remained constant. These results are also shown in Fig. 5. In this case, the value of the "loss tangent" represents the apparent value calculated for the increased losses observed in the chamber. In actuality, losses take place throughout the cavity volume in this case as well as in the capacitor gap. It can be seen that at a pressure of 22 Pa (0.165 torr) the apparent loss tangent decreases by an order of magnitude when the ceramic is removed. but that some increase in cavity loss is still observed. It can also be seen that the apparent loss tangent decreases by a factor of 3 as the pressure is reduced from atmospheric to 22 Pa. This behavior is opposite that observed when the ceramic is present, and is consistent with losses expected for a weakly ionized plasma in which the electron density decreases with the neutral pressure. The electron density was calculated from the observed losses to be $2.8 \times 10^9/cm^3$ at atmospheric pressure and $3.2 \times 10^5/cm^3$ at a pressure of 22 Pa. This reduction in electron density is approximately linear with the reduction in neutral pressure, which would be expected for a source rate proportional to neutral density, as is the case for gamma-induced ionization, and a loss rate independent of neutral density, which would be the case if recombinative losses dominated over diffusive losses.

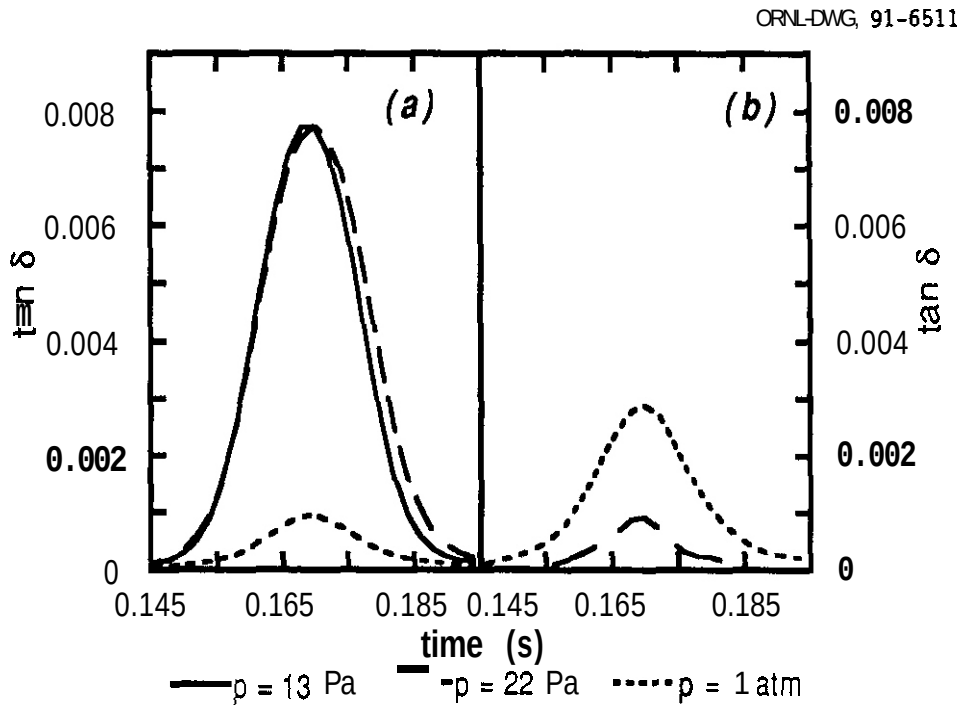

Fig. 5. (a) Time scan showing the measured loss tangent of a 99.5% pure alumina disk for different values of air pressure in the resonant cavity. (b) Time scan showing the apparent loss tangent determined from changes in losses in the cavity with no ceramic present.

Planned Additional Experiments

Additional work is required to verify these preliminary results. The fact that the ionizing dose rate in the TRIGA was about 10 to 100 times higher than that in the HFIF-GIF precludes a firm conclusion regarding the relative importance of ionization and displacement damage. Further experiments will be conducted in the HFIR-GIF using a fresh spent core in order to achieve greater than a factor of 10 increase in the ionizing damage rate. We also hope to achieve a cavity pressure for these experiments of <1 Pa, to confirm that gamma-induced ionization of air in the cavity has little effect below a pressure of about 20 Pa. Both the ionizing and displacive damage rates in the TRIGA are within the range that is expected for CIT and other fusion reactors. Thus, the increases in the loss tangent observed in these initial experiments highlight the need for a careful experimental program to qualify ceramics for use as insulators in fusion reactors. Other variables such as the frequency and the magnitude of the electric field need to be explored. The results of recent in situ dc and low-frequency (50 Hz) ac conductivity measurements by Hodgson and coworkers in Spain[10] indicate that it is particularly important to examine the effect of Sustained irradiation with an applied electric field.

The scope of materials acquired for this work has been expanded to include other ceramic materials that have potential fusion applications. The additional materials include: magnesium aluminate (spinel), silicon carbide, silicon nitride, aluminum nitride, and macor. These irradiations will continue to be conducted in the TRIGA facility at the University of Illinois. In addition, specimens of sapphire and 0.995 alumina have been irradiated in the TRIGA to a neutron fluence of about 5×10^{21} n/m^2. Post-irradiation measurements will be made on these specimens to examine the effect of neutron fluence. This will be followed by in situ property measurements on the same specimens to determine how the accumulated fluence alters the response of the materials during a TRIGA pulse.

REFERENCES

1. R. E. Stoller, R. H. Goulding, and S. J. Zinkle, "In Situ Measurements of Dielectric Properties in Alumina," FRM Semiannu. Prog. Rep., Mar. 31, 1990, DOE/ER-0313/8, USDOE, Office of Fusion Energy, pp. 297–99.
2. M. K. Ferber, H. D. Kimrey, and P. F. Becher, J. Mat. Sci. 19 (1984) 3767–3777.
3. P. F. Becher and M. K. Ferber, J. Mat. Sci. 19 (1984) 3778–3785.
4. R. W. Klaffky, B. H. Rose, A. N. Goland, and G. J. Dienes, Phys. Rev. B 21 (1980) 3610–3634.
5. J. L. Scott, F. W. Clinard, Jr., and F. W. Wiffen, J. Nucl. Mater. 133-134 (1985) 156–163.
6. G. P. Pells and G. J. Hill, J. Nucl. Mater. 141-143 (1986) 375–381.
7. S. N. Buckley and P. Agnew, J. Nucl. Mater. 155-157 (1988) 361–365.
8. G. P. Pells, J. Nucl. Mater. 155–157 (1988) 67–76

9. H. M. Frost, "Millimeter-Wave Properties of Neutron-Irradiated Ceramics for RF-Window MFE Applications," Eighth Annual Progress Report on Special Purpose Materials for Magnetically Confined Fusion Reactors, DOE/ER-0113/5, National Technical Information Service, Springfield, VA, March 1986, pp. 11–16.

10. F. W. Clinard, Jr., IEA Workshop on In-Situ Measurements of Electrical Properties of Irradiated Ceramics, elsewhere in this report.

11. R. H. Goulding *et* al., "ICRF Antenna Design for CIT and ALCATOR C-MOD," (Eighth Topical Conference on Radio Frequency Power in Plasmas, AIP Conf. Proc. No. 190), American Institute of Physics, New York, 1989, pp. 250–253.

12. E. H. Farnum, H. M. Frost, and F. W. Clinard, Jr., "In-Situ Measurement of Radiation Induced Conductivity in Ceramics," elsewhere in this report.

DISLOCATION LOOP FORMATION IN ION-IRRADIATED POLYCRYSTALLINE SPINEL AND ALUMINA — S. J. Zinkle (Oak Ridge National Laboratory)

OBJECTIVE

The objective of this study is to compare the microstructural response to ion irradiation of two oxide ceramics having predominantly ionic bonding. A comparison of the similarities and differences of their microstructure enables basic information to be obtained regarding the effects of radiation on ceramics.

SUMMARY

The microstructure of magnesium aluminate spinel ($MgAl_2O_4$) and alumina (Al_2O_3) has been examined with transmission electron microscopy following ion irradiation to damage levels of 0.1 to 5 keV/atom (1 to 50 dpa) at room temperature and 650°C. The ion irradiation produced interstitial dislocation loops of types a/4<110>{110} and a/4<110>{111} in spinel along with a very low density of a/6<111>{111} loops. Dislocation loops of types a/3[0001](0001) and a/3<1$\bar{1}$00>{1$\bar{1}$00} were tentatively identified in alumina. The loop size increased and the density decreased gradually with increasing fluence in spinel irradiated at 650°C, with the net result that the concentration of interstitials contained in the loops remained nearly constant at ~0.1 at. %. Defect-free regions were observed adjacent to grain boundaries and the irradiated surface in spinel irradiated at 650°C. The denuded zone width was very small for spinel irradiated at 25°C and Al_2O_3 irradiated at 650°C. For a given irradiation temperature, the loops in spinel were larger and of much lower density than the loops in Al_2O_3.

PROGRESS AND STATUS

Introduction

Ceramics are required for numerous applications in a fusion reactor where appreciable radiation fields exist. Previous studies have shown that magnesium aluminate spinel ($MgAl_2O_4$) is resistant to cavity and dislocation loop formation during irradiation to high damage levels.[1-5] Aluminum oxide (Al_2O_3) is a leading candidate for several insulator applications in fusion reactors, largely due to its widespread comnercial availability and also due to the existence of a fairly large data base on its response to radiation. The present study compares the microstructural behavior of spinel and alumina following ion irradiation at room temperature and 650°C.

EXPERIMENTAL PROCEDURE

Polycrystalline specimens of stoichiometric spinel and alpha-alumina (both with a grain size of ≈30 μm) were obtained from Ceradyne, Inc. and General Electric (Lucalox brand alumina), respectively. Transmission electron microscope (TEM) disks of dimensions 3-mm-diam by 0.5 mm were cut and the surface to be bombarded was given a mechanical polish with 0.5 μm diamond paste. Specimens were bombarded in a 3 × 3 array at room temperature or 650°C in the triple ion beam accelerator facility at Oak Ridge National Laboratory (ORNL).[6] The irradiation temperature was determined from a thermocouple attached to the face of a stainless steel specimen that occupied one of the positions in the 9-specimen array.

Table 1 sumnarizes the irradiation conditions for the present study. The displacement damage levels in Table 1 are given for a depth of 0.55 μm, which is approximately halfway between the surface and the calculated peak damage region (Fig. 1). Due to uncertainties in the threshold displacement energies on the various sublattices in $MgAl_2O_4$ and Al_2O_3, the damage levels in Table 1 are given in terms of damage energy density (nuclear stopping power) rather than displacements per atom (dpa). Assuming that a mean displacement energy of 40 eV is appropriate for describing the displacement threshold in Al_2O_3 and $MgAl_2O_4$ (ref. 7), then 1 keV/atom ≈ 10 dpa. The conversion from fluence to damage energy density was determined from an EDEP-1 calculation.[8] Figure 1 shows the calculated depth-dependent displacement profile for 2 MeV Al+ ions incident on $MgAl_2O_4$. Note that the damage level (and damage rate) varies by a factor of 7 between the surface and the damage peak. The ion beam flux during irradiation was maintained at ~1.1 × 10^{17} Al^+/m^2-s for all of the specimens, which corresponds to a damage rate of ~7.2 × 10^{-4} dpa/s at a depth of 0.55 μm. One specimen irradiated with 3.6 MeV Fe^{++} ions was included in this study (Table 1)

The irradiated specimens were glued face-to-face with a polished nonirradiated specimen, sectioned, mechanically dimpled, and ion milled at room temperature (6 kV Ar^+, 15" sputtering angle) until perforation occurred at the interface. TEM analysis was performed with a Philips CM-12 microscope operating at 120 kV. Dislocation loop analysis was performed using the classical inside/outside contrast method in so-called "safe" orientations.[9]

Table 1. Ion Irradiation Conditions for the Ceramic Specimens

Material	Ion Beam	Temperature (°C)	Midrange (0.55 μm) Damage Level (keV/atom)
$MgAl_2O_4$	2 MeV Al^+	25	0.8
$MgAl_2O_4$	2 MeV Al^+	25	2.0
$MgAl_2O_4$	2 MeV Al^+	650	0.3
$MgAl_2O_4$	2 MeV Al^+	650	1.0
$MgAl_2O_4$	2 MeV Al^+	650	2.4
Al_2O_3	2 MeV Al^+	25	0.1
Al_2O_3	2 MeV Al^+	25	0.5
Al_2O_3	3.6 MeV Fe^{++}	650	0.1
Al_2O_3	2 MeV Al^+	650	0.6

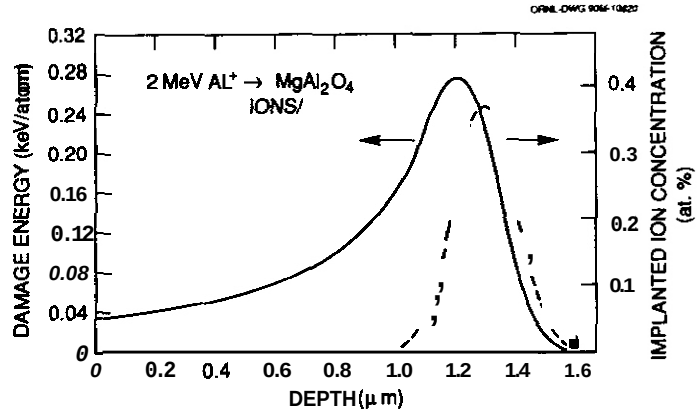

Fig. 1. Depth-dependent displacement damage energy density and implanted ion concentration for ion-irradiated spinel as determined from an EDEP-1[8] calculation.

RESULTS

Figure 2 shows the general cross-section microstructure of spinel irradiated with 2 MeV Al^+ ions to a peak damage level of 1.4 keV/atom (14 dpa) at 650°C. The near-surface region was devoid of any observable radiation-induced defects for depths up to ~0.35 μm. The midrange (0.4 to 1.1 μm depth) damage microstructure consisted of a moderate density of interstitial loops lying on {111} and {110} habit planes. The peak damage region (1.1 to 1.8 μm depth) was strongly influenced by the injected Al^+ ions and will not be analyzed here. The maximum range of observable damage (1.82 μm) was about 0.2 μm greater than predicted by the EDEP-1 calculation (Fig. 1).

The corresponding cross-section microstructure of spinel irradiated to a peak damage level of 10.1 keV/atom (100 dpa) at 650°C is shown in Fig. 3. The microstructure was qualitatively similar to the low-dose case, with a surface-denuded zone of ~0.4 μm.

Figure 4 shows the cross-section microstructure observed near a grain boundary in spinel irradiated at 650°C to a peak damage level of 1.4 keV/atom (14 dpa). A defect-free zone occurs in the matrix region adjacent to both the surface and the grain boundary. The width of the grain boundary denuded zone varies with depth from the bombarded foil surface. According to the established theory on void and dislocation loop nucleation plus growth,[10,11] denuded zones occur near point defect sinks because the point defect concentrations approach thermal equilibrium values and therefore the loop nucleation and growth rates are very low. The grain boundary denuded zone width varies with distance from the bombarded surface due to the spatial dependence of the damage rate (Fig. 1) and defect sink microstructure (Figs. 2 and 3) associated with ion bombardment.

An examination of the grain boundary and surface-denuded zone widths at the same depth from the surface (and therefore same damage rate and sink density) allows a comparison to be made of the relative efficiencies of the two sinks for interstitials. The measurements for spinel found that the grain boundary denuded zone width at a depth of 0.4 um was ~60% of the surface-denuded zone width. Table 2 summarizes some of the denuded zone measurements made on ion-irradiated $MgAl_2O_4$ and Al_2O_3 specimens. The width of the denuded zone near the surface and grain boundaries of spinel irradiated at room temperature was <50 nm.

Figure 5 shows the cross-section microstructure of Al_2O_3 irradiated at 650°C under conditions similar to the spinel case. Oislocation loop formation occurred uniformly within the matrix even at regions very close to the bombarded surface and grain boundaries. The width of the grain boundary and surface-denuded zone in Al_2O_3 irradiated at 650°C was measured to be <15 nm (Fig. 6), which is more than an order of magnitude smaller than the widths observed in spinel subjected to similar irradiation conditions.

ORNL-PHOTO-9031-85

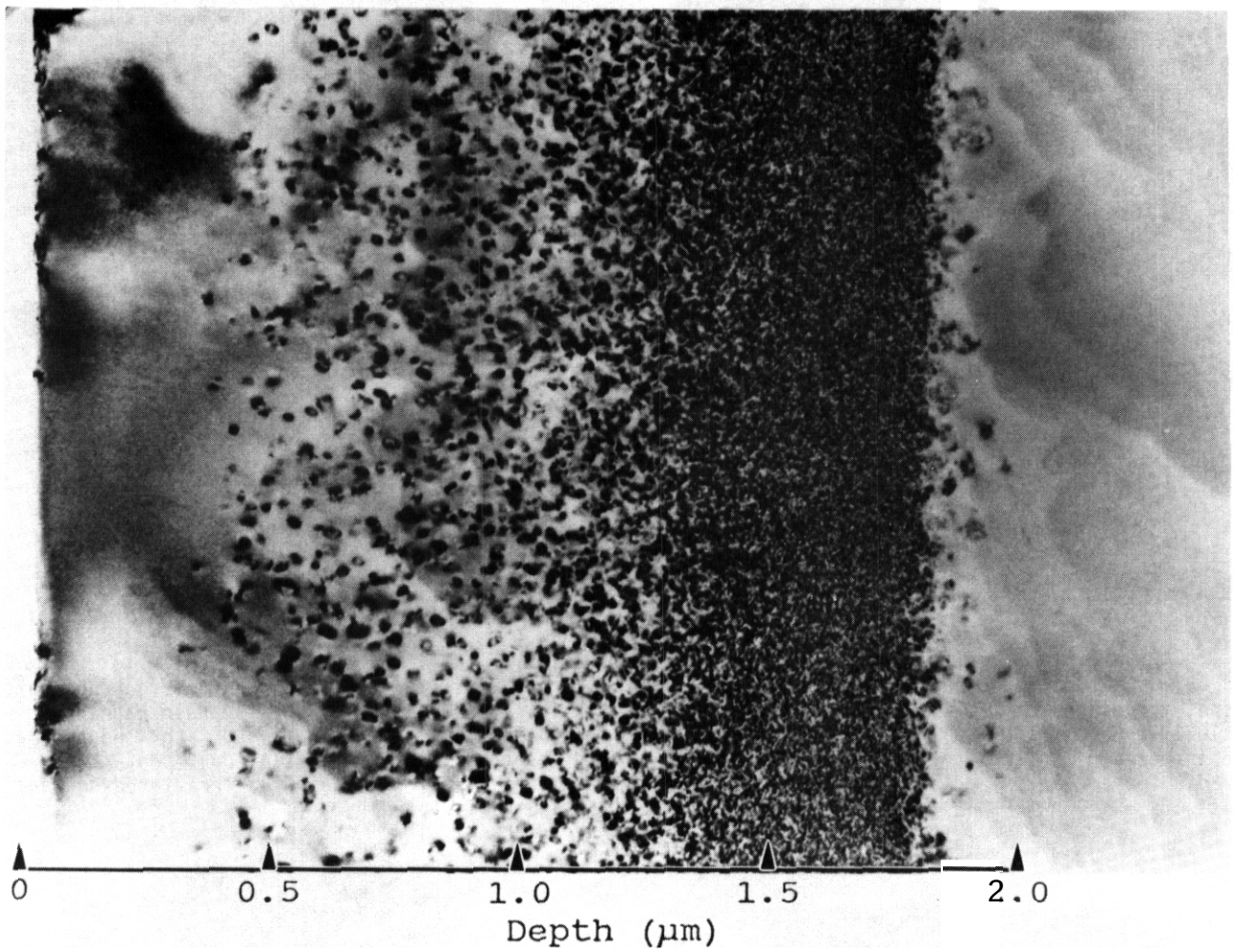

Fig. 2 Depth-dependent microstructure of spinel irradiated at 650°C to a peak damage level of 14 keV/atom (14 dpa).

Figure 7 compares the dislocation loop microstructure in spinel irradiated to three different doses at 650°C. It is evident from this figure that both the size and density of dislocation loops change only a slight amount as the damage level increases from 0.5 to 3.5 keV/atom. The mean loop diameter at a depth of 0.6 μm from the surface increased from 23 to 34 nm over this range of damage levels, and the loop density showed a corresponding decrease from 12 to 3.5 × $10^{21}/m^3$.

Dislocation loop formation in spinel occurred on {110} and {111} habit planes. Table 3 sumnarizes the dislocation loop parameters (measured at an irradiation depth of 0.55 μm) for spinel irradiated at 650°C. Approximately 75% of the loops were observed to be on {110} planes in the lowest dose (0.32 keV/atom) specimen. This fraction increased to ~90% for the two higher dose conditions. Figure 8 shows an example of loops on three different habit planes viewed edge-on. A detailed analysis of the nature and Burgers vector of the loops using weak-beam imaging techniques indicated that all of the loops on {110} were faulted interstitial loops of the type a/4<110>{110}. An analysis of the loops on {111} planes revealed that all of the loops were interstitial-type, and that >90% of the loops were faulted on the cation sublattice but unfaulted on the anion sublattice with Burgers vectors of the type a/4<110>{110}. A very small fraction (<10%) of the interstitial loops on {111} planes were identified as fully faulted loops of the type a/6<111>{111}.

ORNL-PHOTO 4415-90

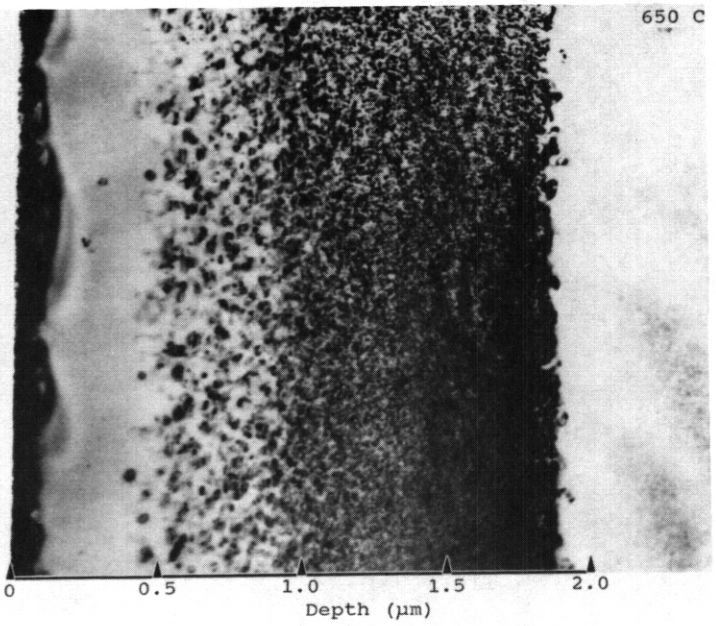

Fig. 3. Depth-dependent microstructure of spinel irradiated at 650°C to a peak damage level of 10.1 keV/atom (100 dpa). The dark features near the irradiated surface are caused by the pre-irradiation mechanical polish.

ORNL-PHOTO-9032-89

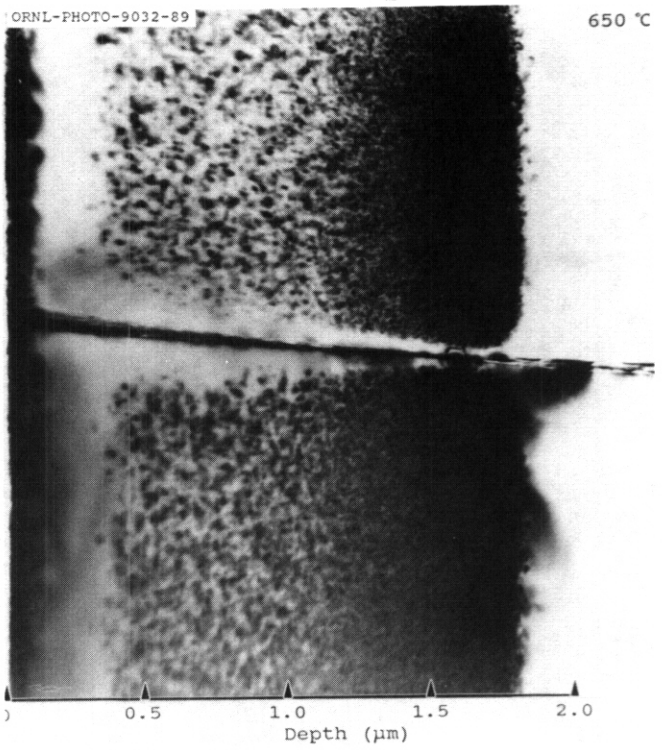

Fig. 4. Depth-dependent microstructure of spinel in the vicinity of a grain boundary following irradiation at 650°C to a peak damage level of 1.4 keV/atom (14 dpa). Note the defect-free zones near the irradiated surface and grain boundary.

ORNL-PHOTO-9035-89

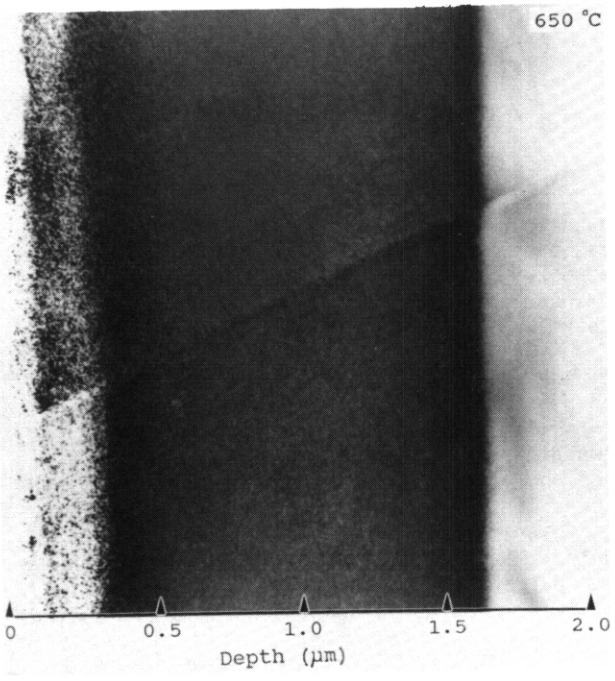

Fig. 5. Depth-dependent microstructure of Al_2O_3 in the vicinity of a grain boundary following irradiation at 650°C to a peak damage level of 2.9 keV/atom (29 dpa).

ORNL-PHOTO 4409-90

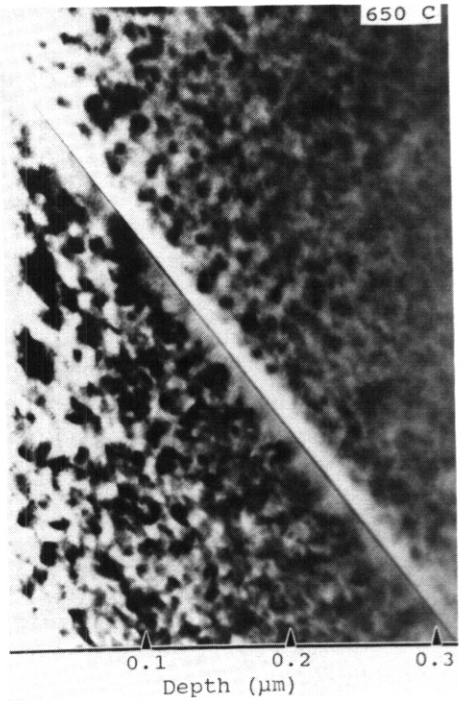

Fig. 6. Near-surface microstructure of Al_2O_3 in the vicinity of a grain boundary following irradiation at 650°C. The calculated damage level at an irradiation depth of 0.15 μm was 0.1 keV/atom (1 dpa).

ORNL-PHOTO-4410-90

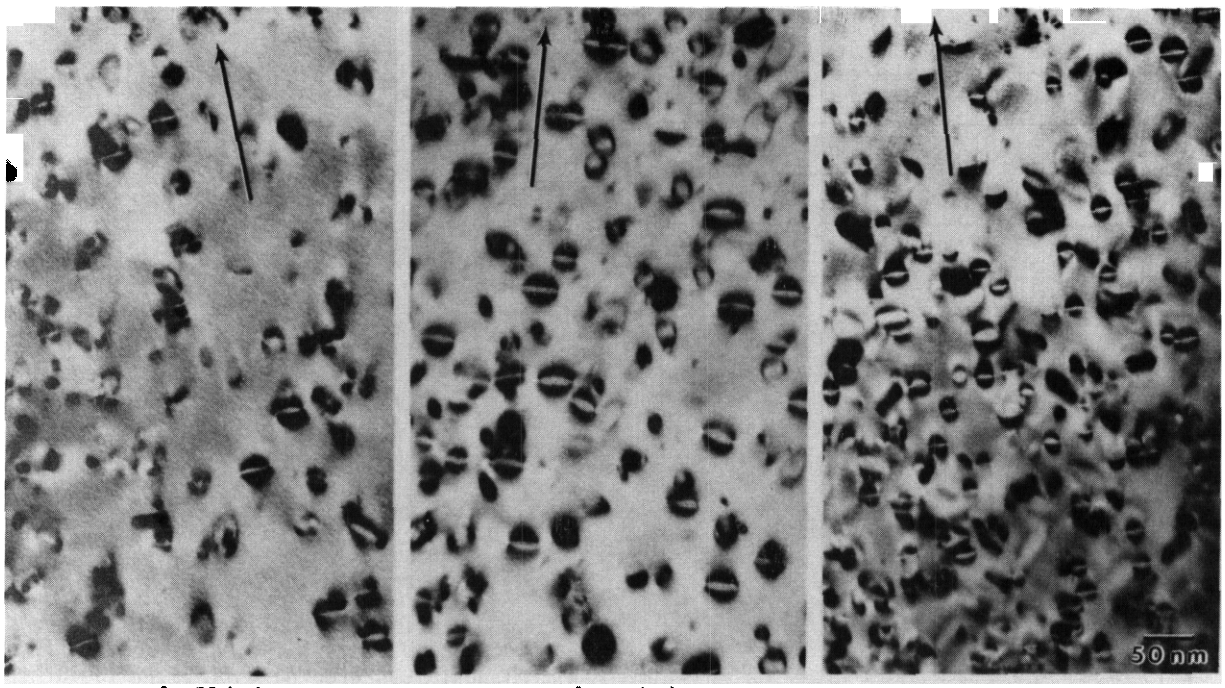

Fig. 7. Dislocation loop formation in spinel following irradiation at 650°C to three different fluences. The calculated damage levels were (left to right): 0.5, 1.5, and 3.5 keV/atom (5, 15, and 35 dpa). The arrows indicate the direction of the diffraction vectors. The imaging conditions were (left to right): B = [111], g = [$\bar{4}40$]; B = [111], g = [0$\bar{4}4$]; B = [001], g = [440].

Table 2. Denuded Zone Width Measurements in Ion-Irradiated Spinel and Alumina

Material	Temperature (°C)	Peak Damage Level (keV/atom)	Denuded Zone Width, nm	
			Surface	Grain Boundary (0.5 μm depth)
Spinel	25	35	<50	~20
Spinel	25	9	<50	~15
Spinel	650	1.4	350	180
Spinel	650	45	350	220
Spinel	650	10	380	170
Al_2O_3	25	0.4	<20	<10
Al_2O_3	25	2.2	<20	15
Al_2O_3	650	0.4	<25	<12

A detailed analysis of the loop habit planes in spinel irradiated at 650°C found that there was a marked anisotropy with respect to the irradiated surface for loop formation on both {110} and {111} planes. Loop formation preferentially occurred on habit planes that were nearly perpendicular to the irradiated surface, whereas loop formation was suppressed on habit planes that were nearly parallel with the irradiated surface. The loop size did not exhibit such a strong anfsotropy with respect to the irradiated surface. Details of the anisotropic loop formation will be published elsewhere.

The dislocation loops in Al_2O_3 were of higher density and smaller size compared to spinel irradiated under comparable conditions. Loop formation in Al_2O_3 was observed on both basal (0001) and prism {$1\bar{1}00$} planes. Figure 9 shows an example of the dislocation loop microstructure in Al_2O_3 irradiated at 650°C to a damage level of ~0.1 keV/atom (~1 dpa). A tentative loop analysis indicates that most of the loops are faulted with Burgers vectors of the type a/3[0001](0001) and a/3<$1\bar{1}00$>{$1\bar{1}00$}, although there is some indication that part of the loop population has unfaulted during irradiation to 0.1 keV/atom (dpa) at 650°C (e.g., presence of visible loops on {1100} prism planes for g = [0006] in the right-hand panel of Fig. 9). The size and density of loops on the basal and prism planes were comparable.

~ a 3. b Measured Dislocation LOW Parameters for Spinel Following Ion Irradiation at 650°C

Damage Level* (keV/atom)	Density (m^{-3})		Mean Diameter (nm)	
	$\{110\}_{loops}$	$\{111\}_{loops}$	$\{110\}_{loops}$	$\{111\}_{loops}$
0.32	9.0 x 10""	3.3 x 10""	25.8	18.1
1.0	3.5 x 10""	2.9 x 10^{20}	34.8	27.4
2.4	2.9 x 10""	3.4 x 10^{20}	34.0	*30.0*

*Measurements were made on crass-sectton specimens within a constant irradiation depth segment of 0.4 to 0.7 μm.

OWL–PHOTO 4412–90

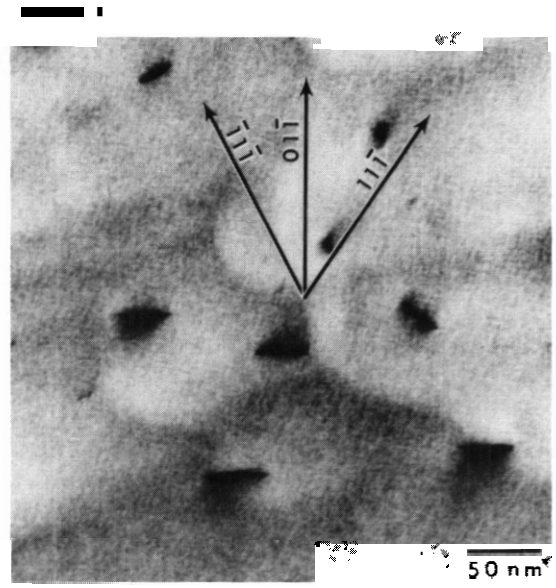

Fig. 8. Dislocation loops in irradiated spinel (650°C, 0.35 keV/atom) lying on several different habit planes. Centered dark field image, B = [011], g = [11$\bar{1}$].

ORNL-PHOTO 4418-90

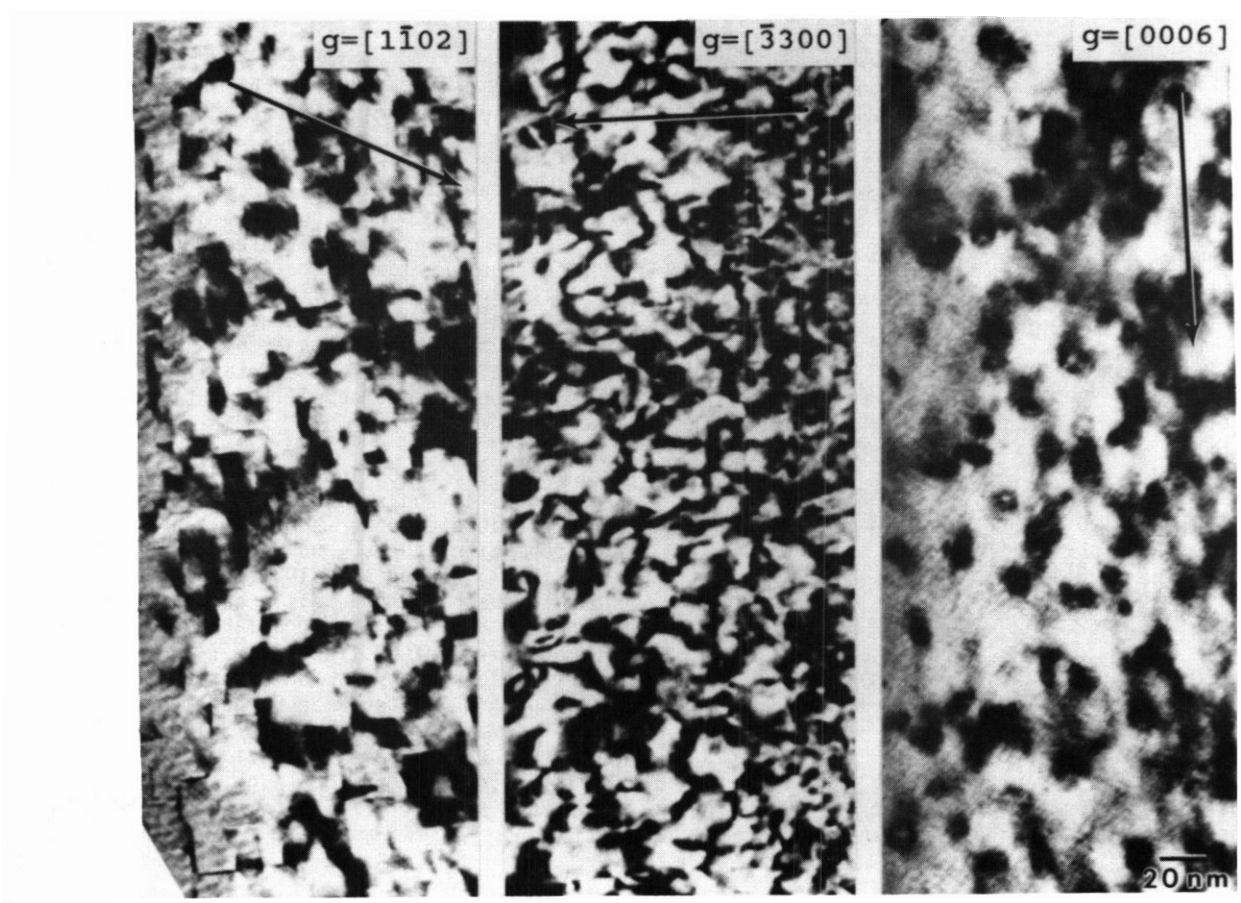

Fig. 9. Dislocation loop contrast in Al_2O_3 irradiated at 650°C to a damage level of 0.1 keV/atom (1 dpa). The zone axis for all three conditions was [1120].

DISCUSSION

Denuded-Zone Width

A previous semi-empirical analysis of metal specimens irradiated in a high voltage electron microscope found that the denuded zone width (L) near a point defect sink such as a free surface was $L \sqrt{D_m/P}$, where D_m is the point defect diffusion coefficient and P is the production rate of point defects.[12] Various authors have derived the steady-state spatial concentration profile of point defects in the vicinity of a free surface.[13-17] In general, the point defect profile cannot be solved analytically. A simplified analysis is presented in the following in order to show the dependence of the point defect gradient on physical parameters.

The steady-state one-dimensional chemical rate equations describing the point defect concentrations in the presence of a sink are given by:[10,13,15,16]

$$\frac{d}{dx}\left[D_i \frac{dC_i}{dx}\right] - \alpha C_i C_v - D_i C_i C_s + P = 0 \quad ; \tag{1}$$

$$\frac{d}{dx}\left[D_v \frac{dC_v}{dx}\right] - \alpha C_i C_v - D_v C_v C_s + P = 0 \quad ; \tag{2}$$

where $D_{i,v}$ and $C_{i,v}$ are the diffusion coefficients and atomic concentrations of interstitials or vacancies, α is the vacancy-interstitial recombination coefficient. C_s is proportional to the concentration of distributed internal sinks for vacancy or interstitial annihilation, and P is the production rate of point defects. If the loss of point defects occurs primarily at sinks (i.e., $D_i C_s \gg \alpha C_v$ and $D_v C_s \gg \alpha C_i$) then the second term in Eqs. (1) and (2) may be neglected. The resultant equation for the sink dominant case is then of the form

$$D_i \frac{d^2 C_i}{dx^2} - D_i C_i C_s + P = 0 \quad . \tag{3}$$

The preceding neglects any dependence of the diffusion coefficients on the point defect concentrations. The solution of Eq. (3) is given by

$$C_i = \frac{P}{D_i C_s} - \left[\frac{P}{D_i C_s} - C_i^{eq}\right] \exp - \sqrt{C_s}\, x \quad , \tag{4}$$

where the boundary conditions $C_i\ (x \to \infty) = P/D_i C_s = C_i^{\infty}$ (bulk interstitial concentration) and $C_i(0) = C_i^{eq}$ (thermal equilibrium interstitial concentration) have been used. Under typical irradiation conditions, C_i^{eq} is negligible compared to the bulk interstitial concentration. Therefore, Eq. (4) simplifies to

$$C_i \simeq C_i^{\infty}\left[1 - \exp - \sqrt{\frac{P}{C_i^{\infty} D_i}}\, x\right] . \tag{5}$$

If $C_i(L)$ is the critical interstitial concentration needed to produce observable loop formation, the denuded zone width is found after rearrangement of Eq. (5) to be

$$L = \sqrt{\frac{C_i^{\infty} D_i}{P}} \ln \left[\frac{C_i^{\infty}}{C_i^{\infty} - C_i^{(L)}} \right] . \qquad (6)$$

The corresponding differential equations for the limiting case where point defect loss occurs primarily via recombination events (*i.e.*, $\alpha C_v >> D_i C_s$ and $\alpha C_i >> D_v C_s$) can be obtained from Eqs. (1) and (2) by invoking the relation[11,15,16] $D_v C_v = D_i C_i$. This leads to an equation of the following form:

$$D_i \frac{d^2 C_i}{dx^2} - \frac{\alpha D_i}{D_v} C_i^2 + P = 0 .$$

The preceding ignores the difference in sink capture efficiencies for vacancies and interstitials, both of which are of order unity.[**] The bulk interstitial concentration for the recombination-dominant case can be obtained directly from Eq. (7),

$$C_i^{\infty} = \sqrt{\frac{P D_v}{\alpha D_i}} .$$

The exact solution of the differential Eq. (7) is given by the Jacobi elliptical function. However, other studies[15,16] have shown that Eq. (5) is also a reasonable approximation to the solution for the recombination dominant case (Eq. 7). Hence, in both the recombination-dominant and sink-dominant limits for point defect annihilation, the characteristic width of the depressed interstitial concentration adjacent to a one-dimensional sink is proportional to $\sqrt{C_i^{\infty} D_i / P}$. The theoretical dependence of this denuded zone on physical parameters can be obtained after substitution of the appropriate relation for the bulk interstitial concentration, C_i^{∞}, for the two limiting cases:

$$L \propto \sqrt{\frac{1}{C_s}} \quad \text{sink dominant} \quad ; \qquad (8)$$

$$L \propto \left[\frac{D_i D_v}{\alpha P} \right]^{Y4} \quad \text{recombination dominant} \qquad (9)$$

The two limits indicate that the denuded zone width should be independent or weakly dependent on the displacement rate.

The ratio of the grain boundary denuded zone widths in spinel irradiated at 650°C (Fig. 4) was 3.3 for depths of 0.5 μm and the implanted ion peak. According to the EDEP-1 calculation (Fig. 1), the corresponding ratio of the damage rates for these two depths was 4.6. Therefore, a grain boundary denuded zone width ratio of $(4.6)^{1/4} = 1.46$ would be expected if the recombination-limited approximation was valid at all depths. However, an inspection of the microstructure indicates that the loop density increases with increasing depth and that the matrix contains a very high density of small defects in the vicinity of the peak damage (injected ion) region, 1.3 to 1.8 um. The large change in the grain boundary denuded zone width in Fig. 4 can therefore be attributed primarily to decreases in the bulk interstitial concentration with increasing depth due to a higher concentration of irradiation-produced traps in the injected ion region which causes a gradual shift from a recombination-dominant to a sink-dominant regime.

In contrast to the case for spinel irradiated at 650°C. the grain boundary denuded zone width was nearly constant at all irradiation depths for spinel irradiated at room temperature and Al_2O_3 irradiated at 650°C. In both of these cases the high density of irradiation-produced defects induced a sink dominant condition for point defect annihilation, with a sink density that was nearly independent of irradiation depth (e.g., Fig. 5). The difference in the denuded zone widths in spinel irradiated at 650°C versus spinel irradiated at 25°C or Al_2O_3 irradiated at 650°C may be attributed to the lower mobility of interstitials in the latter cases along with a change from recombination-dominant to sink-dominant conditions (higher sink density in Al_2O_3 and 25°C spinel due to enhanced interstitial loop nucleation). The denuded zone observations in the present study are in general agreement with previous reports of grain boundary denuded zones in irradiated ceramics.[18-21]

Matrix Dislocation Loop Formation

Most of the general features observed for dislocation loop formation in this study are in qualitative agreement with previous studies on ion- or neutron-irradiated spinel and alumina.[1-5,18-30]

Irradiation of spinel produces loops on {111} and {110} planes, with {110} loops increasingly favored at higher temperatures.[1-3,21-23] Table 4 summarizes the temperature dependence of loop formation on {111} planes in ion-irradiated stoichiometric spinel. The fraction of loops found in {111} planes following irradiation decreases from ~45% at room temperature to 0% at 800°C. The fraction of loops occurring on {111} planes in the present study of spinel irradiated at 650°C decreased from ~25% at a damage level of 0.3 keV/atom (3 dpa) to ~10% at 10 and 24 dpa, which is a further indication of their relative instability. Previous neutron irradiation studies on spinel have reported similar findings with regard to the stability of {110} versus {111} loops as a function of irradiation temperature.[1,22,23] A mixture of loops on both sets of habit planes was observed at irradiation temperatures of 410 to 650°C, whereas only {110} loops were found at 825°C. Parker et al.[2] and Tucker et al.[20] observed loops only on {110} planes following neutron irradiation of stoichiometric spinel at 400 and 540°C. Hyperstoichiometric spinel specimens, $MgO{\cdot}(Al_2O_3)_n$, irradiated at the same conditions formed a mixture of {110} and (111) loops at 400°C and only {110} loops at 540°C for $n = 1.1$ material.[2] The $n = 2$ hyperstoichiometric material formed only {111} loops at both temperatures.[2]

Table 4. Temperature-Dependent Fraction of {111} Loops Observed in Ion-Irradiated Spinel

Irradiation Temperature (°C)	Irradiating Particle	Fraction of Loops Observed on {111} Planes	Reference
25	Mg^+	~45%	3
650	Mg^+	~30%	3
650	Al^+	10 to 25%*	This study
800	Ar^+	~0%	4, 20

*Fluence-dependent (see text).

The lack of {111} loops at high irradiation temperatures in spinel has been cited as evidence for the instability of a/6<111>{111} loops since they do not preserve stoichiometry and are electrically charged.[21,22] The {111} loops observed in the present study were consistently smaller than loops that formed on {110} planes (Table 3).

Essentially all of the loops observed on {111} planes in the present study were of the type a/4<110>{111}, which does not contain an anion fault and is electrically more stable. This partially faulted type of loop was also found in a previous ion irradiation study,[3] but has never been observed in neutron-irradiated specimens. This suggests that there is some feature associated with ion irradiation that induces the formation of a/4<110>{111} loops instead of a/6<111>{111} loops. Likely candidates include differences in the ionizing radiation fields between neutron and ion irradiation along with displacement rate effects and possible electric field effects associated with the implantation of charged particles.

Loops were occasionally observed on habit planes that did not correspond exactly to the {110} or {111} families of planes. This may be evidence that some of the partially faulted a/4<110>{111} loops are rotating along their glide cylinder in the direction of their Burgers vector. Further investigation is needed to confirm this. Knight[4,21] has also reported evidence that a very low density of loops may form on {001} planes in spinel during ion irradiation. We have seen occasional evidence for (001) loops in our studies, but the small loop size (<10 nm) makes an unequivocal determination of the habit plane impossible.

Vacancy loops have not been observed in spinel for any irradiation condition.[1-5,19-23] It is not immediately clear why interstitial clusters form as dislocation loops whereas vacancy clusters occur as cavities. Rechtin reported the presence of a low density of vacancy loops dispersed among a high density of interstitial loops in O^+ ion-irradiated Al_2O_3 (ref. 30).

The concentration of interstitials contained in visible dislocation loops following irradiation is a convenient parameter for gauging the relative radiation resistance of different materials. Previous studies have found that irradiated spinel typically contains an order of magnitude fewer interstitial defects in the form of dislocation loops than simple ceramics such as MgO and Al_2O_3. Very little has been published on the temperature or fluence dependence of this parameter, however. Table 5 summarizes the results of several recent TEM measurements on ion-irradiated spinel.[3-5,21] All of the measurements indicate that the maximum concentration of point defects that can be retained in spinel is on the order of 0.1 at. %. There does not appear to be any large fluence dependence for these temperatures and doses (3 to 24 dpa), which suggests that the saturation concentration of interstitials has already been reached by ~5 dpa. This interstitial concentration is comparable to the saturation concentration of point defects observed in metals following low-temperature irradiation. In the present study, it was observed that the dislocation loops coarsened during irradiation (i.e., the loop density decreased while the loop size increased, Table 3). The net result was that the concentration of interstitials contained in loops remained constant over the dose range of 0.3 to 2.4 keV/atom (3 to 24 dpa). Knight[21] observed a similar behavior in spinel and in $Al_{23}O_{27}N_5$ (which has a spinel-type structure) following ion irradiation at 800°C to comparable doses.

Table 5. Summary of Measured Fraction of Interstitials Retained in Dislocation Loops in Ion-Irradiated Spinel*

Irradiation Temperature (°C)	Damage Level (dpa)	Concentration of Interstitials Retained in Loops (at. %)	Surviving Defect Fraction (%)	Reference
25	10	0.034	0.0034	3
25	20	0.16	0.008	5†
650	10	0.058	0.005	3
650	3.2	0.12	0.038	Present study
650	10	0.10	0.01	Present study
650	24	0.091	0.004	Present study
800	1	0.057	0.057	4, 20
800	6	0.12	0.02	4, 20

*Values for the present study were obtained on cross-section specimens from 0.3-um-wide segments centered at an irradiation depth of 0.55 μm (23% of the peak damage value; see Fig. 1).

†The loop density for this irradiation condition was $7.3 \times 10^{21}/m^3$.

The surviving defect fraction (Table 5) was obtained by dividing the measured concentration of interstitials in loops by the number of initially created defects (displacement damage level). Since the concentration of interstitials in loops was nearly constant, the surviving defect fraction (η) decreased steadily with increasing fluence for a given irradiation temperature.

The microstructural changes observed in the present study of ion-irradiated Al_2O_3 are in agreement with previous TEM observations.[1,24-30] Dislocation loop formation has been found in these studies to obey the following evolution: Faulted interstitial loops of types a/3[0001](0001) and $1/3\langle 10\bar{1}0\rangle\{10\bar{1}0\}$ initially form on the basal and prism planes, respectively. Upon continued irradiation, the loops unfault to form loops—of type $a/3\langle 10\bar{1}1\rangle[0001]$ and $a/3\langle 10\bar{1}1\rangle\{10\bar{1}0\}$. These loops eventually interact to form a dislocation network with a predominant $1/3\langle 10\bar{1}1\rangle$ Burgers vector. Preferential absorption of interstitials by the dislocation network provides a sufficient supersaturation of vacancies to induce growth of cavities.

CONCLUSIONS

Regions devoid of dislocation loops occur near the surface and grain boundaries of spinel irradiated at 650°C. The grain boundary denuded zone width is ~0.2 μm for irradiation at 650°C at a damage rate of 6×10^{-5} keV/atom-s (6×10^{-4} dpa/s), and is independent of fluence for doses between 0.3 and 2.4 keV/atom (3 to 24 dpa). The denuded zone width is very small (≤15 nm) in spinel irradiated at room temperature or in Al_2O_3 irradiated at 25 or 650°C due to enhanced loop nucleation and low interstitial mobility.

The dislocation loop geometry in irradiated spinel depends on the irradiation temperature and, to a lesser extent, dose. Loops of the type $a/4\langle 110\rangle\{110\}$ are preferred at all temperatures and are found exclusive of other loop geometries at high irradiation temperatures. Loops of type $a/4\langle 110\rangle\{111\}$ occur at ion irradiation temperatures <650°C, along with a low density of $a/6\langle 111\rangle\{111\}$ loops.

Ion irradiation studies suggest that spinel can accommodate a maximum interstitial concentration of ~0.1 at. % in the form of dislocation loops for irradiation temperatures of 25 to 800°C. This value is comparable to saturated defect concentrations measured in metals following low-temperature irradiation. The saturated interstitial concentration in spinel is already reached for doses as low as 0.3 keV/atom (3 dpa) at 650°C.

An unusual feature observed in the present study was that the {110} and (111) loop formation was decidedly anisotropic with respect to the irradiated surface. This phenomenon has not been reported in any previous irradiation studies on ceramics. Several possible mechanisms can be formulated, but additional studies are needed to identify the most viable cause.

FUTURE WORK

The microstructure of ceramic specimens irradiated at 650°C with 1-MeV H^+ and He^+ ions will be analyzed and compared with the present results.

ACKNOWLEDGMENTS

The ion irradiations were performed by S. W. Cook, and the TEM specimens were prepared by A. M. Williams, C. P. Haltom, and J. W. Jones. The author thanks Frances Scarboro for manuscript preparation and P. S. Sklad and R. E. Stoller for manuscript review.

REFERENCES

1. F. W. Clinard, Jr., G. F. Hurley, and L. W. Hobbs, J. Nucl. Mater. 1088109 (1982) 655.
2. C. A. Parker, L. W. Hobbs, K. C. Russell, and F. W. Clinard, Jr., J. Nucl. Mater. 133&134 (1985) 741.
3. S. J. Zinkle, J. Am. Ceram. Soc. 72 (1989) 1343.
4. P. A. Knight, M. L. Jenkins, and G. P. Pells, Mat. Res. Soc. Symp. Proc., Vol. 152, Optical Materials: Processing and Science (1989), p. 135.
5. S. J. Zinkle and S. Kojima, Nucl. Instr. Meth. E 46 (1990) 165.
6. M. B. Lewis, W. R. Allen, R. A. Buhl, N. H. Packan, S. W. Cook, and L. K. Mansur, Nucl. Instr. Meth. B 43 (1989) 243.
7. N. M. Ghoniem and S. P. Chou, J. Nucl. Mater. 155-157 (1988) 1263.
8. J. Manning and G. P. Mueller, Comput. Phys. Commun. 7 (1974) 85.
9. D. M. Maher and B. L. Eyre, Phil. Mag. 23 (1971) 409.
10. L. K. Mansur and M. H. Yoo, J. Nucl. Mater. 85&86 (1979) 523.
11. L. K. Mansur, Nucl. Technol. 40 (1978) 5.
12. F. A. Garner and L. E. Thomas, in: Effects of Radiation on Substructure and Mechanical Properties of Metals and Alloys, ASTM STP 529, J. Moteff, Ed. (ASTM, 1973). p. 303.
13. A. Seeger, Phys. Stat. Sol. (a) 28 (1975) 157.
14. M. H. Yoo and L. K. Mansur, J. Nucl. Mater. 62 (1976) 282.
15. N. 4. Lam, S. J. Rothman, and R. Sizmann, Radiat. Eff. 23 (1974) 53.
16. R. Sizmann, J. Nucl. Mater. 69670 (1978) 386.
17. T. Hashimoto, in: Effects of Radiation on Materials: 14th Intern. Symp., N. H Packan et al., eds., ASTM STP 1046, Vol. I (ASTM, Philadelphia, 1989), p. 523.
18. G. F. Hurley, J. C. Kennedy, F. W. Clinard, Jr., R. A. Youngman, and W. R. McDonell, J. Nucl. Mater. 103&104 (1981) 761.
19. T. E. Mitchell and R. A. Youngman, in: 7th Intern. HVEM Conf., eds., R. M. Fisher, R. Gronsky, and K. H. Westmacott, LBL-16031, CDNF-830819 (Aug. 1983), p. 163.
20. D. S. Tucker, T. Zocco, C. O. Kise, and J. C. Kennedy, J. Nucl. Mater. 141—143 (1986) 401.
21. P. A. Knight, D. Phil. thesis, University of Oxford (1989).
22. L. W. Hobbs and F. W. Clinard, Jr., J. de Physique 41, Colloque C6, Suppl. 7 (1980), p. 232.
23. F. W. Clinard, Jr., G. F. Hurley, L. W. Hobbs, D. L. Rohr, and R. A. Youngman, J. Nucl. Mater. 122&123 (1984) 1386.
24. W. E. Lee, M. L. Jenkins, and G. P. Pells, Phil. Mag. A 51 (1985) 639.
25. T. Shikama and G. P. Pells, Phil. Mag. A 47 (1983) 369.
26. R. S. Wilks, J. Nucl. Mater. 26 (1968) 137.
27. A. Y. Stathopoulos and G. P. Pells, Phil. Mag. A 47 (1983) 381.
28. Y. Katano, H. Ohno, and H. Katsuta, J. Nucl. Mater. 155-157 (1988) 366.
29. S. J. Zinkle, in: Processing and Characterization of Materials Using Ion Beams, Eds. L. E. Rehn et al., Mat. Res. Soc. Symp. Proc., Vol. 128 (1989), p. 363.
30. M. D. Rechtin, Rad. Effects 42 (1979) 129.

TECHNIQUE FOR PREPARING CROSS-SECTION TRANSMISSION ELECTRON MICROSCOPE SPECIMENS FROM ION-IRRADIATED CERAMICS -- S.J. Zinkle, C.P. Haltom, L.C. Jenkins, and C.K.H. DuBose (Oak Ridge National Laboratory)

OBJECTIVE

The purpose of this report is to summarize the experimental techniques used at ORNL to prepare cross-section TEM Specimens from ion-irradiated ceramics.

SUMMARY

The general techniques necessary to produce a high-quality cross-sectioned ceramic specimen for transmission electron microscope observation are outlined. A particularly important point is that the width of the glued region between faces of the ceramic specimen must be $<0.2\ \mu m$ to prevent loss of the near-surface region during ion milling. A recently developed vise for gluing ceramic cross-section specimens is described, and some examples of the effect of glue thickness on specimen quality are shown.

PROGRESS AND STATUS

Introduction

In recent years there has been an increasing interest in the microstructure of ion-implanted ceramics, in particular due to applications in surface modification' and radiation effects' studies. The region of interest is typically within one micron of the surface, and the microstructure usually exhibits a strong depth dependence. It is often useful to prepare cross-section specimens for observation in a transmission electron microscope (TEM). There are numerous papers available that describe different techniques for preparing cross-section TEM specimens from metals or ceramics.[3-12]

For monolithic ion-implanted ceramics, the standard cross-section preparation procedure involves the following steps, which are outlined in Fig. 1: First, the ion-implanted specimen is glued face-to-face to another polished specimen (either implanted or nonimplanted) using a commercial epoxy such as M-BOND 610 ADHESIVE (Measurements Group, Raleigh, NC 27611). The glued sandwich is then sectioned. mechanically dimpled, mounted on a support ring (e.g. graphite) and sputter ion milled until perforation occurs near the interface. if the specimen contains multiple phases with dfferent ion milling rates, then special techniques such as sacriicial coatings or other forms of beam shielding"." may be necessary during the ion milling step.

In order to achieve good contrast in the electron microscope, the cross-section specimen must be suitably thin (~100 nm) in the region of interest. Although there are many contributing factors to the preparation of a high-quality cross-section ceramic TEM specimen, it was recognized through experience that a key factor is the width of the glued region separating the two polished faces of the cross-section sandwich. It has been our experience that all commercially available epoxies thin at a faster rate than ceramics such as Al_2O_3 and $MgAl_2O_4$ during the ion milling process. if the width of the glued region is too wide, then a significant portion of the near-surface material is milled away before the foil thickness is electron-transparent. The cause of this near-surface erosion is immediately apparent when the geometry of the ion-milling process is considered. Figure 2 shows an idealized sketch of the glued interface region of a cross-section specimen during ion milling (in practice, there will be gradients in the foil thickness near the interface that depend on the ion milling details). During the initial stages of ion milling, small surface troughs are created in the glued region of the specimen due to the faster ion milling rate of the epoxy compared to the ceramic. When the foil thickness (t) equals a critical value of

$$t = 2W*\tan\alpha \quad , \tag{1}$$

where W is the width of the glued region and a is the milling angle (Fig. 2b), then the interface corresponding to the original surface is completely exposed to the ion milling beams. Continuation of the ion milling process causes material near the interface of interest in the cross-section specimen to be lost due to direct exposure to the ion milling beams (Fig. 2c). Ion mill thinning is usually performed with a milling angle of $\alpha = 15$ deg, which is close to the angle that produces the maximum erosion rate for most materials and hence minimizes the specimen preparation time."." For a final foil thickness of 100 nm and a milling angle of 15 deg, the width of the glued region must therefore be less than 190 nm to avoid any loss of the near-surface material (Eq. 1).

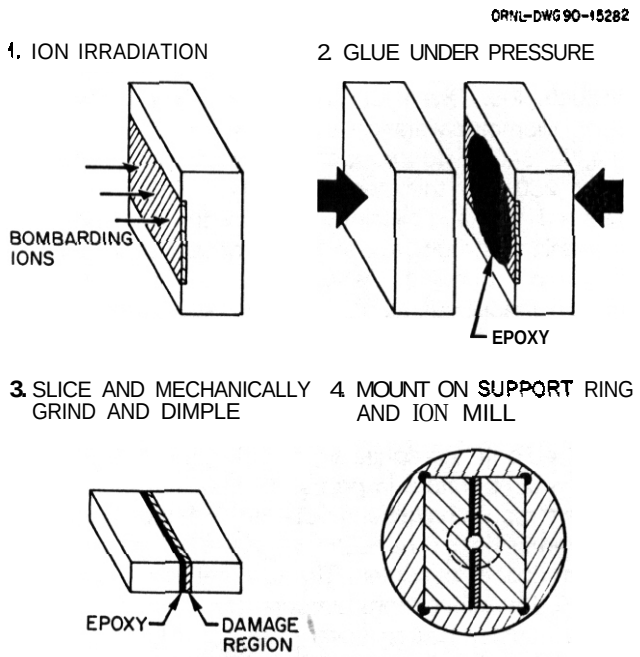

Fig. 1. Schematic of procedure used to prepare cross-section ceramic TEM specimens.

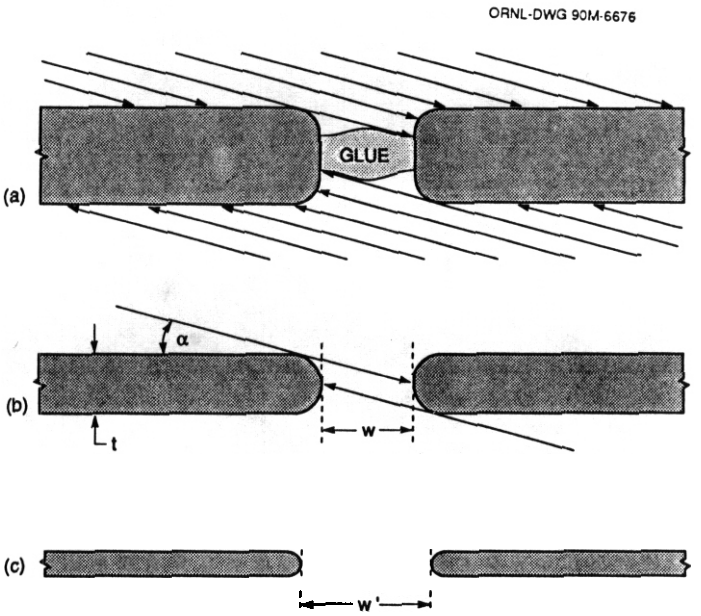

Fig. 2. Schematic of ion milling process. The near-surface regions are milled away if the glue width is large.

In order to achieve this narrow glue width. the surfaces of the specimens must be flat and parallel (i.e., well polished) and glued under pressure. We have designed and built a calibrated vise for making thin, reproducible glue widths in cross-section specimens. There have been several previous descriptions of vises used to prepare cross-section TEM specimens,[""] where the gluing pressure is controlled by finger tightening. The present vise is unique in that it does not rely on operator skill to achieve a known and reproducible pressure on the specimen during gluing.

DESCRIPTION OF CALIBRATED VISE

A vise was designed and built that would produce a known and consistent pressure while the specimen glue was curing in a small laboratory furnace. Due to the inherent brittleness of ceramics. the pressure during gluing must be controllable to avoid the possibility of cracking the specimen as the result of applying excessive force. In addition, since the specimens to be glued are often polished on only one surface, there is a need to eliminate stress concentrators that may occur during clamping due to slightly nonparallel or uneven back surfaces. This was achieved by using Teflon pads on the clamping surfaces of the vise.

The vise consisted of an aluminum base and a stainless steel threaded drive rod and shaft. A photograph of the vise is shown in Fig. 3. With a limiting torque wrench (Utica Tool Co.. Orangeburg, SC 29115), a known pressure can be reproducibly applied. Teflon pads are inserted into machined recesses in the ends of the vise mandrels, which prevents the pads from shifting when pressure is applied. The Teflon pads are 9.5 mm (3/8 in.) diameter by 1.6 mm (1/16 in.) thick and are punched from sheet material. Teflon was chosen for the padding material due to its stability at temperatures appropriate for curing the epoxy (100°C). New pads are used for each specimen to be glued, since the Teflon tends to become scored from indentations associated with the clamping process.

Typically, a small amount of epoxy (M-Bond) is applied between the polished faces of two ceramic pieces, which are then placed on the bottom Teflon pad. The upper mandrel of the vise, which also contains a Teflon pad, is pressed against the glued specimen and torqued by an amount that depends on the strength and fracture toughness of the pieces being glued. The entire vise is then put into a small lab furnace and heated to 100°C for 1 h to cure the epoxy. The force exerted by the upper mandrel for different torque settings was calibrated by making measurements with known mass standards. The relation between torque and applied force is nonlinear due to friction effects in the threaded drive rod. For a torque setting of 2 in.-lb, the applied force is 82 N (18.4 lb_f). The corresponding pressure on a TEM disk of 3 mm diameter is 12 MPa (1700 psi). This pressure is much lower than the typical compressive strength for ceramics of about 1 GPa, but is sufficiently high to produce a narrow glue width in the cross-section specimen.

YE-14477

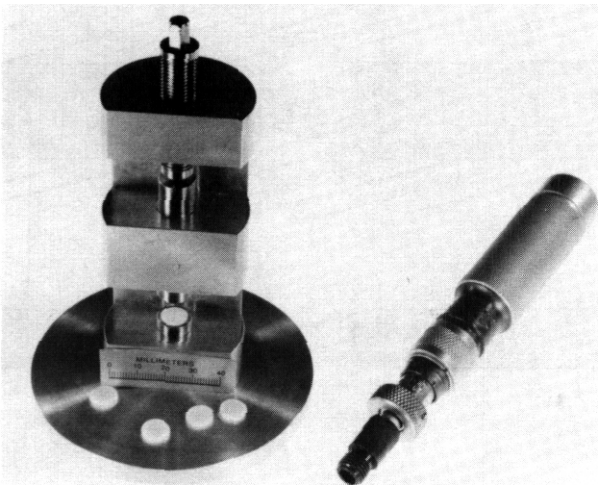

Fig. 3. Photograph of vise with Teflon pads and torque wrench used to control the pressure during gluing of cross-section specimens.

After the specimen has been glued, the sandwich is mounted on a metal cutting block using a commercial mounting wax (Crystalbond, AREMCO Products, Inc., Ossining. NY) and sliced with a low-speed diamond wafering saw (Buehler Ltd.. Lake Bluff, IL 60044) to produce a rectangular foil of about 250 pm thickness (Fig. 1). The foil is mounted on a polishing block with wax and mechanically ground to a thickness of about 150 pm using a grinding wheel or a precision dimpler/grinder (Gatan). The specimen is demounted from the block by soaking in acetone, flipped over, and the back side is ground and mechanically dimpled until the final foil thickness is about 30 μm. The specimen is then demounted and glued onto a graphite support ring with M-Bond at room temperature in preparation for ion milling. The best results have been obtained with a graphite foil of dimensions 3-*mm-diam* by 100-pm thick, with a 1-mm hole in its center. The specimens are then ion milled at either room temperature or in a liquid nitrogen-cooled holder (Gatan) using two beams of 6-keV Ar^+ and an ion milling angle of 15 deg. After foil perforation occurs near the glued interface, the specimen is given a finishing treatment with 3-keV Ar^+ ions to remove some of the surface damaged layer caused by the more energetic 6-keV ions. The milling angle is reduced to 10 deg during the finishing milling of radiation-sensitive materials.

EXPERIMENTAL RESULTS

Cross-section TEM foils prepared from ion-irradiated Al_2O_3 and $MgAl_2O_4$ polycrystalline and single crystal specimens were examined using a Philips CM12 electron microscope operating at 120 keV.

Figure 4 shows a low-magnification view of a spinel specimen that contained a very wide (3.6 pm) glue region. It can be seen that the epoxy has become very thin from the ion milling and has completely disappeared in some regions, whereas the spinel specimen is not thin enough to be transparent to the electron beam.

Figure 5 is a composite view of a single crystal Al_2O_3 specimen that was prepared with a glue width of 1.3 μm. In regions of the cross-section foil where the glue was thin but still intact, the Al_2O_3 was too thick to be electron-transparent. After additional ion milling to produce Al_2O_3 regions that were thin enough to be usable, about 0.7 *pm* was milled away from the near-surface regions of both sides (cf Fig 2b, 2c). Hence, it is not possible to perform detailed TEM analysis of near-surface regions in this specimen.

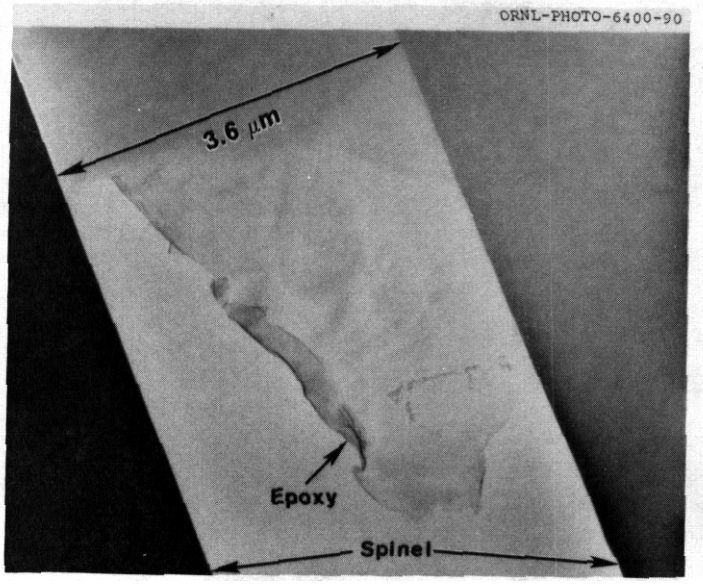

Fig. 4. Transmission electron micrograph of an ion-irradiated spinel specimen with a very wide glue width (compare with Fig. 2b).

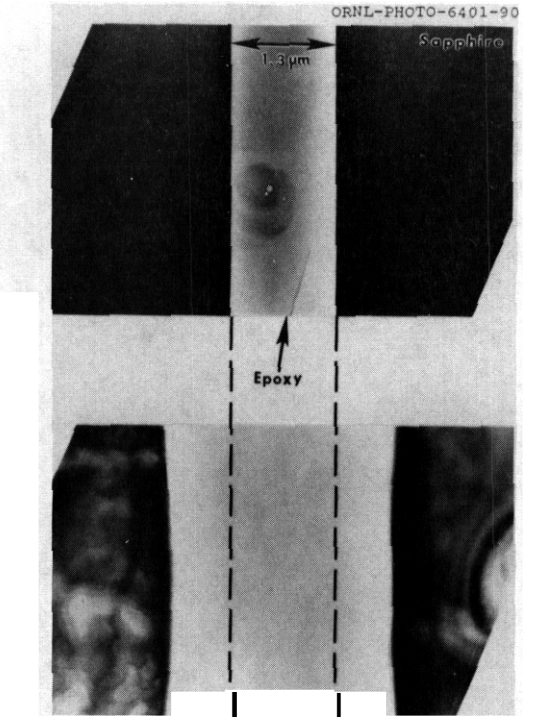

Fig. 5. Transmission electron micrograph of a sapphire specimen with a wide glue width. The ceramic foil thickness is very large in the region where the glue is intact. Approximately 700 nm has been milled away from the original surface in regions where the foil is suitably thin (compare Fig. 2b,c).

Figure 6 shows a single crystal Al_2O_3 specimen that was prepared with a glue width of 0.5 μm. In this case, the glue is beginning to mill away in regions where the Al_2O_3 foil thickness is about 250 nm (this is about the maximum useful thickness for TEM analysis using a microscope operating at 120 keV).

Figures 7 through 9 demonstrate results that were obtained after using the Teflon-padded vise to prepare cross-section foils from ion-irradiated specimens. The ion damaged region in Fig. 7 was contained within 0.53 μm from the bombarded surface, and it was therefore essential for the near-surface region to remain intact. Suitably thin areas were obtained in this specimen, which had a glue width of 0.21 μm. In Fig. 8, the glue width was about 0.17 μm and a foil thickness of <100 nm was obtained without any loss of the near-surface irradiated region. Figure 9 shows part of the extensive thin area that was produced by ion milling of a cross-section specimen with a glue thickness of about 50 nm.

A large number of ion-irradiated ceramic specimens have been prepared for cross-section TEM observation within the past six months in our laboratory. It appears that the success rate of obtaining cross-section specimens with suitable thin area over the entire ion damaged region is >90% with the present technique.

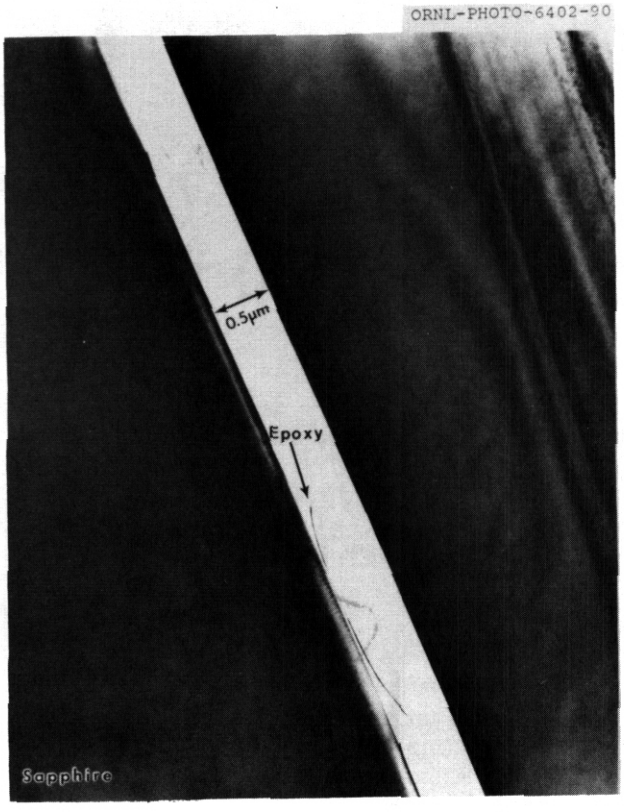

Fig. 6. Transmission electron micrograph of a sapphire specimen with an intermediate glue width and marginal foil thickness (250 nm).

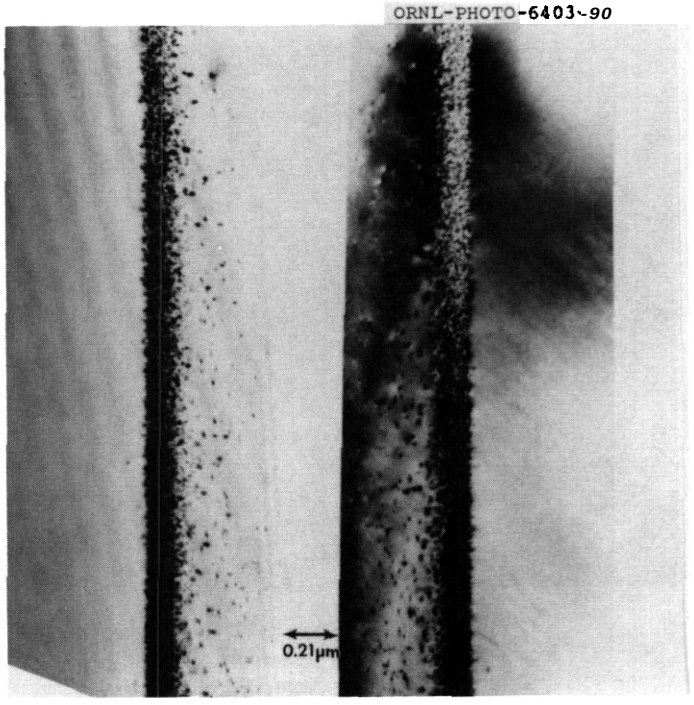

Fig. 7. Cross-section microstructure of single crystal Al_2O_3 implanted along the c-axis with 200-keV $^3He^+$ ions at 800°C to a fluence of 1.8×10^{20} ions/m^2.

CONCLUSIONS

To avoid the loss of the near-surface portion of cross-section ceramic TEM specimens, it is essential that the original interface be "shadowed" from the ion milling beams until the desired foil thickness is achieved. This is most easily carried out by minimizing the width of the glued region between the ceramic faces. Specimens suitable for TEM analysis with a 120 keV electron microscope may be obtained if the glue width is <0.2 μm.

ACKNOWLEDGMENTS

The ion irradiations for the ceramic specimens were performed by S.W. Cook and W. R. Allen. Experimental assistance in preparing the cross-section TEM specimens and comments on the design of the calibrated vise were provided by A.M. Williams and J.W. Jones. We thank L. L. Horton and K. L. More for their efforts in developing the experimental technique and K. B. Alexander and P. S. Sklad for technical comments on the manuscript.

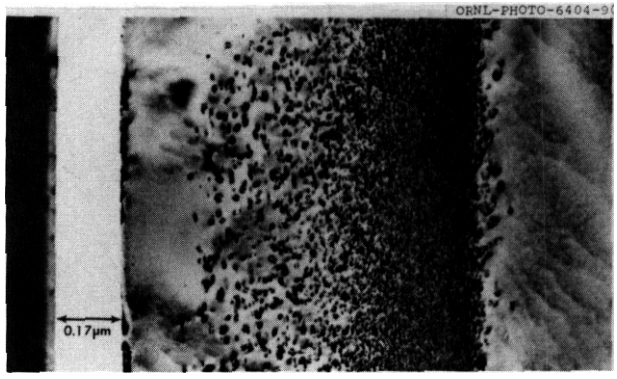

Fig. 6. Microstructure of spinel irradiated with 2-MeV Al+ ions at 650°C to a fluence of $5 \times 10^{20}/m^2$. The glue width is about 170 nm and the foil thickness is about 70 nm.

Fig. 9. Microstructure of spinel inadiated with 2-MeV Al^+ ions at 650°C to a fluence of $1.6 \times 10^{21}/m^2$. The glue width is about 50 nm.

REFERENCES

1. White, C.W., McHargue, C.J. Sklad. P.S., Boatner, L.A. and Farlow, G.C., Ion implantation and annealing of crystalline oxides. Mat. Sci. Reports, 4:41-146 (1989).

2. Lee, W.E., Jenkins, M.L. and Pells. G.P.. The influence of helium doping on the damage microstructure of heavy-ion irradiated Al_2O_3. Phil. Mag. A, 51:639-659 (1985).

3. Spurling, R.A. and Rhodes, C.G., A technique for preparing the cross-section of proton-irradiated 316 stainless steel foils for transmission electron microscopy. J. Nucl. Mater., 44:341-344 (1972).

4. Abrahams, M.S. and Buiocchi. C.J.. Cross-sectional specimens for transmission electron microscopy. J. Appl. Phys., 45:3315-16 (1974).

5. Sheng. T.T. and Marcus, R.B., Advances in transmission electron microscope techniques applied to device failure analysis. J. Electrochem. Soc., 127737-743 (1980).

6. Bravman, J.C. and Sinclair, R.. The preparation of cross-section specimens for electron microscopy. J. Electron Microsc. Tech., 1:53-61 (1984).

7. Newcomb, S.B., Boothroyd, C.B. and Stobbs, W.M., Specimen preparation methods for the examination of surfaces and interfaces in the transmission electron microscope. J. Microsc.. 140:195-207 (1985).

8. Horton, L.L. Bentley, J. and Lewis, M.B., Radiation damage in ion-irradiated MgO. Nucl. Instr. Meth. Phys. Res. B, 16:221-229 (1966).

9. Zinkle, S.J. and Sindelar, R.L. Preparation of ion-irradiated foils for cross-section analysis. Nucl. Instr. Meth. Phys. Res. B, 16:154-162 (1986).

10. Santella, M.L., Fisher, A.T., and Halton, C.P., Technique fo preparing cross-section transmission electron microscopy specimens from ceramic oxide braze joints. J. Electron Microsc. Tech. 8:211-215 (1988).

11. Sklad, P.S., The preparation of TEM specimens from hazardous or difficult materials. Mat. Res. Soc. Symp. Proc. Vol. 115:39-50 (1988).

12. Romano, A. and Vanhellemont, J., Bender, H. and Morante. J.R., A fast preparation technique for high-quality plan view and cross-section TEM specimens of semiconducting materials. Ultramicroscopy, 31:183-192 (1989).

13. Barber, D.J. Thin foils of nonmetals made for electron microscopy by sputter-etching. J. Mater. Sci., 5:1-8 (1989).

14. Oechsner, H., Sputtering--a review of some recent experimental and theoretical aspects. Appl. Phys., 8:185-198 (1975).

15. Rivaud, L., A procedure to prepare cross-sectional samples for TEM. J. Electron Microsc. Tech., 2:577-580 (1985).

16. Flutie, R.E. TEM/STEM sample preparation for the investigation of solid state structures. In: Mat. Res. Soc. Symp. Proc. Vol. 62. L.W. Hobbs et al., eds., pp. 105112 (1986).

DISTRIBUTION

1–16. Argonne National Laboratory, 9700 South Cass Avenue, Argonne, IL 60439

M. C. Billone	P. A. Finn	B. A. Loomis
P. E. Blackburn	A. K. Fisher	R. F. Mattas
O. K. Chopra	A. B. Hull	L. A. Niemark
R. G. Clemmer	C. E. Johnson	D. L. Smith
D. R. Diercks	F. Kassner	S. W. Tam
		H. Wiedersich

17. Argonne National Laboratory, EBR-II Division, Reactor Materials Section, P.O. Box 2528, Idaho Falls, ID 83403-2528
D. L. Porter

18. Auburn University, Department of Mechanical Engineering, 201 Ross Hall, Auburn, AL 36849
B. A. Chin

19–34. Battelle-Pacific Northwest Laboratory, P. O. Box 999, Richland. WA 99352

M. D. Freshley	M. L. Hamilton	J. M. McCarthy
F. A. Garner (5)	H. L. Heinisch	B. D. Shipp
D. S. Gelles	G. W. Hollenberg	O. D. Slagle
L. R. Greenwood	R. H. Jones	J. L. Straalsund

35–36. Carnegie Institute of Technology, Carnegie-Mellon University, Schenley Park, Pittsburgh, PA 15213
W. M. Garrison, Jr. J. C. Williams

37. Department of Energy, Richland Operations Office, Federal Bldg.. MS A590, Richland, WA 99352
Paul Pak

38. EG&G Idaho, Inc., Fusion Safety Program, P.O. Box 1625, Idaho Falls, ID 83415-3523
D. F. Holland

39. GE Astrospace Division, San Jose Operations, 6835 via Deloro, P.O. Box 530954, San Jose, CA 95153-5354
Mike hangilaski

40–43. General Atomics, P.O. Box 85608, San Diego, CA 92138

J. Baur	D. I. Roberts
T. A. Lechtenberg	K. R. Schultz

44. General Dynamics Corporation, 5001 Kearny Villa Road, San Diego, CA 92138
T. L, Cookson

45. Georgia Institute of Technology, School of Textile Engineering, Atlanta, GA 30332
D. S. Tucker

46. Grand Canyon University, Department of Natural Science, 3300 W. Camelback Rd., Phoenix, AZ 85017
W. A. Coghlan

47–48. Hokkaido University, Faculty of Engineering, Kita 13, Nishi 8, Kita-ku, Sapporo 060, Japan
Professor Heishichiro Takahashi Professor Akira Okada

49–52. Japan Atomic Energy Research Institute, Tokai Research Establishment, Tokai-mura, Naka-gun, Ibaraki-ken 319-11, Japan
Or. Tatsuo Kondo Or. Akimichi Hishinuma (3)

53. Kyushu University, Research Institute for Applied Mechanics, 6-1, Kasuga-Koen, Kasuga-Shi, Fukuoka-Ken 816, Japan
Professor Takeo Muroga

54-56. Lawrence Livermore National Laboratory, P.O. Box 808, Livermore, CA 94550

E.C.N. Dalder	J. Perkins
M. Guinan	

57–65. Los Alamos National Laboratory, P.O. Box 1663, Los Alamos, NM 87545

J. L. Anderson	D. J. Dudziak	C. D. Kise
L. D. Caudill	H. M. Frost	R. Liepens
F. W. Clinard	G. Hurley	T. Zocco

66. Manlabs, Inc., 231 Erie Street, Cambridge, MA 02139
O. Tognarelli

67. Massachusetts Institute of Technology, Department of Metallurgy and Materials Science, Cambridge, MA 02139
L. W. Hobbs

68–69. Massachusetts Institute of Technology, Room 13-4069, Cambridge, MA 02139
N. J. Grant — K. C. Russell

70–71. Massachusetts Institute of Technology, Plasma Fusion Center Headquarters, Cambridge, MA 02139
H. D. Becker — D. B. Montgomery

72. McDonnell-Douglas Astronautics Company, East, 0922242, Bldg. 92, P.O. Box 516, St. Louis, MO 63166
J. W. Davis

73–74. Nagoya University, Institute of Plasma Physics, Furo-Cho, Chikusa-ku, Nagoya 464-01, Japan
Professor Akira Miyahara — Dr. Chusei Namba

15. Nagoya University, Department of Nuclear Engineering, Furo-Cho, Chikusa-ku, Nagoya 464-01, Japan
Professor Michio Kiritani

76–77. National Institute of Standards and Technology, Boulder, CO 80302
F. R. Fickett — J. R. Reed

78. National Materials Advisory Board, 2101 Constitution Avenue, Washington, DC 20418
K. M. Zwilsky

79–80. National Research Institute for Metals, Tsukuba Branch, Sengen, Tsukuba-shi, Ibaraki-ken 305, Japan
Dr. Masatoshi Okada — Dr. Haruki Shiraishi

81. Naval Research Laboratory, Washington, DC 20375
J. A. Sprague

82–122. Oak Ridge National Laboratory, P.O. Box 2008, Oak Ridge, TN 37831

Central Research Library	T. D. Burchell	A. F. Rowcliffe (10)
Document Reference Section	R. H. Goulding	R. L. Senn
Laboratory Records Department (2)	M. L. Grossbeck	J. Sheffield
Laboratory Records—RC	E. A. Kenik	L. Snead
Patent Section	R. L. Klueh	R. E. Stoller
D. J. Alexander	Eal Lee	K. R. Thoms
C. C. Baker	A. W. Longest	P. F. Tortorelli
G.E.C. Bell	L. K. Mansur	S. J. Zinkle
J. Bentley	P. J. Maziasz	R. Yamada
E. E. Bloom	T. C. Reuther	
D. N. Braski	T. K. Roche	

123–124. Princeton University, Princeton Plasma Physics Laboratory, P.O. Box 451, Princeton, NJ 08540
H. Furth — Long-Poe Ku

125. Rensselaer Polytechnic Institute, Troy, NY 12181
D. Steiner

126. Rockwell International Carporation, NA02, Rocketdyne Division, 6633 Canoga Avenue, Canoga Park, CA 91304
D. W. Kneff

127–128. Sandia National Laboratories, P.O. Box 5800, Albuquerque, NM 87185-5800
M. J. Davis — W. B. Gauster

129–130. Sandia National Laboratories, Livermore Division 8316, Livermore, CA 94550
W. Bauer — W. G. Wolfer

131. San Diego State University, Mechanical Engineering Dept., San Diego, CA 92182-0191
L. D. Thompson

132. Tohoku University, Institute for Materials Research, Katahira 2-1-1, Sendai 980, Japan
Professor Hideki Matsui

133. Tohoku University, Institute for Materials Research, Orai Branch, Oarai, Higashi-Ibaraki-gun, Ibaraki-ken 311-13, Japan
Professor Hideo Kayano

134. Tohoku University, Department of Nuclear Engineering, Tohoku University, Roba, Rramaki, Sendai 980, Japan
Professor Katsunori Abe

135–136. University of California, Department of Chemical and Nuclear Engineering, Santa Barbara, CA 93106
G. E. Lucas
G. R. Odette

137–139. University of California, Department of Chemical, Nuclear and Thermal Engineering, Los Angeles, CA 90024
M. 8. Abduo
R. W. Conn
N. M. Ghoniem

140. University of Michigan, Department of Nuclear Engineering, Ann Arbor, MI 48109
T. Kammash

141. University of Missouri, Department of Nuclear Engineering, Rolla, MO 65401
A. Kumar

142. University of Tokyo. Department of Materials Science & Technology, 2641 Yamazaki Noda City, Chiba Prefecture 278 Japan
N. Igata

143–144. University of Tokyo, Department of Nuclear Engineering, 3-1, Hongo 7-Chome, Bunkyo-ku, Tokyo 113 Japan
Professor Shiori Ishino (2)

145146. University of Tokyo, Department of Materials Science, 3-1, Hongo 7-Chome, Bunkyo-ku, Tokyo 113, Japan
Professor Akira Kohyama
Professor Yutaka Kohno

147. University of Wisconsin, Nuclear Engineering Dept., 1600 Johnson Drive, Madison, WI 53706
G. L. Kulcinski

148–153. Westinghouse Hanford Company, P. O. Box 1970, Richland, WA 99352
H. R. Brager
A. M. Ermi
G. D. Johnson
F. M. Mann
R. J. Puigh
R. L. Simons

154. Department of Energy, Oak Ridge Operations Office, P.O. Box 2001, Oak Ridge, TN 37831
Assistant Manager for Energy Research and Development

155. Department of Energy, Oak Ridge Operations Office, P. O. Box 2001, MS 6269, Oak Ridge. TN 37831
S. D. Frey

156–161. Department of Energy, Office of Fusion Energy, Washington, DC 20585
S. E. Rerk
M. M. Cohen
N. A. Davies
R. J. Dowling
R. E. Price
F. W. Wiffen

162–211 Department of Energy, Office of Scientific and Technical Information, Office of Information Services, P.O. Box 62, Oak Ridge, TN 37831
For distribution as shown in DOE/TIC-4500, Distribution Categories UC-423 (Magnetic Fusion Reactor Materials) and UC-424 (Magnetic Fusion Energy Systems)